Alternative Energy Sources for Green Chemistry

RSC Green Chemistry

Editor-in-Chief:
Professor James Clark, *Department of Chemistry, University of York, UK*

Series Editors:
Professor George A. Kraus, *Department of Chemistry, Iowa State University, Ames, Iowa, USA*
Professor Andrzej Stankiewicz, *Delft University of Technology, The Netherlands*
Professor Peter Siedl, *Federal University of Rio de Janeiro, Brazil*

Titles in the Series:
1: The Future of Glycerol: New Uses of a Versatile Raw Material
2: Alternative Solvents for Green Chemistry
3: Eco-Friendly Synthesis of Fine Chemicals
4: Sustainable Solutions for Modern Economies
5: Chemical Reactions and Processes under Flow Conditions
6: Radical Reactions in Aqueous Media
7: Aqueous Microwave Chemistry
8: The Future of Glycerol: 2nd Edition
9: Transportation Biofuels: Novel Pathways for the Production of Ethanol, Biogas and Biodiesel
10: Alternatives to Conventional Food Processing
11: Green Trends in Insect Control
12: A Handbook of Applied Biopolymer Technology: Synthesis, Degradation and Applications
13: Challenges in Green Analytical Chemistry
14: Advanced Oil Crop Biorefineries
15: Enantioselective Homogeneous Supported Catalysis
16: Natural Polymers Volume 1: Composites
17: Natural Polymers Volume 2: Nanocomposites
18: Integrated Forest Biorefineries
19: Sustainable Preparation of Metal Nanoparticles: Methods and Applications
20: Alternative Solvents for Green Chemistry: 2nd Edition
21: Natural Product Extraction: Principles and Applications
22: Element Recovery and Sustainability
23: Green Materials for Sustainable Water Remediation and Treatment
24: The Economic Utilisation of Food Co-Products
25: Biomass for Sustainable Applications: Pollution Remediation and Energy
26: From C-H to C-C Bonds: Cross-Dehydrogenative-Coupling
27: Renewable Resources for Biorefineries
28: Transition Metal Catalysis in Aerobic Alcohol Oxidation
29: Green Materials from Plant Oils

30: Polyhydroxyalkanoates (PHAs) Based Blends, Composites and Nanocomposites
31: Ball Milling Towards Green Synthesis: Applications, Projects, Challenges
32: Porous Carbon Materials from Sustainable Precursors
33: Heterogeneous Catalysis for Today's Challenges: Synthesis, Characterization and Applications
34: Chemical Biotechnology and Bioengineering
35: Microwave-Assisted Polymerization
36: Ionic Liquids in the Biorefinery Concept: Challenges and Perspectives
37: Starch-based Blends, Composites and Nanocomposites
38: Sustainable Catalysis: With Non-endangered Metals, Part 1
39: Sustainable Catalysis: With Non-endangered Metals, Part 2
40: Sustainable Catalysis: Without Metals or Other Endangered Elements, Part 1
41: Sustainable Catalysis: Without Metals or Other Endangered Elements, Part 2
42: Green Photo-active Nanomaterials
43: Commercializing Biobased Products: Opportunities, Challenges, Benefits, and Risks
44: Biomass Sugars for Non-Fuel Applications
45: White Biotechnology for Sustainable Chemistry
46: Green and Sustainable Medicinal Chemistry: Methods, Tools and Strategies for the 21st Century Pharmaceutical Industry
47: Alternative Energy Sources for Green Chemistry

How to obtain future titles on publication:
A standing order plan is available for this series. A standing order will bring delivery of each new volume immediately on publication.

For further information please contact:
Book Sales Department, Royal Society of Chemistry, Thomas Graham House, Science Park, Milton Road, Cambridge, CB4 0WF, UK
Telephone: +44 (0)1223 420066, Fax: +44 (0)1223 420247
Email: booksales@rsc.org
Visit our website at www.rsc.org/books

Alternative Energy Sources for Green Chemistry

Edited by

Georgios Stefanidis
KU Leuven, Belgium
Email: georgios.stefanidis@cit.kuleuven.be

Andrzej Stankiewicz
Delft University of Technology, Netherlands
Email: a.i.stankiewicz@tudelft.nl

ROYAL SOCIETY
OF CHEMISTRY

THE QUEEN'S AWARDS
FOR ENTERPRISE:
INTERNATIONAL TRADE
2013

RSC Green Chemistry No. 47

Print ISBN: 978-1-78262-140-9
PDF eISBN: 978-1-78262-363-2
EPUB eISBN: 978-1-78262-872-9
ISSN: 1757-7039

A catalogue record for this book is available from the British Library

Published by The Royal Society of Chemistry,
Thomas Graham House, Science Park, Milton Road,
Cambridge CB4 0WF, UK

Registered Charity Number 207890

For further information see our web site at www.rsc.org

Printed in the United Kingdom by CPI Group (UK) Ltd, Croydon, CR0 4YY, UK

Preface

The use of alternative energy sources, such as alternating electromagnetic fields at different operating frequencies, acoustic and hydrodynamic cavitation, magnetic fields, plasma and high gravity fields in chemical processing are some of the key approaches of process intensification to enable greener chemical processes and sustainable chemical manufacturing. Some of these technologies have already been commercialized for certain niches. However, the breadth of industrial implementation will depend on the production and operating costs, robustness, flexibility and safety. The progress in the development of alternative energy source-based processes in various disciplines of chemicals and materials manufacturing reported in the open and patent literature gives confidence that the above criteria will be met. In this book, world leading researchers demonstrate the potential of several alternative energy transfer technologies to enable greener chemical processing in different industries through attainment of resource- and energy-efficient reaction and separation processes. Rather than being comprehensive in a specific application area or technology, the book aims at highlighting the broad impact that the aforementioned technologies may have in various application areas.

In *Chapter 1*, the impressive impact of microwave irradiation in the field of organic chemistry is discussed. The ability of microwaves to deliver energy rapidly and selectively to those components of the reaction mixture that are strongly microwave-dissipative, whether a reagent, a catalyst or a solvent, can enable greener chemistry in terms of decreased process times, higher energy efficiency and processing under solvent-free or green solvent conditions.

Chapter 2 presents different strategies for the application of microwaves to extract high value chemicals from plant matter. The volumetric heating of microwaves allows for their direct interaction with the plant matrix, intracellular water heating and vaporization, overpressure inside the plant matrix

RSC Green Chemistry No. 47
Alternative Energy Sources for Green Chemistry
Edited by Georgios Stefanidis and Andrzej Stankiewicz

Published by the Royal Society of Chemistry, www.rsc.org

and, eventually, more effective cell wall rupture. This effect combined with rapid heating of a polar solvent may result in significantly faster extraction kinetics and improved materials efficiency, in terms of using less solvent and producing higher yields, compared to conventional heating.

Chapter 3 places the focus on the potential use of microwave technology for low temperature (and thus energy efficient) decomposition of biomass and biomass constituents (cellulose, lignin, hemicellulose) to high value chemicals. Although most of the relevant work in this area has been carried out with lab-scale microwave equipment, microwave process upscaling possibilities are also discussed.

Chapter 4 concludes the first part of the book devoted to microwave technology. The chapter discusses design aspects of different microwave applicator concepts suitable for chemical processing. The discussion extends beyond standard off-the-shelf monomode and multimode cavities to advanced non-cavity applicator types that can be used for efficient and tailored microwave activation of chemical reactors. In this context, an important suggestion put forward is that well-controlled and optimized microwave-assisted chemical processing requires transition from the current processing paradigm of chemical reactors activated by standing wave fields, as in conventional resonant cavity-based equipment, to chemical reactors activated by travelling electromagnetic fields.

Chapter 5 gives an overview of applications of cavitational (ultrasonic and hydrodynamic) reactors to different reactive and separation processes and the associated benefits in terms of greener and intensified processing. Faster chemical syntheses, improved yields and selectivities and safer operation at ambient conditions, mostly due to radical formation and mass transfer intensification, are some of the benefits expected in reactive processes. Cavitation, in synergy with oxidants, can also enable effective decontamination of wastewater. Regarding separation processes, application of ultrasound to crystallization can affect the crystal size distribution and product polymorphism. Further, ultrasound can enable shorter extraction processes with improved recovery at milder temperatures and lower amounts of solvents, compared to conventional extraction. Ultrasound can also improve adsorbents' activity and enhance adsorptives' desorption. Finally, it has been reported that ultrasound can improve vapor–liquid mass transfer and possibly break azeotropes in distillation processes.

Chapter 6 and 7 are concerned with magnetic fields. *Chapter 6* presents applications of magnetic fields to separation processes in the chemical and biotechnology industries. In particular, an overview of mechanical magnetic separations, magnetic separations involving magnetic solids with non-tailored surfaces and magnetic separations involving tailored and functionalized magnetic solids is presented.

Chapter 7 introduces magnetic field-assisted mixing concepts. In most chemical reactive processes, the mixing rate determines the spatiotemporal distribution of the temperature and concentration fields, which in turn determine the reaction rates and product yield and distribution. Chapter 7 highlights intensification of mixing of fluids using magnetic fields in the context of ferrohydrodynamics and magnetohydrodynamics.

Chapter 8 discusses past achievements and future trends in the field of heterogeneous photocatalysis for solar fuel synthesis and pollutant degradation. The chapter is organized in two parts. First, novel developments in catalyst design are presented with a special focus on the application of MOFs. Second, the current state-of-the-art and challenges in the design of photocatalytic reactors are discussed including alternative options for the light source to enhance efficiency.

Chapter 9 reviews the most important reactor design concepts, which form building blocks for photocatalytic reactor designs aimed at wastewater treatment. The two popular performance indicators used in the literature to assess photocatalytic reactors are the photonic efficiency and the pseudo-first order rate constant. The former does not account for the total electricity consumption; the latter is process volume dependent. In this work, a new benchmark is introduced, the photocatalytic space-time yield, to address these limitations. The new benchmark has been demonstrated by comparing three different photocatalytic reactor designs, namely a microreactor, a membrane reactor and a parallel plate reactor. This comparative study points at a new direction in the research field of photocatalytic wastewater treatment. This is the efficient illumination of existing reactor geometries, instead of seeking new reactor geometries.

Plasma reactors are seen as an enabling technology for decentralized chemicals and fuels production and efficient utilization of renewable electricity generation from solar energy or wind. In this vein, *Chapter 10* summarizes and evaluates plasma-assisted nitrogen fixation reactions (NO, NH_3 and HCN synthesis) in different types of plasma reactors. Despite the current limitation in scalability of plasma reactors, non-thermal plasma processing in certain operating windows in combination with solid catalysts has the potential to enable energy efficient chemistries.

The last two chapters of the book give an overview of applications of high gravity fields to green intensified chemical processing through intensification of mixing, heat and mass transfer and the enablement of ideal flow patterns and short contact times. In this context, *Chapter 11* reviews the application of spinning disc reactors and rotating packed beds, including some novel recent versions of the latter, on polymerization, reactive-precipitation, catalytic and enzymatic transformation and adsorption processes. *Chapter 12* introduces the concept of rotating fluidized beds in static vortex chambers. The hydrodynamic aspects and design characteristics of the vortex chambers are discussed in detail based on experiments and CFD simulations. The technology can intensify various processes, including low temperature pyrolysis and gasification of biomass, and particle drying and coating, when compared to conventional fluidized beds.

Georgios D. Stefanidis
Andrzej I. Stankiewicz

Contents

RSC Green Chemistry No. 47
Alternative Energy Sources for Green Chemistry
Edited by Georgios Stefanidis and Andrzej Stankiewicz

Published by the Royal Society of Chemistry, www.rsc.org

CHAPTER 1

Microwave-Assisted Green Organic Synthesis

ANTONIO DE LA HOZ*[a], ANGEL DÍAZ-ORTIZ[a] AND PILAR PRIETO[a]

[a]Facultad de Ciencias y Tecnologías Químicas, Universidad de Castilla-La Mancha, Avda. Camilo José Cela, 10, E-13071 Ciudad Real, Spain
*E-mail: Antonio.Hoz@uclm.com

1.1 Introduction

Due to the ability of some compounds (solids or liquids) to transform electromagnetic energy into heat, microwave (MW) radiation has been widely employed in chemistry as an energy source. Microwave irradiation has several advantages over conventional heating and these include homogeneous and rapid heating (deep internal heating), spectacular accelerations in reactions as a result of the heating rate (which frequently cannot be reproduced by classical heating) and selective heating. Consequently, microwave-assisted organic reactions produce high yields and lower quantities of side-products, purification of products is easier and, in some cases, selectivity is modified. Indeed, new reactions and conditions that cannot be achieved by conventional heating can be performed using microwaves. The use of microwaves in organic synthesis has been reviewed in numerous recent books, book chapters,[1] and reviews.[2]

RSC Green Chemistry No. 47
Alternative Energy Sources for Green Chemistry
Edited by Georgios Stefanidis and Andrzej Stankiewicz

Published by the Royal Society of Chemistry, www.rsc.org

Absorption and transmission of microwave energy is completely different from conventional heating (Table 1.1). Conventional heating is a superficial heating process and the energy is transferred from the surface to the bulk by convection and conduction. This is an inefficient mode of heating because the surface is at a higher temperature than the bulk and the vessel must be overheated to achieve the desired temperature. In contrast, microwave irradiation produces efficient internal heating by direct coupling of microwave energy with the bulk reaction mixture. The magnitude of the energy transfer depends on the dielectric properties of the molecules. As a guide, compounds with high dielectric constants tend to absorb microwave energy whereas less polar substances and highly ordered crystalline materials are poor absorbers. In this way, absorption of the radiation and heating can be very selective.

Considering the twelve principles of Green Chemistry reported by Anastas and Warner (Table 1.2),[3] the use of microwaves may be applicable to principle 6 (increased energy efficiency).

It has been reported that energy efficiency is higher with microwaves than with conventional heating.[4] Clark described an 85-fold reduction in energy demand on switching from an oil bath to a microwave reactor for a Suzuki reaction.[5] However, some reports consider that the relative "greenness" of microwave-assisted transformations is a complex issue in which numerous different factors must be considered. Firstly, the efficiency of the magnetron is low, with 65% conversion of electrical energy into electromagnetic radiation.

Table 1.1 Characteristics of microwave and conventional heating.

Microwave heating	Conventional heating
Energetic coupling	Conduction/convection
Coupling at the molecular level	Superficial heating
Rapid	Slow
Volumetric	Superficial
Selective (dependent upon the properties of the material)	Non-selective (independent of the properties of the material)

Table 1.2 The twelve principles of Green Chemistry[3]

1. Prevent waste
2. Maximize atom economy
3. Design less hazardous chemical syntheses
4. Design safer chemicals and products
5. Use safer solvents and reaction conditions
6. Increase energy efficiency
7. Use renewable feedstocks
8. Avoid chemical derivatives
9. Use catalysts, not stoichiometric reagents
10. Design chemicals and products to degrade after use
11. Analyze in real time to prevent pollution
12. Minimize the potential for accidents

Secondly, transformation of the electromagnetic radiation into heat could be low in apolar systems. The authors consider that it is highly questionable whether microwaves as a heating source should be labelled as being green, based on energy efficiency considerations.[6,7] Similarly, Ondrushka *et al.* reported energy efficiency data for a Suzuki–Miyaura reaction carried out under solvent-free conditions and determined that ball milling was more efficient than microwave irradiation.[8] However, Hessel *et al.* carried out a complete cost analysis on a production plant and they considered that integrated microwave heating and microflow processing led to a cost-efficient system on using a micropacked-bed reactor in comparison to wall-coated microreactor (Figure 1.1).[9]

Regardless of the considerations outlined above, it is clear that microwave irradiation is more efficient when using a substrate with a high loss tangent (tan δ), *i.e.*, a good microwave absorber that can easily transform microwave energy into heat.

In this chapter, we will review the applications of microwave irradiation related to Green Chemistry. In this regard, we will consider reactions that are performed under solvent-free conditions where radiation is absorbed

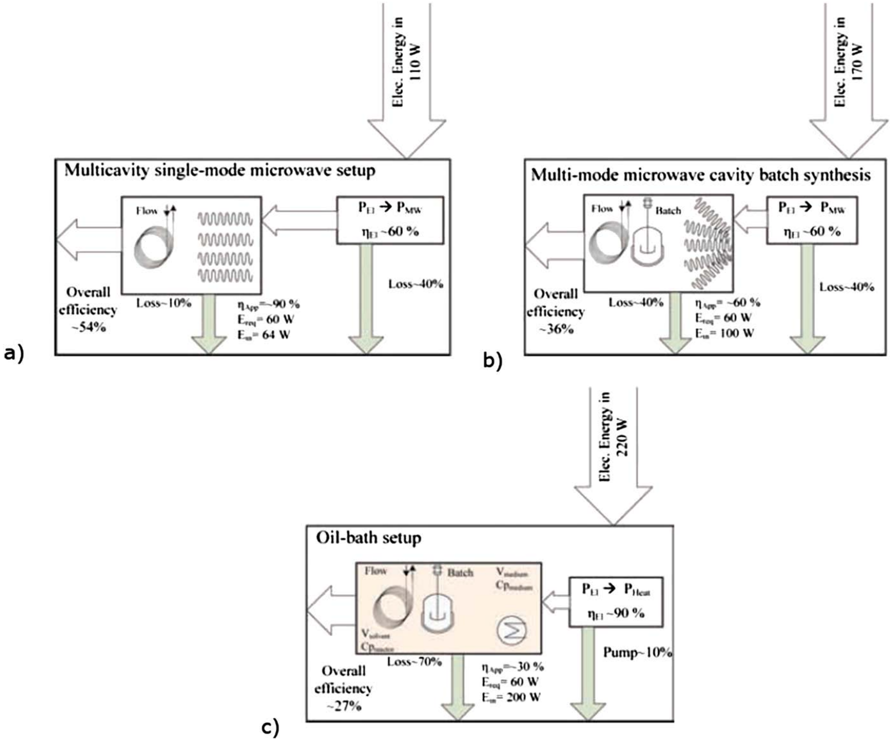

Figure 1.1 Energy flow diagrams for (a) single-mode, (b) multimode microwave and (c) oil-bath heating. Reproduced from ref. 9 with permission.

directly by the reagents and, as a consequence, energy is not diffused in the solvent. The use of neoteric and green solvents that couple efficiently with microwaves will also be discussed. The synergic use of microwave irradiation with other non-conventional energy sources will not be considered in this chapter.

1.2 Solvent-Free Reactions

Although microwave irradiation is a safe source of heating, uncontrolled reaction conditions involving volatile reactants and/or solvents at high pressure may result in undesirable results. This problem has been addressed and organic syntheses have been made more sustainable processes through the use of open-vessel solvent-free microwave conditions.[10]

The absence of organic solvents in reactions leads to a clean, efficient and economical technology; safety is increased significantly, the work-up is simplified considerably, costs are reduced, larger amounts of reactants can be employed, the reactivity is enhanced and, in some cases, the selectivity is modified without dilution. In summary, the absence of solvent in conjunction with the high yields and short reaction times that are characteristic of microwave-assisted processes make these procedures very attractive for sustainable synthesis.

In solvent-free conditions, the radiation is directly absorbed by the substrates and not by the solvents, thus increasing the benefits of microwave irradiation. Energy savings are increased and the effects on yield and selectivity are more marked.

Loupy classified solvent-free microwave-assisted processes into three types:[10c] (i) reactions between neat reactants, needing at least one liquid polar molecule, where the radiation is absorbed directly by the reagents; (ii) reactions between supported reagents in dry media by impregnation of compounds on alumina, silica or clays; and (iii) phase transfer catalysis (PTC) conditions in the absence of organic solvent, with a liquid reagent acting both as a reactant and an organic phase.

In 1993, Loupy reported that potassium acetate can be alkylated in the absence of solvent in a domestic oven using equivalent amounts of salt and alkylating agent in the presence of Aliquat 336 (10% mol) (Scheme 1.1).[11] Yields are practically quantitative within 1–2 min regardless of the chain length, the nature of the halide leaving group and the scale (up to 500 mmol).

Quinolines are known not only for their important biological activities but also for the formation of conjugated molecules and polymers that combine enhanced electronic or nonlinear optical properties with good mechanical

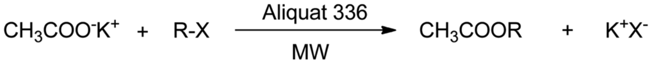

$$CH_3COO^-K^+ + R\text{-}X \xrightarrow[\text{MW}]{\text{Aliquat 336}} CH_3COOR + K^+X^-$$

Scheme 1.1 Alkylation of potassium acetate under microwave irradiation in solvent-free conditions.

properties. Kwon described the preparation of a mini-library of 12 quinoline derivatives by Friedlander coupling condensation between an acetophenone and a 2-aminoacetophenone in the presence of diphenylphosphate (0.1–0.5 equiv.) within 4 min under microwave irradiation in the absence of solvent (Scheme 1.2).[12] This procedure afforded product yields of up to 85%, whereas the yield obtained with classical heating under similar conditions did not exceed 24%.

Styrylquinolines are valuable derivatives as imaging agents for β-amyloid plaques on human brain sections in Alzheimer patients. Menéndez reported a microwave-assisted solvent-free synthesis of 2-styrylquinolines by condensation of 2-methylquinolines with benzaldehydes or cinnamaldehydes in the presence of acetic anhydride (Scheme 1.3).[13]

Thermal hydrazone/azomethine imine isomerization usually requires long reaction times (several hours or days) under reflux in high-boiling solvents (*e.g.* xylenes). However, this reaction can be easily promoted by microwave irradiation in the absence of solvent, as can the subsequent 1,3-dipolar cycloaddition with electron-deficient dipolarophiles. Thus, the use of pyrazolyl hydrazones led to valuable products such as bipyrazoles within a few minutes in 30–84% yields (Scheme 1.4).[14] The application of classical heating led to considerably lower yields and, indeed, several dipolarophiles did not react at all.

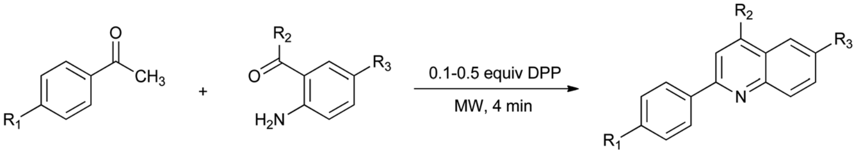

Scheme 1.2 Preparation of quinoline derivatives under microwave irradiation in the absence of solvent.

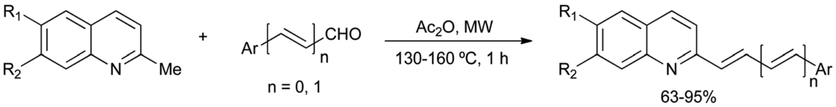

Scheme 1.3 Synthesis of 2-styrylquinolines under microwave irradiation in solvent-free conditions.

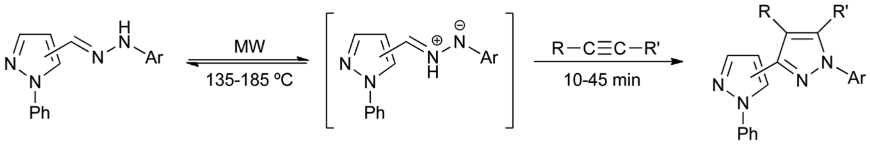

Scheme 1.4 Preparation of bipyrazoles by microwave-induced hydrazone/azomethine imine isomerization in solvent-free conditions.

In 2008 Varma described the preparation of ring-fused aminals through microwave-assisted α-amination of nitrogen heterocycles in a high-yielding process that was solvent- and catalyst-free (Scheme 1.5).[15]

In the absence of solvents, carbon nanoforms (fullerenes, carbon nanotubes, graphene, *etc.*) absorb microwave radiation directly and it is possible to take full advantage of the strong microwave absorption characteristics of these structures. Very high temperatures are obtained in a few seconds, thus providing extremely time-efficient reactions and making new transformations possible. In 2002 Prato reported the azomethine ylide cycloaddition reaction on carbon nanotubes (CNTs).[16] This process required large amounts of DMF to disperse the CNTs and long reaction times (five days). On using microwave activation in solvent-free conditions the same reaction takes place in 1 h (Scheme 1.6).[17] This methodology has also been applied in the functionalization of carbon nanohorns (CNHs)[18] and to produce multifunctionalized nanostructures using a combination of this reaction and the addition of diazonium salts (in this case employing water as the solvent).[17*b*]

β-Enaminones and β-enaminoester derivatives are versatile synthetic intermediates for a wide range of bioactive heterocycles, pharmaceuticals and naturally occurring alkaloids. For this reason, several catalytic and non-catalytic methods have been applied for the synthesis of these compounds. In 2013 Das described the microwave-assisted synthesis of novel classes of β-enaminoesters within 5–10 min by reaction between ethyl 3-(2,4-dioxocyclohexyl) propanoate and different amines under solvent- and catalyst-free conditions (Scheme 1.7).[19] The reactions did not require work-up and clean product formation was achieved under milder reaction conditions, thus making this process in an environmentally benign method.

Recently, Jain reported an efficient and facile solvent-free peptide synthesis assisted by microwave irradiation using *N*,*N*′-diisopropylcarbodiimide

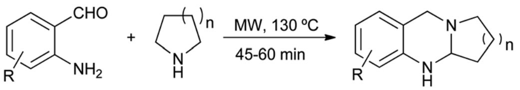

Scheme 1.5 Solvent- and catalyst-free synthesis of ring-fused aminals under microwave induction (MWI).

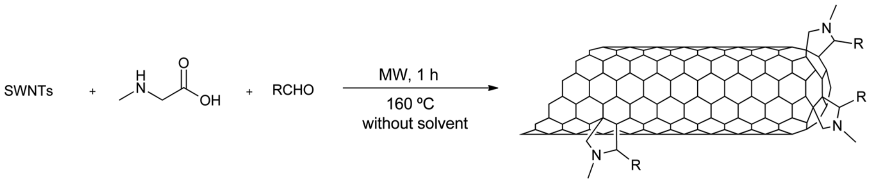

Scheme 1.6 Microwave-assisted functionalization of CNTs in solvent-free conditions.

(DIC) as the coupling reagent and *N*-hydroxy-5-norbornene-*endo*-2,3-dicarbodiimide (HONB) as an auxiliary nucleophile (Scheme 1.8).[20] Peptides were obtained in 15 min at 60 °C in high yield and with high purity without racemization.

Difunctional triazinyl mono- and bisureas possess very interesting self-assembly properties that allow them to form supramolecular nanostructures as a result of non-covalent interactions in aqueous or hydrophobic environments. These abilities have resulted in applications such as ambipolar thin film devices and polyurea networks with 2D porous structures. de la Hoz reported an efficient and sustainable microwave-assisted solvent-free approach for the preparation of a wide range of 1,3,5-triazinyl mono- and bisureas.[21] Under these conditions non-reactive amino groups attached to the triazine ring are able to react with phenylisocyanate to yield selectively mono- and bisureas (Scheme 1.9). Products were obtained with a simple purification procedure, which simply involved washing with a solvent (diethyl ether or ethanol).

1,3-Diynes have received considerable attention in materials science due to their use for the construction of π-conjugated structures. The most widely used method for the synthesis of diynes involves the self-coupling of terminal acetylenes. Several palladium-free syntheses have been described in which copper salts are used as catalysts. However, these protocols require bases and/or additives as well as toxic and carcinogenic solvents.

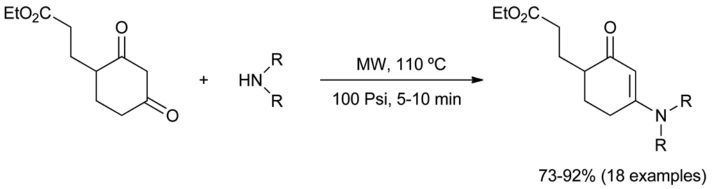

Scheme 1.7 Solvent- and catalyst-free synthesis of β-aminoesters under MWI.

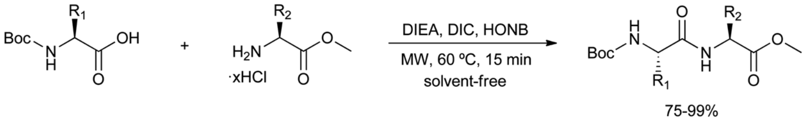

Scheme 1.8 Synthesis of peptides under microwave irradiation in solvent-free conditions.

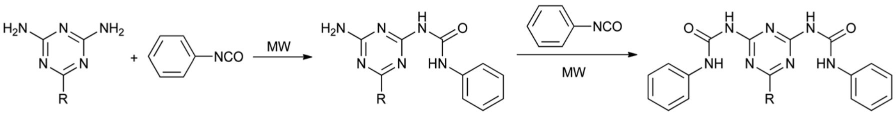

Scheme 1.9 Synthesis of 1,3,5-triazinyl mono- and bisureas under microwave irradiation in dry media.

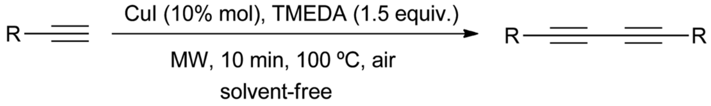

Scheme 1.10 Microwave-assisted synthesis of 1,3-diynes in the absence of solvent.

Braga recently described a microwave-assisted synthesis of 1,3-diynes from terminal acetylenes catalysed by CuI and tetramethylenediamine, in the presence of air as the oxidant, at 100 °C for only 10 min under solvent-free conditions (Scheme 1.10).[22] The same protocol can also applied for the synthesis of unsymmetrical 1,3-diynes.

1.3 Microwave Susceptors

The nature of the radiation means that non-polar substances are poorly heated by microwaves. In other cases, the reaction requires very high temperatures that cannot be achieved by the absorption of the reagents. These problems can be overcome by the use of a susceptor, an inert compound that efficiently absorbs microwave radiation and transfers the thermal energy to other compounds that are poor radiation absorbers or to the reaction medium.

1.3.1 Graphite As a Microwave Susceptor

Most forms of carbon interact strongly with microwaves. Powdered amorphous carbon and graphite rapidly (within 1 min) reach very high temperatures (>1000 °C) upon irradiation and, for this reason, graphite has been widely employed as a microwave susceptor. The amount of graphite can be varied. In some cases, a catalytic amount of graphite (10% or less than 10% by weight) is sufficient to induce rapid and strong heating of the reaction medium. However, in most cases the amount of graphite is at least equal to or greater than the amount of reagents, thus resulting in a graphite-supported microwave process.[23]

In 1996, Dubac described the Diels–Alder cycloaddition between anthracene and diethyl fumarate supported on graphite in a dry medium (Scheme 1.11).[24] Sequential irradiation (irradiation with “battlements”) at moderate power, 3 × 1 min at 30 W, allowed the reaction temperature to be controlled and avoided the retro-Diels–Alder process, which would diminish the product yield of unstable adducts. On applying classical heating, a reaction time of 60 h in refluxing dioxane was required to achieve a similar yield.

The efficiency of the graphite-supported process is all the more noteworthy because reagents are frequently volatile, but the adsorption power of graphite retains these components and this enhances the reaction. For example, the cycloaddition reaction between isoprene and ethyl glyoxylate affords 73% yield within 10 × 1 min (final temperature 146 °C) whereas only 10% can be obtained by classical heating (Scheme 1.12).[25]

Besson reported that a quinazolin-4-one ring can be fused onto a benzimidazo[1,2-*c*]quinazoline skeleton by a modified Niementowski reaction. Thermal heating of the two reagents at 120 °C or in refluxing butanol for 48 h gave only 50% of the target compound. The reaction time was reduced to 6 h in a microwave-assisted process, albeit without an improvement of the yield. However, irradiation of the quinazoline derivative and an excess of anthranilic acid (6 equiv.), absorbed on graphite, led to the desired product in 1.5 h with 95% yield (Scheme 1.13).[26] Furthermore, the fact that by-products were not detected allowed the easy purification of the product.

The thiazole and benzothiazole rings are present in various natural compounds. Likewise, indolo[1,2-*c*]quinazoline and benzimidazo[1,2-*c*]quinazoline skeletons are often present in potent cytotoxic agents. For these reasons, Besson described the fusion of these two systems under microwave irradiation in the presence of graphite as a sensitizer (10% by weight) and the expected products were obtained in good yields and in short reaction times (Scheme 1.14).[27]

Graphene is a one atom-thick two-dimensional carbon structure that has attracted considerable attention due to its amazing properties and potential applications in material science. In 2011 Kim described the fabrication of high quality graphene nanosheets within 1 min by solid-state microwave

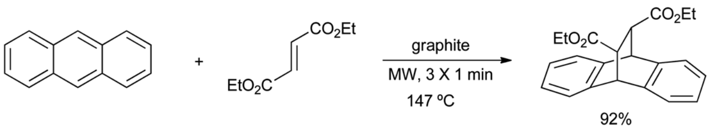

Scheme 1.11 Microwave-assisted cycloaddition between anthracene and diethyl fumarate supported on graphite in a dry medium.

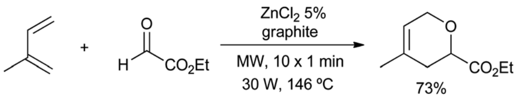

Classical heating: $SnCl_4$ 5%, CH_2Cl_2, 20 °C, 18 h, 10%

Scheme 1.12 Microwave-assisted cycloaddition between isoprene and ethyl glyoxylate adsorbed on graphite.

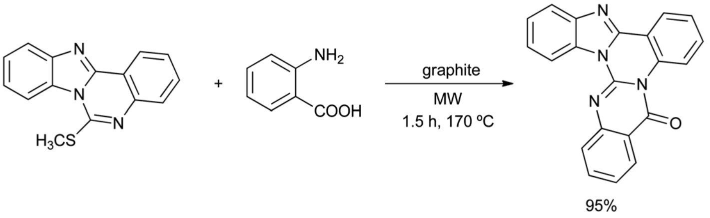

Scheme 1.13 Preparation of polyheterocyclic derivatives under microwave irradiation in conjunction with graphite.

irradiation of a mixture of graphite oxide and graphene nanosheets (10 wt%) under a hydrogen atmosphere.[28] The graphene nanosheets in the mixture acted as a microwave susceptor providing sufficiently rapid heating for the effective exfoliation of graphite oxide (Figure 1.2). The hydrogen atmosphere plays an important role in improving the quality of the graphene nanosheets by promoting the reduction of graphite oxide and preventing the formation of defects.

Carbon nanotubes can act as microwave susceptors in the curing of epoxy polymers. The presence of carbon nanotubes (0.5 or 1.0 wt%) within an epoxy matrix has proven to shorten the curing time, which decreased as the carbon nanotube concentration was increased (Figure 1.3).[29] Substantial changes were not observed in the mechanical behaviour of the carbon nanotube-reinforced polymers. However, the energy saving was quantified to be at least 40% due to the reduction in the curing time.

1.3.2 Silicon Carbide (SiC) As a Microwave Susceptor

It is well known that silicon carbide (SiC) is thermally and chemically resistant (melting point *ca.* 2700 °C) and that it is a strong microwave absorber. The use of SiC as a microwave susceptor has been reported in materials and ceramics science.[23] Sintered SiC has a very low thermal expansion coefficient and no phase transitions that would cause discontinuities in thermal

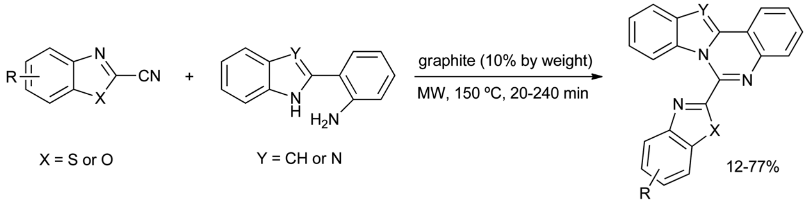

Scheme 1.14 Preparation of quinazoline derivatives under microwave irradiation using graphite as a sensitizer.

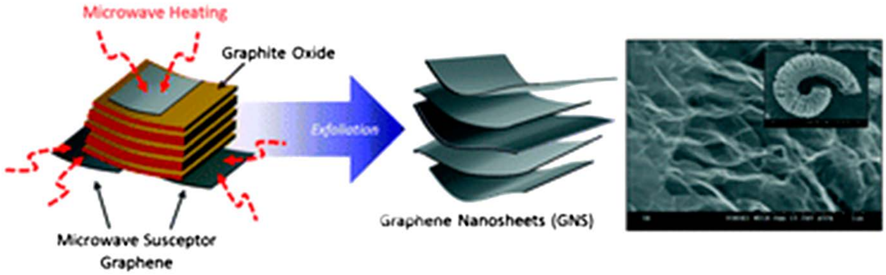

Figure 1.2 Preparation of graphene nanosheets under microwave irradiation using graphene as a susceptor. Reproduced from ref. 28 with permission from the Royal Society of Chemistry.

expansion. Thus, SiC cylinders sintered at 2000 °C, which are stable to corrosion and temperatures up to 1500 °C, have been developed for use as microwave susceptors in organic processes (Figure 1.4).[30]

Non-polar solvents can be rapidly and deeply heated by microwave irradiation in the presence of SiC as a susceptor, and chemical transformations can

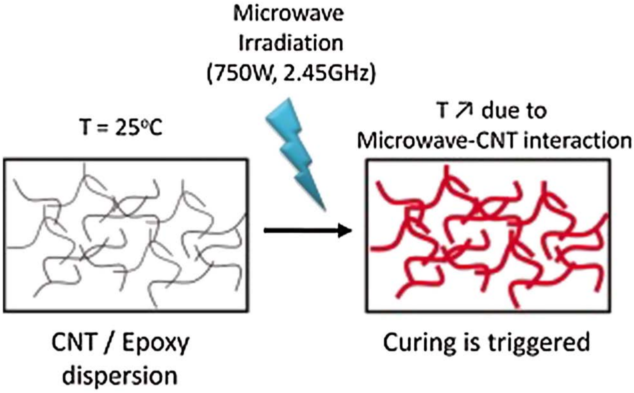

Figure 1.3 Carbon nanotubes as a microwave susceptor in the curing of epoxy polymers. Reproduced from I. Fotiou *et al.*, *J. Appl. Poly. Sci.* with permission from John Wiley and Sons. Copyright © 2013 Wiley Periodicals, Inc.[29]

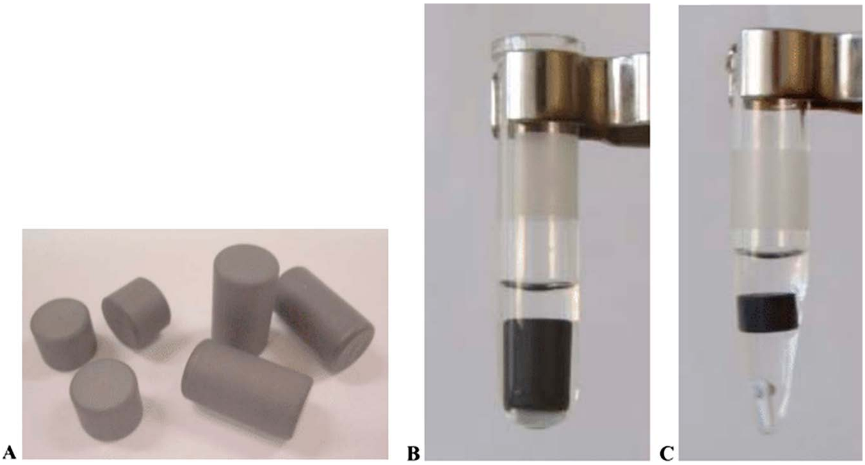

Figure 1.4 (a) SiC cylinders: 10 × 8 mm (1.94 g) and 10 × 18 mm (4.35 g). (b) SiC cylinder (10 × 18 mm) inside a standard 10 mL microwave vial used in single-mode microwave apparatus, solvent volume 2 mL. (c) SiC cylinder (10 × 8 mm) inside a standard 5 mL conical microwave vial, solvent volume 2 mL. Reproduced with permission from J. M. Kremsner and C. O. Kappe, *J. Org. Chem.* 2006, **71**, 4651–4658. Copyright (2006) American Chemical Society.[30]

be performed at temperatures as high as 300 °C (Table 1.3).[30] These passive heating elements are compatible with any solvent or reagent, they are virtually indestructible and they can be re-used indefinitely without loss of efficiency.

Kappe described the use of SiC in several transformations. Michael addition of methyl acrylate and piperazine in toluene as the solvent afforded the bis-Michael adduct in 98% yield within 10 min at 200 °C (Scheme 1.15).[30] However, despite the presence of piperazine the microwave absorbance of the reaction mixture was not sufficient: after 7 min of irradiation at 300 W the maximum temperature was 170 °C and very low conversion to the final product was observed. Full conversion to the product at room temperature in toluene required 2 days.

In another example, Kappe studied the high-temperature rearrangement of a heterocyclic derivative bearing a nucleophilic free amino group. Since ionic liquids cannot be used as microwave susceptors owing to the presence of a nucleophilic group, SiC was employed as a heating element. Thus, the thermal Dimroth rearrangement was performed within 30 min at 220 °C and the product was isolated in 68% yield (Scheme 1.16).[23] The reaction did not proceed at all in the absence of SiC (maximum temperature after 4 min: 140 °C).

Table 1.3 Microwave-induced temperatures of non-polar solvents in the presence and absence of SiC as a microwave susceptor.[a]

Solvent	T without SiC (°C)	T with SiC (°C)	Time[b] (s)	B.p. (°C)
CCl_4	40	172	81	76
Dioxane	41	206	114	101
Hexane	42	158	77	69
Toluene	54	231	145	111
THF	93	151	77	66

[a] 150 W constant magnetron output power, 2 mL solvent, sealed 10 mL quartz (pure solvent) or Pyrex (solvent with SiC) reaction vessel, magnetic stirring.

[b] Time until the maximum pressure limit of the microwave apparatus employed by the researchers (20 bar). Significantly higher solvent temperatures can be obtained using different instrumentation with higher pressure limits.

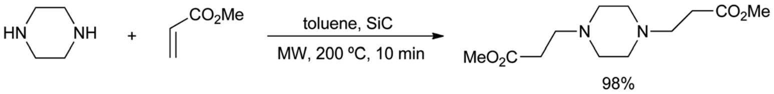

Scheme 1.15 Michael addition of methyl acrylate and piperazine in the presence of SiC as a microwave susceptor.

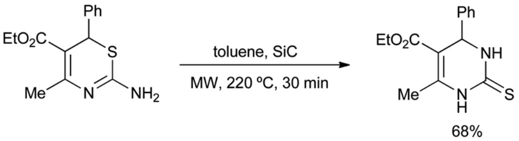

Scheme 1.16 Dimroth rearrangement of a 2-amino-1,3-thiazine using SiC as a microwave susceptor.

It is noteworthy that chemical transformations using SiC cylinders as heating elements generally require only a fraction of the magnetron output power (30–70%), which represents a significant energy saving.

In order to facilitate the penetration of radiation into the reaction mixture, microwave vessels are typically made from materials that have low microwave absorption or are microwave transparent (Pyrex, quartz or Teflon™). However, these useful materials do have some drawbacks, which include lack of stability under extreme reaction conditions (very high temperature or pressure, or aggressive chemical media). In an effort to solve these problems a sintered SiC ceramic reaction vessel with the exact same geometry as a standard 10 mL Pyrex vial has been produced (Figure 1.5).[31]

Kappe studied 21 selected chemical transformations and compared the results obtained in microwave-transparent Pyrex vials with experiments carried out in SiC vials at the same reaction temperature.[31] As an example, SiC vials were used to carry out microwave-assisted aliphatic fluorine–chlorine exchange reactions using trimethylamine trihydrofluoride (TREAT-HF, $Et_3N{\cdot}3$ HF) as a reagent in benzene at 250 °C (Scheme 1.17).[31] Since TREAT-HF can release hydrogen fluoride at high temperatures, a significant level of corrosion of standard Pyrex vials was observed in the vapour space above the reaction mixture. This corrosion represents a serious safety risk as the pressure rating of the heavy-walled Pyrex vials (20–30 bar) cannot be maintained. In contrast, the SiC vial was completely resistant to TREAT-HF even at 250 °C for prolonged periods.

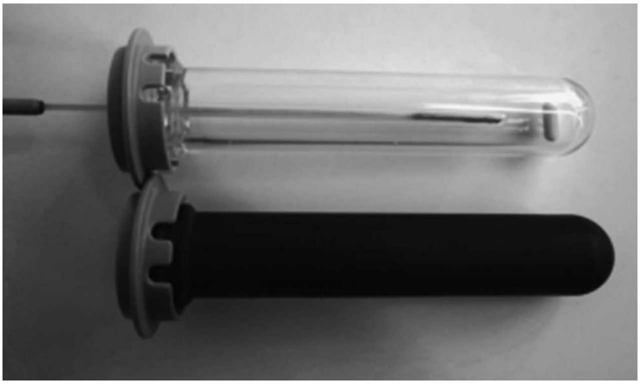

Figure 1.5 Reaction vial made from sintered SiC (lower). For comparison a standard 10 mL Pyrex vial with a snap cap, internal FO probe and a magnetic stirrer bar is also included (upper). Reproduced from B. Gutmann, *Chem. Eur. J.*, with permission from John Wiley and Son. Copyright © 2010 WILEY-VCH Verlag GmbH & Co. KgaA, Weinheim.[31]

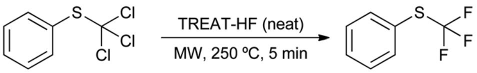

Scheme 1.17 Microwave-assisted aliphatic fluorine–chlorine exchange in a SiC vial.

Parallel microwave synthesis has received a great deal of attention in recent decades due to the benefits of these two technologies. The most important issue in this application was to achieve a uniform temperature distribution in all of the plates. This problem was addressed by developing deep-well plates made of Weflon™ (Teflon™ doped with 10 wt% graphite). However, a significant limitation of all early microtiter plate systems is that is was impossible to perform microwave chemistry under sealed-vessel conditions in a pressure range similar to those operating in single-mode reactors (20–30 bar). In 2007 the first sealed microtiter plate system made from SiC for use in a dedicated multimode microwave instrument was described.[32] At present, these systems allow high-speed microwave chemistry to be carried out in a highly parallelized and miniaturized format (0.02–3.0 mL) at a maximum temperature and pressure limit of 200 °C and 20 bar, respectively. Up to 192 reactions can be performed depending on the specific plate and rotor configuration (Figure 1.6).[33]

1.3.3 Other Microwave Susceptors

Other substances that are strong microwave absorbers have also been used as microwave susceptors. Metal particles (Fe or Ni) were employed in microwave-assisted pyrolysis processes that require temperatures of up to 1200 °C.[34] The use of ionic liquids to reach high temperatures in microwave-assisted reactions is described in Section 1.4.2.

In 1996 Díaz-Ortiz described the microwave-assisted 1,3-dipolar cycloaddition of nitriles with nitrones or nitrile oxides in solvent-free conditions using an alumina–magnetite (Fe_3O_4) (5 : 1) bath as an external microwave susceptor.[35] The product yields decreased significantly in the absence of a microwave susceptor or when using classical heating.

A few years later our research group demonstrated the reproducibility and scalability of solvent-free microwave-assisted reactions from domestic

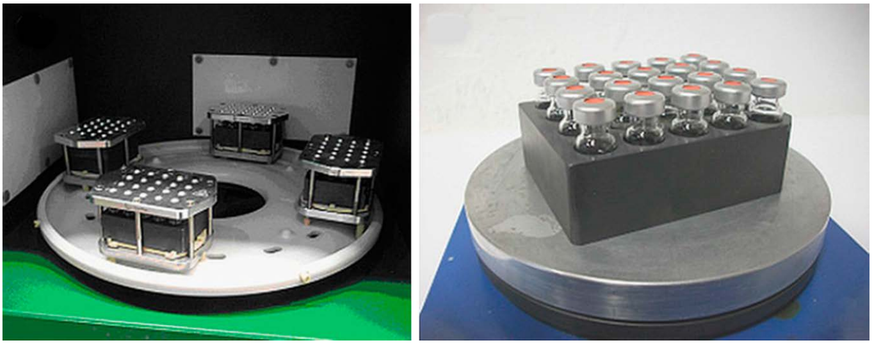

Figure 1.6 Fully equipped systems with SiC well plates commercialized by Anton Paar GmbH. Reprinted from Molecular Diversity, Parallel Microwave Chemistry in Silicon Carbide Microtiter Platforms: A Review, 16, 2011, C. O. Kappe, with permission from Springer.[33]

ovens to a dedicated microwave apparatus. In this study the 1,3-dipolar cycloaddition between nitriles and nitrile oxides was selected and 24 reactions were carried out in a multiwell plate (Scheme 1.18).[36] The reactions were performed in a Weflon™ multiwell plate. This system not only acted as a microwave susceptor to raise the reaction temperature, but it ensured identical conditions for each individual reaction.

1.4 Reactions in Solution

The vast majority of reactions in organic synthesis, on both the industrial and laboratory scales, are performed in solution.

The use of solvents allows the following:

- Obtaining an efficient mixture of reagents at the molecular level.
- Placing in contact the reagents at the appropriate concentrations to achieve a suitable reaction rate.
- Transporting reagents and/or products and facilitating the dosage for introduction into the reactor.
- Controlling the temperature of the reaction.
- In endothermic processes, increasing the temperature within the limit of the boiling point of the solvent.
- In exothermic processes, absorbing excess heat and controlling the temperature by reflux of the solvent or by cooling the solvent directly.

However, the use of solvent does present several problems and is not environmentally friendly. Solvents are used in large excess, *i.e.*, 10–100 times the quantity of reagents, and most of them are volatile (VOC's). Solvents are used not only during the reaction but also in the separation, purification (recrystallization, chromatography) and, possibly, in a final separation (evaporation, distillation, decantation, filtration or centrifugation) to obtain the final product.

On the other hand, solvents are the most likely contaminants amongst the auxiliary products because of their volatile and fluid nature. Solvents may have occupational toxicity, ecotoxicity, flammability or carry the risk of explosion and they may have drawbacks such as persistent contamination and pollution. Moreover, solvents may increase the greenhouse effect and contribute to the destruction of the ozone layer.

Water is an obvious choice in green chemistry to replace common organic solvents but it is hardly used because of the low solubility of organic

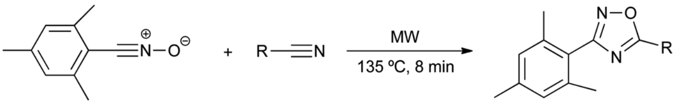

Scheme 1.18 Microwave-assisted 1,3-dipolar cycloaddition between nitriles and nitrile oxides.

compounds at room temperature. The development of neoteric solvents, supercritical fluids, ionic liquids and fluorous solvents has led to the development of a new sustainable chemistry. All of these systems have been used in efficient processes under microwave irradiation.

1.4.1 Reactions in Water

Water is considered as a paradigm green solvent. Water is readily available and is non-toxic and non-flammable. The use of water in organic synthesis has been hampered by the low solubility of organic compounds, however, new strategies have been designed to overcome this problem, for instance the use of an organic cosolvent, the exploitation of hydrophobic effects (chemistry "on-water") and the use of water at high temperatures. The latter conditions can be exploited easily under microwave irradiation. Water at elevated temperatures, close to the critical point, has unique properties that are very different from those observed at room temperature (Table 1.4).[37]

High temperature near-critical water (NCW) shows interesting properties for applications in organic synthesis. The dielectric constant of water changes from 78.5 at 25 °C to 27.5 at 250 °C (similar to acetonitrile at 25 °C) and 20 at 300 °C (similar to acetone at 25 °C). This means that at these temperatures water can be considered as a pseudo-organic solvent. In addition to the advantages of using water, the isolation of materials is simplified as pure products could be obtained by crystallization on cooling the aqueous solution.

The ionic product of water increases by 3 orders of magnitude from room temperature to 250 °C. As a consequence, at this temperature water can be used as a strong acid and a strong base, thus avoiding the use of mineral acids and bases which have to be neutralized when the reaction is complete.

The reactions studied under microwave irradiation in water include palladium-catalysed coupling reactions, heterocycle synthesis, multicomponent reactions, nucleophilic substitutions, cycloadditions, decarboxylations, hydrolyses and radical reactions. These reactions have recently been reviewed.[38]

Table 1.4 Properties of water under different conditions[37]

Fluid	Ordinary water, $T < 150$ °C, $p < 0.4$ MPa	Near-critical water (NCW), $150 < T < 350$ °C, $0.4 < p < 20$ MPa	Supercritical water (SCW), $T > 374$ °C, $p > 25$ MPa	Steam
Temp (°C)	25	250	400	400
Pressure (bar)	1	50	250	1
Density (g cm^{-3})	1	0.8	0.17	0.0003
Dielectric constant, ε'	78.5	27.1	5.9	1
pK_w	14	11.2	19.4	—

In this chapter some representative examples will be highlighted.

Leadbeater and Marco[39] described a Suzuki coupling in water under microwave irradiation (Scheme 1.19). The addition of TBAB as a phase transfer agent facilitated the reaction because it enhances the solvation of the organic substrate in water and increases the rate of the coupling reaction through the formation of a complex with the boronate. The authors reported that the reaction can be performed without the use of a palladium catalyst.

In a second paper it was reported that ultralow levels of palladium (50 ppb) found in the sodium carbonate base were responsible for the reaction.[40] In all cases, a clear reduction in the reaction time was observed on using microwave irradiation (from 120 to 5 min). Finally, an *in situ* Raman detection system was employed to show that the reaction had reached completion after 135 s.[41]

Ericsson and Engman reported the microwave-assisted group-transfer cyclization of organotellurium compounds in a radical reaction performed in different solvents including water (Scheme 1.20).[42]

It was found that the reaction was substantially improved under these conditions. The reaction time was shortened and the process could be performed in water without additives and in the absence of toxic tin mediators. The only drawback was the loss of diastereoselectivity due to the higher temperatures used.

Baran reported the total synthesis of the antiviral marine alkaloid ageliferin from sceptrin by a tautomerization/ring expansion.[43] The reaction was only successful in water under microwave irradiation and was complete in 1 min to give 40% yield (Scheme 1.21). Longer reaction times or the use of conventional heating led to decomposition of this unstable compound.

Reactions in near-critical water are scarce but they have especially been used for hydrolysis and degradative purposes. The first reactions were reported by Strauss[44] with the MBR microwave reactor developed at the CSIRO in Australia.

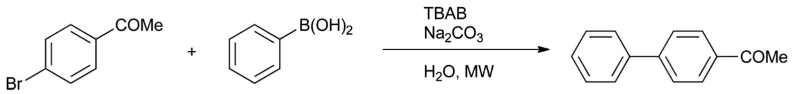

MW, 100 W, 150°C, 5 min 100%
CH, 150°C, 120 min 94%

Scheme 1.19 Suzuki reaction in water.

R = Bn, Ethyleneglycol, 250 °C, 6 min 74%, endo/exo, 1/1,8
Water, 180°C, 10 min <10%, endo/exo, 1/2,4

Scheme 1.20 Group transfer cyclization of organotellurium compounds.

As an example, degradative hydrolysis of an indole 2-carboxylic ester was carried out in which, by controlling the temperature, it was possible to control the hydrolysis and the subsequent decarboxylation (Scheme 1.22).

Kremsner and Kappe performed a proof-of-concept study that involved a wide range of reactions in water at temperatures up to 300 °C and pressures up to 80 bar in a dedicated multimode microwave reactor (Scheme 1.23).[45] They concluded that microwave–NCW technology is ideally suited to perform organic synthesis in this high-temperature region as it combines the advantages of both techniques.

Santra and Andreana reported an Ugi/Michael/aza-Michael cascade reaction in aqueous media at high temperature to obtain azaspiro tri- and tetracyclic compounds.[46] The process generates a quaternary centre, four stereogenic centres and six contiguous bonds, and provides good to excellent yields and regioselectivities with appreciable diastereoselectivity (Scheme 1.24).

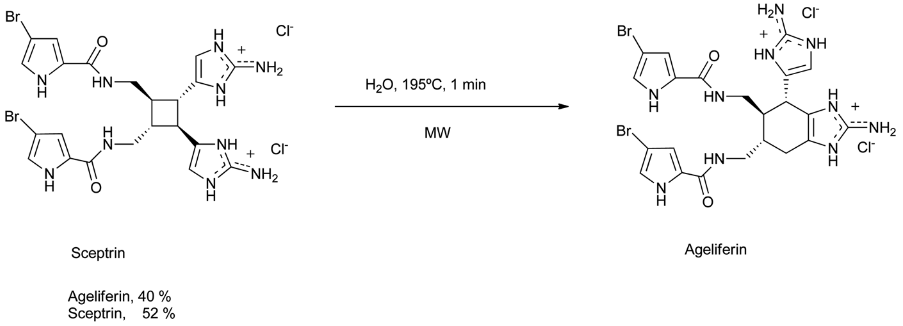

Scheme 1.21 Microwave-assisted transformation of sceptrin into ageliferin.

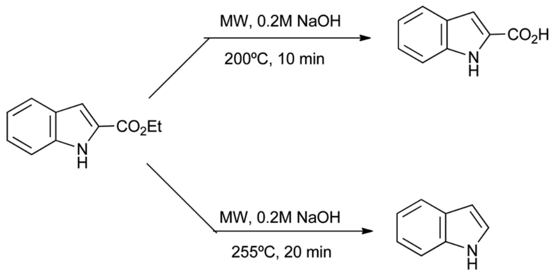

Scheme 1.22 Hydrolysis of indole 2-carboxylic ester in water.

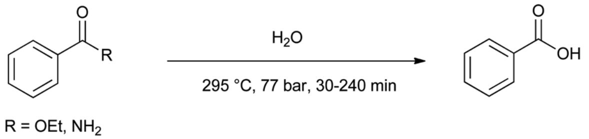

Scheme 1.23 Hydrolysis of benzoic esters and amides in subcritical water.

Finally, the Tour reaction of single-walled carbon nanotubes (SWCNTs) in water under microwave irradiation was described as a green process for the functionalization of CNTs.[47] Pristine SWCNTs were dispersed in water with aniline derivatives in a microwave glass vessel. After sonication for a few minutes, isoamyl nitrite was added and a condenser was attached. The mixture was irradiated for 90 min at 80 °C in a focused microwave reactor (Scheme 1.25). TGA showed the presence of one functional group for each 68 carbon atoms approximately.

1.4.2 Reactions in Ionic Liquids (ILs)

Ionic liquids (ILs) are an excellent green alternative to VOCs. ILs are organic salts that remain liquid at room temperature. The properties of ILs that make them suitable for applications in synthesis are:

- Non-volatility: ILs present negligible vapour pressure over a wide range of temperatures.
- High thermal and chemical stability.
- Broad solubility range: ILs can dissolve a wide variety of organic, inorganic and organometallic compounds. They are also miscible with several organic solvents.
- Low combustibility: ILs are considered to be non-flammable compounds.

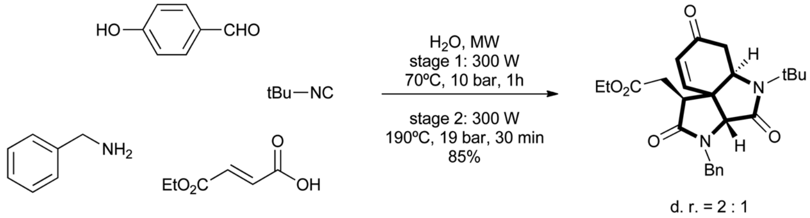

Scheme 1.24 Microwave-assisted cascade reactions in water.

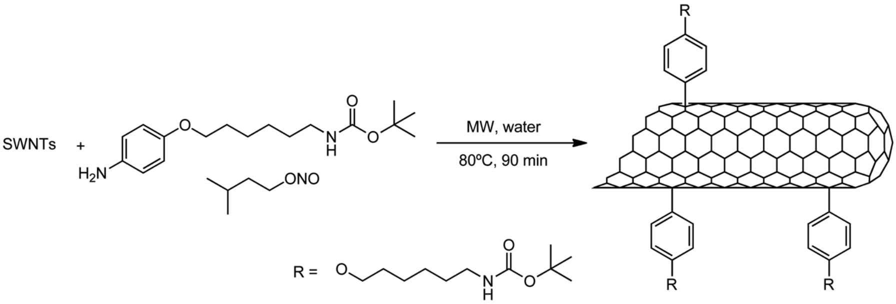

Scheme 1.25 Tour reaction of CNT in water.

- Catalytic properties: ILs can act as catalysts, for example as Lewis acid catalysts.
- Large electrochemical window and relatively high electrical conductivity.

The main mechanisms for the transformation of electromagnetic radiation into heat are dipolar rotation and ionic conduction. Due to their ionic character, ILs absorb microwave irradiation very efficiently and transfer energy quickly by ionic conduction. As a result, ILs can reach very high temperatures in very short times. The ionic conduction mechanism produces superheating of an ionic substance due to the motion generated by an electric field. The transfer of energy becomes more efficient as the temperature increases. However, for organic reactions performed in ionic liquids under consecutive microwave irradiation, overheating is an inevitable problem because of the non-volatile nature of these solvents.

The combination of ILs and microwave irradiation in organic synthesis has been reviewed.[48] A number of representative examples of the advantages of the IL–MW combination are discussed in this section.

Leadbeater and Torrenius investigated the effect of the addition of a small quantity of ionic liquid in apolar solvents (hexane and toluene). They showed that these solvents can be heated above their boiling points in sealed vessels by adding just 2 mmol of IL for each 1 mL of solvent. This technique permitted the use of solvents with very low loss tangents in microwave-assisted reactions (Table 1.5).[49]

Table 1.5 The microwave heating effects on adding a small quantity of **1** and **2** to hexane, toluene, THF, and dioxane.[a,d]

Solvent used	Ionic liquid added	Temp attained (°C)	Time taken (s)	Temp without ionic liquid[b] (°C)	Boiling point[c] (°C)
Hexane	**1**	217	10	46	69
	2	228	15		
Toluene	**1**	195	150	109	111
	2	234	130		
THF	**1**	268	70	112	66
	2	242	60		
Dioxane	**1**	264	90	76	101
	2	246	90		

[a] Experiments run using a microwave irradiation power of 200 W.
[b] Temperature attained during the same microwave irradiation time but without any ionic liquid added.
[c] Boiling point of the solvent used (for comparison purposes).
[d]

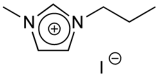

1

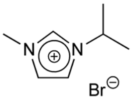

2

These solvent mixtures were used in Diels–Alder reactions, Michael additions and alkylation reactions. Improvements were observed in most reactions on using this protocol, with the exception of the alkylation reactions. The alkyl halide must react with the IL at the elevated temperatures used in the reaction and this leads to decomposition of the IL (Scheme 1.26).

Microwaves have shown significant benefits in the preparation of ILs. Conventional methods require several hours at high temperatures to afford acceptable yields. Under microwave irradiation, however, reactions can be performed in solvent-free conditions in short reaction times. The first example was reported by Varma for the synthesis of 3-methylimidazolium halides by alkylation of imidazoles in solvent-free conditions (Scheme 1.27).[50]

Task-specific ionic liquids (TSIL) have been used successfully under microwave irradiation. Applications include the use of solid-supported ILs and grafted ILs as substrates for the liquid-phase combinatorial synthesis of small molecules and as matrices for multicomponent reactions.

Bazureau described a microwave-assisted Knoevenagel condensation and Schiff base formation using a TSIL prepared by esterification of 1-(2-hydroxyethyl)-3-methylimidazolium tetrafluoroborate (Scheme 1.28).[51]

The use of deep eutectic solvents (DES) under microwave irradiation is rare. These systems consist of a mixture of compounds that has the lowest melting point. Depression of freezing point is related to the strength of interactions between the two components. Many components are inexpensive, non-toxic, non-flammable, biodegradable and versatile. As such they are

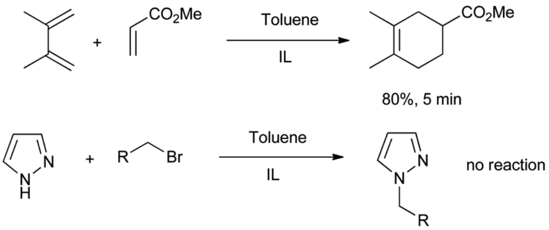

Scheme 1.26 Microwave-assisted reactions in toluene with addition of ionic liquids.

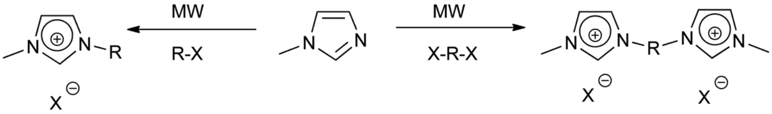

Scheme 1.27 Microwave-assisted alkylation of imidazoles in solvent-free conditions.

considered to be green solvents and they have properties related to those of ILs. However, DES materials show unusual solvent properties:

- They dissolve a wide range of solutes, *e.g.* salts, polar organics, metal oxides, amino acids, enzymes and surfactants.
- Solvent properties can be markedly changed by altering the hydrogen bond donor (HBD).

The most common DES is a mixture of choline chloride and urea.

These materials have been used in combination with microwave irradiation, particularly for extraction processes,[52] and there are only a few examples in which organic synthesis has been carried out such media. For example, Nagarkar described the use of a deep eutectic mixture of choline chloride and urea (1:2) in the synthesis of nitriles from aldehydes under microwave irradiation in solvent-free conditions.[53] The eutectic mixture was used as an eco-friendly catalyst (Scheme 1.29).

1.4.3 Fluorous Chemistry

The chemistry of highly fluorinated compounds has grown significantly since its inception in 1994. This type of chemistry is related to the characteristics of highly fluorinated materials, molecular fragments or solvents and it is based on carbon with a sp^3 hybridization. This area also concerns fluorous media or solvents, fluorous separation techniques, fluorous tags and

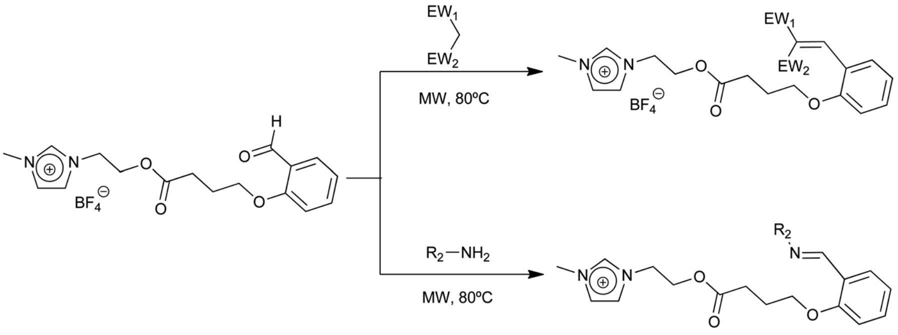

Scheme 1.28 Reactions with task-specific ionic liquids (TSIL).

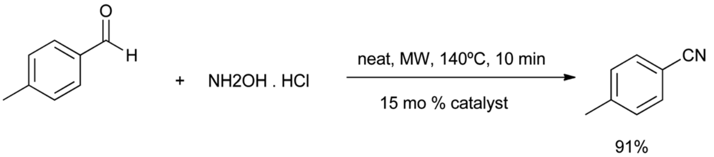

Scheme 1.29 Microwave-assisted reaction with a deep eutectic mixture as catalyst.

fluorous reagents and substrates. In this way, fluorous reactions and fluorous chemistry can be defined as concerning those materials in which a highly fluorous component is used in the reaction or synthesis.

The green character of fluorous chemistry is associated with the solvophobicity to aqueous and organic solvents at room temperature, a property that is exploited in the development of new phase-tag-based separation techniques. In many cases, a simple extraction can be employed to obtain the pure products, thus avoiding the use of distillation, recrystallization or chromatography, and this advantage leads to significant savings in energy and solvents.

However, it should be noted that fluorous solvents have debatable toxicological properties; many perfluorocarbons are environmentally persistent and the low boiling point of perfluorocarbons is believed to be responsible for ozone depletion and global warming.[54]

Fluorous solid-phase extraction (F-SPE) increases the synthetic efficiency and reduces the amount of solvent required for purifications. Because of their solvophobic and fluorophilic nature, fluorous molecules can be retained in fluorous silica gel cartridges when eluted with a fluorophobic solvent. After separation of the non-fluorous molecules, the fluorous component is washed out from the cartridge with a stronger solvent.[54]

Microwave-assisted fluorous chemistry combines the advantages of microwave irradiation during the reaction and the advantages of F-SPE, since microwave irradiation has a strong influence on the reaction but not on the separation and purification steps.

Curran and Hallberg reported the first example of fluorous chemistry under microwave irradiation.[55] They described a series of coupling reactions, reductions, cyclizations and additions using tin derivatives with an F-21 tag. The high reaction rate under microwave irradiation and the subsequent easy purification makes this procedure an interesting alternative for use in combinatorial chemistry. The use of microwave irradiation makes compounds with F-21 an alternative to F-13. The corresponding tin derivatives with the F-21 tag are highly insoluble in organic solvents, thus facilitating their purification on silica gel or by liquid–liquid extraction (Scheme 1.30).

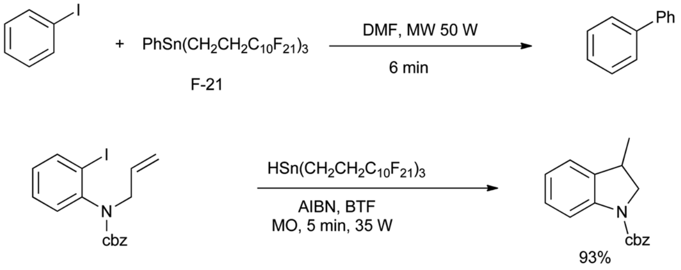

Scheme 1.30 Microwave-assisted Stille coupling and radical cyclizations with fluorous reagents.

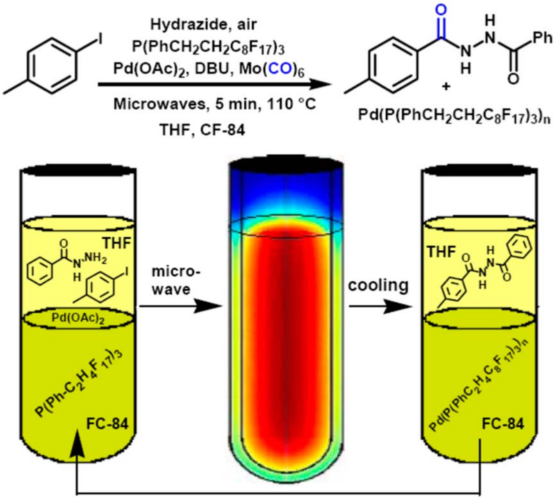

Figure 1.7 Synthesis of diacylhydrazines with a fluorous phosphine. Reproduced from ref. 56 with permission © Georg Thieme Verlag KG.

Larhed described the synthesis of diacylhydrazines by *in situ* carbonylation of aryl iodides using $Mo(CO)_6$ as the carbon monoxide source. A fluorous phosphine ligand was used and the authors demonstrated that the catalytic system can be recycled up to six times (Figure 1.7).[56]

1.5 Flow Chemistry

The synergistic combination of microwave irradiation and flow chemistry is an interesting approach to solve the problems associated with the scale-up of reactions under microwave irradiation and this will further enhance the synthetic possibilities.

Microwave irradiation is a volumetric limited heating process. At the typical microwave frequency (2.45 GHz), the penetration depth is of the order of a few centimetres depending on the dielectric properties of the material. The composition and consequently the polarity of the reaction medium changes during the reaction and this determines the penetration depth and the total absorption of the microwave energy. Therefore, the ability to scale-up a reaction is always dependent on the reaction conditions. These characteristics have prevented the scale-up of microwave reactions in batch to a few litres and prevent their use in the production of compounds on a large scale.

An excellent review of microwave reactions under continuous flow conditions has been published[57] and in this section a selection of some key systems are discussed.

Synergy between microwave irradiation and flow was described by Strauss *et al.*,[58] who developed a continuous microwave flow reactor (CMR) that enabled a complete range of parameters to be controlled (temperatures to

200 °C, pressures up to 14 bar and flow rates of 15–20 mL min^{-1}). The application of these conditions with a residence time of 1–2 min allowed the processing of 1 L of reaction mixture in 1 h (Figure 1.8).

They described a series of reactions that included esterification, elimination, substitution and oxidation amongst others (Scheme 1.31).

Today microwave vendors provide commercially available flow systems (pumps, reactors, injection systems, *etc.*) that can be attached to the standard microwave systems – both single-mode and multimode.

However, several flow systems have been designed in-house for particular applications.

Haswell described a microreactor for the continuous-flow Suzuki reaction using a palladium catalyst and a gold bed.[59] Use of microwave irradiation enabled the localized heating of the catalyst.

Two reactors shown in Figure 1.9 were designed, the first reactor had a catalyst channel that was 1.5 mm wide, 0.08 mm deep and 15 mm long. The

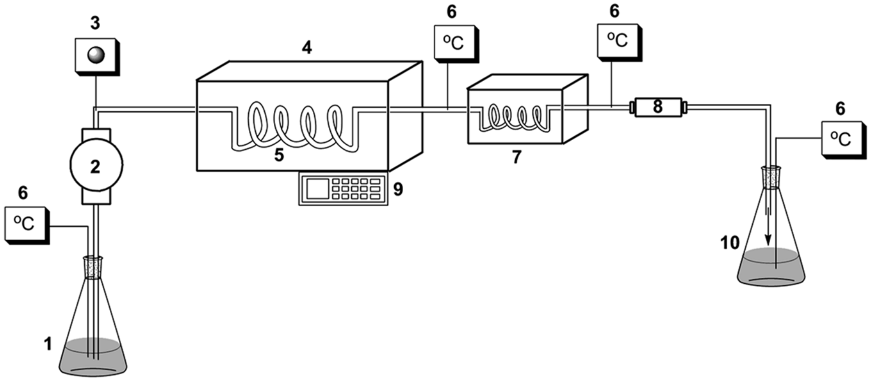

Figure 1.8 Schematic illustration of the CMR. 1. Reaction mixture, 2. Pump, 3. Pressure sensor, 4. Microwave cavity, 5. Reaction coil, 6. Temperature sensor, 7. Heat exchanger, 8. Pressure control valve, 9. Electronic key pad and display and 10. Product mixture. Reproduced with permission from T. Cablewski, A. F. Faux and C. R. Strauss, *J. Org. Chem.* 1994, **59**, 3408–3412. Copyright (1994) American Chemical Society.[58]

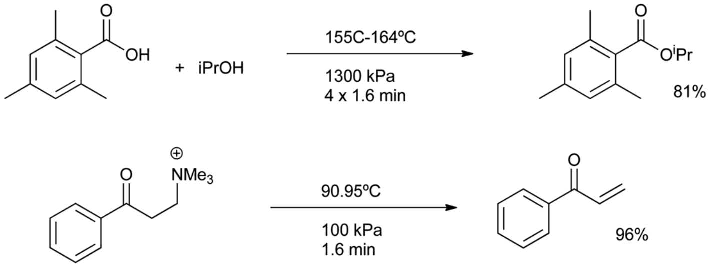

Scheme 1.31 Examples of microwave reactions in flow with the CMR reactor.

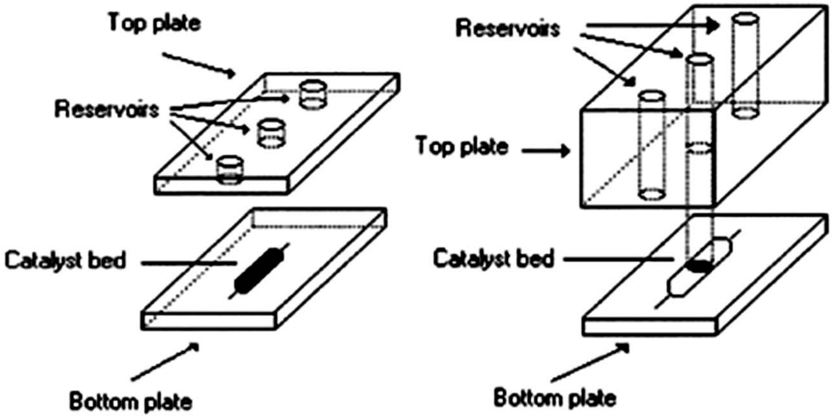

Figure 1.9 Continuous-flow Suzuki coupling in microchannels. Reproduced from ref. 59 with permission from the Royal Society of Chemistry.

catalyst is introduced as a monolayer with a thickness of 45–63 mm. The efficiency of the catalyst is reduced after the first cycle but in the next four cycles the loss of activity is very low. The main problem encountered with this system was the difficulty in measuring the temperature with an IR sensor.

Organ described a microreactor for microwave-assisted organic synthesis using microcapillaries.[60] The internal diameter of the capillary was 200–1200 mm and the flow rate varied from 2 to 40 mL min^{-1}, which corresponds to an irradiation time of 4 min. Capillaries were impregnated internally with a thin layer of Pd(0) and the system showed a great acceleration in coupling reactions such as the Suzuki reaction (Figure 1.10). Reagents can be injected into the capillary system and mixing and reaction occurs without the usual laminar flow problems that occur in microreactors. The authors described the impregnation with other metal catalysts and developed a multireactor, which can be applied to the preparation of libraries of compounds (Figure 1.10).

Bagley described a flow reactor to be used with supports.[61] In this system a standard pressure-rated glass tube (10 mL) was fitted with a custom-built steel head. The flask was filled with sand (10 g) between two drilled frits (Figure 1.11) to minimize dispersion and effectively create a lattice of microchannels. The system was charged with solvent (5 mL), sealed using PTFE washers and connected to an HPLC flow system with a back-pressure regulator. Reagents were introduced in the bottom of the vessel and they flowed to the top of the reactor. An IR detector in the bottom of the reactor was used to determine the reaction temperature. The authors tested the system in two previously reported reactions and they observed a significant improvement in yield and demonstrated the ease of scale-up.

Ley described the use of polyurea microencapsulated palladium (PdEnCat) as a catalyst for the microwave-assisted Suzuki reaction described in

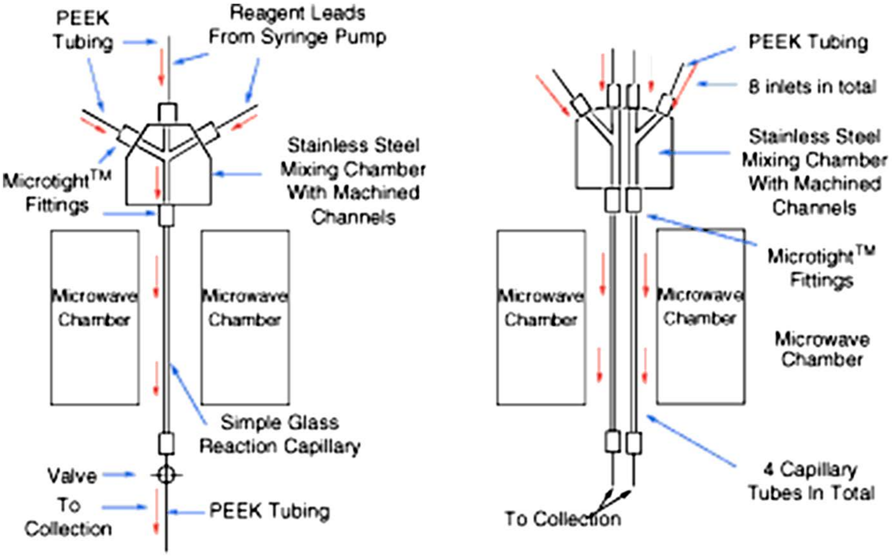

Figure 1.10 Flow reactions in microcapillaries. Reproduced from ref. 60 with permission.

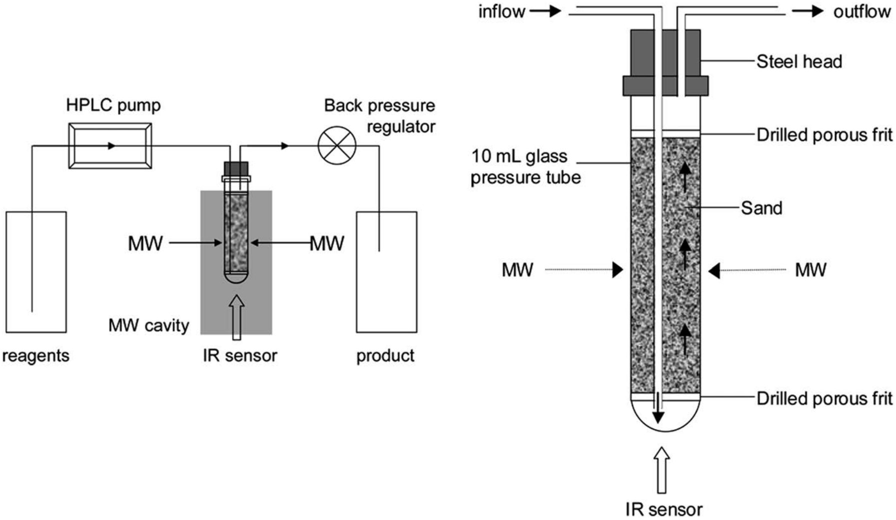

Figure 1.11 Set-up for flow reactions with solid support (sand). Reproduced from ref. 61 with permission.

Figure 1.12.[62] The authors reported a 48-fold rate increase under microwave irradiation and considered that selective heating by direct coupling of metallic species with microwave irradiation was responsible for this improvement.

This procedure was applied for library synthesis and a modified protocol for flow-based Suzuki reactions was also described. In this system pulsed microwaves, 50 W for 30 s followed by 18 s of cooling with no power application, were used in order to avoid the collapse of the polymer matrix which could melt and eventually block the tube.

Larhed described a non-resonant cavity that can be applied to a flow reactor.[63]

Microwaves are transmitted through a coaxial connector to the microwave applicator and they are applied to the reaction mixture in a tubular reactor. The axial-field microwave applicator uses a non-resonant structure that suppresses mode patterns (standing waves) in the applicator, thus avoiding hot and cold spots. The field is generated in a coil surrounding the flow reactor and this allows the microwave field to be concentrated axially inside the coil. The reactor consists of a straight tube made of microwave-transparent borosilicate glass (Figure 1.13).

The authors tested the system in several known palladium-catalysed coupling reactions.

An important requirement for a continuous flow reactor and a key principle of green chemistry is the ability to continuously monitor and adjust the reaction parameters whilst in operation. This facilitates both easy reaction optimisation and the introduction of automated safety controls.

Gómez *et al.* described a flow microwave system with on-line monitoring by nanoliter NMR.[64] They reported the design and implementation of a microliter microwave reactor hyphenated with a custom-made nanolitre-NMR set-up, comprising a less than 2 mL reaction volume for the microwave flow cell and a 6 nL detection volume microfluidic NMR chip (Figure 1.14).

As the detection volume of the NMR chip was much smaller than that of the microwave cell, the reaction volumes were submitted to microwave

Figure 1.12 Experimental set-up for a Suzuki coupling catalysed by PdEnCat. Reproduced from ref. 62 with permission.

heating at different irradiation times. In this way, different starting positions in the capillary can be analysed within the same on-flow experiment. This set-up was used for the on-line monitoring and optimisation of a Diels–Alder reaction between 2,5-dimethylfuran and dimethyl acetylenedicarboxylate, with reaction volumes in the order of μL (Figure 1.15).

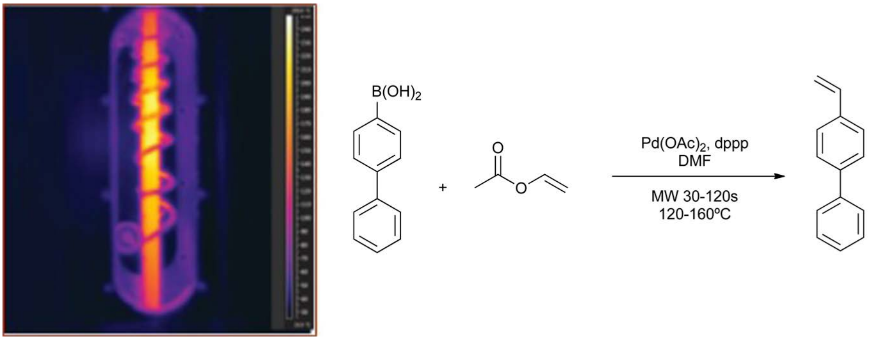

Figure 1.13 Non-resonance cavity. Application to a flow Suzuki reaction. Reproduced from ref. 63 with permission from the authors.

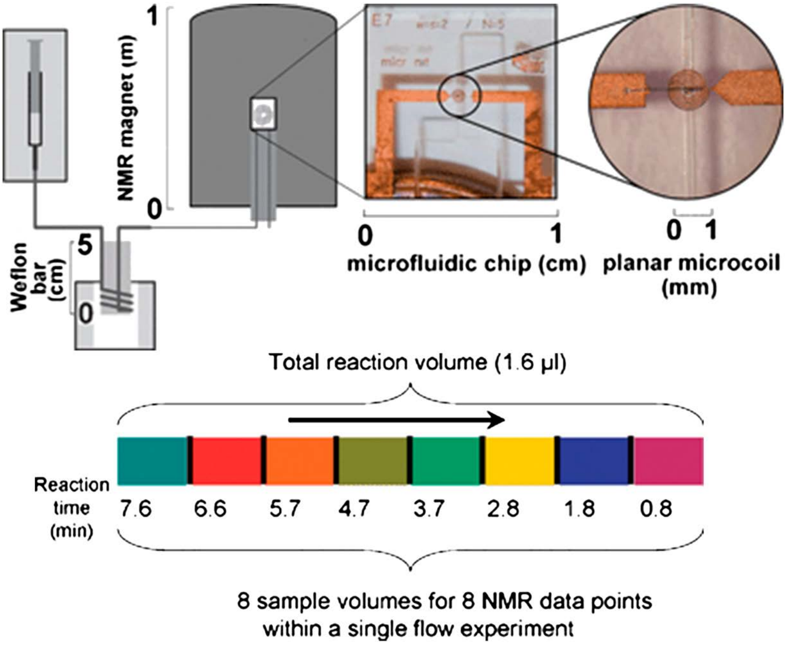

Figure 1.14 Set-up for on-line NMR analysis of a flow microwave-assisted reaction. Reproduced from ref. 64 with permission from the Royal Society of Chemistry.

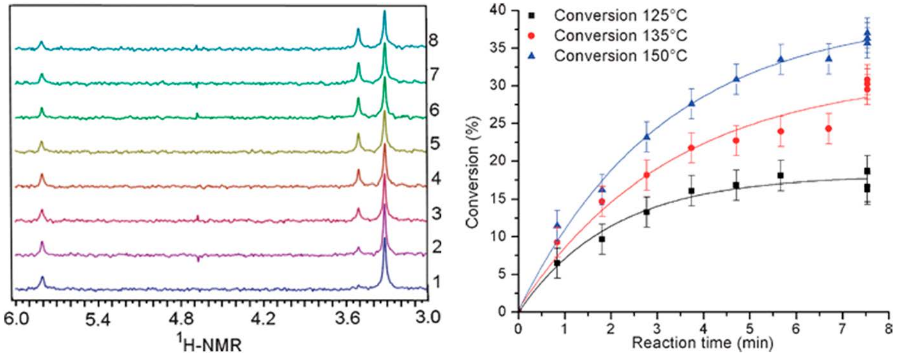

Figure 1.15 NMR optimisation and analysis of a Diels–Alder reaction. Reproduced from ref. 64 with permission from the Royal Society of Chemistry.

1.6 Conclusions

In conclusion, in this review we have attempted to show how microwave irradiation can be used under green and sustainable conditions. Rather than providing a comprehensive review, we have tried to highlight the green applications of this methodology and the synergy with other green conditions. The most obvious advantage, namely energy efficiency, requires a strong absorption of microwave irradiation by one component of the reaction mixture—either the solvent, reagents, catalyst or a susceptor. In addition to energy efficiency, the application of microwaves in conjunction with other green conditions, *e.g.* solvent-free reactions, reactions in water or neoteric solvents, has enabled the green applications of this methodology to be expanded. Finally, the use of flow conditions have solved the problem of scale-up under microwaves, a step that is hindered by the small penetration depth of the radiation at 2.45 GHz. Flow conditions also allow the on-line monitoring by NMR and the optimisation of reactions in a single experiment on a very small scale.

References

1. For example, see: (a) *Microwaves in Organic Synthesis*, ed. A. de la Hoz and A. Loupy, Wiley-VCH, Weinheim, 3rd edn, 2012; (b) *Green Chemistry for Environmental Remediation*, ed. R. Sanghi and V. Singh, Wiley, Hoboken, 2012; (c) M. P. Pollastri and W. G. Devine, *Microwave Synthesis In Green Techniques for Organic Synthesis and Medicinal Chemistry*, ed. W. Zhang and B. Cue, Wiley, Chichester, 2012, ch. 12, pp. 325–342; (d) *Microwaves in Nanoparticles Synthesis: Fundamentals and Applications*, ed. S. Horikoshi and N. Serpone, Wiley-VCH, Weinheim, 2013; (e) *Microwave Assisted Organic Synthesis*, ed. J. P. Tierney and P. Lidström, Blackwell Publishing Ltd., Oxford, 2009; (f) N. E. Leadbeater, Organic Synthesis

Using Microwave Heating, in *Comprehensive Organic Synthesis: Second Edition*, ed. P. Knochel and G. Molander, Elsevier Ltd., Oxford, 2014, ch. 10, vol. 9, pp. 234–286; (g) C. O. Kappe and A. Stadler, *Microwaves in Organic and Medicinal Chemistry*, Wiley, Weinheim, 2nd edn, 2012.

2. For example, see: (a) R. B. N. Baig and R. S. Varma, *Chem. Soc. Rev.*, 2012, **41**, 1559–1584; (b) S. L. Pedersen, A. P. Tofteng, L. Malik and K. J. Jensen, *Chem. Soc. Rev.*, 2012, **41**, 1826–1844; (c) S. R. Takkellapati, *Curr. Org. Chem.*, 2013, **17**, 2305–2322; (d) C. O. Kappe, *Chem. Soc. Rev.*, 2013, **42**, 4977–4990; (e) Z. Wu, E. Borreto, J. Medlock, W. Bonrath and G. Cravotto, *ChemCatChem*, 2014, **6**, 2762–2783; (f) G. D. Stefanidis, A. N. Muñoz, G. S. J. Sturm and A. Stankiewicz, *Rev. Chem. Eng.*, 2014, **30**, 233–259; (g) A. de la Hoz, A. Díaz-Ortiz and A. Moreno, *Chem. Soc. Rev.*, 2005, **34**, 164–178.
3. P. T. Anastas and J. Warner, *Green Chemistry. Theory and Practice*, Oxford University Press, Oxford, 1998.
4. B. König, *Sustainability in the organic chemistry lab course*, http://www.oc-praktikum.de/nop/en-entry, last accessed on 10th January, 2015.
5. M. J. Gronnow, R. J. White, J. H. Clark and D. J. Macquarrie, *Org. Process Res. Dev.*, 2005, **9**, 516–518.
6. T. Razzaq and C. O. Kappe, *ChemSusChem*, 2008, **1**, 123–132.
7. J. D. Moseley and C. O. Kappe, *Green Chem.*, 2011, **13**, 794–805.
8. F. Schneider, T. Szuppa, A. Stolle, B. Ondruschka and H. Hopf, *Green Chem.*, 2009, **11**, 1894–1899.
9. F. Benaskar, A. Ben-Abdelmoumen, N. G. Patil, E. V. Rebrov, J. Meuldijk, L. A. Hulshof, V. Hessel, U. Krtschil and J. C. Schouten, *J. Flow Chem.*, 2011, **1**, 74–89.
10. (a) A. Loupy, A. Petit, J. Hamelin, F. Texier-Boullet, P. Jaquault and D. Mathé, *Synthesis*, 1998, 1213–1234; (b) S. K. Das, *Synlett*, 2004, 915; (c) K. Bougrin, A. Loupy and M. Soufiauoi, *J. Photochem. Photobiol., C*, 2005, **6**, 139–167; (d) J. A. Seijas and M. P. Vázquez-Tato, *Chim. Oggi*, 2008, **26**, 4; (e) V. Pistarà, A. Rescifina, M. A. Chiacchio and A. Corsaro, *Curr. Org. Chem.*, 2014, **18**, 417–445; (f) M. B. Gawande, V. D. B. Bonifácio, R. Luque, P. S. Branco and R. S. Varma, *ChemSusChem*, 2014, **7**, 24–44.
11. A. Loupy, A. Petit, M. Ramdani, C. Yvanaef, M. Majdoub, B. Labiad and D. Villemin, *Can. J. Chem.*, 1993, **71**, 90–95.
12. S. J. Song, S. J. Cho, D. K. Park, T. W. Kwon and S. A. Jenekhe, *Tetrahedron Lett.*, 2003, **44**, 255–257.
13. M. Staderini, N. Cabezas, M. L. Bolognesi and J. C. Menéndez, *Synlett*, 2011, 2577–2579.
14. A. Arrieta, J. R. Carrillo, F. P. Cossio, A. Díaz-Ortiz, M. J. Gómez-Escalonilla, A. de la Hoz, F. Langa and A. Moreno, *Tetrahedron*, 1998, **54**, 13167–13180.
15. V. Polshettiwar and R. S. Varma, *Tetrahedron Lett.*, 2008, **49**, 7165–7167.
16. V. Georgakilas, K. Kordatos, M. Prato, D. M. Guldi, M. Holzinger and A. Hirsch, *J. Am. Chem. Soc.*, 2002, **124**, 760–761.
17. (a) F. G. Brunetti, M. A. Herrero, J. de M. Muñoz, S. Giordani, A. Díaz-Ortiz, S. Filippone, G. Ruaro, M. Meneghetti, M. Prato and E. Vázquez, *J.*

Am. Chem. Soc., 2007, **129**, 14580–14581; (b) F. G. Brunetti, M. A. Herrero, J. de M. Muñoz, A. Díaz-Ortiz, J. Alfonsi, M. Meneguetti, M. Prato and E. Vázquez, *J. Am. Chem. Soc.*, 2008, **130**, 8094–8100; (c) E. Vázquez, F. Giacalone and M. Prato, *Chem. Soc. Rev.*, 2014, **43**, 58–69.

18. N. Rubio, M. A. Herrero, M. Meneguetti, A. Díaz-Ortiz, M. Schiavon, M. Prato and E. Vázquez, *J. Mater. Chem.*, 2009, **19**, 4407–4413.
19. D. Sharma, Bandna, C. B. Reddy, S. Kumar, A. K. Shil, N. R. Guha and P. Das, *RSC Adv.*, 2013, **3**, 10335–10340.
20. A. Mahindra, N. Patel, N. Bagra and R. Jain, *RSC Adv.*, 2014, **4**, 3065–3069.
21. A. Ruiz-Carretero, J. R. Ramírez, A. Sánchez-Migallón and A. de la Hoz, *Tetrahedron*, 2014, **70**, 1733–1739.
22. L. Bettanin, G. V. Botteselle, M. Godoi and A. L. Braga, *Green Chem. Lett. Rev.*, 2014, **7**, 105–113.
23. T. Besson and C. O. Kappe, Microwave Susceptors, in *Microwaves in Organic Synthesis: Third Edition*, ed. A. de la Hoz and A. Loupy, Wiley-VCH, Weinheim, 2012, ch. 7, vol. 1, pp. 297–346.
24. B. Garrigues, C. Laporte, R. Laurent, A. Laporterie and J. Dubac, *Liebigs Ann.*, 1996, 739–741.
25. C. Laporterie, A. Oussaid and B. Garrigues, *C. R. Acad. Sci., Ser. IIc: Chim.*, 2000, **3**, 321.
26. M. Soukri, G. Guillaumet, T. Besson, D. Aziane, M. Aadil, E. M. Essassi and M. Akssira, *Tetrahedron Lett.*, 2000, **41**, 5857–5860.
27. S. Frère, V. Thiéry, C. Bailly and T. Besson, *Tetrahedron*, 2003, **59**, 773–779.
28. S.-H. Park, S.-M. Bak, K.-H. Kim, J.-P. Jegal, S.-I. Lee, J. Lee and K.-B. Kim, *J. Mater. Chem.*, 2011, **21**, 680–686.
29. I. Fotiou, A. Baltopoulos, A. Vavouliotis and V. Kostopoulos, *J. Appl. Polym. Sci.*, 2013, **129**, 2754–2764.
30. J. M. Kremsner and C. O. Kappe, *J. Org. Chem.*, 2006, **71**, 4651–4658.
31. B. Gutmann, D. Obermayer, B. Reichart, B. Prekodravac, M. Irfan, J. M. Kremsner and C. O. Kappe, *Chem.–Eur. J.*, 2010, **16**, 12182–12194.
32. J. M. Kremsner, A. Stadler and C. O. Kappe, *J. Comb. Chem.*, 2007, **9**, 285–291.
33. C. O. Kappe and M. Damm, *Mol. Diversity*, 2012, **16**, 5–25.
34. B. Yahaya, S. Izman, M. Konneh and N. Redzuan, *Adv. Mater. Res.*, 2014, **845**, 426–433.
35. A. Díaz-Ortiz, E. Díez-Barra, A. de la Hoz, A. Moreno, M. J. Gómez-Escalonilla and A. Loupy, *Heterocycles*, 1996, **43**, 1021–1030.
36. A. Díaz-Ortiz, A. de la Hoz, J. Alcázar, J. R. Carrillo, M. A. Herrero, A. Fontana and J. de M. Muñoz, *Comb. Chem. High Throughput Screening*, 2007, **10**, 163–169.
37. P. Krammer and H. Vogel, *J. Supercrit. Fluids*, 2000, **16**, 189–206.
38. D. Dallinger and C. O. Kappe, *Chem. Rev.*, 2007, **107**, 2563–2591.
39. N. E. Leadbeater and M. Marco, *Angew. Chem., Int. Ed.*, 2003, **42**, 1407–1409.
40. R. K. Arvela, N. E. Leadbeater, M. S. Sangi, V. A. Williams, P. Granados and R. D. Singer, *J. Org. Chem.*, 2005, **70**, 161–168.

41. N. E. Leadbeater and R. J. Smith, *Org. Lett.*, 2006, **8**, 4589–4591.
42. C. Ericsson and L. Engman, *J. Org. Chem.*, 2004, **69**, 5143–5146.
43. P. S. Baran, D. P. O'Malley and A. L. Zografos, *Angew. Chem., Int. Ed.*, 2004, **43**, 2674–2677.
44. C. R. Strauss, *Aust. J. Chem.*, 1999, **52**, 83–96.
45. J. M. Kremsner and C. O. Kappe, *Eur. J. Org. Chem.*, 2005, 3672–3679.
46. S. Santra and P. R. Andreana, *Angew. Chem., Int. Ed.*, 2011, **50**, 9418–9422.
47. N. Rubio, M. A. Herrero, A. de la Hoz, M. Meneghetti, M. Prato and E. Vázquez, *Org. Biomol. Chem.*, 2010, **8**, 1936–1942.
48. R. Martínez-Palou, *Mol. Diversity*, 2010, **14**, 3–25.
49. N. E. Leadbeater and H. M. Torrenius, *J. Org. Chem.*, 2002, **67**, 3145–3148.
50. R. S. Varma and V. V. Namboodiri, *Chem. Commun.*, 2001, 643–644.
51. J. Fraga-Dubreuil and J. P. Bazureau, *Tetrahedron Lett.*, 2001, **42**, 6097–6100.
52. F. Pena-Pereira and J. Namiesnik, *ChemSusChem*, 2014, **7**, 1784–1800.
53. B. Patil, S. S. Shendage and J. M. Nagarkar, *Synthesis*, 2013, **45**, 3295–3299.
54. (a) W. Zhang, *Green Chem.*, 2009, **11**, 911–920; (b) W. Zhang, *Top. Curr. Chem.*, 2006, **266**, 145–166.
55. K. Olofsson, S.-Y. Kim, M. Larhed, D. P. Curran and A. Hallberg, *J. Org. Chem.*, 1999, **64**, 4539–4541.
56. M. A. Herrero, J. Wannberg and M. Larhed, *Synlett*, 2004, 2335–2338.
57. I. R. Baxendale, J. J. Hayward and S. V. Ley, *Comb. Chem. High Throughput Screening*, 2008, **10**, 802–836.
58. T. Cablewski, A. F. Faux and C. R. Strauss, *J. Org. Chem.*, 1994, **59**, 3408–3412.
59. P. He, S. J. Haswell and P. D. I. Fletcher, *Lab Chip*, 2004, **4**, 38–41.
60. (a) E. Comer and M. G. Organ, *J. Am. Chem. Soc.*, 2005, **127**, 8160–8170; (b) E. Comer and M. G. Organ, *Chem.–Eur. J.*, 2005, **11**, 7223–7227.
61. M. C. Bagley, R. L. Jenkins, M. C. Lubinu, C. Mason and R. Wood, *J. Org. Chem.*, 2005, **70**, 7003–7006.
62. I. R. Baxendale, C. M. Griffiths-Jones, S. V. Ley and G. K. Tranmer, *Chem.–Eur. J.*, 2006, **12**, 4407–4416.
63. P. Öhrngren, A. Fardost, F. Russo, J.-S. Schanche, M. Fagrell and M. Larhed, *Org. Process Res. Dev.*, 2012, **16**, 1053–1063.
64. M. V. Gómez, H. H. J. Verputten, A. Díaz-Ortíz, A. Moreno, A. de la Hoz and A. H. Velders, *Chem. Commun.*, 2010, **46**, 4514–4516.

CHAPTER 2

Microwave-Assisted Plant Extraction Processes

RAFAEL B. MATO CHAÍN*[a], JUAN MONZÓ-CABRERA[b]
AND KATALIN SOLYOM[c]

[a]Departamento de Ingeniería Química y Tecnología del Medio Ambiente, Universidad de Valladolid, c/ Dr Mergelina S/N, 47011 Valladolid, Spain; [b]Departamento de Tecnologías de la Información y las Comunicaciones, Universidad Politécnica de Cartagena, Campus Muralla del Mar S/N, 30202 Cartagena, Spain; [c]Fraunhofer Institute for Interfacial Engineering and Biotechnology, Physical Process Technology, Nobelstraße 12, 70569 Stuttgart, Germany
*E-mail: rbmato@iq.uva.es

2.1 Introduction

The biodiversity of plants has provided a boundless source of chemical compounds with uses in medicine and as food, feed, cosmetics, fibre and energy throughout human history. Therefore, the exploration and exploitation of their inherent potential has always been at the centre of attention. Nowadays, numerous species are commonly used as first resources of edible oils, flavours, fragrances, pigments, and bioactive compounds. Also the re-use of industrial waste streams and by-products of plant origin is being widely considered in order to obtain high added-value components, fibres and energy sources, thus promoting an energy- and resource-effective future.

RSC Green Chemistry No. 47
Alternative Energy Sources for Green Chemistry
Edited by Georgios Stefanidis and Andrzej Stankiewicz

Published by the Royal Society of Chemistry, www.rsc.org

In order to selectively separate these compounds from the plant matrix, different extraction processes are applied. As the substances of interest mostly have intracellular localization, the natural cells have first to be damaged in order to facilitate accessibility to the product in question. This primary stage of the processes is often recognised as the rate limiting step, causing slow process kinetics and therefore leading to long operation times, low recovery efficiencies or high operating costs. Among other novel cell disruption technologies, the use of microwaves has emerged as an effective and environmentally friendly technology, since microwave irradiation can improve cell wall rupture of high moisture plant materials. Due to the rapid heating and evaporation of intracellular water, the resulting pressure gradient may lead to cell wall damage.

Microwave technology is already widely used for analytical purposes, achieving greener and more economical procedures and using less harmful solvents in rapid procedures. Despite the large number of research articles on this topic, the industrialization of microwave-assisted extraction processes has not spread to the market. The use of expensive electrical energy to transfer microwaves into a material and the high cost of equipment can lead to high capital and operating costs in industrial-scale applications. For this reason, an effective and short microwave pre-treatment of the natural material may be more convenient prior to conventional processing. This additional stage would not replace the existing process, but may modify the cell structure in order to facilitate the conventional method, thus improving the kinetics of the conventional process.

This chapter aims to review first the basics of microwave heating, the interaction of plant matrixes with the electromagnetic field providing examples, and also the available bench-, pilot- and industrial-scale applications in the field of extraction processes. Second, some possible compounds of interest are outlined, and microwave-assisted extraction procedures are strategically explained, depending on conditions such as the presence or absence of solvents or the operating pressure. In this section, the main driving parameters (energy, power, time, temperature, solvent, pressure and particle size) and their influence on process performance are also reviewed. Finally, extraction kinetics and modelling are discussed, and special attention is paid to the scalability of these extraction processes considering experimental quantification of the absorbed microwave energy.

2.2 Microwave Heating Foundations

It is very well known that dielectric materials are heated when high-frequency electromagnetic waves are applied to them. Many scientists such, as Debye,[1] Fröhlich[2] and Daniel[3] showed that the origin of microwave heating is based mainly on the capability of the electric field to polarise dipolar molecules and to move ionic charges within the dielectric materials. These materials are usually characterised by their electric permittivity, which is a macroscopic property that includes all the polarization effects occurring at microscopic levels within the material volume.[4]

The absolute permittivity of a material, ε^*, is a complex quantity that provides a description of the macroscopic interaction between the electric displacement field vector $\vec{D}$, and the electric field intensity vector, $\vec{E}$, as expressed in eqn (2.1):[5]

$$\vec{D} = \varepsilon^* \vec{E} = \varepsilon_0 \varepsilon_r \vec{E} = \varepsilon_0 (\varepsilon' - j\varepsilon'') \vec{E} \tag{2.1}$$

where $\varepsilon_0 = 8.8541 \times 10^{-12}$ is the vacuum permittivity, ε_r is the so-called complex relative permittivity, ε' is the dielectric constant, and ε'' the loss factor. It should be noted that despite this nomenclature the dielectric constant, in fact, presents a variable behaviour with frequency, temperature and humidity, and therefore some authors prefer to use the term 'real part of the relative permittivity' to refer to the dielectric constant of materials.

The dielectric constant is responsible for electric field reflection at the material's surfaces. In fact, the higher the dielectric constant, the lower the electric field magnitude within the material. Additionally, when the dielectric constant value increases then the electric wavelength within the material decreases and, thus, maxima and minima of the electric field are closer within the material.[6]

The loss factor is responsible for converting electromagnetic energy into heat within the material. Usually, the loss factor includes several loss mechanisms such as dipolar or polarization losses, conduction effects, Maxwell–Wagner losses, *etc.*, although at microwave frequencies dipolar and conduction losses are predominant.[4] When the electric field goes straight through the dielectric material, electromagnetic energy turns into heat due to dielectric losses. This means that, as long as the electric field travels across the dielectric, it decreases its energy and the dielectric increases its temperature.

The ratio of the loss factor to the dielectric constant is called the loss tangent, given in eqn (2.2), and is used to characterize dielectric losses.

$$\tan\delta = \frac{\varepsilon''}{\varepsilon'} \tag{2.2}$$

In polar materials (such as water or products containing humidity—with molecules presenting asymmetric charge distributions) electric field changes force the reorientation of the dipolar molecules. At low frequencies the dipolar molecules have enough time to follow the electric field's sinusoidal variations and the dielectric constant shows a very high value, but at microwave frequencies the dipoles are not able to reach their original positions when trying to follow the electric field reversals and under these conditions the dielectric constant decreases and the loss factor increases.

Table 2.1 shows the dielectric properties of some usual solvents and food products used in microwave-assisted extraction (MAE) processes at 2.45 GHz. It has been extracted and adapted from several authors.[7–11]

Obviously, when mixing solvents and solid products in order to perform MAE, the whole mix will also vary its properties when compared to individual components, and additional permittivity measurements are needed. Temperature dependent measurements are also needed in order to determine

Table 2.1 Permittivities of solvents, fresh fruits and vegetables at 2.45 GHz. Adapted from ref. [7–11]

Material	ε'	ε''	Temperature (°C)	References
Acetone	20.7	11 499	20	7–9
Acetronitrile	37.5	N/A	20	7–9
Apple	54	10	23	10 and 11
Banana	60	18	23	10 and 11
Cantaloupe	66	13	23	10 and 11
Carrot	56	15	23	10 and 11
Cucumber	69	12	23	10 and 11
Ethanol	24.3	6075	20	7–9
Ethyl acetate	6.02	3200	20	7–9
Grape	65	17	23	10 and 11
Grapefruit	73	15	23	10 and 11
Hexane	1.89	N/A	20	7–9
Kiwi fruit	66	17	23	10 and 11
Lemon	71	14	23	10 and 11
Mango	61	14	23	10 and 11
Methanol	32.6	20 864	20	7–9
Onion	64	14	23	10 and 11
Orange	69	16	23	10 and 11
Peach	67	14	23	10 and 11
Pear	64	13	23	10 and 11
Potato	57	17	23	10 and 11
2-Propanol	19.9	8933	20	7–9
Radish	67	15	23	10 and 11
Squash	62	13	23	10 and 11
Strawberry	71	14	23	10 and 11
Water	78.3	12 293	20	7–9

the behaviour of the solvent-solid mixture's permittivity during MAE. Unfortunately, few data have been found for the dielectric properties of mixtures involved in MAE processes. These properties are, however, of the utmost importance for several reasons:

- They characterize how the electric field will distribute within the vessels or ducts during MAE and thus how heat will distribute within the mixture.
- The knowledge of permittivity and the volume to be processed are necessary to predict resonant frequencies of microwave applicators and their power efficiencies which are required for the proper design of microwave applicators[12] and their associated filters.[13]

2.2.1 Volumetric Heating Term

The volumetric heat (W m^{-3}) caused by microwave energy can be derived by using the Poynting vector, some of Maxwell's laws and the divergence theorem as explained in ref. 4. Since the electric field is not constant within the sample or liquid to be heated, and also the dielectric constant will vary with temperature, the spatial volumetric heating term will depend both on the electric field spatial distribution and the dielectric properties at each point of the body to be heated.

Eqn (2.3) shows the volumetric heat term as a function of these spatial distributions:

$$Q_{\text{gen}}(x,y,z) = \tfrac{1}{2}\,\omega\varepsilon_0\varepsilon''(x,y,z)\,|\vec{E}\,(x,y,z)|^2 = \omega\varepsilon_0\varepsilon''\,|\vec{E}_{\text{rms}}(x,y,z)|^2 \tag{2.3}$$

where Q_{gen} (x,y,z) is the volumetric heat distribution (W m^{-3}), $\varepsilon''(x,y,z)$ is the loss factor distribution, $E(x,y,z)$ is the electric field vector distribution, $\vec{E}\,(x,y,z)$ is the electric field vector spatial distribution expressed in peak values, and $\vec{E}_{\text{rms}}(x,y,z)$ is the electric field vector spatial distribution expressed in effective values.

Figure 2.1 shows the scheme of a cylindrical microwave applicator where the magnetron is directly applied to the cavity, whereas Figure 2.2 shows the volumetric heat pattern in the liquid contained in the inner PTFE Tube. The scheme simulates a PTFE tube containing a solvent with ethanol and water mixture and grape mill solid particles. The dielectric constant for the liquid–solid mixture employed in these simulations was $\varepsilon_r = 28 - 12i$.

As can be seen from Figure 2.2, the volumetric heat pattern is not uniform for this applicator. However, in the case of liquids containing particles, three mechanisms will homogenize the temperature distribution:

- Internal convection movements due to density differences in the liquid
- Vaporisation processes
- Liquid turbulence due to liquid movement.

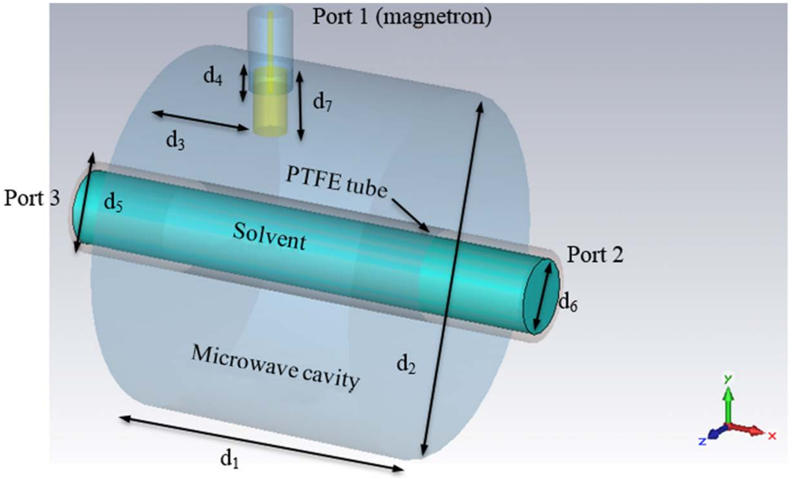

Figure 2.1 Scheme of a cylindrical microwave applicator with a PTFE tube containing ethanol/water solvent and grape mill particles. Internal dimensions (cm): $d_1 = 13$, $d_2 = 16.5$, $d_3 = 0.5$, $d_4 = 4$, $d_5 = 4.2$, $d_6 = 3.4$ and $d_7 = 2.8$.

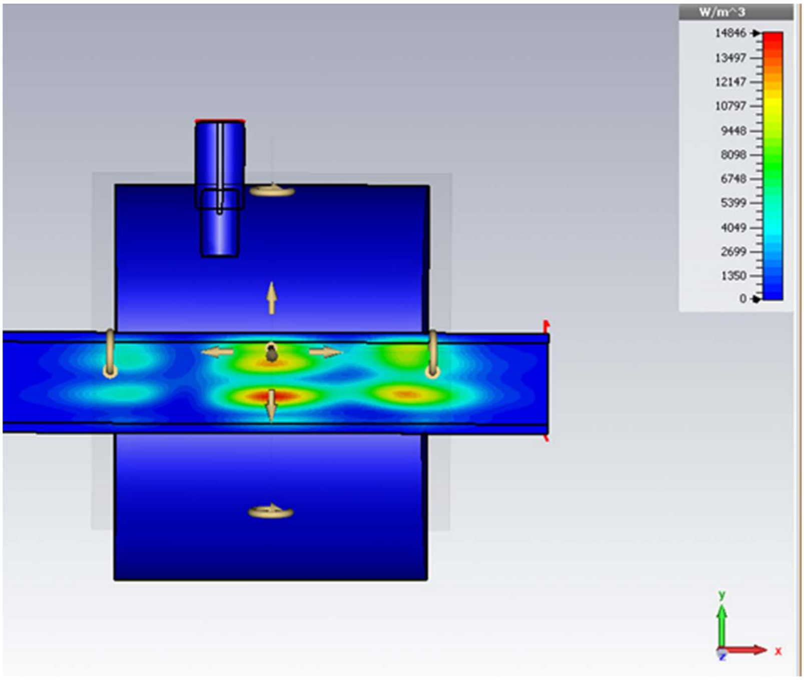

Figure 2.2 Volumetric heat distribution within the tube.

However, despite these effects, correct microwave heating patterns should be validated by using proper measuring techniques such as thermographic cameras or by having optical fibre thermometers properly positioned.

2.3 Microwave-Assisted Extraction Systems

Nowadays, MAE publications mainly describe three types of microwave systems: modified domestic microwave ovens, commercial MAE systems including, in most cases, closed vessels with temperature and pressure monitoring, and continuous microwave applicators. Each of them has its own features, advantages and drawbacks that will be analysed in next sections.

Basically, a microwave heating system usually consists of a magnetron that irradiates at a power level controlled by a power supply. Waveguides transport the irradiated power into a microwave cavity where the chemical reactor is inserted. Depending on the microwave heating device used, these basic elements can be very different. Additional elements such as circulators for magnetron protection, directional couplers for incident and reflected power measurements, and temperature and weight sensors can be included in high quality microwave extractors also, thus increasing the system cost.

2.3.1 Usage of Modified Domestic Microwave Ovens

Although nowadays there are specialized microwave ovens for extraction purposes, the prices of domestic ovens make them very attractive for carrying out MAE tests at low cost. Many works in literature make use of domestic ovens with some modifications to be able to extract the irradiated substances. For instance, domestic microwave ovens have been used for MAE of natural antioxidants from spent espresso coffee grounds[14] and also to extract compounds from other vegetable substances such as *Myrtus communis* L. leaves,[15] dragon fruit peel,[16] mulberry leaves,[17] *Dunaliella tertiolecta,*[18] *Equisetum arvense* waste,[19] cocoa (*Theobroma cacao* L.) leaves,[20] carrot peel,[21] grape seeds,[22] cottonseed oil,[23] *etc.*

Figure 2.3 shows a scheme of a typical configuration of a MAE test setup that makes use of a modified domestic microwave oven. Usually, the flask containing the solvent and materials to be processed is sealed, and a tube transports the evaporated substances into an external condenser and then to a graduated cylinder.[22–24]

Despite their low cost, researchers should take into account some important features of domestic microwave ovens when carrying out the MAE tests with these devices:

- Microwave power cannot be controlled in these domestic ovens. The only available control of irradiation power is a very simple one: ON/OFF. The indicated power, if any is present, is just an effective one since domestic ovens always irradiate at maximum power and then include some OFF working cycles to simulate different power level regimes. For instance, for a typical microwave oven irradiating at around 800 watts, the only way to produce an effective power of 400 watts is to use an OFF working cycle for 50% of the time.

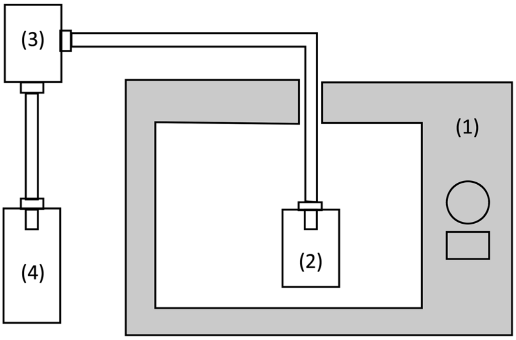

Figure 2.3 Typical modified domestic microwave oven for MAE purposes: (1) microwave oven, (2) flask, (3) external condenser and (4) graduated cylinder.

- The temperature of the magnetron will rise during the process due to poor air refrigeration and, sometimes, high temperatures can switch off the microwave oven. Additionally, this temperature rise will also change magnetron power efficiency.
- When using flasks rotating at the oven cavity or even for low loss conditions within the microwave cavity, power and frequency pulling will occur. This means that both the power and operating frequency of the microwave oven will change as the reflection coefficient of the cavity changes during the process. Irradiated power levels could vary by up to 15% of the nominal value and the frequency could vary by around ±0.2%.[4] This means that for 800 watts of nominal power, the real irradiated power of the domestic microwave oven could be around 680 watts under some reflection conditions. Therefore, good matching levels should be ensured in order to avoid these effects.

Due to these considerations, researchers using domestic microwave ovens for MAE should be aware that it is very complicated to know the real power used within the microwave cavity, and only thermodynamic measurements including evaporation, conduction, radiation and convection losses can be used for these purposes.[4,25]

2.3.2 Usage of Commercial Microwave Reactors

In order to produce an efficient conversion of electromagnetic energy into heat in the most reproducible way, laboratory-dedicated microwave reactors should be chosen instead of domestic ovens. These systems use power supplies able to produce continuous microwave irradiation, which allows easier power control. Additionally, the fixed containers and structures within the microwave cavity produce better process reproducibility.[26]

The basic features of these commercial microwave reactors can be summarized as follows:[26]

- homogeneous temperature profiles by using mode stirrers and/or vessel rotation
- flask geometry design taking into account the penetration depth
- temperature and pressure control within the reaction chamber for continuous monitoring and control of MAE
- vessel safety mechanisms and proper microwave leakage filters.

Table 2.2 shows a summary of different commercial microwave reactors for extraction with different specifications.[27–31] It can be appreciated that most of them allow working at high pressure levels, high power control, and high temperature values. Additionally, most of them allow vapour and gas extraction when certain pressure levels are detected within the vessels and computer control and temperature uniformity are often offered in these systems.

Table 2.2 Summary of commercially available microwave-assisted extraction systems.

Producer/model	Max. power (watts)	Max. pressure (bar)	Max. working temperature (°C)	Max. number of vessels	Vessel vol. (ml)	Vessel materials	Cavity	Vessel	Website
Anton paar/monowave 300	850	30	300	1	Up to 30	PEEK	Monomode	Closed	27
Anton paar/masterwave BTR	1500	30	250	1	1000	PTFE	Multimode	Closed	27
Biotage/biotage advancer	1200	20	250	1	350	PTFE	Multimode	Closed	28
CEM/star	N/A	Ambient pressure	N/A	2	250	Pyrex, quartz and PTFE	Monomode	Open	29
CEM/MARS 6	1800	103	300	Up to 40	80	Silicon carbide, rhodium, glass, PFA teflon	Multimode	Closed	29
Milestone/FlowSYNTH	1000	30	200	Continuous	100/min	Glass	Multimode	Closed	30
Milestone/UltraCLAVE	1000	200	300	Up to 40	From 12 to 2000	TFM, quartz	Multimode	Closed	30
Sineo microwave/JUPITER	1300	40	250	12	100	PTFE and fiber composite	Multimode	Closed	31

2.3.3 Continuous and High-Scale Microwave Applicators for MAE

Some continuous systems for MAE have been found in the scientific literature and in commercial firms. An industrial continuous microwave-assisted system to condition olive paste was built and implemented as an industrial process. The developed system was tested to assess its performance during implementation in an industrial olive oil extraction plant, showing great potential to become an alternative technique with which to condition olive paste. The reduced process time of the microwave system resulted in lower oxidation of the olive oil and consequently in a reduction in the peroxide value compared to the traditional method.[32]

Additionally, this also caused a reduction of the phenolic compounds usually associated with the spicy and bitter notes of olive oil. The microwave heater was manufactured in this case by EMitech.[33]

Advanced Microwave Technologies (AMT) produces a scalable continuous-flow microwave applicator to heat liquids such as blood or fruit juices that can also be applied to microwave-assisted extraction processes.[34] This patented technology is based on a metallic cylindrical cavity containing an inner dielectric tube that allows the material to be processed while flowing along the cylindrical applicator.[35]

Sairem also offers microwave continuous flow reactors working at 2.45 GHz and 915 MHz frequencies.[36] These reactors are equipped with auger-type stirring systems to ensure good homogeneity of heating and good product transfer. Püschner manufactures a 100 kW/915 MHz microwave flow-reactor for 1–2 ton h^{-1} production working at up to 30 bar and 300 °C.[37]

C-Tech Innovation has developed a continuous flow reactor that allows the scale-up of chemical reactions from lab scale to production scale.[38] Their standard products allow power levels from 1 to 6 kilowatts, flow rates up to 1 L min^{-1}, pressure levels up to 30 bars and working temperatures up to 250 °C. Even higher yields have been achieved by Microwave Chemical.[39] They have successfully developed a large-scale microwave flow reactor with a production rate of 12 tons per day.

A very interesting literature review of self-assembled continuous flow microwave reactors can be found in ref. 39. Most of the systems described therein use a pump to flow the solvent and materials through a microwave cavity. Monomode or multimode microwave applicators are used to heat the moving fluid, and PTFE, PEEK and glass are the materials most used to direct the liquid flow through the microwave cavity.

2.4 Plants and Components of Interest for Microwave-Assisted Extraction Processes

2.4.1 Essential Oils from Herbs

Essential oil extraction from more than 3000 plants possesses considerable history within extraction technology and is of great interest also to the present world market. The oils are used mainly by the cosmetic and flavour industries but also by the food and pharmaceutical industries as preservatives and flavour components.

Essential oils are found in special secretory tissues (for example, oil-containing glands and trichomes) on the plant surface or within the plant tissues, producing and discharging substances in order to provide healing and defensive capabilities to the plant.[40] In order to induce the release of these compounds steam distillation is used, where the high temperature steam flows through the oil-containing secretory tissues and lets the oil content be released. The remaining secretory structure becomes deflated through the loss of its content.[41] The conventional steam distillation and hydrodistillation processes can be replaced by microwave extraction technology offering a fast rupture of the oil-containing glands and thereby accelerating the process kinetics.[42–44]

2.4.2 Phenolic Compounds and Antioxidants

Phenolic compounds belong to the group of widely variable secondary metabolites in plant tissues, where they are involved in the defensive reaction against ultraviolet radiation or the aggression by pathogens. Polyphenols can be classified into different groups according to the number of contained phenol rings and to the ring-binding structural elements. Groups are distinguished as follows: phenolic acids, flavonoids, stilbenes, and lignans, and their subcategories. In addition to this diversity, polyphenols may be associated with various carbohydrates and organic acids and with one another.[45]

The great interest in the food industry has emerged not only due to their colouring and organoleptic functions, but also to their biological effects such as antioxidant capacity, antimicrobial activity and supposed anti-carcinogenic power. Through these features polyphenols improve the quality and nutritional value of foods as they are believed to protect against chronic human diseases such as heart disease, cancer, diabetes and hypertension.[46,47]

Among a wide variety of plants, herbs and fruits containing different polyphenol classes, microwave-assisted extraction of flavonoids was reviewed and compared to other novel extraction technologies such as pressurized extraction, ultrasound extraction or supercritical extraction.[45,48] More recently, maritime pine containing considerable amounts of condensed tannins,[49] as well as pomace of Red Delicious and Jonathan apple varieties[50] and eucalyptus leaves[51] were studied using microwave extraction technologies in order to obtain biologically active polyphenol agents. Beside the comparable or superior extraction quality and quantity obtained by microwaves, thermal degradation of the labile phenolic compounds (especially anthocyanins) can be avoided due to the short treatment required at high temperature.

2.4.3 Oils, Lipids and Fatty Acids

The analysis of lipids and the fatty acid methyl ester profile of edible oils, such as soybean, rape and sunflower oil, are of interest to the food industry. Microwave technology enabled their faster qualitative and quantitative determination, generating less solvent waste during the analytical process compared to the existing ISO methods.[52]

Lately, the quality of the oils and their bioactive constituents came to be the focus of attention from the nutritional point of view due to their positive effects. Plants and seeds containing considerable amounts of polyunsaturated fatty acids (PUFA), including omega-fatty acids, docosahexaenoic acid (DHA), triglycerides and triterpenoids, which have antioxidant, antiseptic and antifungal characteristics, have been studied using novel extraction technologies, also applying microwave irradiation with positive outcomes. The structural degradation of neem seeds due to microwave energy reduced the extraction time of oil from 10 h in a Soxhlet extractor to 24 min with MAE, without quality changes in the fatty acid profile of the extract.[53] Likewise, the microwave extraction of soybean germs, seaweed[54] or pitaya oil[55] resulted in enhanced kinetics and extraction yield.

Another use of extracted lipids from non-edible plant tissues is the conversion into biodiesel as was proposed in the case of Chinese Tallow seeds with a lipid content of 32.5%.[56] Nevertheless, in the field of biodiesel production, the lipid extraction from microalgae covers a remarkable research area in the field of lipid recovery from plant tissues.[57]

2.4.4 Polysaccharides and Pectin Extraction

Among polysaccharide extraction processes the extraction of pectin is widely used in order to valorise waste streams of fruit and vegetable processing. Pectin is a complex polysaccharide composed of α-D-(1 → 4) galacturonic acids, which can be found in primary cell walls and in the middle lamellae of higher plant tissues. These high molecular weight compounds are closely connected with the other polymer components in the cell walls in order to inhibit their release from the cell matrix. Pectin is abundantly used by the food industry as a gelling, stabilizing and thickening agent. Conventional extraction methods involve the use of hot dilute mineral solutions imlying long extraction times depending on the raw material and the desired pectin quality.[58] Due to the long processing times the extracted pectin suffers from degradation, thus several pre-treatment processes have been proposed to enhance process kinetics by cell disruption and enzyme inactivation.[59] Microwave pre-treatments and microwave-assisted extractions have been used in the case of citrus fruit residues such as orange,[59] lime[60] and grapefruit[58] peels. Other fruit wastes such as apple pomace,[61] jackfruit rinds[62] and dragon fruit peel[63] were also used as raw materials. In all cases microwave irradiation highly improved the extraction kinetics and resulted in equal, or even better, extract quality.

2.5 Microwave-Assisted Extraction Techniques

Conventional extraction and maceration processes suffer from large amounts of solvent use, long processing times, sometimes at elevated temperatures, and thus the degradation of thermo-labile bioactive compounds. The use of microwaves, due to their special heating mechanism, was first reported as a promising new technology in organic extraction intensification in 1986 by the development of extraction protocols for lipids, anti-nutritive and pesticides from different materials including seeds and other foods.[64–66] Besides its use for analytical purposes, considering the upscaling option, microwave extraction was proposed for further research concerning extraction processes on an industrial scale.[67–69]

Two main principles can be distinguished in microwave extraction techniques:[65] first, when the microwave irradiation is used for direct heating of the plant matrix and microwaves are absorbed by the material releasing the extractable components into the hot absorbing solvent, or releasing the components together with the *in situ* water inside the plant, which evaporates during the process. Solvent-free microwave extraction (SFME), microwave-assisted extraction (MAE) with non-polar solvents and microwave pre-treatments can be classified under this first criterion. The second criterion is based on the absorption of microwaves by the polar solvent, which acts as a hot solvent with improved diffusion into the plant matrix and therefore achieves more effective extraction of the compounds of interest. Most of the MAE processes belong to this group, where polar solvents are used under microwave irradiation.

Another classification criterion considers the use of opened or closed vessels in the process.[66] Opened extraction vessels only permit atmospheric pressure in the system, where the evaporating solvent and compounds may be collected outside or directed back through a reflux connection. This technique allows mild conditions as the maximum temperature depends on the solvent's atmospheric boiling point. With proper solvent selection or internal water heating, thermo-labile compounds can be successfully extracted. SFME techniques for essential oil extraction are based on such a system, but numerous refluxed open vessel processes can be also found throughout the literature.[70] On the contrary, closed vessel extractions operate under high pressure, which enables extraction at a higher temperature and, in consequence, extraction kinetics are accelerated.[48] Pressurized systems can be used both in the presence of solvent[71] or in the absence of solvent.[72]

Besides the two above-mentioned classification criteria, processes are differentiated according to the presence or absence of solvent in the system. Thus, SFME processes cover extractions where no additional solvent is used during the process, MAE processes encompass all extractions with solvent used under the microwave irradiation, including the possibility of different pressures. Finally, microwave pre-treatments are classified separately. When no solvent is used during microwave irradiation all the energy is absorbed by the plant material, damaging the cellular structure. In a later stage the solvent is added to the system, and the extraction itself takes place without the use of microwave energy.

Classification of microwave-assisted extraction technologies can be seen in Figure 2.4.

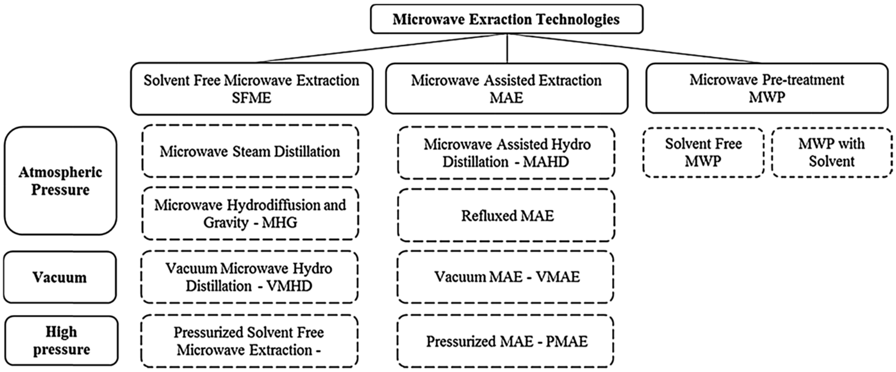

Figure 2.4 Microwave-assisted Extraction Technologies.

2.5.1 Solvent-Free Microwave Extraction

This technique has been widely used for the extraction of essential oils. During microwave irradiation to the plant material, heating and evaporation of the *in situ* water inside the plant takes place. Simultaneously, the irradiation destroys the oil-containing glands and the essential oil evaporates and is transferred, together with the produced steam, out of the extraction vessel.[73] The outgoing steam is collected by condensation outside of the microwave equipment and oil-water phases are separated. From the first conceptual designs of domestic microwaves[74,75] this technology has been improved and has reached the interest of commercialization and pilot scale use,[76] both at atmospheric pressure.

Another approach in the field of atmospheric pressure SFME has been microwave hydrodiffusion and gravity (MHG).[77] This extraction technique combines microwave heating and the earth's gravity at atmospheric pressure. It has been used for the extraction of essential oils from different aromatic plants. Based on a relatively simple principle, this method involves placing plant material in a microwave reactor, without any added solvent or water, such as in the case of primary SFME explained above. In contrast to the first technique, here the mass transfer of the essential oil does not have to depend on steam production under microwave heating because the physical phenomenon known as hydrodiffusion allows the extract (water and essential oil) to diffuse outside the plant material and drop by under gravity out of the microwave reactor, falling through a perforated Pyrex disc. Water and essential oil are collected and separated in an external vessel. After the design of a successful laboratory application the process received interest for commercialization.

Additionally, microwave hydro distillation under vacuum (VMHD) has been used in order to obtain thermally-sensitive crude extracts, which may degrade under the conventional extraction method. In this case, the dry raw material is first hydrated by the addition of water. Next, microwave irradiation is applied on the refreshed plant material which releases its extractable content. In a third step, due to a pressure reduction to 100–200 mbar, an azeotropic mixture of the water-volatile oil evaporates from the plant matrix.[78]

Pressurized SFME (PSFME) has been used for the extraction of antioxidants from sea buckthorn berries.[79] The technique is based on the repeated irradiation of the fresh plant material of high moisture content (>70%) in a closed microwave cavity. Microwaves penetrate into the plant matrix through their interaction with polar molecules, such as water, heat up the *in situ* water and the high pressure inside the cell destroys the cell wall structures releasing the solutes. Due to evaporation, the overall pressure in the cavity increases and as a consequence a higher temperature can be obtained inside the cells. This pressurized condition allows the dissolution and the extraction of less polar compounds (*e.g.* flavonol aglycons) which are not soluble in water at ambient pressure. A drawback of this technique is its limitation owing to the high moisture content required of the raw material and the thermo-labile extractable compounds.[78,79]

2.5.2 Microwave-Assisted Extraction

In the present process classification it is understood that MAE processes always occur under microwave irradiation when solvent and plant material are placed together in the reactor. Consequently, both the solvent and the plant matrix absorb microwave energy and, according to their proportion and dielectric properties, the energy will be distributed in the sample. As a synergetic effect of the improved diffusion of the solvent due to heating and the altered plant matrix, effective extraction can be achieved in a very short time.[66] This approach also makes possible the extraction of thermolabile substances and the effective recovery of compounds which occur only in small quantity in the plant matrix. Both features are very important for the development of isolation procedures for accurate analysis of bioactive compounds in natural sources.[48]

MAE processes can be further divided into closed or open systems, where open systems are necessarily working at atmospheric pressure up to the boiling point of the solvent. When the extract is collected during the irradiation *via* condensation in an external condenser, the process is named microwave-assisted distillation or rather microwave assisted hydrodistillation (MAHD). Water is mainly used as a solvent for the extraction of essential oils and aromatic compounds.[80–82] Otherwise, the evaporating solvent can be directly refluxed back to the microwave cavity whereafter the extract must be obtained through a separation process. However, this additional step increases the complexity of the extraction technique. Most of the conventional extraction processes are already connected to extract-specific separation steps which can be used after a microwave extraction technique also.

Closed microwave systems may work under pressure, so-called pressurized MAE (PMAE), where higher temperatures can be achieved than the atmospheric boiling temperature, or under vacuum, called vacuum-MAE (VMAE), where a lower boiling temperature applies during the extraction.

Processes under pressure come with better diffusivity of the solvent into the matrix causing enhanced extraction kinetics. When this phenomenon is coupled with microwave extraction, treatment times may be lowered drastically and in addition thermo-labile compounds can be extracted avoiding thermal degradation. This behaviour was observed in the case of winemaking by-products.[83] Although extraction rate and efficiency are enhanced in this procedure, safety precautions must be taken in order to avoid hazards due to the use of high pressure and temperature in the presence of flammable solvents.[84] PMAE procedures are also common in analytical applications where small sample amounts are treated under accurate pressure and temperature control. For example, triazine herbicides in infant nutrient cereal-based foods were determined by pressurized microwave-assisted extraction, coupled with high performance liquid chromatography-electrospray ionization mass spectrometry, resulting in a more efficient and faster method compared to microwave-assisted extraction at atmospheric pressure, ultrasonic extraction or Soxhlet extraction.[85] In another paper ginsenosides from Panax ginseng roots were successfully obtained under PMAE (4–6 bar) with enhanced kinetics and higher extraction yield compared to Soxhlet extraction, ultrasound-assisted extraction and heat reflux extraction.[86] In a more recent approach, pressurization and microwave irradiation were applied consecutively to peanut roots in order to obtain resveratrol-rich extracts. Under optimized conditions of treatment time and solid/solvent ratio, a 1.72-fold yield increment was obtained compared to the conventional solvent extraction method.[87]

In VMAE the boiling of the extraction solvent is achieved at lower temperature, thus avoiding the degradation of thermo-labile compounds such as many bioactive agents. Due to the vacuum process the synergetic effect of low temperature and an oxygen-free environment favours the extraction of colouring and antioxidant compounds.[88,89] Vacuum MHG was used to extract polyphenolic compounds from the by-products of common yellow onion, applying reduced pressure between 200 and 900 mbar. Optimal extract yield was obtained at 700 mbar, where cell disruption was promoted, while a lower vacuum did not allow cell wall rupture due to lower temperatures.[88] A low vacuum (270 mbar) also caused similar or lower extraction yields compared to MAE in the case of pigment extraction from phytoplankton, although both processes were completed in minutes instead of 0.5–1 hour.[90] Another study focused on the vitamin C and E content of guava, green pepper, soy bean and tea leaves. These antioxidants are extremely sensitive to oxygen and high temperatures, thus being good candidates to evaluate the positive effects of vacuum-MAE (VMAE) compared to the MAE process at atmospheric pressure. The VMAE process was performed at 400 mbar vacuum, where temperatures, extraction times and solid/liquid ratios were all varied. The results showed that higher yields (up to 40% increment) of vitamin C and E were obtained using VMAE compared to MAE at atmospheric pressure, indicating the potential of an efficient microwave process at moderate temperature and in an oxygen deficient environment for the extraction of sensitive natural plant antioxidants.[89]

2.5.3 Microwave Pre-Treatment

A special class of microwave processes has emerged among microwave extraction techniques. As mentioned before, many MAE procedures are limited to analytical purposes. However, MAE has also evoked industrial interest due to the reported reductions in energy requirements and operating time. The cost of microwave extraction has two undesirable characteristics which diminish the advantages of the reduced energy and shorter extraction times: first, the high cost of a continuous microwave oven and, second, the cost of electrical energy in comparison to the less expensive heat from fuels. These drawbacks lead to a conceptual change, where microwaves are only used for a short time as a pre-treatment. After the pre-treatment, a more efficient conventional process can take place. Depending on the extraction process and compounds of interest, the addition of solvent can be performed prior to, or just after, the pre-treatment. Such a pre-treatment procedure was proposed for the enhanced steam distillation of essential oils from rosemary. It was found that there was a specific energy range ($0.3–0.6\ \mathrm{kJ\ g_{dry\ plant}}^{-1}$) where the essential oil containing glands are disrupted and the content is released on the plant surface where it can easily be removed by the steam flow in a shorter time. The energy consumption of the process can be kept low if the wall breakage of the glands is fast and no steam is generated from plant moisture at this stage. Additionally, no vapour recovery is required in the continuous microwave oven.[42] Another example of microwave pre-treatment is the juice extraction from apple mash by pressing. Heat treatment prior to juice pressing is necessary in order to avoid enzymatic oxidation and to enhance the solubility of the phenolic compounds into the juice, thus improving juice quality. While conventional heat treatments are not able to homogenously heat large volumes, microwave pre-treatment leads to increased juice yield and antioxidant content and simultaneously faster enzyme inactivation, thus avoiding browning of the end product.[91]

2.6 Extraction Fundamentals

Experimental evidence of the successful performance of MAE has been frequently reported in the literature. However, to understand the complex behaviour of this extraction method, the fundamentals must be properly considered. This knowledge will allow assessment of the influence of the operating variables on the performance of the process and permit correct planning of the experimental setup to obtain reproducible and scalable results.

MAE is a complex technique in terms of its fundamentals because of the numerous elemental phenomena to consider in order to obtain the whole picture of the process: electric field development, heat generation, transformation and transfer, cell structure changes, degradation reactions, mass transfer, and thermodynamic equilibrium relationships (compound solubility and phase changes). In addition, the extraction system suffers changes in temperature and composition during the extraction process altering its thermodynamic and dielectric properties. This is particularly relevant when there is a significant reduction in sample moisture because of evaporation. Moisture is often a major contributor to the dielectric property of the sample and its loss can cause a dramatic change in the dielectric constant and the loss factor of the medium.

The combination of these phenomena determine the efficiency of the process, which can be assessed in terms of yield, extraction kinetics and product degradation.

These individual phenomena are described below along with the main aspects to consider in the case of each one.

2.6.1 Heat Generation

Volumetric heat generated by microwaves was presented in Section 2.2.1. Eqn (2.3) shows how the corresponding electric field established at a certain location in the sample ($\vec{E}$), in combination with the dielectric properties of the material (ε'') and the frequency of the radiation (ω), determine the volumetric heat power released at that point (Q_{gen}). The volumetric distribution of the electric field is governed by Maxwell equations. Because of the strong interaction of electromagnetic waves with the media (reflection, refraction, diffraction), even systems with homogeneous dielectric properties always show uneven distributions of the electric field. This makes it very difficult to achieve processes with homogenous heat distributions, even in customized setups specifically designed for a particular system, such as the one shown in Figure 2.2. Several papers in the literature describe the use of finite element methods to calculate temperature and concentration evolution in microwave extraction processes.[21,73]

The most immediate and effective way to reduce heat generation inhomogeneities is by using a stirring system. Unfortunately, when large solid samples are processed, stirring is not practicable. However, in most MAE processes small solid samples are suspended in the solvent and the use of an impeller or a pumping system may be effective enough to improve homogeneity. In solvent-free microwave extraction (SFME) processes the solid samples are irradiated in the absence of solvent and stirring is more difficult to accomplish.

The volumetric heat generated by microwaves is absorbed by the media. This heat ultimately may split into four different destinations, depending on the media properties and conditions, as shown in Figure 2.5:

1. Sensible heat. If the media temperature is below its boiling point some of the heat will be absorbed as sensible heat, increasing the local temperature. This is the usual destination for the main fraction of the total generated energy at the beginning of the MAE process.
2. Evaporation. If the sample container is not operating at a high enough pressure, the temperature of the solvent can reach boiling point and part of the solvent will evaporate, absorbing from the media the

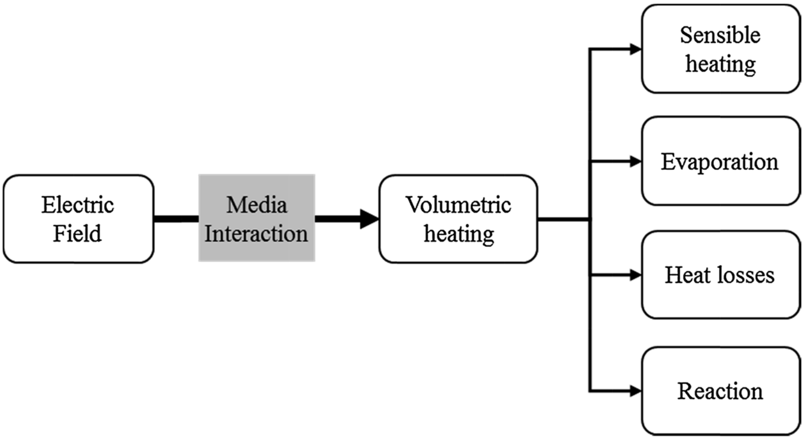

Figure 2.5 Scheme of volumetric heat transformation.

corresponding enthalpy of vaporization. This enthalpy has a large value compared with the sensible heat and so this vapor may be responsible for a considerable fraction of the energy absorbed by the sample provided that a significant amount of vapor is generated in the microwave oven.

3. Heat losses. Temperature differences between the sample container and the surrounding environment lead to heat losses. This phenomenon is enhanced by air blowing inside the microwave oven. For short microwave processing extractions of a few minutes length this loss is usually negligible. However, it is usual to find extraction processes in the literature where extraction times of 30 minutes or even more than an hour are reported. In these cases, the fraction of absorbed energy converted into heat loss may be considerable.
4. Reaction. Reaction processes can also be responsible for consuming/producing energy. However—"*the microwave photon is not sufficiently energetic to break hydrogen bonds; it is also much smaller than that of Brownian motion and obviously cannot induce chemical reactions*".[92] Comparisons between conventional and MAE extraction processes generally show similar composition of extract and final extraction media. This provides evidence that, under the range of conditions used in extraction processes, relevant chemical reactions do not take place and that this fraction of absorbed energy can be neglected.

2.6.2 Mass Transfer

Mass transfer is caused by the natural tendency of soluble compounds to be transferred from the raw material to the extraction solvent. The difference of concentration of the compound of interest between the raw material and the solvent is the driving force. However, this transfer is not immediate because of mass transfer resistances, both internal and external:

- Internal mass transfer. Before being extracted into the solvent the compounds must be released from the interior of the raw material matrix. The location of compounds is very diverse depending on the type of compounds and the raw material. In the case of ferulic acid, for example, only 10% is found in a soluble, free form in wheat bran. Most of it is found chiefly in the *trans* form, esterified to arabinoxylans and hemicelluloses in the aleurone and pericarp, and several dimers of ferulic acid are also found in cereals and form bridge structures between chains of hemicellulose.[93] However, in the case of rosemary, the essential oil is inside glandular trichomes,[94] and it is readily accessible once the trichome cell wall is opened. Internal mass transfer usually becomes the limiting process in solvent extraction because of some or all of the following resistances to release of the compounds: compounds linked to cell structure, wall cell transfer resistance and mass transfer diffusion within the solid.
- External mass transfer. Once the compound gets out of the matrix into the interface with the external solvent, it is distributed into the global phase of the solvent. This stage is determined by the external mass transfer coefficient (k_x):

  $$W_i = k_x A \left(c_i^* - c_i\right) \tag{2.4}$$

  where W_i is the flow rate of component i transferred from the surface of the matrix to the solvent, A is the area of the matrix surface, and c_i^* and c_i are the concentrations of component i in the surface interface and the global phase, respectively. A reduction in the particle size of the material matrix will increase the area A, enhancing the external mass transfer. This size reduction will also improve internal mass transfer when diffusion is the main resistance but not when the binding of compounds to the cell structure or cell wall penetrability are the main resistances. Solvent and matrix mixing by proper stirring will boost external mass transfer by increasing the mass transfer coefficient (k_x) by orders of magnitude, leaving internal mass transfer as the rate-limiting stage in the extraction process. This reason, together with microwave heating homogeneity, highly favours stirring during microwave-assisted extraction.

The success of MAE in solid-solvent extraction responds well to the combined effect of fast heating and solvent action on internal mass transfer. Temperature increase and solvent interaction help to alter or damage cell structures facilitating solvent penetration into the matrix, component release from bound forms and solvent diffusion through cell walls. In some cases, as in the solvent-free microwave extraction (SFME) of rosemary, the effect of microwave heating is strong enough to burst the walls of the glandular trichomes ensuring immediate release of the essential oil–water emulsion.[95,96]

2.6.3 Kinetics Modelling

Measurement and correlation of extraction kinetics is a powerful tool to get a deeper knowledge of MAE processes. Total yield determination is a valuable parameter as it reports information about the overall performance of the extraction. However, for complete information on the development of the process extraction, the kinetics should be measured and correlated since they report not only the final yield, but also allow determination of the effect of MAE on release rates.

To illustrate the benefits of measuring extraction kinetics, Figure 2.6 shows possible results from two MAE experiments performed using different conditions.

If only the final yield is measured (the last experimental point), the only conclusion inferred from the experiments is a higher yield for case B. When the kinetics are measured (all experimental points), a relevant additional conclusion may be obtained from the slope of the graph at the beginning of the extraction process—in case A the component has been extracted at a higher rate than in case B. This fact may be used to better assess the influence of MAE on the extraction process and to get a better understanding of the extraction mechanism and of the influence of the operating variables.

To quantify the information contained in extraction kinetics graphs, experimental values of concentration-time pairs should be regressed using mathematical models. For example, exponential models are extensively used to model extraction processes:

$$c_i = c_i^{\mathrm{f}}\left(1 - \mathrm{e}^{-kt}\right) \tag{2.5}$$

where c_i is the concentration of component i in the solvent at time t. The equation has two parameters: c_i^{f}, the final concentration of component i in the solvent ($t = \infty$), and k, the kinetic parameter. The value for the initial slope of the curve is given in eqn (2.6).

$$V_0 = \lim_{t \to 0} \frac{\mathrm{d}c_i}{\mathrm{d}t} = c_i^{\mathrm{f}} k \tag{2.6}$$

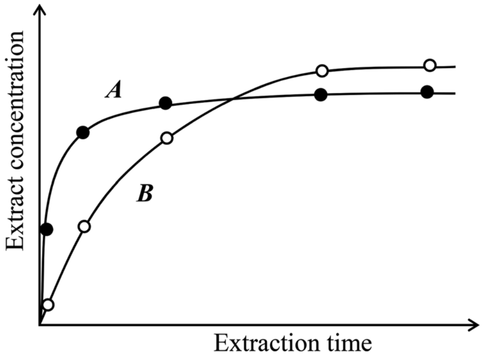

Figure 2.6 Evolution of extract concentration in MAE experiments A and B.

Correlation of experimental values to eqn (2.5) allows the effect of MAE to be quantified by using these two parameters (c_i^{f}, V_0) and enables proper assessment the effects of operating variables on process performance.

Many mathematical models are proposed in the literature to represent the behaviour of MAE processes.[97,98]

2.7 Operating Variables

Operating variables used in microwave-assisted extraction are the same as those in conventional solid-solvent extraction processes (temperature, pressure, solvent, particle size and time), plus those corresponding to the microwave heating process (power, energy and dielectric properties).

2.7.1 Time

Extraction time plays a double role in MAE processes: the contact time between the matrix and the solvent, and the microwave irradiation period.

The contact time between the matrix and the solvent allows components inside the matrix to be released into the solvent. Figure 2.6 shows the usual behaviour of conventional or MAE extraction processes. The rapid release of component at the beginning progressively slows until complete extraction is achieved. The main advantage when using MAE is the large reduction in the time required to complete the extraction. For example, the extractions of tea polyphenols and tea caffeine with MAE for 4 min were higher than those of extractions at room temperature for 20 h.[99] However, reductions in extraction time are not always so marked, and extraction times of hours are not unusual in the literature.

The microwave irradiation period runs simultaneously with the extraction, however, they rarely have the same duration. Only in the case of short MAE treatments of a few minutes might the material be irradiated during the entire process. In all other cases, and for longer treatments, the use of continuous heating would lead to highly undesirable elevated temperatures unless very intensive cooling is provided or microwave irradiation is controlled by ON/OFF regulation cycles. In the latter case, the actual value of the irradiation period would be uncertain. Although the magnetron power might be controlled, the power used in the process would be uncertain unless the irradiation power is properly monitored.

For analytical or research purposes long extraction times may be used. However, in industrial processes with larger processing capacities, maintaining the sample in the oven for a long residence time requires large volume ovens. This is a complicated or expensive solution because of typical low penetration depths of microwaves in MAE systems. Should this be the case, the use of a short and intense microwave pre-treatment, followed by a conventional extraction period out of the oven, should be considered.[100,101] The purpose of this intense microwave pre-treatment is to produce destructive changes in the plant tissue, facilitating the release of the compounds in the later extraction process.[59] This means of operation exploits the main advantage of MAE while reducing the irradiation time and the size of the oven.

2.7.2 Microwave Power and Energy

Microwave power and energy appear as critical operation variables in many MAE processes. However, in conventional microwave ovens it is difficult to know the actual value of these variables.

In the case of power, the actual heating value is hidden by the efficiency of absorption of the microwave irradiation, as explained in Section 2.2 (Microwave Heating Foundations). This efficiency may be as low as 40% in domestic ovens with low absorbing samples, or as high as 99% in laboratory equipment under ideal and controlled conditions.[102] In addition, the use of ON/OFF working cycles implemented in some equipment to control the average power may create difficulties in estimating the actual value of the applied power unless specific measurement equipment, such as a high power reflectometer, is used.

Often, the value of the energy used in the MAE process is calculated as the product of the selected power multiplied by the irradiation time. However, as previously explained, the selected power does not correspond to the actual heating power, nor does the extraction time match the irradiation time in domestic microwave ovens. The measurement of the electrical energy demands of the microwave during the MAE process also provides a value exceeding the energy absorbed by the sample, as the efficiencies in the magnetron and in irradiation absorption should be considered.

Reliable values of power and energy are, however, essential to obtain reproducible experimental conditions, or for scale-up purposes. This is probably the main source of discrepancy when authors report different, or even contradictory, results when studying the same system under similar conditions.[103] Moreover, energy values should preferably be reported in specific values (kJ kg^{-1} or kJ L^{-1}) to make them independent of the size of the sample.

The amount of energy absorbed by the sample may be estimated from an energy balance. This microwave energy absorbed by the medium is split into four different terms, as explained in Section 2.6.1. (Heat Generation) and illustrated in Figure 2.5. These terms may be calculated from basic measurements.[103] Since the heat of reaction is usually negligible in MAE processes, the amount of energy absorbed by the sample (E_{absorbed}) will be the sum of the sensible, latent and heat loss terms:

$$E_{\text{absorbed}} \approx Q_{\text{sensible}} + Q_{\text{latent}} + Q_{\text{heat loss}} \tag{2.7}$$

The sensible heat (Q_{sensible}) is calculated from the masses of solvent (m_s) and matrix (m_m), their respective specific heats ($C_{p,s}$ and $C_{p,m}$) and the temperature increment between the beginning and the end of the process (ΔT):

$$Q_{\text{sensible}} = m_s C_{p,s} \Delta T + m_m C_{p,m} \Delta T \tag{2.8}$$

The latent heat term (Q_{latent}) appears in processes were solvent evaporation takes place, and is calculated from the amount of evaporated solvent (m_{vap}) measured by weight loss after microwave treatment and its enthalpy of vaporization (ΔH_{vap}):

$$Q_{\text{latent}} = m_{\text{vap}}\Delta H_{\text{vap}} \tag{2.9}$$

The heat loss term ($Q_{\text{heat loss}}$) from the container wall to the surroundings is calculated from the global heat transfer coefficient (UA) and the evolution with time of ambient (T_{a}) and matrix (T_{m}) temperatures:

$$Q_{\text{heat loss}} = -\text{UA}\int_0^{t_{\text{final}}} \left(T_{\text{m}} - T_{\text{a}}\right)\text{d}t \tag{2.10}$$

The experimental value of the global heat transfer coefficient (UA) may be easily obtained in one experiment, where the sample in the microwave oven is allowed to cool at ambient temperature (T_{a}) by switching off the heating power from an initial temperature (T_{initial}) to a final temperature (T_{final}) over a time t_{final}:

$$\text{UA} = \frac{m_{\text{s}}C_{\text{p,s}}\Delta T + m_{\text{m}}C_{\text{p,m}}\Delta T}{t_{\text{final}}}\ln\frac{T_{\text{initial}} - T_{\text{a}}}{T_{\text{final}} - T_{\text{a}}} \tag{2.11}$$

2.7.3 Temperature

A higher extraction temperature helps to enhance extraction yield and kinetics. The benefits from a higher temperature are higher compound solubilities, improved mass transfer, because of higher diffusion coefficients and lower viscosity, and enhanced effect on components' internal binding and cell tissue damage.

Unfortunately, higher extraction temperatures can lead to thermal degradation of heat-labile compounds, as is the case of many compounds obtained by MAE processes from natural products, such as pigments,[90] isoflavones,[104] carotenoids,[105,106] *etc.* MAE, however, can reduce this undesirable effect in the extraction process if fast cooling follows intense microwave pre-treatment. This is possible because the progress of degradation reactions depends not only on the temperature, but also on the time of exposure at a certain temperature.[83]

The boiling point of the solvent sets the maximum temperature level that may be reached in the extraction process. To exceed this value the extraction must be carried out under pressure.

2.7.4 Particle Size

Particle size reduction also improves extraction kinetics. Size reduction favours internal mass transfer as it reduces the mass transfer path in the matrix when diffusion is the rate-controlling stage for release of the compounds. Also, external mass transfer is enhanced due to an increase in the external surface area, although this is rarely the rate-controlling stage of extraction processes.

Care must be taken with size reduction of natural products, since mechanical reduction can alter the internal structure of the matrix and enhance the release of undesirable components into the solvent.

2.7.5 Solvent

The solvent in MAE plays an important role as it is involved in phenomena, all of which affect the performance of the extraction process.

First, the choice of solvent, coupled with the extraction temperature, determines the solubility of the compounds in the solvent. This value limits the maximum amount of compound that can be obtained in the solvent but it can also determine the driving force for mass transfer.

Secondly, the dielectric properties of the solvent determine the volumetric heating by the microwaves. Solvents like water, methanol or acetone, with high dielectric constants, are easily heated with microwaves, while others like hexane or toluene are more difficult to heat because of their low dielectric constants. In addition to the solvent, the dielectric properties of the matrix are also relevant to evaluate the volumetric heating produced by microwaves. In this case, the moisture content of natural products often makes the largest contribution to the final value.

Finally, the effect of the selected solvent, in combination with microwave heating, on the degradation of cell tissues is also an important effect. This is the effect through which MAE sometimes displays outstanding performance when compared to conventional or alternative extraction processes. However, the limited experience collected at present concerning this effect does not allow one to predict the effect of solvents on different natural structures under microwave conditions.

The combination of these three effects is the reason why sometimes mixtures of different solvents are used in MAE to achieve optimal performance.

An additional operational variable to determine when evaluating optimal conditions for MAE is the solvent/matrix ratio. The optimal value for this ratio will depend on the choice of solvent, since solubility, polarity, dielectric constant and effects on the matrix structure will vary depending on the nature of the solvent.

2.7.6 Pressure

Pressure must be considered an operational variable in MAE processes when the desired extraction temperature is higher than the boiling point of the mixture. Table 2.3 shows the minimum pressure required in the extraction container to avoid the boiling of the solvent as a function of the extraction temperature.

Table 2.3 Minimum extraction pressure to prevent boiling of solvent.

	P_{min} (bar)				
T (°C)	Water	Methanol	Ethanol	Ethyl acetate	Hexane
80	0.47	1.81	1.08	1.11	1.42
100	1.01	3.52	2.25	2.03	2.44
120	1.98	6.38	4.27	3.46	3.95
140	3.61	10.84	7.54	5.55	6.07
160	6.17	17.51	12.52	8.47	8.98
180	10.01	27.07	19.72	12.41	12.85
200	15.52	40.37	29.70	17.61	17.94

2.8 Conclusions

Microwaves can be successfully used to improve the extraction of natural products from plants. This improvement mainly affects extraction yield with a substantial reduction in processing time. Positive use of microwave-assisted extraction has been proven in a wide variety of raw material extractions including herbs, fruits and algae or biomass residues. It has been used to extract a full spectrum of compounds of interest (essential oils, phenolics, antioxidants, lipids and fatty acids, polysaccharides, pectin, herbicides, *etc.*). This prolific number of extraction circumstances has led to the development of different extraction techniques able to take advantage of microwave irradiation under very different process conditions: microwave steam distillation, microwave hydrodiffusion, microwave hydrodistillation, microwave-assisted extraction (MAE), vacuum MAE and pressurized MAE.

There are a large number of references in the literature describing microwave extraction processes, most of them for analytical purposes, but also many others for industrial application. In order to provide relevant information that can be helpful to other researchers, special attention must be paid to microwave fundamentals. Experiments must be performed and reported in such a way that conditions and results are reproducible. Experimental conditions, such as absorbed power and energy or irradiation homogeneity are critical to validate experimental results.

References

1. P. Debye, *Polar Molecules*, Chemical Catalog, New York, 1929.
2. H. Fröhlich, *Theory of Dielectrics*, Clarendon Press, 1949.
3. V. Daniel, *Dielectric Relaxation*, Academic Press, New York, 1967.
4. A. C. Metaxas and R. J. Meredith, *Industrial Microwave Heating*, London, 1983.
5. A. Díaz-Morcillo, J. Monzó-Cabrera and M. A. García-Fernández, *High Frequency Electromagnetic Dosimetry*, Norwood, 2009, pp. 23–45.
6. P. Plaza-Gonzalez, J. Monzo-Cabrera, J. M. Catala-Civera and D. Sanchez-Hernandez, *IEEE Trans. Microwave Theory Tech.*, 2005, **53**(5), 1699.

7. *Microwave-assisted Extraction for Bioactive, Compounds: Theory and Practice*, ed. F. Chemat and G. Cravotto, 2012, Food Engineering Series, Book 4, p. 18.
8. L. Jassie, R. Revesz, T. Kierstead, E. Hasty and S. Matz, *Microwave Enhanced Chemistry Fundementals, Sample Preparation, and Applications*, ed. H. M. Kingston and S. J. Haswell, American Chemical Society, Washington, DC, 1997, ch. 12, pp. 569–612.
9. A. Zlotorzynski, *Crit. Rev. Anal. Chem.*, 1995, **25**, 43.
10. M. S. Venkatesh and G. S. V. Raghavan, *Biosyst. Eng.*, 2004, **88**(**1**), 1.
11. S. O. Nelson, Jr, W. R. Forbus and K. C. Lawrence, *Trans. ASAE*, 1994, **37**(**1**), 183.
12. T. V. Chow Ting Chan and H. C. Reader, *Understanding Microwave Heating Cavities*, Artech House, 2000.
13. F. J. Clemente-Fernández, J. Monzó-Cabrera, J. M. Catalaá-Civera, J. L. Pedreño-Molina, A. J. Lozano-Guerrero and A. Diáaz-Morcillo, *Electron. Lett.*, 2012, **48**(**13**), 772.
14. M. Ranic, M. Nikolic, M. Pavlovic, A. Buntic, S. Siler-Marinkovic and S. Dimitrijevic-Brankovic, *J. Cleaner Prod.*, 2014, **80**, 69.
15. F. Dahmoune, B. Nayak, K. Moussi, H. Remini and K. Madani, *Food Chem.*, 2015, **166**, 585.
16. K. Thirugnanasambandham, V. Sivakumar and J. Prakash Maran, *Carbohydr. Polym.*, 2014, **112**, 622.
17. K. Thirugnanasambandham, V. Sivakumar and J. Prakash Maran, *Int. J. Biol. Macromol.*, 2015, **72**, 1.
18. X.-Y. Qv, Q.-F. Zhou and J.-G. Jiang, *J. Sep. Sci.*, 2014, **37**, 2991.
19. M. Milutinović, N. Radovanović, M. Rajilić-Stojanović, S. Šiler-Marinković, S. Dimitrijević and S. Dimitrijević-Branković, *Ind. Crops Prod.*, 2014, **61**, 388.
20. C. H. Chan, R. Yusoff and G. C. Ngoh, *Chem. Eng. Sci.*, 2014, **111**, 41.
21. N. Chumnanpaisont, C. Niamnuy and S. Devahastin, *Chem. Eng. Sci.*, 2014, **116**, 442.
22. Y. Y. Dang, H. Zhang and Z. L. Xiu, *J. Chem. Technol. Biotechnol.*, 2014, **89**, 1576.
23. M. Taghvaei, S. M. Jafari, E. Assadpoor, S. Nowrouzieh and O. Alishah, *Food Chem.*, 2014, **160**, 90.
24. C. S. Eskilsson and E. Björklund, *J. Chromatogr. A*, 2000, **902**, 227.
25. J. Monzó-Cabrera, A. Díaz-Morcillo, J. M. Catalá-Civera, A. J. Canós and E. de los Reyes, *Microwave Opt. Technol. Lett.*, 2001, **31**(**6**), 470.
26. *Production of Biofuels and Chemicals with Microwave*, ed. Z. Fang, R. L. Smith Jr and X. Qi, Springer, 2015, pp. 17–40.
27. http://www.anton-paar.com/.
28. http://www.biotage.com/.
29. http://www.cem.com/.
30. http://www.milestonesci.com/.
31. http://www.sineomicrowave.com/.
32. A. Leone, A. Tamborrino, R. Romaniello, R. Zagaria and E. Sabella, *Biosyst. Eng.*, 2014, **125**, 24–35.

33. http://www.emitech.it/.
34. http://www.advancedmicrowavetechnologies.com/.
35. Y. V. Zadyraka, S. I. Gritsinin, M. A. Misakyan, I. A. Kossyl and E. M. Barkhudarou, *Apparatus for treating a fluid with microwave radiation, U. S. Pat.*, US-2012/0305496, 2012.
36. http://www.sairem.com/.
37. http://www.pueschner.com/.
38. http://ctechinnovation.com/.
39. J. M. Sauks, *A continuous flow microwave reactor for organic synthesis*, Ph.D. thesis, Chemical Engineering and Applied Chemistry, University of Toronto, 2011.
40. K. P. Svoboda and G. T. Svoboda, *Secretory Structures of Aromatic And Medicinal Plants*, ed. P. M. Syred, Microscopix Publications, Middle Travelly, Beguildy, Knighton UK, 2000.
41. M. G. Cerpa, R. B. Mato, M. J. Cocero, R. Ceriani, A. J. A. Meirelles, J. M. Prado, P. F. Leal, T. M. Takeuchi and M. A. A. Meireles, *Extracting Bioactive Compounds for Food Products*, ed. M. A. A. Meireles, CRC press, Taylor and Francis Group, 2009, ch. 2, pp. 9–74.
42. A. Navarrete, S. Wallraf, R. B. Mato and M. J. Cocero, *Ind. Eng. Chem. Res.*, 2011, **50**, 4667.
43. M. A. Desai and J. K. Parikh, *ACS Sustainable Chem. Eng.*, 2015, **3**(**3**), 421.
44. V. P. Pavićević, M. S. Marković, S. Ž. Milojević, M. S. Ristić, D. S. Povrenović and V. B. Veljković, *J. Chem. Technol. Biotechnol.*, 2016, **91**(4), 883.
45. C. Manach, A. Scalbert, C. Morand, C. Rémésy and L. Jimenez, *Am. J. Clin. Nutr.*, 2004, **79**, 727.
46. C. Proestos and M. Komaitis, *LWT – Food Sci. Technol.*, 2008, **41**, 652.
47. E. Durmaz, G. Sumnu and S. Sahin, *Sep. Sci. Technol.*, 2015, **50**(13), 1986–1992.
48. W. Routray and V. Orsat, *Food Bioprocess Technol.*, 2012, **5**, 409.
49. L. Chupina, S. L. Maunub, S. Reynaudc, A. Pizzid, B. Charriera and F. Charrier-EL Bouhtoury, *Ind. Crops Prod.*, 2015, **65**, 142.
50. V. Chandrasekar, M. F. San Martin-Gonzalez, P. Hirst and T. S. Ballard, *J. Food Process Eng.*, 2015, **38**(6), 571.
51. D. J. Bhuyan, Q. V. Vuong, A. C. Chalmers, I. A. van Altena, M. C. Bowyer and C. J. Scarlett, *Ind. Crops Prod.*, 2015, **69**, 1.
52. L. E. García-Ayuso, J. Velasco, M. C. Dobarganes and M. D. Luque de Castro, *Chromatographia*, 2000, **52**, 103.
53. D. B. Nde, D. Boldora and C. Astete, *Ind. Crops Prod.*, 2015, **65**, 233.
54. G. Cravotto, L. Boffa, S. Mantegna, P. Perego, M. Avogadro and P. Cintas, *Ultrason. Sonochem.*, 2008, **15**, 898.
55. H. Rui, L. Zhang, Z. Li and Y. Pan, *J. Food Eng.*, 2009, **93**, 482.
56. D. Boldor, A. Kanitkar, B. G. Terigar, C. Leonardi, M. Lima and G. A. Breitenbeck, *Environ. Sci. Technol.*, 2010, **44**, 4019.
57. Y. Chisti, *Biotechnol. Adv.*, 2007, **25**, 294.
58. H. Bagherian, F. Z. Ashtiani, A. Fouladitajar and M. Mohtashamy, *Chem. Eng. Process.*, 2011, **50**, 1237.

59. M. Kratchanova, E. Pavlova and I. Panchev, *Carbohydr. Polym.*, 2004, **56**(**2**), 181.
60. M. L. Fishman, H. K. Chau, P. D. Hoagland and A. T. Hotchkiss, *Food Hydrocolloids*, 2006, **20**, 1170.
61. S. Wang, F. Chen, J. Wu, Z. Wang, X. Liao and X. Hu, *J. Food Eng.*, 2007, **78**(**2**), 693.
62. P. C. Koh, C. M. Leong and M. A. Noranizan, *Int. Food Res. J.*, 2014, **21**(**5**), 2091.
63. S. Rahmati, A. Abdullah, E. Momeny and O. L. Kang, *Int. Food Res. J.*, 2015, **22**(**1**), 233.
64. K. Ganzler, A. Salgó and K. Valkó, *J. Chromatogr.*, 1986, **371**, 299.
65. M. Letellier and H. Budzinski, *Analusis*, 1999, **27**, 259.
66. C. H. Chan, R. Yusoff, G. K. Ngoh and F. Wai-Lee Kung, *J. Chromatogr. A*, 2011, **1218**, 6213.
67. M. L. Clodoveo and R. H. Hbaieb, *Food Res. Int.*, 2013, **54**(**2**), 1926.
68. A. Filly, X. Fernandez, M. Minuti, F. Visinoni, G. Cravotto and F. Chemat, *Food Chem.*, 2014, **150**, 193.
69. A. Leone, A. Tamborrino, R. Zagaria, E. Sabella and R. Romaniello, *J. Food Eng.*, 2015, **146**, 44.
70. P. C. Veggi, J. Martinez and M. A. A. Meireles, *Microwave-assisted Extraction for Bioactive Compounds: Theory and Practice*, ed. F. Chemat and G. Cravotto, Springer Science+Business Media New York 2013, ch. 2, pp. 15–52.
71. V. Camel, *Trends Anal. Chem.*, 2000, **19**, 229.
72. T. Michel, E. Destandau and C. Elfakir, *Food Chem.*, 2011, **126**, 1380.
73. A. Navarrete, R. B. Mato and M. J. Cocero, *Chem. Eng. Sci.*, 2012, **68**, 192.
74. M. E. Lucchesi, F. Chemat and J. Smadja, *J. Microwave Power Electromagn. Energy*, 2004, **39**, 135.
75. F. Chemat, M. E. Lucchesi, J. Smadja, L. Favretto, G. Colnaghi and F. Visinoni, *Anal. Chim. Acta*, 2006, **555**, 157.
76. A. Filly, X. Fernandez, M. Minuti, F. Visinoni, G. Cravotto and F. Chemat, *Food Chem.*, 2014, **150**, 193.
77. A. Vian, X. Fernandez, F. Visinoni and F. Chemat, *J. Chromatogr. A*, 2008, **1190**, 14.
78. Y. Li, A. S. Fabiano-Tixier, M. A. Vian and F. Chemat, *Trends Anal. Chem.*, 2013, **47**, 1.
79. T. Michel, E. Destandau and C. Elfakir, *Food Chem.*, 2011, **126**, 1380.
80. J. K. Parikh, *ACS Sustainable Chem. Eng.*, 2015, **3**, 421.
81. V. P. Pavićević, M. S. Marković, S. Ž. Milojević, M. S. Ristić, D. S. Povrenović and V. B. Veljković, *J. Chem. Technol. Biotechnol.*, 2016, **91**(4), 883.
82. P. C. Veggi, J. Martinez and M. A. A. Meireles, *Microwave Assisted Extraction for Bioactive Compounds: Theory and Practice*, ed. F. Chemat and G. Cravotto, Springer, 2013, ch. 2, Fundamentals of Microwave Extraction.
83. K. Sólyom, R. Solá, M. J. Cocero and R. B. Mato, *Food Chem.*, 2014, **159**, 361.

84. A. Kaufmann and P. Christen, *Phytochem. Anal.*, 2002, **13**, 105.
85. J. You, H. Zhang, H. Zhang, A. Yu, T. Xiao, Y. Wang and D. Song, *J. Chromatogr. B*, 2007, **856**, 278.
86. Y. Wang, J. You, Y. Yu, C. Qu, H. Zhang, L. Ding, H. Zhang and X. Li, *Food Chem.*, 2008, **110**(**1**), 161.
87. A. Qiong-Ling, L. Hong-Zhi, L. Li, H. Xuan-Hui and W. Qiang, *Food Sci.*, 2013, **34**(**20**), 43.
88. Zill-e-Huma, M. Abert-Vian, M. Elmaataoui and F. Chemat, *J. Food Eng.*, 2011, **105**, 351.
89. X. Xiao, J. Wang, G. Wang, J. Wang and G. Li, *J. Chromatogr. A*, 2009, **1216**, 8867.
90. V. Pasquet, J. R. Chérouvrier, F. Farhat, V. Thiéry, J. M. Piot, J. B. Bérard, R. Kaas, B. Serive, T. Patrice, J. P. Cadoret and L. Picot, *Process Biochem.*, 2011, **46**(**1**), 59.
91. J. S. Roberts and K. A. Gerard, *J. Food Process Eng.*, 2004, **27**, 29.
92. D. Stuerga, Microwave-Material Interactions and Dielectric Properties, Key Ingredients for Mastery of Chemical Microwave Processes, in *Microwaves in Organic Synthesis*, ed. A. Loupy, Wiley-VCH Verlag GmbH, Weinheim, Germany, 2nd edn, 2008, p. 6.
93. C. Manach, A. Scalbert, C. Morand, C. Rémésy and L. Jiménez, *Am. J. Clin. Nutr.*, 2004, **79**, 727.
94. M. Marin, V. Koko, S. Duletić-Laušević, P. D. Marin, D. Rančić and Z. Dajic-Stevanovic, *S. Afr. J. Bot.*, 2006, **72**, 378.
95. M. E. Lucchesi, F. Chemat and J. Smadja, *J Chromatogr. A*, 2004, **1043**(**2**), 323–327.
96. M. E. Lucchesi, F. Chemat and J. Smadja, *Flavour Fragrance J.*, 2004, **19**, 134.
97. I. Hartatia, L. Kurniasari and Y. Anas, *Procedia Chem.*, 2015, **14**, 186.
98. Z. Dong, F. Gu, F. Xu and Q. Wang, *Food Chem.*, 2014, **149**, 54.
99. X. Pan, G. Niu and H. Liu, *Chem. Eng. Process.*, 2003, **42**, 129.
100. M. Mubarak, A. Shaija and T. V. Suchithra, *Algal Res.*, 2015, **7**, 117.
101. Y. Tong, L. Gao, G. Xiao and X. Pan, *J. Food Process Eng.*, 2012, **35**, 792.
102. K. Sólyom, *Enhanced extraction of natural substances using microwave energy*, PhD thesis, University of Valladolid, 2013.
103. K. Sólyom, R. B. Mato, S. I. Pérez-Elvira and M. J. Cocero, *Bioresour. Technol.*, 2011, **102**, 10849.
104. M. A. Rostagno, M. Palma and C. G. Barroso, *Anal. Chim. Acta*, 2007, **588**, 274.
105. R. M. El-Abassy, P. Donfack and A. Materny, *Food Res. Int.*, 2010, **43**, 694.
106. L. Zhao, G. Zhao, F. Chen, Z. Wang, J. Wu and X. Hu, *J. Agric. Food Chem.*, 2006, **54**, 8346.

CHAPTER 3

Low-Temperature Microwave Pyrolysis and Large Scale Microwave Applications

JIAJUN FAN[a], VITALIY BUDARIN*[a], MARK J. GRONNOW[b]
AND JAMES H. CLARK[a]

[a]Green Chemistry Centre of Excellence, Department of Chemistry, University of York, York YO10 5DD, UK; [b]Biorenewables Development Centre, The Biocentre, York Science Park, York, YO10 5NY, UK
*E-mail: vitaliy.budarin@york.ac.uk

3.1 Microwave Technology

The definition of "microwaves" is somewhat arbitrary. According to the conventional definition the term "microwave" refers to electromagnetic radiation with wavelengths ranging from as long as one metre to as short as one millimetre, with frequencies between 300 MHz and 300 GHz (see Figure 3.1).[1] The wavelengths between 1 cm and 25 cm are extensively used for RADAR transmissions with the remaining wavelengths used for telecommunications. In order not to interfere with these uses, domestic and industrial microwave heaters are required to operate at either 12.2 cm (2.45 GHz) or 33.3 cm (915 MHz) unless the apparatus is shielded in such a way that no radiation losses occur. Domestic microwave ovens generally operate at 2.45 GHz (see Figure 3.1B).

RSC Green Chemistry No. 47
Alternative Energy Sources for Green Chemistry
Edited by Georgios Stefanidis and Andrzej Stankiewicz

Published by the Royal Society of Chemistry, www.rsc.org

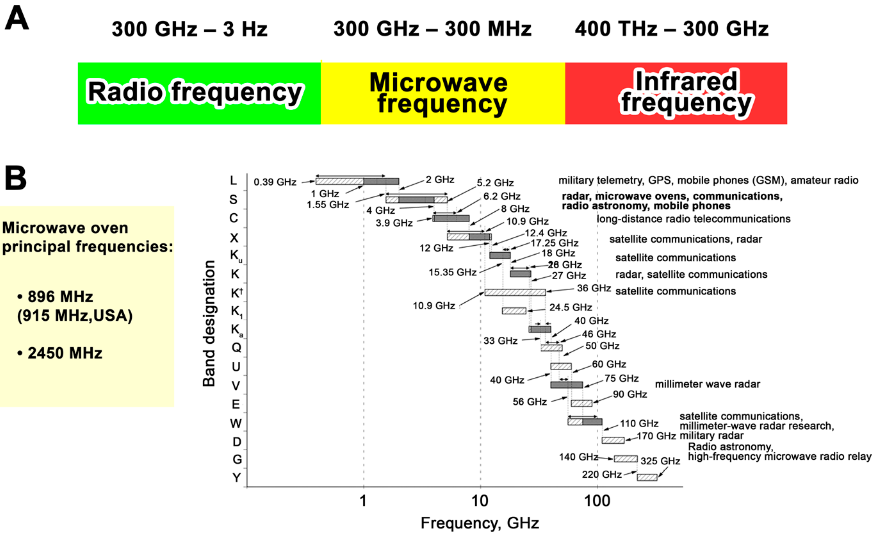

Figure 3.1 (A) Radio frequency (RF), microwave and infrared (IR) frequency band designations. (B) Industrial and IEEE designations. Diagonal hashing indicates variation in the definitions found in the literature; dark regions in the bars indicate the IEEE radar band definitions.

3.1.1 Microwave Technology Applications

Microwave (MW) technology is extensively used for communication,[2] medical (*e.g.* diathermy or hyperthermia)[3] applications, microwave power transmission[4] and radio detection and ranging (RADAR) systems. For many years the driving application of microwave technology was military RADAR. The small wavelength of microwaves permits the realization of narrowly-focused beams to be achieved with antennae small enough to be practically steered, resulting in adequate resolution of target location. Long-distance terrestrial communications for telephony as well as satellite uplink and downlink for voice and video were among the first commercially viable applications of microwave technology. These commercial communication applications were successful because microwave frequency carriers (f_c) offer the possibility of very wide absolute signal bandwidths (Δf) while still maintaining relatively narrow fractional bandwidths (*i.e.*, $\Delta f/f_c$). This allows many more voice and data channels to be accommodated than would be possible with lower frequency carriers or baseband transmission. Microwave application in RADAR systems stimulated design and production of very powerful magnetrons (a high-powered vacuum tube that generates microwaves) which are one of the major elements of microwave technology. Microwave magnetrons used in RADAR systems span a wide range of applications, operating at frequencies from 300 MHz to 300 GHz with output powers from a few hundred watts to more than 10 megawatts.[2]

3.1.2 History of Heating Application of Microwave Irradiation

Before World War II, there is little evidence of work on RF heating, much less on microwave heating—since microwaves were still in their infancy. Still, the patent literature shows some loose reference to the use of microwave energy to affect materials for industrial purposes. Kassner, a German refugee living in England and Switzerland in the late thirties, mentions such industrial application of microwaves in two of his patents on spark-gap microwave generators. More specifically, another of his patents in 1937 discussed a "process for altering permanently as well as temporarily the energy content of dipolar substances by exposing them to rapidly oscillating electromagnetic fields". Thus he was particularly interested in the "range of quasi-optical waves" ... "having wavelengths of the range of fractions of a millimetre upwards". This clearly is the presently recognized regime of microwaves. However, Kassner believed that he could achieve useful changes in materials without heating. He states that the object of the invention is not a rise in temperature but a change in the internal "energy content of dipolar substance", *i.e.* a change in the molecular state and hence its chemistry. In his belief in such a "non-thermal" effect, he no doubt was influenced by widespread belief in the non-thermal "specific" effects from diathermy, that widely entertained by medical doctors, especially in Germany.[1] A reliable device for generating fixed frequency microwaves was designed by Randall and Booth at the University of Birmingham as part of the development of RADAR during the Second World War. This device, the magnetron, was produced in large numbers during the war with the aid of United States industrial expertise. By almost universal acknowledgement, the first microwave oven was made by the Raytheon Manufacturing Company during 1945–46 with Percy Spencer as the inventor and those who helped design and build the first model (Table 3.1).[5]

Table 3.1 Development of microwave technology

Year	No.	Title	Assignee	Author
1937	US2089966 A	Process for altering the energy content of dipolar substances	None	Kassner
1939	US 2161292 A	Radiating device	Lorenz C Ag	W. M. Hahnemann
1944	US 2407075 A	Ultra high frequency power measurement	Gen Electric	A. Gurewitsch
1946	US 2400777 A	Electrical power absorber	Westinghouse Electric Corp	E. C. Okress
1948	US 2442114 A	Method of and apparatus for subjecting materials to a radio-frequency field	RCA Corp	G. H. Brown

1949	US 2461372 A	Tube forming device	William F Stahl	F. V. Collins
	US 2463569 A	Apparatus for treating gaseous media	Raytheon Mfg Co	C. G. Smith
	US 2467230 A	Ultra high frequency dielectric heater	Gen Electric	H. E. Revercomb and E. W. Donald
	US 2480679 A	Prepared food article and method of preparing	Raytheon Mfg Co	P. L. Spencer
	US 2480682 A	Microwave heating apparatus using circularly polarized horn	Raytheon Mfg Co	K. J. Stiefel
	US 2483933 A	Ultra high frequency dielectric heater	Gen Electric	E. H. Revercomb and P. W. Morse
1950	US 2495170 A	Microwave heating of dielectric materials	Westinghouse Electric Corp	T. P. Kinn
	US 2495415 A	High-frequency electromagnetic cooking apparatus	Raytheon Mfg Co	L. K. Marshall
	US 2495429 A	Method of treating foodstuffs	Raytheon Mfg Co	P. L. Spencer
1955	US 2714070 A	Microwave heating apparatus and method of heating a food package	Raytheon Mfg Co	A. E. Welch

Since World War II, there have been major developments in the use of microwaves for heating applications. The main applications of microwave heating today include food processing, wood drying, plastic and rubber treatment and the curing and preheating of ceramics.[5]

3.1.3 Microwave Equipment

Microwave equipment consists of three major components: the power supply together with microwave generator, the applicator, and the control circuitry. The power supply and microwave generator provide microwaves at the appropriate frequency. The power supply must be matched to the microwave source to ensure correct operation. The most common microwave sources are the magnetron and klystron, the former being robust, efficient, frequency-stable and readily available, while the latter is more expensive, available in higher powers, but with a somewhat shorter operating life (80 000 *versus* 100 000 hours). Low power magnetrons for laboratory use typically come in the power range 1–6 kW and may be of fixed or variable power type, while higher power magnetron systems up 100 kW are available, usually at 915 MHz rather than the more common low power frequency of 2450 MHz. Power output from low power permanent magnet magnetrons can be achieved by thyristor control of the anode voltage, while high power systems usually use an electromagnet to vary the anode current. It is usual to insert a circulator between the magnetron and the load. This is a 3-port structure that couples power clockwise between adjacent ports. As microwave power can be reflected, the circulator protects the magnetron from excessive reflected power by diverting reflected power to a water-cooled matched load, which may also be equipped with a power meter. The circulator is particularly important in preliminary investigations where the dielectric properties of the load are not well known and where a general purpose applicator is being used which may result in significant amounts of reflected power. To provide a good impedance match between the magnetron and the load a stub tuner is often provided. Even with the use of a circulator it is sometimes found that significant power pulling (20% of nominal power) due to impedance mismatches can still occur. Both the stub tuner and the circulator are expensive and cope with powers of up to about 6 kW. For these reasons they are not generally used in high power industrial systems. Microwave applicators are metallic enclosures that contain the material to be heated, and their design depends on the processing requirements. Travelling wave applicators are used for processing thin webs of material and would be of limited use in minerals processing. Single mode cavities, in which the electromagnetic field exists in a well-defined form, are useful for processing small quantities of material (*e.g.* filaments), particularly those with low effective loss factors. Full descriptions are given in Metaxas and Meredith, 1983.[6] The most common applicator is the multimode cavity, which is basically a large box, with at least one dimension somewhat larger than the free space wavelength of the radiation (122 mm at 2450 MHz). Microwave radiation entering a multimode cavity undergoes multiple reflections to form a complex standing wave pattern, governed by the dimensions of the cavity and the nature of the load. The multimode cavity is versatile and suited to heating large loads and can be adapted for continuous processing. Unfortunately, its convenience is offset by problems of poor electromagnetic uniformity and difficulties in modelling and design. Specialized features such as mode stirrers and slotted waveguide feeds can overcome the former.[7] The mode stirrer is the most common of these devices, consisting of a rotating, vaned metallic fan.[8]

3.2 Heating

3.2.1 General Discussion

The microwave dielectric heating effect uses the ability of some liquids and solids to transform electromagnetic energy into heat and thereby drive chemical reactions. This *in situ* mode of energy conversion has many attractions to the chemist because its magnitude depends on the properties of the molecules. This allows some control of the material's properties and may lead to reaction selectivity.[9]

3.2.2 Mechanism of Microwave Heating

A material can be heated by applying energy to it in the form of high frequency electromagnetic waves. However, not all materials can be heated rapidly by microwaves. Materials may be classified into three groups: conductors, insulators and absorbers. This classification is illustrated in Figure 3.2.

Materials that absorb microwave radiation are called dielectrics, thus, microwave heating is also referred to as dielectric heating.[10]

In dielectric materials the microwave energy is converted irreversibly into heat. The level of this conversion is estimated by using a special characteristic of the dielectric material, its "dielectric loss". The term dielectric loss originated from the fact that in an ideal dielectric, energy cannot be lost but only accumulate in the form $W = \varepsilon_0 \varepsilon E^2/2$, where ε_0 is the permittivity of free space ($\varepsilon_0 = 8.86 \times 10^{-12}$ F m^{-1}); ε is the relative dielectric constant and E is an electric field. In real materials a part of the microwave energy could be transformed into heat (another form of energy). The two main loss mechanisms for non-magnetic materials are dielectric (dipolar) loss and conduction loss. Conduction losses dominate in metallic, high conductivity materials and dipolar losses dominate in dielectric insulators. Dielectric heating, also known as the re-orientation loss mechanism, arises when a high frequency electric field is established within a material which is a poor electrical conductor. When microwaves penetrate and propagate through a dielectric material the internal field generated within the affected volume induces rotation of charge complexes, such as dipoles. A sample's heating is due to rotational excitation of its molecules and irreversible energy transfer to translational energy by molecular collisions. Inertial, elastic and frictional forces resist these induced motions (the dipoles are unable to follow the rapid reversals in the field) and cause losses, a consequence of which is volumetric heating. As a result of this phase lag, power is dissipated in the material. To describe the ability of a dielectric to dissipate energy in an electric field, engineering practice most often uses the angle of dielectric losses

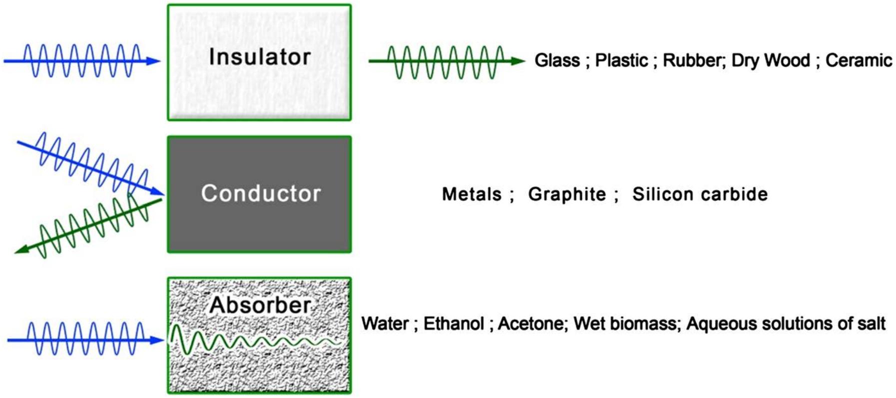

Figure 3.2 Microwave absorption in insulators, conductors and absorbers.

as well as the tangent of this angle, often named the dissipation factor. The dielectric loss angle δ is the angle complementary to the 90° phase angle φ between the current and voltage in the capacitive circuit (see Figure 3.3). The word "loss" refers to the input microwave energy that is lost to the sample by being dissipated as heat. A high value for $\tan\delta$ indicates a high susceptibility to microwave energy. The tangent loss factor could also be expressed as the quotient, $\tan\delta = \varepsilon''/\varepsilon'$, where ε'' is the dielectric loss factor, indicative of the efficiency with which electromagnetic radiation is converted to heat, and ε', is the dielectric constant describing the ability of molecules to be polarized by the electric field.[11]

The power P absorbed per unit volume ($\mathrm{W\,m^{-3}}$) of the sample at any instant of time has been described by Sutton[12] as

$$P = 2\pi f \varepsilon_0 \varepsilon' \tan\delta |E|^2 \tag{3.1}$$

where E ($\mathrm{V\,m^{-1}}$) is the magnitude of the internal electric field and f is the frequency.

As stated earlier, two phenomena play a role in the dielectric heating of a material: (1) the polarization (represented by ε') and (2) the 'rubbing' between the polarized molecules ($\tan\delta$). Both elements are contained in the definition of the loss factor ε'' ($\varepsilon'' = \varepsilon' \tan\delta$). The loss factor is not a constant value for a given material. It is, among other things, dependent on frequency and temperature. The key for generating the heat by microwaves in liquid media containing polar molecules or ions is that the frequency of the oscillating field should be appropriate to enable inter-particle interaction. If the frequency is very high, intermolecular bonds will not allow the charged particles to even start to move to follow the electromagnetic field, resulting in a lack of inter-particle interaction. On the other hand, if the frequency is too low, the charged particles will have sufficient time to align themselves in phase with the electromagnetic field. In both cases, no random interaction (friction and hence heat release) will take place between the neighbouring particles. The absence of the random interaction is also one of the reasons why sample temperature influences the efficiency of microwave heating. For example, hot water is significantly less well heated than water at room

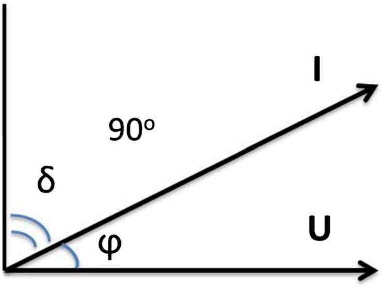

Figure 3.3 Dielectric loss angle.

temperature, because the more mobile electric dipoles are able to follow the microwave field with less phase lag due to reduced friction.[13]

With increasing temperature, the loss factor will often increase. A material whose loss factor has a positive temperature coefficient will, starting from a critical temperature T_c, suddenly absorb much more energy. It is known as thermal runaway and can damage the product. Critical temperatures often arise around phase changes in the material. For example, the loss factor of food products typically demonstrates stepwise change around the melting point of ice as shown in Figure 3.4.[14]

It is important to note that water in an ice phase and bound water are scarcely heated because the electric dipoles cannot rotate due to the tightly hydrogen-bonded network of water molecules.[13,15] This fact could be explained due to the very low energy of the microwave photon compared to the typical energy required to break molecular bonds (see Table 3.2). However, the dielectric loss tangent of water increases 178-fold from 0.0009 in ice to 0.16 in water at 25 °C.[16]

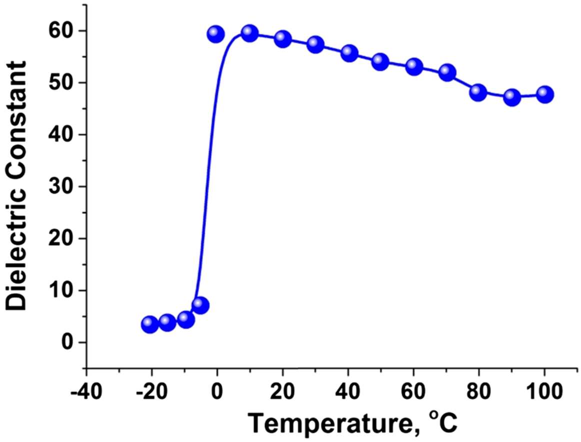

Figure 3.4 Dielectric constant in different food products with temperature.

Table 3.2 Comparison of bond energies with microwave energy.

Bond type	Bond energy (kJ mol^{-1})	Bond energy/MW energy
Microwaves (2.45 GHz)	0.001	1
van der Waals	0.4–4	400–4000
Hydrogen bonds	10–40	10 000–40 000
Dipole attraction between molecules	40–400	40 000–400 000
Covalent single bonds	200–500	200 000–500 000
Covalent double bonds	500–700	500 000–700 000
Covalent triple bonds	800–1000	800 000–1 000 000
Ionic bonds	700–4000	700 000–4 000 000

Therefore, microwave-caused excitation does not affect the structure of the molecules, and the rate of microwave heating (efficiency of interaction) increases around the temperature of phase transitions—events such as melting and softening.

3.3 Microwave Pyrolysis/Torrefaction

3.3.1 Introduction

The vast majority of research establishments have explored the thermal processes of pyrolysis and torrefaction extensively, with significant focus over the past two decades on the conversion of biomass to gaseous and liquid biofuels. From these studies, it has been established that the thermo-chemical route of pyrolysis provides one of the simplest paths for the production of chemicals that can be adapted for use with current liquid fuel-based technology. Nevertheless, significant challenges have arisen in these processes due not only to the desired, but also to undesired chemical species being produced. These possess significant undesirable properties such as wide product distributions, high oxygen contents, high water contents, low pH values and the presence of significant levels of alkali metals.

The literature on low-temperature pyrolysis using microwaves or conventional heating is very limited. This is due to the infancy of the research topic, hindered by the research community using microwave heating to replicate conditions of high temperature conventional heating. Using microwaves as a heating source is not as efficient as conventional heating, however using microwaves as a "catalyst" allows their power to be realised.

However, recently the application of microwave energy has been explored as a potential route for the conversion of biomass, with microwave pyrolysis and torrefaction becoming prevalent in the research community as far back as 1980, with journal articles reporting microwave pyrolysis of biomass and its constituent components. The main focus of these studies has utilised microwaves to heat lignocellulosic materials to high temperatures, in excess of 500 °C, which has been shown to have some advantages over conventional thermal routes but still presents a significant challenge in the refinement of the products produced, with many of the limitations seen in conventional pyrolysis work still present, as evident in the work of Domínguez *et al.*[17] However, little work has been performed to establish whether the conversion of biomass can be achieved through the use of low temperatures (<400 °C), especially on the individual components of cellulose, hemicellulose and lignin.[18] Nevertheless, the work that has been performed showed the potential for the collection of higher value chemicals with simpler product distributions and the potential for production of high value platform molecules.[19–21]

Low-temperature microwave pyrolysis and torrefaction has had a limited range of research performed, however, fundamental investigations have been undertaken looking at the decomposition of the constituents of biomass, these being cellulose, hemicellulose and lignin,[20,22,23] as well as investigations into biomasses such as oil palm, wheat straw, reed canary grass, softwood, bracken, waste office paper, barely dust, macro algae, oil palm shell, tea waste, coffee hulls, sewage sludge, willow, bagasse and corn cob.

3.3.2 Low-Temperature Pyrolysis of Constituent Biomass Components

The technical challenge of understanding and developing conventional pyrolysis-based chemicals has been largely examined from basic principles, with products being controlled to the greatest extent by manipulating reaction conditions, such as heating rate and maximum pyrolysis temperature.[24] However, the microwave heating process is very much dependent on the fundamental dielectric properties of a material, the reaction temperature and the density and wavelength of microwaves. As such, logical progression in the field would benefit by understanding the fundamental interactions between microwaves and biomass constituent components.

The first experiments on the microwave decomposition of cellulose were undertaken by Allan *et al.*,[25] in which the solid, liquid and gaseous products were examined. Following this, two research groups led by J. H. Clark from the University of York in the UK and the other by Y. Fernandez from the National Institute of Carbon in Spain, published a number of papers on the microwave pyrolysis of biomass and the components of cellulose and lignin.[20,26–29]

Of these, only a handful have been undertaken by us in the Green Chemistry Centre of Excellence, University of York, in which the low-temperature microwave pyrolysis of cellulose or lignin has been investigated and currently no work has been published on hemicellulose.[30]

3.3.2.1 Cellulose

The low-temperature microwave pyrolysis of cellulose has been presented in a number of papers. Of these, Allan *et al.*[25] demonstrated the principle of microwave pyrolysis of cellulose, with a deeper understanding developed by Ollivon *et al.*[23] in which the dielectric changes of cellulose were investigated. From ref. 23 (see Figure 3.5) it was possible to determine that a temperature of 180 °C demonstrated a significant change in the dielectric properties of cellulose, with a maximum being reached. At this point, the rate at which temperature increases is at its greatest, after which a reduction in the dielectric properties of cellulose occurs as the temperature increases and the sample undergoes decomposition.

The change in the dielectric properties of cellulose is accompanied by its phase transition, the point at which cellulose changes from a glass state to an elastic state.[31,32] This occurs at approximately 220–250 °C for dry cellulose.[33] This is extremely high, close to the temperature at which initiation of conventional thermal decomposition of cellulose occurs—approximately 250 °C.

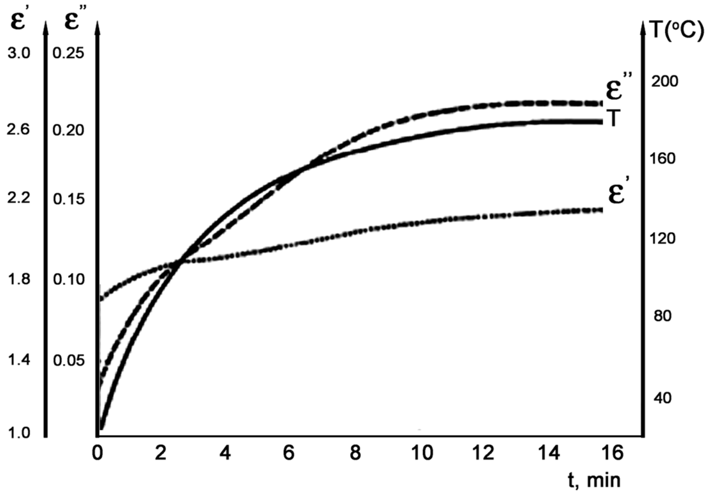

Figure 3.5 The dielectric properties (right: T = temperature, left: ε' and ε'') of cellulose with increasing temperature.[23] Reproduced from Thermochimica Acta, volume 125, M. Ollivon, S. Quinquenet, M. Seras, M. Delmotte and C. More, Microwave dielectric measurements during thermal analysis, page 151, Copyright 2016, with permission from Elsevier.

Budarin *et al.* examined the changes in crystallinity of cellulose with temperature, finding that a significant reduction occurred at 180 °C.[20] This was subsequently linked to major dielectric changes when the sample underwent microwave heating. It has to be proposed that it was the changes in crystallinity within the regions undergoing phase transition that gave the increased dielectric response. The author further proposed that cellulose was considered to have greater molecular freedom as the structure became amorphous, resulting in an increasing number of CH_2OH groups within the intra-molecular arrangement to undergo microwave heating by dipolar polarisation (see Figure 3.6).

The interaction of microwaves dependent upon the crystallinity of cellulose and the resulting changes in its dielectric properties have also been linked to changes in product distributions during the decomposition process.

When looking at char/torrified material it was found that when comparing chars prepared under microwave and conventional thermal conditions, microwave-produced chars have significantly greater calorific values (LHV) (see Figure 3.7).[20]

The significant shift in the calorific values of chars obtained from microwave pyrolysis at 180 °C was observed to correlate with the glass transition temperature of cellulose, with amorphous areas of the cellulose most likely initiating the decomposition process. This was confirmed within this study by deuteration of the amorphous regions of cellulose, with the results displaying a much slower decomposition of the deuterated cellulose than of the protonated form.[20]

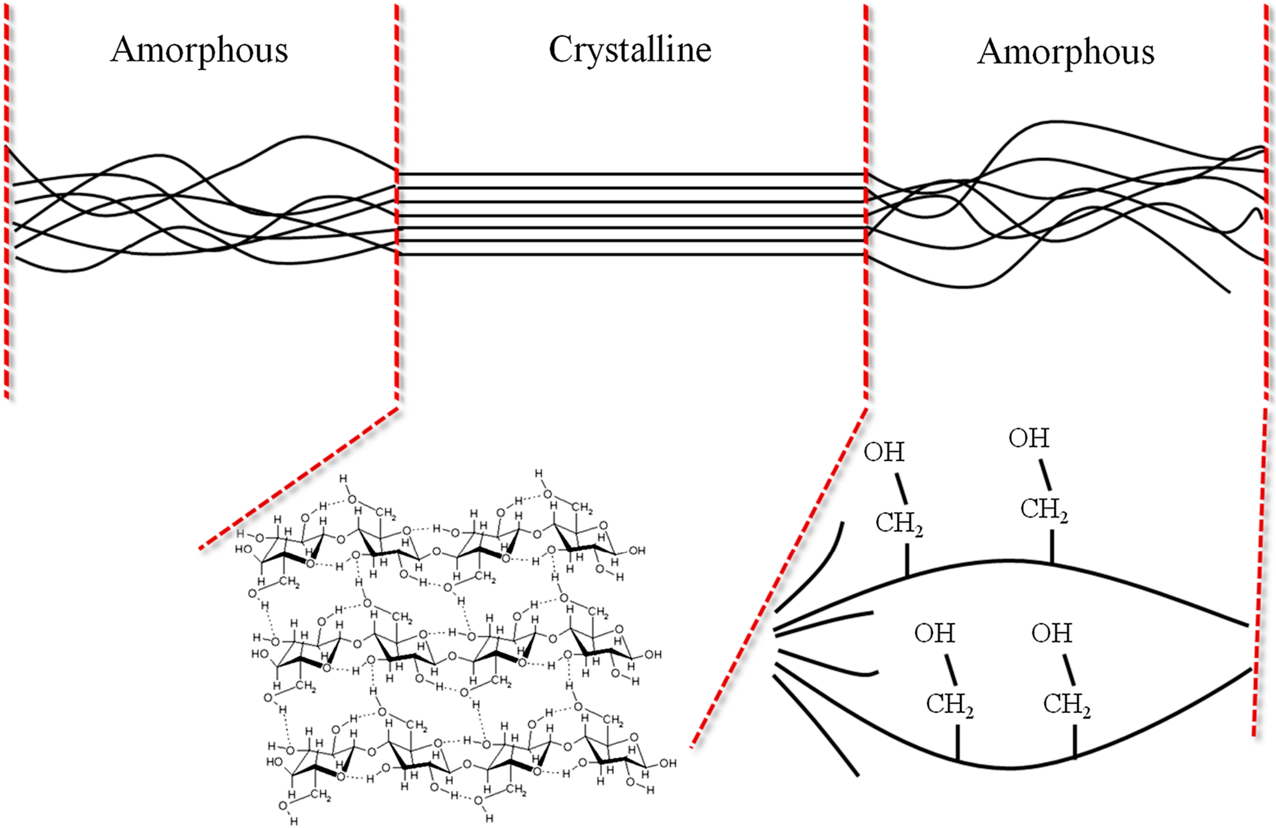

Figure 3.6 Crystalline and amorphous regions of cellulose.

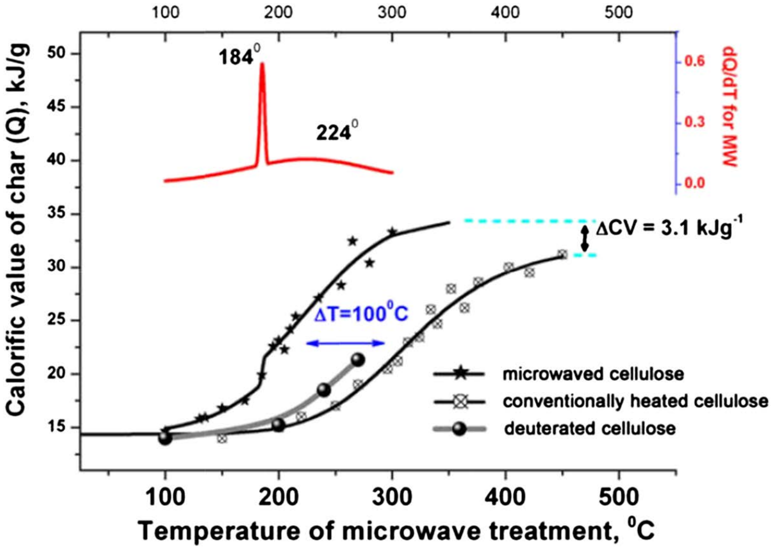

Figure 3.7 Calorific value of char obtained from cellulose processed conventionally and in the presence of microwaves. Cellulose that was initially deuterated and then microwave treated is also shown. The calorific value derivative of the microwave treated cellulose is shown emphasising a peak at 184 °C.[20] Reproduced from Bioresource Technology, volume 101, V. L. Budarin, J. H. Clark, B. A. Lanigan, P. Shuttleworth and D. J. Macquarrie, Microwave assisted decomposition of cellulose: A new thermochemical route for biomass exploitation, page 3777, Copyright 2016, with permission from Elsevier.

During the low-temperature microwave decomposition of cellulose it is found that four major components are formed, these being levoglucosan, 1,6-anhydro-β-D-glucofuranose, 1,4 : 3,6-dianhydro-α-D-glucopyranose and levoglucosenone. These have been recognised as the major decomposition products of cellulose pyrolysis from a conventional thermal process[24,34–37] and indicate that the fundamental chemistry of cellulose decomposition is largely unchanged. A generalised model of cellulose decomposition is proposed and is shown in Figure 3.8.

The model summarises that the first stage of cellulose decomposition is to form active cellulose, undergoing depolymerisation to oligosaccharides. These undergo further depolymerisations until individual sugar units are formed. The first of these is levoglucosan, formed through the cleavage of the 1,4-glycosidic linkage in the polymer followed by intramolecular rearrangement of monomer units.[37] Levoglucosan undergoes further dehydration reactions to form 1,4 : 3,6-dianhydro-α-D-glucopyranose with the loss of one water and levoglucosenone from the loss of two waters. The route that this decomposition takes is unclear with simultaneous competing pathways forming both products directly, however it is also possible to form levoglucosenone from further dehydration of 1,4 : 3,6-dianhydro-α-D-glucopyranose.

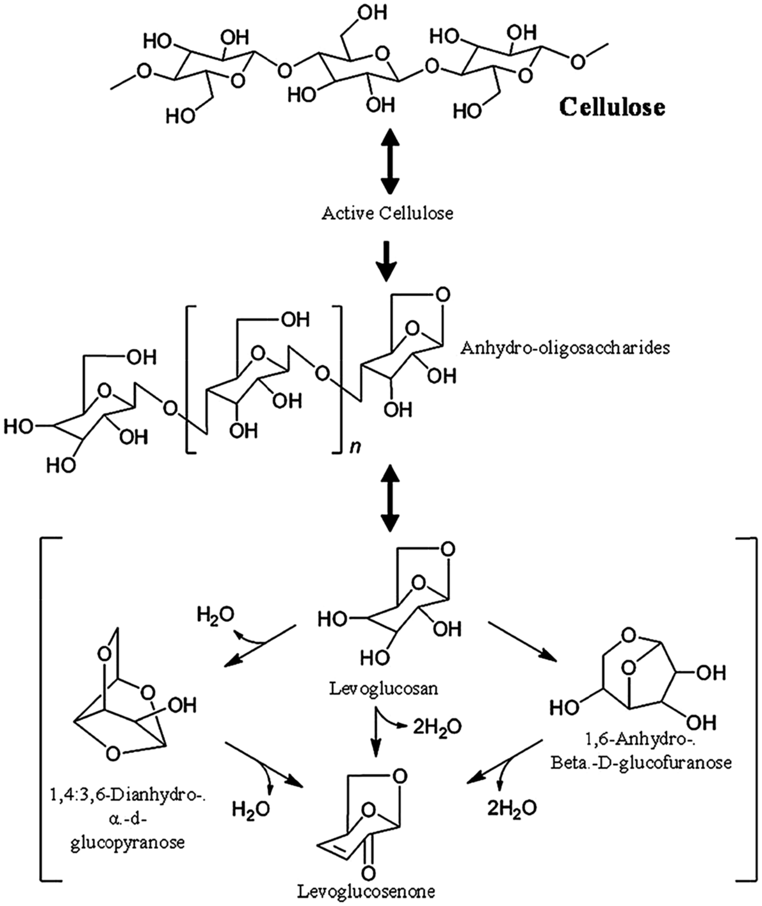

Figure 3.8 Proposed route of cellulose pyrolysis.

Nevertheless, the isomer of levoglucosan, 1,6-anhydro-β-D-glucofuranose is also present during this decomposition process and is thought to go through dehydration losing two waters to form leveglucosenone (Figure 3.9).

The phase transition temperature of cellulose is important in the microwave decomposition process.

The use of MDSC was employed so that the structural changes of crystallisation and melting could be determined. The technique offers increased sensitivity over that of conventional differential scanning calorimetry (DSC).[38,39] Like DSC, MDSC determines phase changes by measuring the difference in heat flow between a sample and a reference, quantifying endothermic and exothermic events from this. MDSC modulates the heating rate the sample is exposed to, allowing for the simultaneous detection of both endothermic and exothermic events. This is subsequently mathematically corrected so that reversing and non-reversing heat flows can be derived.[40,41]

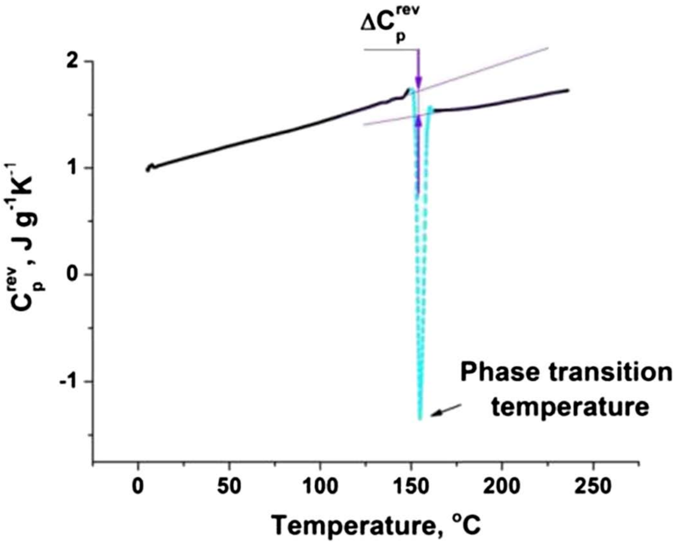

Figure 3.9 MDSC reverse heat capacity traces for unprocessed microcrystalline cellulose.

From the MDSC trace, it was possible to determine the phase transition temperature (T_{phase}) and the reverse heat capacity (ΔC_p^{rev}). The MDSC shows the reverse heat flow trace, which does not directly show the phase transition temperature, but rather the change from a metastable to the thermodynamically stable crystalline state, hence the reverse heat flow. This is the reverse phase transition.

3.3.2.2 Hemi-Cellulose

Little work has been published on the microwave decomposition of hemi-cellulose apart from that performed by Lanigan (2010) in which the microwave and thermal decomposition of hemicellulose was investigated for changes in calorific value by irradiating hemi-cellulose at between 120 and 300 °C and by conventional thermal conditions from 250–450 °C, respectively. The results of this can be observed in Figure 3.10.

The pyrolysis of hemi-cellulose appeared to proceed at temperatures around 100 °C lower during microwave decomposition than during conventional thermal decomposition, whilst also occurring 130 °C lower than cellulose—at 250 °C,[30] a result of the depolymerisation arising through rearrangement of the more heterogeneous polysaccharide structure. Decomposition of oligosaccharides and monosaccharides then occurs at 300 °C to produce char, CO, CO_2 and H_2O.[22] Further to this, the study found that a significant increase in the calorific value of hemi-cellulose char could be achieved in comparison to conventional thermal means with final differences of 6.0 kJ g^{-1} achieved by the comparable temperature at approximately

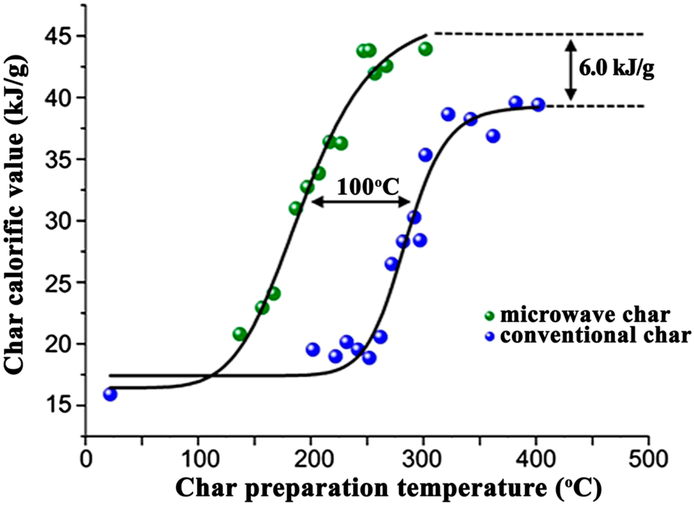

Figure 3.10 Calorific values of chars obtained from hemicellulose (xylan) processed conventionally and in the presence of microwaves.[22] Reproduced with permission of Brigid Lanigan.

300 °C. When compared to the changes observed in cellulose, it was found that an increase of *circa* 30 kJ g^{-1} as opposed to 24 kJ g^{-1}, for hemi-cellulose and cellulose after microwave irradiation respectively, is, believed to be as a result of hemi-cellulose thermal degradation taking place at significantly lower temperatures.[22]

To date, studies of the microwave decomposition of hemi-cellulose have not been able to identify the decomposition mechanisms that occur. However, if the mechanisms recognised in the microwave decomposition of cellulose are applied to hemi-cellulose, then it can be surmised that the increased molecular freedom of movement due to its amorphous structure allows for groups within hemi-cellulose to undergo dipolar polarisation and increase the interaction between microwaves and hemi-cellulose. This is thought to decrease the barrier of activation to degradation, leading to decomposition at lower temperatures. No further investigations have been performed on the low-temperature microwave pyrolysis of hemi-cellulose, hence understanding of the decomposition process and resulting materials is limited at this time.

3.3.2.3 *Lignin*

The nature of lignin is such that a high degree of variability can be seen across different sources of the material; this is considered to be largely dependent on the species from which it was derived.[42] However, it is commonly defined as an amorphous, polyphenolic material arising from the enzymatic polymerisation of three phenylpropanoid monomers, each having a three carbon chain attached to a six atom carbon ring structure and called phenylpropane. Issues arise in the microwave heating of lignin due to the largely sterically hindered complex structure, in which the lack of hydroxyl groups does not promote the heating of its mass. The result being that it is highly resistant to degradation and poses a poor dielectric in comparison to cellulose and hemi-cellulose making it less susceptible to microwave heating, requiring significantly greater microwave powers to induce pyrolysis.[43]

It is generally recognised that in lignocellulosic materials the presence of cellulose is required as an initiating compound, triggering the breakdown of the relatively inactive compounds (lignin) during microwave decomposition. As such, there are few investigations into the microwave decomposition of lignin itself, but rather investigations into lignocellulosic materials.

Nevertheless, key investigations have indicated that the microwave pyrolysis process displays a number of key differences over that of a conventional pyrolysis process with results demonstrating fundamental changes in the balance of decomposition pathways over those normally seen.

3.3.3 Microwave Pyrolysis of Lignocellulosic Biomass

The increasing number of studies performed on the microwave pyrolysis of biomass has increased significantly since the mid-2000s with both the number of patents and articles published reaching new heights in 2010.[44] The range of biomass investigated is noteworthy but with a distinct focus on biomass wastes, *e.g.* agricultural and forestry residues or food wastes, due to the diversification away from food-competitive crops. This has led to few studies looking at grains and grasses but rather industrial by-products such as softwood, wheat straw, rice straw, corn cob, oil palm, coffee hulls and then the cultivated micro/macro algae. This means there is little research on any one given source of material at this moment in time, but rather a number of short studies investigating each of these potential new resources.

3.3.3.1 Wood

Woods have been investigated substantially both by conventional thermal pyrolysis and in the microwave pyrolysis community. Wood constitutes the greatest body of research over any other given type of biomass. The first significant piece of research undertaken was by Miura *et al.*[19] in which the microwave pyrolysis of larch (*Lalix leptolepis* Gordon) was undertaken. During this experimentation larch samples were irradiated for given periods of up to 14 minutes, after which mass balance and compositional analysis of oils were performed. From the mass balance it was found that it was possible to decompose the wood block by up to ~80 wt% and from that collect ~26 wt% tar. When analysed for its composition the tar largely consisted of levoglucosan, furfural, phenol, *o*-cresol, veratorol, guaiacol, levoglucosenone, xylosan, eugenol, galactosan, mannosan, alcohols and aldehydes. Of significant interest during this study was the significant production of levoglucosan (~2.6 wt%) which can be used as a platform molecule for the production of many different chemicals.

Further studies have also been performed into Douglas fir by Ren *et al.*[45] in which the torrefaction (pyrolysis) of Douglas fir took place by low-temperature microwave pyrolysis with maximum temperatures reaching 310 °C. The results of his investigations are summarised in Table 3.3.

In his experimentation he found that, with increased reaction temperature and time, the mass of torrefied biomass decreased whilst bio-oil and non-condensable gases were increased. The bio-oils produced from the microwave torrefaction of Douglas fir contained valuable products such as furans, guaiacols, ketones/aldehydes, and sugars, furans ranged in percentage from 18.49% to 29.07% and were primarily composed of β-methoxy-(*S*)-2-furanethanol, furfural, 2-furanmethanol and tetrahydro-2,5-dimethoxyfuran. Sugars in bio-oils ranged from 2.74% to 17.9% and comprised 1,6-anhydro-β-D-glucopyranose, 1,4:3,6-dianhydro-α-D-glucopyranose, and D-mannose. Non-condensable gases comprised mainly CO_2 and CO with their proportions significantly influenced by reaction temperature. The calorific values (HHVs) of torrefied Douglas fir pellets ranged from 20.3 MJ kg^{-1} to 25.4 MJ kg^{-1} and were also increased as the reaction temperature and time increased, with energy yields of 67.03% to 90% which decreased with higher reaction temperature.

3.3.3.2 *Wheat Straw and Rice Straw*

Straws present themselves as an interesting source of biomass as they are often co-products of food production with both wheat and rice straw having little use in comparison with other types of straw, which are often used as

Table 3.3 Summary of experimental results from torrefaction of Douglas fir,[45] reproduced with permission from S. Ren *et al.*, *Energy & Fuels*, 2012, 26, 5936–5943. Copyright 2016, American Chemical Society.

Actual Value		Yield (%)		
Reaction temperature X_1	Reaction time X_2	Bio-oil	Non-condensable gases	Torrefied biomass
250	10	13.12	3.74	83.15
300	10	32.57	8.33	59.11
250	20	17.66	5.82	76.52
300	20	36.35	11.04	52.61
240	15	14.06	3.55	82.39
310	15	32.62	11.32	56.07
275	7.93	22.08	5.61	72.31
275	22	26.79	7.29	65.93
275	15	23.41	5.75	70.85
275	15	25.56	6.25	68.20
275	15	24.56	7.15	68.29

cattle fodder or bedding. Further to this, the high volumes produced on an annual basis around the world are potentially a substantial resource. However, a number of disadvantages related to its density present themselves.

Nevertheless, a number of studies have been completed on these two straw types with the authors Budarin *et al.*,[20,26] Zhao *et al.*[46] and Huang *et al.*[47] having performed research into their low-temperature microwave pyrolysis.

Budarin *et al.*[26] examined the low-temperature microwave pyrolysis of wheat straw at temperatures less than 180 °C. This resulted in identifying trends in the decomposition process and when volatiles were released from the wheat structure (see Figure 3.11).

Budarin *et al.*[48] demonstrated that during the microwave decomposition of wheat straw, volatiles produced showed two major fractions at 110 °C containing low molecular weight carboxylic acids and aqueous soluble components (FTIR spectra I and II, Figure 3.11) and a second fraction at 180 °C thought to correspond to an organic fraction with low water content (FTIR spectrum III, Figure 3.11). This supported the finding from previous investigations that the decomposition initiation temperature of cellulose is within its amorphous range and indicates that that cellulose is likely to be the active component in MW pyrolysis of wheat straw. Within the bio-oil it was found that the major component formed was benzofuran (~28%), with less abundant chemicals such as levoglucosan (~10%) and phenols (~11%). Furthermore the oils were found to have extremely low water contents (<1%).

Microwave pyrolysis of rice straw was performed by Huang *et al.*,[47] in which the use of a single mode microwave was employed and the key findings were that increased microwave power resulted in greater heating rates

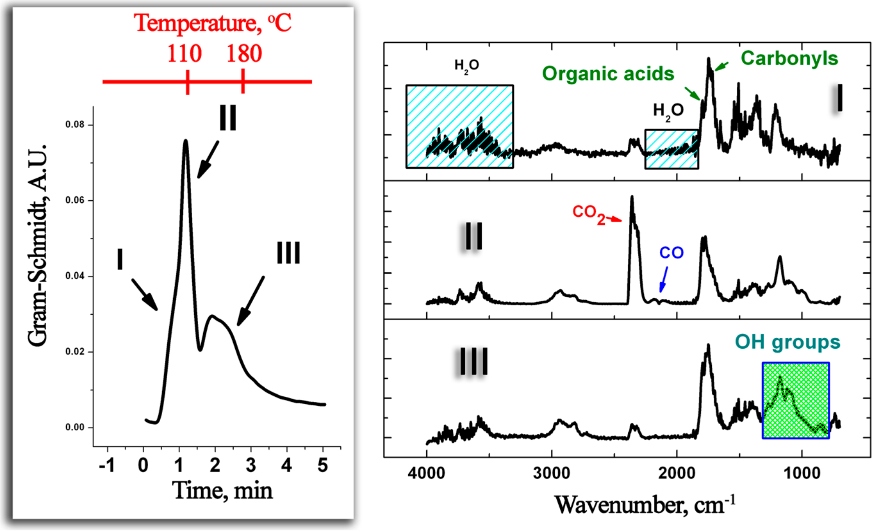

Figure 3.11 *In situ* FTIR analysis of volatiles during pyrolysis.[48] Reproduced from ref. 48 with permission from The Royal Society of Chemistry.

and maximum temperatures, both of which demonstrated a linear relationship, hence they concluded that the results of microwave operating conditions could be relatively predictable in the consequent thermal conditions. The resulting products from the pyrolysis were analysed and the liquids produced were shown to contain alkanes, polycyclic aromatic hydrocarbons and phenols as major components. The fraction of gas produced form the decomposition was found to be significant with around 40% of the rice straw converted to gas. The major components were hydrogen: 50.67%, carbon dioxide: 22.56%, carbon monoxide: 16.09% and methane: 7.42%—together comprising 96.73% of the total. This large production volume of gas was suspected to be a result of catalysis due to the large volume of inorganic compounds found within the rice straw.

3.3.3.3 Macro and Micro Algae

Further work on macro and micro algae was largely performed by Budarin *et al.*[49] and Du *et al.*[50] Unfortunately, the experiments performed by Du *et al.*[50] were at high temperature hence do not fall within the category of low-temperature microwave pyrolysis. Macro algae, including seaweed, are a significant source of polysaccharides, these being alginates, polygalactose and anhydrogalactopyranose. Budarin *et al.*[49] found that upon microwaving the seaweed *Digitata* and *Ascophyllum nodosum* significant gaseous release was achieved at very low temperatures, in the region of 130 °C. With the whole microwave process performed at 200 W (single mode) this produced up to 16 wt% oil and 70 wt% char, with the low overall yields of oil and gas being accounted for by the extremely high levels of inorganic material found within the seaweed. During these investigations it was also found that the mass of seaweed used was critical, with smaller masses resulting in the production of sugars and anhydro- sugars, while greater masses were dominated by the production of phenolic compounds. This indicated that differing decomposition pathways could be elucidated by varying the mass of sample used.

3.3.3.4 Oil Palm

Oil palm was largely investigated by Salema *et al.*[51] wherein the components of oil palm fibre and shell were examined. From this it was found that microwave heating was highly effective in pyrolysing the material which would otherwise have been difficult by conventional techniques. It was found that the temperature of the material used could not be raised above 200 °C when only the raw material was present (see Figure 3.12).

A microwave absorber was added in ratios of 25 wt% and 50 wt% which served to raise the temperature of the pyrolysis process. However it was found that this only had a significant effect for oil palm fibre with temperatures well in excess of 1000 °C being achieved. Bio-oil produced during this process was found to contain phenols, ketones, aldehydes and carboxylic acids. Salma concluded that low-temperature microwave pyrolysis of oil palm shell was

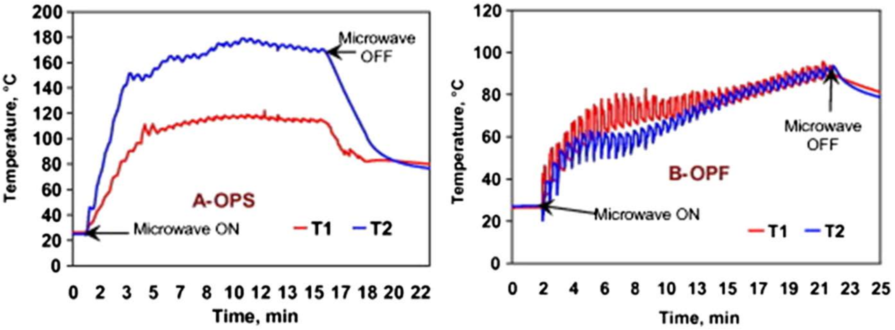

Figure 3.12 Real temperature profiles of oil palm shell (left) and oil palm fibre (right) when exposed to 450 W microwave irradiation (T_1 = bed temperature, T_2 = surface temperature).[51] Reproduced from Bioresource Technology, volume 102, A. A. Salema and F. N. Ani, Microwave induced pyrolysis of oil palm biomass, page 3391, Copyright 2016, with permission from Elsevier.

an efficient route to bio-oil production, but the use of a microwave absorber could assist operation at low power input, reducing the need for high-power microwave pyrolysis.

3.4 Commercial Applications of Microwaves

One of the common feedback comments received on academic microwave chemistry research is that microwave processing is not able to progress to a commercial scale. This comment is unfounded, however, and this part of the chapter aims to highlight the established and broad range of applications in which microwaves are employed. Studies have been carried out investigating the efficiency of microwave processing for various chemical transformations[16,52] and these describe the cases under which microwave processing is more efficient than conventional heating. However, the real world is more telling than the academic literature, so here are various examples of commercial microwave usage. For example, most pre-cooked bacon for sandwiches and pasta sauces is cooked by microwave.[53] The systems employed typically offer smaller footprints, lower capital cost, higher throughput and reduced operating costs along with a reduction in acrylamide formation. The examples shown are all in the public domain, however, the companies involved in reactor design produce many more systems for their customers for applications which are under confidentiality agreements. This secrecy in the industry may be responsible for the lack of public awareness. It is not clear whether the use of microwaves is kept secret due to the innovation in the processes or to protect reputation, as the public perceive the microwave to be a "shortcut" just as it is in the home kitchen environment.

Large commercial microwave systems are built through additive waveguides where multiple magnetrons are combined to produce higher power. As described in Section 2.3 various microwave sources are available, from low (sub-200 W), to very high (>100 kW), powers. Any magnetron size is, in theory, possible, however the microwave industry tends to work with a smaller number of well-developed, well-understood and easy-to-replace units such as the 6 kW at 2.45 GHz, and 100 kW at 915 MHz, ones. These can be relatively easily combined additively to create systems of hundreds of kilowatts, thereby allowing either:

- Higher power input to a modest size static system to achieve a high power density.
- High power input to a continuous system for high product throughput.
- High power input across a large static system for larger batch sizes.

Application systems can be developed in a number of ways including tunnels for continuous processing of solids, ovens/cavities for batch processing and flow systems for liquids/slurries. There are also a number of specialist application systems which will be described below in the application case studies. The most common microwave processing systems are for cooking (*e.g.* ready meals) and food-related processing, such as sterilising and pasteurising.[54] Microwave heating can be used for tempering of products such as meat and gums (see Figure 3.13). By using microwave tempering, products can be prepared, frozen for long-term storage then defrosted in a rapid but controlled manner, whereby product quality is maintained. The technique is often used in the meat supply chain and for managing stock *e.g.* at Christmastime.

3.4.1 Drying Apparatus

Drying is one of the most common applications of large commercial microwave systems. For example, a search of *www.alibaba.com* indicates over 15 000 microwave drying systems available in August 2015.

This is a natural technology solution, with microwaves specifically heating the water rather than the bulk leading to less product damage and, in theory,

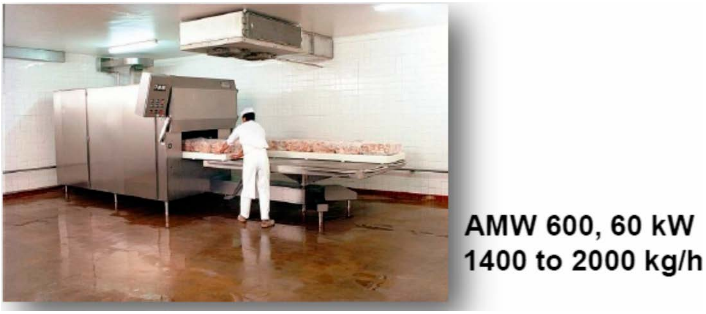

Figure 3.13 Tunnel for tempering, thawing and defrosting of meat blocks.[72] Reproduced with kind permission of Sairem SAS – http://www.sairem.com/.

lower energy costs. However low-temperature drying can be less efficient due to the energy costs of generating microwaves. Furthermore, microwaves can cause issues in certain drying situations if not applied correctly due to channelling of the water vapour. Ceramic drying and curing is one area which benefits from microwave heating.

One unusual benefit of microwave heating is the ability to not influence the non-water part of a product to be dried. The drying of herbs and other plant materials is particularly interesting. When drying lavender or basil under air flow and microwave heating, less flavour/fragrance is lost as volatiles and furthermore better colour in the plant is maintained. This is a distinct advantage as clients prefer the bright green or purple plant material over a dulled, browned or discoloured one.

Some of the largest single microwave cavities have been developed for timber drying applications. Two such batch systems are shown in Figure 3.14. Due to the tightly-bound lignocellulosic structure, water is traditionally very slow to diffuse from wood during drying; furthermore, rapid, forced drying can cause warping of the wood. Microwave heating has been proven to speed this process up, thereby offering savings.

3.4.2 Other Processes

The following applications are variations on heating at relatively low temperatures: drying, cooking, thawing and defrosting. The academic literature has provided examples of much stronger applications using microwave heating whereby microwave systems can offer transformations which cannot be achieved without microwave heating, ones which are better with microwave heating and applications where microwaves are simply more effective/efficient heaters. Some of these applications are gradually being developed into commercial processes.

Combined 50 kW, 27.12 MHz & steam pressure (2 bars)

Drying time: 6 h for coniferous trees, 8 - 9 h for oak

Figure 3.14 Large batch microwave cavities for wood drying.[72] Reproduced with kindpermission of Sairem SAS – http://www.sairem.com/.

Exfoliated vermiculite is a low density material used for insulation, as a growth medium, in packaging, for holding water and for other applications. Traditionally it is manufactured by heating crude vermiculite mineral in a furnace until exfoliation occurs. Researchers at the National Centre for Microwave Processing at the University of Nottingham[55] and E2V have collaborated to commercialise the ProWave® system.[56] The system offers a 90% energy saving by directly heating the water and not the bulk mineral. Furthermore, product quality improves by offering greater control and reducing waste. This is a superb example of utilising the selective heating phenomenon of microwaves through selectively heating the water trapped in pores; both energy-savings and improved exfoliation are possible. The same scenario is possible during steam distillation whereby oils can be extracted from plant products through selective boiling of the water.

Radient Technologies Inc. (Canada) have commercialised the extraction of natural products using microwave assisted processing.[57] Their technology (MAP™) offers increased product purity, increased yield and reduced waste along with the more traditional microwave advantages of lower footprint and lower energy consumption.

Advanced Microwave Technologies Ltd. have developed a very high power density system and currently promote its use in pasteurisation applications.[58] They have proven that microwave heating achieves the same level of microbe kill as conventional thermal pasteurisation at 15–20 °C lower temperatures and reduced contact times. Less product degradation therefore occurs and a better tasting product can be produced. The unique feature of the system is the extremely high power density offered by Dr Zadyraka's patented waveguide/magnetron design; with high microwave field density rapid heating rates can be achieved.

C-Tech Innovation UK[59] have developed a novel process and product combination which utilises microwave heating to deconstruct garments at the end of life or end of season which allows better recycling or even reuse by allowing separation of embroidered logos and different fabric components.

Pressurisation and microwave heating is an emerging area. By employing the advantages of microwave energy input to feedstock above the boiling point, additional benefits may be possible. The majority of laboratory research synthesis and digestion microwaves allow this,[60–62] however the ability to take this from millilitre bench scale to pilot or commercial scale has been limited. Sairem have developed a novel microwave "wand" applicator.[63,64] This allows microwaves to be introduced into batch or flow vessels which can be pressure vessels. This appears to be a solution to the dichotomy of the thick, mechanically strong walls required for holding pressure limits trading-off against microwave transparency.

3.4.3 Microwave-Assisted Biomass Activation

Despite all the good reasons outlined earlier in this chapter, commercial use of microwaves for thermochemical processing has been very limited. With a small footprint and no penalty for small units, microwaves lend themselves to biomass processing as they can be taken to the biomass processing site seasonally thereby leaving by-products such as water on-site allowing the products to be transported directly to their user. However, the distributed *versus* centralised processing argument for biomass has other aspects, including downstream processing, to be considered.

In the arena of microwave-assisted torrefaction targeting biochar, Carbonscape of New Zealand[65] are the most active company. They have progressed through pilot scale to commercial, and produce biochar and pyrolysis oils. Initially the biochar was marketed as a soil improver but their technology has now matured and it is suitable for use as green coke in the steel industry and activated carbon.

Pyrolysis, the thermochemical process for making bio-oil and other liquid products, struggles within product markets. Bio-oil has the potential for direct use as a heavy oil, can be upgraded for use in transport fuels or refined into chemical feedstocks. However, due to the relative immaturity of the technology, upgrading solutions are still in infancy. One of the leaders in development of these technologies is Future Blends.[66] Initially created by the UK government's Carbon Trust organisation, Future Blends has worked actively in conventional bio-oil formation, microwave pyrolysis and bio-oil upgrading. In Norway, the Scandinavian Biofuels Company[67] has large equipment carrying out microwave pyrolysis of a range of waste materials including sludge, plastics and biomass. To aid the commercialisation of the technology, demonstration centres exist in York, UK at the Biorenewables Development Centre[68] and in Minnesota, USA at the Center for Biorefining's Department of Bioproducts and Biosystems Engineering.[69] These facilities offer access to demonstration-scale microwave equipment to allow users to trial the technology.

Gasification has not been reported using microwave heating, however microwave-induced plasma gasification is gaining interest as a methodology.[70] Plasma gasification generates syngas (carbon monoxide and methane) which can subsequently be rebuilt into conventional chemical building blocks using Fischer–Tropsch chemistry. Microwave-induced plasma is, however, different to microwave activation of biomass and beyond the scope of this discussion.

Beyond biomass, pyrolysis lends itself to processing waste plastics and packaging. Currently, at best, plastics can be recovered as recycled plastics or burnt for energy recovery in a solid recovered fuel (SRF) system. Most packaging is however composite and therefore not suitable for simple recycling and energy recovery is the bottom of the value chain in comparison to pyrolysis. Alternatively, pyrolysis and microwave induced pyrolysis have been applied to plastic packaging, where products including monomers and liquid fuels have been produced. On searching for microwave pyrolysis one is overwhelmed with used tyre pyrolysis systems. Due to the nature of tyre rubber, pyrolysis is relatively easy—the carbon black filler acts as a strong absorber which allows for the depolymerisation of the rubber. With the steel reinforcement, carbon black and rubber separated, the waste issue is dealt with. However, carbon black has limited market value and, due to the high sulfur content, the bio-oil has yet to find a commercial outlet. Within the UK a system for recovering energy and the aluminium metal from laminates and Tetrapak® cartons using microwave pyrolysis has been developed by the University of Cambridge spin-out, Enval.[71] The system is attracting strong interest from many large food producers.

3.5 Conclusion

The wide range of academic papers and commercial applications presented in this review shows that microwave pyrolysis is a feasible process at low temperatures (below 300 °C). The link between the maximum microwave interaction and specific thermodynamic phase transitions of structure components of biomass has been demonstrated. The observed changes were reproduced by independent calorimetric measurement, for each component changes were shown to be below 250 °C reinforcing the observed low-temperature process.

It is very important to note that there are a lot of commercially-available microwave processes which operate at low temperature (below 300 °C). For example, microwaves have been used for many years for drying and cooking purposes; they are highly suitable due to the strong interaction between microwaves and water. However, microwaves also offer other benefits including better flavour retention. It is to be noted that the low-temperature pyrolysis process temperatures are in the range of standard materials of construction—PTFE and Pyrex®—and therefore apparatus already in existence is suitable for low-temperature microwave pyrolysis.

The systems employed typically offer smaller footprints, lower capital cost, higher throughput and reduced operating costs along with other process benefits such as less side-product formation. Naturally, this is not always the case and microwaves cannot replace every heating process, there are examples where microwave heating does not compete. The generation of microwave energy is not as efficient in comparison to burning gas to generate steam or hot air for example.

We have not even touched on the neighbouring technologies of RF and ohmic heating, or the complimentary infra-red heating, but the authors hope technologists will start to consider heating methods beyond the conventional direct convective heating as the benefits often far exceed those of the latter.

Acknowledgements

The authors would like to acknowledge Marilena Radiou of Sairem and all the team at Advanced Microwave Technologies for fascinating insights and discussion. The authors would like to thank members of the Green Chemistry Centre of Excellence and Biorenewables Development Centre for their support and stimulating discussion. The authors also acknowledge funding from the EPSRC (EP/K014773/1).

References

1. J. M. Osepchuk, *IEEE Trans. Microwave Theory Tech.*, 1984, **32**, 1200–1224.
2. *The RF and Microwave Handbook*, ed. M. Golio, CRC Press, Taylor & Francis Group Boca Raton London New York, 2nd edn, 2008.
3. A. W. Guy, *IEEE Trans. Microwave Theory Tech.*, 1984, **32**, 1182–1200.
4. W. C. Brown, *IEEE Trans. Microwave Theory Tech.*, 1984, **32**, 1230–1242.
5. J. M. Osepchuk and Ieee, *2009 Ieee/Mtt-S International Microwave Symposium*, 2009, vol. 1–3, pp. 1397–1400.
6. A. C. Metaxas and R. J. Meredith, *Industrial Microwave Heating*, Peter Peregrimus Ltd., London, UK, 1983.
7. S. C. Kashyap and W. Wyslouzil, *J. Microwave Power*, 1977, **12**, 223–230.
8. S. M. Bradshaw, E. J. van Wyk and J. B. de Swardt, *J. S. Afr. Inst. Min. Metall.*, 1998, **98**, 201–210.
9. D. M. P. Mingos and D. R. Baghurst, *Chem. Soc. Rev.*, 1991, **20**, 1–47.
10. D. A. Jones, T. P. Lelyveld, S. D. Mavrofidis, S. W. Kingman and N. J. Miles, *Resour., Conserv. Recycl.*, 2002, **34**, 75–90.
11. Y. Fernandez, A. Arenillas and J. A. Menendez, in *Advances in induction and microwave heating of mineral and organic materials*, ed. Grundas, Lublin, 2011, vol. 31.
12. W. H. Sutton, *Am. Ceram. Soc. Bull.*, 1989, **68**, 376–386.
13. M. Tanaka and M. Sato, *J. Chem. Phys.*, 2007, **126**, 03450.
14. J. Chen, K. Pitchai, S. Birla, R. Gonzalez, D. Jones and J. Subbiah, *Trans. ASABE*, 2013, **56**, 1457–1467.
15. A. K. Datta and R. C. Anantheswaran, *Handbook of Microwave Technology for Food Application*, CRC Press, USA: Marcel Dekker, Inc, 2001.
16. M. J. Gronnow, R. J. White, J. H. Clark and D. J. Macquarrie, *Org. Process Res. Dev.*, 2005, **9**, 516–518.
17. A. Domínguez, J. A. Menendez, M. Inguanzo and J. J. Pis, *Bioresour. Technol.*, 2006, **97**, 1185–1193.
18. J. A. Menéndez, A. Domínguez, Y. Fernández and J. J. Pis, *Energy Fuels*, 2006, **21**, 373–378.
19. M. Miura, H. Kaga, T. Yoshida and K. Ando, *J. Wood Sci.*, 2001, **47**, 502–506.
20. V. L. Budarin, J. H. Clark, B. A. Lanigan, P. Shuttleworth and D. J. Macquarrie, *Bioresour. Technol.*, 2010, **101**, 3776–3779.
21. P. Shuttleworth, V. Budarin, M. Gronnow, J. H. Clark and R. Luque, *J. Nat. Gas Chem.*, 2012, **21**, 270–274.
22. B. Lanigan, Microwave processing of lignocellulosic biomass for production of fuels, PhD thesis, University of York, 2010.
23. M. Ollivon, S. Quinquenet, M. Seras, M. Delmotte and C. More, *Thermochim. Acta*, 1988, **125**, 141–153.
24. Y. C. Lin, J. Cho, G. A. Tompsett, P. R. Westmoreland and G. W. Huber, *J. Phys. Chem. C*, 2009, **113**, 20097–20107.
25. G. G. Allan, B. B. Krieger and D. W. Work, *J. Appl. Polym. Sci.*, 1980, **25**, 1839–1859.

26. V. L. Budarin, J. H. Clark, B. A. Lanigan, P. Shuttleworth, S. W. Breeden, A. J. Wilson, D. J. Macquarrie, K. Milkowski, J. Jones, T. Bridgeman and A. Ross, *Bioresour. Technol.*, 2009, **100**, 6064–6068.
27. J. A. Menendez, A. Arenillas, B. Fidalgo, Y. Fernandez, L. Zubizarreta, E. G. Calvo and J. M. Bermudez, *Fuel Process. Technol.*, 2010, **91**, 1–8.
28. Y. Fernandez and J. A. Menendez, *J. Anal. Appl. Pyrolysis*, 2011, **91**, 316–322.
29. J. A. Menendez, A. Dominguez, M. Inguanzo and J. J. Pis, *J. Anal. Appl. Pyrolysis*, 2004, **71**, 657–667.
30. D. J. Macquarrie, J. H. Clark and E. Fitzpatrick, *Biofuels, Bioprod. Biorefin.*, 2012, **6**, 549–560.
31. F. Roig, E. Dantras, J. Dandurand and C. Lacabanne, *J. Phys. D: Appl. Phys.*, 2011, **44**, 045403.
32. L. Szcześniak, A. Rachocki and J. Tritt-Goc, *Cellulose*, 2008, **15**, 445–451.
33. A. T. Kalashnik, S. P. Papkov, G. V. Rudinskaya and L. P. Milkova, *Polym. Sci. U.S.S.R.*, 1991, **33**, 107–112.
34. F. Shafizadeh and Y. L. Fu, *Carbohydr. Res.*, 1973, **29**, 113–122.
35. F. Shafizadeh, *J. Anal. Appl. Pyrolysis*, 1982, **3**, 283–305.
36. M. J. Antal, Jr. and G. Varhegyi, *Ind. Eng. Chem. Res.*, 1995, **34**, 703–717.
37. D. K. Shen and S. Gu, *Bioresour. Technol.*, 2009, **100**, 6496–6504.
38. P. Gill, S. Sauerbrunn and M. Reading, *J. Therm. Anal. Calorim.*, 1993, **40**, 931–939.
39. M. Reading, A. Luget and R. Wilson, *Thermochim. Acta*, 1994, **238**, 295–307.
40. A. Boller, C. Schick and B. Wunderlich, *Thermochim. Acta*, 1995, **266**, 97–111.
41. S. L. Simon, *Thermochim. Acta*, 2001, **374**, 55–71.
42. N. D. Bonawitz and C. Chapple, *Annu. Rev. Genet.*, 2010, **44**, 337–363.
43. R. W. C. Chan and B. B. Krieger, *J. Appl. Polym. Sci.*, 1981, **26**, 1533–1553.
44. R. Luque, J. A. Menendez, A. Arenillas and J. Cot, *Energy Environ. Sci.*, 2012, **5**, 5481–5488.
45. S. Ren, H. Lei, L. Wang, Q. Bu, Y. Wei, J. Liang, Y. Liu, J. Julson, S. Chen, J. Wu and R. Ruan, *Energy Fuels*, 2012, **26**, 5936–5943.
46. X. Zhao, M. Wang, H. Liu, L. Li, C. Ma and Z. Song, *Bioresour. Technol.*, 2012, **104**, 673–678.
47. Y. F. Huang, W. R. Chen, P. T. Chiueh, W. H. Kuan and S. L. Lo, *Bioresour. Technol.*, 2012, **123**, 1–7.
48. V. L. Budarin, P. S. Shuttleworth, J. R. Dodson, A. J. Hunt, B. Lanigan, R. Marriott, K. J. Milkowski, A. J. Wilson, S. W. Breeden, J. J. Fan, E. H. K. Sin and J. H. Clark, *Energy Environ. Sci.*, 2011, **4**, 471–479.
49. V. L. Budarin, Y. Z. Zhao, M. J. Gronnow, P. S. Shuttleworth, S. W. Breeden, D. J. Macquarrie and J. H. Clark, *Green Chem.*, 2011, **13**, 2330–2333.
50. Z. Y. Du, Y. C. Li, X. Q. Wang, Y. Q. Wan, Q. Chen, C. G. Wang, X. Y. Lin, Y. H. Liu, P. Chen and R. Ruan, *Bioresour. Technol.*, 2011, **102**, 4890–4896.
51. A. A. Salema and F. N. Ani, *Bioresour. Technol.*, 2011, **102**, 3388–3395.
52. J. D. Moseley and C. O. Kappe, *Green Chem.*, 2011, **13**, 794–806.

53. K. T. Higgins, *Food Progressing*, http://www.foodprocessing.com/articles/2015/industrial-microwave-technology/, 2015.
54. Y. V. Zadyraka, S. I. Gritsinin, M. A. Misakyan, I. A. Kossyl and E. M. Barkhudarou, US **20120305496** A1, Apparatus for treating a fluid with microwave radiation, 2009.
55. O. Folorunso, C. Dodds, G. Dimitrakis and S. Kingman, *Int. J. Miner. Process.*, 2012, **114**, 69–79.
56. E2V bring life to technology, http://www.e2v.com/news/e2v-launches-prowave-pioneering-vermiculite-exfoliation-system/, 2011.
57. Microwave Assisted Processing, Radient, http://www.radientinc.com/.
58. Advanced Microwave technologies, http://www.advancedmicrowave-technologies.com/, 2010.
59. C-Tech innovation, http://ctechinnovation.com/funded-projects/wear2-microwave-textile-disassembly/, 2015.
60. CEM Corporation, http://www.cem.com/chemical-synthesis.html, 2015.
61. Milestone Inc, http://www.milestonesci.com/products/microwave-synthesis.html, 2014.
62. Anton-Paar, http://www.anton-paar.com/corp-en/products/group/microwave-synthesis/, 2015.
63. A. Grange, J. M. Jacomino and A. Grandemenge, WO2009122101 A1, 2008.
64. A. Grange, J. M. Jacomino and A. Grandemenge, WO2009122102 A1, 2008.
65. CarbonScape, http://carbonscape.com/, 2015.
66. Future Blends and Carbon Trust Enterprise, http://www.futureblends.com, 2015.
67. Scandinavian Biofuel Company, http://www.sbiofuel.com/pyrolysis.html, 2012.
68. Biorenewables Development Centre, http://www.biorenewables.org/machine/microwave-pyrolysis-unit/, 2015.
69. Centre for Biorefining, University of Minnesota, http://biorefining.cfans.umn.edu/, 2015.
70. T. Freyberg, *Waste Management World*, 2012.
71. Enval, http://www.enval.com/, 2015.
72. http://www.sairem.com/, 2015.

CHAPTER 4

Microwave Reactor Concepts: From Resonant Cavities to Traveling Fields

GUIDO S. J. STURM[a], ANDRZEJ I. STANKIEWICZ[b]
AND GEORGIOS D. STEFANIDIS*[c]

[a]Process and Energy Department, Delft University of Technology, Leeghwaterstraat 39, 2628 CB Delft, The Netherlands; [b]Process and Energy Department, Delft University of Technology, Leeghwaterstraat 39, 2628 CB Delft, The Netherlands; [c]Chemical Engineering Department, Katholieke Universiteit Leuven, Willem de Croylaan 46, 3000 Leuven, Belgium
*E-mail: G.S.J.Sturm@TUDelft.nl, A.I.Stankiewicz@TUDelft.nl, georgios.stefanidis@cit.kuleuven.be

4.1 Introduction: The Limitations of Thermal Reactor Activation

Enabling chemical reactor operation under tailored and selective heating at macro- and microscale is a major chemical reaction engineering challenge. Thermal activation of chemical reactors is conventionally done by means of conductive heating through the reactor walls. Conventional heating is inherently (1) non-selective towards chemically active and inert elements of the reactor (reactants, products, solvents, catalyst, support,

RSC Green Chemistry No. 47
Alternative Energy Sources for Green Chemistry
Edited by Georgios Stefanidis and Andrzej Stankiewicz

Published by the Royal Society of Chemistry, www.rsc.org

walls) and (2) slow (in most cases), giving rise to uncontrolled spatial and temporal temperature gradients. Both limitations are detrimental in terms of energy and chemical efficiency (yield and product distribution). On the contrary, electromagnetic fields, mainly in the form of microwaves (almost exclusively at the operating frequency of 2.45 GHz), have been investigated for three decades[1,2] mainly by chemists as an unconventional heating method to perform chemical reactions. In several cases, significant process enhancement compared to conventional heating is reported; the enhancements usually include reduction in process time, improved selectivity and the enabling of reactions that would otherwise be impossible.[3–43] For certain systems the positive results obtained can be attributed with a fair degree of certainty to specific microwave heating characteristics, such as fast volumetric heat generation, superheating of polar molecules above the boiling point and selective heating of catalytic sites. In other cases, some researchers claim what are known as non-thermal microwave effects. Non-thermal effects are usually reflected in higher pre-exponential factor in the Arrhenius law or lower activation energy. The former is justified on the basis of increased molecular collision efficiency, due to effective mutual orientation of polar molecules involved in the reaction. Lower activation energy is assumed to occur due to the lower contribution of entropy to its value, as dipolar polarization tends to decrease the extent of randomness or disorder in a system. Nevertheless, despite the potential of microwaves for process intensification,[44] and despite the undisputed distinct heating characteristics mentioned above, there is still a fair amount of uncertainty as to: when the technology enhances a process; under what conditions; through which thermochemical mechanisms; and the overall efficiency compared to conventional processing.[45–55]

Further, in spite of several success stories, a very limited number of applications in the chemical industry are reported. To a large extent, the reasons behind these issues are to be attributed to known limitations of standard microwave equipment for chemical processing including poor definition and controllability of the electromagnetic field, limited scalability and mediocre energy efficiency.

Tailoring heating patterns is crucial for a number of applications. Some obvious ones include multistep chemistries in which different chemical steps are optimized at different conditions. For example, in catalytic partial oxidation reformers involving combustion, steam reforming and water gas shift, optimal thermal coupling and temperature profiling between the different chemistry zones in the reactor is important. In other applications, temperature uniformity is a requirement. For example, in material syntheses, local temperature gradients in a solution arising from conventional heating would cause crystallization at different locations and times, resulting in various coexisting intermediate compounds which would potentially interact with each other, or in poor product quality.

Spatially uniform thermal conditions are also required in applications targeted at fundamental chemistry studies and kinetic measurements. In order to achieve a tailored microwave field pattern, heating rate and temperature distribution as well as electrodynamics and electromagnetic engineering aspects must be taken into consideration. It will be shown in this chapter that microwave equipment currently used in microwave-assisted processing research is limited in its ability to generate tailored electromagnetic patterns. For successful microwave-enhanced processing, one should aim for integrated concepts of microwave field applicator and reactor design. Although it cannot be excluded that for some applications the currently used equipment types yield satisfactory results, more advanced novel integrated equipment types are proposed here that may serve more demanding process applications.

This chapter primarily deals with microwave field applicator concepts and how they can be integrated into the design of combined reactor-applicator systems. As control over the microwave field is a major issue in microwave-assisted processing, the applicator concepts are discussed in order of increasing control over the spatial microwave field distribution. Commonly, microwave equipment that is typically used in microwave-assisted chemistry research is classified as either a single mode or a multimode system. What these devices have in common is that they are resonant cavity systems in which the microwave field is characterized by non-uniform and unpredictable interference patterns. This results in unpredictable patterns of heat generation. This chapter first discusses the resonant cavity systems and the nature and limitations of the microwave fields that they employ. The types included here are generic multimode systems, the celebrated CEM Discover microwave synthesis system, and custom-built TE_{10n} systems. This is followed by a discussion on novel applicator systems that aim to have better performance in terms of predictability, controllability and efficiency of microwave activation in chemical processes. In this frame, the LABOTRON system built by SAIREM is presented first; this type of equipment uses an internal transmission line to enhance the distribution of the microwave field. Finally, the concept of a coaxial traveling microwave reactor is discussed, which is a novel concept that does away with resonant fields.

Several simulation results are presented to illustrate the topics in this chapter; the environment of these simulations is COMSOL Multiphysics 3.5[56] and dielectric data were taken from Meredith.[57]

4.2 Resonant Microwave Cavities

Usually, when microwave heating is applied, it is done by means of an applicator cavity.[58] This is essentially a metal box – a Faraday cage – which contains the microwave field. The walls of this box form one single interconnected electrically conducting entity. As opposed to a system with multiple conducting terminals, this means that the cavity can only support electromagnetic field patterns whose wavelength is short enough to *fit inside*. Furthermore, due to the cavity being fully enclosed, the microwave fields reflect back and forth in it, interfering constructively and destructively in an alternating standing wave pattern. The following two facts are essential to understand the properties of cavity applicator systems:

1 There is an integer number of wave patterns that can be supported by a cavity. Above a certain wavelength threshold or, equivalently, below a frequency threshold, no field pattern fits; just below the critical wavelength, one wave pattern fits and with decreasing electromagnetic wavelength more wave patterns will fit.
2 The microwave fields resonate. They are a superposition of multiple wavefields traveling in different directions. The interference between these fields causes a non-uniform distribution of field intensity, heating rate and, ultimately, temperature distribution. In addition, phase shifts in the wave fields caused, for example by varying medium properties, result in hard-to-predict shifts in the resonant wave patterns.

The resonant nature of the standing wave patterns is what hampers control over the electromagnetic field; the alternating standing wave pattern results in strong variations in heat generation and temperature. Mode stirrers and chemical sample rotation and/or agitation/stirring are frequently applied in an effort to improve heating uniformity, but this does not prevent the electromagnetic energy from being dissipated non-uniformly inside the process fluid. Heating therefore occurs through a process of combined microwave, convective and conductive heating with the latter two homogenizing the non-uniformities of the former. Consequently, processes become partially conventionally heated and any direct microwave effect would be limited in cases where it would occur. Often, continuous and vigorous stirring is proposed as a means to improve the uniformity of processing conditions, but this can only apply to temperature and concentrations; the distribution of the intensity of resonant microwave fields is inherently non-uniform. Moreover, in processes where mechanical mixing is impossible, ineffective or undesired (*e.g.*, fixed-bed reactors, viscous liquids, tubular reactors), the problem of uncontrolled heating patterns is even more difficult to resolve.

This section continues with a discussion on specific types of cavity applicators. As their name implies, multimode cavities support multiple resonant electromagnetic patterns. This is a consequence of their large size relative to the electromagnetic wavelength. This microwave applicator is well known, as it has spread worldwide in the form of the domestic microwave oven. Single mode cavities are rarer. Typically, they are smaller and aimed at specific fields of application. The following section discusses the performance and limitations of multimode cavities in general, followed by a discussion on single mode cavities. In the latter context, two particular types of single mode applicators used in microwave-assisted chemistry research are discussed: the CEM Discover and the TE_{10n} class of cavity applicators.

4.2.1 Multimode Cavities

The best known microwave applicator type is the multimode cavity. The most common example of this type is the domestic microwave oven, but dedicated multimode heating devices for laboratory applications have been developed as well. Its construction amounts to a relatively simple rectangular metal box with dimensions ranging in the order of 20 cm to 50 cm, with a door on the front side. Typically microwave energy is generated by a magnetron tube and this energy is led into the cavity by a short waveguide. For microwave-assisted chemistry research, the cavities are usually fitted with attenuated access pipes to accommodate fluid inlets and outlets, stirring rods and sensor access.

As its name implies, this type of cavity supports multiple resonance modes in the vicinity of the operating frequency.[57,59] This is a consequence of the size of the cavity relative to the wavelength of the microwave field. Despite its geometrical simplicity, the electromagnetic analysis of this type of systems is very complicated. The difficulty lies in the resonance modes that are excited simultaneously; it cannot be determined practically how energy is distributed over these modes. Typically, resonance modes are very sensitive to variations in geometries and medium properties involved with the electromagnetic field, as well as the frequency of the field. In addition, a number of phenomena summarized below render the electromagnetic field pattern highly complex and, for practical purposes, impossible to predict. These phenomena are listed as follows:

- Electromagnetic medium properties are changing with respect to both the composition of the reacting media and its temperature,
- Manufacturing tolerances of glassware are limited,
- The media are flowing *i.e.* continuously moving,
- The operating frequency of magnetron tubes is not stable and can spread over a range of around 50 MHz.

Although mode stirrers have been suggested to improve uniformity, these add an additional source of complexity to the problem. Therefore, mode stirrers cannot be expected at all to improve the predictability of the microwave field. The complexity is illustrated by thermal imaging and simulations in COMSOL 3.5. Figure 4.1 presents modal patterns in a multimode cavity[60] by means of thermal images (SP Thermoview 8300) of an expanded polystyrene plate supporting a thin water film heated in a multimode cavity (Sharp R-2S57); these images were made with a similar procedure as in Karstädt

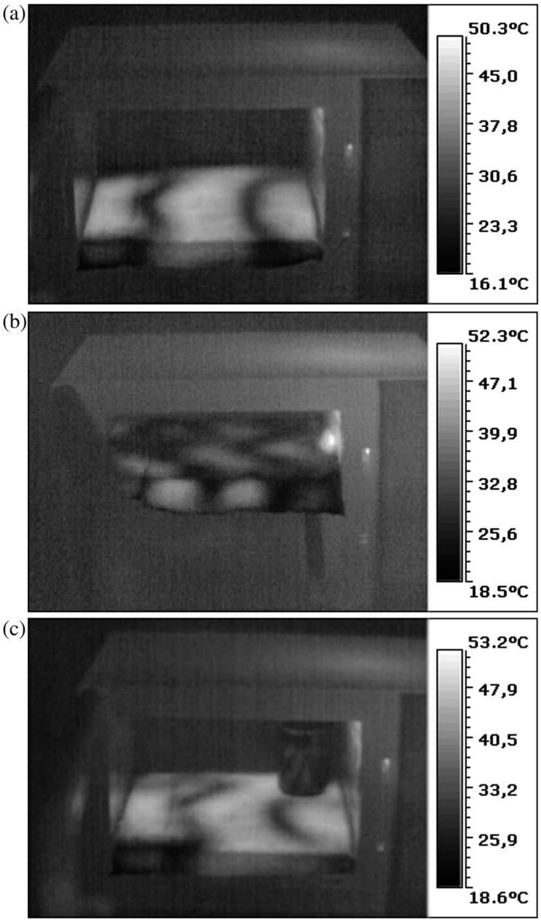

Figure 4.1 Thermal imaging of a water film in a multimode cavity, (a) with the film at 40 mm from the bottom; (b) at a height of 120 mm above the bottom; and (c) with the film at 40 mm and with a water-filled beaker placed in the cavity. The complex field patterns in the plane of the film change both with the height and with introduction of the beaker.[60] (Reprinted from *Chem. Eng. J.*, **243**, G. S. J. Sturm *et al.*, Microwaves and Microreactors: Design challenges and remedies, 147–158, Copyright (2014) with permission from Elsevier.)

et al.[61] The images clearly show the non-uniformity of the resonant microwave field in the horizontal direction. Furthermore, these images demonstrate the dependence of the microwave field on the vertical direction; compare Figure 4.1a and b, where the wet surface is at a height of 40 and 120 mm, respectively, above the cavity bottom. The resonance patterns between these images bear no similarity, although it cannot be ruled out that the three-dimensional electromagnetic field is affected by the changed position of the plate. Compare also the differences between Figure 4.1a and c. In Figure 4.1c, a water-filled beaker is introduced into the cavity. The microwave field pattern that presents itself in the empty space of the cavity *via* thermal imaging is affected by the introduction of the beaker, which is most notable in the far left corner. The resonant pattern emerges from an electromagnetic field that is coupled throughout the entire microwave system of the device. Any disturbance that locally affects the microwave field is apparent over the total microwave field.

The thermal imaging results demonstrate the sensitivity of the microwave field in multimode cavities around a heated object, but they do not reveal the effects on the heating rate distribution in the load. In order to illustrate the heating rate distribution inside a load, the microwave field in a multimode cavity with a 250 ml beaker containing 200 ml water placed inside is simulated. Figure 4.2 presents slice plots at a height of 30 mm above the beaker bottom at a frequency of 2.45 GHz (Figure 4.2a) and 2.46 GHz (Figure 4.2b). This 10 MHz shift in frequency would fit well within the frequency spectrum generated by a typical magnetron tube.

The simulation results demonstrate that there is a high degree of sensitivity to disturbances of the multimode microwave field inside the load too—a relatively small frequency shift may double the total energy absorption. Furthermore, the results show that there is an interference pattern of alternating high and low electromagnetic dissipation inside the water volume. Notably, this interference pattern *does not follow the exponentially decaying trends*

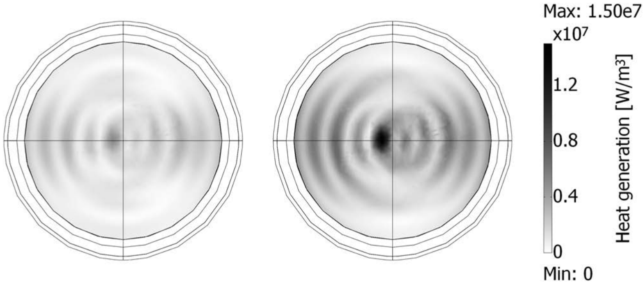

Figure 4.2 Slice plot of heating rate 30 mm above beaker bottom in a 250 ml beaker filled with 200 ml water ($\varepsilon_r = 77 - 13i$) placed in the middle of a 190 mm × 290 mm × 285 mm ($h \times d \times w$) cavity with a 1000 W field fed into the cavity. In (a) the field has the nominal frequency of 2.45 GHz and in (b) the frequency has shifted slightly by 10 MHz. In both simulation results, the interference pattern is quite apparent; note that the shape has varied subtly. More obvious is the increase in heating rate for the shifted frequency; the overall heat generation in the water has more than doubled. At 2.45 GHz the absorbed power is 370 W, while at 2.46 GHz it is 770 W. Note that an inverted color map has been applied to improve the clarity of the figure.[60] (Reprinted from *Chem. Eng. J.*, **243**, G. S. J. Sturm *et al.*, Microwaves and Microreactors: Design challenges and remedies, 147–158, Copyright (2014) with permission from Elsevier.)

that would follow from the often-mentioned penetration depth limitation of microwave fields. Furthermore, there are variations in the morphology of the microwave field too due to the frequency shift.

4.2.2 Single Mode Cavities

One of the drawbacks of multimode cavities, which is often mentioned as being mitigated by the use of single mode cavities, is their limited field intensity. This is said to be traded-off against the volume of the cavity, which results in limited scale-up possibilities of single mode cavities. This explanation may be too simplistic, however. Behind the performance of single mode cavities lies the fact that the smaller volume of these cavities in theory should only support one single microwave field pattern. Consequently, if, due to the design of the cavity, this single modal pattern absorbs microwave energy well, then it follows that the cavity will perform well in terms of energy absorption and efficiency—at least, better than multimode cavities that support far more resonance modes, which cannot all be expected to perform well in terms of energy absorption, thus compromising the overall performance. However, it cannot be guaranteed that the single resonance mode of a single mode cavity always performs well, it requires careful design and tuning to ensure this. In terms of predictability, however, the single mode cavity can be expected to outperform multimode systems, because there is only one single modal pattern to consider.

Two types of single mode cavities are discussed here to demonstrate the behavior of the resonant field. These two cavities represent two design philosophies for single mode resonant microwave cavities. The two types are the CEM Discover and a class of system known as TE_{10n} cavities.

4.2.2.1 CEM Discover

The CEM Discover[62] is a celebrated microwave heating device for laboratory applications. Its performance follows from the unique design of the microwave circuit[63] (Figure 4.3) consisting of a cylindrical cavity that is small when compared to multimode cavities. It is therefore limited in the number of microwave field patterns it supports and hence is a single mode cavity. The cavity is enclosed by a rectangular waveguide, which is connected to a magnetron microwave source. The wall between the cavity and the waveguide is slotted, so the microwave field generated by the magnetron is coupled *via* the waveguide through these slots into the cavity and the load. The slotted or radiating waveguide[57,64] is an effective structure to expose a load that is placed in its proximity to a microwave field. Consequently, the Discover is able to heat small samples efficiently and rapidly, making it an ideal tool for small scale non-contact laboratory heating.

Although the Discover generates a stable and relatively intense microwave field, this does not mean its microwave field is uniform or well defined.

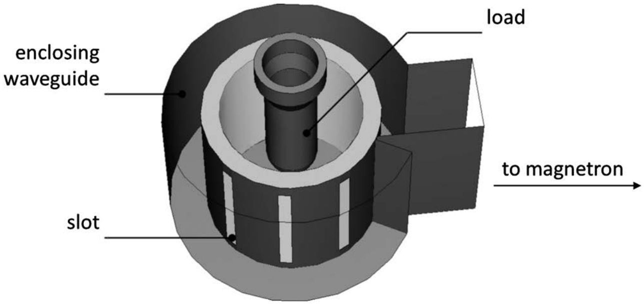

Figure 4.3 Microwave circuit[63] of the Discover. The load is placed in a cylindrical cavity that is enclosed by a rectangular waveguide. One end of the waveguide is connected to a magnetron microwave source. Microwave energy is coupled through slots in the wall of the waveguide into the cavity and the load.

In fact the distribution of the microwave field forms quite complex three-dimensional patterns. We demonstrate this by experiment and simulation. In Figure 4.4, results of a study[65] on microwave heating with the Discover of a water filled vial are presented. Figure 4.4a shows two strips of thermal fax paper that were immersed in the water contained by the vial while it was being heated. This paper decolorizes irreversibly when it reaches a temperature of around 67 °C. From the strips it is apparent that heating occurs rather non-uniformly; the front view strip has two hot zones to the side of the strip, while the side view strip has a dominant hot zone in the back. This trend is also found in the simulated three dimensional electromagnetic heating rate distribution in the vial presented in Figure 4.4b. In the front view of Figure 4.4b, two hot zones to the side are found; in the side view slice plot, a dominant hot zone against the back wall appears.

Another study that investigates heating with the Discover is concerned with methanol steam reforming in a packed bed.[66] Figure 4.5 presents the reactor setup. It consists of a glass vial with a catalytic bed placed into it. The bed is fed with a gas phase mixture of water and methanol, which is led underneath the bed with a glass tube and then passes through the bed upwards towards the outlet. For comparison, the reactor assembly is heated in two separate experiments by either a microwave field in the Discover or conventionally by an electric heating coil. Two glass sensor guides are placed in the bed for temperature measurement, one in the center of the bed and the other near the wall of the vial. These sensor guides enable variation of the vertical sensor position, so the temperature can be evaluated at different axial positions in the bed.

It was found that strong temperature gradients exist in the bed; these gradients are more pronounced for microwave heating than for conventional heating. As opposed to the inwards heat flux, which is the case for conventional heating, the heat flux in the case of microwave heating is outwards as heat

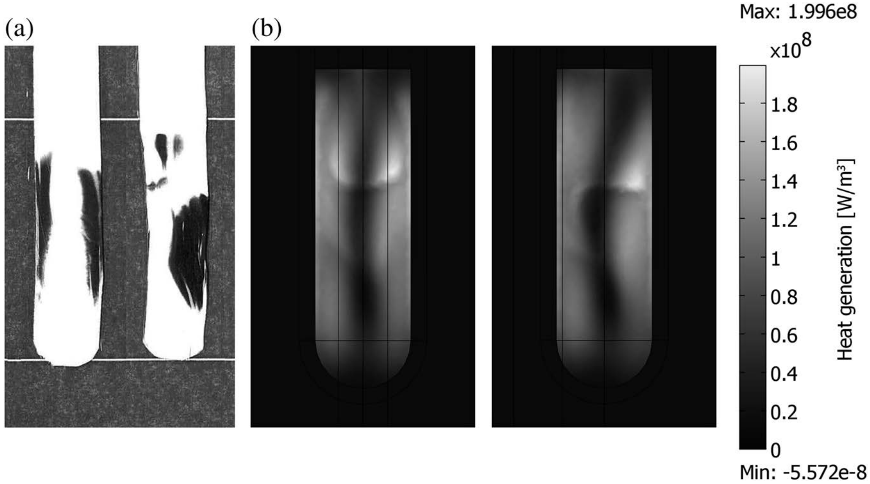

Figure 4.4 Distribution of heating rate in a 12 mm inner diameter vial filled to a level of 40 mm with water that is heated in the CEM Discover.[62] In (a), strips of thermal fax paper inserted in the vial are presented followed by one second exposure to a microwave field at the maximum power of the device. The left strip was positioned with the ink covered site facing the front of the device and the right strip was positioned with the rightmost edge of the strip pointing towards the back of the device. The thermal paper strips indicate that there are two hot zones on either side of the vial and one dominant hot zone in the back of the vial. In (b), simulation results with COMSOL 3.5 of the microwave field in the Discover and the vial indicate a similar distribution of heating rate; a slice plot crossing the front/back dividing plane indicates distribution with two more or less symmetrical hot zones on either side of the vial, while a slice plot in the left/right dividing plane indicates a dominant hot zone in the back of the vial. Moreover, both the experiments and the simulation indicate a highly non-uniform and complex spatial distribution of heat generation.

is generated inside the catalytic bed. This results in an inverted temperature profile over the bed with the lowest temperatures on the outside. Figure 4.6 presents the temperature profiles obtained during the steam reforming process. The case presented in Figure 4.6 has a spatially-averaged temperature of 210 °C. It was found that for this same average temperature, methanol conversion to syngas is 1.23 times as high for microwave heating as it is for conventional heating, which indicates that selective heating of the catalytic sites may indeed occur. However, the temperature is non-uniformly distributed in complex patterns and the spatial distribution of heating rate and temperature are beyond any form of manipulation in this particular microwave field applicator. Consequently, despite the indications of the existence of selective heating, the complex non-uniform resonant microwave field patterns inhibit harnessing the full potential of this phenomenon if it indeed exists.

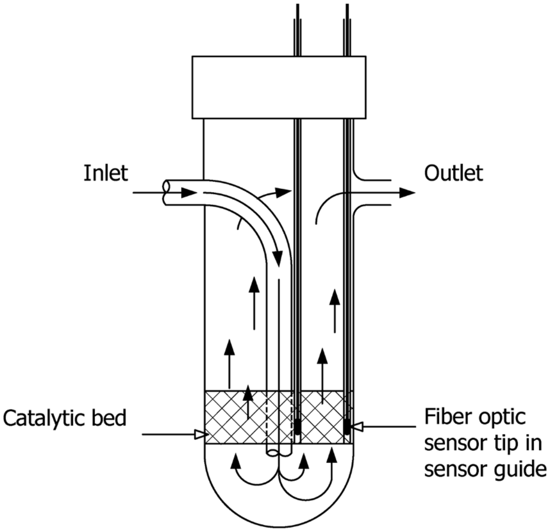

Figure 4.5 Layout of the methanol steam reforming reactor as reported in Durka *et al.*[66] indicating the catalytic bed and the sensor positions. (Reprinted from *Int. J. Hydrogen Energy*, **55**, T. Durka *et al.*, Microwave-activated methanol steam reforming for hydrogen production, 12843–12852, Copyright (2014) with permission from Elsevier.)

4.2.2.2 TE_{10n} Cavities

A different design philosophy is found in the TE_{10n} resonance cavity. Instead of the slotted waveguide that couples energy into an applicator cavity, as used in the Discover, the TE_{10n} cavity has the load placed directly into the waveguide. These systems usually are custom built. This approach towards applicator design has been suggested in the past for heating materials and fluids,[57,64,67] and since it has been proposed to supply energy to reactive processes, such as reactive distillation processes,[68] flow reactors,[69–71] and high-temperature reactions.[72] It typically consists of the following parts as indicated in Figure 4.7:

- A microwave source
- An isolator that absorbs reflected fields before they can travel back to the source
- An impedance matching section that can be tuned to prevent reflection out of the applicator section. Proper tuning of this part keeps microwave fields inside the applicator where they can be dissipated into useful heat instead of being reflected out of the applicator and lost in other parts of the system
- An applicator section in which a load is placed to be exposed to the microwave field
- An adjustable reflector at the end of the cavity to vary the position of the microwave field in the applicator section

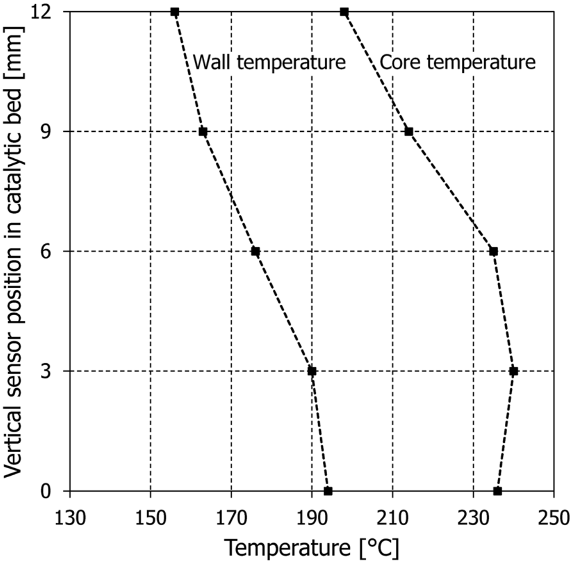

Figure 4.6 Temperature distribution in the catalytic bed of the methanol steam reforming from Durka *et al.*[66] Temperature is measured at different heights, both along the centerline of the bed and near the wall. (Reprinted from *Int. J. Hydrogen Energy*, **55**, T. Durka *et al.*, Microwave-activated methanol steam reforming for hydrogen production, 12843–12852, Copyright (2014) with permission from Elsevier.)

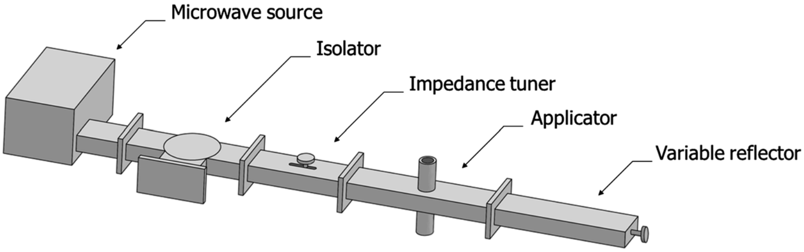

Figure 4.7 General layout of a TE_{10n} microwave heating system. The basis of the microwave system is a standard rectangular waveguide size, for example WR-340 with dimensions of 86 × 43 mm that is typically used with an operating frequency of 2.45 GHz. The system consists of a source that generates microwave fields and sends them into an isolator that lets the fields pass in the forward direction, but absorbs them when reflected back, thus preventing exposure of the source to reflected fields. When the impedance transformer is properly tuned it enables highly efficient operation. Connected to the impedance transformer is the applicator cavity, which applies the microwave field to the load that is to be heated. The applicator can take a variety of forms, depending on the particular requirements on the system. The microwave system is terminated by a variable reflector that houses a reflective wall whose position can move along the length of the circuit. The reflector can thus be used to position the standing microwave field inside the microwave circuit.

The waveguide is typically a standard size waveguide, for example WR-340 (86 × 43 mm cross-section), used for the 2.45 GHz frequency. The microwave field is constrained in this kind of cavity to relatively simple and predictable patterns[73] (Figure 4.8). When oriented with the broad side of the waveguide sections in the horizontal plane, this waveguide has a height of less than half a wavelength, which is too short for an empty cavity to support a standing microwave pattern in that direction. Therefore, the microwave field is invariant with height. The width of the waveguide on the other hand is narrow enough to support just one standing wave antinode. The length of the waveguide is such that it supports a number of standing wave antinodes. The designation 10*n* for this type of waveguide refers to the number of standing wave antinodes in *an empty cavity* in the three spatial directions: one over the width, none over the height and a number *n* over the length. Introducing a load in the cavity influences the field to an extent that depends on the geometry and medium properties of this load; typically, a smaller load has a

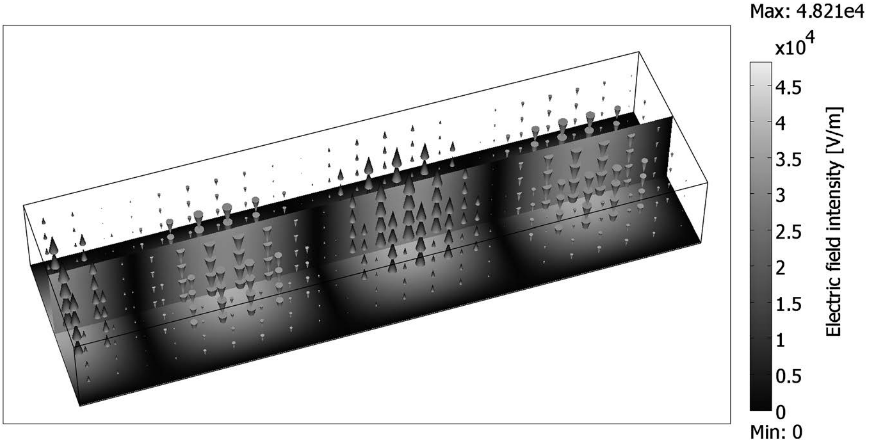

Figure 4.8 Simulation in COMSOL 3.5 of the electric field component of a microwave field at 2.45 GHz in a WR-340 rectangular (86 × 43 mm) waveguide. The field, incident from the open left end with a power of 1.0 kW, travels through the waveguide and is reflected at the closed right end. The reflected field then travels back toward the open end and exits there. The forward and backward traveling wavefields interfere: they combine constructively and destructively in a standing wave pattern of alternating high and low field intensity. Two slice plots are included in the geometry of the time-average electric field intensity. The cones indicate the electric field direction and intensity *at an instant in time*; it is not a static field, but it oscillates with the field vectors continuously reversing their directions. The field has *one* antinode (field maximum) over the width of the waveguide, it is *invariant* with height, and an unspecified number, *n*, of antinodes occur over the length of the waveguide. Furthermore, the electric field vector—rather than the magnetic field vector—is *perpendicular* to the direction of propagation of the microwave field. The standing wave pattern thus formed is therefore denoted *transverse electric one zero n*—or TE_{10n}.

weaker effect. Consequently, for a small object heated in this type of cavity, the simple empty cavity field patterns already give an adequate description of the microwave field. To demonstrate the operation of this type of cavity we present results of a study with a TE_{10n} cavity concerning the effective coupling of microwave fields with flowing process fluids.

Placing a narrow cylindrical load, a vial or a continuous flow tube, vertically in this type of cavity has the additional advantage that the wavelength of the microwave field is long enough to have relatively little variation in the planar cross-section of this load, which means that the load is heated uniformly; the narrower the load is, the more uniform the heating.[74] Moreover, due to the field being invariant with height—whether truly or by approximation—a uniform heating pattern can be achieved in three dimensions.

The orientation of an object in a microwave field plays an important role in the transmission and dissipation of energy. Figure 4.9 presents a photograph of a tube (LDPE, outer diameter 2.5 mm, wall thickness 0.3 mm) entering a TE_{10n} cavity from the bottom, running along its axis for approximately 30 cm, and exiting through the bottom again. Note that this cavity has a removable top side. It was found that in the vertical orientation the interfacial interactions between the tube and the cavity space are optimized, because the electric field vector of the microwave field runs parallel to the tube/air interface over the full circumference of the tube. This is not the case when the tube is oriented horizontally; in that case, the electric field is also oriented perpendicularly with respect to the tube/air interface. Figure 4.10 presents the boundary conditions for the electric field over the interface in both parallel and perpendicular orientation.[73] For the parallel orientation, which is the case for vertically oriented tubes, the electric field intensity is constant over the interface, whereas in the perpendicular orientation it is not. In the perpendicular orientation, which occurs over a large portion of the interface in the horizontal tube orientation,

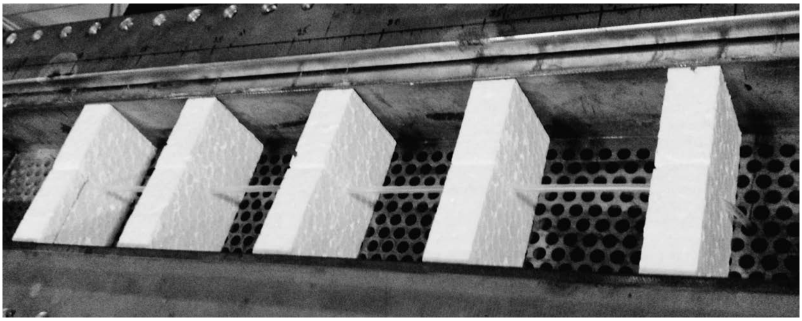

Figure 4.9 Thin water-filled polyethylene tube inside a TE_{10n} cavity. Most of the tube is horizontally oriented and running along the centerline of the cavity. The inlet and outlet though are bent towards the holes in the bottom of the cavity to accommodate inlet and outlet of a continuous flow medium. The tube has an outer diameter of 2.5 mm with a wall thickness of 0.3 mm.

the field intensity is reduced with the ratio of the electric permittivities inside and outside of the tube. Effectively, in the horizontal orientation, the microwave field is pushed out of the tube according to the boundary condition.

The configuration in Figure 4.9 had water flowing in it at a rate of 15 ml min^{-1}. It was heated by a microwave field while the temperature inside was measured with a thin fiberoptic probe (uncladded Neoptix T1[75]). The temperature distribution measured over the length of the tube is presented in Figure 4.11. It can be seen that in the vertical sections that enter and exit the

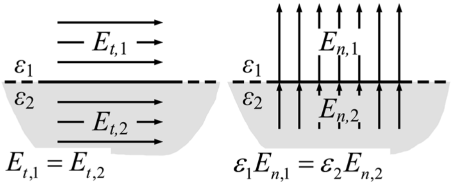

Figure 4.10 Boundary conditions over an interface with different electric permittivities on either side. It depends on the direction of the electric field vector how its intensity changes over the interface. If the electric field vector direction is tangent—or parallel—to the interface (left), then its intensity does not change over the interface. On the other hand, if the electric field vector direction is normal—or perpendicular—to the interface (right), its intensity is scaled by the ratio of the permittivities, reducing when going to a medium with increasing permittivity as indicated by the equation in the right-hand figure.

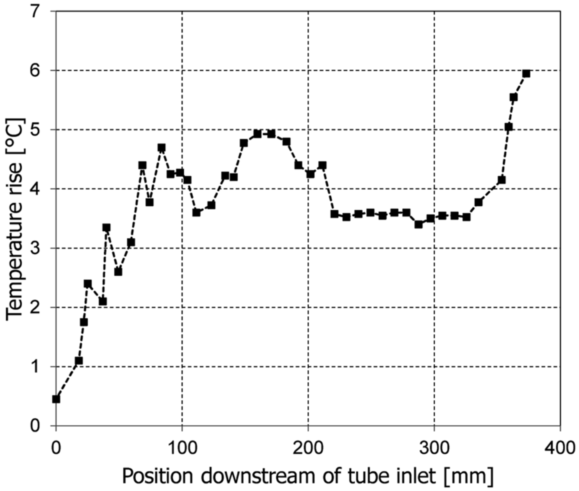

Figure 4.11 Temperature distribution along the length of the tube in the configuration in Figure 4.9 for a water flow rate of approximately 15 ml min^{-1}. The vertically oriented section near the inlet and the outlet of the tube experience a heating rate that is much higher than the middle section, which is horizontally oriented.

waveguide the temperature increase is much higher than in the horizontal middle section of the tube, even though the middle section is much longer. This is a result of the electric boundary conditions with respect to the tube orientation. This is verified by a simulation in COMSOL 3.5 (Figure 4.12) that shows that in the two vertically oriented sections near the inlet and outlet the field strength inside the tube is relatively large. This contrasts with the horizontal section where hardly any heating occurs.

From the results presented above it follows that in order to have an effective coupling of microwave energy in a load, the load has to be in a vertical orientation. This can pose a rather limiting constraint on the residence time in continuous flow systems as the length available in the vertical orientation is short. To resolve this, one could consider a system with multiple vertical sections inside a TE_{10n} cavity. Although in such systems the standing resonant wave patterns in the microwave field will cause differences in the field distribution between the vertical sections, such an approach allows efficient coupling of microwave energy in a long flow system. Additionally, because of the strongly constrained microwave field, the heating rate distribution is still quite predictable.

Figure 4.13 presents a similar tube in a spiral structure supported by an expanded polystyrene block that is placed in the TE_{10n} cavity. As the photograph shows, a large proportion of the tube is in a near vertical orientation. Figure 4.14 presents a thermal image (SP Thermoview 8300) of the tube after heating and removal of the top side of the cavity. It demonstrates that high temperatures can be reached over the entire length of the continuous flow configuration. The heating rate is not perfectly uniform however; there are short horizontal sections in the tube and the standing wave pattern in the cavity is superimposed over the heating rate distribution too. In spite of

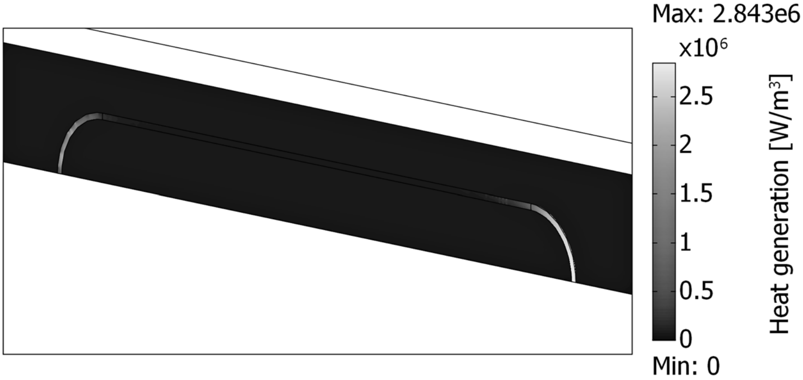

Figure 4.12 Simulation in COMSOL 3.5 of the heating rate distribution of a thin water-filled tube entering a TE_{10n} cavity from the bottom, running along the centerline of the cavity for some length and then exiting the cavity though the bottom. The vertical inlet and outlet sections are heated considerably more than the horizontal middle section.

this, the configuration has a number of notable advantages. Aside from the efficient energy coupling and the high temperatures, the field is stable and well-predictable. Furthermore, the concept can be tailored to specific applications by varying the length of the spiral and, if needed, the cavity.

The spiral configuration was used as a microwave reactor system for the synthesis of *n*-propyl propionate from the esterification of *n*-propanol with propionic acid. The reaction mixture was fed with a flow rate of 0.5 ml min^{-1} into the spiral in a 1 : 1 molar ratio and was catalyzed by zinc triflate dissolved

Figure 4.13 Spiral flow configuration in TE_{10n} cavity. A thin tube is wound around an expanded polystyrene placeholder. As such a configuration is created with a relatively large portion of tube length that is oriented vertically, parallel with the electric field vector of the microwave field supported in the cavity.

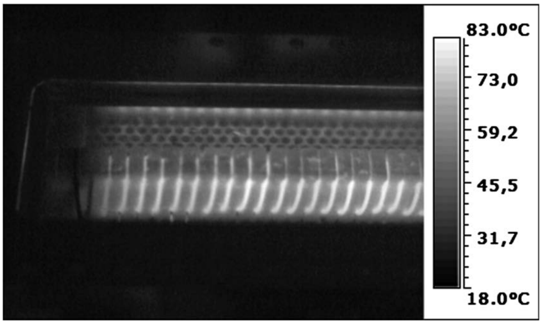

Figure 4.14 Thermographic image (SP Thermoview 8300) of the tube surface with an *n*-propanol/propionic acid reactant mixture heated in it. The experiment was run with a continuous flow of reactants at a 0.5 ml min^{-1} flow rate and a microwave power of 80 W. The microwave power was stopped and the lid on top of the cavity was opened to view the temperature development inside with the thermal camera. This configuration enables heating up to the boiling point of the liquids.

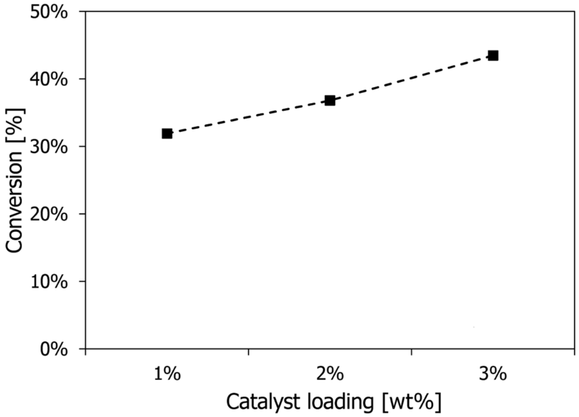

Figure 4.15 Conversion *versus* catalyst loading in a continuous esterification reaction. The reaction is the synthesis of *n*-propyl propionate from *n*-propanol and propionic acid in a 1 : 1 molar ratio with zinc triflate as the homogeneous catalyst. The average reaction temperature is between 50 and 60 °C and the residence time is 30 minutes. The catalyst loading is varied and presented *versus* conversion.

in the reactant mixture as a homogeneous catalyst. The total tube length was 4.5 m, resulting in a residence time of 30 minutes. Three experiments were conducted at different catalyst loadings of 1, 2 and 3 wt%. The power applied was 80 W in all three experiments. Boiling and condensation phenomena in the reacting mixture caused an oscillating outlet flow with a temperature varying between 50 and 60 °C. Analysis of the thermal imaging results of the surface temperature of the tube reveals that the average temperature of the process lies in the same temperature range. The outlet conversions in the three experiments are presented in Figure 4.15. It can be seen that over 30 minutes of residence time satisfactory conversions are attained (equilibrium conversion 66%[76]), which increase with increased catalyst loading.

4.3 Advanced Non-Cavity Applicator Types

In the previous section, different cavity applicator systems were presented for the application of microwave fields to heating processes. It was demonstrated that these systems only allow for limited predictability, control and optimization of the distribution of microwave energy supplied to the process. These drawbacks were linked to the resonant field, which is inherent to cavity systems.

In contrast to microwave heating, radio frequency heating applications never use cavity applicators. What is interesting about radio frequency heating in the context of microwave-assisted chemistry is that it causes heating by the same mechanisms of dipole rotation and charge translation, but that the relation between the characteristic dimensions are entirely different.

More specifically, while the electromagnetic wavelength in microwave heating applications is of the same order of magnitude as the heated objects, in radio frequency heating, the wavelength is much larger. Consequently, cavity applicators would be far too large to accommodate the electromagnetic field. Instead, a variety of electrode configurations is used for radio frequency heating;[64,77] the electrodes are terminals that support the electric component of the electromagnetic field. The long radio frequency wavelengths render resonant patterns much less of an issue and due to the freedom in shaping the geometry of the electrodes there is much greater potential to predict and control the radio frequency field. The heating rate is more limited when compared to microwave heating though, as the heat generation rate is proportional to frequency. Nevertheless, radio frequency heating has already been applied by Izadifar *et al.*[78] enabling a uniform temperature in a packed-bed extraction process.

Since microwaves are essentially short radio frequency waves, it follows that they do not necessarily have to be applied by cavities, and that the difficulties linked with resonant field patterns may be avoidable. The following section presents a discussion on advanced microwave field applicator concepts. First, the LABOTRON system pioneered by SAIREM is presented. This system uses a transmission line to improve the distribution of microwave energy. Then, a novel coaxial traveling microwave reactor concept is discussed. This concept circumvents resonant field patterns altogether and enables a high degree of optimization with respect to the morphology of the microwave field.

4.3.1 Internal Transmission Line

Recently, SAIREM (microwave and radio frequency technology provider) launched a new range of integrated reactor and microwave transmission systems, under the generic name LABOTRON,[79,80] especially designed to carry out microwave-assisted synthesis and extraction processes in batch or in continuous flow both at laboratory and pilot scale. The novelty in this type of equipment, as opposed to conventional single mode or multimode cavity types lies in the use of an internal transmission line to bring selectively a great quantity of energy directly inside the reaction mixture. Most importantly, this working principle enables the possibility of scaling up microwave-assisted multiphase processes in both batch and continuous flow. SAIREM claims that the LABOTRON equipment covers a wide area of chemical processes ranging from a few grams per hour to more than 1 kg hour^{-1}. Two types of reactor/applicator systems are available (Figure 4.16):

- Batch reactor with volumes from 1.5 to 20 liter. A 100 liter scaled-up version is currently under development. The reactor is made of stainless steel and is equipped with a cooling jacket and a mechanical stirrer.
- Continuous flow helix-type reactor mounted on the U-shaped waveguide. The available internal volumes range from 40 to 150 ml.

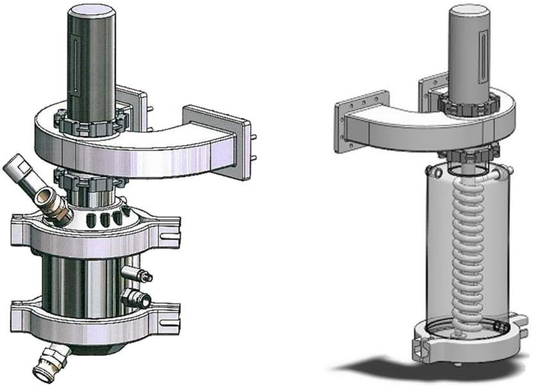

Figure 4.16 Batch reactor (left) and SPIN M (right) continuous flow reactor that mount on the LABOTRON microwave processing system.[79,80] (© 2013 Springer Science + Business Media, reprinted from Li *et al.*[79] with permission from Springer Science + Business Media.)

In these systems, a microwave field is fed *via* a U-shaped waveguide and transmitted into the reactor *via* the internal transmission that is placed in the middle of the reactor in direct contact with the reaction mixture. SAIREM lists a number of advantages among which are the following: the internal transmission line helps to overcome the penetration depth limitation; the system is adaptable for specific processing needs in terms of volume and batch *versus* continuous operation; control of forward and reflected power, minimization of reflected power and a high utilization efficiency of microwave energy; high power density; and efficient cooling *via* a cooling jacket.

4.3.2 Traveling Microwave Reactor

The grand challenge in the context of microwave-assisted chemistry is to engineer microwave fields to enable chemical processing under tailored and controlled heating conditions at macro- and microscale. Macroscale refers to optimization of spatial and temporal heating patterns; microscale refers to optimization of selective microwave-matter (*e.g.* catalyst, reactant) interactions.

As was shown earlier, resonant fields are limited in terms of spatial control over microwave fields. Therefore, an alternative approach is presented here based upon the use of traveling electromagnetic waves as opposed to standing electromagnetic waves as an unconventional means of thermochemical activation. Traveling electromagnetic waves do not occur in confined spaces. They travel through a medium in one direction without being reflected by reflective surfaces, such as the cavity walls. As they move, part of the electromagnetic energy is dissipated to heat, according to the dielectric properties of the medium, and the remainder of the energy is transported downstream. Due to the absence of interference between the traveling waves incident in one direction and reflected portions of the these waves traveling in the opposite direction, resonant standing wave patterns arising from superposition of interfering waves do not occur. Contrary to resonant standing wave fields, non-resonant traveling wave fields can be precisely controlled and optimized according to different objectives for chemical reactor activation.

Figure 4.17 shows a photograph of a typical coaxial cable. It consists of two concentric conductors with dielectric filler between them. Between both conductors a microwave field is supported. In the coaxial traveling wave reactor concept this is a traveling microwave field that propagates in only one direction along the system. Because there is no microwave field traveling in opposite direction, no interference pattern emerges that would be detrimental for uniformity and predictability of the microwave field intensity distribution. The concept has the process fluids positioned between the conductors, thus being exposed to the microwave field. Two process system configurations are presented here to demonstrate the concept of a coaxial traveling microwave reactor (TMR): a liquid phase process and a gas phase/solid catalyst process. We show how both reactor concepts can be geometrically optimized to fulfill a specific set of requirements. A two-step approach towards optimization is employed. First, the cross-section is optimized, followed by the inner conductor diameter profile in the axial direction in order to bring the axial heating rate distribution in accordance with the specification.

An important feature of the TMR is operation below the cut-off frequency of higher order modes. Electromagnetic propagation in waveguiding

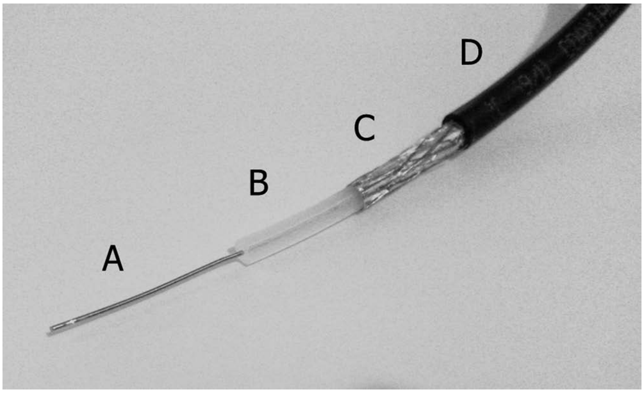

Figure 4.17 RG-59 coaxial cable. It consists of (A) an inner conductor, (B) a dielectric filler, (C) an outer conductor, and (D) an outer insulator.

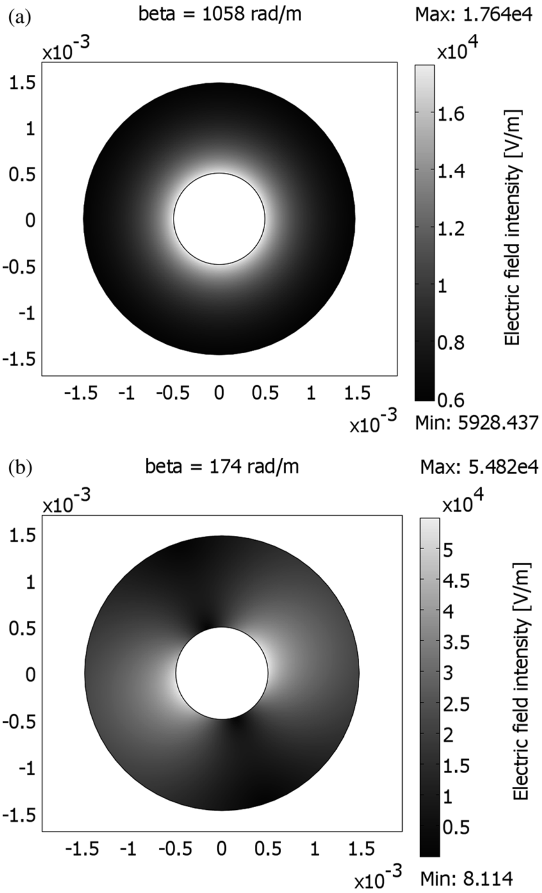

Figure 4.18 Modal patterns at 1 W power transmission of (a) the fundamental transverse electric magnetic (TEM) propagation mode and (b) the TE_{11} propagation mode in a RG-141 coaxial cable at a frequency of 35 GHz. The TEM mode propagates at all frequencies, while the TE_{11} mode only propagates above a 34.5 GHz cut-off frequency. The relatively low propagation mode $\beta = 174$ rad m^{-1} indicates that the TE_{11} mode is close to the cut-off condition. It can be seen that for the TEM mode, the field intensity does not fall to zero at the outer conductor and that the intensity distributes uniformly over the circumference. Therefore, an array of channels positioned in the field against the outer conductor will be exposed to uniform field. This is not the case though for the TE_{11} mode. Care must be taken to prevent operation in any other mode than the TEM mode.

structures has an integer number of propagation modes that is, ways in which the electromagnetic waves propagate. Figure 4.18 presents the lowest, fundamental propagation mode and the next higher order propagation mode of a coaxial waveguide; these propagation modes are denoted TEM (transverse electro-magnetic) and TE_{11} (transverse electric), respectively. The TEM mode can always propagate in a coaxial waveguide, the TE_{11} can only propagate above a certain frequency for a given waveguide. Effectively, the electromagnetic wavelength has to be sufficiently small (or, equivalently, the frequency has to be high enough) for the TE_{11} mode to "fit into" the waveguide.

The concept of TMR requires that it is dimensioned such that only the TEM propagation mode can propagate and that all higher order modes are cut off. In fact, the tangential non-uniformity observed in the TE_{11} mode in Figure 4.18b is a standing wave pattern, whose avoidance is the primary aim of the TMR concept. Moreover, limiting the propagation modes to only the TEM mode enables predictable microwave fields, because energy can only be distributed over this single mode.

Finally, we note that the electromagnetic field pattern cannot attain a true TEM mode in systems with a non-homogeneous medium distributed between the conductors, so the propagation mode is more correctly referred to as quasi-TEM.

4.3.2.1 Liquid Phase Process Configuration

For liquid phase processes, microchannels in the filler are cut against the outer conductor. In the concept presented in Figure 4.19, the one-directional microwave field would be supported by these conductors. Fluids or reactants that flow in the channels would thus be exposed to and heated

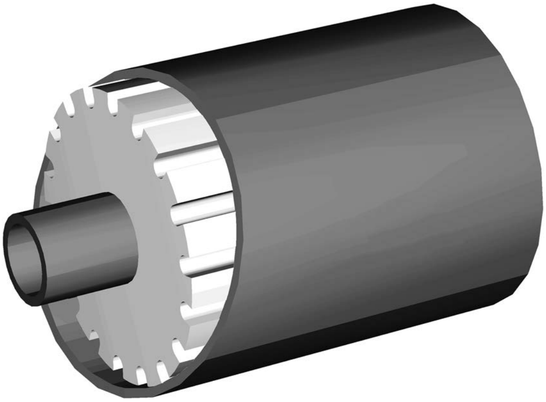

Figure 4.19 Coaxial traveling microwave multichannel liquid phase reactor concept.

by the microwave field. The goal is to achieve a uniform three-dimensional heating rate distribution in the process fluid. This is important as the present resonant microwave cavities perform partial and non-uniform exposure of the process fluid to the microwave field in an uncontrolled manner. It is reasonable to assume that for those processes that can be intensified *via* microwave exposure, the effect can be optimized and fully harnessed only when the entire process fluid is exposed to uniform and controlled microwave field conditions. Besides, it is only under such conditions that one can decouple microwave from thermal effects and study microwave–chemistry interactions.

As shown in Figure 4.18, the field intensity in TEM or quasi-TEM distributes uniformly over the circumference of the outer conductor.[73] Heat generation would thus be distributed uniformly among the channels. Note here that the channels can be cooled through the outer conductor surface. Doing so would not expose the coolant to the microwave field. This avoids the need for special coolants that do not absorb microwave energy. Besides, optimization of the field distribution can be locally controlled through the structural parameters of the TMR that is, optimization of size, shape and materials of the different structures of the TMR.

The optimization of this system is presented for a case of a liquid phase TMR configuration that consists of 12 water filled channels with a 0.2 mm^2 cross-sectional area each.[60,81] Figure 4.20 presents the degrees of freedom that are available to actuate on heat generation over the cross-section. A constant temperature of 25 °C is assumed. The system is analyzed *via* modal

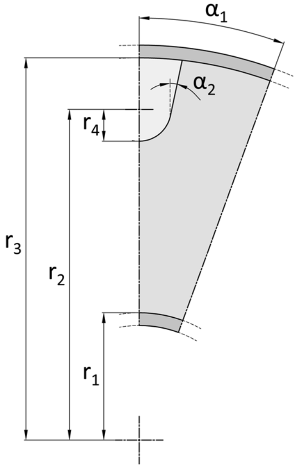

Figure 4.20 Geometrical degrees of freedom in the cross-section of the coaxial traveling microwave multichannel liquid phase reactor concept. The radii r_2 and r_4 and the angle α_2 are available for optimization of the channel cross-section. The inner conductor radius r_1 can be varied to manipulate the axial distribution of heat generation.

analysis of the waveguide configuration involving an electromagnetic model combined with optimization routines. Figure 4.21 presents the heating rate distribution in the optimized segmental cross-section.

In a second step, the axial heating rate distribution is optimized by manipulating the profile of the inner conductor diameter. If the inner conductor were to be constant over the length of the reactor, the field intensity and heating rate would attenuate exponentially over the length of the reactor. To compensate for this, the inner conductor diameter can be increased over the length of the reactor to gradually concentrate the microwave field more into the channels. The approach taken in the optimization is to calculate the characteristic impedance of the system for a set of inner conductor diameters. The impedance in this context is the ratio between the electric potential between the conductors and the electric current that flows through them; impedance is related to the measure of wave reflection and transmission between waveguide sections. The reactor is then discretized; for each discrete part the impedance is interpolated and from this the axial heating rate distribution is determined. Then, an optimal diameter profile resulting in uniform heating rate distribution is determined by means of an optimization routine. Figure 4.22 presents the diameter profile of the inner conductor for a 1.6 m long reactor with the channel cross-section mentioned above. In Figure 4.23 the axial heating rate distribution over the system is presented. The two-step approach was successfully validated by means of a three-

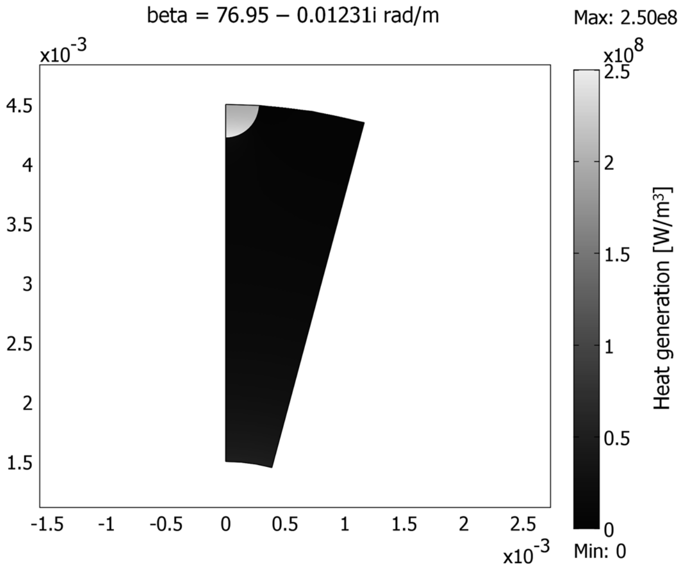

Figure 4.21 Segment of the coaxial traveling microwave multichannel liquid phase reactor with an optimized channel cross-section. The channel is optimized for a 0.2 mm^2 cross-sectional area and a uniform heating rate distribution.

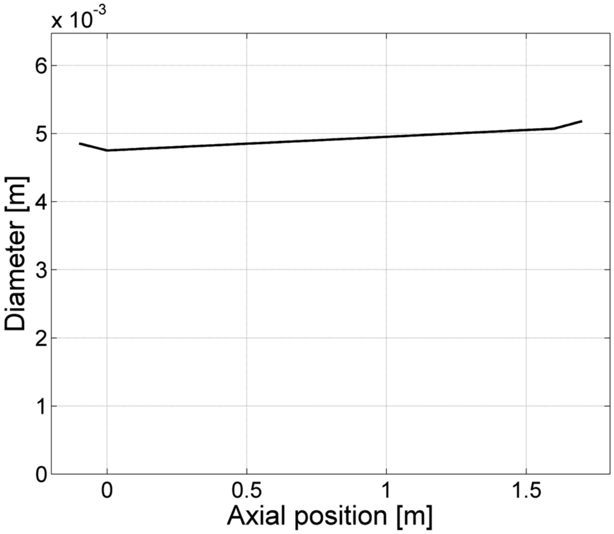

Figure 4.22 Optimized diameter profile over the length of the liquid phase reactor.

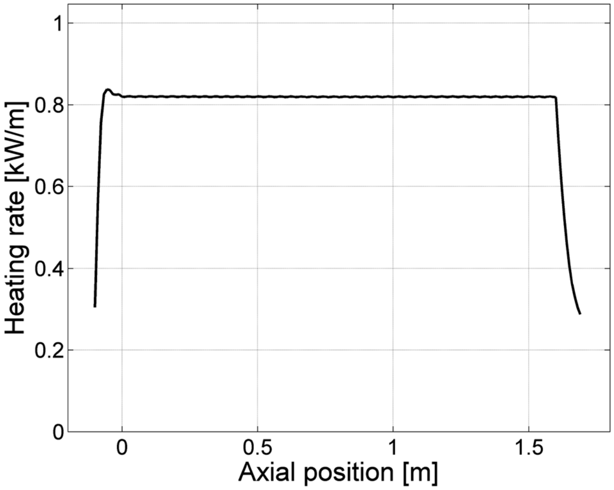

Figure 4.23 Optimized axial heating rate distribution over the length of the liquid phase reactor.

dimensional simulation of a segment of the coaxial traveling microwave reactor. The 3D simulation results are shown in Figure 4.24. It was found that the greatest variation of ~15% occurs in the cross-section rather than in the axial direction. The performance in terms of heating rate uniformity is much better than can be achieved in resonant systems.

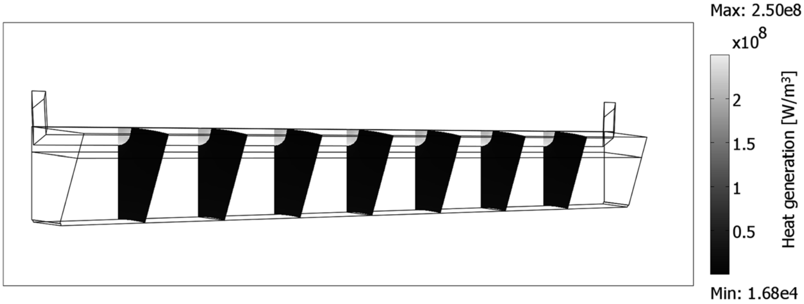

Figure 4.24 Three dimensional simulation of heating rate of one optimized liquid phase reactor segment. The slices are spaced 0.2 m apart. Note that this figure has a high degree of perspective distortion, the geometry is only about 2 mm high, while it is 1.6 meter long.

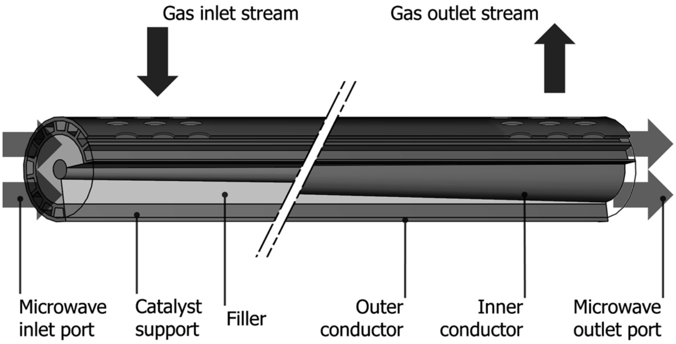

Figure 4.25 Coaxial traveling microwave gas phase monolith reactor concept.

4.3.2.2 Gas–Solid Phase Process Configuration

Another possible application of coaxial traveling microwave reactors concerns selective and uniform catalyst heating in heterogeneous gas–solid chemistries.[37] As opposed to the liquid phase reactor, the focus now lies in selective catalyst heating. This is, in principle, beneficial not only in terms of energy savings, as inert parts of the reactor are not directly heated, but also in terms of chemical efficiency as undesired side-reactions in the bulk phase may be suppressed. In the concept proposed herein, the space between the inner and outer conductor contains a dielectric material and a monolithic (cordierite/silica) multichannel layer adjacent to the outer conductor. The channels' volume will be occupied by the gas phase. The channel walls transverse to the outer conductor will be functionalized with metal catalyst. Unlike the system for liquid phase processing discussed in the previous section, the goal here is to *focus* the electric field on the metal nanoparticles (selective/direct catalyst heating) in the monolith walls and to attain heating rate uniformity along the axial (flow) direction. The latter

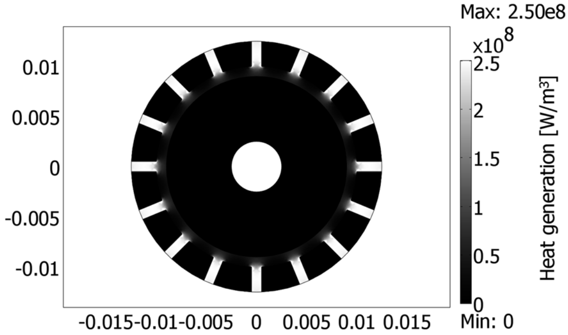

Figure 4.26 Simulation of the heating rate distribution over the cross-section of the gas phase monolith reactor.

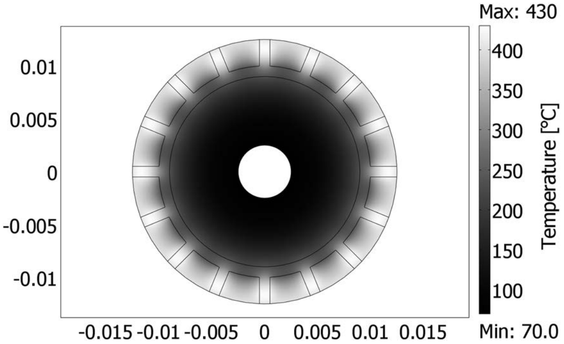

Figure 4.27 Simulation of the temperature distribution over the cross-section of the gas phase monolith reactor after 12 s of microwave exposure.

can be achieved by gradually increasing the radius of the inner conductor, as shown in Figure 4.25, in order to compensate for wave attenuation along the reactor length.

Figures 4.26 and 4.27 are based on a preliminary modeling study of the configuration in Figure 4.25. Figure 4.26 shows the electromagnetic energy dissipation (heat generation) over a cross-section of the TMR. Due to the filler material having a higher permittivity compared to the effective permittivity of the outer monolithic layer containing the gas phase, the electric field is "pushed" towards the outer conductor. The densified field in the monolithic layer results in evenly distributed and focused heating of the transverse channel walls as shown in Figure 4.27. The transverse channel walls represent monolithic walls functionalized with metal catalyst nanoparticles which have a high dielectric loss factor thereby selectively absorbing the microwave energy.

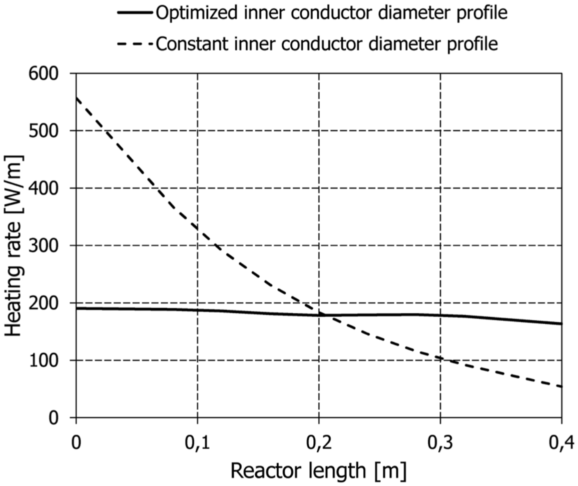

Figure 4.28 Axial heating rate distribution for both the constant inner diameter profile and the inner diameter profile optimized for a constant axial heating rate distribution.

Finally, the exact inner radius profile is optimized according to the approach described for the liquid phase system. The results for optimized and non-optimized (constant) radius profiles are shown in Figure 4.28. The solid line in Figure 4.28 corresponds to the optimized inner conductor diameter profile and shows that the heating rate along a 40 cm length remains almost invariant although >70% of the microwave power at the inlet has been absorbed along the way (not shown).

As the take home message, locally-tailored heating patterns at macro- and microscale can be achieved in TMRs through iterative numerical optimization of the channels' cross-sectional geometry, the inner conductor diameter as function of length and the filler material permittivity. This can be achieved neither with conventional heating nor with conventional microwave equipment used for chemical processing.

4.4 Conclusions

This work discusses design aspects of different microwave applicator concepts suitable for chemical processing. Up to now, in the research area of microwave-assisted chemistry, discussion of the design of electromagnetic field applicators and their integration into reactor systems has been limited to single mode cavity *versus* multimode cavity arguments. Herein, we extend the discussion beyond this limited scope by presenting advanced non-cavity applicator types that can be used for microwave activation of chemical reactors. In this context, our main conclusion is that well-controlled and optimized microwave-assisted chemical processing requires transition from the current processing paradigm of chemical reactors activated by standing wave fields in conventional resonant cavity-based equipment to chemical reactors activated by traveling electromagnetic fields.

Acknowledgements

We thank the chair of Chemical Reactor Engineering, Eindhoven University of Technology for the use of custom glassware and we thank the Design Engineering Department, Product Engineering Section, Delft University of Technology for use of the thermal camera.

References

1. R. Gedye, F. Smith, K. Westaway, H. Ali, L. Baldisera, L. Laberge and J. Rousell, *Tetrahedron Lett.*, 1986, **27**, 279.
2. R. J. Giguere, T. L. Bray, S. M. Duncan and G. Majetich, *Tetrahedron Lett.*, 1989, **27**, 4945.
3. K. Adlington, G. J. Jones, J. El Harfi, G. Dimitrakis, A. Smith, S. W. Kingman, J. P. Robinson and D. J. Irvine, *Macromolecules*, 2013, **46**, 3922.
4. R. K. Arvela, N. E. Leadbeater, T. L. Mack and C. M. Kormos, *Tetrahedron Lett.*, 2006, **47**, 217.
5. S. Bag, S. Dasgupta and B. Torok, *Curr. Org. Synth.*, 2011, **8**, 237.
6. J. M. Bermúdez, D. Beneroso, N. Rey-Raap, A. Arenillas and J. A. Menéndez, *Chem. Eng. Process.*, 2015, **95**, 1.
7. D. Bogdal, *Microwave-assisted organic synthesis: one hundred reaction procedures*, Elsevier, Amsterdam, 2005.
8. V. L. Budarin, P. S. Shuttleworth, M. De bruyn, T. J. Farmer, M. J. Gronnow, L. Pfaltzgraff, D. J. Macquarrie and J. H. Clark, *Catal. Today*, 2015, **239**, 80.
9. R. Cherbanski, M. Komorowska-Durka, G. D. Stefanidis and A. I. Stankiewicz, *Ind. Eng. Chem. Res.*, 2011, **50**, 8632.
10. S. J. Choi, J. Kuwabara and T. Kanbara, *ACS Sustainable Chem. Eng.*, 2013, **1**, 878.
11. A. de la Hoz, A. Diaz-Ortiz and A. Moreno, *Chem. Soc. Rev.*, 2005, **34**, 164.
12. C. Ebner, T. Bodner, F. Stelzer and F. Wiesbrock, *Macromol. Rapid Commun.*, 2011, **32**, 254.
13. B. Fidalgo, A. Arenillas and J. A. Menendez, *Fuel Process. Technol.*, 2011, **92**, 1531.
14. K. Y. Foo and B. H. Hameed, *Bioresour. Technol.*, 2012, **119**, 234.
15. T. N. Glasnov and C. O. Kappe, *Chem.–Eur. J.*, 2011, **17**, 11956.
16. M. J. Gronnow, R. J. White, J. H. Clark and D. J. Macquarrie, *Org. Process Res. Dev.*, 2005, **9**, 516.
17. M. D. Johnstone, A. J. Lowe, L. C. Henderson and F. M. Pfeffer, *Tetrahedron Lett.*, 2010, **51**, 5889.

18. C. O. Kappe, D. Dallinger and S. S. Murphree, *Practical Microwave Synthesis for Organic Chemists*, Wiley-VCH, Weinheim, 2009.
19. C. O. Kappe and E. van der Eycken, *Chem. Soc. Rev.*, 2010, **39**, 1280.
20. M. Komorowska-Durka, M. Barmen' t Loo, G. S. J. Sturm, M. Radoiu, M. Oudshoorn, T. Van Gerven, A. I. Stankiewicz and G. D. Stefanidis, *Chem. Eng. Process.*, 2013, **69**, 83.
21. K. Kranjc and M. Kocevar, *Curr. Org. Chem.*, 2013, **17**, 448.
22. K. Kranjc and M. Kocevar, *Curr. Org. Chem.*, 2013, **17**, 457.
23. M. Larhed, C. Moberg and A. Hallberg, *Acc. Chem. Res.*, 2002, **35**, 717.
24. N. E. Leadbeater, T. M. Barnard and L. M. Stencel, *Energy Fuels*, 2008, **22**, 2005.
25. P. Lidstrom, J. Tierney, B. Wathey and J. Westman, *Tetrahedron*, 2001, **57**, 9225.
26. A. Loupy, L. Perreux, M. Liagre, K. Burle and M. Moneuse, *Pure Appl. Chem.*, 2001, **73**, 161.
27. R. T. McBurney, F. Portela-Cubillo and J. C. Walton, *RSC Adv.*, 2012, **2**, 1264.
28. A. Navarrete, M. Herrero, A. Martin, M. J. Cocero and E. Ibanez, *J. Food Eng.*, 2011, **104**, 196.
29. P. D. Patil, V. G. Gude, L. M. Camacho and S. G. Deng, *Energy Fuels*, 2010, **24**, 1298.
30. P. D. Patil, V. G. Gude, A. Mannarswamy, P. Cooke, S. Munson-McGee, N. Nirmalakhandan, P. Lammers and S. G. Deng, *Bioresour. Technol.*, 2011, **102**, 1399.
31. G. Perin, G. Alvaro, E. Westphal, L. H. Viana, R. G. Jacob, E. J. Lenardao and M. G. M. D'Oca, *Fuel*, 2008, **87**, 2838.
32. L. Perreux and A. Loupy, *Tetrahedron*, 2001, **57**, 9199.
33. W. L. Perry, D. W. Cooke, J. D. Katz and A. K. Datye, *Catal. Lett.*, 1997, **47**, 1.
34. W. L. Perry, A. K. Datye, A. K. Prinja, L. F. Brown and J. D. Katz, *AIChE J.*, 2002, **48**, 820.
35. X. H. Qi, M. Watanabe, T. M. Aida and R. L. Smith, *Green Chem.*, 2008, **10**, 799.
36. X. H. Qi, M. Watanabe, T. M. Aida and R. L. Smith, *Catal. Commun.*, 2008, **9**, 2244.
37. G. D. Stefanidis, A. Navarrete Muñoz, G. S. J. Sturm and A. Stankiewicz, *Rev. Chem. Eng.*, 2014, **30**, 233.
38. W. K. Teng, G. C. Ngoh, R. Yusoff and M. K. Aroua, *Chem. Eng. J.*, 2016, **284**, 469.
39. Z. S. Wei, G. H. Zeng, Z. R. Xie, C. Y. Ma, X. H. Liu, J. L. Sun and L. H. Liu, *Fuel*, 2011, **90**, 1599.
40. H. Will, P. Scholz and B. Ondruschka, *Top. Catal.*, 2004, **29**, 175.
41. Y. Y. Wu, Z. H. Fu, D. L. Yin, Q. Xu, F. L. Liu, C. L. Lu and L. Q. Mao, *Green Chem.*, 2010, **12**, 696.
42. S. Yamada, A. Takasu and K. Kawamura, *J. Polym. Sci., Part A: Polym. Chem.*, 2013, **51**, 3732.

43. X. L. Zhang and D. O. Hayward, *Inorg. Chim. Acta*, 2006, **359**, 3421.
44. T. Van Gerven and A. Stankiewicz, *Ind. Eng. Chem. Res.*, 2009, **48**, 2465.
45. M. H. C. L. Dressen, J. E. Stumpel, B. H. P. van de Kruijs, J. Meuldijk, J. A. J. M. Vekemans and L. A. Hulshof, *Green Chem.*, 2009, **11**, 60.
46. M. H. C. L. Dressen, B. H. P. V. van de Kruijs, J. Meuldijk, J. A. J. M. Vekemans and L. A. Hulshof, *Org. Process Res. Dev.*, 2009, **13**, 888.
47. A. K. Gupta, N. Singh and K. N. Singh, *Curr. Org. Chem.*, 2013, **17**, 474.
48. R. Hoogenboom, T. F. A. Wilms, T. Erdmenger and U. S. Schubert, *Aust. J. Chem.*, 2009, **62**, 236.
49. M. Irfan, M. Fuchs, T. N. Glasnov and C. O. Kappe, *Chem.–Eur. J.*, 2009, **15**, 11608.
50. C. O. Kappe, B. Pieber and D. Dallinger, *Angew. Chem., Int. Ed.*, 2013, **52**, 1088.
51. M. Komorowska, G. D. Stefanidis, T. Van Gerven and A. I. Stankiewicz, *Chem. Eng. J.*, 2009, **155**, 859.
52. V. P. Mehta and E. V. Van der Eycken, *Chem. Soc. Rev.*, 2011, **40**, 4925.
53. J. D. Moseley, P. Lenden, M. Lockwood, K. Ruda, J. P. Sherlock, A. D. Thomson and J. P. Gilday, *Org. Process Res. Dev.*, 2008, **12**, 30.
54. I. Plazl, S. Leskovsek and T. Koloini, *Chem. Eng. J. Biochem. Eng. J.*, 1995, **59**, 253.
55. E. Caliskan, J. M. Bermudez, J. B. Parra, J. A. Menendez, M. Mahramanlioglu and C. O. Ania, *J. Environ. Manage.*, 2012, **102**, 134.
56. *Comsol Multiphysics 3.5® with RF-module*, Comsol AB, Stockholm, 2008.
57. R. Meredith, *Engineers' Handbook of Industrial Microwave Heating*, Institution of Electrical Engineers, London, 1998.
58. B. Ondruschka, W. Bonrath and D. Stuerga, Development and design of reactors in microwave-assisted chemistry, in *Microwaves in organic synthesis*, ed. A. de la Hoz and A. Loupy, Wiley-VCH, Weinheim, 2012.
59. T. V. Chow Ting Chan and H. C. Reader, *Understanding microwave heating cavities*, Artech House, Boston, 2000.
60. G. S. J. Sturm, M. D. Verweij, A. I. Stankiewicz and G. D. Stefanidis, *Chem. Eng. J.*, 2014, **243**, 147.
61. D. Karstädt, K. Möllmann and M. Vollmer, *Phys. Unserer Zeit*, 2004, **35**, 90.
62. CEM corp, *Discover legacy systems – Microwave Synthesizers*, http://it.cem.com/discover-labmate.html, accessed 8 August 2015.
63. W. E. Jennings, *Microwave-assisted chemical synthesis instrument with fixed tuning*, U.S. Patent 6753517, 2004.
64. G. Roussy, and J. A. Pearce, *Foundations and Industrial Applications of Microwave and Radio Frequency Fields: Physical and Chemical Processes*, Wiley, Chichester, 1995.
65. G. S. J. Sturm, M. D. Verweij, T. van Gerven, A. I. Stankiewicz and G. D. Stefanidis, *Int. J. Heat Mass Transfer*, 2012, **55**, 3800.
66. T. Durka, G. D. Stefanidis, T. Van Gerven and A. I. Stankiewicz, *Int. J. Hydrogen Energy*, 2011, **36**, 12843.
67. A. C. Metaxas, *J. Microwave Power*, 1974, **9**, 123.

68. E. Altman Restrepo, *Microwave Enhanced Reactive Distillation*, PhD thesis, Delft University of Technology, Delft, 2011.
69. N. G. Patil, F. Benaskar, J. Meuldijk, L. A. Hulshof, V. Hessel, J. C. Schouten, E. D. C. Esveld and E. V. Rebrov, *AIChE J.*, 2014, **60**, 3824.
70. N. G. Patil, A. I. G. Hermans, F. Benaskar, J. Meuldijk, L. A. Hulshof, V. Hessel, J. C. Schouten and E. V. Rebrov, *AIChE J.*, 2012, **58**, 3144.
71. P. Zhou, X. Yang, K. Huang and G. Jia, *Chem. Eng. Technol.*, 2015, **38**, 1334.
72. E. R. de Castro, M. B. Mourao, L. A. Jermolovicius, C. Takano and J. T. Senise, *Steel Res. Int.*, 2012, **83**, 131.
73. D. M. Pozar, *Microwave Engineering*, Wiley, Hoboken, 2005.
74. G. S. J. Sturm, G. D. Stefanidis, M. D. Verweij, T. D. T. Van Gerven and A. I. Stankiewicz, *Chem. Eng. Process.*, 2010, **49**, 912.
75. Neoptix Canada LP, *T1 Fiber Optic Temperature Probe*, http://www.neoptix.com/t1-sensor.asp, accessed 24 August 2015.
76. E. Altman, G. D. Stefanidis, T. van Gerven and A. Stankiewicz, *Ind. Eng. Chem. Res.*, 2012, **51**, 1612.
77. G. H. Brown, C. N. Hoyler and R. A. Bierwirth, *Theory and Application of Radio-Frequency Heating*, Van Nostrand, New York, 1947.
78. M. Izadifar, O. D. Baik and G. S. Mittal, *Chem. Eng. Process.*, 2009, **48**, 1437.
79. Y. Li, M. Radoiu, A.-S. Fabiano-Tixier and F. Chemat, From laboratory to industry: scale-up, quality, and safety consideration for microwave-assisted extraction, in *Microwave-assisted extraction for bioactive compounds*, ed. F. Chemat and G. Cravotto, Springer US, New York, 2013.
80. Sairem SAS, *The INTLI Technology and Laboratory & Pilot*, http://www.sairem.com/the-new-intli-technology-for-performing-clean-fast-and-energetic-chemistry-58.htmlresp, http://www.sairem.com/laboratory-et-pilot-59.html, accessed 24 August 2015.
81. G. S. J. Sturm, M. D. Verweij, T. Van Gerven, G. D. Stefanidis and A. Stankiewicz, *Proceedings of the 13th International Conference on Microwave and RF Heating AMPERE*, 2011, pp. 48–51 (electronic version).

CHAPTER 5

Greener Processing Routes for Reactions and Separations Based on Use of Ultrasound and Hydrodynamic Cavitation

PARAG R. GOGATE[a]

[a]Chemical Engineering Department, Institute of Chemical Technology,
Matunga, Mumbai – 400 019, India
*E-mail: pr.gogate@ictmumbai.edu.in, paraggogate@yahoo.co.in

5.1 Introduction

Cavitational reactors based on the use of sound energy or the energy associated with the fluid flow, offer immense potential for process intensification. The driving mechanism in the case of cavitational reactors is the generation of cavities based on alterations of pressure followed by growth and collapse of the cavities, releasing a significant amount of the accumulated energy during the growth phase.[1–3] The active area of cavitational events and the release of energy are at the microscopic level, which could also mean that the energy is released at the specific point of transformation thereby increasing the energy efficiency. Due to significant energy release over a very small active area, it is expected that conditions of very high pressures and temperatures (a few thousand atmospheres and a few thousand degrees) are generated locally at

---

RSC Green Chemistry No. 47
Alternative Energy Sources for Green Chemistry
Edited by Georgios Stefanidis and Andrzej Stankiewicz

Published by the Royal Society of Chemistry, www.rsc.org

microscopic levels.[4] Due to entrapment of vapours in the cavitating bubbles, free radicals are generated by pyrolytic dissociation reactions, which can lead to intensification of chemical reactions or may even result in the propagation of certain reactions.[5–7] The physical effects of cavitation in terms of the generation of local turbulence and acoustic streaming dominate the intensification of physical processing applications as well as reactions limited by mass transfer, as it is expected that the physical effects would enhance the rates of transport processes.

In practice, cavitation can be generated in the reactor using different approaches to energy transfer, and a basic distinction in terms of the type of cavitation can be made based on the mode of energy dissipation. Acoustic cavitation is based on the use of sound energy (mostly ultrasound) whereas hydrodynamic cavitation is based on the use of fluid energy in terms of pressure/velocity alterations based on the principle of Bernoulli's equation.[8] The two other types of cavitation, though not having significant potential for physicochemical transformations, are based on the use of light energy (optic cavitation) and energy associated with moving particles (particle cavitation). Another approach to distinguishing cavitation is on the basis of the type of collapse of the generated cavities. In the case of transient cavitation, it is expected that the generated cavity grows to a few hundred times the original size and then collapses within a very short duration generating very high energy densities. The effects of transient cavitation would be mostly chemical in terms of hot spots or the generation of free radicals and suited more to the intensification of chemical processing applications. On the other hand, stable cavitation involves multiple cycles of growth and slow collapse of the generated cavities creating milder conditions in terms of pressure and temperature. Also, the maximum growth of cavities associated with the stable cavitation is much lower as compared to the case of transient cavitation. The mild effects of stable cavitation would be more suited for physical processing applications or chemical reactions limited by mass transfer as in the case of heterogeneous reactions. It is important to identify the controlling mechanisms for intensification and tune the type of cavitation for the desired effects so that the intensification per unit energy input can be maximized.

The efficacy of the cavitational reactors, especially in large-scale operations, is decided by the active cavitational volume and the cavitational intensity which can be quantified in terms of the collapse pressure or the quantum of free radicals generated.[9] The important aspects in deciding the active volume and intensity would be the maximum size reached during the growth phase, the lifetime and type of the cavity and the number of cavities. The maximum size would govern the energy released by the collapsing cavity whereas the lifetime of cavity and the number of cavities generated in the reactor would govern the active cavitational volume. The type of cavity produced *i.e.* cavity containing gas or vapour, or mixture of gas and vapour also affects the final collapse conditions and the quantum of energy released. The aim of any equipment designer dealing with large-scale designs should be to maximize both the cavitational volume and collapse intensity which can be achieved by a proper selection of the geometry of reactor (including the arrangement of transducers in the case of acoustic cavitation-based reactors) and set of operating parameters including the equipment and the liquid physicochemical properties.

After providing a basic understanding of cavitation, the chapter will now provide an overview of the mechanism for intensification, design configurations for both acoustic and hydrodynamic cavitation, guidelines for selection of operating/geometric parameters and finally some case studies related to process intensification in the areas of green chemistry and separations.

5.2 Mechanism of Cavitation-Based Process Intensification

The exact mechanism of intensification due to the use of cavitational reactors would be dependent on the type of system *i.e.* homogeneous or heterogeneous, and the controlling effects governing the specific transformation.[6,7] It is expected that the homogenous systems, especially in the case of chemical reactions, would be more affected by chemical effects such as local hot spots and the generation of radicals, whereas for heterogeneous systems, physical effects in terms of liquid turbulence and circulation would be dominant for the intensification.

In the case of homogeneous liquid phase reactions, the generated cavity is likely to contain vapors of the liquid and these vapors would be subjected to hot spots in the collapsing cavities (the temperature inside the cavity would be an order of magnitude higher than the bulk liquid and the cavity liquid interface) generating highly reactive free radicals. In the specific case of wastewater treatment applications,[10] water would be dissociated into hydroxyl radicals which can oxidize the majority of the contaminants present in the wastewater and, in addition, a variety of other oxidants will be generated based on the series of radical reactions. The generated radicals can react either within the collapsing bubble or migrate into the bulk liquid and react with the non-volatile components present in the bulk. It is also expected that the rate of chemical reactions in the collapsing cavity would be significantly higher compared to that observed in the bulk liquid. Another mechanism that can drive the intensification in homogeneous systems is the sudden collapse of the cavities which can create significant shear forces in the surrounding liquid capable of breaking chemical bonds.

In the case of heterogeneous systems, the processing rates would be decided by the rates of transport processes which can be intensified due to the turbulence generated by cavitation. In a solid/liquid system, where the solid can be either a reactant or a catalyst, the micro-scale turbulence can lead to enhanced surface areas as well as activation. The collapse near the surface of solids can create an asymmetrical inrush of the liquid, generating effects similar to the high-pressure/high-velocity liquid jets used for cleaning.

The net effect would be either in terms of activation or cleaning of the solids or even in terms of breakage of the solids leading to an enhanced surface area available for reaction. The turbulence and liquid circulation leads to enhanced mass transfer to and from the surface based on the disruption of the interfacial boundary layers whereas the ability to dislodge the material occupying the active sites leads to cleaning effects. The collapse intensity and the impact on the surface transfers enough energy to cause fragmentation of the solids, which would be more suited to the case of solid reactants or where agglomeration of solids needs to be avoided. Depending on the specific application, for example involving a catalyst or solids, the cavitational intensity needs to be controlled so as to maximize the benefits.

In the case of heterogeneous liquid/liquid reactions, cavitational energy dissipation at, or near, the interface results in the formation of very fine emulsions and the available surface area for the reaction between the two phases is significantly increased due to the formation of fine emulsions—generally the drop sizes would be in the micro range or even sometimes in the nano range. These effects of cavitation can also be beneficial in the cases of a reaction catalyzed by a phase–transfer catalyst although it is important to note here that usually cavitation cannot replace the need of a phase–transfer catalyst.

The use of cavitational reactors either as a complete replacement for conventional reactors or as a supplement would be dependent on the controlling mechanism of the expected intensification.[1] If the cavitational enhancement only results in an improved mixing or enhanced surface area, especially in the case of heterogeneous systems, cavitation pretreatment or treatment at intermittent conditions (for cleaning or avoiding agglomeration) would be sufficient to give intensification at much lower energy input. The time of application and the exact duration of treatment using cavitational reactors can be decided based on the identified controlling mechanisms so as to optimize the energy consumption. The approach of pretreatment or intermittent application can also be very useful in the case of crystallization where a tailor-made crystal size distribution can be obtained using the approach of periodic application. The scale-up of the pretreatment vessel would be a relatively simple task when compared to designing a new main cavitational reactor. If the effect is truly based on cavitation chemistry involving the formation of radicals or hot spots driving the reactions, then the application of cavitation would be required continuously throughout the transformation.

The scientific database established using the laboratory study or the analysis of reported literature can be used to understand the most effective parametric window of operation based on the controlling effects of the operating parameters on the cavitational intensity and hence on the expected levels of process intensification.[1] An important step in this approach would also be to understand the mechanisms of interaction so that the effect can be maximized at minimum possible energy consumption. Proper design guidelines would also be required to generate a uniform cavitation field of desired intensity at a larger scale.[11] The physicochemical properties of the medium will also play a major role in deciding the extent of benefits and the required costs for the expected intensification. For example, high viscosity media will require higher energy to generate cavitation whereas the presence of gases or solid particles will facilitate cavitation. Overall, it can be said that a detailed analysis in terms of controlling mechanisms for the intensification and interaction of the operating/design parameters with the cavitational effects is very important and will decide the balance between the degree of process intensification and economic implications.

5.3 Reactor Configurations

5.3.1 Sonochemical Reactors

Reactors based on acoustic cavitation generated by the passage of ultrasound are more commonly described as sonochemical reactors. Passage of ultrasound (frequencies in the range of 16 kHz–2 MHz) through liquid media results in pressure variations due to alternate compression and rarefaction cycles. When a sufficiently large negative pressure is applied to the liquid based on the pressure amplitude and operating frequency, a cavity will be formed if the average distance between the molecules due to the stretching action exceeds the critical molecular distance required to hold the liquid intact. The oscillating pressure field created by the compression and rarefaction cycles drives the different stages of cavitation.[4] The passage of ultrasound is usually effected with the help of a transducer and the energy transfer efficiency into the reactor, as well as the cavitationally active volume, strongly depends on the type and geometry of the transducer. Transducers typically operate at a fixed frequency of irradiation but can be tuned to give variable power dissipation, also the area of irradiation can be varied based on the number of transducers or the dimensions of a single transducer. The different types of transducers commonly used are electromechanical, liquid-driven and gas-driven. The electromechanical transducers *viz.* piezoelectric and the magnetostrictive transducers are the most versatile and widely used types of transducers. Piezoelectric transducers work on the principle that the piezoelectric material expands and contracts in an oscillating electric field resulting in the propagation of sound waves (pressure waves) into the liquid medium. On the other hand, magnetostrictive transducers expand and contract in an alternating magnetic field and the typical materials that are used are nickel alloys. Liquid-driven transducers (*e.g.* a liquid whistle) are not so commonly used for chemical processing applications requiring significant power dissipation, and are generally recommended for homogenization and generation of very fine emulsions. Similarly, gas-driven transducers (simple whistles such as dog whistles and sirens with high frequency output) are only used to break foams and agglomerates of dust or for the acceleration of drying processes. Most of the earlier designs were based on the use of transducers in direct contact or attached to flat surfaces such as the bottom of reactors. Recent developments allowing the bonding of transducers to reactor walls has led to development of new designs giving much higher flexibility in operation.[12]

The ultrasonic horn has been the most commonly used design, especially at the laboratory scale of operation and is recommended for all exploratory studies. In this design the transducer is usually attached to the tip of the horn and systems can deliver large power directly to the medium giving significantly higher cavitational intensity around the transducer. The power dissipation can be controlled by changing the amplitude and these designs operate at constant frequency of irradiation. The flexibility of operation in terms of introducing pulses also gives the designer a means to control the cavitational intensity which would be very important in the case of delicate applications such as enzymatic reactions. Most of the ultrasonic horn type designs have been used in a batch mode of operation although continuous designs are indeed possible by inserting ultrasonic horns at multiple locations in flow systems.[13] Using a number of such transducers in series can give extended treatment times though the design (Figure 5.1) would have some problems associated with possible leakage especially in the case of high pressure operation. One major disadvantage of the ultrasonic horn is due to direct contact of the process fluid with the immersed transducer which can lead to possible contamination of the processed liquids. Also, the cavitational activity is concentrated very close to the transducer and diminishes at a distance of few cm away from the transducer in both (axial and radial) directions depending on the dissipated power and the geometry of the transducer. Use of a horn with vibrations in the lateral area and a significantly higher area of irradiation[14,15] compared to the conventional design allows efficient processing at the pilot-scale capacity with higher

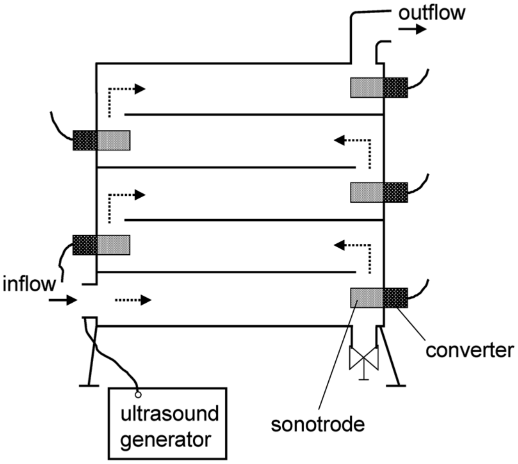

Figure 5.1 Schematic representation of flow systems based on ultrasonic horn. Reprinted from Ultrasonics Sonochemistry, 14, K. Nickel and U. Neis, Ultrasonic disintegration of biosolids for improved biodegradation, 450–455, Copyright (2007) with permission from Elsevier.[13]

energy efficiencies, established by calorimetric measurements. The design provides dual advantages of higher irradiating surface area (lower intensity of irradiation and higher active volume) coupled with better distribution of the energy in multiple directions. Dion[16] has also described a new design that can be operated in a continuous manner based on the high-power converging acoustic waves in a tube. The design is reported to produce an acoustic cavitation zone spreading over a relatively large volume and leads to better cavitational activity distribution.

Cleaning tank type configurations, also commonly described as ultrasonic baths, are the other most commonly used designs, especially when an indirect mode of irradiation is preferred, for example, to avoid contamination of the processed liquids or to prevent exposure to high intensity cavitation such as in the case of enzymatic reactions. The transducers are typically attached to the bottom and either single or multiple transducers can be used depending on the volume of the reactor. The active cavitational zone is typically restricted to a vertical plane just above the transducers and the arrangement of the transducers can be altered so as to achieve good distribution of the incident energy.[17] During the processing, a reaction vessel can be immersed in the coupling fluid though this will restrict the applications especially in terms of operating temperature. On the other hand, the ultrasonic bath can also be used as the reaction vessel but this might restrict the use of any toxic or corrosive materials and would also require additional mixing equipment, especially for large-scale application.

The development of continuous flow systems is essential, especially for large volume systems or where the ultrasonic reactor is to be operated as a supplement to the main conventional reactor. The design of continuous systems can be based on transducers attached to the walls of the reactor or on the coupling of multiple ultrasonic horns/baths sequentially. Multiple horns can be inserted in a flow system either in the external flow loop or by using *T* sections. Recent improvements in the bonding method have allowed the development of flow cells with different geometries including parallel plate reactors,[18] hexagonal reactors[19] and cylindrical reactors. Use of multiple transducers with lower power dissipation levels allows achievement of uniform distribution of the cavitational activity and avoids the possible decoupling losses giving a higher energy transfer efficiency. The multi-transducer units can effectively concentrate intensity at the central zone of the reactor and, most importantly, away from the vessel walls, which can reduce the problems of erosion and particle shedding. Multiple frequency operation can also be facilitated in these configurations to give intense cavitational activity compared to single frequency reactors under conditions of similar power dissipation.[20] Certain modifications in the designs as demonstrated in Figure 5.2 can also allow the use of simultaneous irradiations with incorporation of the ultraviolet lamp in the central annular tube giving irradiations from the center to the outside, along with ultrasonic irradiations from the walls towards the center.

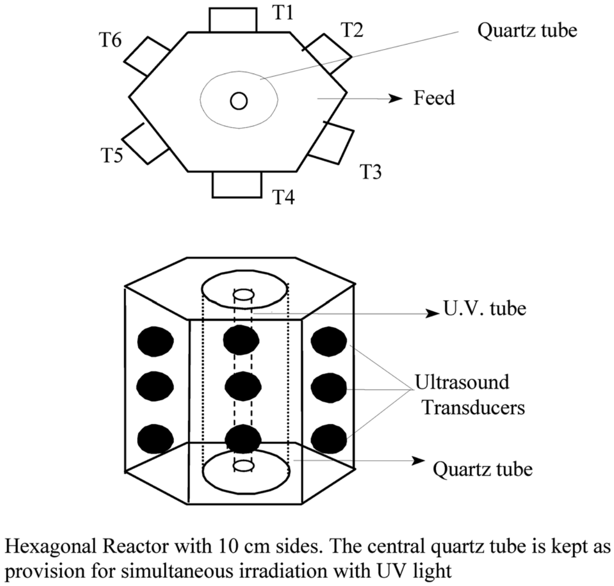

Figure 5.2 Schematic representation of hexagonal flow cell with possibility of simultaneous irradiations.

Although most of the research into sonochemical reactors has been at laboratory/pilot scale, there have been some reports dealing with large-scale operation at a capacity suitable for commercial applications. Son *et al.*[21] reported the use of a design with a working volume of 250 L having a rectangular type cross-section with dimensions 1.2 m × 0.6 m × 0.4 m. The design is based on a transducer module consisting of nine transducers located on the walls of the reactor and having different frequencies in the range 35–170 kHz but having a fixed power rating of 400 W per transducer. Asakura *et al.*[22] also reported a similar design based on the use of twelve transducers (frequency of 500 kHz and maximum power rating of 620 W with location at the bottom or on the walls), though with a lower capacity of 112 L. Vinatoru[23] has also reported the application of a sonochemical reactor with a working capacity of 750–800 L for the extraction of active ingredients from herbs.

5.3.2 Hydrodynamic Cavitation Reactors

The governing principle in the case of hydrodynamic cavitation reactors is the alterations of fluid velocity and local pressure based on the classical Bernoulli principle. If the kinetic energy associated with the liquid increases significantly due to the incorporation of a constriction such as simple valve, orifice or venturi, the local pressure can fall below the vapor pressure generating cavities.[24] Similar increases in the local velocity can also be achieved using high speed rotational equipment. Usually downstream of the constriction or away from the impeller/rotor blade, the pressure is recovered due to sudden or gradual increase in the flow area driving the different stages of cavitation. There is a significant loss of energy in the form of pressure drop across these constrictions or during the flow, which is utilized in generating high intensity turbulence. The intensity of turbulence and, in turn, the cavitational intensity would be dependent on the design of the constriction and the flow conditions of the liquid in terms of driving pressure or the speed of the rotational equipment.

One of the earliest designs for hydrodynamic cavitation reactors is the high-pressure homogenizer based on the use of a high-pressure positive displacement pump supported by a throttling device. The liquid pumped at very high pressure is subjected to sudden constriction, most commonly in the form of two-stage valves, generating cavities. The typical range of operating pressure is 50 atm to 300 atm and usually cavitation is observed only beyond a critical discharge pressure.[25] Intense shear is also generated in these reactors due to the fluid flow and impingement of high velocity jets on the solid wall.

The high-speed homogenizer is another design mainly based on the use of a stator–rotor assembly and the typical operating range for speed of rotation is 4000 to 20 000 rpm. The stator–rotor assembly will be mostly of cylindrical cross-section and different surface indentations/irregularities can be introduced on the rotor to increase the cavitational intensity. As with the high-pressure homogenizer, there exists a critical speed for obtaining significant benefits of cavitation.[26] It is imperative to note here that the energy consumption in these types of reactors is significant and also there is not much flexibility in the design parameters so as to control the intensity of cavitation.

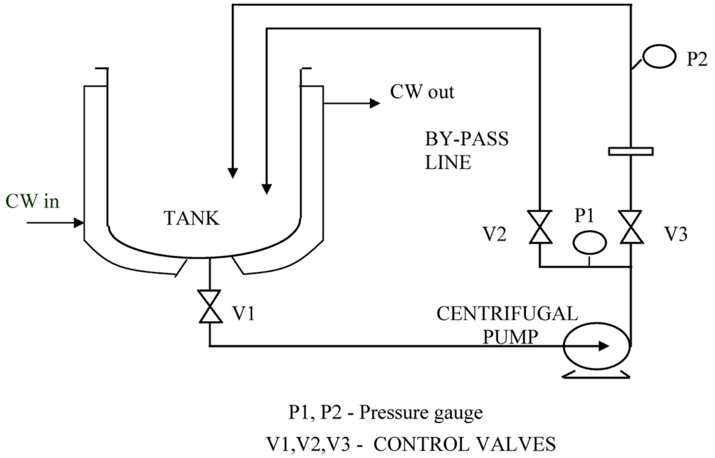

Figure 5.3 Schematic representation of hydrodynamic cavitation setup based on a flow loop housing a cavitation chamber.

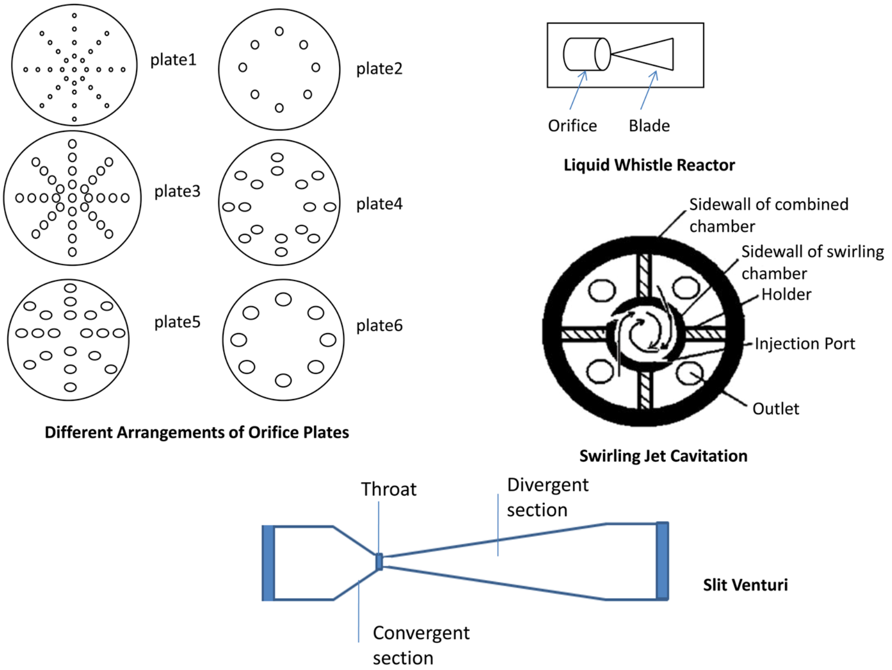

Different Arrangements of Orifice Plates

Liquid Whistle Reactor

Swirling Jet Cavitation

Slit Venturi

Figure 5.4 Types of cavitating devices used in hydrodynamic cavitation reactors.

A versatile design of hydrodynamic cavitation reactor based on the use of a cavitation chamber in a recirculation loop has been described by Gogate *et al.*[18] A schematic representation of the setup has been presented in Figure 5.3. The flow through the main line passes through a cavitation chamber and a bypass line can also be used to control the flow through the main line and that being subjected to the cavitating conditions. The cavitation chamber can be based on the use of a venturi, a single hole orifice, multiple holes on an orifice plate or use of sequential orifice plates.[8] Schematic representations of different types of cavitating devices have been given in Figure 5.4. The recirculation type setup allows a good control over the cavitational activity based on the variation in the operating parameters such as inlet pressure and flow rate as well as geometric parameters such as the different designs of cavitation chamber. Sampathkumar and Moholkar[27] reported a new design based on the use of a converging–diverging nozzle with a facility of introducing bubbles or nuclei in the flow. The design provides flexibility for introducing different gases at varying conditions of flow rate, pressure and bubble size (based on the variation in the gas distributor).

In a recent work, Gogate *et al.*[28] have described a reactor based on the static mixing elements to generate hydrodynamic cavitation. The specific arrangement of mixing elements within a pipe creates conditions similar to the use of multiple orifices generating cavitation as well as efficient mixing, which is key to the explored application of water treatment based on the utilization of ozone. The combined operation of hydrodynamic cavitation and sonochemical reactors has also been utilized in this advanced oxidation reactor with great success in water recycling operations for oil and gas explorations.

5.4 Guidelines for the Selection of Cavitational Reactor Designs and Operating Parameters

The degree of intensification obtained due to the use of cavitational reactors will be strongly dependent on operating and geometric parameters, as the cavitational intensity is usually controlled by these parameters. Typically most of the applications of cavitation have been based on the use of ultrasound-based (sonochemical) reactors and only recently have hydrodynamic cavitation reactors been proposed as an alternative to ultrasound-based processing. Sonochemical reactors generate higher intensities of cavitation but offer scale-up limitations whereas hydrodynamic cavitation has been shown to be more energy efficient, offering good possibilities for scale-up, but these reactors generate less intense cavitation and only limited areas such as synthesis and wastewater treatment, *etc.* have been explored so far.

The important parameters in the case of sonochemical reactors are the power dissipation (intensity of irradiation and power density are affected), frequency of irradiation, liquid phase physicochemical properties (determines the ease of generation of cavities as well as their initial size), temperature, arrangement of the transducers (number, size and pitch in the case of multiple transducer units) and geometry of the reactor. For hydrodynamic cavitation, the important parameters are inlet pressure (initial speed depending on the reactor), type of cavitation chamber, geometry of the reactor, temperature and liquid phase physicochemical properties. A detailed understanding of the effect of operating parameters on the overall cavitational intensity and its distribution can be established on the basis of bubble dynamics simulations.[29–34] Such a detailed analysis can be helpful in obtaining an efficient design for the large-scale operation and can be used effectively for improved processing as well.

In the case of sonochemical reactors, the frequency of irradiation is usually fixed for the transducer used in the reactor. Generally it has been observed that low frequency operation (over the range 20 to 50 kHz) gives dominant physical effects, in terms of turbulence and liquid streaming, with some chemical effects. Use of high frequency irradiations (usually optimum over the range 200 to 500 kHz) result in dominant chemical effects in terms of the generation of free radicals. Use of multiple frequency operation can intensify the cavitational intensity which also permits good control over the active cavitational volume due to the use of multiple transducers. Typically a combination of low frequency irradiation over the range

20 kHz to 50 kHz is the most efficient way of intensifying the cavitational activity with only minimal drawbacks in terms of possible erosion or high power requirements.

Power dissipation is another important parameter as it affects the intensity of irradiation, deciding the cavitational intensity as well as the number of cavitation events in the reactor. Typically, as higher power dissipation as possible until an optimum[35] (the value depends on the specific application and the reactor system), using higher areas of irradiation, gives higher cavitational yields (*viz.* net output per unit power dissipation).

The important liquid phase physicochemical properties having similar effects in both sonochemical and hydrodynamic cavitation reactors are vapor pressure, viscosity and surface tension. Usually liquids with lower vapor pressure, lower viscosity and higher surface tension are preferred to give maximum cavitational activity in the reactor. Water is the most favored liquid medium for efficient processing in the various applications of cavitational reactors.

The effect of operating temperature is usually 'double-edged' and hence optimum selection would be required based on the specific application. On the one hand, enhanced temperature would favor generation of cavities as well as enhanced kinetic rates, on the other the presence of vapors in the formed cavities significantly reduces the cavitational intensity. Energy analysis studies[36] have confirmed that the energy released in a vaporous cavity collapse is much lower compared to a gaseous cavity due to the cushioned collapse of cavities.

The cavitational intensity can be enhanced based on the use of process-intensifying parameters such as the presence of dissolved gases (air, ozone and argon), salts (NaCl, $NaNO_2$ and $NaNO_3$) or solid particles (TiO_2, CuO and MnO_2). Such an approach would be more efficient in the case of chemical processing applications and some of the used additives can also act as a catalyst. It is important to note here that optimum loading of the additives would be required to maximize the effects.[37,38]

In terms of the geometric parameters for sonochemical reactors, using higher areas of irradiation and multiple transducers is beneficial for large-scale processing and optimum values of the ratio of the diameter of the transducer to the reactor diameter, the immersion depth or the liquid height need to be selected. The positioning of transducers in the reactors based on the multiple transducer arrangement should be tailored to obtain maximum and uniform cavitational activity. Overall it can be said that the, multiple transducer design would be the most suitable option for large-scale processing, giving advantages of better cavitational activity distribution with a lower degree of problems like erosion of the surface.

In the case of hydrodynamic cavitation reactors, a reactor design based on the use of a recirculation flow loop through a cavitation chamber *viz.* a venturi, orifice or a series of orifice plates is most flexible. This design would allow the generation of different levels of cavitational intensity depending on the application and hence can give a cost-effective operation. Among the venturi and orifices, the use of a venturi results in dominant stable oscillatory radial bubble motion due to a linear pressure recovery gradient, whereas in the case of an orifice, the presence of an additional oscillating pressure gradient due to turbulent velocity fluctuation results in a transient cavity behavior more suited for chemical processing requiring intense conditions. The extent of permanent pressure drop across an orifice is higher compared to a venturi meaning that a larger fraction of energy is available for cavitation. However, a higher pressure drop would also mean higher pumping energy requirements and this needs to be weighed against the possible benefits that can be obtained in the processing. The geometrical design of the venturi as well as the orifice also plays an important role in deciding the cavitational intensity. For the venturi, a higher intensity can be obtained by using a lower length of venturi or lower venturi throat to pipe diameter ratio. For an orifice plate, a lower flow area would give higher intensity and the possibility of adjusting the number of orifices and the diameter of individual holes gives enhanced flexibility in the operation.

Higher inlet pressures into the system or the use of higher rotational speeds in the case of high speed homogenizers would result in higher cavitational intensity, though beyond a certain limit there is a possibility of supercavitation where a large cavity cloud is formed giving much lower cavitational effects. The optimum conditions for the operating pressure or speed would be dependent on the geometry of the reactor as well as the specific application in question.

5.5 Comparison of Two Modes of Cavity Generation

Passage of ultrasound through the liquid medium creates a fluctuating pressure field which drives the cavitation phenomena, while in the case of hydrodynamic cavitation, fluctuations are brought about by alterations in the geometry of the fluid flow. The majority of earlier research concentrated on the use of ultrasonic reactors for process intensification whereas in the last decade or so, the use of hydrodynamic cavitation has been reported to show promise for intensification of applications such as chemical synthesis and wastewater treatment. It is interesting to compare these two modes of cavity generation especially in terms of the similarity of the operating parameters in controlling the bubble dynamics and the net effects obtained per unit energy dissipation. Typically the amplitude of oscillation of cavity/bubble radius and the lifetime of the bubble are the two important parameters deciding the cavitational intensity and the active cavitational volume, which in turn will control the net effects per unit power dissipation—generally described as the cavitational yield.

Moholkar *et al.*[39] compared the effects of operating parameters on the bubble dynamics in both ultrasonic and hydrodynamic cavitation reactors and reported that the operating parameters in both these types of reactors showed similar effects on the cavitational intensity. It was established that the time required for the pressure recovery in hydrodynamic cavitation and frequency of irradiation in the case of acoustic cavitation had similar effects on the lifetime of the cavity (and hence the cavitationally active volume). Similarly, the amplitude of cavity oscillations (and hence the collapse pressure) was strongly dependent on the intensity of ultrasonic irradiation and the magnitude of pressure in hydrodynamic cavitation (both depicting the energy dissipation into the reactors). The study was one of the earliest studies to establish that hydrodynamic cavitation can also be used for the physicochemical transformations being intensified by the use of ultrasonic reactors.

In the case of hydrodynamic cavitation reactors, the degree of cavitation can be suitably controlled by operating parameters such as inlet pressure and geometric parameters such as the design of the cavitation chamber (type of constriction, shape and number of holes). Similarly for acoustic cavitation, the controlling parameters are frequency and intensity of irradiation as the operating parameters, and number of transducers, mode of irradiation and geometry of the transducer as the geometric parameters. Significantly higher variations are possible in the case of hydrodynamic cavitation reactors to control the cavitational effects thereby prompting an energy-efficient operation. The modifications can be in terms of using orifice, venturi, valve or a rotating valve as the cavitating device; using multiple such devices or deliberately introducing nuclei at the upstream location or at the constriction. Different studies have been reported in the literature confirming the superiority of the hydrodynamic cavitation reactors as compared to the acoustic cavitation-based sonochemical reactors.[40–42] The effects have been mainly quantified in terms of the cavitational yields (described as net chemical or physical effects per unit power dissipation). The lower energy effectiveness of ultrasound-based reactors is attributed mainly to the significantly higher pressure amplitudes (3 to 10 atm) in the case of ultrasound reactors than that required for cavitation inception (typically 1 atm for systems containing nuclei, which most of the time are presented by the dissolved gases or impurities). On the other hand, for the case of hydrodynamic cavitation reactors, such high amplitudes are not used giving higher energy efficiencies. Also due to the recirculating operation of the hydrodynamic cavitation reactors, significantly higher cavitationally active volumes would be obtained, whereas in the case of ultrasonic reactors the active cavitational zone is concentrated very near to the transducer surface. The scale-up of hydrodynamic cavitation reactors has also been considered to be comparatively easier as vast amounts of information about the fluid dynamics downstream of the constriction is readily available.[8] The use of sophisticated mathematical simulation programs is easy for predicting the pressure fields and cavitational intensities as a function of geometry in order to arrive at optimum designs.

5.6 Overview of Intensification of Chemical Synthesis

Sonochemistry or, in general, the use of cavitational reactors is a lucrative option for obtaining greener synthesis routes, mainly on the basis of the following distinct advantages.[2,6]

a. The possibility to change the course of a reaction giving enhanced selectivity, which also means reduction in the waste generation.
b. The improvement in the rates of chemical reactions, giving higher yields coupled with energy savings.
c. The possibility to use greener reagents, even aqueous media, giving reduction in the use of hazardous chemicals.
d. Use of ambient conditions leading to inherently safer operation and energy savings.

The degree of cavitational effects and the beneficial effects for process intensification will be dependent on the type of the reaction, mainly homogeneous or heterogeneous. The mechanisms of intensification in these types of reaction need to be understood first so as to obtain significant benefits by the application of cavitational reactors and result in an energy-efficient operation. In the case of homogeneous reactions, cavitational effects will mainly affect reactions which proceed *via* radical or radical-ion intermediates and this also means that the ionic reactions will not be affected much by the use of cavitational reactors. This is attributed to the fact that the sudden collapse of bubbles in the case of homogeneous systems results in an inrush of liquid to fill the void generated by the collapsing cavity. This inrush is so powerful and produces significant shear forces in the surrounding bulk liquid capable of breaking the chemical bonds leading to radical formation. In the case of heterogeneous reactions, the mechanical effects of cavitation, mainly in terms of the liquid turbulence and acoustic streaming, are more dominating when compared to the chemical effects, such as free radical formation. In the case of heterogeneous liquid–liquid reactions, the enhanced rates of processing can be obtained mainly on the basis of generation of fine emulsions which can provide a large surface area for the reaction. Also, these emulsions are stable and require little or no surfactant to maintain stability. In the case of solid–liquid reactions, the beneficial effects would again be mainly in terms of higher surface areas if the solid is a reactant or in terms of both enhanced surface area and cleaning action on the solid particles if the solid used is a catalyst. The cleaning action would be significantly useful especially when the catalyst is getting deactivated during the reaction as this can enhance the life of catalyst giving higher productivity. It is also important to understand that the use of cavitational reactors is not a substitute for the catalysts, especially in the case of the phase transfer type, but can serve as a useful supplement giving beneficial results in terms of significantly faster processing.

Apart from its use in the actual chemical reactions, ultrasound can play an effective role in obtaining better quality catalysts in terms of the lower size and/or better distribution of active ingredients on the supports. Application of ultrasound during the synthesis provides essential nuclei as well as avoids the formation of agglomerates leading to the formation of catalyst particles with lower mean size and narrow particle size distribution. Ultrasound application in the catalyst synthesis leads to a more active catalyst as compared to the more commonly used synthesis routes such as sol–gel, microemulsion, reverse micelles, wet impregnated and hydrothermal methods *etc.* In addition, increasing the ultrasonic irradiation time during the synthesis (in some cases optimum time would be essential) leads to decrease in the agglomerations of the catalyst. Ultrasound treatment also improves the catalytic activity of the material and hence increases the yield and rate of the specific reaction. Some of the examples of catalyst synthesis[43–45] where ultrasound has been shown to be effective are nanosized metals like gold, silver, platinum, palladium *etc.*, metal carbides, metal oxides, bimetallic catalysts and different types of supported catalysts such as palladium on carbon.

After understanding the different benefits and the possible mechanisms for intensification, we now present a brief overview of earlier studies to get an idea about the quantitative benefits that can be obtained from the use of cavitational reactors.

Waghmare *et al.*[46] investigated the application of ultrasound for the transesterification of glycerol to glycerol carbonate (GlyC) from dimethyl carbonate (DMC) using commercial immobilized lipase (Novozym 435). A detailed understanding into the effect of operating parameters revealed that the optimum ultrasound parameters were 25 kHz frequency, 100 W rated power with 50% duty cycle. Under these conditions, application of ultrasound treatment resulted in significant intensification in the process with reduction in the reaction time by 10 h as compared to the conventional stirring method. Use of the conventional approach required 14 h for a conversion of about 95% whereas ultrasound coupled with stirring resulted in a conversion of 99.75% in only 4 h of reaction. It was also demonstrated that ultrasound alone could not give enough mixing of the reaction mixture and the conversion using only ultrasound was around 64%. Thus a combination of ultrasound and stirring was essential so as to give beneficial results. The other demonstrated advantages of the combined processing were the requirement of lower enzyme loading and the use of milder conditions (atmospheric pressure and 60 °C) throughout the processing.

Mannich reaction is one of the carbon–carbon bond forming reactions of significant value in organic synthesis because it produces synthetically and biologically important β-aminocarbonyl compounds, the intermediates for the construction of various nitrogen-containing natural products and pharmaceuticals. Zeng *et al.*[47] investigated the use of ultrasound for intensifying the synthesis of β-aminocarbonyl under ambient conditions based on the following scheme of reaction:

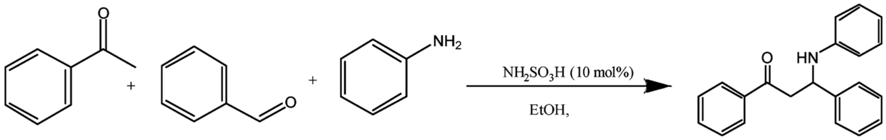

Table 5.1 Important results for the Mannich reaction study[47] (Ultrasound operating frequency of 40 kHz and power of 600 W). Reprinted from Ultrasonics Sonochemistry, 16, H. Zeng *et al.*, One-pot three-component Mannich-type reactions using Sulfamic acid catalyst under ultrasound irradiation, 758–762, Copyright (2009) with permission from Elsevier[47]

Entry	NH_2SO_3H (mole%)	Method	Time (h)	% yield
1	10	High speed stirring	18	88
2	3	Ultrasound	1.5	79
3	5	Ultrasound	1.5	88
4	10	Ultrasound	1.5	95
5	15	Ultrasound	1.5	94

A summary of the important results obtained in the work have been reproduced in Table 5.1 and it can be clearly seen that the use of ultrasound resulted in significant intensification. It was demonstrated that the use of ultrasound reduced the reaction time from 18 h to 1.5 h and also the requirement of reagents (NH_2SO_3H) reduced from 10 mol% to 5 mol% to obtain similar levels of conversion (88%). Use of a loading of 10 mol% in the ultrasound assisted approach could improve the conversion to 95% but any further increase in reagent loading could not intensify the reaction.

Bandyopadhyay *et al.*[48] reported a green synthesis approach in terms of the ultrasound-assisted aza-Michael reaction being performed in water without non-benign solvent as per the following reaction scheme.

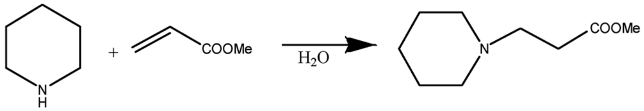

The comparison between conventional stirring and the effect of ultrasonication (US) confirmed significant process intensification benefits. It was reported that the conventional approach resulted in a yield of 92% in 30 min reaction time whereas the ultrasound-assisted approach was six-fold faster than conventional stirring with a 98% yield in only 5 min.

Safari and Javadian[49] investigated the application of ultrasound in a one-pot synthesis of 2-amino-4*H*-chromenes by condensation of aldehydes with malononitrile and resorcinol in water using magnetic Fe_3O_4-chitosan nanoparticles as the catalyst as per the following reaction scheme:

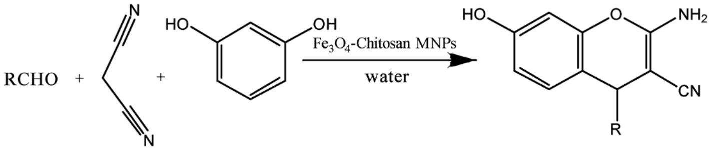

The reported results have been reproduced in Table 5.2 and it can be clearly seen that under optimum conditions the reaction could be intensified though the degree of intensification was limited compared to some

Table 5.2 The effect of ultrasonic power on the synthesis of 2-amino-4*H*-chromene.[49] Reprinted from Ultrasonics Sonochemistry, 22, J. Safari and L. Javadian, Ultrasound-assisted green synthesis of 2-amino-4*H*-chromene derivatives catalyzed by Fe_3O_4-functionalized nanoparticles with chitosan as a novel and reusable magnetic catalyst, 341–348, Copyright (2015) with permission from Elsevier.

Entry	Max. power (%)	Intensity (W)	Time (min)	% yield
1	High speed stirring (w/o US)		31	90
2	20	40	29	72
3	40	80	25	75
4	60	120	22	76
5	80	160	20	99
6	100	200	21	86

of the earlier illustrations. In addition, it was demonstrated that using too much power to generate high cavitational intensity does not give better results and hence it is very important to evaluate the benefits in laboratory-scale operation before actual application at the commercial scale can be decided.

Apart from the illustrative examples of the process intensification benefits that can be achieved using cavitational reactors, a brief summary[50–57] of the ultrasound intensified reactions, highlighting the benefits, has been presented in the Table 5.3. Overall it can be said that the application of cavitational reactors intensifies conventional routes of chemical synthesis leading to greener processing with higher yields, faster processing, and the requirement of ambient conditions as well as use of greener reagents in lower quantum.

5.7 Overview of Applications in the Area of Wastewater Treatment

Cavitation can be used effectively for the destruction of the contaminants in water because of the generation of conditions of local hot spots (significantly higher temperature and pressure) along with the generation of oxidizing species such as hydroxyl radicals and hydrogen peroxide. The efficacy of treatment would strongly depend on the type of the pollutants present in the effluent stream and typically the nature of the compound (hydrophobic or hydrophilic) plays a major role. Hydrophobic compounds usually migrate towards the collapsing cavity and hence the extent of degradation is likely to be higher due to maximum cavitational activity in and around the collapsing cavity. Hydrophilic compounds are likely to accumulate in the liquid bulk and react with radicals that can migrate from the collapsing cavity, but the quantum of these radicals is significantly lower. The degree of intensification can be enhanced by suitable optimization of the operating parameters such as energy density, energy intensity, frequency of irradiation and the nature and properties of the saturating gas or any additives that can intensify the cavitational activity.

Table 5.3 A summary of different reactions intensified using ultrasound.

Sr.	Reaction	Effect of ultrasound	Reference
1	Oxidation of cyclohexanol in presence of PTC	• Reaction time reduced • Reaction yield improved • Milder reaction conditions	Chatel *et al.*[50]
2	Oxidative esterification of 4-nitrobenzaldehyde	• Reaction time reduced • Reaction yield improved • Milder reaction conditions	Mirza-Aghayan *et al.*[51]
3	Synthesis of substituted 2-amino-3-cyano-4*H*-pyran derivatives	• Reaction time drastically reduced • Reaction yield improved • High temperature requirement avoided	Tabassum *et al.*[52]
4	Aldol condensation reaction	• Catalyst use avoided • Water as solvent • Improved yields in less time	Cravotto *et al.*[53]
5	*N*-alkylation of imidazole	• Use of solvent avoided • Improved yields and conversion	López-Pestaña *et al.*[54]
6	Bromination of aromatic compounds	• Mo-catalyzed bromination of various aromatic compounds was accelerated by ultrasound • Reaction did not proceed without catalyst	Lévêque *et al.*[55]
7	Dehydrogenation of 2-oxo-1,2,3,4-tetrahydropyrimidine-5-carboxamides	• Use of ultrasound reduced the reaction time • The required amount of oxidant was also reduced • The nature of 4-substituent greatly influenced the time of oxidation	Memarian and Soleymani[56]
8	Stille coupling reaction	• Improved yields in less time	Domini *et al.*[57]

The variety of contaminants that have been degraded using cavitational reactors, though in different equipment and on different scales of operation are pesticides, such as triazophos, dichlorovos, methyl parathion and alachlor; pharmaceutical compounds such as ibuprofen, ciprofloxacin, oflaxacin *etc.*; dyes such as acid orange, rhodamine B, brilliant green *etc.*; phenolic compounds such as *p*-nitrophenol, 2,4,6-trichlorophenol, 2,4-dinitrophenol *etc.* and halogenated compounds such as trichloroethane, pentachlorophenate, CFC 11 and CFC 113, *o*-dichlorobenzene and dichloromethane as well as inorganic compounds such as potassium iodide, sodium cyanide, carbon tetrachloride among many others. The detailed discussion on the kinetic aspects and mechanisms of degradation can be obtained from some of the excellent reviews available in the literature.[58,59]

Cavitational reactors can also be combined with other advanced oxidation processes resulting in synergistic effects. The similarity between the mechanism of destruction, mainly in terms of generation and subsequent attack of the hydroxyl radical, points towards the possible synergism between these methods and the fact that combination with advanced oxidation processes should give better results compared to individual techniques.[60] The different combinations involving cavitational reactors that have been synergistically used for degradation include cavitation/ozone, cavitation/H_2O_2, sonophotocatalytic oxidation, cavitation/Fenton, cavitation/perfulfate *etc.* Combination approaches work on the principle of enhanced generation of hydroxyl radicals which can eventually result in higher oxidation rates, of course depending on the type of the pollutant. The efficacy of the process and the extent of synergism depend strongly on the reaction rates between the radicals and the pollutants and also on the type of the oxidation approaches used in the combination. The mechanistic details about the combined techniques, its applicability for different wastewater streams and the optimum conditions for obtaining the synergistic effects can be obtained from published literature.[61–66]

Although the use of cavitational reactors has been very successful in laboratory-scale applications, the treatment costs associated with the cavitational reactors (especially the ultrasound-based reactors) have been reported to be higher[64] compared to some of the conventional approaches such as chemical or biological oxidation. Cavitational reactors can be effectively harnessed as a pre-treatment to increase the biodegradability so that conventional biological oxidation occurs at a faster rate and with enhanced effectiveness. The pretreatment would be highly effective for a complex stream where bio-refractory compounds are present in the effluent stream, as these compounds significantly reduce the efficacy of the biological oxidation techniques. Sangave and Pandit[65] investigated the efficacy of ultrasonic irradiation as a pretreatment step for the treatment of one of the most polluting industrial effluents, the distillery spent wash, especially in countries such as India and Brazil having maximum production of sugars. Use of an ultrasonic bath resulted in negligible change in the COD value and hence it was established that the role of ultrasonic irradiation was only to restructure the molecules present in the waste, which can generate more utilizable molecules for subsequent biological oxidation. It was reported that the extent of degradation achieved using the ultrasound pretreated sample was 44%, which was about twice that obtained using the fresh sample (untreated, where the extent of degradation was only 25%) in similar treatment times (72 h).

It is important to note here that there have been some studies related to the use of cavitational reactors for the treatment of real industrial effluents, and even demonstrated on the commercial scale. Some representative case studies have been presented now for a better understanding into the capability of cavitational reactors in water treatment applications.

Hydraulic fracturing is one of the common operations that has been applied to increase the productivity of oil and gas wells. In this process, water is pumped into the well at a high pressure so that it fractures the rock permitting the extraction of the petroleum gas. A significant quantum of water is required in this operation and water recycling is one of the important factors deciding the economic efficiency of the operation as the expected transportation costs are significant due to the remote locations of the oil wells.

About 10–30% of the water sent into the wells is expected to come back to the surface (described as the flowback water or frac water). It is imperative that this water must be treated so as to avoid the problems associated with contaminants such as microorganisms and recycled to avoid the need to make up fresh water that would enhance the treatment costs. Gogate *et al.*[28] described a hybrid oxidation reactor that has been applied successfully over 1200 installations in the USA. The Ozonix® reactor is based on the combination of hydrodynamic cavitation, acoustic cavitation, electrochemical oxidation/precipitation and ozone. The reactor is scalable, modular and can be fitted on a trailer which makes it an efficient onsite treatment solution. The optimized combination of the oxidation processes significantly enhance the treatment rates attributed to the enhanced utilization of ozone, generation of additional oxidants including hydroxyl radicals and chlorine-based species and the elimination of mass transfer resistances. It has been reported that the mobile reactor was deployed and commercialized at different shale plays in the USA *viz.* Woodford, Fayetteville, Marcellus, Haynesville, Permian Basin and Eagle Ford. Apart from treating the water for microorganisms and other organic contaminants, treatment also provides advantages in terms of zero scale deposition and increased flowability confirmed by the dynamic tube blocking test method.

Rasheed *et al.*[67] investigated the treatment of wastewater from petroleum refining using a combination of ultrasound and dispersed zero-valent iron particles. The wastewater obtained from a local petrochemical complex had a COD of 40 000 mg L^{-1} and a pH of 5.4. It was reported that the degradation of organic pollutants using the combination approach followed first-order reaction kinetics. Detailed investigation into the effect of operating parameters revealed that optimum treatment conditions as: initial pH of 5 and loading of the iron nanoparticles as 0.15 g L^{-1} where more than 90% reduction in the COD was obtained. It has been also reported that the combination of iron with sonication gave better results compared to sonication alone. The better efficacy for the combined approach has been attributed to enhanced cavitational activity due to the presence of solid particles (nucleation due to the deformities giving an enhanced number of cavitation events) as well as generation of enhanced oxidants in the system. It is important to note that loading of the solid particles plays an important role as having too many particles in the system reduces the energy transfer giving lower cavitational effects.

Phenolic derivates are another class of organic compounds most commonly found in the effluents of many types of industry and give high levels of toxicity and also foul odor even at small levels. It becomes imperative to develop efficient treatment strategies and hydrodynamic cavitation has been reported to be effective for the treatment of real industrial effluent containing phenolic derivatives as the major constituent. Chakinala *et al.*[68] investigated the combination of hydrodynamic cavitation and an advanced Fenton process (iron metal particles with hydrogen peroxide). The effect of important operating parameters, such as operating pressure and oxidant loading as well as the extent of dilution on the extent of degradation has been elucidated. A dilution ratio of 50, operating pressure of 1500 psi and stage-wise addition of hydrogen peroxide (in each stage loading is kept constant at 1900 ppm) have been reported to give a maximum extent of removal of the TOC as 60% within a treatment time of 150 min. It is important to note here that proper optimization of geometry and the flow conditions can allow use of much lower operating pressures giving an energy-efficient operation. Another approach for giving an economic treatment is based on the concept of latent remediation where the use of cavitation treatment in combination with oxidants is restricted for an optimized duration beyond which the residual oxidants bring about the desired reduction. The combined treatment offers flexibility in terms of the operation by way of selection of multiple orifice plates, oxidant loading (ratio of iron particles and hydrogen peroxide), stagewise addition of oxidant, *etc.*, and hence can be optimized to give an energy-efficient operation especially at lower dilution ratios which should make this process industrially feasible.

This overview of studies related to water and wastewater treatment has established considerable promise for cavitational reactors for treating a variety of contaminants, also studies have demonstrated actual commercial level applications or using real industrial effluents. Combined treatment strategies based on the optimized conditions can give synergistic results as compared to the individual operations and in an energy-efficient manner.

5.8 Overview of Cavitational Reactors for Intensified Separations

Cavitational reactors can be effectively applied for intensifying separations mostly on the basis of physical effects such as turbulence and liquid circulation which help in eliminating the mass transfer resistances and also sometimes in altering the thermodynamics of the process. Application of cavitational reactors can also give better productivity especially in terms of the desired characteristics. The important separation processes discussed in the present work include crystallization, extraction, adsorption and distillation.

5.8.1 Crystallization

Separation and purification of a desired component from a solution is achieved by the process of crystallization. The important characteristics deciding the efficacy of the process are polymorphism, morphology of the crystals, size of the crystals and particle size distribution. All these characteristics must be maintained within standard limits especially in the case of pharmaceutical applications, as the important properties of the drugs or the active ingredients are strongly dependent on these characteristics. The different approaches used to crystallize the component are cooling crystallization, evaporative crystallization, reactive crystallization and antisolvent crystallization. The application of ultrasound in these crystallization processes (mostly described as sonocrystallization) can have positive effects on the nucleation stage as well as in controlling the particle size distribution with reduced mean size due to avoidance of particle agglomeration. Sonocrystallization induces rapid nucleation that generally yields smaller crystals with a more narrow size distribution compared to conventional crystallization processes.

The application of ultrasound to improve crystallization has been reported over decades now though the use of hydrodynamic cavitation has not been much reported perhaps due to lack of indirect operation and the problems of particle settling on the walls of the reactor in possible direct contact type operation. Some of the representative literature dealing with sonocrystallization will be presented now to understand the important concepts and guidelines for the operating parameters.

Miyasaka *et al.*[69] investigated the ability of ultrasound to induce primary nucleation, and the possibility of the existence of a threshold energy input for the crystallization of acetylsalicylic acid. Ultrasonic irradiation was applied using a titanium probe operating at 20 kHz and the effect of time and power dissipation was investigated. Optical microscopy was used to determine the number of crystals formed after primary nucleation and the total number of crystals after 72 h. The obtained results confirmed that a low amount of ultrasonic energy (<100 J) was found to inhibit crystal nucleation as compared to the crystallization performed in the absence of ultrasound. Beyond the threshold ultrasonic energy, ultrasound was able to eliminate the induction period completely, confirming that nucleation was dominant in the presence of ultrasound. The duration of ultrasound also showed similar effects and a narrow band for the treatment time was observed to give beneficial results based on the power input.

Dalvi and Yadav[70] investigated the dependency of the induction time, metastable zone width, nucleation rates and solid–liquid interfacial energies for antisolvent crystallization of curcumin solution in ethanol on the application of ultrasound and stabilizers. Ultrasound-assisted crystallization (with or without stabilizer) was reported to decrease the metastable zone width (MSZW) significantly as compared to the conventional mode, which can be attributed to an enhanced frequency of inter-particle collisions in the presence of ultrasound. The presence of stabilizers increased the MSZW in the absence of ultrasound due to the interaction of stabilizer with curcumin. The nucleation rates of curcumin were reported to be enhanced by two orders of magnitude in the presence of ultrasound. The application of ultrasound was also reported to decrease the induction time and the effect was significant only at lower antisolvent mole fractions.

Devi *et al.*[71] investigated the crystallization of glycine in the presence of ultrasound (high frequency over the range of 1–10 MHz) and compared the effect with the conventional approach. It has been reported that high frequency ultrasound creates a feasible environment for crystallization with formation of smaller and larger numbers of bubbles significantly promoting the nucleation and formation of crystals. Application of ultrasound was reported to give reduction in the induction time and also the metastable zone width changed favorably. It was also established that the α form of glycine is formed dominantly under the influence of high frequencies.

Jordens *et al.*[72] investigated the effect of application of ultrasound on the crystallization of paracetamol over a wider range of operating frequencies. Whereas on one hand, where ultrasound has favorable effect on the crystallization, it also has a detrimental effect on the compound as the production of free radicals can induce degradation. The effect of frequency was investigated using a single reactor setup, with exchangeable ultrasound transducers, and the power dissipation was kept constant at 8 W as established using the calorimetric measurements. It was reported that all frequencies gave a reduction in the MSZW as compared to the conventional approach. Interestingly, all the frequencies also gave degradation of paracetamol *via* the radical mechanism confirmed using addition of the radical scavenger 1-butanol. A detailed study revealed that lower frequency (typically 20 or 41 kHz) gave the most favorable results with improved crystallization. The low frequency application allowed faster nucleation with lower sonochemically induced degradation of the products as compared to the higher frequencies.

An overview of the literature on the sonocrystallization confirms that the positive influence of ultrasound (US) on crystallization is in terms of reduction in the induction period as well as favorable changes in the supersaturation conditions and metastable zone width. Application of ultrasound during the growth phase also enhances the mass transfer rates and promotes the crystal formation making the crystallization process faster. Also the energy dissipation at the microscale avoids agglomeration of the crystals maintaining the desired crystal size distribution. The important variables that play a major role in deciding the degree of intensification include the ultrasound variables such as frequency, intensity, ultrasound time and power as well as the geometrical characteristics such as reactor type, size and the transducer arrangement. In summary, some of the important guidelines for effective utilization of the ultrasound in the crystallization operation are as follows:

1. Application of ultrasound helps in reducing the induction time for the onset of crystallization and the observed effect is predominant at lower supersaturation levels.
2. Ultrasound can induce spontaneous nucleation and hence can avoid the requirement to introduce seeds into the solution. However, some seeding may be required especially in the case of racemic mixtures as the final dominant form of crystals obtained is dependent on the introduced seeds.
3. Ultrasound application at low power dissipation levels is sufficient for reducing the metastable zone width and, in these cases, it is not recommended to introduce higher power as this can lead to detrimental effects in terms of degradation of the compounds.
4. The solvent properties such as vapor pressure and surface tension usually do not significantly affect the nucleation process (including the MSZW) though some effect may be observed on the cavitational intensity and hence the expected process intensification benefits.

5. The typically recommended frequency range of ultrasound is the low-frequency range. Higher operating frequencies (>100 kHz) are not recommended due to the possibility of radical-induced degradations.
6. The crystal size distribution is affected by the ultrasonic power dissipation, time of application of ultrasound as well as the total duration and the geometry of the ultrasonic transducers. A proper optimization of these parameters (especially the time and duration of ultrasound pulse) can allow tailoring a specific crystal size distribution.
7. Application of ultrasound to a polymorphic system at the right level of supersaturation can help in obtaining the ground-state polymorph (the most thermodynamically favored and less soluble), which is of significant importance particularly in the pharmaceutical industry.
8. In crystallization processes where supersaturation is induced by the addition of an antisolvent or in the case of reactive crystallization, there is a chance that high supersaturation levels are produced locally and very rapidly. In such cases, application of ultrasound ensures uniform mixing of the added antisolvent or the reactants, and helps in achieving the desired crystal size distribution as well as intensifying the crystal formation process.

It is important to note here that commercial-scale technologies are available for sonocrystallization. Ruecroft *et al.*[12] have presented a detailed overview of the different options that can be applied at varying capacities of operation. The scaling-up is mainly based on the use of multiple transducers and using a flow cell type configuration. The possibility of direct bonding of the transducers to the walls of the reactor has allowed development of these configurations and the designs can give a uniform acoustic pattern above the cavitational threshold and, more importantly, throughout the entire working volume. The use of low power output transducers also avoids the problems related to the acoustic decoupling as the power density close to the tip of transducer is not significantly higher. The multiple transducer units can be tailored using suitable geometry to concentrate the ultrasonic intensity towards the central axis and definitely away from the vessel walls, which reduces the problems of material erosion. It has been reported that these ultrasonic vessels can be operated in batch mode or, for larger scale operation, in continuous mode with units being combined in a modular fashion, which also gives increased residence time.

5.8.2 Extraction

Solid–liquid extraction using a specific solvent is an important operation in many biotechnological, food and pharmaceutical sectors and the main objective is the recovery of valuable ingredients. The operation can also be of vital importance even in the wastewater treatment applications so as to separate the toxic contaminants present in the effluent stream, though this area is still an often neglected one. The increasing demand towards the use of natural products especially in the pharmaceutical, perfume manufacturing and dyes sectors has given significant importance to research into developing intensifying approaches for solid–liquid extraction. Vegetable sources usually contain only a small fraction of the active solute on a weight basis but the high value associated with these active compounds justifies the need for developing high-performance separations. An important need of these processes is also to maintain the activity of the ingredients, though this can induce some restrictions on the operating conditions. The conventional extraction techniques are often limited by the mass transfer resistances due to the multi-phase nature of the process and hence these methods can require significantly longer time and also complete recovery may not be possible, sometimes making the overall process economically unfeasible.

Solvent extraction of organic compounds contained within the bodies of plants and seeds can be significantly improved by the use of power ultrasound. The observed intensification will be dominantly affected by the mechanical effects of ultrasound which provide a greater solvent penetration into the cellular materials coupled with the enhanced mass transfer. The collapse of cavities near the surface results in significant shear forces and the impingement by micro-jets which results in surface peeling, erosion and particle breakage. All these effects create additional surface area which is very important in deciding the rate of extraction. The dominant effects of ultrasound on the solid materials and creation of additional surfaces has been clearly established on the basis of scanning electron microscopy analysis of the specific samples of soybean flakes[73] and almond powder.[74] Also the application of ultrasound can result in the disruption of biological cell walls which can also facilitate the release of contents. The cavitational effects especially the microscale turbulence induces cracks in the cell wall increasing the overall permeability, which in turn facilitates the entry of the solvent into the inner part of the material as well as washing out of the extracts back to the surface. It is also important to note that the effects will be observed only until a specific energy dissipation limit[75] and this optimum would be dependent on the specific system that can be established using the laboratory scale investigations.

The different classes of products that have been extracted using the intensified approach based on ultrasound include flavonoids, aroma compounds, essential oils, citrus compounds, natural dyes, pigments, medicinal products, *etc.* Some of the specific examples include vanillin from vanilla pods, health-promoting phenolic compounds like ferulic, syringic, *p*-coumaric, *p*-hydroxybenzoic, and vanillic acids from wheat bran, tannins from myrobalan nuts, salvianolic acid B from the roots of *Salvia miltiorrhiza*, anthraquinones from *Morinda citrifolia* (noni), tartaric and malic acids from grapes and grape seeds, *etc.* Vinatoru[76] and Shirsath *et al.*[77] have reported an exhaustive overview of the different products that can be recovered using ultrasonically assisted extraction. Similarly, Vilkhu *et al.*[78] have also discussed the applications of the ultrasound-assisted extraction for the specific food industry sectors.

The optimum selection of the operating parameters is also a must so that the maximum benefits are obtained giving an economically feasible operation. The controlling factors include the reactor configuration, power dissipation, frequency of irradiation, sonication time, temperature and the type of solvent. The selection of the reactor configuration is often dictated by the ease of extraction decided by the location of the product inside the source as well as the stability of the product. Direct immersion reactors such as ultrasonic horn give significantly higher cavitational intensity as compared with the reactors such as ultrasonic bath or the flow cells where an indirect mode of irradiation exists. For the case of thermally unstable compounds, it is important to select the indirect mode of irradiation with the transducers being attached to the walls or the bottom of the reactor. Similar to crystallization, low frequency operation is recommended and most of the literature dealing with extractions reports the use of frequencies over the range of 20–50 kHz. Selection of optimum power dissipation is also essential and the value will depend on the specific application under question as well as the ultrasonic system used for the extraction. Sonication time also plays a major role in deciding the efficacy of operation and the required time depends on the type of material and the distribution of the active ingredient in the cell matrix. Many a times an optimum treatment time would exist beyond which either no intensification could be obtained or even reduced yields can be observed possibly due to the degradation of the product.

A distinct advantage of the ultrasound-assisted extraction is that similar levels of extraction can be obtained using much lower operating temperatures as compared to the conventional approaches. Most investigations have revealed the use of lower temperatures over the range of 30–40 °C in the case of the ultrasound-assisted approach as compared to the reflux conditions being used in the conventional approach. The feasibility of using lower temperatures offers promise for the recovery of the heat-sensitive materials using the ultrasonic extraction.

The selection of the solvent is more controlled by the extraction parameters than the efficacy for the cavitational effects. Solvents such as alcohols, acetone and ether, *etc.* are generally preferred for the extraction of bioactive substances from natural sources. Water is the most preferred solvent to extract polar ingredients such as carbohydrates, glycosides and amino acids. All these solvents offer the desired properties in terms of the surface tension and viscosity providing enough cavitational intensity such that the application of ultrasound can give the suitable levels of intensification.

Ultrasound-assisted extraction can also be coupled with other extraction approaches[79–81] such as enzymatic extraction, microwave-assisted extraction and supercritical fluid extraction. The combined approach can give enhanced effectiveness and possibly synergistic effects for intensification.

Overall, it can said that ultrasound-assisted extraction offers significant advantages when compared to the conventional mode in terms of reduction in the processing time, operation at lower temperature, requirement of lower quantum of solvents and higher recoveries. Use of ultrasound for extraction of high-cost raw materials can be an economical alternative offering excellent prospects for commercial-scale application.

5.8.3 Adsorption

Adsorption is the process by which a solid adsorbent can remove a pollutant from either a liquid or gas stream by forming an attachment based on the formation of a physical or chemical bond. The typical advantages of adsorption process are simplicity in operation, lower treatment costs compared to other separation methods and no sludge formation. Adsorption using activated carbon has become a widely acceptable method especially for the pollutant removal from liquid effluents. It is a simple operation giving high efficiency though the costs of producing good quality activated carbon are significant and the regeneration or disposal of the spent carbon is often problematic. The high cost of adsorption operations on commercial activated carbons has motivated the search for alternative adsorbents, which can be based on cheaper alternatives involving agricultural and other wastes. A number of low cost, biodegradable and effective adsorbents obtainable from natural resources have been developed but the operation is hampered by reduced adsorption capacities and hence higher treatment times as compared to the commercial form of activated carbon. An intensification approach for reducing the treatment times as well as increasing the adsorption capacities can be in terms of application of ultrasound either in the actual adsorption process or in the preparation of efficient adsorbents.

Hamdaoui and Naffrechoux[82] investigated the adsorption of 4-chlorophenol (4-CP) from aqueous solution containing *tert*-butyl alcohol (10% v/v) using granular activated carbon (GAC) in the presence of ultrasound operating at different frequencies (516, 800 and 1660 kHz) and acoustic powers (15.2, 21.5, 31.1 and 38.3 W). The obtained results showed that both the adsorption rate and adsorbed amount were significantly enhanced in the presence of ultrasound for all the studied frequencies and powers with enhanced effects being obtained at higher power dissipation levels. The reported values of the intra-particle diffusion coefficient in the presence of ultrasound confirmed that the transfer rates were increased due to the physical effects of ultrasound. The diffusion coefficient was also reported to increase with an increase in the power dissipation for all frequencies. The initial adsorption rate as well as the intra-particle diffusion coefficient were higher at lower frequencies with the order of 516 kHz > 800 kHz > 1660 kHz.

Hamdaoui *et al.*[83] investigated the use of dead needles of Aleppo pine (*Pinus halepensis*) as a possible adsorbent for the removal of malachite green from aqueous solutions in the absence and presence of ultrasound. It was reported that both the rate and the quantum of malachite green adsorbed markedly increased in the presence of the ultrasonic field. The combination of stirring and ultrasound led to a significant improvement in the removal of dye, confirming that the bulk liquid circulation induced using the ultrasonic irradiations is not sufficient to ensure complete dispersion of adsorbent particles. Estimations of the intra-particle diffusion coefficient revealed that combined operation gave 3.6 times higher value as compared to the conventional approach. The effect of ultrasound on the improvement of dye adsorption was attributed to a variety of mechanical effects of cavitation phenomena.

Roosta *et al.*[84] investigated the optimization of ultrasonic assisted adsorption of safranin O using tin sulphide nanoparticles loaded on activated carbon and it was reported that the adsorption rate of safranin O (SO) on the tin sulfide nanoparticles loaded on activated carbon (SnS-NPAC) was accelerated by ultrasound. It was demonstrated that optimized conditions of 4 min of sonication time, 0.024 g of adsorbent loading, pH of 7 and 18 mg L^{-1} SO initial concentration resulted in near complete removal of the dye (98%) and the adsorption capacity was 50.25 mg g^{-1}. It was clearly established that equilibrium was reached much faster in the presence of ultrasound, attributed to the enhanced rates of transfer processes.

Sayan and Esra Edecan[85] investigated the decolorization of reactive blue 19 using different approaches based on ultrasound and activated carbon prepared from sustainable resources. Under the optimum conditions, the use of only ultrasound, only activated carbon and combined ultrasound/activated carbon resulted in the extent of decolorization as 36%, 91% and 99.9%, respectively. The results established the beneficial effect of ultrasound power on the decolorization using the combined ultrasound activated carbon approach. It was also established that the dye concentration, time of treatment and activated carbon loading are important process parameters affecting the decolorization. It was reported that the physical effects of sonication enhanced the decolorization from aqueous solutions by adsorption.

It is also important to understand that even though ultrasound enhances the rate of adsorption significantly, it can also have an effect on the rate of desorption from the adsorbent especially if weak interactions are present between the adsorbate and the adsorbent molecules. Hamdaoui *et al.*[86] investigated the effect of ultrasound (frequency of 21 kHz) on the adsorption–desorption characteristics of *p*-chlorophenol on granular activated carbon (GAC). It was reported that the extent of desorption of *p*-chlorophenol on GAC was more dominantly affected by the cavitational effects generated by the ultrasound. It was also established that the stronger the power intensity of the ultrasonic field, the smaller was the adsorption capacity of *p*-chlorophenol on the activated carbon, which was attributed to the stronger effect on the desorption. Thus, depending on the system, proper adjustments need to be made (such as selection of pH or the operating temperature or the ultrasonic power dissipation and time of treatment) so as to inhibit the desorption process and yield higher extents of adsorptive removals from the process.

In addition to the use of ultrasound in enhancing the actual adsorptive separations, ultrasound can also be used to synthesize an effective adsorbent, especially in the polymer composites. Shirsath *et al.*[87] investigated the use of ultrasound for synthesis of poly(acrylic acid) hydrogel composite with kaolin clay (PAA-K hydrogel) and subsequent application for the removal of brilliant green dye. Transmission electron microscopic (TEM) images of the dried PAA-K hydrogel revealed that the particle size of the kaolin clay was found to be in the range of 20–50 nm and fine and homogeneous clay dispersion was achieved in the hydrogel matrix due to the ultrasound effects during the synthesis.

In summary, it can be said that use of ultrasound can give improved adsorbents with higher activity and also the rate of adsorptive removals can be intensified using ultrasonic irradiations. The ultrasound operating parameters need to be optimized with the important objective of reducing the rate of desorption of the compound from the adsorbent, but this would be more specifically dependent on the type of system.

5.8.4 Distillation

Distillation is one of the preferred separation processes though it is also one of the most energy intensive operations and also offers significant difficulties in separating mixtures with very close boiling points and mixtures where there is a possibility of formation of an azeotrope. Continuous improvements have been targeted to either add-on facilities or use alternative technologies. Use of ultrasonic equipment in assistance to the distillation system can result in higher separation efficiencies and the cavitational energy in this case is useful in altering the physical properties of the mixtures and enhancing the mass and heat transfer processes giving an intensified vapor–liquid separation. Though, there have not been many investigations in the area of ultrasound assisted distillation operations, recent works from some groups have highlighted the benefits that can be obtained using the application of ultrasound.[88–92] Ultrasound application has been reported to give enhanced relative volatility of the mixtures as well as enhanced separation efficiency in the actual vapor liquid separations.

Mudalip *et al.*[88] investigated the application of ultrasound for the separation of a mixture of cyclohexane (Chx) and benzene (Bz), which is one of the most complicated separation processes in the petrochemical industry due to the very small differences in the boiling points (about 0.6 °C). The study reported a detailed investigation into the effect of different frequencies and intensity of irradiation on the relative volatility. It was demonstrated that the ultrasonic waves at different intensity and frequency had the potential to change the relative volatility of Chx/Bz mixtures and the optimum conditions for the maximum benefits were established as an intensity of $100\ \mathrm{W\ cm^{-2}}$ and frequency of irradiation of 40 kHz. Any increase in the intensity as well as frequency beyond this optimum resulted in a decrease in the relative volatility and also altered the azeotropic point of Chx/Bz unfavourably. An increase in the frequency beyond the optimum results in lower duration of the rarefaction cycle, which also means that there is formation of smaller cavitation bubbles and smaller vacuum effects within the liquid medium, which reduces the degree of vaporization of the more volatile component. Similarly, higher acoustic intensities beyond the optimum result in formation of too many cavitation bubbles giving a cushioning effect and hence lower degree of separation. Under the optimum conditions, it was reported that maximum relative volatility of 2.505 was obtained and the azeotropic point was totally eliminated. Ripin *et al.*[89,90] have also reported similar results for the enhancement in the relative volatility of methanol–water and methyl *tert*-butyl ether–methanol mixtures. It is important to understand that the degree of intensification would indeed be dependent on the type of mixtures. Also the optimum conditions of frequency and intensity of irradiation for maximum benefits are dependent on the type of mixture. Ripin *et al.*[89] reported that the maximum average relative volatility for the methanol–water mixture was obtained as 29.413 under the optimum conditions of intensity (200 W cm^{-2}) and frequency (25 kHz).

In continuation of the work on identifying the effect of ultrasound on the relative volatility, Mahdi *et al.*[91] developed a mathematical model for the single stage distillation system based on conservation principles, vapor–liquid equilibrium and sonochemistry. The model results were validated using the ethanol–ethyl acetate mixture data and the model was demonstrated to explain the effects of the intensity of irradiation and operating frequency. It was demonstrated that the model is only able to explain the intensification at lower intensities of irradiation as it could not consider the effects of cushioned collapse of the cavitation bubbles at very high intensities of irradiation. The presented results confirmed that the azeotropic point of the ethanol–ethyl acetate mixture can be totally eliminated using optimized sonication parameters, and the maximum relative volatility of 3.1 was obtained under the optimum conditions of intensity of irradiation (485 W cm^{-2}) and frequency (26.3 kHz).

It is also important to understand that the exact mechanism of intensified separation due to the use of ultrasound has not been conclusively established. Spotar *et al.*[92] investigated the application of ultrasound for separation of ethanol from the binary mixture of ethanol and water and demonstrated that the enhanced separation is purely due to the intensified heat effects. It was established that there is an enhancement in the total vapor–liquid interfacial area due to the generation of atomized mist droplets but this is with the same composition as the bulk liquid under similar conditions of temperature and pressure.

Overall, it can be said that the application of ultrasound for intensified distillation is an upcoming area and detailed investigations are required to elucidate the controlling mechanisms and demonstrate the working prototypes before commercial-scale applications can be thought of. Some of the presented studies do confirm the significant benefits that can be obtained using ultrasound in terms of easier separation and possible conversion of the azeotropic distillation into a simple one-stage process due to the elimination of the azeotropic points.

5.9 Summary

Cavitational reactors show considerable promise for intensification of different chemical processing applications, such as synthesis using greener routes and wastewater treatment, that can lead to a greener environment. Also, cavitational reactors (especially based on the use of ultrasound) offer a lucrative option for intensified separations including crystallization, extraction, adsorption and distillation. The current chapter has given a detailed understanding into the mechanistic details, the types of reactor configurations and guidelines for optimum selection of geometric and operating parameters so as to achieve maximum benefits. The different experimental illustrations depicted in the work have clearly established the benefits that can be obtained using the application in a quantitative manner. Overall, cavitation is a well-established technology for greener processing at laboratory-/pilot- scale and some applications in recent years have also been harnessed at an industrial scale of operation, especially for the water treatment and crystallization applications.

References

1. T. J. Mason, *Practical Sonochemistry: Users Guide in Chemistry and Chemical Engineering*, Chichester, UK, 1992, Ellis Horwood series in Organic chemistry.
2. P. R. Gogate, *Chem. Eng. Process.*, 2008, **47**, 515.
3. J. L. Luche, *Synthetic Organic Chemistry*, Plenum Press, New York, USA, 1999.
4. F. R. Young, *Cavitation*, McGraw Hill, London, UK, 1989.
5. J. Lindley and T. J. Mason, *Chem. Soc. Rev.*, 1987, **16**, 275.
6. L. H. Thompson and L. K. Doraiswamy, *Ind. Eng. Chem. Res.*, 1999, **38**, 1215.
7. G. Cravotto and P. Cintas, *Chem. Soc. Rev.*, 2006, **35**, 180.
8. P. R. Gogate and A. B. Pandit, *Rev. Chem. Eng.*, 2001, **17**, 1.
9. P. R. Gogate and A. B. Pandit, *Ultrason. Sonochem.*, 2004, **11**, 105.
10. Y. G. Adewuyi, *Ind. Eng. Chem. Res.*, 2001, **40**, 4681.
11. V. S. Sutkar and P. R. Gogate, *Chem. Eng. J.*, 2009, **155**, 26.
12. G. Ruecroft, D. Hipkiss, T. Ly, N. Maxted and P. W. Cains, *Org. Process Res. Dev.*, 2005, **9**, 923.
13. K. Nickel and U. Neis, *Ultrason. Sonochem.*, 2007, **14**, 450.
14. O. Dahlem, J. Reisse and V. Halloin, *Chem. Eng. Sci.*, 1999, **54**, 2829.
15. U. S. Bhirud, P. R. Gogate, A. M. Wilhelm and A. B. Pandit, *Ultrason. Sonochem.*, 2004, **11**, 143.
16. J. L. Dion, *Ultrason. Sonochem.*, 2009, **16**, 212.
17. P. R. Gogate, P. A. Tatake, P. M. Kanthale and A. B. Pandit, *AIChE J.*, 2002, **48**, 1542.
18. P. R. Gogate, I. Z. Shirgaonkar, M. Sivakumar, P. Senthilkumar, N. P. Vichare and A. B. Pandit, *AIChE J.*, 2001, **47**, 2526.
19. P. R. Gogate, S. Mujumdar and A. B. Pandit, *J. Chem. Technol. Biotechnol.*, 2003, **78**, 685.
20. A. V. Prabhu, P. R. Gogate and A. B. Pandit, *Chem. Eng. Sci.*, 2004, **59**, 4991–4998.
21. Y. Son, M. Lim and J. Khim, Investigation of acoustic cavitation energy in a large-scale sonoreactor, *Ultrason. Sonochem.*, 2009, **16**, 552.

22. Y. Asakura, K. Yasuda, D. Kato, Y. Kojima and S. Koda, *Chem. Eng. J.*, 2008, **139**, 339.
23. M. Vinatoru, *Ultrason. Sonochem.*, 2001, **8**, 303.
24. P. R. Gogate and A. B. Pandit, *Ultrason. Sonochem.*, 2005, **12**, 21.
25. P. S. Kumar and A. B. Pandit, *Chem. Eng. Technol.*, 1999, **22**, 1017.
26. I. Z. Shirgaonkar, R. R. Lothe and A. B. Pandit, *Biotechnol. Prog.*, 1998, **14**, 657.
27. K. Sampathkumar and V. S. Moholkar, *Chem. Eng. Sci.*, 2007, **62**, 2698.
28. P. R. Gogate, D. McGuire, S. Mededovic Thagard, R. Cathey, J. Blackmon and G. Chapas, *Ultrason. Sonochem.*, 2014, **21**, 590.
29. P. R. Gogate, A. M. Wilhelm and A. B. Pandit, *Ultrason. Sonochem.*, 2003, **10**, 325.
30. V. S. Sutkar and P. R. Gogate, *Chem. Eng. J.*, 2009, **155**, 26.
31. J. Klima, A. Frias-Ferrer, J. Gonzalez-Garcý, J. Ludvyk, V. Saez and J. Iniesta, *Ultrason. Sonochem.*, 2007, **14**, 19.
32. P. A. Tatake and A. B. Pandit, *Chem. Eng. Sci.*, 2002, **57**, 4987.
33. V. S. Moholkar and A. B. Pandit, *Chem. Eng. Sci.*, 2001, **56**, 6295.
34. P. R. Gogate and A. B. Pandit, *AIChE J.*, 2000, **46**, 1641.
35. M. Sivakumar and A. B. Pandit, *Ultrason. Sonochem.*, 2001, **8**, 233.
36. N. P. Vichare, P. Senthilkumar, V. S. Moholkar, P. R. Gogate and A. B. Pandit, *Ind. Eng. Chem. Res.*, 2000, **39**, 1480.
37. A. G. Chakinala, P. R. Gogate, A. E. Burgess and D. H. Bremner, *Ultrason. Sonochem.*, 2007, **14**, 509.
38. S. N. Katekhaye and P. R. Gogate, *Chem. Eng. Process.*, 2011, **50**, 95.
39. V. S. Moholkar, P. Senthilkumar and A. B. Pandit, *Ultrason. Sonochem.*, 1999, **6**, 53.
40. K. K. Jyoti and A. B. Pandit, *Biochem. Eng. J.*, 2001, **7**, 201.
41. M. Sivakumar and A. B. Pandit, *Ultrason. Sonochem.*, 2002, **9**, 123.
42. M. A. Kelkar, P. R. Gogate and A. B. Pandit, *Ultrason. Sonochem.*, 2008, **15**, 188.
43. L. M. Cubillan-Aguilera, M. Franco-Romano, M. L. A. Gil, I. Naranjo-Rodríguez, J. L. Hidalgo-Hidalgo de Cisneros and J. M. Palacios-Santander, *Ultrason. Sonochem.*, 2011, **18**, 789.
44. P. Estifaee, M. Haghighi, N. Mohammadi and F. Rahmani, *Ultrason. Sonochem.*, 2014, **21**, 1155.
45. M. Abdollahifar, M. Haghighi and A. A. Babaluo, *J. Ind. Eng. Chem.*, 2014, **20**, 1845.
46. G. V. Waghmare, M. D. Vetal and V. K. Rathod, *Ultrason. Sonochem.*, 2015, **22**, 311.
47. H. Zeng, H. Li and H. Shao, *Ultrason. Sonochem.*, 2009, **16**, 758.
48. D. Bandyopadhyay, S. Mukherjee, L. C. Turrubiartes and B. K. Banik, *Ultrason. Sonochem.*, 2012, **19**, 969.
49. J. Safari and L. Javadian, *Ultrason. Sonochem.*, 2015, **22**, 341.
50. G. Chatel, C. Monniera, N. Kardosa, C. Voironc, B. Andriolettib and M. Drayea, *Appl. Catal., A*, 2014, **478**, 157.

51. M. Mirza-Aghayan, S. Zonoubi, M. M. Tavana and R. Boukherroub, *Ultrason. Sonochem.*, 2015, **22**, 359.
52. S. Tabassum, S. Govindaraju, R. R. Khan and M. A. Pasha, *Ultrason. Sonochem.*, 2015, **24**, 1.
53. G. Cravotto, A. Demetri, G. M. Nano, G. Palmisano, A. Penoni and S. Tagliapietra, *Eur. J. Org. Chem.*, 2003, 4438.
54. J. M. López-Pestaña, M. J. Avila-Rey and R. M. Martín-Aranda, *Green Chem.*, 2002, **4**, 628.
55. J. M. Lévêque, M. Fujita, A. Bosson, H. Sohmiya, C. Petrier, N. Komatsu and T. Kimura, *Ultrason. Sonochem.*, 2011, **18**, 753.
56. H. R. Memarian and M. Soleymani, *Ultrason. Sonochem.*, 2011, **18**, 745.
57. C. E. Domini, G. F. Silbestri, B. B. Fernández and A. B. Chopa, *Ultrason. Sonochem.*, 2012, **19**, 410.
58. P. R. Gogate, *Adv. Environ. Res.*, 2002, **6**(**3**), 335.
59. Y. G. Adewuyi, *Ind. Eng. Chem. Res.*, 2001, **40**, 4681.
60. P. R. Gogate and A. B. Pandit, *Adv. Environ. Res.*, 2004, **8**, 553.
61. P. R. Gogate, *Ultrason. Sonochem.*, 2008, **15**, 1.
62. M. V. Bagal and P. R. Gogate, *Ultrason. Sonochem.*, 2014, **21**, 1.
63. C. G. Joseph, G. Li Puma, A. Bono and D. Krishnaiah, *Ultrason. Sonochem.*, 2009, **16**, 583.
64. N. N. Mahamuni and Y. G. Adewuyi, *Ultrason. Sonochem.*, 2010, **17**, 990.
65. P. C. Sangave and A. B. Pandit, *Ultrason. Sonochem.*, 2004, **11**, 197.
66. P. R. Gogate and P. N. Patil, *Ultrason. Sonochem.*, 2015, **25**, 60–69.
67. Q. J. Rasheed, K. Pandian and K. Muthukumar, *Ultrason. Sonochem.*, 2011, **18**, 1138.
68. A. G. Chakinala, P. R. Gogate, A. E. Burgess and D. H. Bremner, *Ultrason. Sonochem.*, 2008, **15**, 49.
69. E. Miyasaka, S. Ebihara and I. Hirasawa, *J. Cryst. Growth*, 2006, **295**, 97.
70. S. V. Dalvi and M. D. Yadav, *Ultrason. Sonochem.*, 2015, **24**, 114.
71. K. R. Devi, A. Raja and K. Srinivasan, *Ultrason. Sonochem.*, 2015, **24**, 107.
72. J. Jordens, B. Gielen, L. Braeken and T. Van Gerven, *Chem. Eng. Process.*, 2014, **84**, 38.
73. H. Li, L. Pordesimo and J. Weiss, *Food Res. Int.*, 2004, **37**, 731.
74. Q. A. Zhang, Z. Q. Zhang, X. F. Yue, X. H. Fan, T. Li and S. F. Chen, *Food Chem.*, 2009, **116**, 513.
75. M. Romdhane and C. Gourdon, *Chem. Eng. J.*, 2002, **87**, 11.
76. M. Vinatoru, *Ultrason. Sonochem.*, 2001, **8**, 303.
77. S. R. Shirsath, S. H. Sonawane and P. R. Gogate, *Chem. Eng. Process.*, 2012, **53**, 10.
78. K. Vilkhu, R. Mawson, L. Simons and D. Bates, *Innovative Food Sci. Emerging Technol.*, 2008, **9**, 161.
79. Z. Lianfu and L. Zelong, *Ultrason. Sonochem.*, 2008, **15**, 731.
80. A. Hu, S. Zhao, H. Liang, T. Qiu and G. Chen, *Ultrason. Sonochem.*, 2007, **14**, 219.
81. Z. Lou, H. Wang, M. Zhang and Z. Wang, *J. Food Eng.*, 2010, **98**, 13.

82. O. Hamdaoui and E. Naffrechoux, *Ultrason. Sonochem.*, 2009, **16**, 15.
83. O. Hamdaoui, M. Chiha and E. Naffrechoux, *Ultrason. Sonochem.*, 2008, **15**, 799.
84. M. Roosta, M. Ghaedi, A. Daneshfar and R. Sahraei, *Spectrochim. Acta, Part A*, 2014, **122**, 223.
85. E. Sayan and M. Esra Edecan, *Ultrason. Sonochem.*, 2008, **15**, 530.
86. O. Hamdaoui, E. Naffrechoux, L. Tifouti and C. Petrier, *Ultrason. Sonochem.*, 2003, **10**, 109.
87. S. R. Shirsath, A. P. Patil, R. Patil, P. R. Gogate and S. H. Sonawane, *Ultrason. Sonochem.*, 2013, **20**, 914.
88. S. K. A. Mudalip, A. Ripin, R. M. Yunus, S. Z. Sulaiman and R. C. Man, *Proc. Int. Conf. Adv. Sci. Eng. Inf. Tech.*, 2011, 72(ISBN 978-983-42366-4-9).
89. A. Ripin, S. K. A. Mudalip and R. M. Yunus, *J. Teknologi*, 2008, **48**, 61.
90. A. Ripin, S. K. A. Mudalip, Z. Sukaimi, R. M. Yunus and Z. A. Manan, *Sep. Sci. Technol.*, 2009, **44**, 1.
91. T. Mahdi, A. Ahmad, A. Ripin, T. A. T. Abdullah, M. M. Nasef and M. W. Ali, *Ultrason. Sonochem.*, 2015, **24**, 184.
92. S. Spotar, A. Rahman, O. C. Gee, K. K. Jun and S. Manickam, *Chem. Eng. Process.*, 2015, **87**, 45.

CHAPTER 6

Magnetically Assisted Separations in Chemical Industry and Biotechnology: Basic Principles and Applications

JORDAN HRISTOV[a]

[a]Department of Chemical Engineering, University of Chemical Technology and Metallurgy, 8 Kliment Ohridsky, blvd., Sofia 1756, Bulgaria
*E-mail: jordan.hristov@mail.bg
http://hristov.com/jordan

6.1 Introduction

Magnetic separation techniques are widely encountered in practice from the laboratory to industrial plants and are part of everyday practice in science and engineering.[1] Addressing specific applications in chemical engineering and biotechnology, we have to take into account specific issues not well explained in the classical books on magnetic separations.[1,2] The chapter refers to techniques based on magnetic particles with non-functionalized (native) and functionalized (tailored) surfaces as well as mechanical magnetic separations such as aerosol filtration and sedimentation. At the beginning the main issues will be briefly outlined.

RSC Green Chemistry No. 47
Alternative Energy Sources for Green Chemistry
Edited by Georgios Stefanidis and Andrzej Stankiewicz

Published by the Royal Society of Chemistry, www.rsc.org

6.1.1 Magnetic Separations at a Glance

The traditional areas of application of conventional separation techniques are numerous, being applied to problems of chemical engineering, metals industries, food, drink and tobacco manufacturing, minerals processing industries and environmental protection and remediation technologies. Magnetic fields are already commonly applied to achieve the separation or filtration of particles, cells, substances, *etc.* The most significant applications are encountered in the separation and filtration techniques in the minerals processing industries.[1,2] In the last decade the breadth of area where magnetic separation may be successfully applied has potentially (and in some cases, effectively) increased. In this context, chemical engineering and biotechnology are scientific areas which contain broad spectra of problems and relevant separation applications.

There are some typical industries in which magnetic separations are well-established techniques, namely:

1. *Steel industry* – where resultant waste waters contain different pollutants with non-negligible magnetic susceptibility values.[1,2]
2. *Power plants* – with corrosion products within equipment parts such as iron-, cobalt- and nickel-based composites.[1,2] Moreover, coal-based and thermal power plants release huge amounts of fly ash[1] containing pollutants such as aluminium, iron or titanium oxides.
3. *Water treatment* – where contaminant removal by application of magnetic fields is a continuously evolving area based on developments in magnetic tagging and carrier technologies.
4. *Reaction chemistry* – where fluidized catalytic cracking (FCC), common in the petroleum industry, uses catalysts contaminated with nickel, iron and other heavy metals with high magnetic susceptibility values. Some methods based on drum magnetic separators have been developed[3,4] for catalyst recovery.

These are well-known applications, but the present chapter presents another structured presentation of magnetic separations applicable in chemical engineering and biotechnology. The structure of this analysis is based on the type of magnetic particles used and the technologies of their organization in separation devices. Complicated equations are avoided and the emphasis is on the physics of the processes. In this context, the illustrations (the figures) used present the basic ideas and do not copy the original published counterparts.

6.1.2 Topics Analyzed at a Glance

The term "magnetic separation" can, of course, have widely differing meanings for different areas of application[5] and the proper discussion requires a clear presentation of the technical information. The overview will be developed in three principal directions relevant to chemical and biochemical applications of magnetic separation techniques.

6.1.2.1 Mechanical Magnetic Separations

The magnetic particle attraction and separation from flow to surfaces of large magnetic bodies is an old technique involving fixed-bed operations in the so-called magnetic matrix filters.[6] This separation technique has a well-developed theory with good support from experimental data. Aerosol filtration is among the oldest application of magnetically-assisted beds. It is thoroughly analyzed on the basis of published experimental data and the new insights developed through models.[9] Magnetically-assisted gravity sedimentation together with high-gradient magnetic separation is among the oldest technique used in the mining industry for removing fine minerals from liquid–solid suspensions.

6.1.2.2 Separations Involving Non-Tailored Magnetic Solids

The second trend in magnetic separation envisages specific involvement of magnetic solids such magnetite (natural or synthetic) and iron for separation of hazardous species from aqueous solutions including dangerous organic contaminants, heavy metals, *etc.* The principal point here is that the surfaces of the magnetic solids employed are natural, *i.e.* they are not tailored or functionalized. Cementation of metals by iron in magnetically-assisted particle beds is a good example. Here, the magnetic separation itself is the second step in the final stage of the process, where the magnetic solids with deposited species on their surfaces have to be removed and subsequently treated (utilized, deposited or processed).

6.1.2.3 Separations Involving Magnetic Solids with Tailored and Functionalized Surfaces

Separations with tailored solids having magnetic properties form the third major trend in magnetic separations. Here, the mechanical magnetic separation from liquids is a secondary step, while the principal one is the specific adsorption onto the functionalized particle's surface.

6.2 Mechanical Magnetic Separations

Mechanical separations by gravity (or other physical fields) are old processes encountered in the mining industry and process separation units as well as in many technologies such chemical and pharmaceutical and in modern biotechnology, *etc.* There are no published systematic analyses relevant to such applications even though some particular reviews on coal beneficiations[7,8] and mechanical separations by magnetically-assisted fluidized beds[9] were published in the last decade.

We start with particle–particle separation, exploiting the possibility of the magnetically-assisted fluidized beds to attain different regimes controlled by the fluid flow and the field intensity. Hence, the controllable apparent bed density and rheological parameters form the background for development of the solids–solids separation based on the "dense medium" approach—the lighter components of the mixture float upwards to the top surface while the heavier ones sink.

The fluidized bed is always recognized as a technique that can be used for particle separation either by size or density. Since the minimum fluidization velocity depends on the size and the density of the fluidized bodies, we get directly a possibility for segregation along the bed depth. The easily-fluidizable particles go to the top while the others requiring a high energy to be fluidized remain in the bottom section. Hence, with equal density, the finest particles float to the top and the particle size increases with depth towards the supporting grid. Alternatively, with almost equal particle sizes but in a mixture of powders with different densities, the heavier form the bottom section while the lighter ones flow to the top. Some basic features of magnetically-assisted fluidization which form the basis of separation processes are present next.

6.2.1 Magnetically-Assisted Fluidization (MAF)

Magnetic field-assisted fluidization, in general, employs magnetic solids as catalysts, bubble breakers or bio-supports, whose motions and spatial arrangements within the working volume can be controlled by external magnetic fields. From a general point of view, the possibility to control the solid-phase motion affects the external diffusion resistance with respect to heat and mass transfer, depending on the hydrodynamic conditions at the vicinity of the solid–fluid interface. The latter, as a well known fact, is pre-determined by the size of solids used and the fluid viscosity—increase in the particle size increases the working flow rate but reduces the fluid–solid contact area and *vice versa*. These comments are valid for all mass transfer (separation) operations where solids back-mixing is undesirable, such as adsorption, ion-exchange and special separations based on the same principles. In fact, the limits just mentioned above are natural restrictions imposed by the fact that all existing chemical technologies are gravity-dependent ones. That is to say, fluid–solids contact can be performed in either fixed-, fluidized beds or in transport flows.

The possibility of applying an external physical fields, *i.e.* magnetic, results in additional body and surface forces acting on the magnetic solids and leads to: (1) particle arrangements impossible in the gravitational field alone;[10] (2) operations beyond the point of minimum fluidization[9,10] (in the absence of a magnetic field) without particle mixing, or in conventional terminology—*we get fixed bed conditions at high fluid throughput and low hydraulic resistance*[10] (see later in this chapter); (3) point 1 and 2 simply mean that particle size reduction is possible, affecting both external diffusion resistance and intra-particle transport (in the case of porous solids).

In a magnetically-assisted reactor (separator) *the field assists the process acting on the magnetic solids* inside the reactor but the main energy source creating mixing of all phases involved is *due to the fluid flow*, as in the classical fixed- and fluidized bed reactors widely encountered in practice.[10]

6.2.1.1 Operating Modes

MAF can operate with two-phase (fluid–solids)[10–16] and three-phase (gas–liquid–solids)[17,18] systems as can all non-magnetic counterparts encountered in contemporary fluidization technologies. With respect to flow organization of the phases, we have: (a) fixed-bed with upward and downward fluid flow (two-phase systems); (b) moving-bed with countercurrent (upward) fluid flow, mainly for gas–solids systems; and (c) fluidized bed mode.

The magnetic field is additional to the existing gravitational one (affecting all phases) and can be applied in two basic operation (magnetization) modes: (a) Magnetization FIRST and (b) Magnetization LAST.

- *Magnetization FIRST*[10,11] implies application of the field on an initially fixed bed, *i.e.* batch solids mode, and then the fluid flow starts to increase—the bed is undergoing fluidization. This is the classical operational mode with many advantages because it allows creation of a "meta-stable" fixed bed, known as a "magnetically-stabilized bed" (MSB) with a structure depending on both the field strength and fluid flow, and predetermined, of course, by the field-lines orientation. The break-up of the MSB is the fluidization onset.[10]
- *Magnetization LAST*[10,12] means application on an already fluidized bed. The field action results in particle aggregation, bed collapse (reduction in bed height) and increase in the solid–fluid slip velocity. The increase in the field intensity results ultimately in a fixed bed, known as a "frozen bed", where all solids are completely settled at the column bottom (supporting grid). The structure of the final "frozen bed" is entirely dependent on the orientation of the field applied.[13]
- *On–Off (Pulsed field) magnetization*. This is a rarely-employed technique, but there are literature sources,[10,14] mainly on gas–solids systems. The bed alters between a completely fluidized state and a "frozen bed", *i.e.* this is a rapidly performed *Magnetization Last* during the *On* periods (field turned on).[15]

6.2.1.2 Magnetic Fields Used

Magnetically-assisted reactors employing magnetizable solids operate (in general) with steady state (DC) magnetic fields.[10] There are some attempts[10] with alternating (50–60 Hz) current-energized magnetic systems but the results are unsatisfactory with respect to those obtained with DC. The coils generating alternating fields have high inductances and reluctance resistances thus reducing the field intensities required to attain sufficient interparticle forces to allow control of the bed structure.

The fields are mainly generated by coils without iron elements and based mainly on long solenoid systems (Figure 6.1a), multicoil systems (Figure 6.1b) or Helmholtz pair (Figure 6.1c) or saddle coils (Figure 6.2). The first three types of magnetic systems (Figure 6.1) generate fields parallel to their axes of symmetry. In contrast, the saddle coils create a field with lines transverse to the coils' vertical symmetry axes. Taking into account the traditional design of chemical reactors as columns with cylindrical cross-section arranged vertically, when such reactors are magnetically-assisted we get two principal configurations: *Axial fields* and *Transverse fields*.[10]

When the magnetic field has a strong non-homogeneity, mainly in a lateral direction (*i.e.* along the column radius), then significant body forces

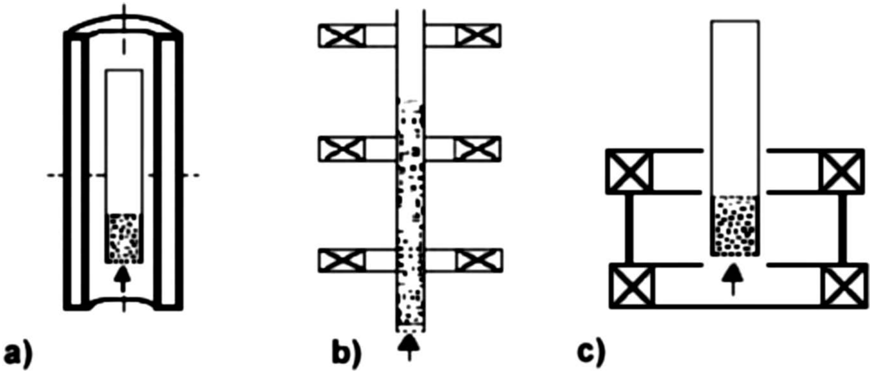

Figure 6.1 Schematic of magnetic systems used in MAF for homogeneous axial fields (a) solenoids; (b) multicoil system; (c) Helmholtz pair, more details area available elsewhere.[10]

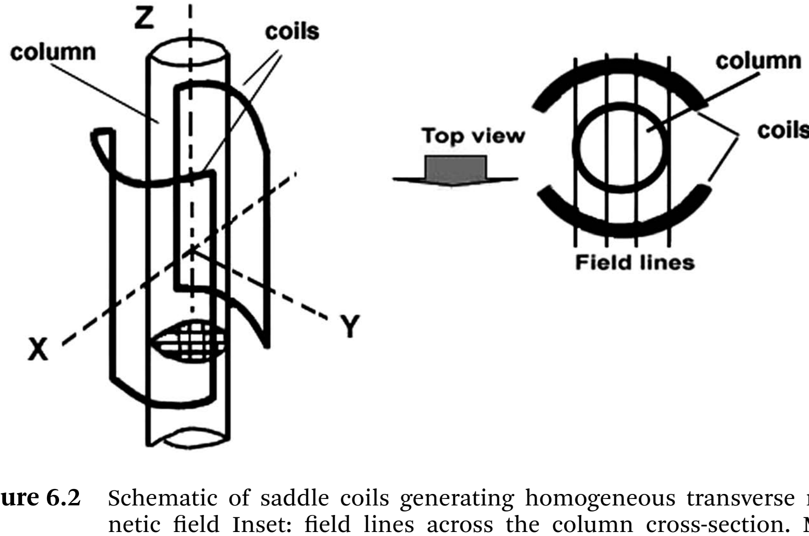

Figure 6.2 Schematic of saddle coils generating homogeneous transverse magnetic field Inset: field lines across the column cross-section. More details area available elsewhere.[10]

pulling the suspended particles (*e.g.* in Magnetization LAST mode) toward the windings of the magnetic system occur and they adhere on the column wall. Therefore, the non-homogeneous fields lead to non-homogeneous distribution of the particles in the volume of the fluidization vessel and decrease the efficiency of the fluid-particle contacts. *This is the reason for widespread use of homogeneous fields (see also the comments in the next section) despite the fact that, from a physical point of view, any field may act in accordance with the scenarios described above.*

6.2.1.3 Hydrodynamic Background

6.2.1.3.1 Solids Flow Through the Reactor: Operating Modes. There are two operating modes with respects the solids flow through the reactor volume:[10]

- *Solids batch* – an amount of solids is charged into the reactor and when the process is over the particles may be removed, or not, for the next step of regeneration. Solids Batch operations are also applicable to particle beds of admixtures of magnetic particles and non-magnetic bio-supports.[10,18]
- *Moving solids (or moving beds)* – there is a continuous particle flow through the reactor. The creation of moving beds is possible with all the magnetization modes – Magnetization FIRST, Magnetization LAST and On–Off.[15]

6.2.1.3.2 Fluidization Vessels. In general, fluidization is performed in cylindrical vessels (columns) allowing a homogeneous gas distribution across the bed cross-section. This a basic principle of fluidization and its magnetic version is generally studied in such devices.[9,10,13–18] An alternative version to the classical "cylindrical" fluidization is the spouted bed created in conical vessels (see Figure 6.3) which is a relatively new trend in this

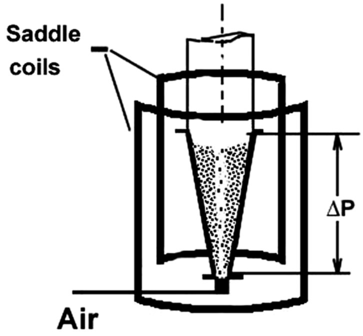

Figure 6.3 Magnetically-assisted gas-fluidization in a tapered vessel (transverse field) More details are available elsewhere[10,19–21]

fluid–solid contacting technique.[19–21] The conical vessel is encircled by a saddle coil magnetic system tall enough to cover the entire volume of the bed, creating a field transverse with respect to the cone symmetry axis. The axial fields are not suitable for these systems due to the induced preferential channeling and the impossibility to cover deep beds.

6.2.1.3.3 Bed Regimes Map. Commonly, the original studies are motivated by the need to operate either: *at high working velocities, impossible in fixed bed regimes* or *to retain low-density magnetic bio-supports in the working volume due to their low minimum fluidization velocities*. This is true, but the main idea, from a chemical engineering standpoint, is quite simple: to achieve *high particle-fluid slip velocity, i.e.*, to decrease mass transfer diffusional resistance in the liquid phase that finally yields enhanced mass transfer operations. This is an essential formulation of the main idea—how to apply external magnetic fields to fluidized magnetic solids, either on preliminary fluidized-particle or on fixed beds, enabling creation of a "stabilized bed" regime. Mass transfer and separation operations impose additional requirements[17] such as low axial dispersion, almost plug-flow regime, *etc.* The phase diagrams in Figure 6.4 demonstrate the principle bed regimes in axial and transverse fields.[10]

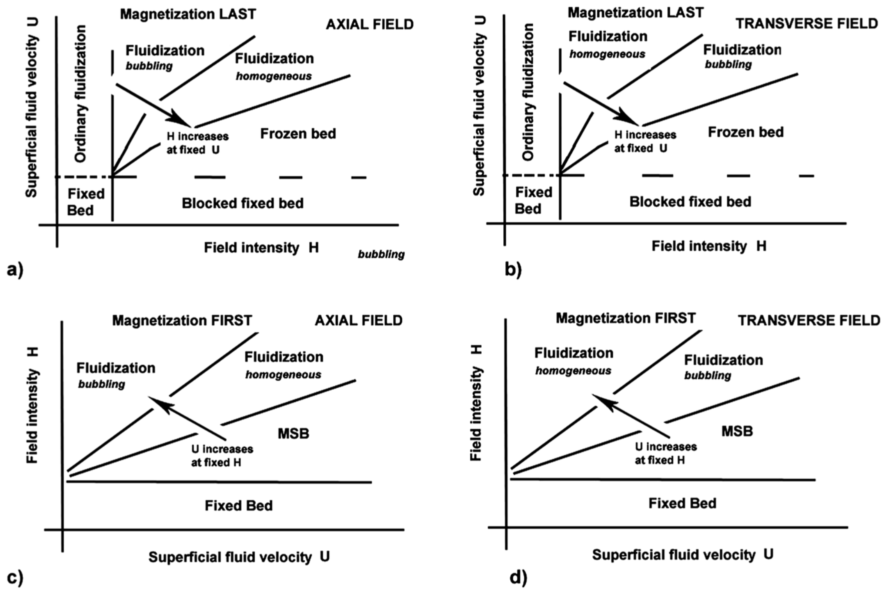

Figure 6.4 Schematic representations of phase diagrams (regime maps) (a) fluidization LAST (axial field); (b) fluidization LAST (transverse field); (c) fluidization FIRST (axial field); (d) fluidization FIRST (transverse field) Comprehensive information is available elsewhere.[10]

6.2.2 Magnetically-Assisted Particle–Particle Separations by Density

6.2.2.1 Batch-Solids Separations

If a mixture of magnetic and non-magnetic particles undergoes fluidization in a magnetic field[10] then segregation by size and density occurs.[22] The segregation is a time-dependent process and its duration can be controlled by either the fluid flow or the field intensity.[23] When the magnetic component in the mixture dominates, the separation process is easier, needs shorter times, lower gas flow rates and relatively low field intensities.[23]

Batch separations of particles were thoroughly investigated[24,25] for removal of fluorite, barite, tantalite and tin with specific gravities of 3.2, 4.5, 6.6 and 7.4, respectively, in the size range 2.00–2.38 mm by settling through magnetically-assisted beds (axial fields). Separation of materials which are practically inseparable (Fe, Cr and Ca from limonite) by conventional techniques was successfully carried out considering such beds as magnetically controllable heavy media.[26]

The magnetic beneficiation of coal can produce fuels containing lower levels of sulphur and ash-forming minerals.[27] Gas-fluidized magnetically-assisted beds of magnetic pearls were used extensively for studying possibilities of coal beneficiation.[28–32] The pearls (recovered from coal ashes) are by-products of coal combustion in conventional plants and mainly comprise Fe_3O_4 in the form of hollow spheres with a density in the range 1300–2200 kg m^{-3}.

The separation in magnetically-assisted beds is strongly affected by the bed rheology which is strongly non-linear,[13] exhibits Bingham-like flow properties with a field-dependent yield stress[33] and depends on the regime attained beyond the fixed-bed regime of the magnetically-stabilized bed (MSB) with Magnetization FIRST mode.[10]

Magnetically-assisted fluidization was successfully tested in high-gradient magnetic separations of copper oxide superconducting particles.[34,35] The experiments with YBCO pellets (Y_2O_3, $BaCO_3$ and CuO), backed at 960 °C and ranged from 38–105 μm. The composition included 25 wt% orthorhombic and 75 wt% tetragonal phases of YBCO compound. The fluidization was performed with Magnetization FIRST mode[10] in an axial magnetic system generating a field with a strong vertical gradient. In fact, this is the unique magnetically-assisted fluidization carried out under cryogenic conditions of 77 K. Looking for the mechanism of separation, the Meissner effect force F_M acting on a particle with volume V_p and magnetic susceptibility χ_p has to be taken into account, namely

$$F_M = \frac{V_p}{\mu_0}\left(\frac{\chi_p}{1+\chi_p/3}\right)B\frac{dB}{dz} \tag{6.1}$$

Since the YBCO material exhibits a strong anisotropy, the Meissner force depends on the particle orientation with respect to the field lines. The Meissner force effect is that the free particles suspended in the gas particles are selectively driven towards the direction of the field gradient dB/dz. Short fluidization runs of about 30 min are enough to attain the equilibrium in the superconducting concentration profile. This separation technique requires almost calm conditions with ceased bubbling that can be achieved by approaching a fluidization of the Geldart's group A[36] through *reduction in the particle diameter* or by control of the *magnetic interparticle forces*.[9]

6.2.2.2 Continuous Cross-Flow MSB for Particle–Particle Separations

The cross-flow magnetically-assisted bed consists of a channel (Figure 6.5) with a bottom having slight inclination to enhance the movement due to gravity in a direction transverse to the fluid flow.[13,32,37] The field can be created in any direction by a magnetic system surrounding the channel, thus controlling the mobility of the magnetic particles.

A mixture of non-magnetic solids of different densities entering the bed near the bottom at the left end of the channels will be separated in components floating towards the top with different speeds. The speed of motion of particular solids towards the bed top surface depends on the density and the size of the particles and can be controlled by the fluidizing flow and the field intensity, both of them affecting the density and fluidity of the dense magnetic medium.[9,13]

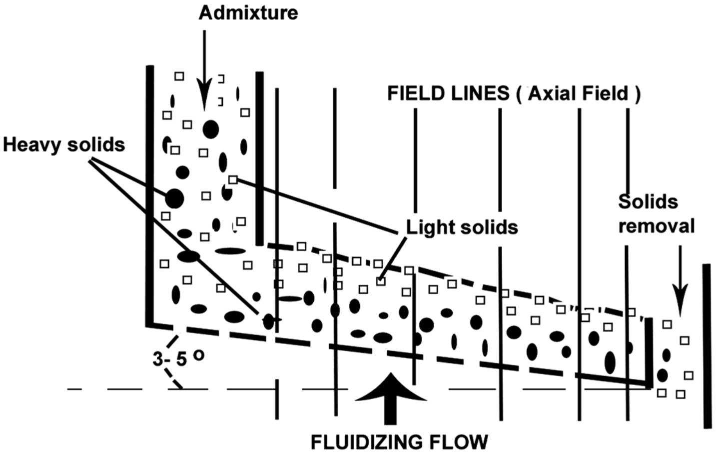

Figure 6.5 Schematic of continuous cross-flow magnetically-assisted bed for solids–solids separation.

6.2.3 Particle Separation from Flow

6.2.3.1 Magnetic Matrix Filters

Magnetic separation involves the selective capture of particles through the application of a magnetic force to overcome competing forces, such as hydrodynamic drag, gravity and, for <10 μm particles, interparticle surface forces. The magnetic force acting on a paramagnetic particle in a field of intensity H is given by[38]

$$F_{\mathrm{m}} = V_{\mathrm{p}}\left(kH\frac{\mathrm{d}H}{\mathrm{d}x}\right) \tag{6.2}$$

The high-gradient magnetic separation (HGMS) devices are based on solenoids as magnets, being the most economic devices for the generation of large uniform magnetic fields with strong enough field (H). By packing the solenoids with fine ferritic steel wire (*called the matrix*), the uniform fields produced by the solenoids are perturbed and very high field gradients are produced at points where the grains (or the wires) are in contact. The magnetic force on a given particle can, therefore, be increased by increasing the field intensity H and the field gradient $\mathrm{d}H/\mathrm{d}x$ inside the magnetic packing of the matrix.

In general, the HGMS separation requires a preliminary treatment of the system containing particles that have to be removed. This initial step is mainly flocculation: magnetic flocculation by brief application of a magnetic field, chemical flocculation by adding flocculants or magnetic seeding (a heterogeneous flocculation of a magnetic host particle and a non-magnetic target particle). As a result of particle flocculation, the formed aggregates easily attract to the element of the magnetic matrix due to high field gradients inside the matrix structure. HGMS was successfully applied to magnetic seed filtration,[39,40] copper removal,[41] environmental applications combating eutrophication of inland waters,[42] dissolved heavy metals (by an initial chemical coagulation and subsequent magnetic seeding),[43] paramagnetic dust filtration,[44] radionuclides removal from technological wastewaters.[45]

We refer to HGMS as a step in separation technologies because, as it was mentioned, this is not a separate process, but more a stage in a technological chain. In cases where *flocculation is not needed*, the flow with particles to be captured passes directly through the matrix[46] and in these cases are cases of so-called *magnetic filtration*. The magnetically-assisted granular filters are almost the same as the classical deep-bed filters widely encountered for cleaning liquids and gases but the packing is magnetic, mainly iron spheres[6,47–50] or strings (wires).[51] The magnetic filter is a dynamical system with time-dependent accumulation of solids depending on the performance of the capture properties of the single elements building the matrix. In general, the matrix should have porosity in the range 0.4–0.5 and the steady-state filtration efficiency Ψ[47] depends on the filter length (depth) L_{filter}

$$\Psi = \alpha_{\text{m}} \left[1 - \exp\left(\frac{\lambda_{\text{f}}}{L_{\text{filter}}} \right) \right] \tag{6.3}$$

The filter coefficient $\lambda_{\text{f}}[m]$ is known also as absorption coefficient $\beta[m]$. The filter efficiency depends on the size of the particle to be removed and this effect becomes more prominent in the micron and sub-micron range.[51,52] The filtration efficiency is inversely proportional to the fluid superficial velocity[51] and this effect is strongly related to the capturing mechanism by adhesion and magnetic attractive forces in the cavities close to the contact points of the magnetic beads.[53] The common assumption is that the flow is within the Stokes' regime, that is the Reynolds number based on the particle (the grain forming the bed) size is $\text{Re}_{\text{p}} = 1$. Both the capture and the collection in the cavities close to the contact points are limited from above by the critical distance, named the saturation radius r_{sat}.[53] Accumulation of particles beyond this limit leads to detachment and re-emission from the filter.

6.2.3.2 MSB-Based Aerosol Filters

The magnetically-stabilized bed (MSB) is a meta-stable state with a fixed structure due to strong interparticle forces of induced magnetic cohesion[10] and suitable to be used as a magnetic filter.[9] Some principle features of the MSB[9,10] relevant to the filter performance should be outlined as:

(1) MSB operates at velocities beyond the minimum fluidization point of the ordinary fixed bed (zero field intensity) forming the magnetic filter medium.
(2) MSB has a structure dependent on the simultaneous action of both the fluid flow and the field intensity.
(3) MSB filters are easily renewed by switching off the field and vigorous fluidization.
(4) MSB can be created in various magnetic field orientations and the existing literature data reveal only two distinct situations:[9] (a) MSB filters in axial magnetic fields and (b) MSB filters in transverse magnetic fields.

Because the field controls the particle arrangements in the bed body it is desirable to create structures having maximum capturing efficiencies. Obviously, any channeling, gaps and pockets in the bed body would reduce the capturing efficiency. Taking into account the knowledge about the MSB structure[9,10] then particle arrangements almost transverse to the fluid flow are suitable solutions. This idea directly leads to application of MSBs created in transverse fields as filter media.

We have started speaking about MSB filters, which implicitly indicates we suggested the Magnetization FIRST mode as the operation for the creation of the filter medium. This is a natural stage in the development of the idea since the initial fixed bed undergoing fluidization is already well-known as a filter medium; thus, we only go beyond the minimum fluidization point in the absence of a field, enhancing the granular medium properties by applying external magnetic fields. However, we have to remember that magnetically-assisted fluidization in the Magnetization LAST mode can create the so-called "frozen bed[12,13] when a sufficiently strong field intensity arrests any particle motions of the preliminary fluidized particles. This bed has loose and strongly anisotropic structure with bad filtration properties, as will be commented upon further in this chapter. However, the transverse magnetic systems based on saddle coils[54] (see Figure 6.6) create deep beds with structures suitable for effective particle capture.

6.2.3.2.1 Aerosols Capture in Magnetization FIRST Mode: Axial Fields. This is the oldest application of MSB filters based on the doctoral thesis of Paul Geuzens[55,56] with a magnetite bed assisted by an external axial magnetic field. The filtration efficiency, in general, decreases in time and depends on the bed depth L_f, namely:

$$\Psi = 1 - \exp\left[-1.5\left(\frac{1-\varepsilon}{\varepsilon}\right)\left(\frac{L_\mathrm{f}}{d_\mathrm{pf}}\right)E_\mathrm{SC}^\mathrm{T}\right], \tag{6.4a}$$

$$\lambda_\mathrm{f} = \frac{1.5}{d_\mathrm{pf}}\left(\frac{1-\varepsilon}{\varepsilon}\right) \tag{6.4b}$$

The filtration coefficient λ_f is a function of the overall bed porosity ε and is inversely proportional to the filter grain diameter d_pf. In contrast to the dominating studies with talc and non-ferrous dusts, the group of Macias-Machin[57]

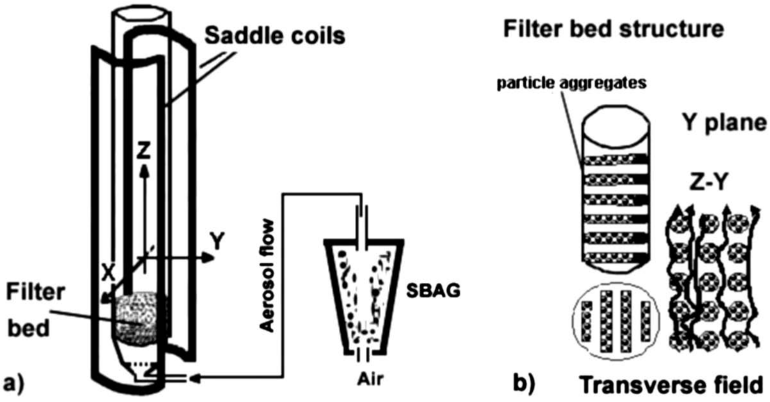

Figure 6.6 Aerosol filter in a transverse field. (a) filter bed with saddle coil magnetic systems and spouted-bed aerosol generator (SBAG), (b) schematic representation of the bed structure and flow paths.

reported filtrations of iron oxide particles (axial fields). In general, these studies do no differ too much from the ones performed with non-ferrous dusts. However, the increase in the field intensity yields increased filter efficiency attaining a value of about 93% because some of the dust particles exhibit remanent magnetism allowing the capture mechanism to be enriched by a magnetic cohesion.

6.2.3.2.2 Aerosols Capture in Magnetization LAST Mode: Axial Fields. The group of Tien[58–60] developed the idea for MSB filters in more detail, applying the Magnetization LAST mode. These experiments of Albert and Tien[58] performed in the frozen bed filters[9,10] revealed increased efficiency with respect to the bubbling bed.

6.2.3.2.3 Aerosols Capture in Magnetization FIRST Mode: Transverse Fields. In axial fields, in order to create an almost homogeneous particle arrangement, the beds should be relatively short,[9,10] which affects the filtration efficiency. Transverse field magnetic systems are rare in MSB filtration[61] but fields created by saddle coils allowed use of filters with depths about 3 times the column diameter[61] (bed heights never attained in axial magnetic systems). In addition, such MSB filters avoid bed channeling, and the reduced filtration efficiency per unit bed length (due to the looser bed structure) is compensated by use of tall beds.

6.2.3.3 Aerosol Filtration by Magnetically Semi-Fluidized Beds

A successful combination of the features of the fluidized and fixed beds controlled by a magnetic field is magnetic semi-fluidization (MSF).[62,63] In contrast to the classical non-magnetic semi-fluidization[64,65] MSF uses a top screen (see Figure 6.7) with an aperture greater than the particle size, *i.e.*, the particles flow through the screen in the absence of a magnetic field. The

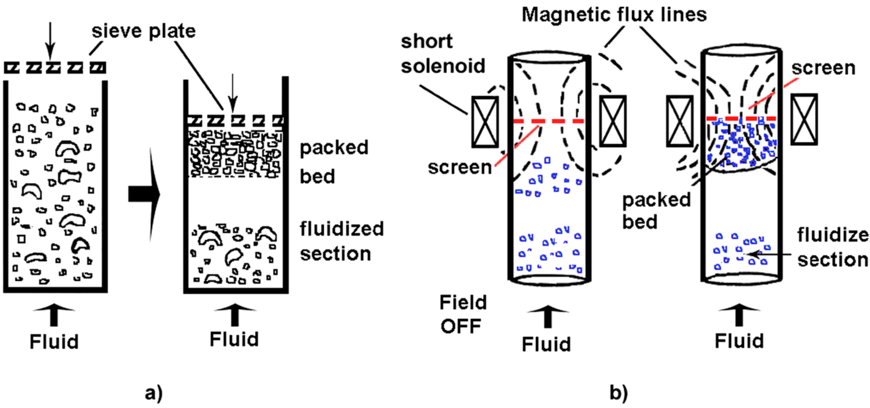

Figure 6.7 Semi-fluidized beds – basic schematics (a) non-magnetic version; (b) magnetic semi-fluidization.

idea of MSF is to create a flexible partition over which permeability can be controlled by an external magnetic field.

In accordance with the classification of MAF,[10] magnetically semi-fluidization belongs to batch solids fluidized beds with the Magnetization FIRST mode. The mode suitable for aerosol filtration is the so-called "Type A"[13,63] when the field intensity at the position of the initial static bed is not enough to cause bed stabilization at the column bottom and the fluidization onset is unaffected. However, the field intensity is enough to stop the magnetic particle entrainment through the top screen and enables the formation of a fixed bed beneath it. This fixed bed filters the aerosols. The decontamination of the saturated bed is simple: the field should be turned off and the gas flow rate reduced to a value insufficient to transport particles to the top screen; hence it easily elutriates the accumulated aerosol from the bottom fluidized bed and ensures easy collection in bins or other vessels.

6.2.3.4 *Magnetically-Assisted Cake Filtration*

This filtration, the oldest technique, was successfully enhanced by additional magnetic action[66,67] by simple attachment of a magnetic system (a solenoid) to a filter press cell. The axial field (see Figure 6.8) generated by a superconducting magnet (up to 5 T) allows one to collect natural hematite with an average particle diameter of 4.7 μm. The filtration rate through the cake is governed by the Darcy law and the main idea comes from the basic law of magnetic flocculation caused by existing magnetic gradients. As a criterion for aggregation of a particulate system, the number E_G,[22] the inverse of the magnetic Bond number $\mathrm{Bo}_{\mathrm{mg}}$,[16,68] was used:

$$E_{\mathrm{G}} = 24\frac{\rho_{\mathrm{s}} g d_{\mathrm{p}}}{\mu_0 M^2} \equiv \frac{1}{\mathrm{Bo}_{\mathrm{mg}}}, \tag{6.5a}$$

$$\mathrm{Bo}_{\mathrm{mg}} = \frac{\mu_0 H^2}{2\rho_{\mathrm{S}} g d_{\mathrm{p}}} \tag{6.5b}$$

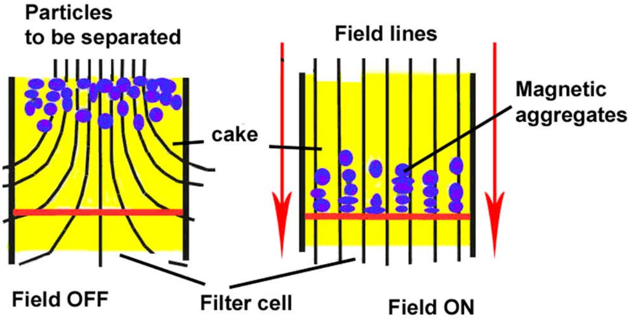

Figure 6.8 Schematic of basic principle of the magnetically-assisted cake filtration.

The magnetic Bond number $\mathrm{Bo}_{mg} = \dfrac{\text{attractive forces between two grains}}{\text{Particle weight}}$ is a measure of the stability of aggregates created by an external magnetic field against the destructive action of the forces of gravity.

6.2.4 Magnetically-Assisted Gravity Sedimentation

Many processes in the production of hydrocarbons[18] are catalyzed by iron, nickel or cobalt (see ref. 18 for many examples). In the slurry following the process, there are fine magnetic particles that have to be removed, recycled and used again. The main problems emerge when the particles are so fine that this results in a low settling velocity and a long processing time. However, when huge magnetic separators and strong magnetic fields have to be avoided, magnetically-boosted sedimentation is the clean, low-energy, easily-handled process avoiding complex equipment and maintenance.

In general, magnetically-assisted sedimentation (MAS) employs gravity as a driving physical field creating a relative motion of the solids with respect to the liquid (commonly almost stagnant) and does not require magnetic gradients to be created. There exist two principal scenarios for magnetically-assisted sedimentation to be carried out: (i) temporal, short time magnetization (STM) of the suspension and consequent gravity sedimentation without field assistance and (ii) continuous magnetization (CM) during the entire process. Additional conditions such as field line orientation and duration of the magnetization process also affect the process efficiency.

Particles in a suspension exposed to an external magnetic field get induced magnetic moments. They start to aggregate when the magnetic attraction forces are strong enough to prevail over the fluid drag and any other surface or body forces stabilizing the suspension. The kinetics of flocculation is of key importance and of either fundamental or practical interest. Since the degree of flocculation depends on the intensity of the field applied at given properties of the suspended particles in weak fields, the attractive forces are comparable as an order of magnitude to the repulsive forces. Hence, there is threshold intensity for strong magnetic flocculation.[9] Low field intensities promote the sedimentation of the aggregates because they are heavier and larger than the primary particles, so they settle rapidly. Further increase in the field intensity leads to strong aggregate–aggregate interaction, the formation of large masses of particles, formation of skeletons of particles that actually do not allow the formation of sediment with the aggregates either as strings or rings.[9]

The experiments of White and Amornraksa[69] (temporal magnetization) were motivated by the separation process of the Australian “Sirofloc” process developed for potable and waste water treatment using magnetic materials (finely ground mineral magnetite) to remove impurities.[70] The fine magnetite was too costly, so its separation and recovery from the suspension was a mandatory step to reduce the process costs.[71] Temporal magnetization is a natural way to provoke flocculation of the induced magnetic dipoles, widely applied in the separation of minerals. It was successfully applied by Saxena[72] to the separation of micro-sized iron particles from hydrocarbons.

Refined tests concerning the field orientation effects and the magnetization mode were carried out[9,73] in magnetic systems used for magnetically assisted fluidization[11] (without vertical gradients). The main outcomes of this study concerning the initial flocculation process can be summarized as:[9,73] (i) stronger fields lead to shorter flocculation processes. (ii) The time required for particle aggregation increases in parallel with the liquid viscosity, and (iii) the flocculation time is proportional to the single-particle settling velocity.

6.3 Magnetic Separations Involving Magnetic Solids with Non-Tailored Surfaces

This section addresses separation involving magnetic particles with non-tailored surfaces such as natural or synthetic magnetite, nickel, cobalt, iron and iron oxides. The principle of this separation approach is that target particles or species from aqueous solutions should have the ability to be adsorbed onto the surfaces of magnetic materials. The second separation stage could then be either filtration, sedimentation or high-gradient magnetic separations, all of them already discussed in the preceding section. Two principal directions are discussed next:

- *Magnetic seeding*, a process where fine, at a colloidal state, particles are attached at the surfaces of large magnetic particles by electrostatic, van der Waals and London forces, *etc.*, thus allowing the larger aggregate to be removed by mechanical magnetic process as a subsequent step.
- *Adsorption of heavy metals and hazardous (non-metallic) species from* aqueous solutions by native or synthetic magnetic particles.

6.3.1 Magnetic Seeding

Magnetic seeding flocculation, or more generally, *particle–particle magnetic flocculation* is a separation technique aimed primarily at separating non-magnetic or weakly magnetic particles from a suspension.[74,75] The basic idea is that strongly magnetic particles, such as magnetite, are "*seeded*" into a fluid suspension where they coagulate with the "*target*" particles of interest. This technique has been widely used in the textile industry, the field of biology and in environmental protection.[76–79] Furthermore, magnetic seeding flocculation extends magnetic separation to include the removal of non-magnetic substances from a suspension. Additionally, magnetic seeding flocculation may be of enormous value in the remediation of radioactive groundwater contamination.[80] In many applications,[76,77,80] the overall goal is to maximize the amount of target particles removed from the suspension while minimizing the amount of time required to carry out the separation process.

Although the feasibility and efficacy of magnetic seeding as a particle separation technique have been recognized for almost two decades,[76–79] its mechanics are not very well studied. In the majority of magnetic seeding applications, a two-step process is employed (see Figure 6.9):

- First, coagulation between magnetic seeds and target particles is promoted either by exploiting the differences in magnetic susceptibilities of particles or by regulating their surface chemical properties.
- Next, the removal of magnetic agglomerates from the fluid phase is facilitated by passing the suspension through a magnetized filter consisting of a wire matrix, for example. Alternatively, the magnetic seed particles are removed from the fluid by a combination of magnetic and gravitational forces. An external magnetic field gradient exerts a net magnetic traction force.

For the separation of target particles that are weakly magnetic or non-magnetic, particles of higher magnetic susceptibility are introduced to form aggregates with the target particles. The aggregates have paramagnetic properties and thus can be easily removed by a magnetic filter. This process is called *magnetic-seeding filtration*. Magnetic-seeding filtration consists of two steps: (1) heterogeneous particle flocculation of magnetic and non-magnetic particles in a stirred tank and (2) high-gradient magnetic filtration (HGMF).

6.3.2 Adsorption: Focusing on Magnetite as Adsorbent

We refer to the adsorption/desorption possibilities of the magnetite, both natural and synthetic, with respect to hazardous species dissolved in aqueous solutions.[81] The analysis stresses the attention on typical hazardous contaminants such as uranium, cadmium, cobalt, europium and arsenic. This point

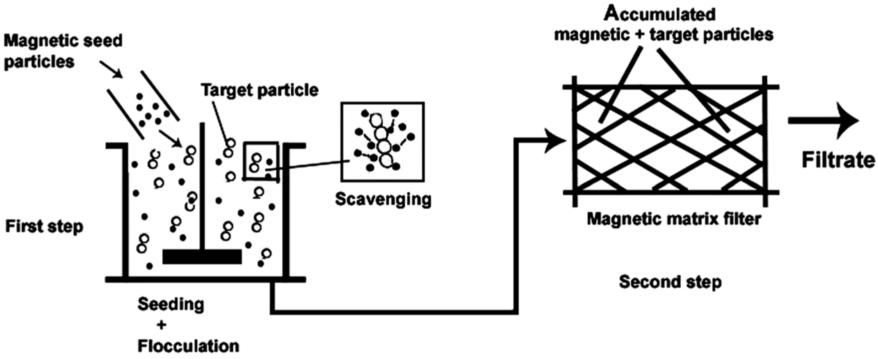

Figure 6.9 Schematic representation of two-step magnetic seeding operation.

is of primary importance when fashionable nano-scale magnetite particles are used for sorption. The choice of magnetite is special because this mineral exhibits strong magnetic properties easily allowing creation of devices and processes for both upstream (adsorption) and downstream (deposition) processes carried out in fixed beds and magnetically-assisted beds. In addition, magnetite easily allows magnetic separation and remote deposition of the dangerous materials being handled.

Magnetite, or iron ferrite ($FeO \cdot Fe_2O_3$) is a naturally occurring mineral, but can also be easily prepared in the laboratory from solutions containing ferric and ferrous ions[82,83] in an Fe(III)/Fe(II) ratio of 2 (see more detailed analysis in ref. 81). Moreover, magnetite exhibits good adsorption characteristics with respect to a wide variety of species, such as dissolved metals, particulate matter, and organic and biological materials, as an economical and environmentally inert material. Magnetite has a relatively low solubility in pure water where the pH is close to its point of zero charge (PZC) (established as PZC = 6–6.8),[84,85] but the solubility varies by changing pH and/or in the presence of complexing agents. In aqueous systems, iron oxides act as Lewis acids and adsorb water or hydroxyl groups (singly, doubly and triply coordinated to Fe atoms). Moreover, two OH groups can coordinate to one iron atom. The coordination of hydroxyl groups and number of surface sites depends on the crystal structure and morphology of the iron oxide.

There is an astonishing plethora of articles published on magnetite and its application in wastewater treatment. We focus the attention on two groups of magnetite particles: *coarse particles* and *nanoparticles*. The *coarse magnetite particles* dominated in the literature before the era of modern nanotechnology. The coarse magnetite-based adsorbents exhibit surface areas comparable to all other natural metal oxides used for the same purposes, *i.e.* water decontamination. The *magnetite nanoparticles*, in the last 10 years, and at present, are the only ones used for sorption processes in some aspects.

Coarse magnetite particles are sometimes found in large quantities in beach sand. Such black sands (mineral sands or iron sands) are found in various places, such as California and the west coast of New Zealand. Silicates, carbonates and other traces that affect both the color and the surface sorption properties commonly contaminate the grain surfaces. Desired fractions can be easily obtained by sieving.

Magnetite nanoparticles exhibit small particle size, large surface area, low cost and ease of preparation. Especially, with respect to wastewater treatment, the nanoparticles offer great applicability but at the same time challenge development of new devices and operating conditions different from the classical ones operating with classical coarse adsorbents. These particles are easily separable from >98% of water solutions by the high-gradient magnetic separation (HGMS). Particularly for magnetite-based nanoparticles, an extremely small size of about 10 nm can be easily obtained thus providing a high contact surface area. The high surface area to some extent compensates for the increase in the mass transfer resistance due to increase in the thickness of the stagnant liquid layer at the vicinity of the solid surface. Magnetic nanoparticles display the phenomenon of super-paramagnetism, not keeping magnetized after the action of a magnetic field, which offers the advantage of reducing the risk of particle aggregation.

6.3.2.1 Adsorption of Hazardous Species: Examples

6.3.2.1.1 Radioactive contaminants

Cesium. Milonjic and Ruvarac[86] reported the adsorption of cesium (Cs), cobalt (Co^{2+} as less than 5 wt%) and cerium (Ce^{+}) by magnetite at pH 2.2 by batch experiments. In this context, the adsorptive properties of magnetite with respect to alkali metal ions were also investigated in batch experiments.[85] Tamura *et al.*[87] reported adsorption of the long-lived isotope $^{60}Co^{2+}$ onto spherical magnetite particles, a corrosion product from the inner layer of the cooling pipe systems in nuclear power stations. Catalette *et al.*[91] used natural magnetite with some impurities (Fe_3O_4: 96 ± 0.6 wt%, SiO_2: 2.4 ± 0.5 wt%, CaO: 0.2 ± 0.1, Al_2O_3: 0.1 ± 0.1 wt%) in laboratory batch experiments for cesium sorption. The magnetite fraction <180 μm exhibited about 18.3 ± 0.2 $m^2\ g^{-1}$ specific surface area determined by the BET method. Marmier and Fromage[92] commented especially on the cesium sorption on magnetite with silicate impurities. The experiments performed reveal that silicates can bind to the magnetite surface over a wide pH range with a maximum sorption different from 100%. According to Marmier and Fromage,[92] the greater affinity of cesium for silanol surface sites than for magnetite surface sites could explain the cesium sorption on natural magnetite with impurities.

Cobalt. Cotten and Navratil[88] observed the adsorption of cobalt in a static field of a neodymium–iron–boron permanent magnet irradiating a fixed bed of magnetite. According to the authors, the ionic sorption is small in comparison to the particle sorption capacity: recall that cobalt is also magnetic, so the external field boosts the magnetic attraction to the magnetite surfaces. Tewari *et al.*[89] reported absorption of Co^{2+} by oxides (Fe_3O_4, Al_2O_3 and MnO_2) as a function of the solute concentration, pH and temperature. In all cases the adsorption increases with increase in pH within the range from 5.0–7.5.

Uranium. Uranium and associated radionuclides, in particular radium and radon, pose significant health risks to humans due to both radiotoxicity and chemical toxicity. Because isotopes of uranium have relatively long half-lives (ranging from approximately 4.5 billion years for ^{238}U to 245 thousand years for ^{234}U,[89]) human ingestion of uranium causes only slightly increased risk of cancer. However, a more immediate risk is posed by the potential for kidney damage resulting from chemical toxicity. The mixed oxide, magnetite is assumed to be the main corrosion product of iron under anoxic conditions. Thus, the role of magnetite in immobilizing uranium may be crucial. Because of the semiconductor character of magnetite, it can potentially function as a mediator of electrons in the reduction on the iron surface, leading to the precipitation of more insoluble UO_2.[90] In addition, magnetite contains ferrous iron, which may also be able to reduce U(VI) species. The source of carbonate seemed to have no effect on the U(VI) removal by magnetite.

Europium. Being a typical member of the lanthanide series, europium (Eu), usually assumes the oxidation state of +3, but due to Eu^{2+} ion electron configuration stability, europium also forms common compounds in oxidation state 2+, which are all slightly reducing. Europium has no significant biological role and appears not to be particularly toxic compared to other heavy metals. It is as hard as lead but is the most reactive of the rare earth elements and rapidly oxidizes in air. Europium is produced by nuclear fission, also, but the fission products yield isotopes which are near the top of the mass range for fission products. Sorption experiments with natural magnetite[91,93] revealed the effect of silica content on the efficiency of the process.

6.3.2.1.2 Heavy Metals

Chromium. Namdeo and Bajpai[93] investigated deposition of a hexavalent chromium Cr(VI) onto synthetic magnetite nanoparticles from aqueous solutions in the temperature range 30–50 °C. The adsorption process follows Langmuir-type behavior and the sorption free energy (calculated by Dubinin-Radushkevich as about 13.51 kJ mol^{-1}) indicates the chemical nature of the adsorption process. The rate of chromium removal is reduced as the pH in the solution increases.[94]

Selenium. Selenium (a metalloid found in group VI of the periodic table below sulfur) is a natural trace element found in bedrock, but it is also introduced into the environment by anthropogenic activities, such as mining and combustion of fossil fuels.[95] Its environmental impact strongly depends on its speciation and concentration. In decomposition processes, $Se^{2-}$is transformed into Se(IV) (SeO_3^{2-}) or Se(VI) (SeO_4^{2-}). The former is more strongly adsorbed on the surface of iron oxyhydroxides and the adsorption process is largely pH-dependent. Martınez *et al.*[96] studied the sorption of ^{79}Se (Se(IV) and Se(VI)) onto magnetite because it is a mineral presented in the near-field of nuclear waste repositories that might represent an important retardation factor for the mobility of many radionuclides. For example, ^{79}Se is one of the principal components of the radioactive wastes and the main selenium radioactivity will be due to the ^{79}Se isotope (with a half-life of 6×10^4 years).

Arsenic. Arsenic is a heavy metal occurring in the environment in different oxidation states and form various species, *e.g.*, As as As(V), As(III), As(0) and As(−III). Arsenic cannot be easily destroyed but can only be converted into different forms or at least transformed into insoluble compounds by contacts with other elements, such as iron, for instance. Inorganic arsenic generally exists in two predominant oxidation states, arsenite $NaAsO_2$ and arsenate-Na_2HAsO_4, both of which are toxic to man and plants.[98] Arsenic is a metal that can generate multiple adverse health effects because of the many chemical forms it takes on. Arsenic-contaminated groundwater used as drinking water has been a severe problem worldwide, especially in Bangladesh, India, some parts of Europe, South America and the United States.[97,98] Conventionally, there are several methods for arsenic removal[98] which include the following steps: coagulation and flocculation, precipitation, adsorption and ion exchange, and membrane filtration. In the context of the topic of the present analysis, we address the adsorption process, mainly by iron oxides, and onto magnetite in particular among these sorbents.

The iron oxides have a high affinity for the adsorption of arsenite and arsenate.[99–101] Researchers have studied the effect of magnetite nanoparticle size on the adsorption and desorption of arsenite and arsenate for water cleaning purposes. It was observed that decrease in the particle size results in increased adsorption maximum capacity for both arsenite and arsenate. On the other hand, the arsenic desorption was hysteretic, an effect demonstrated strongly with decrease in the particle size. According to these authors, the hysteresis is due to higher arsenic affinity of the magnetite nanoparticles. All adsorption data were fitted with the Langmuir isotherm, but the As(III) adsorption demonstrated pH independence.

6.3.2.1.3 Post-Adsorption Separations. The next step, after the adsorption, is the removal of the magnetic adsorbents from the solution. Commonly, high-gradient magnetic separation (HGMS) is applied. As already mentioned in the cases of *magnetic seeding* and *magnetic matrix filters*, the conventional HGMS processes use fine steel wools or fixed beds of steel spheres to form a magnetic matrix.[1,2,45,102–106] A common step in this process is the preliminarily flocculation in order to create large particles (>1 μm in diameter). This approach is now widely applicable when magnetite nanoparticles are used as adsorbents. With coarse magnetic adsorbents, either HGMS is the suitable separation technique if large amounts of water have to be treated, or other techniques from the conventional "arsenal" of the chemical engineering can be applied.

Therefore, as a natural consequence of the analysis of the absorption processes we like to focus attention on three principal issues affecting both the adsorption process performance and the separation step of magnetic particle removal from the aqueous solutions, namely:[81]

(a) *Perfect mixing in tanks* (batch operations) followed by separations, either mechanical or magnetic, but this operating mode needs large volumes for the adsorption stage. The consequent separation process is either by filtration (membranes) or other magnetic methods.[108]
(b) *Adsorption in fixed-bed* operations (in columns) where the deposited substances on the magnetic grain surfaces can be safely deposited afterwards. With respect to the magnetic adsorbent this operation is a batch one, while the wastewater flows continuously through the bed up the break-through point.

The classical fluid–solids contacting techniques using fixed or fluidized bed operations are limited by the particle size used. Decreasing the particle size, we get the high surface area required for an efficient sorption process but at the same time this leads to reduction in the fluid flow rate which is limited from above by the minimum fluidization velocity. Moreover, the decrease of particle size results in bad flow distribution through the bed cross-section, channeling and fluid by-pass. The sorption process should avoid the solids back-mixing, so any problems emerging in the organization of a good fixed-bed operation should be avoided.

6.3.2.1.4 Coarse Particles *vs.* Nanoparticles As Adsorbents. The main problem in the sorption by nanoparticles is the impossibility to organize an efficient fixed-bed operation, because this contacting technique works quite well with particle sizes beyond 100 μm. Even with some micron-sized natural magnetite particles, the channeling and limited flow rate range do not allow the fixed-bed operation to be applied.

Hence, from the point of view of process organization, nanoparticles can operate in the batch perfect mixing mode, *i.e.*, the same as in the laboratory flask, but at a larger scale, and then be removed by HGMS. The HGMS is not low-cost equipment and its application should be carefully analyzed before designing the entire separation process. On the other hand, coarse particles work quite well in fixed beds that are proven by many sorption operations and widely applicable.

What should be the technical solution following the laboratory experiments? Nowadays, the answer is straightforward: the nanoparticles are better due to the high surface area provided but inapplicable in large scale processes. The coarse particles are natural, have some impurities and work well in fixed beds, despite the fact that their specific surface area is lower than that exhibited by their nanoscaled counterparts. As usual, in the modern world, the common answer is: the choice is yours! However, realistic engineering should take into account all issues mentioned above and take a realistic decision.

6.3.2.1.5 Magnetically-Assisted Fluidization: An Alternative in the Adsorption Separations. The sorption with magnetic adsorbents should compromise the fixed-bed operation properties avoiding solids back-mixing and the use of coarse particles. The MSB operation practically avoids the use of a consequent magnetic recovery step when fine particles are collected from large liquid volumes. When the adsorption process is over, only a simple switching of the flow to another "fresh" column is necessary. Because, in the case of hazardous contaminants, either desorption or adsorbent recovery is undesirable, a remote removal of the saturated bed and a consequent safe deposition are necessary. Separations of various species from either gaseous or liquid flows are well analyzed.[9,109]

6.3.3 Metal Recovery by Cementation

Cementation is a term describing an electrochemical precipitation of a metal, usually from an aqueous solution of its salts, by a more electropositive metal.[110,111] It has been used for a long time in the industry for the recovery of value metals, for example copper from iron scrap,[112] from mine waters and process streams. The cementation (or contact reduction) is a process by which a more noble metal ion is precipitated from solution and replaced in solution by a metal higher in electromotive series. The general reaction for the cementation process is:[113]

$$m\mathrm{N}^{n^+} + n\mathrm{M} = n\mathrm{M}^{m^+} + m\mathrm{N} \tag{6.6}$$

where N represents the noble metal and M denotes the reductant metal.

6.3.3.1 Copper Cementation by Iron

Cementation by iron is used commercially to remove impurities from electrowinning and electroplating solutions and to remove copper from a variety of leach solutions.[114–116] Although there are many feasible cementation systems, the most intensively studied metal pair must be copper cementation by iron[113]

$$\mathrm{Cu}^{2+} + \mathrm{Fe} = \mathrm{Cu} + \mathrm{Fe}^{2+} \tag{6.7a}$$

due to different standard reduction potentials

$$\mathrm{Cu}^{2+} + 2\mathrm{e} = \mathrm{Cu}\ (E^0 = +0.34\ \mathrm{V}) \tag{6.7b}$$

and

$$\mathrm{Fe}^{2+} + 2\mathrm{e} = \mathrm{Fe}\ (E^0 = -0.44) \tag{6.7c}$$

The cementation occurs through shorted electrochemical cells in which the electrons for reduction of copper are transferred from the precipitant through the growing copper deposit.[117] Cupric ion is reduced at the copper dendrite surface and iron, which supplies the electrons, is oxidized at anodic surface sites. The cementation process allows recovery of copper in a form of metal particles acceptable (when dry) in copper metallurgy. The cementation rate can be expressed as a first order chemical reaction[113]

$$-\frac{\mathrm{d}\left[\mathrm{Cu}^{2+}\right]}{\mathrm{d}t} = k_\mathrm{c} A_\mathrm{p} \left[\mathrm{Cu}^{2+}\right] \tag{6.8}$$

$[\mathrm{Cu}^{2+}]$ is the copper concentration, k_c is the rate constant and A_p is the precipitant surface area.

The cementation process can be performed either in a fixed particle bed[115,116] or in a suspended particle mode[113,118] irrespective of the cementation couple, thus including fluidized beds.[119] Particularly for copper cementation, Fisher[113,120] recognized the fluidized-bed electrode and demonstrated the concept. In accordance with this concept, copper deposits broken away from the precipitant surfaces create a fluidized section near the iron surface.

Gros *et al.*[121,122] used spherical martensitic steel shots (2.5 mm average diameter ρ_S = 7440 ± 50 kg m^{-3}) for copper cementation in magnetically-assisted fluidized beds using a flat (*i.e.* 2D column placed between poles of an electromagnet with iron cores). The principal process variable is the *liquid volumetric flow rate* because *the hydrodynamic effect on the external mass transfer diffusion resistance is of primary importance*: this is the only way to control both the boundary layer thickness around the particles and the deposit detachment. The facts confirm the mass transfer in copper cementation is under external diffusion control and may be manipulated by the fluid convection. Gros[121] clearly demonstrated that a magnetically stabilized bed of iron and zinc particles works quite well for copper cementation as a result of synergism of both the magnetic stabilization, assuring good hydrodynamic conditions, and the combination of two cementation couples, *copper–iron* and *copper–zinc*, in same fixed bed.

6.3.3.2 Silver Cementation by Iron

Silver is a naturally occurring element and a precious metal used in large quantities for many purposes, particularly in the photographic (and X-ray) industry as a unique light-sensitizing agent. When exposed to light, silver halides such as AgBr on photographic films are reduced to metallic silver. The waste X-ray/photographic films are very good sources for silver recovery with an amount of silver between 1.5 and 2.0 wt%. Silver recovery of spent photographic fixer solutions is of great economic and ecological importance; the ecologically acceptable concentration is <5 mg L^{-1}Ag.[123,124]

Two of the most common methods of silver recovery from the fixer and bleach fix processing solutions are electrolytic recovery[125,126] and metallic replacement[127,129] (cementation). Silver ions will displace many of the common metals from their solid state. Cementation by iron (steel wool, iron shots, spheres or plates,[130] and zinc plates[131]) and copper[132] are among the oldest ones.[133] Recently, natural magnetite was used for silver recovery.[134]

Silver cementation by iron spheres was carried out in magnetically-assisted beds created in axial fields.[135] The magnetic field, in general, does not boost the cementation process itself, but the main effects on the silver recovery are due to particle arrangement in the fluid flow and the larger fluid–solid contact area in the MSB. It was established[135] that slightly expanded MSBs with increased fluid–solid contact areas and acceptable anisotropy in their particle arrangement are optimal for performance of high-efficiency recovery processes. In any case the increase in the fluid flow rate yields increased silver recovery due to reduction of the external mass transfer resistance, irrespective of the particle bed structures used for cementation.[135]

6.4 Magnetic Separations Involving Tailored and Functionalized Magnetic Solids

The presence of magnetic particles for separations in the literature is astonishing and they are normally acceptable as *materials that have to be developed for certain applications*. However, we have to define the main targets in the development of magnetic particles for separations in an explicit way.

Magnetic separations in biochemistry and biotechnolog have been restricted and of limited use up to the 1970's,[136] before the boom in the performance of nanotechnology. Since then, magnetic separation has found many useful and interesting applications in various biosciences and biotechnology. Generally speaking, there are two types of magnetic bio-separations.[136–138] In the first type, *material to be separated is intrinsically magnetic* so that magnetic separations can be performed without any modifications. Examples, such as red blood cells containing paramagnetic haemoglobin, magnetotactic bacteria containing small magnetite particles are just a few of the applications in biosciences. In the second type, *one or more non-magnetic components or a mixture have to be rendered magnetic by the attachment of a magnetically responsive entity*. The new-formed complexes have magnetic properties and can be manipulated by an external magnetic field.[136]

6.4.1 Why Magnetic Beads?

Controlling the particle motion by the field is the primary objective, well-known from the development of magnetic separations. The basic magnetic materials such as iron, nickel, cobalt and magnetite, do not work well as adsorbents for cells, proteins and viruses, which raises the problem for the creation of bio-compatible magnetic composite materials. Moreover, after the sorption of the target species from the solution subsequent downstream operations should be carried out. Separations by magnetic beads can be carried out by two approaches: *Conventional downstream separations* and *separation focusing*.

Separation of cells or enzymes from the culture medium is a mandatory step in downstream biotechnological processing. The *traditional downstream operations* such as thermal shock, filtration and disintegration techniques create stresses in the liquids containing the metabolic products, which are the final targets of the upstream processes. The thermal and mechanical stresses reduce the content and quality of useful metabolic products. The magnetic particles allow easy removal of immobilized cells, enzymes or other metabolite products from the processing fluid to avoid the negative effects on the classical downstream processing.

Separation focusing is another advantage of magnetic bio-carriers in the downstream processing. This simply means, making the particles magnetic with functionalized surfaces to be specific for adsorption of targeted substances of the multicomponent liquid.

6.4.2 Magnetic Bead Manufacturing

Magnetic beads can be manufactured using inorganic materials or a number of synthetic and natural polymers.[18] High mechanical strength, thermal stability, solvent resistance and resistance to microbial attacks are commonly desired features. The ease manufacturing and the excellent shelf-life make inorganic materials ideal supports. The main disadvantage of inorganic supports is their limited functional groups for selective binding: the most useful method is the addition of reactive organic functional groups in silane coupling.

Magnetic beads are more commonly manufactured from polymers since they have a variety of functional groups that can be tailored to suit specific applications.[139–141] The techniques described for the production of magnetic particles can be used for a variety of polymers. The polymer used as binding or coating agent will depend on the final application.[18] The carriers must fulfill a number of criteria relating to their shape, size, rigidity, porosity, chemical inertness, density, magnetic properties, hydrophilicity, surface charge, surface concentration of reactive groups, cost, ease of manufacture, sterilizability, aggregation properties and mechanical strength.[142–144]

The magnetically susceptible supports are mainly *porous beads* created using different conventional materials applied as biocarriers or in chemical adsorption. Since many materials (polymers) are available as potential bio-supports from separations of proteins and cells from liquids, the key problems is: *how to make them magnetic and selective*?

There many methods to make the magnetic particle functionalized. We do not try to encompass all methods and types of particles available, but some examples are: magnetite distributed in cross-linked polysaccharide (chitin, agar, agarose, κ-carrageenan, dextran) beads and magnetite/calcium alginate mixture,[139,145–149] chitosan/polymer encapsulating magnetic particles,[149,150] aminoalkylsilylated magnetite,[151] poly(methyl methacrylate) doped by magnetic particles;[152,153] poly(methyl methacrylate) magnetic latex,[154] magnetite included in polyacrylamide gel,[155] thermo-sensitive polystyrene beads,[156] composites based on vinylic templates,[157] macroporous polystyrene beads,[139,158] duolite–polystyrene composite particles,[140] low-cost magnetic nitrocellulose[159] and magnetically resposive carbons.[160] In general, the functionalized magnetic beads allow quick and efficient purification of crude cell extracts or recovery from other samples rich in cell debris, thereby eliminating the need for most of the pre-treatment steps, including centrifugation, filtration and membrane separation.[161] Therefore, there is a demand for low-cost, robust and reusable magnetic adsorbents.[162]

The use of *non-porous magnetic particles* for separations avoid problems emerging in the application of porous adsorbents since *no intraparticle diffusion and binding are required to attain the desired separation*.[18] However, the incorporation of magnetic particles into the non-magnetic bio-active adsorbent materials may offer a possibility for it to bind specific proteins, for example, from the bulk of the liquid where the supports are immersed.

To complete this section we give some examples of magnetic affinity adsorbents, among them:

(a) *Protein adsorptions*:
  - Matrix containing magnetite colloids[163] for protein adsorption.
  - Ni–Fe–B alloy-densified agarose gel for protein adsorption.[164]

  - Magnetic macroporous cellulose cation exchangers for lysozyme recovery.[165]
  - Capture of lactoferrin from whey using magnetic micro-ion exchangers.[166]
  - Adsorption of bovine serum albumin on nanosized magnetic particles.[167]

(b) *Bacteria capture and detection*:

  - Vancomycin combined with FePt magnetic nanoparticles allows a sensitive and quick assay to allow Gram-negative bacteria, such as *E. coli*, to be captured and analyzed.[168,169]

(c) *Enzyme removal*:

  - Alginate microparticles as affinity adsorbent for removal of α-amylases.[170]
  - Covalently binding polyacrylic acid (PAA) on Fe_3O_4 superparamagnetic nanoparticles for the recovery of lysozyme.[171,172]

The key problem in protein recovery by MSB is the particle design. We cannot encompass all specific problems of particle surface functionalization but recommend some references for further reading.[137,138]

6.4.3 Examples of Bio-Separation Processes

6.4.3.1 *Affinity Chromatography*

Magnetic supports with covalently-immobilized affinity ligands have proved to be effective in cell biology for affinity chromatography and human, animal and plant cell separation.[145,173,174] Highly selective separation is achieved using the reversible complex formation between two or more interacting biological species. Enzymes are coupled specifically with substrates, inhibitors, activators and coenzymes;[175] antibodies bind to antigens; hormones to receptors; lectins bind to specific surface antigens, red blood cells and carbohydrates,[176] and magnetic agarose[177] for protein adsorption.

Burns conceived a continuous contacting system with adsorption–desorption processing in an MSB-based device.[145] The magnetically susceptible solids are introduced at the top of the bed in the *magnetically stabilized bed* (MSB) regime. The feed mixture containing the product is injected at the bottom of the bed. The desired product adsorbs on the supports while the non-adsorbed components travel up with the solvent. The magnetic solids are continuously removed from the bottom of the column and transported to a second stage with any MSB for a washing procedure and finally moved to a MSB-fluidized bed for desorption.

An MSB-based separator of proteins employing an axial field with a lysate entering the column at the bottom was developed by Noble.[178] The examples in the patent[178] claim that with increase in the free volume of the MSB, the lysate will pass through the separator without forming clogging, *i.e.* no fouling and plugging in the bed. The negative effect of the channeling was compensated by recirculation of feedstock through the bed thus extending the residence time. In this context, magnetic agarose support (MAS) for protein adsorption in liquid–solid MSB was conceived.[177]

6.4.3.2 MSB-Based Cell Affinity Separations

The separation of specific cells from mixed populations is essential for a complete understanding of the role of these cells in complex normal and pathological processes. In this context, Molday and Molday[179] were pioneers in the field by using iron–dextran micro-particles and a high-gradient separator. The dextran was conjugated to Protein A to allow specifically labeling of red blood cells (RBC). The approach[179,180] resembles *screened magnetically-stabilized beds*[13] where the particles adhere magnetically on bars or wires with strong magnetic properties.

6.4.3.3 Magnetic solid-phase extraction

Magnetic solid-phase extraction (MSPE) means adsorption of a desired component onto a magnetic adsorbent recoverable from the suspension by appropriate magnetic separators.[138,181,182] With this approach *fine magnetic seed particles* of magnetite (or silanized magnetite) were attached to yeast cell wall envelopes making them magnetic and amenable to separation.[183,184] In a similar way chitosan magnetic beads were developed for heavy metal removal.[141,185,186]

In MSPE, *magnetic particles* are added into the sample solution and the *target analyte* is adsorbed on the surface of the magnetic beads which are separated from the aqueous solution by means of an external magnetic force. In fact, the technique *magnetic solid-phase extraction* means *a selective magnetic seeding*. Making the surfaces of the coarse magnetic particles selective to specific substances by surface tailoring, it is possible to remove (extract) from the processing liquor only desired substances, in contrast to the classical magnetic seeding which is not selective with respect to the substances and particles attached.

Magnetic solid phase extraction methodology overcomes problems such as column packing and phase separation, which can be easily performed by applying an external magnetic field.[138] To some extent, the MSPE technique resembles the *one-step magnetic seeding* as it was commented upon in the preceding sections of the chapter.

6.4.4 Magnetic Membrane Separations

Gas separation and purification by polymer membranes is a promising technology with many advantages[187] over the current separation methods such as cryogenic distillation and gas absorption. The low-energy consumption and process flexibility when impurities have to be removed as well as the process's ability in allowing to separate molecules by size and shape are attractive features, appealing for the feasibility of this separation technology.[188–190] The effectiveness of the membrane separation depends on interaction of the active component to separate and the mainly active components of the membrane material. The contact between the penetrant and the polymer and the dispersion in the membrane body are of primary importance.[187]

Recently, a new concept to enhance gas separation processes, more precisely oxygen–air enrichment, by polymer membranes filled with magnetic powder (and consequently magnetized in a strong field up to 2 T), termed *magnetic membrane separation*,[190–192] has been conceived.[193] The common approach is to use polymer membranes prepared from ethyl cellulose and poly(2,6-dimethyl-1,4-phenylene oxide) (PPO) and filled with neodymium powder or iron oxides.[194–197]

The presence of the magnetic particle additives has an impact on the separation properties of the polymer matrix. Using this type of membranes in separation of gaseous mixtures restrains permeation of paramagnetic constituents and promotes diffusivity of the diamagnetic component.[197] In addition, the diffusion coefficient of nitrogen, for instance, increases from 8.66×10^{-4} cm^2 s^{-1} for the pure PPO membrane to 42.00×10^{-4} cm^2 s^{-1} for that loaded with 10 wt% of Fe_3O_4 nanoparticles. However, under the same conditions,[197] in contrast to the nitrogen whose diffusivity increases about 5 times, the change in the diffusion coefficient of the oxygen is only from 8.71×10^{-4} to 10.20×10^{-4} cm^2 s^{-1}.

If the membrane is made from a dense polymer, then the single gas diffusion model can be described by the nonlinear Smoluchowski equation,[198]

$$\frac{\partial C}{\partial t} = D\frac{\partial^2 C}{\partial x^2} - k(x)\frac{\partial C}{\partial x} \tag{6.9}$$

where $k(x)$ is the coordinate-dependent drift coefficient and D is the diffusion coefficient. The drift coefficient may vary from 0.1 up to 10 and is strongly affected by the presence of potential field (magnetic field in this case).[193] In the simulations of Strzelewicz and Grzywna[197] a value of $k = 0.7$ corresponding to a field of about 0.3 T was used. Experimentally and by simulations, an almost linear relationship was established between the oxygen enrichment and the magnetic field strength.

Magnetic membrane separations offer a large area of application due to the possibility to control the process selectivity not only by the polymer properties but also by the external magnetic field applied to the filtration cell. This is a new and promising technology requiring much new experimental data and adequate mathematical models.

6.5 Final Comments

These final comments avoid long and complicated decisions and standpoints. Magnetically-assisted separation is a dynamic, developing area with novelties appearing every day in the scientific literature and practice. We believe that the overview and the analysis made in this chapter and will serve as comprehensive source of information despite its limited format. However, for the scholars more interested in the field some further reading is recommended.[1,7–10,12–18,109,136,138]

References

1. J. Svoboda, *Magnetic Techniques for the Treatment of Materials*, Kluwer Acad. Publ., Dordrecht, 2004, ch. 1, pp. 39–45.
2. R. R. Gerber, *J. Phys. D: Appl. Phys.*, 1978, **11**, 2119.
3. S. I. Andersson and T. Myrstad, *Appl. Catal., A*, 1997, **159**, 291.
4. M. C. Leaper, S. W. Kingman and J. P. K. Seville, *Magn. Electr. Sep.*, 2002, **11**, 141.
5. M. R. Parker, *Contemp. Phys.*, 1977, **18**, 279.
6. T. Abbasov, *China Particuol.*, 2007, **5**, 71.
7. R. K. K. Dwari and R. H. Rao, *Miner. Process. Extr. Metall. Rev.*, 2007, **28**, 177.
8. A. K. Sahu, S. K. Biswal and A. Parida, *Int. J. Coal Prep. Util.*, 2009, **29**, 216.
9. J. Hristov, *Rev. Chem. Eng.*, 2012, **28**, 243.
10. J. Hristov, *Rev. Chem. Eng.*, 2002, **18**, 295.
11. J. Hristov, *Powder Technol.*, 1996, **87**, 59.
12. J. Hristov, *Powder Technol.*, 1998, **97**, 35.
13. J. Hristov, *Rev. Chem. Eng.*, 2003, **19**, 1.
14. J. Hristov, *Rev. Chem. Eng.*, 2003, **19**, 229.
15. J. Hristov, *Rev. Chem. Eng.*, 2004, **20**, 377.
16. J. Hristov, *Rev. Chem. Eng.*, 2006, **22**, 195.
17. J. Hristov, *Rev. Chem. Eng.*, 2009, **25**, 1.
18. J. Hristov, *Rev. Chem. Eng.*, 2010, **26**, 55.
19. J. Hristov, *Can. J. Chem. Eng.*, 2008, **86**, 470.
20. J. Hristov, *Particuology*, 2009, **7**, 24.
21. J. Hristov, *Particuology*, 2009, **7**, 183.
22. R. E. Rosensweig, W. K. Lee and J. Siegell, *Sep. Sci. Technol.*, 1987, **22**, 25.
23. R. L. Sonolikar, A. B. Pande, S. B. Gaidhani and M. G. Kher, *Proc. 3rd World Congress of Chemical Engineering*, Tokyo, 1986, pp. 481–484.
24. O. Harel, W. Resnik and Y. Zimmels, *J. Magn. Magn. Mater.*, 1990, **83**, 498.
25. O. Harel, Y. Zimmels and W. Resnik, *Powder Technol.*, 1991, **61**, 159.
26. U. Andres and W. O'Reilly, *Powder Technol.*, 1992, **69**, 279.
27. S. E. Male, *Magn. Sep. News*, 1985, **2**, 1.
28. M. Fan, Q. Chen, Y. Zhao and Z. Luo, *Int. J. Miner. Process.*, 2001, **63**, 225.
29. M. Fan, Q. Chen, Y. Zhao, Z. Luo, Y. Guan and B. Li, *Powder Technol.*, 2002, **123**, 208.
30. M. Fan, Q. Chen, Y. Zhao, Z. Luo and Y. Guan, *Coal Prep.*, 2003, **23**, 47.
31. Z. Luo, Y. Zhao, Q. Chen, M. Fan and X. Tao, *Fuel Proc. Technol.*, 2002, **79**, 63.

32. Z. Luo, Y. Zhao, Q. Chen and X. Tao, *Fuel Proc. Technol.*, 2003, **85**, 173.
33. W. K. Lee, *Powder Technol.*, 1991, **64**, 69.
34. S. Labroo, Y. Ebrahimi and J. Y. Park, *IEEE Trans Magn.*, 1992, **28**, 1895.
35. S. Labroo, J. Y. Park, R. J. Kearney and W. J. Yeh, *Cryogenics*, 1993, **33**, 1063.
36. D. Geldart, *Powder Technol.*, 1973, **7**, 285.
37. J. Siegell, Magnetically frozen beds, *Powder Technol.*, 1988, **55**, 127.
38. G. Dobby and J. A. Finch, *Powder Technol.*, 1997, **17**, 73.
39. T. Y. Ying, C. J. Chin, S. C. Lu, S. Yiacoumi, M. R. Chattin, M. A. Spurrier, D. W. DePaoli and C. Tsouris, *Sep. Sci. Technol.*, 1999, **34**, 1371.
40. T. Y. Ying, S. Yiacoumi and C. Tsouris, *Chem. Eng. Sci.*, 2000, **55**, 1101.
41. W. I. Wu, C. F. Lin, S. C. Panchangam, C. H. Wu and A. P. K. Hong, *Environ. Technol.*, 2011, **32**, 817.
42. A. Merino-Martos, J. de Vicente, L. Cruz-Pizarro and I. de Vicente, *J. Hazard. Mater.*, 2011, **186**, 2068.
43. Y. Terashima, H. Ozaki and K. Sekine, *Water Res.*, 1986, **20**, 537.
44. R. F. Boucher and O. O. Okeke, *Aerosol Sci. Technol.*, 1990, **12**, 300.
45. A. D. Ebner, J. A. Ritter and L. Nufiez, *Sep. Sci. Technol.*, 1999, **34**, 1333.
46. L. Chen, Z. Qian, S. Wen and S. Huang, *Miner. Process. Extr. Metall. Rev.*, 2013, **34**, 340.
47. S. Herdem, T. Abbasov and M. Koksal, *Powder Technol.*, 1999, **106**, 176.
48. T. Abbasov, *Powder Technol.*, 2001, **115**, 215.
49. T. Abbasov, M. Yuceer, Z. Yildiz and E. Sener, *Int. Rev. Chem. Eng.*, 2011, **3**, 101.
50. T. Abbasov, M. Yuceer and Z. Yildiz, *Int. Rev. Chem. Eng.*, 2011, **3**, 755.
51. T. Abbasov, S. Herdem and M. Koksal, *J. Phys. D: Appl. Phys.*, 1999, **32**, 1097.
52. T. Abbasov, Z. Yildiz and A. Sarimeseli, *Int. Rev. Chem. Eng.*, 2010, **2**, 289.
53. T. Abbasov and A. R. Bahadır, *J. Dispersion Sci. Technol.*, 2007, **28**, 463.
54. I. Penchev and J. Hristov, *Powder Technol.*, 1990, **62**, 1.
55. P. Geuzens, *Some aspects of magnetically stabilized fluidization*, PhD Thesis, Tech. Univ. Eindhoven, The Netherlands, 1985.
56. P. Geuzens and D. Thoenes, *Chem. Eng. Commun.*, 1988, **67**, 229.
57. J. M. Rodriguez, A. Macias-Machin, A. Alvaro, J. R. Sanchez and A. M. Estevez, *Ind. Eng. Chem. Res.*, 1999, **38**, 276.
58. R. V. Albert and C. Tien, *AIChE J.*, 1985, **31**, 288.
59. M. Warrior and C. Tien, *Chem. Eng. Sci.*, 1986, **41**, 1711.
60. A. H. Cohen and C. Tien, *Powder Technol.*, 1991, **64**, 147.
61. J. Hristov and A. Hristov, *Proc. 7th World Filtration Congress*, Hungarian Chemical Society Publ., Budapest, 1996, vol. 2, pp. 743–747.
62. J. Hristov, *Proc. FILTECH Conference*, Filtration Society Publ., Karlsruhe, 1991, vol. 2, pp. 611–622.
63. J. Hristov, *Hung. J. Ind. Chem.*, 1998, **26**, 69.
64. L. T. Fan and C. Y. Yang, *AIChE J.*, 1959, **5**, 407.
65. L. T. Fan and C. Y. Wen, Method of filtration using convertible (Semifluidized) beds, U.S. Patent 4 157 959, 1979.

66. M. Stolarski, B. Fuchs, S. B. Kassa, C. Eichholz and H. Nirschl, *Chem. Eng. Sci.*, 2006, **61**, 6395.
67. C. Eichholz, M. Stolarski, V. Goertz and H. Nirschl, *Chem. Eng. Sci.*, 2008, **63**, 3193.
68. J. Hristov, *China Particuol.*, 2007, **5**, 103.
69. D. A. White and S. Amornraksa, *Chem. Eng. J.*, 2000, **79**, 165.
70. R. B. Brocks and D. J. Twining, *Environ. Prot. Bull.*, 1993, **23**, 3.
71. B. A. Bolto and T. H. Spurling, *Environ. Monit. Assess.*, 1991, **19**, 139.
72. S. C. Saxena, R. S. Miao, M. Shalabi and M. J. Mcnallan, *AIChE J.*, 1994, **40**, 1594.
73. J. Hristov and V. Girenko, *Proc. of 8th World Filtration Congress*, Brighton, 2000, pp. 1213–1216.
74. S. Relle and S. B. Grant, *Langmuir*, 1998, **14**, 2316.
75. T. J. Wan, S. M. Shen, S. H. Siao, C. F. Huang and C. Y. Cheng, *Water Res.*, 2011, **45**, 6301.
76. C. J. M. Chin, P. W. Chen and L. J. Wang, *Chemosphere*, 2006, **63**, 1809.
77. V. Rocher, J. M. Siaugue, V. Cabuil and A. Bee, *Water Res.*, 2008, **42**, 1290–1298.
78. S. L. Lo, Y. L. Wang and C. Y. Hu, *Res. J. Chem. Environ.*, 2008, **12**, 40.
79. Y. Li, J. Wang, Y. Zhao and Z. Luan, *Sep. Purif. Technol.*, 2010, **73**, 264.
80. S. Yiacoumi, D. A. Rountree and C. Tsouris, *J. Colloid Interface Sci.*, 1996, **184**, 477.
81. T. Petrova, L. Fachikov and J. Hristov, *Int. Rev. Chem. Eng.*, 2011, **2**, 134–152.
82. G. Sposito, *The Chemistry of Soils*, Oxford University Press, New York, 1989, ch. 8 and 9, pp. 363–369.
83. Z. Sun, F. Su, W. Forsling and P. Samskog, *J. Colloid Interface Sci.*, 1998, **197**, 151.
84. R. M. Cornell and U. Schwertmann, *The Iron Oxides, Structure, Properties, Reactions, Occurrences and Uses*, Wiley-VCH, New York, 2nd edn, 2003, ch. 11, pp.135–140.
85. S. K. Milonic and M. M. Kopecni, *J. Radioanal. Chem.*, 1983, **78**, 15.
86. K. Milonic and A. L. Ruvarac, *Bull. Boris Kidric Inst. Nucl. Sci*, 1970, **21**, 21.
87. H. Tamura, E. Matijevic and L. Meitess, *J. Colloid Interface Sci.*, 1983, **92**, 303.
88. G. B. Cotten, J. D. Navratil and H. Bradley, *Proc. Of Waste Management '99 Conference*, Tucson, Arizona, March 1999, Article AZ INEEL/Con-98–00749.
89. P. H. Tewari, A. B. Campbell and W. Lee, *Can. J. Chem.*, 1972, **50**, 1642.
90. M. Rovira, S. El Armani, L. Duro, L. Gimenez, J. de Pablo and J. Bruno, *J. Hazard. Mater.*, 2007, **147**, 726.
91. H. Catalette, J. Dumonceau and Ph. Ollar, *J. Contam. Hydrol.*, 1998, **35**, 151.
92. N. Marmier and F. Fromage, *J. Colloid Interface Sci.*, 2000, **223**, 83.
93. M. Namdeo and S. K. Bajpai, *EJEAFChe*, 2009, **8**, 367.

94. M. M. Amin, A. Khodabakhshi, M. Mozafari, B. Bina and S. Kheiri, *Environ. Eng. Manage. J.*, 2010, **9**, 921.
95. N. Zhang, L. S. Lin and D. C. Gang, *Water Res.*, 2008, **42**, 3809.
96. M. Martınez, J. Gimenez, J. de Pablo, M. Rovira and L. Duro, *Appl. Surf. Sci.*, 2006, **252**, 3767.
97. M. Bissen and F. H. Frimmel, *Acta Hydrochim. Hydrobiol.*, 2003, **31**, 9.
98. T. S. Y. Choong, T. G. Chuaha, Y. Robiaha, F. L. G. Gregory and I. Azni, *Desalination*, 2007, **217**, 139.
99. M. L. Pierce and C. B. Moore, *Water Res.*, 1982, **15**, 1247.
100. K. P. Raven, A. Jain and R. H. Loeppert, *Environ. Sci. Technol.*, 1998, **32**, 344.
101. S. Yean, L. Cong, C. T. Yavuz, J. T. Mayo, W. W. Yu, A. T. Kan, V. L. Colvin and M. B. Tomson, *J. Mater. Res.*, 2005, **20**, 3255.
102. J. A. Oberteuffer, *IEEE Trans. Magn.*, 1976, 444.
103. T. Oka, H. Kanayama, S. Fukui, J. Ogawa, T. Sato, M. Ooizumi, T. Terasawa, Y. Itoh and R. Yabuno, *Physica C*, 2008, **468**, 2128.
104. G. D. Moeser, K. A. Roach, W. H. Green and A. T. Hatton, *AIChE J.*, 2004, **50**, 2835.
105. C. T. Yavuz, A. Prakash, J. T. Mayo and V. L. Colvin, *Chem. Eng. Sci.*, 2009, **64**, 2510.
106. G. Mariani, M. Fabbri, F. Negrini and P. L. Ribani, *Sep. Purif. Technol.*, 2010, **72**, 47.
108. S. K. R. Yadanaparthi, D. Graybill and R. von Wandruszka, *J. Hazard. Mater.*, 2009, **171**, 1.
109. J. Hristov and L. Fachikov, *China Particuol.*, 2007, **5**, 11.
110. P. H. Strickland and P. Lawson, in *Proc. International Symposium on Hydrometallurgy*, ed. D. J. I. Evans and R. S. Shoemaker, The American Institute of Mining, Metalurgical &Petroleum Engineers, Inc., Chicago, February, 1973, ch. 13, pp. 293–328.
111. G. P. Power and I. M. Ritchie, *Electrochem. Acta*, 1977, **22**, 365.
112. J. S. Jacobi, The recovery of copper from dilute process streams, in *Unit Operations in Hydrometallurgy*, ed. M. E. Wadsworth and F. T. Davis, Gordon and Breach, New York, 1964, pp. 617–644.
113. W. W. Fisher, *Hydrometallurgy*, 1986, **16**, 55.
114. W. S. Sheffer and L. G. Evans, *U.S. Bur. Mines, Inf. circ.*, 1968, **8341**, 57.
115. K. Kubo, A. Mishima, T. Aratani and T. Yano, *J. Chem. Eng. Jpn.*, 1979, **12**, 495.
116. A. Dib and L. Makhoufi, *Chem. Eng. Process.*, 2004, **43**, 1265.
117. R. S. Rickard and M. C. Fuerstenau, *Trans. Metall. Soc. AIME*, 1968, **242**, 1487.
118. J. D. Miller, R. Y. Wan and J. R. Parga, *Hydrometallurgy*, 1990, **24**, 373.
119. B. Boyanov, J. D. Donaldson and S. M. Grimes, *J. Chem. Technol. Biotechnol.*, 1988, **41**, 317.
120. W. W. Fisher and R. D. Groves, *U.S. Bur. Mines, Rep. Invest.*, 1976, **8098**, 22.

121. F. Gros, *Intensification of copper recovery from solutions: Cementation in fixed and fluidized beds, mono and bi-component, affected by a magnetic field*, PhD thesis, INPG, Grenoble, France, October, 2005(in French).
122. F. Gros, S. Baup and M. Aurousseau, *Chem. Eng. Process.*, 2008, **47**, 295.
123. E. Y. Yazici, H. Deveci and R. Yazici, *Sep. Sci. Technol.*, 2011, **46**, 2231.
124. A. D. Bas, E. Y. Yazici and H. Deveci, *Hydrometallurgy*, 2012, **121–124**, 22.
125. C. V. Reyes, M. T. Oropeza, I. Gonzalez and C. Ponce-De-Leon, *J. Appl. Electrochem.*, 2002, **32**, 473.
126. J. P. Chen and L. L. Lim, *Chemosphere*, 2005, **60**, 1384.
127. E. A. Abdel-Aal and F. E. Farghaly, *Powder Technol.*, 2007, **178**, 51.
129. W. Djoudi, F. Aissani-Benissad and S. Bourouina-Bacha, *Chem Eng. J.*, 2007, **133**, 1.
130. G. D. Sulka and M. Jaskuła, *Electrochim. Acta*, 2006, **51**, 6111.
131. S. Aktas, *Hydrometallurgy*, 2010, **104**, 106.
132. G. D. Sulka and M. Jaskuła, *Hydrometallurgy*, 2002, **64**, 13.
133. R. Ramesh and B. S. Sheshadri, *Indian J. Technol.*, 1992, **30**, 19.
134. T. M. Petrova, V. A. Karadjova, L. Fachikov and J. Hristov, *Int. Rev. Chem. Eng.*, 2012, **4**, 373.
135. T. M. Petrova, B. Tzaneva, L. Fachikov and J. Hristov, *Chem. Eng. Process.*, 2013, **71**, 83.
136. I. Safarik and M. Safarikova, in *Scientific and Clinical Applications of Magnetic Carriers*, ed. U. Hafeli, W. Schutt, J. Teller and M. Zborowski, Plenum Press, New York, 1997, pp. 323–340.
137. I. Safarik and M. Safarikova, *J. Chromatogr. B: Biomed. Sci. Appl.*, 1999, **722**, 33.
138. I. Safarik and M. Safarikova, *J. Magn. Magn. Mater.*, 1999, **194**, 108.
139. M. S. Griffiths and G. A. Bosley, *Enzyme Microb. Technol.*, 1993, **15**, 109.
140. D. Demirel, A. R. Ozdural and M. Mutlu, *J. Food Eng.*, 2004, **62**, 203.
141. K. Z. Elwakeel, A. A. Atia and A. M. Donia, *Hydrometallurgy*, 2009, **97**, 21.
142. B. R. Pieters, R. A. Williams and C. Webb, in *Colloid and Surface Engineering: Applications in the Process Industries*, ed. R. A. Williams, Butterworth-Heinemann, Oxford, 1991, pp. 248–286.
143. D. Bozhinova, B. Galunsky, G. Yueping, M. Franzreb, R. Köster and V. Kasche, *Biotechnol. Lett.*, 2004, **26**, 343.
144. Z. Y. Ma and H. Z. Liu, *China Particuol.*, 2007, **5**, 1.
145. M. A. Burns and D. J. Graves, *Biotechnol. Prog.*, 1985, **1**, 95.
146. T. Hamaya, T. Takizawa, H. Hidaka and K. Horikoshi, *J. Chem. Eng. Jpn.*, 1993, **26**, 223.
147. I. Safarik, Z. Sabatkova and M. Safarikova, *J. Agric. Food Chem.*, 2008, **56**, 7925.
148. I. Safarik, Z. Sabatkova and M. Safarikova, *J. Magn. Magn. Mater.*, 2009, **321**, 1478.
149. Z. D. Zhou, G. Y. Li and Y. J. Li, *Int. J. Biol. Macromol.*, 2010, **47**, 21.

150. D. Hritcu, M. I. Popa, N. Popa, V. Badescu and V. Balan, *Turkish J. Chem.*, 2009, **33**, 785.
151. E. Sada, S. Katoh, M. Shiozawa and T. Fukui, *Biotechnol. Bioeng.*, 1981, **23**, 2561.
152. E. Pollert, K. Knizek, M. Marysko, K. Zaveta, A. Lancok, J. Bohacek, D. Horak and M. Babic, *J. Magn. Magn. Mater.*, 2006, **306**, 241.
153. Y. H. Chen, Y. Y. Liu, R. H. Lin and F. S. Yen, *J. Appl. Polym. Sci.*, 2008, **108**, 583.
154. R. Y. Hong, B. Feng, X. Cai, G. Liu, H. Z. Li, J. Ding, Y. Zheng and D. G. Wei, *J. Appl. Polym. Sci.*, 2009, **112**, 89.
155. T. Ivanov, V. Ivanova and M. Kamburo, *Int. Rev. Chem. Eng.*, 2009, **1**, 316.
156. A. Kondo, H. Kamura and K. Higashitani, *Appl. Microbiol. Biotechnol.*, 1994, **41**, 99.
157. N. Tudorachi and A. P. Chiriac, *J. Appl. Polym. Sci.*, 2008, **108**, 3690.
158. C. L. Yang, Y. P. Guan, J. M. Xing, J. G. Liu, G. B. Shan, Z. T. An and H. Z. Liu, *AIChE J.*, 2005, **51**, 2011.
159. D. Tanyolac and A. R. Ozdural, *React. Funct. Polym.*, 2000, **45**, 235.
160. I. Safarik, K. Horska, K. Pospiskova and M. Safarikova, *Int. Rev. Chem. Eng.*, 2012, **4**, 346.
161. N. Tuzmen, F. Akdogan, T. Kalburcu, S. Akgol and A. Denizli, *Process Biochem.*, 2010, **45**, 556.
162. T. C. Willett, *Magnetic Adsorbents Displaying Switchable Ion-Exchange Behaviour*, Ph.D. thesis, University of Birmingham, UK, 2009.
163. B. Xue and Y. Sun, *J. Chromatogr. A*, 2002, **947**, 185.
164. X. D. Tong and Y. Sun, *J. Chromatogr. A*, 2001, **943**, 63.
165. I. Safarik, Z. Sabatkova, O. Tokar and M. Safarikova, *Food Technol. Biotechnol.*, 2007, **45**, 355.
166. A. Meyer, S. Berensmeier and M. Franzreb, *React. Func. Polym.*, 2007, **67**, 1577.
167. Z. G. Peng, K. Hidajat and M. S. Uddin, *J. Colloid Interface Sci.*, 2004, **271**, 277.
168. H. Gu, P. L. Ho, K. W. T. Tsang and B. Xu, *Chem. Commun.*, 2003, **15**, 1966.
169. H. Gu, P. L. Ho, K. W. T. Tsang and B. Xu, *J. Am. Chem. Soc.*, 2003, **125**, 15702.
170. M. Safarikova, I. Roy, M. N. Gupta and I. Safarik, *J. Biotechnol.*, 2003, **105**, 255.
171. P. Kopacek, R. Vogt, L. Jindrak, C. Weise and I. Safarik, *Insect Biochem. Mol. Biol.*, 1999, **29**, 989.
172. M. H. Liao and D. H. Chen, *Biotechnol. Lett.*, 2002, **24**, 1913.
173. B. E. Terranova and M. Burns, *Biotechnol. Prog.*, 1989, **5**, 98.
174. M. A. Burns and D. J. Graves, *React. Polym.*, 1987, **6**, 45.
175. I. Safarik and M. Safarikova, *J. Biochem. Biophys. Methods*, 1993, **27**, 327.
176. G. Moffat, R. A. Williams, C. Webb and R. Stirling, *Min. Eng.*, 1994, **7**, 1039.
177. X. D. Tong and Y. Sun, *Biotechnol. Prog.*, 2003, **19**, 1721.

178. R. D. Noble, C. A. Koval and G. F. Slaff, Stationary magnetically stabilized fluidized bed for protein separation and purification, US Patent 5084169, 1989.
179. R. S. Molday and L. L. Molday, *FEBS Lett.*, 1984, **170**, 232.
180. J. J. Chalmers, M. Zborowski, L. Sun and L. Moore, *Biotechnol. Prog.*, 1998, **14**, 141.
181. F. Sebesta, in *Natural Microporous Materials in Enviromental Technology*, ed. P. Misaelides and F. Macasek, Kluwer Acad. Publ, 1999, pp. 473–484.
182. J. John, F. Sebesta and A. Motl, *Radiochim. Acta*, 1997, **78**, 131.
183. M. Patzak, P. Dostalek, R. V. Fogarty, I. Safarik and J. M. Tobin, *Biotechnol. Tech.*, 1997, **11**, 483.
184. Y. Q. Ji, Y. T. Hu, Q. Tian, X. Z. Shao, J. Y. Li, M. Safarikova and I. Safarik, *Sep. Sci. Technol.*, 2002, **45**, 1499.
185. G. L. Rorrer, T. Y. Hsien and J. D. Way, *Ind. Eng. Chem. Res.*, 1993, **32**, 2170.
186. L. M. Zhou, Z. R. Liu, J. H. Liu and Q. W. Huang, *Desalination*, 2010, **258**, 41.
187. R. W. Baker, *Membrane Technology and Applications*, John Wiley and Sons, Chichester, 2nd edn, 2004, ch. 1, pp. 1–14.
188. D. J. Malik, C. Webb, R. G. Holdich, J. J. Ramsden, G. L. Warwick, I. Roche, D. J. Williams, A. W. Trochimczuk, J. A. Dale and N. A. Hoenich, *Sep. Purif. Technol.*, 2009, **66**, 578.
189. I. Agirre, M. B. Guemez, H. M. van Veen, A. Motelica, J. F. Vente and P. L. Arias,*J. Membr. Sci.*, 2011, **371**, 179.
190. J. Albo, E. Santos, L. A. Neves, S. P. Simeonov, C. A. M. Afonso, J. G. Crespo and A. Irabien, *Sep. Purif. Technol.*, 2012, **97**, 26–33.
191. M. Mihoub, A. El May, A. Aloui, A. Chatti and A. Landoulsi, *Int. J. Food Microbiol.*, 2012, **157**, 259.
192. M. Vazquez, M. Hernandez-Velez, A. Asenjo, D. Navas, K. Pirota, V. Prida, O. Sanchez and J. L. Baldonedo, *Phys. B*, 2006, **384**, 36.
193. A. Strzelewicz and Z. J. Grzywna, Studies on the air membrane separation in the presence of a magnetic field,*J. Membr. Sci.*, 2007, **294**, 60.
194. A. Rybak, Z. J. Grzywna and W. Kaszuwara, On the air enrichment by polymer magnetic membranes,*J. Membr. Sci.*, 2009, **336**, 79.
195. Z. J. Grzywna, A. Rybak and A. Strzelewicz, in *Membrane Gas Separation*, ed. Y. Yampolskii and B. Freeman, A John Wiley & Sons, Chichester, 2010, ch. 9, pp.159–182.
196. M. Krasowska, A. Rybak, G. Dudek, A. Strzelewicz, K. Pawelek and Z. Grzywna,*J. Membr. Sci.*, 2012, **415–416**, 864.
197. G. Dudek, R. Turczyn, A. Strzelewicz, M. Krasowska, A. Rybak and Z. J. Grzywna, *Sep. Purif. Technol.*, 2013, **109**, 55.
198. H. Risken, *The Fokker–Planck Equation*, Springer-Verlag, Berlin, 2nd edn, 1996, ch. 1, pp. 1–11.

CHAPTER 7

Prospects of Magnetic Nanoparticles for Magnetic Field-Assisted Mixing of Fluids with Relevance to Chemical Engineering

SHAHAB BOROUN[a] AND FAÏÇAL LARACHI*[a]

[a]Department of Chemical Engineering, Laval University, Québec, QC,
Canada, G1V0A6
*E-mail: faical.larachi@gch.ulaval.ca

7.1 Introduction

Development of efficient unit operations in chemical processing has always been one of the main goals in process intensification (PI). An efficient operation encompasses several subcategories from the safety, economy, environmental and sustainability points of view. It results in diverse research fields and remarkable efforts to develop intensified technologies with beneficial consequences. Among the various aspects in the field of process intensification, maximizing the effectiveness of transport phenomena has tremendous impact on intermolecular interactions, and interfacial and bulk materials processing.[1] In every transport process, mixing has a crucial role in

RSC Green Chemistry No. 47
Alternative Energy Sources for Green Chemistry
Edited by Georgios Stefanidis and Andrzej Stankiewicz

Published by the Royal Society of Chemistry, www.rsc.org

homogenization of a specific property such as temperature or concentration and its effectiveness determines the unit energy consumption and size. This significant designation has a deterministic influence in chemical reactions that mixing and reaction rates are in the same order of magnitude in terms of characteristic time constants. In this case, mixing effectiveness affects product distribution as well.[2]

In recent years, various external energy fields such as centrifugal, electric and ultrasonic were the subject of multiple studies to offer an alternative energy source for PI purposes. In this contribution, the magnetic field is introduced as a potential energy source to enhance homogenization in fluid phases. Basically, magnetic field energy transfer to a medium requires interaction with a magnetic material. The nonmagnetic nature of conventional fluids makes the magnetic-assisted mixing supposedly impractical. Nevertheless, magnetic suspensions obtained from dispersing magnetic particles in organic or aqueous liquid media make the general idea feasible. In addition, the considerable, and also tunable, magnetization of magnetic suspensions and also well-established theories describing magnetic hydrodynamics enables modeling and design of magnetic-assisted mixing systems. In particular, the benign nature of most magnetic particles to biological samples, beside their multi-functionality and targetability, makes them attractive tools for lab-on-chip or micro-total-analysis systems.[3] However, utilization of magnetic manipulation is not limited to this classification and can be extended to the broad concept of micromixing in chemical synthesis and processing with its advantageous features in PI.[4] Besides the mixing mechanisms based on particle–field interaction, an electromagnetic field and an electrically conducting fluid lead to another type of interaction which is widely studied in the framework of magnetohydrodynamics. This type of interaction provides another opportunity for fluidic manipulations without using a fluid with artificially bestowed magnetism but necessarily reliant on its electrical conductivity.

In this contribution, the main properties of magnetic nanoparticles (MNP) are introduced and subsequently the properties of their colloidal dispersions are discussed. After a brief presentation of the governing equations of motion of polar fluids, an analysis of how magnetic fluids can be actuated, driven and exploited in a mixing application is presented. Finally, the latest theoretical and experimental findings regarding the application of magnetic fields in the actuation of magnetic fluids for mixing purposes are thoroughly presented. In the last section, the theory of magnetohydrodynamics is briefly outlined to highlight the potential mechanisms envisaged in mixing applications despite the paucity of research activities in this emerging field.

7.2 Mixing Based on Ferrohydrodynamics (FHD)

The application of magnetic nanoparticles in mixing processes has been studied for nearly a decade, however, the physical and mathematical principles of magnetic-assisted mixing phenomena have a substantial precedent in the context of FHD and magnetism. Accordingly, introducing an overview in both of these topics can be instructive prior to the presentation of any practical application. Understanding the basic physical properties of magnetic nanoparticles (MNPs) is essential because they bestow the hosting fluid medium with a polar nature that is the main consideration in the derivation of the governing equations of motion for such nanofluids. The medium of interest in this current subject of mixing is basically fluid-phase, hence the properties MNPs when dispersed in a liquid carrier should also be studied form both magnetic and hydrodynamic aspects. It should be noted that such colloidal dispersions of MNPs are also known as ferrofluids. While Brownian agitation prevents nanoparticle sedimentation and, to some extent, magnetic dipole–dipole induced agglomeration, it is insufficient to undo agglomeration by the short-range van der Waals attraction, thus requiring surfactant agents and/or the nanoparticles to be electrically charged to achieve stability of the colloidal system by providing sufficient steric or electrostatic repulsion forces on each particle surface in the carrier aqueous or organic liquid.[5]

Magnetization of magnetic particles is a size-dependent property. In the length scales ranging from several to tens of nanometers, MNPs are single domains and before approaching a critical diameter they exhibit superparamagnetism.[5] This category of particle shows considerable saturation magnetization in magnetic fields while their magnetization drastically declines when the magnetic field drops to zero and consequently results in zero coercivity. Hence, superparamagnetic nanoparticles (SMNPs) are known as soft magnets since they intrinsically have no permanent magnetism.

Aligned magnetic moments of SMNPs in the absence of magnetic fields are randomized due to thermal fluctuations. Accordingly, an important parameter for characterization of soft magnets is defined as Neelian relaxation characteristic time, which determines the time scales of randomization of magnetic moments inside the crystalline structure as a result of thermal agitation. This time scale is described by an expression in the form of eqn 7.1[6]

$$\tau_{\mathrm{n}} = \tau \mathrm{e}^{\frac{KV_{\mathrm{p}}}{k_{\mathrm{B}}T}} \tag{7.1}$$

where k_{B} is Boltzmann's constant, V_{p} is the magnetic particle core volume, K is an anisotropy constant, τ is the reciprocal of the Larmor frequency of the magnetization vector in the anisotropic nanoparticle field, and T is the temperature. As the size of nanoparticle increases, the magnetic energy barrier (KV_{p}) of domains becomes stronger and Neelian relaxation time increases exponentially. In this state, MNPs turn into hard magnets showing coercivity in their magnetization curve.[7] As the particle size further increases, the single domain of magnetic moments splits into subdomains. This energetically-favoured transition from single domain to multi-domain structure occurs at a critical diameter which is unique for each magnetic material. As an example, the magnetite critical transition diameter is estimated to be 128 nm.[5] Multi-domain magnets still show coercivity in their magnetization curves but it decreases drastically when the size of the nanoparticles increase.

The decay of magnetization by the Neelian relaxation mechanism is insignificant for hard MNPs. However, this type of MNPs can exhibit another mechanism of magnetization shuffling in the colloidal state, known as Brownian relaxation. This mechanism stems from the fact that the dispersed particles are uninterruptedly exposed to the Brownian movement of molecules in the carrier fluid the result of which is the perturbation of the magnetic moments *via* bodily movements of the nanoparticle. This relaxation time is given by eqn 7.2[6]

$$\tau_{\mathrm{b}} = \frac{3V_{\mathrm{H}}\eta}{k_{\mathrm{B}}T} \tag{7.2}$$

where V_{H} denotes the hydrodynamic volume of the particle including the surfactant layer and η is the dynamic viscosity of the liquid. It is important to note that as particle size increases τ_{n} increases exponentially while τ_{b} grows linearly. Thus, for larger particles, Neelian relaxation can be neglected when compared to Brownian relaxation.[8]

7.2.1 FHD Transport Equations

Description of the governing equations of motion for an incompressible and polar fluid makes the inference of possible mixing mechanisms theoretically possible. Derivation of FHD transport equation as accomplished by Shliomis[9] requires analysis of both linear and angular momentum transport phenomena. We can here provide a brief description of the physical basics of the mathematical derivation. In the absence of magnetic field, each nanoparticle follows the fluid velocity field (u) and can spin if the velocity field has a nonzero vorticity ($\nabla \times u \neq 0$). In the presence of a magnetic field, the exerted magnetic torque can impede or augment the intrinsic spin of nanoparticles.[10] The particles, as a result of external torque, gain an internal angular momentum which is in continuous exchange with external angular momentum of the entire fluid resulting in a net total angular momentum of the colloidal suspension. Assuming magnetic colloids as a polar continuum—each fluid sub-continuum element is in both angular and linear momentum exchange with its surrounding classical linear momentum transport—is no longer valid in such systems. The asymmetric nature of the stress tensor in the equation of motion modifies the linear momentum transport formulation in the form given by eqn (7.3).

$$\rho\frac{\mathrm{D}\mathbf{u}}{\mathrm{D}t} = -\nabla p + \rho\mathbf{F} + 2\zeta\nabla \times \boldsymbol{\omega} + (\zeta + \eta)\nabla^2\mathbf{u} \tag{7.3}$$

where ρ is the fluid density, $\boldsymbol{\omega}$ is the spin density vector, p is the hydrodynamic pressure, ζ is the vortex viscosity and $\mathbf{F}$ is the sum of gravitational and magnetic body forces.

For the angular momentum transport, one has:

$$\rho I\frac{\mathrm{D}\boldsymbol{\omega}}{\mathrm{D}t} = \rho\mathbf{G} + \mathbf{A} + (\lambda' + \eta')\nabla\nabla \cdot \boldsymbol{\omega} + \eta'\,\nabla^2\boldsymbol{\omega} \tag{7.4}$$

where λ' is the bulk spin viscosity, η' is the shear spin viscosity and $\rho\mathbf{G}$ is the magnetic angular momentum received from the external magnetic field ($\mu_0\mathbf{M} \times \mathbf{H}$) to the magnetic body and its value is reduced or augmented by **A**. Physically, **A** is an outcome of the asynchrony between the rotation of fluid sub-continuum originating from inherent vorticity and magnetically-driven spin. Thus, this parameter should be a function of their difference correlated with a coefficient referred to as vortex viscosity:

$$\mathbf{A} = 2\zeta(\nabla \times \mathbf{u} - 2\boldsymbol{\omega}) \tag{7.5}$$

For a magnetic material, the magnetic body force density ($\mathbf{F_m}$), also known as Kelvin force, is expressed as follows:[6]

$$\mathbf{F_m} = \mu_0(\mathbf{M}\cdot\nabla)\,\mathbf{H} \tag{7.6}$$

where μ_0 is the vacuum permeability, **M** is the magnetization vector and **H** is the magnetic field vector. Kelvin force manifests itself when there is a spatial heterogeneity in the applied magnetic field or magnetic susceptibility of the colloidal suspension.

The magnetization vector in eqn (7.3) and (7.4) is not necessarily aligned with the applied magnetic field lines and may be shifted and perturbed from the saturation magnetization ($\mathbf{M}_0$) in a fluid experiencing a magnetic field. By introducing a mathematical description of each phenomenon playing a role in magnetization, a phenomenological equation for magnetization can be derived in the following form:[9]

$$\frac{\mathrm{D}\mathbf{M}}{\mathrm{D}t} = \boldsymbol{\omega} \times \mathbf{M} + \tau^{-1}\left(\mathbf{M} - \mathbf{M}_0\right) \tag{7.7}$$

The first term in the right hand side of this equation represents the shift of the magnetization vector while rotating in an average angular velocity $\boldsymbol{\omega}$ whereas the second term defines perturbation of the magnetization as a result of relaxation. MNPs exhibit dissimilar behaviors in response to various magnetic fields. Consequently, in the following sections, the interplay between magnetic fields and MNPs, possible realizable mixing mechanisms and the most recent practical approaches will be explained.

7.2.2 Mixing with Static Magnetic Fields (SMF)

SMF are invariant in time and can be spatially uniform or non-uniform. While a moderate intensity magnetic field applied to a stagnant and homogeneous ferrofluid cannot trigger any directional manipulation and movement of nanoparticles,[8] a magnetic field applied to a sheared ferrofluid may affect the linear momentum or the angular movement of suspended particles. Any individual particle in a velocity field such that $\nabla \times u \neq 0$ freely rotates with fluid vorticity as result of hydrodynamic torque. A normal to vorticity magnetic field impedes free rotation of particles whereas the stationary magnetic torque resists the hydrodynamic torque. This resistance to rotation induces an additional dissipation of fluid kinetic energy and is known as positive magnetoviscosity.[11] In Section 7.2.4 the experimental attempts to explore mixing in this condition will be discussed.

If the magnetic field direction is in the same direction as the vorticity vector, the magnetization vector is superposed on the axis of rotation without any interference with the exerted hydrodynamic torque and accordingly particles have no angular momentum exchange with their carrier. In this condition, a linear momentum transport balance with an additional term accounting for magnetic body force (Kelvin force) will suffice to describe fluid flow.[12] We will show how this situation can be exploited in a mixing application but primarily, to better unveil the potential of Kelvin force on mixing, a vector operation on eqn (7.6) can be instructive. By using the vector identity:

$$(\mathbf{H}\cdot\nabla)\,\mathbf{H} = \tfrac{1}{2}\nabla(\mathbf{H}\cdot\mathbf{H}) - \mathbf{H}\times(\nabla\times\mathbf{H}) \tag{7.8}$$

Assuming the magnetic susceptibility (χ_i) as being equal to the ratio of magnetization vector to magnetic field, then the Kelvin force can be rewritten as:

$$\mathbf{F_m} = \tfrac{1}{2}\mu_0\nabla(\chi_i\mathbf{H}\cdot\mathbf{H}) - \mathbf{H}\times(\nabla\times\mathbf{H}) \tag{7.9}$$

By applying Ampere's law for magnetic fields ($\nabla \times \mathbf{H} = 0$):

$$\mathbf{F_m} = \frac{1}{2}\mu_0|\mathbf{H}|^2\,\nabla(\chi_i) + \frac{1}{2}\mu_0\chi_i\nabla(\mathbf{H}\cdot\mathbf{H}) \tag{7.10}$$

Eqn (7.10) suggests two conceivable mechanisms for driving a magnetic fluid. The first mechanism is based on the spatial heterogeneity of magnetic field intensity as expressed in the second term of the right-hand side of eqn (7.10). The second mechanism is based on the fact that magnetic susceptibility is a concentration-dependent parameter. This means that, even in a uniform magnetic field and gradient magnetic concentration, a driving force for the movement of MNPs also possibly exists.

Tsai *et al.*[13] presented the first application of SMF in mixing by placing a permanent magnet with moderate magnetization (2.2 Kg) underneath the channel of a Y-mixer with the magnetic field perpendicular to the flow direction. Mixing performance, characterized based on visualization in an observation window downstream of the channel, shows near complete mixing between magnetic and nonmagnetic fluids flowing alongside each other in Reynolds numbers of about unity. Mixing between (nonmagnetic) water and a ferrofluid on the basis of pure diffusion shows no prominent evolution downstream of the channel, however, the indistinct and blurred interface confirms that MNPs protruded into the contiguous stream when the magnet was placed under the channel.

Characterization of mixedness based on visualization can reveal how MNPs are dispersed into a sample for specific applications when MNPs are the targeted materials and their uniform dispersion in another sample is crucial. However, one may expect a thorough homogenization between fluids wherein MNPs act exclusively as mixers. The unique property of ferrofluids makes the latter objective possible. Every magnetic particle dispersed in a carrier liquid is in intermolecular interactions with chemisorbed surfactant and solvent molecules. Particles moving in a specific direction will drag the accompanying solvent molecules inducing bulk movement of the whole nanofluid, a phenomenon analogous to electroosmotic flow. Zhu *et al.*[14] experimentally verified such behavior in a microfluidic device designed for water/ferrofluid mixing studies and confirmed simultaneous homogenization of both MNPs and solvents. The geometry of the studied system is a circular chamber, 1 mm in diameter with three inlets. With such configuration of inlet channels, two flow patterns can be established. In one pattern, ferrofluid is the core stream and in the other one is the cladding one. A uniform magnetic field with adjustable intensities up to 10 mT is applied perpendicular to the main flow direction as depicted in Figure 7.1.

Prior to experimental investigations, the mixing efficiency between ferrofluid and water was predicted by solving the coupled linear momentum transport and advection–diffusion equation of concentration in the conditions that Reynolds number is close to 1. By assuming a linear relationship between magnetic susceptibility and MNP concentration, velocity of the suspension and concentration distribution of MNPs can be calculated. Despite

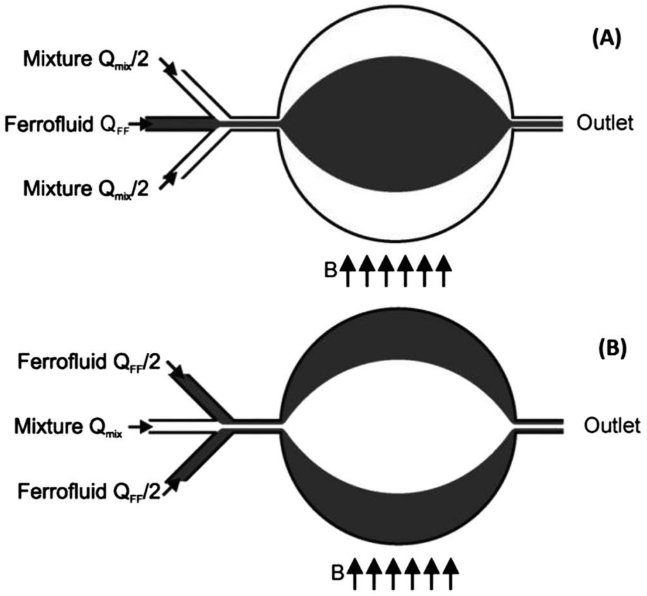

Figure 7.1 Schematics of the flow of ferrofluid and water in (A) ferrofluid-core and (B) ferrofluid-cladding configurations. (Reproduced from ref. 14 with permission from the Royal Society of Chemistry.)

the magnetic field direction being apparently normal to fluid vorticity the effect of angular momentum exchange on velocity profiles is neglected in the adopted formulation. Nonetheless, the simulation results depicted in Figure 7.2 show that in the absence of magnetic force all the velocity vectors include axially directed components while magnetic actuation can produce vertical components as well. This deviation from parabolic profile is even more severe in the cladding pattern in which the flow field in some regions exhibits remarkably irregular and vortical patterns. Thus, it is expected that the magnetic force perpendicular to the flow direction can drag magnetic fluid toward nonmagnetic regions and reduce the diffusion path.

Calculated and measured mixing efficiencies in the ferrofluid cladding configuration are higher for specified flow rates. However, for both configurations, a magnetic flux *ca.* 10 mT is required to reach the maximum mixing efficiency and also a minimum magnetic intensity is required to trigger magnetic force and evince its effect.

Since the simulated and experimental mixing efficiencies are based on concentration distribution of MNPs, an uncertainty in concentration uniformity of carriers in both flow patterns exist. To resolve this ambiguity, the authors devised an experiment in which a mixture of water and fluorescent dye flows on one side and ferrofluid flows next to it in the same fluidic cell. Analysis of fluorescent dye intensity in the entire cell under the action of SMF reveals a relatively uniform pattern and validates homogeneous distribution of the carrier fluid as well as the magnetic nanoparticles in the entire volume of the mixing chamber.

Wen *et al.*[15] further scrutinized the mixing mechanism under SMF and demonstrated the effect of magnetic fields on stretching magnetic fluids and on the inception of instabilities in micro-devices. The observed and simulated transient concentration patterns provide a more vivid understanding of the dominant mechanism for the enhanced mixing. As depicted in Figure 7.3, the studied mixer consists of an electromagnet placed alongside the exit channel of a Y-mixer with a 1000 × 150 μm cross-section.

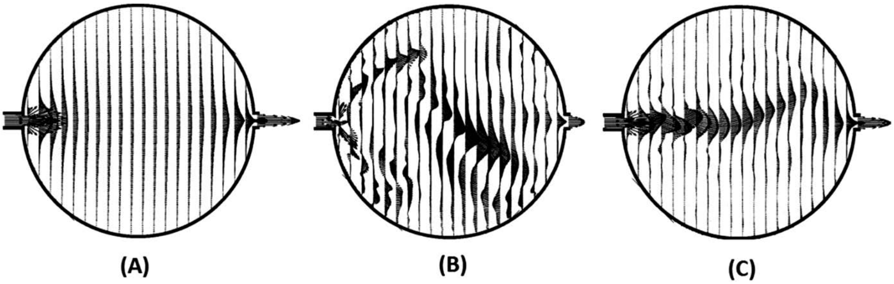

Figure 7.2 Simulated velocity profiles (A) with no magnetic field, (B) with applied uniform magnetic field in ferrofluid-cladding and (C) ferrofluid-core configurations. (Reproduced from ref. 14 with permission from the Royal Society of Chemistry.)

The fluids in contact are water and a ferrofluid consisting of 10 nm magnetite nanoparticles. The degree of mixing is quantified by grayscale analysis of three observation windows nearby: up-, mid- and downstream of the channel. The adopted formulation to model the fluid motion is similar to the approach of Zhu *et al.*, however, in the magnetic body force term, the gradient of magnetic susceptibility is neglected without justification and, instead, a magnetic force field as a result of gradient magnetic field is considered as a body force. Spatial non-uniformity in the magnetic field imposes some difficulties in the calculation of the magnetic force field. It requires numerically solving Maxwell–Ampere's law and Gauss's law for magnetic flux density provided that the coil geometry and current in the electromagnet are known.

A mixing process without application of magnetic field would result in less than 20% homogeneity while a magnetic field having 90 Oe peak strength improves mixing up to nearly 95%. The simulated and observed concentration profiles confirm development of instabilities in the shape of narrow finger structures in up- and downstream channel regions as illustrated in Figure 7.4.

These structures reduce the diffusion path from the length scale of the device to the fingers. By virtue of a scaling analysis of diffusional transport, the role of instabilities in promoting mixing can be interpreted with order of magnitude estimations:[16]

$$t_{\mathrm{m}} = l^2/D_{\mathrm{i}} \tag{7.11}$$

where t_{m}, l and D_{i} are, respectively, the diffusion time, length and coefficient. The mixing time between two parallel streams in the length scale of 1 mm with an approximate diffusion coefficient in the order of 10^{-9} m^2 s^{-1} can be estimated to amount to *ca.* 1 ks. The length of observation window

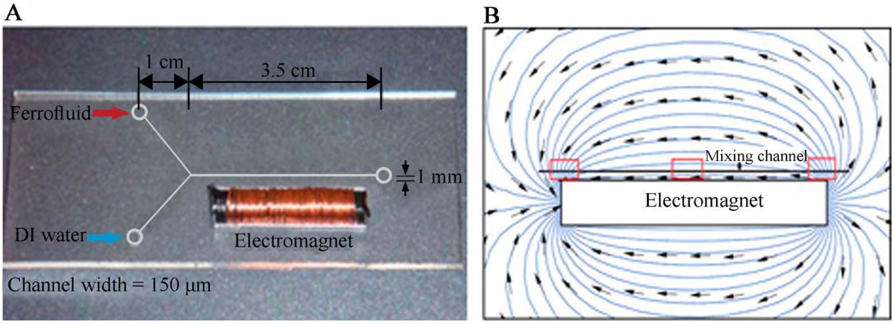

Figure 7.3 (A) Microfluidic chip with electromagnet (B) simulated magnetic field lines with corresponding peak strength of $H = 60$ Oe. The three rectangles in (B) represent observation windows for mixing quality evaluation based on grayscale analysis. (Reproduced from ref. 15 with permission from John Wiley and Sons. Copyright © 2011 WILEY-VCH Verlag GmbH & Co. KGaA, Weinheim.)

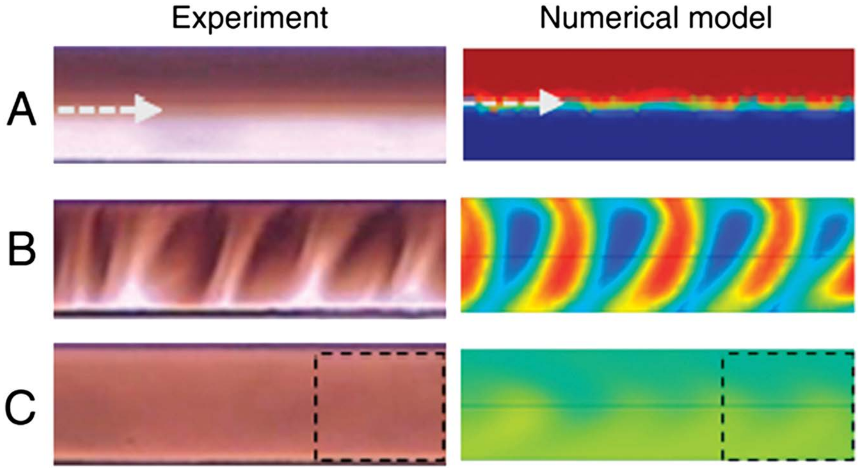

Figure 7.4 Experimental observation and numerical prediction of finger-shaped instabilities development in the observation windows at t = (A) 0 s (B) 0.5 s (C) 2 s for magnetic field peak strength H = 60 Oe. (Reproduced from ref. 15 with permission from John Wiley and Sons. Copyright © 2011 WILEY-VCH Verlag GmbH & Co. KGaA, Weinheim.)

in Figure 7.4 tests is 700 μm leading to finger lengths of the order of 100 μm corresponding to a time scale of diffusion *ca.* 10 s. In accordance with scaling analysis, the experimental time for a complete mixing is about three seconds. It is important to note that development of fingers cannot be generalized to all the processes in which a magnetic fluid penetrates into an aqueous nonmagnetic fluid on account of the ferrofluid viscosity which is typically multiple times that of water.

In addition, magnetic field orientation has a pronounced impact on the formation of instabilities. In fact, the finger structuring is favored in the regions where the magnetic field is oblique to flow direction. In contrast, the parallel magnetic field lines between two poles have a stabilizing effect and can transmogrify fingers into parallel strips. In the downstream region, fingers are formed once again and finally the concentration gradients fade away. Such a stabilizing effect of parallel magnetic fields has been previously reported by Rosensweig.[17]

7.2.3 Mixing with Oscillating Magnetic Fields (OMF)

Various parameters influence nanoparticle motion in an OMF and before any attempt to deduce a mixing mechanism, it is important to clarify nanoparticle and magnetic field interactions. The response of MNPs to an OMF is acutely reliant on intensity and frequency of the OMF, the relaxation time constant of MNPs (τ_B) and the hydrodynamic time constant ($\tau_h = 1/|\nabla \times \mathbf{v}|$).[10,18] When the magnetic field oscillation time scale ($\tau_{AC} = 1/f_{AC}$) exceeds the nanoparticle Brownian characteristic time or the nanofluid hydrodynamic relaxation, the magnetic field will not single out a preferred direction for a collection of rotating nanoparticles. Incidentally, as soon as the magnetic field intensity falls from the amplitude peak to zero or rises from the amplitude valley to zero, in those brief moments where the field reaches nearly zero value, the magnetization vector becomes very loosely locked to the magnetic field direction and can thus be disrupted through hydrodynamic shear or, randomly, through Brownian relaxation. Thus, when the magnetic intensity reaches its highest algebraic value over the next quarter of an oscillation, the magnetic moment vector of each nanoparticle aligns itself anew with that of the magnetic field. Such random orientation in each half-cycle will not allow the MNPs to rotate in single direction.[18] In such case ($\tau_{AC} > \tau_h$ or $\tau_{AC} > \tau_B$, see Figure 7.5a and b) the measured viscosity known in the literature as positive rotational viscosity ($\nabla\eta > 0$) is inflated.[8] On the other hand, when the period of oscillation is fast enough ($\tau_B > \tau_h > \tau_{AC}$), the competing phenomena are not able to significantly deviate the magnetization vector and the nanoparticles are forced to rotate in synchrony with the magnetic field. In the brief moment of zero intensity, the hydrodynamic torque will flip the nanoparticles to rotate in the same direction as the fluid vorticity. Furthermore, owing to the exerted magnetic torque, the nanoparticle angular velocity is accelerated to align its magnetization vector parallel to the magnetic field direction. This sequence replicates itself over each half-period and leads to a nonzero macroscopic angular velocity of nanoparticles.[18] In this case, energy transfer from the AC magnetic field to the fluid flow *via* rotating MNPs occurs. This oriented energy transfer decreases apparent viscosity of the ferrofluid and leads to a negative rotational viscosity ($\nabla\eta < 0$, see Figure 7.5c).

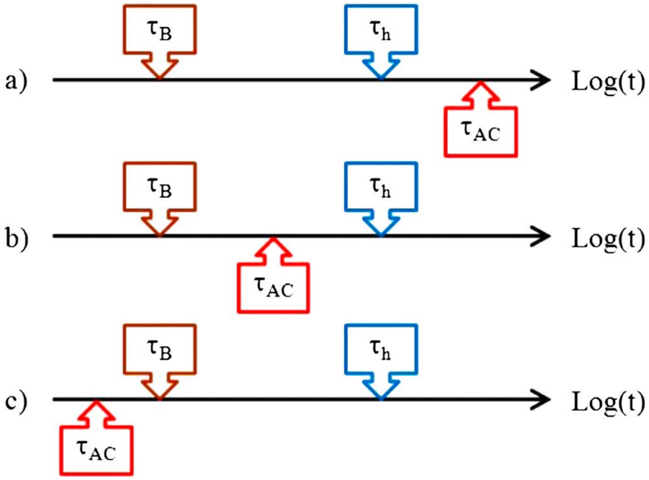

Figure 7.5 Impact of AC-field magnetoviscosity phenomena with respect to the relative order of Brownian, hydrodynamic and AC time scales: (a) $\tau_{AC} > \tau_h > \tau_B$, $\Delta\eta > 0$; (b) $\tau_h > \tau_{AC} > \tau_B$, $\Delta\eta > 0$; (c) $\tau_B > \tau_h > \tau_{AC}$, $\Delta\eta < 0$

Rotating microparticles and nanoparticles, as theoretically and experimentally evidenced,[19–21] can resemble a magnetic stirrer and can have a profound impact on mixing. If one wishes to implement mixing with OMF with a mechanism tantamount to rotating microparticles, the operating parameters should be appropriately adjusted. Normally, Brownian relaxation time of MNPs in the size of 10 nm in aqueous media, in the order of 10 μs, necessitates application of the OMF typically with frequencies as high as 100 kHz. Hence, moderate frequencies are practically inoperative in mixing applications. Experimental proof of this statement will be described in Section 7.2.4. However, an oscillating field with moderate frequency can also stir magnetic fluids to promote mixing on the basis of a similar Kelvin force-driven mixing mechanism as for SMF. Whether the Kelvin force is based on application of a spatially non-uniform magnetic field or magnetic susceptibility, the governing equations of motion are those described in Section 7.2.4 but in case of an OMF, the magnetic field intensity is time dependent, often sine wave-like.

Wen *et al.*[15,22] investigated the mechanism for enhanced mixing between magnetic and nonmagnetic fluids in Y-mixers with similar characteristics as described earlier in Section 7.2.2 The pathway of mixing in the observed and simulated transient evolution of concentration profiles is analogous to what has been investigated in the case of SMF. Finger-shaped arrays similarly developed under the action of OMF in the regions where the oscillating field is oblique to the flow direction while in the midstream the interface is stabilized and perturbed again when passing the second pole of the electromagnet. The findings of Wen *et al.* also show that a magnetic field normal to the water/ferrofluid interface can produce fingers if the magnetic field intensity passes a threshold and a critical magnetic intensity exists for the onset of instabilities on the interface. When the magnetic field intensity is less than a critical value, the narrow fingers evolve into broader shark-like fins whereby the mixing performance drops as a consequence.

Munir *et al.*[23] reported application of residence time distribution (RTD) analysis in theoretical characterization of ferrofluid flow in a rectangular channel under OMF. The RTD of magnetic fluid was numerically predicted while the fluid is flowing in a channel with two current-carrying conductors on the top and bottom surfaces of the conduit (see Figure 7.6).

The direction of current in each conductor is perpendicular to the flow direction and can be in the same or opposite direction with respect to one another. In such configuration, each conductor generates a non-uniform circular magnetic field with higher intensity near the conductor surface. Once a concentration pulse of MNPs suspension is fed into the channel, the average concentration of MNPs at a point downstream of the channel can be calculated by solving the coupled convection–diffusion and linear momentum transport equations. According to these authors' simulations, the residence time distribution of the nanofluid in a magnetically-actuated system with various actuation scenarios is narrower in shape,

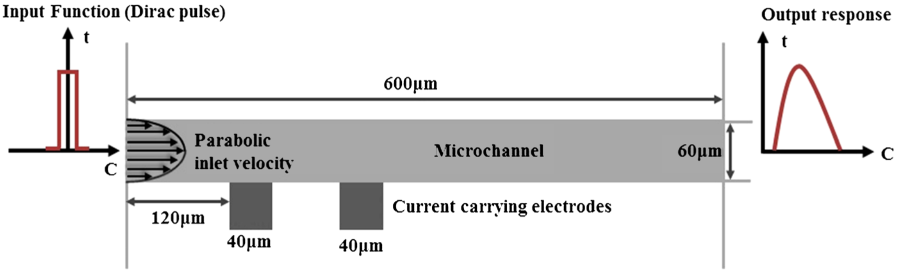

Figure 7.6 Schematic representation of confined space for numerical analysis of RTD.[29] (Reproduced from *Microfliud. Nanofluid.*, **10**, 2010, Residence time distribution analysis of magnetic nanoparticle-enhanced mixing using time-dependent magnetic actuation in microfluidic system, A. Munir, © Springer-Verlag 2010. Reprinted with kind permission from Springer Science and Business Media.)

i.e., of slimmer variance, in comparison to the conditions when axial dispersion is governed by diffusion and advection. The dependency of magnetic susceptibility on the MNPs' concentration triggers a Kelvin force and by manipulating the current direction in each conductor, periodic pulling and pushing forces on the MNPs prompt secondary vertical velocity components. However, these simulations kept silent about the computed velocity profiles though in accordance with the narrower RTD signals, the magnetic field might possibly have altered the parabolic character of the velocity profile.[24]

The approach of Munir *et al.* to induce magnetic disturbances in a fluid flow undeniably requires MNPs concentration gradients. In absence of concentration gradients, thermal agitation is in permanent interference with magnetic energy to undertake nanoparticles' motion and would oppose magnetic forces to harness the MNPs. Therefore, the effectiveness of a magnetic field should be quantitatively assessed in comparison to thermal perturbation of nanoparticles. To perform such analysis, a dimensionless number expressing the ratio of magnetic energy to Brownian kinetic energy can be used.[8] This ratio is described by eqn (7.12).

$$R = \frac{\mu_0 M \pi d^3 H}{6 k_B T} \tag{7.12}$$

where d is the diameter of the MNPs. For a suspension of magnetite nanoparticles with the average size of 10 nm, the intensity of magnetic field should be larger than 100 kA m^{-1} to ensure $R \approx 1$. This analysis reveals that nanofluid flow characteristics such as RTDs cannot be manipulated magnetically using a moderate OMF. An effective mechanism of mixing even in homogeneous ferrofluids will be explained in the category of rotating magnetic fields in the Section 7.2.4.

7.2.4 Mixing with Rotating Magnetic Fields (RMF)

Application of RMF in mixing with the assistance of magnetic particles was first theoretically conceived by Calhoun.[25] A collection of magnetic particles can form various types of assemblies bound together by interacting magnetic dipoles. These assemblies rotate when they are subjected to RMF and can promote the mixing rate in two different regimes identified by the structure of chains. In the first regime, whenever stronger dipole interactions prevail between particles in comparison to the shear forces exerted on the assembly's body, a collection of particles leads to stable magnetic chain stirrers. In the second regime, on the contrary, the shear forces are able to overcome and weaken the dipole interactions undoing the chains which experience continual formation and breakup. Demarcation between these two regimes is characterized by a dimensionless number proposed by Gao *et al.*[26] which accounts for the ratio of hydrodynamic torque to magnetic torque for a collection of N particles in a RMF rotating with frequency f:

$$R_{\mathrm{T}} = \frac{16\eta f N^3}{\mu_0 \chi_{\mathrm{i}}^2 H^2 \left(N-1\right)\left(\mathrm{Ln}\left(\frac{N}{2}\right)+2.4N\right)} \tag{7.13}$$

It is experimentally shown and theoretically proven[25,26] that rotation of particle assemblies is subject to reformation and breakup sequences for $R_{\mathrm{T}} < 1$ whereby mixing times are lesser than for the conditions when $R_{\mathrm{T}} > 1$. When used in typical mixing applications, this method requires mixing times in the order of several minutes. In addition, Wittbracht *et al.*[27] estimated effective diffusion coefficient with magnetic particle stirrers to be only 32% higher than pure diffusion.

It was argued earlier in Section 7.2.1 that rotating MNPs can exchange their magnetic angular momentum (or internal angular momentum) with the surrounding fluid. In an oscillating magnetic field, the state of momentum transport is frequency dependent and also fluid vorticity is *sine qua non* a trigger for rotation. In a rotating magnetic field, in contrast, a magnetic torque is constantly exerted on the nanoparticles setting them into rotation even in the absence of bulk advective fluid flow. Magnetically-excited angular momentum can drive the carrier fluid and produce an external angular momentum which manifests itself as a torque-driven flow.[28] Besides this macro scale effect of internal rotation of a magnetic fluid, another phenomenon pinpointed in smaller scales by Hajiani and Larachi[19] can prove to be an efficient mixing tool. The mechanism supporting this phenomenon is based on a conception that every nanoparticle will drag the surrounding fluid by means of viscous forces prompting vortex formation around each nanoparticle. Spinning of the nanoparticles causes entrainment of their neighboring fluid elements resulting in an effective reduction of the diffusion length scales. The discussion to follow provides experimental evidence in support of such a postulated mechanism for the mixing ability of dispersed MNPs in a fluid carrier subject to RMF. It is first instructive to have a glimpse on a recent study by Gravel *et al.*[29] who used an optical method for the visualization of the MNP suspension stimulated by RMF. An example of microscopic images of a suspension consisting of 16 nm MNPs at 0.005 volume fraction is shown in Figure 7.7.

Although vortices in the submicron range cannot be detected at such level of scrutiny in Figure 7.7, the coherent vortical structures in the larger scales are discernible. The work of Gravel *et al.* confirmed that formation of vortices and their size depends on various operating variables such as RMF frequency and intensity, and magnetic volume fraction and nanoparticle size. Prior to providing any explanation for the emergence of such vortices, it is worth mentioning that every two co-rotating vortices when reaching a critical distance go through an elliptical deformation, diffuse into each other and grow in size. The two deformed vortices will finally form a single structure. This phenomenon, known as vortex merger, is strongly dependent on vortex radius, a, and inter-vortex separation distance, b. Various criteria for the merging condition as a function of a/b ratio have been reported.[30] By extension an analogy can be drawn between vortex merger at the micron scale, as discussed above, and the merger of vortices prompted by the rotating magnetic nanoparticles at

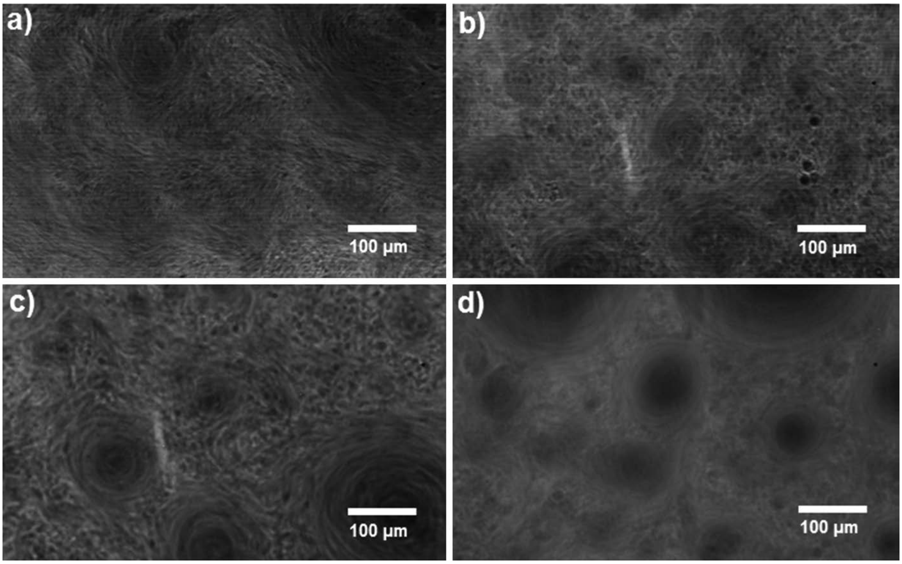

Figure 7.7 Optical images of magnetic suspension of 16 nm magnetite nanoparticles submitted to a uniform RMF of 31.4 kA m^{-1} with a frequency of (a) 10 Hz (b) 50 Hz (c) 100 Hz (d) 200 Hz. Suspension consists of 0.005 volume fraction of MNPs.[29] (Reproduced from *Chem. Eng. J.*, **260**, O. Gravel *et al.*, Inception of vortical coherent structures from spinning magnetic nanoparticles in rotating magnetic fields – New nanofluid microscale mixing tool, 338–346, Copyright (2015) with permission from Elsevier.)

the nanometer scale. Interestingly, as RMF frequency is increased, the coherent structures become larger in size which is conceivably due to the larger spheroids around each nanoparticle as illustrated in Figure 7.7.

Vortex size cannot grow limitless but showcases a limiting size after a certain frequency of rotation is attained. Such a growth limit may be explained by considering the act of hydrodynamic forces on the larger assembly of MNPs inside a vortex and their subsequent breakdown, a process similar to deformation of rotating chains of magnetic microparticles. Ultimately, merging and deformation reaches an equilibrium state leading to a specified distribution of vortex size. Larger MNP concentrations tantamount to reduced inter-particle distances increase the likelihood of merging. Emergence of these vortices within the MNP suspension is evocative of turbulent eddies in which motion is manifested into pseudo-turbulence by conversion of magnetic energy, *via* magnetic torque, into kinetic energy transferred to the carrier fluid.

Experimental studies by Hajiani and Larachi[19] revealed that stimulated transport at such small scales in ferrofluids subject to RMF is prone to reduce significantly the diffusion time scales. For this purpose, self-diffusion coefficients of diluted ferrofluid in a capillary tube have been measured by means of an electrical conductimetry method. The capillary has 1 mm inner diameter and 40 mm length with two pairs of conductivity wire electrodes located at equal distances from both ends. By injecting a brief tracer pulse at one end, the transient evolution of electrical conductivity near each probe can be monitored over time. A uniform rotating magnetic field is generated by six current-carrying coils on the periphery of a hollow cylinder and the capillary tube is placed in the bore space normal to the cylinder central axis as illustrated in Figure 7.8. Each pair of coils located across each other is energized with an alternating current (AC) with a specific frequency and the currents in

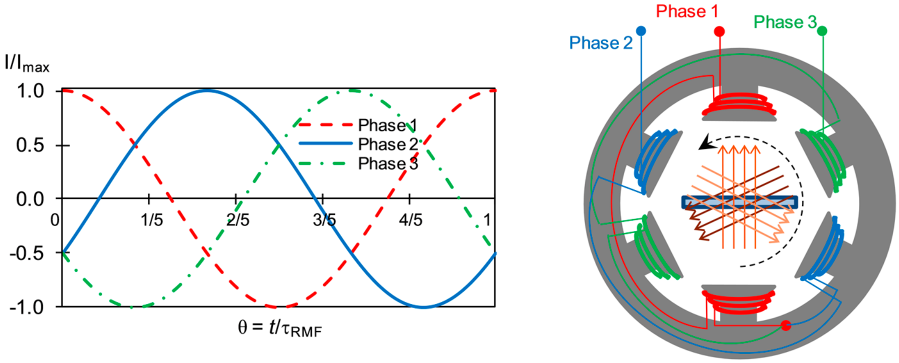

Figure 7.8 Schematic of 2-pole 3-phase magnetic field generator top view and the inserted capillary cell.[19] (Reproduced form *Chem. Eng. Process.*, **71**, P. Hajiani and F. Larachi, Giant effective liquid self-diffusion in stagnant liquids by magnetic nanomixing, 77–82, Copyright (2013) with permission from Elsevier.)

each pair are phase shifted by 2π/3 thus providing a rotating magnetic field with a rotation frequency equal to the frequency of the AC currents. If two adjacent coils with the corresponding ones across them are energized with an AC current, the resulting magnetic field will be an oscillating one with the direction normal to the center axis of the magnet bore. A SMF with similar direction can also be generated if the AC current is switched to DC.

It was observed that the time required to reach equilibrium with equalized conductivities registered at both capillary ends is reduced from about 1300 min to 10 min upon enabling RMF with frequency and intensity as high as 100 Hz and 31.4 kA m^{-1}, respectively. Initiation of other mixing mechanisms, such as those induced by Kelvin force, is precluded under such experiments because the injected tracer pulse consisted of the same magnetic concentration as the ferrofluid already present inside the cell. The estimated diffusion coefficient of such a magnetically-actuated system neared two hundred times the normal self-diffusion coefficient of the diluted ferrofluid. Furthermore, the diffusion coefficient increases with the magnetic field rotational frequency though the enhancement tends to plateau beyond a certain frequency. This is in accordance with optical observations of Gravel *et al.*[29] which reveal that after a specified frequency, vortex growth was halted. Likewise, amplification of the magnetic field follows qualitatively a similar trend by strengthening the nanostirrers' agitation. Measurement of the diffusion coefficient at high frequencies as a function of RMF intensity shows an ascending trend confirming the advantageous effect of magnetic field intensity.

The concept of nanostirrers active within stagnant fluids has also been extended to dilute (0.001 to 0.005 volume fraction) ferrofluids in motion by Hajiani and Larachi.[24,31] The authors showed that RMF active in the plane transverse to the flow direction can notably modify the flow characteristics reducing the axial dispersion coefficient (D) in laminar flow and also enhancing the lateral mixing. Dispersion was quantified by means of tracer pulse tests and by fitting an open–open axial dispersion RTD model.[32] The axial dispersion coefficients thus obtained were found to decrease upon enabling the RMF. This can be visually picked up from the narrower residence time distributions despite Reynolds numbers corresponding to purely laminar flows. Figure 7.9 illustrates such dependency *versus* Reynolds number for various RMF frequencies. The magnetic field parameters have also considerable effects on axial dispersion in a manner similar to that exemplified earlier in the case of self-diffusion coefficients. Similarly, higher frequencies of RMF drastically reduce axial dispersion while after a certain frequency, this exhibits no further reduction.

7.2.4.1 Comparison of RMF with OMF and SMF in Lateral Nanomixing of Ferrofluid Capillary Flows

It was previously explained that low frequency OMF cannot result in any single oriented rotation of MNPs. Yet another experimental evidence of such a phenomenon can be observed when the capillary tube is perpendicular

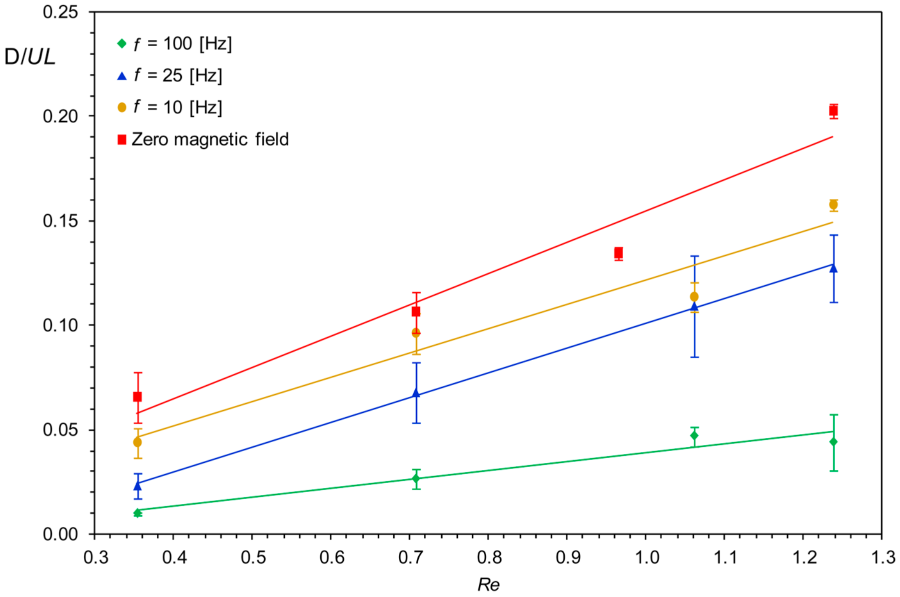

Figure 7.9 Effect of Reynolds number and RMF frequency on axial dispersion coefficient shown as a dimensionless number. Experiments performed with $\varphi = 0.001$, $H = 31.4$ kA m^{-1}.[24] (Reproduced from *Chem. Eng. J.*, P. Hajiani and F. Larachi, Reducing Taylor dispersion in capillary laminar flows using magnetically-excited nanoparticles: Nanomixing mechanism for micro/nanoscale applications, 492–498, Copyright (2012) with permission from Elsevier.)

to the OMF direction. In the range of tested frequencies, *i.e.*, 10 to 100 Hz, no pronounced variation in axial dispersion can be observed. Undoubtedly, Brownian relaxation for *ca.* 16 nm MNPs of the order of 10 µs is notably shorter than the RMF period (0.1 to 0.01 s). The momentary zero passage of OMF will reshuffle randomly the orientation of the MNP magnetic moments, thus over the whole cycle the net rotation direction of the nanoparticles is zero. Therefore a mechanism for mixing similar to RMF cannot be expected from low frequency OMF. Figure 7.10 portrays how RMF and OMF affect axial dispersion coefficients as a function of frequency.

The effect of SMF has also been studied by Hajiani and Larachi[31] but in that case flow direction and magnetic field were set parallel to each other to investigate how competing magnetic and hydrodynamic torque affect the flow characteristics. SMF, depending on its intensity and also MNP concentration, can evince different impacts on axial dispersion. In low intensity fields, the magnetic torque exerting on the nanoparticles is not strong enough to overcome the hydrodynamic torque, while after a certain magnetic field intensity, RTD signals broadened corresponding to inflating axial dispersion coefficients in contrast to the effect of RMF. This dependency is depicted in Figure 7.11.

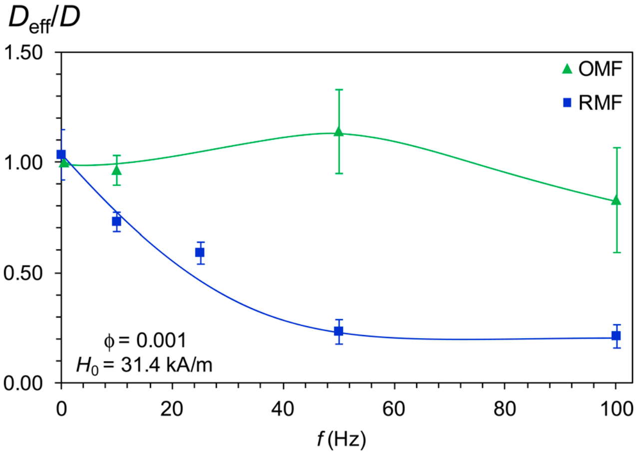

Figure 7.10 Ratio of axial dispersion coefficient under the effect of magnetic field (D_{eff}) to reference axial dispersion coefficient at $H = 0$ and $\varphi = 0$ (D) as a function of RMF and OMF frequency.[31] (Reproduced from *Chem. Eng. J.*, **223**, P. Hajiani and F. Larachi, Controlling lateral nanomixing and velocity profile of dilute ferrifluid capillary flows in uniform stationary, oscillating and rotating magnetic fields, 454–466, Copyright (2013) with permission from Elsevier.)

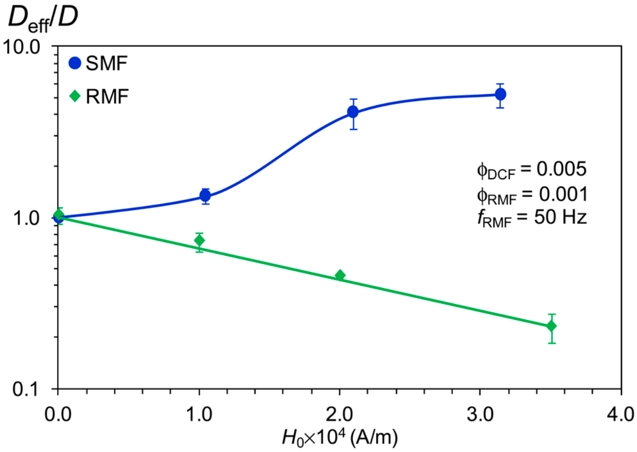

Figure 7.11 Relative axial dispersion evolution under RMF and SMF *versus* magnetic field strength. Magnetic volume fractions in RMF and SMF are 0.001 and 0.005, respectively.[31] (Reproduced from *Chem. Eng. J.*, **223**, P. Hajiani and F. Larachi, Controlling lateral nanomixing and velocity profile of dilute ferrifluid ferrifluid capillary flows in uniform stationary, oscillating and rotating magnetic fields, 454–466, Copyright (2013) with permission from Elsevier.)

SMF with enough strength locks the MNPs to prevent their free rotation as a result of flow vorticity. These locked nanoparticles will impede the regular sliding of fluid layers in which the MNPs are present. Therefore, fluid velocity in these layers is flattened and a zero gradient region appear locally in the entire velocity profile. In return, the adjacent layers showcasing MNP depletion will compensate fluid mass continuity by an increased axial velocity. This would result in a protruding axial velocity profile, the increased variance of which subsequently leads to inflated axial dispersion coefficients.

Alteration of the velocity profile under the action of RMF can also be conjectured since every rotating nanoparticle imposes a velocity component on the plane perpendicular to the flow direction. In addition, the reduced axial dispersion coefficient specifies a more flattened velocity profile whereas the fluid layers smear the injected tracer blob less than a parabolic distribution. Besides, the mixing ability of MNPs and their influence on velocity profile could prove promising in process intensification applications.[1]

7.3 Lorentz Force-Driven Mixing

Unlike FHD, whose theoretical framework addresses fluid motion by means of magnetically stimulated MNPs, the study of the interactions between electromagnetic fields and electrically conducting fluids pertains to the realm of magnetohydrodynamics (MHD). In this section, the governing theory, as well as experimental and theoretical achievements in MHD-assisted mixing will be discussed. Since Lemoff and Lee[33] divulged the ability of MHD for non-mechanical pumping of fluids, especially for applications in micro total analysis systems, numerous attempts have been devoted to exploit MHD in micro-pumps, heat exchangers, analytical and biomedical devices.[34] In addition, Bau *et al.*[35] reported the first application of MHD for stirring. Similar to the subject of FHD-assisted mixing, an introduction to MHD is instructive to better understand, compare and predict the behavior of conducting fluids subject to electromagnetic fields.

The principle of MHD is based on the Lorentz body force experienced by a current-carrying body in a magnetic field. The linear momentum transport equation including this body force is:

$$\rho\frac{\mathrm{D}\mathbf{u}}{\mathrm{D}t} = -\nabla p + \mathbf{J}\times\mathbf{B} + \eta\nabla^2\mathbf{u} \qquad (7.14)$$

Where $\mathbf{J}$ is the current density which, according to Ohm's law, can be written as

$$\mathbf{J} = \sigma(\mathbf{E} + \mathbf{u}\times\mathbf{B}) \qquad (7.15)$$

thus establishing a relationship between current density, electric field ($\mathbf{E}$) and electrical conductivity of the solution (σ). The curl operator applying to

J and **B** in eqn (7.14) implicitly necessitates judicious implementation of magnetic and electric fields to induce a body force in the desired direction. The devices for generating electric and magnetic fields should be mounted on the fluidic devices in such a way that the produced fields result in a body force acting in the favored directions. This requirement imposes complexity in the design and manufacture when compared to devices utilized for MNPs-assisted mixing.

By rewriting eqn (7.14) in a dimensionless form, shown in eqn (7.16), a scaling analysis can be performed to predict the effectiveness of the Lorentz body force by using specific electromagnetic energy:

$$\mathrm{Re}\frac{\mathrm{D}\bar{\mathbf{u}}}{\mathrm{D}\bar{t}} = -\frac{LP}{U\eta}\nabla\bar{\mathrm{p}} + \nabla^2\bar{\mathbf{u}} + K_{\mathrm{e}}\left(-\nabla\bar{V} \times \bar{\mathbf{B}}\right) + Ha^2\left(-\nabla\bar{V} \times \bar{\mathbf{B}}\right) \times \bar{\mathbf{B}} \qquad (7.16)$$

where $\bar{V}$ is the dimensionless voltage and the Hartmann number $\left(Ha = LB\sqrt{\frac{\sigma}{\eta}}\right)$ represents the ratio of electromagnetic force to viscous force and takes significant values for liquid metals.[35] For an aqueous electrolyte with an electrical conductivity in the order of one S m^{-1}, Ha^2 is rather negligible in comparison to $K_{\mathrm{e}} = L\sigma VB/U\eta$.

Bau *et al.*[35] were the first group to numerically predict flow patterns in a conduit designated for mixing purposes and also verified experimentally their MHD-stimulated mixing simulations. The studied conduit is a rectangular channel with a set of narrow band-shaped electrodes on the bottom surface, connected alternatively to positive and negative poles of a DC current. Therefore, the current density direction in the channel varies in each section between two pairs of electrodes and at the same time interacts with the uniform magnetic field perpendicular to the bottom surface. Assuming a two-dimensional geometry, the momentum transport equations in x and y directions are solved to predict the velocity components in x and y directions. The coordination of magnetic and electric fields results in periodic upward and downward electromagnetic forces. In accordance with this arrangement, the velocity components taken among three adjacent electrodes, exhibit upward and downward horizontal components with central symmetry with respect to the coordinates' origin. The vertical velocity components are also symmetric with respect to the center of coordinate. The aforesaid velocity components, as illustrated in Figure 7.12, induce a circulatory pattern of motion in a set of adjacent electrodes.

In an experimental verification of the predicted motion of fluid, it was observed that an injected strip of dye on the conduit axis previously filled with water with conductance 2.23 10^{-4} S m^{-1} deforms once the currents are maintained and as the process continues eddy like patterns form in each paired section (see Figure 7.13). However these researchers approach for the evaluation of mixing is rather qualitative without providing any information on the mixing time or quantification of the mixing level.

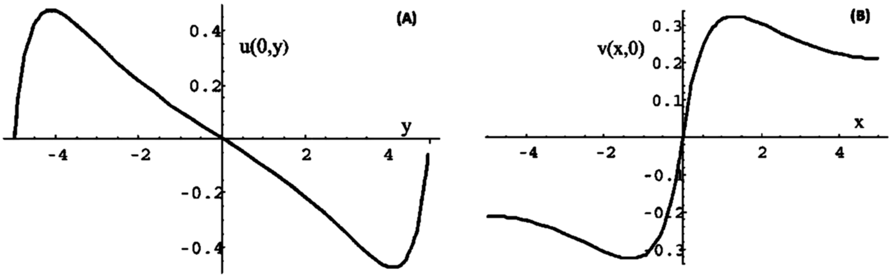

Figure 7.12 (A) Horizontal and (B) vertical velocity components as a function of x and y in space between dashed lines in Figure 7.13. Direction of x and y components are also shown in Figure 7.13.[35] (Reproduced from *Sens. Acutators, B*, **79**, H. H. Bau *et al.*, A minute magneto hydro dynamic (MHD) mixer, 207–215, Copyright (2001) with permission from Elsevier.)

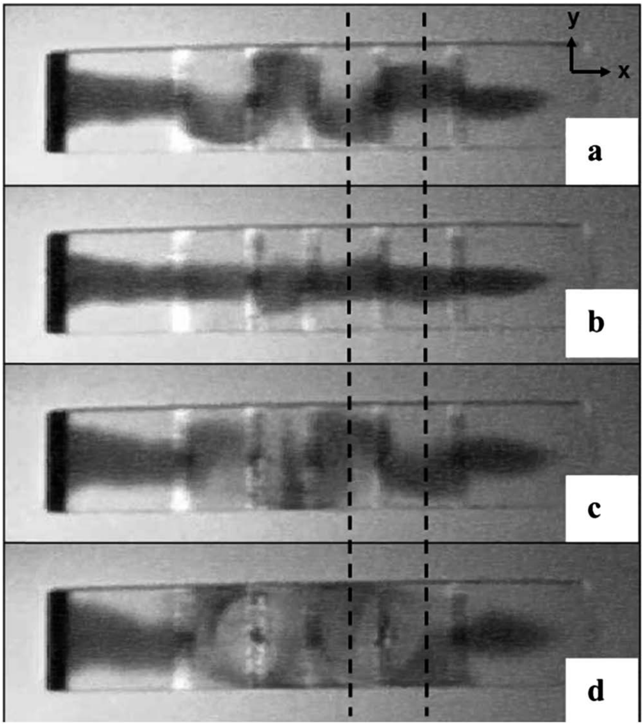

Figure 7.13 (a) The experimental observation of deformation of an injected dye strip with the application of Lorentz force. (b) By reversing the polarity of the electrodes, the dye strip returns to its initial shape. (c) In the subsequent reversal of Lorentz force direction, the dye strip continues to deform in opposite direction. (d) With the passage of time, eddies become apparent, resulting in more uniform dispersion of dye strip in the channel.[35] (Reproduced from *Sens. Actuators, B*, **79**, H. H. Bau *et al.*, A minute magneto hydro dynamic (MHD) mixer, 207–215, Copyright (2001) with permission from Elsevier.)

Qian *et al.*[36] expanded the MHD-assisted mixing concept to continuous flow systems by utilizing another configuration of electrodes. In their approach, as depicted in Figure 7.14, electrodes are assembled across each other on the side walls of the conduit and the magnetic field is perpendicular to the bottom surface.

The odd numbered electrodes on one side and the even numbered ones on the other side are connected separately to DC current poles. Periodic energization of each electrode pair generates electric currents diagonal to channel axis resulting in a Lorentz force normal to current vector in the (x,y) plane. The y-component of the Lorentz force changes its sign when the energized pairs are switched from odd numbered electrodes to even and *vice versa*. The inferable effect of the Lorentz force is a wave-shaped force field that periodically stretches fluid filaments toward the channel side walls. Qian *et al.* predicted the mixing performance of such an MHD device by coupling advection–diffusion transport equation to eqn (7.14) for two initially separated fluids in the channel with concentrations of a passive tracer to be 0 and 1 in the two streams. Typical conditions used in the simulation are a magnetic field intensity of 0.4 T, a potential difference of 2.5 V and a conductivity of two streams 2.56 S m^{-1}. Figure 7.15 illustrates the simulated concentration distribution in the channel middle plane over time.

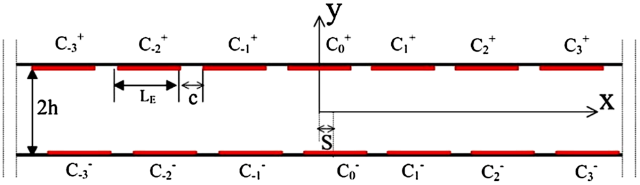

Figure 7.14 Schematic top view of the stirring channel. Electrodes are denoted with C_i^+ and C_i^- on the side walls.[36] (Reproduced from *Sens. Actuators, B*, 106, S. Qian and H. H. Bau, Magneto-hydrodynamic stirrer for stationary and moving fluids, 859–870, Copyright (2005) with permission from Elsevier.)

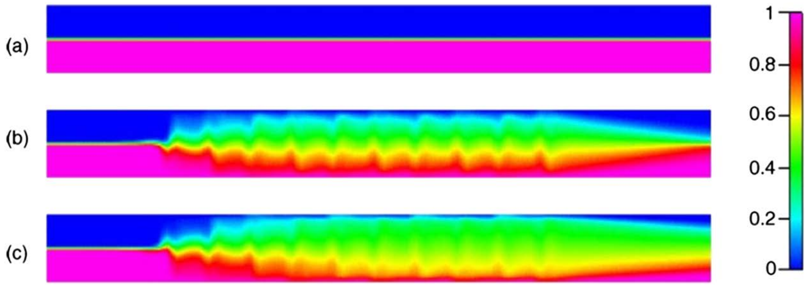

Figure 7.15 MHD-simulated concentration distribution of two fluids over time at (a) 0 s (b) 2 s (c) 6 s.[36] (Reproduced from *Sens. Actuators, B*, **106**, S. Qian and H. H. Bau, Magneto-hydrodynamic stirrer for stationary and moving fluids, 859–870, Copyright (2005) with permission from Elsevier.)

Formation of a mixed region between the two streams by the oscillatory motion of fluid gradually eliminates vertical concentration gradients. By defining a mixing index in terms of standard deviation of dimensionless concentration, the theoretical evolution of mixing as a function of time can be estimated. According to that index, Qian *et al.* performed an analysis to evaluate the Lorentz force order of magnitude on mixing quality.

Ha^2 for the studied system is in the order of 10^{-3} and its order of magnitude in comparison to K_e which is in the order of unity, is negligible. Qian *et al.* studied the effect of K_e on mixing effectiveness in a flow-through mixer by defining it as $JBL^2 \cos\theta / U\eta$ where θ is the angle between the diagonal line that connects the center of two electrodes in a pair and the y-axis. Simulations show that the mixing quality rapidly increases when K_e approaches unity and finally achieves an asymptotic value near 100% when $K_\mathrm{e} > 2$. This analysis gives a practical criterion for the minimum required electromagnetic energy and electrolytic conductance to maintain an effective MHD-induced secondary flow for a typical MHD-based mixing process. Experimental implementation of the simulated mixer is qualitatively in accordance with theoretical predictions.

In the above mentioned approaches for exploiting the Lorentz force in mixing, the role of secondary flows in stretching fluid elements and shortening the diffusion path is dominant while the ultimate resultant flow field has no chaotic characteristics. It means that a trajectory of a hypothetical passive tracer is independent of its initial conditions and the tracer always follows the same streamline if injected at various positions. A mixing mechanism based on chaotic advection is also possible[37,38] by electrodes energization in a cavity. Qian *et al.*[37] accomplished this idea by assuming point electrodes on the bottom surface of a channel with the magnetic field perpendicular to it and two parallel rectangular electrodes on the side walls, see Figure 7.16. Each point electrode and the plate electrodes on the sides account for an independent electrode pair. When the potential difference is imposed across a pair, the resultant Lorentz force drives the electrolytic solution with a circulatory motion around the point electrode. The whole electrode pairs can be energized based on various algorithms but two possible ones, carried out in the work of Qian *et al.* are adopted to generate counter- and co-rotating flow fields with only two point electrodes across the channel, alternately energized with various time intervals.

Flow field simulation is based on solving eqn (7.14) for momentum balance where advection is neglected for small Re numbers. Potential alterations between electrode pair are sufficiently slow so that for each pair the flow field is calculated based on steady solution of the momentum balance equation. Although the flow field for each pair of active electrodes is static, the entire field is time dependent as a result of applied on–off protocol in electrodes alterations. The electric field in each electrode pair can be calculated by solving Laplace's equation of electric potential in a charge-free space. Finally, by solving the equations of motion in two dimensions, the velocity field for individual pairs can be calculated. By superposition of individual

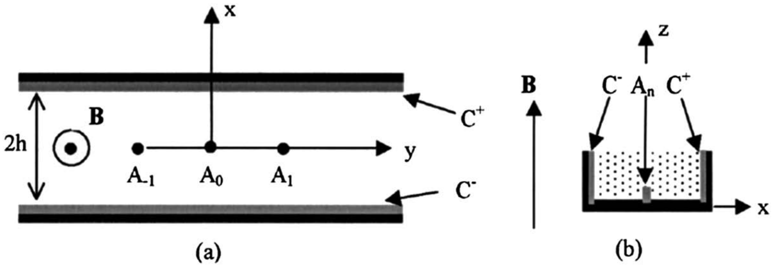

Figure 7.16 (a) Top view (b) and side view of the stirring channel geometry for numerical simulation with rectangular electrodes (C^+,C^-) and three point electrodes (A_{-1},A_0,A_1).[37] (Reproduced with permission from S. Z. Qian, J. Z. Zhu and H. H. Bau, *Phys. Fluids*, 2002, 14, 3584–3592. Copyright (2002), AIP Publishing LLC.)

fields associated with each pair, the resulting field can be obtained. Qian *et al.* utilized trajectories of a passive tracer to study the chaotic nature of the flow field. These trajectories can be calculated by integrating the position vector (**x**) equation with various initial conditions:

$$\frac{\mathrm{d}\mathbf{x}}{\mathrm{d}t} = u(\mathbf{x},t) \tag{7.17}$$

Valuable conclusions deduced from the stroboscopic images of passive tracer locations in the beginning and end of a period include the dependency of tracer deformation pattern on the switching intervals (T_s) between two electrode pairs. This interval is a time scale equal to the ratio of velocity scale over the half-width of the channel. When $T_s \rightarrow 0$, the system resembles two co-rotating flow fields with one hyperbolic fixed point between the point electrodes and two elliptic fixed points on the point electrodes. In this case, any tracer has only two groups of streamlines to follow. The first is a group of orbits encircling the elliptic fixed points and the second refers to orbits encircling both of them. In contrast, as the time interval becomes longer, the flow pattern becomes more chaotic with shrinking regions where the tracer can travel in one single streamline. Any passive tracer in the center, in both visualized and calculated flow fields, changes its streamline as a result of chaotic motion until it is totally deformed and dispersed in the conduit. Figure 7.17 portrays the streamlines of both situations by both stroboscopic image and visualization of the process with an injected point of dye. The experimental and mathematical analysis proves the emergence of chaotic motion of fluid, but mixing evaluation is qualitative and homogenization of injected dye spot is not sensibly quantified.

Although MHD-based mixing seems an attractive approach for mixing especially in micro-devices, there are some serious drawbacks associated with this method. There is always a limit in maintaining DC current in the electrodes which is due to the possible electrochemical interactions. Depending on electrolyte concentration, formation of bubbles and also degradation

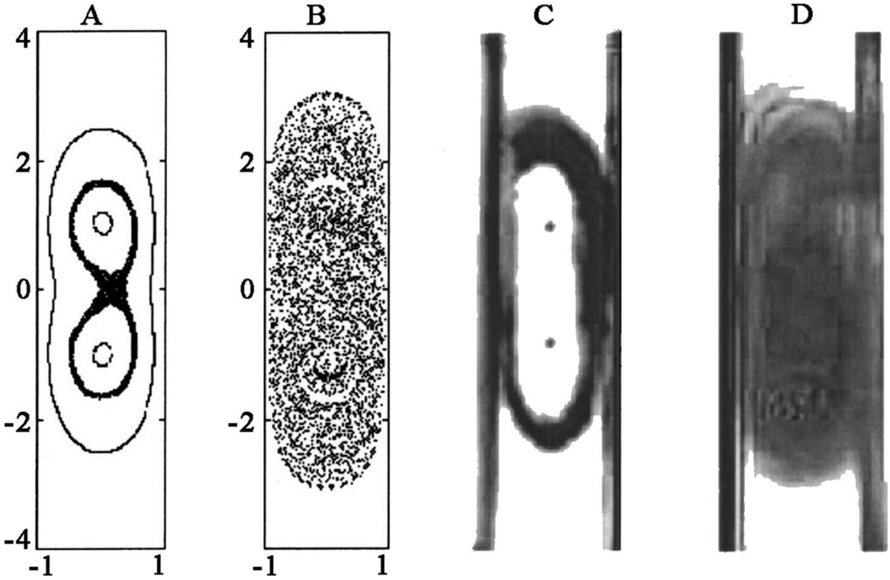

Figure 7.17 Illustration of stroboscopic images and experimental observation of a tracer when (A,C) $T_s = 4$ (s) and tracer is initially located at {0,0}, {0,±9} and {0,2.5}, (B,D) $T_s = 8$ (s) and tracer is initially located at {0,0}.[37] (Reproduced with permission from S. Z. Qian, J. Z. Zhu and H. H. Bau, *Phys. Fluids*, 2002, **14**, 3584–3592. Copyright (2002), AIP Publishing LLC.)

of electrodes after a certain voltage is inevitable.[37] Application of AC current can be a possible solution, however, Lemoff and Lee[33] experimentally confirmed that even in the case of AC currents, bubble formation may persist. Nevertheless, increasing frequency allows operation with higher currents whilst preventing bubble formation.

7.4 Conclusion

This contribution briefly introduced, both theoretically and experimentally, the magnetic field-assisted mixing concept. In the subcategory of mixing with magnetic nanoparticles (MNP), the governing equations of fluid motion help gain insights into grasping the MNPs' interaction with magnetic fields and exploiting specific interactions in mixing applications. In static magnetic fields (SMF), the mixing mechanism is mainly due to the Kelvin body force as a result of inhomogeneity in magnetic field strength and material magnetic susceptibility. In oscillating magnetic fields (OMF), besides a similar mechanism to SMF, translation of magnetic energy into kinetic energy of MNPs is theoretically and experimentally proven, albeit this mechanism has not been used practically in mixing applications. Rotating magnetic fields (RMF) highlight another mechanism able to perform magnetic energy conversion into kinetic energy though with technically simpler methods. Experimental evidence of RMF effectiveness in mixing applications makes it a promising tool to expand its applicability from microfluidics to larger scale processes.

Analogous to ferrohydrodynamics (FHD), which requires a magnetic medium to translate magnetic energy into kinetic energy, magnetohydrodynamics (MHD) can also actuate fluids owing to the interaction of magnetic fields with a current-carrying fluid. By appropriate induction of magnetic and electric fields and adjusting electrical conductivity of the fluid, the generation of complex flow fields to enhance mixing is attainable. However, according to the scaling analysis, the effectiveness of the MHD-based mixing method strongly depends on electromagnetic energy and electrical conductivity of working fluids. Although sufficient electrical conductivity might be inherent in the working fluids, electrochemical degradation of electrodes and electrolyte is always a serious obstacle.

Nomenclature

$\mathbf{A}$ (**N Kg m^{-5}**)	Exchange between internal and external angular momentum vectors
$\mathbf{B}$ (**T**)	Magnetic flux density
$\bar{\mathbf{B}}$	Dimensionless magnetic flux density
$\mathbf{E}$ (**V m^{-1}**)	Electric field vector
d (**m**)	Diameter of magnetic nanoparticle
D_i (**m^2 s^{-1}**)	Diffusion coefficient
f (**s^{-1}**)	Frequency of magnetic field rotation
f_0 (**Hz**)	Larmor frequency of the magnetization vector
f_{AC} (**s^{-1}**)	Frequency of AC magnetic field
$\mathbf{F}$ (**N m^{-3}**)	External body force density
$\mathbf{F_m}$ (**N m^{-3}**)	Kelvin body force density
$\mathbf{G}$ (**Pa**)	Body couple density vector
$\mathbf{H}$ (**A m^{-1}**)	Magnetic field vector
$\lvert\mathbf{H}\rvert$ (**A m^{-1}**)	Value of magnetic field vector
Ha	Hartmann number
I (**m^2**)	Moment of inertia density of magnetic nanoparticles
$\mathbf{J}$ (**A m^{-2}**)	Current density vector
L (**m**)	Characteristic length
l (**m**)	Scaled diffusion length
K (**J m^{-3}**)	Anisotropy constant
K_e	Dimensionless number in eqn (7.16)
k_B (**J K^{-1}**)	Boltzmann's constant
L (**m**)	Length
$\mathbf{M}$ (**A m^{-1}**)	Magnetization vector
$\mathbf{M}_0$ (**A m^{-1}**)	Saturation magnetization vector
N	Number of magnetic particles
p (**Pa**)	Pressure
$\bar{p}$	Dimensionless pressure

R	Ratio of magnetic energy to Brownian kinetic energy
Re	Reynolds number
R_{T}	Dimensionless number in eqn (7.13)
V $\mathbf{(V)}$	Voltage
$\bar{V}$	Dimensionless voltage
V_{H} $\mathbf{(m^3)}$	Hydrodynamic volume of nanoparticles
V_{p} $\mathbf{(m^3)}$	Magnetic particle core volume
t $\mathbf{(s)}$	Time
$\bar{t}$	Dimensionless time
t_{m} $\mathbf{(s)}$	Scaled diffusion time
T $\mathbf{(K)}$	Absolute temperature
U $\mathbf{(m\ s^{-1})}$	Value of characteristic velocity vector
$\mathbf{u}$ $\mathbf{(m\ s^{-1})}$	Velocity vector
$\bar{\mathbf{u}}$	Dimensionless velocity vector
$\mathbf{x}$ $\mathbf{(m)}$	Position vector
ζ $\mathbf{(Pa\ s)}$	Vortex viscosity
$\boldsymbol{\eta}$ $\mathbf{(Pa\ s)}$	Dynamic viscosity
$\boldsymbol{\eta}'$ $\mathbf{(Kg\ m\ s^{-1}\ rd^{-1})}$	Shear spin viscosity
$\boldsymbol{\lambda}'$ $\mathbf{(Kg\ m\ s^{-1}\ rd^{-1})}$	Bulk spin viscosity
μ_0 $\mathbf{(N\ A^{-2})}$	Absolute magnetic permeability of vacuum
$\boldsymbol{\rho}$ $\mathbf{(Kg\ m^{-3})}$	Density
$\boldsymbol{\sigma}$ $\mathbf{(S\ m^{-1})}$	Electrical conductivity
$\boldsymbol{\tau}$ $\mathbf{(s)}$	Effective relaxation time
$\boldsymbol{\tau}_{\mathrm{AC}}$ $\mathbf{(s)}$	AC magnetic field oscillation time scale
$\boldsymbol{\tau}_{\mathrm{b}}$ $\mathbf{(s)}$	Brownian relaxation time
$\boldsymbol{\tau}_{\mathrm{h}}$ $\mathbf{(s)}$	Hydrodynamic time scale
$\boldsymbol{\tau}_{\mathrm{n}}$ $\mathbf{(s)}$	Neelian relaxation time
χ_{i}	Initial magnetic susceptibility
$\boldsymbol{\omega}$ $\mathbf{(rd\ s^{-1})}$	Spin density vector

References

1. S. Borukhova and V. Hessel, in *Process Intensification for Green Chemistry: Engineering Solutions for Sustainable Chemical Processing*, ed. K. Boodhoo and A. Harvey, John Wiley & Sons, United Kingdom, 1st edn, 2013, ch. 4, pp. 91–156.
2. J. Baldyga and J. R. Bourne, *Chem. Eng. Sci.*, 1990, **45**, 907–916.
3. A. van Reenen, A. M. de Jong, J. M. J. den Toonder and M. W. J. Prins, *Lab Chip*, 2014, **14**, 1966–1986.
4. K. Boodhoo and A. Harvey, in *Process Intensification for Green Chemistry: Engineering Solutions for Sustainable Chemical Processing*, ed. K. Boodhoo and A. Harvey, John Wiley & Sons, United Kingdom, 1st edn, 2013, ch. 1, pp. 1–31.
5. D. L. LesliePelecky and R. D. Rieke, *Chem. Mater.*, 1996, **8**, 1770–1783.
6. R. E. Rosensweig, *Ferrohydrodynamics*, Dover Publications, United States of America, 1st edn, 1997.

7. N. Poudyal and J. P. Liu, *J. Phys. D: Appl. Phys.*, 2013, **46**, 1.
8. S. Odenbach and S. Thurm, in *Ferrofluids: Magnetically Controllable Fluids and Their Applications*, ed. S. Odenbach, Springer, Germany, 2002, vol. 594, pp. 185–201.
9. M. I. Shliomis, *Sov. Phys. JETP-USSR*, 1972, **34**, 1291.
10. J. C. Bacri, R. Perzynski, M. I. Shliomis and G. I. Burde, *Phys. Rev. Lett.*, 1995, **75**, 2128–2131.
11. A. Zeuner, R. Richter and I. Rehberg, *Phys. Rev. E*, 1998, **58**, 6287–6293.
12. Q. Cao, X. Han and L. Li, *Lab Chip*, 2014, **14**, 2762–2777.
13. T.-H. Tsai, D.-S. Liou, L.-S. Kuo and P.-H. Chen, *Sens. Actuators, A*, 2009, **153**, 267–273.
14. G.-P. Zhu and N. Nam-Trung, *Lab Chip*, 2012, **12**, 4772–4780.
15. C.-Y. Wen, K.-P. Liang, H. Chen and L.-M. Fu, *Electrophoresis*, 2011, **32**, 3268–3276.
16. N. Kockmann, *Transport Phenomena in Micro Process Engineering*, Springer, Germany, 1st edn, 2008.
17. M. Zahn and R. E. Rosensweig, *J. Magn. Magn. Mater.*, 1987, **65**, 293–300.
18. M. I. Shliomis and K. I. Morozov, *Phys. Fluids*, 1994, **6**, 2855–2861.
19. P. Hajiani and F. Larachi, *Chem. Eng. Process.*, 2013, **71**, 77–82.
20. T. G. Kang, M. A. Hulsen, P. D. Anderson, J. M. J. den Toonder and H. E. H. Meijer, *Phys. Rev. E*, 2007, **76**, 066303.
21. Y. Gao, A. van Reenen, M. A. Hulsen, A. M. de Jong, M. W. J. Prins and J. M. J. den Toonder, *Microfluid. Nanofluid.*, 2014, **16**, 265–274.
22. C.-Y. Wen, C.-P. Yeh, C.-H. Tsai and L.-M. Fu, *Electrophoresis*, 2009, **30**, 4179–4186.
23. A. Munir, J. Wang, Z. Zhu and H. S. Zhou, *Microfluid. Nanofluid.*, 2011, **10**, 735–747.
24. P. Hajiani and F. Larachi, *Chem. Eng. J.*, 2012, **203**, 492–498.
25. R. Calhoun, A. Yadav, P. Phelan, A. Vuppu, A. Garcia and M. Hayes, *Lab Chip*, 2006, **6**, 247–257.
26. Y. Gao, M. A. Hulsen, T. G. Kang and J. M. J. den Toonder, *Phys. Rev. E*, 2012, **86**, 041503.
27. F. Wittbracht, A. Weddemann, B. Eickenberg, M. Zahn and A. Huetten, *Appl. Phys. Lett.*, 2012, **100**, 123507.
28. R. Moskowit and R. Rosenswe, *Appl. Phys. Lett.*, 1967, **11**, 301–303.
29. O. Gravel, J. Lauzon-Gauthier, C. Duchesne and F. Larachi, *Chem. Eng. J.*, 2015, **260**, 338–346.
30. C. Cerretelli and C. H. K. Williamson, *J. Fluid Mech.*, 2003, **475**, 41–77.
31. P. Hajiani and F. Larachi, *Chem. Eng. J.*, 2013, **223**, 454–466.
32. O. Levenspiel, *Chemical reaction engineering*, Wiley, USA, 3rd edn, 1999.
33. A. V. Lemoff and A. P. Lee, *Sens. Actuators, B*, 2000, **63**, 178–185.
34. S. Qian and H. H. Bau, *Mech. Res. Commun.*, 2009, **36**, 10–21.
35. H. H. Bau, J. H. Zhong and M. Q. Yi, *Sens. Actuators, B*, 2001, **79**, 207–215.
36. S. Qian and H. H. Bau, *Sens. Actuators, B*, 2005, **106**, 859–870.
37. S. Z. Qian, J. Z. Zhu and H. H. Bau, *Phys. Fluids*, 2002, **14**, 3584–3592.
38. M. Q. Yi, S. Z. Qian and H. H. Bau, *J. Fluid Mech.*, 2002, **468**, 153–177.

CHAPTER 8

Photocatalysis: Past Achievements and Future Trends

FATEMEH KHODADADIAN[†a], MAXIM NASALEVICH[†b],
FREEK KAPTEIJN[b], ANDRZEJ I. STANKIEWICZ[a], RICHARD
LAKERVELD[c] AND JORGE GASCON*[b]

[a]Department of Process and Energy, Delft University of Technology,
Leeghwaterstraat 39, Delft, The Netherlands; [b]Department of Chemical
Engineering, Delft University of Technology, Julianalaan 136, Delft, The
Netherlands; [c]Department of Chemical and Biomolecular Engineering,
The Hong Kong University of Science and Technology, Clear Water Bay,
Kowloon, Hong Kong
*E-mail: J.Gascon@tudelft.nl

8.1 Introduction

Heterogeneous photocatalysis is receiving much attention for its promise to enable more efficient and sustainable chemical processes. Since the discovery of photocatalysis in 1972 by Fujishima and Honda,[1] a great deal of effort has been devoted to improve the relatively low efficiency of photocatalytic transformations. Fujishima and Honda[1] observed that when illuminated

---

[†]These authors contributed equally to this work.

RSC Green Chemistry No. 47
Alternative Energy Sources for Green Chemistry
Edited by Georgios Stefanidis and Andrzej Stankiewicz

Published by the Royal Society of Chemistry, www.rsc.org

TiO_2 is used as a photoanode for water splitting in combination with Pt as a cathode, the reaction occurs at a much lower potential than one would expect for the ordinary water electrolysis. Thereafter, much research has been conducted on hydrogen production *via* water splitting with heterogeneous photocatalysis to convert solar energy to fuel. Later studies also demonstrated that organic and inorganic compounds can be oxidized with illuminated semiconductors in both liquid and gas phases.[2] More recently, photocatalysis has been successfully applied to degrade a large variety of organic contaminates including alkanes, alcohols, carboxylic acids, alkenes, aromatics, phenols, dyes and pesticides.[3–5] The possibility of full mineralization of pollutants to harmless compounds has raised much interest from academia and industry. Moreover, heterogeneous photocatalysis can degrade very low concentrations of pollutants. Therefore, heterogeneous photocatalysis is expanding rapidly as one of the main so-called *advanced oxidation technologies* (AOT) for water and air purification. Also, the demand for renewable energy resources is increasing dramatically due to depleting fossil fuels reservoirs and enhanced global warming from CO_2 emissions. In recent years, a renewed interest has been raised in the reduction of carbon dioxide over a photocatalyst as one of the promising solutions to convert harmful CO_2 to valuable chemicals such as methanol and acetaldehyde.[6] Although significant progress has been achieved, the process efficiency of CO_2 reduction remains low and detailed mechanistic insights are lacking, which hampers economic viability.

Since the pioneering work of Fujishima and Honda,[1] a great number of scientists in catalysis attempted to enhance the so-called quantum efficiency, defined as ratio between the number of molecules produced in a photocatalytic reaction and the number of incident photons. Unfortunately, despite the efforts, in the vast majority of reported cases the efficiency does not exceed 10%.[3,7] After 40 years of intense research TiO_2 remains the most investigated photocatalyst (*ca.* 50% of the publications in the field) and, to the best of our knowledge, the only one applied commercially. The constantly growing scientific attention to this problem is reflected in the impressive 4200 publications in 2014.[8] The captivation of photocatalytic reactions can be attributed to the abundancy of sunlight as an energy source. However, titania is only capable of operating under illumination of light with a wavelength shorter than *ca.* 400 nm that corresponds to its bandgap energy of 3.2 eV.[9] The sun irradiation spectrum contains only 5% of photons with such desired energies.[10] Therefore, one of the main pathways for obtaining highly active titania photocatalysts lies in sensitization of the semiconductor towards visible light absorption. Applied synthetic strategies and a few representative examples will be briefly given in this chapter. Since photocatalysis proceeds at the surface of semiconductors, another generally accepted solution for increasing activity is employing TiO_2 materials with high surface area. Addition of noble metals was proven to yield substantially higher photocatalytic rates, this applies to TiO_2 and other semiconductors. Zinc oxide, CdS, WO_3 and many other inorganic compounds were subjected to successful evaluation in a variety of photocatalytic transformations. Despite the progress achieved with these more traditional semiconductors, the absence of the ultimate photocatalyst triggers the endeavours in seeking for new alternative materials. Oxides like TiO_2, ZnO and ZrO_2 and many others suffer from the undesirably large bandgap energies,[11,12] hematite (Fe_2O_3) is characterized by fast electron–hole recombination,[13,14] whereas sulphides such as CdS experience deactivation.[15] The ultimate photocatalyst should have a narrow bandgap for capturing a large fraction of solar light, must be free of noble metals, be of heterogeneous nature and remain stable after multiple cycles of photocatalytic reactions while demonstrating a high quantum efficiency. Many novel materials emerged as potential photocatalysts over the last decades including perovskites and heteropolyacids.

Another new class of advanced materials for photocatalysis is metal–organic frameworks (MOFs), porous solids of hybrid organic–inorganic nature. Although the first reports on photocatalytic activity of MOFs appeared in the early 2000's, these coordination polymers are receiving massive attention primarily due to their excellent tunability as well as extremely high surface areas. The idea to apply MOFs in photocatalysis most likely originates from the similarity between metal–organic frameworks based on a given metal and their corresponding metal oxides. However, this 'at first sight' analogy is false, as these solids possess properties very distinct from the ones found in classical semiconductors. This class of materials will be discussed in detail.

As with any heterogeneous catalytic process, the conversion of chemicals with heterogeneous photocatalysis follows several steps: (1) reactants transfer from bulk to the catalyst surface, (2) reactants adsorb on the catalyst surface, (3) conversion of reactants on the catalyst surface, (4) desorption of products from the catalyst surface, (5) products transfer from the catalyst surface to the bulk. An important difference in heterogeneous photocatalysis is the method of catalyst activation. A photocatalytic process is driven by photon absorption to provide the required energy for the reduction–oxidation reaction. Favourable properties of heterogeneous photocatalysis that can make photocatalysis a suitable alternative for implementation of redox reactions are, (a) availability of cheap semiconductors such as TiO_2 that can be used as a catalyst, (b) mild reaction conditions, (c) ability to use solar energy directly, (d) possibilities for applications in both liquid and gas phases. However, industrial applications of photocatalysis require scalable photocatalytic reactors with high efficiency, which remains notoriously challenging. Therefore, improving the efficiency of a photocatalytic process requires both the development of more efficient photocatalysts as well as innovative reactor equipment.

Several design challenges exist for photocatalytic reactors. First, an efficient photocatalytic reactor needs to optimize the mass transfer of reactants and products. Second, a major challenge in the design of a photocatalytic reactor is efficient catalyst illumination.[16] The former challenge is not unique for photocatalytic reactors, but applies equally well to any other catalytic reactor. However, the latter challenge complicates the design of photocatalytic reactors compared to conventional catalytic reactors. Photons can be obtained directly from the sun or, indirectly, *via* electricity and subsequent use of artificial light sources. In any case, effective photon utilization within the reactor is important for economic feasibility. Scale-up of a photocatalytic reactor is a complex process, which has to take into account many factors including providing high catalyst surface area that is uniformly illuminated with an optimal dose and allows for high mass transfer of reactants and products. Despite important research efforts and significant progress, the development of photocatalytic processes for commercial purposes has been hindered by, amongst others, these scale-up complexities.[17] Fundamental research to develop improved photocatalysts and novel design methods for improved reactor equipment that would provide a higher effective utilization of photons is needed to enable future sustainable chemical processes that are driven by photocatalysis.

This chapter is organized as follows. First, novel developments in catalyst design will be discussed with a special focus on the application of MOFs. Second, the current state-of-the-art and challenges in the design of photocatalytic reactors are discussed including alternative options for the light source to enhance efficiency. The chapter ends with a summary and an outlook for both catalyst and reactor developments.

8.2 Catalyst Development

The development of photocatalytic systems originates from using TiO_2 as an electrode in photo-electrocatalytic water splitting in the early 70's. At that time, carrying out a photocatalytic reaction on a titania slurry was not a straightforward task.[18] In one of the pioneering works published by Kawai *et al.* in 1980, the researchers tackled the problem of water splitting on a powdered $RuO_2/TiO_2/Pt$ system by adding various organic compounds, such as methanol, to the reaction mixture. This resulted in a quantum efficiency of 44%.[19] Already in this early work they speculated that most likely the reduction of protons occurs on the platinum surface whereas the oxidation counterpart takes place at the ruthenium oxide component of the composite. This system demonstrated an activity two orders of magnitude higher than that of bare titania. Even from the early days of research in photocatalysis it was understood that pristine bulk titanium dioxide could not serve as an efficient catalyst unless modified or combined with other materials.

In a traditional sense, a photocatalytic process on a heterogeneous semiconducting catalyst proceeds as follows: at first the light of the energy exceeding the bandgap energy is absorbed by a semiconductor and the charge separation takes place. Electrons are promoted from the valence band of the semiconductor to the conduction band leaving behind positively charged holes. Further, the free charges can undergo several pathways as they are travelling within the semiconductor bands. They can recombine and loose the acquired energy in radiative (photoluminescence) or non-radiative way (heat). In photocatalysis this scenario is undesired and different strategies are applied in order to avoid a fast charge recombination. A few of them will be touched upon below. Another possibility for the photogenerated charge carriers is to migrate to the surface of the semiconductor crystallite and to react with various chemical species residing on the surface. It is worth noting that there is a driving force for the charge carriers to travel to the surface. This force is mainly caused by the charge concentration gradient as the charge carriers are spent on the surface due to the redox chemical transformations. Another factor contributing to this concentration gradient is band bending.[20] Once the charge carriers reach the surface, oxidation and reduction of substrates are carried out by holes and electrons, respectively. For a long time it was generally accepted that the oxidation and reduction take place at different well defined crystal facets[21,22] whereas the recent investigations show that this phenomenon is more complex.[23] Moreover, redox reactions on the surface can only occur if the thermodynamic potentials of the valence and conductance band of the semiconductor are suitable for a given substrate, *i.e.* the valence band maximum is more positive on the NHE potential scale (more negative in the absolute energy scale) than the oxidation potential of a substrate and the conduction band minimum is more negative on the NHE potential scale (more positive in absolute energy scale) than the reduction potential of the same or another substrate. This very simplistic representation of the mechanism of photocatalysis is essential for understanding the basic concepts behind the development strategies of heterogeneous catalysts. The important aspects of this mechanism in the view of this work can be split into the following: (1) absorption of light is the first vital step in initiating any photocatalytic reaction; (2) charge handling properties (mobility, recombination rate, *etc.*) are of crucial importance; (3) photocatalysis is a phenomenon taking place on surfaces similar to any other heterogeneous catalytic process; (4) valence band and conduction band positions on the absolute energy scale are the ones defining thermodynamic capabilities of a certain photocatalyst to oxidize and reduce given substrates.

Nearly 40% of all solar photons reaching the surface of our planet have energies falling into the visible region of electromagnetic radiation. Therefore the predictable trend in photocatalyst development was in tailoring absorption edges of catalysts towards visible light. Theoretically, the full water splitting can be accomplished by a catalyst with a bandgap of 1.23 eV. Proton reduction has a potential of 0 V *vs.* NHE while oxygen evolution happens at the potential of +1.23 V. In practice, an overpotential is often required and the more negative the conduction band potential the greater is the thermodynamic force for the proton reduction. Depending on the application of choice, one can select a photocatalyst with desired valence band and/or conduction band potentials. Applications such as water and air purification would favor semiconductors with largely positive valence band potentials while the reduction of CO_2 and H_2 evolution demand negative conduction band potentials. The conduction band electrons can be of great reduction potential of +0.5 to −1.5 V *vs.* NHE while the valence band holes typically have oxidative power of +1 to +3.5 V *vs.* NHE.[3,24] The bandgap requirements are, however, more universal and do not depend on a specific application—the lower the bandgap, the more photons captured. Balancing the low bandgap requirement and the band potentials yields an appropriate catalyst. In this part we will briefly discuss the synthetic strategies for lowering the bandgap of TiO_2.

Among the most exploited pathways for increasing the visible light absorption, doping of titania is probably the most robust and has the greatest industrial potential. Titania can be doped with metals as well as non-metals. Chemical doping by metals is commonly carried out by adding Fe^{3+},[25,26] Cr^{3+},[27,28] Ce^{4+},[29] V^{5+}[30] and many other cations to TiO_2.[7,31] Such treatment leads to enhanced light absorption by the semiconductor, improved separation of charge carriers and often an increase in the photocatalytic activity. In these materials the cations exist on the titania surface in the form of small metal-oxide isles. However, sometimes these dopants may serve as recombination sites reducing the photogenerated charge carriers' lifetimes and thus photocatalytic activity.[27] This drawback can be avoided by using the ion-implantation technique (bombarding TiO_2 with high energy ions) developed by Anpo and co-workers instead of chemical doping.[32] Another useful strategy is to dope titania with light elements like N,[33] C,[34] B[35] and F.[36] In the case of anion chemical doping the dopants can be incorporated into the TiO_2 lattice without disturbing the charge handling properties. Moreover, these materials have superior thermal stability with respect to the metal-doped titania. Sensitizing titanium dioxide with organic dyes was also documented in a number of reports.[37,38] This approach was successfully implemented by Grätzel and colleagues in his dye-sensitized solar cells,[39] however it was not widely applied in powdered photocatalysis due to the instability of organic molecules under the photocatalytic conditions. This particularly applies to photocatalytic oxidations in which the great oxidative power of TiO_2 causes the destruction of the sensitizers. A special case of increasing the visible light absorption of TiO_2 is achieved *via* the surface plasmon resonance (SPR) of gold nanoparticles residing at the semiconductor surface.[40,41] The improved photocatalytic performance is not only due to the visible light absorption of the composite but also due to the suitable catalytic sites for hydrogen evolution at, or close to, the gold nanoparticles in the Au/TiO_2 material.[42]

In photocatalysis by semiconductors such as TiO_2 the lifetime of photogenerated charge carriers is of crucial importance as well as the mobility of these species. Obviously, in a dense crystallite, charges can only react with substrates at the surface, meaning that charges generated in the bulk of the semiconductor have to reach this surface. The charge mobility within a TiO_2 crystal depends on a number of parameters such as preparation method, crystallinity, *etc.* It is worth noting that, on one hand high charge carrier mobility is beneficial as the charges can reach the surface faster, but on the other hand the high mobility increases the chances of electron–hole recombination, unless one of the charge carriers is trapped. To date, a variety of methods for trapping charge carriers has been documented. Electrons may be commonly trapped by noble metal nanoparticles whereas alcohols are used for hole trapping. Instead of increasing the mobility (speed with which charge carriers propagate over the crystal), one could also think of decreasing the distance these charges have to travel. This can be accomplished by employing TiO_2 nanoparticles as well as particles of desired morphologies.[43] At the same time, lowering the size of titania particles leads to an increased surface area that is immediately reflected in improved photocatalytic performance. Unfortunately, this positive influence is achieved at the cost of bandgap energy, as it increases while lowering the size, due to the quantum size effects in semiconductors.[44,45] Moreover, synthesizing nanosized TiO_2 retaining its high crystallinity is challenging since a high crystallinity is generally achieved *via* thermal treatment causing particle agglomeration.[46] An alternative route to increasing specific surface area in titania catalysts is to induce mesoporosity.[47]

In addition to the aforementioned functions of noble metal nanoparticles immobilized on TiO_2, such as SPR and electron capture, another important role in the overall performance of M/TiO_2 systems is to provide appropriate catalytic surfaces for assembling and/or splitting of certain molecules. Noble metals like Pt and Pd are known to promote photocatalytic hydrogen evolution as well as a variety of other chemical transformations.[48,49] Fortunately, the use of additional catalytic sites is not restricted only to precious metals. Examples of employing cobalt-based molecular complexes[50,51] as well as enzymes[52] for this purpose are documented by Reisner and co-workers.

Metal–organic frameworks (MOFs) emerged as potential photocatalysts in the early 2000's.[53,54] Most of the pioneering research was carried out on Zn-based coordination polymers[55,56] that offered relatively high stability compared to their predecessors of the same class.[57] In the early beginning these solids were classified as semiconductors analogously to their corresponding metal oxides.[55] The main argument supporting the semiconducting nature of MOFs was based on the UV-vis studies that demonstrated band-like spectral features as well as bandgap energies similar to the ones found in inorganic semiconductors.[58,59] In spite of distinct differences between photocatalysis by MOFs and that by semiconductors revealed by further studies, this first false judgment triggered the interest of the scientific community. The characteristic aspects of MOFs as photocatalysts, as opposed to TiO_2 as a representative example of heterogeneous photocatalysis by semiconductors, will be highlighted in this chapter as well as the clear similarities in the strategies for MOF-based catalyst development.

Metal–organic frameworks (MOFs) are crystalline solids constituted by infinite lattices of the inorganic secondary building unit (SBU: metal ions/clusters) interconnected by organic linkers. This moderately strong bonding has a coordinative character. In contrast to traditional inorganic materials, MOFs are assembled from well-defined molecular building blocks due to the reliability of molecular synthesis and the hierarchical organization governed by crystal engineering. MOFs can therefore be seen as coordination complexes arranged in a crystalline lattice.[60] Extremely large surface areas and remarkable tunability have triggered applications in gas storage, separation and molecular sensing.[61–65] Bio-compatible scaffolds hold promise for medical applications.[66,67] Due to the affinity of MOFs for either organic or inorganic materials, depending on the composition, various composites may be fabricated with applications ranging from (opto)electronic devices to food packaging materials and membrane separation.[68,69] Finally, their tunable adsorption properties, outstanding dispersion of metal sites, uniform pore size and topology, along with their intrinsic hybrid nature, all point toward applications in heterogeneous catalysis.[70–72]

One of the first MOFs discovered to have photocatalytic properties was MOF-5. In this material Zn_4O tetrahedra are interconnected by terephthalates as shown in Figure 8.1.

Very shortly after the first reports on the MOF, a number of scientists computed electronic properties of MOF-5 in order to assess the nature of electronic transitions possessed by the solid. The theory predicted a quantum dot-like behavior where Zn_4O moieties can be considered as zinc oxide quantum dots spaced by organic antennas.[54] Despite the fact that the calculated bandgap energy for MOF-5 was 5 eV which would determine this material to be an insulator, the computational study revealed another important feature characteristic of this solid: the HOMO was mainly localized at the organic ligand (linker) whereas the LUMO was located at the inorganic SBU.[73] This type of transition is referred to as ligand to metal charge transfer (LMCT). The authors also speculated that the HOMO–LUMO gap must be strongly influenced by the substituents on the aromatic rings of the linkers while the variations in metal nodes (Zn, Cd, Be, Mg, Ca) would not affect the bandgap energy, as predicted by Widom *et al.*[74] Indeed, in 2008 Gascon and co-workers experimentally proved this concept by altering the bandgap of MOF-5 using various aromatic dicarboxylic acids (Figure 8.1). They found that, unlike classical semiconductors such as TiO_2, ZnS and ZnO, MOFs possess excellent optical tunability. The energy required to induce LMCT transitions depends on the level of conjugation of the aromatic system of the ligand. Recent theoretical studies by Han and co-workers revealed that bandgap energies of materials adopting MOF-5 topology can also be tuned by substituting the oxygen atoms within the Zn_4O tetrahedra by S, Se and Te,[75] however this strategy is not yet synthetically accessible.

Later on, the photocatalytically active MOF-5 being unstable upon exposure to water[76] was replaced by more robust metal–organic frameworks based on Ti,[77] Zr,[78] Fe[79] and others. At the moment, functionalized linkers such as 2-aminoterephthalic acid (ATA) are employed. For instance, the NH_2 group, once introduced to the aromatic system of the ligand, offers the lone pair of nitrogen for interaction with the π^* orbitals of the benzene ring, donating electron density to the antibonding orbitals. As a result of this interaction, a new HOMO level, less positive on the potential scale, is obtained shifting the absorption to the visible region.[80] This approach was documented for the first time by Garcia and colleagues.[81] Using ATA instead of terephthalic acid for the synthesis of Zr-based UiO materials allowed them to sensitize the parent deep-UV-absorbing MOF to a fraction of the visible region. The enhancement

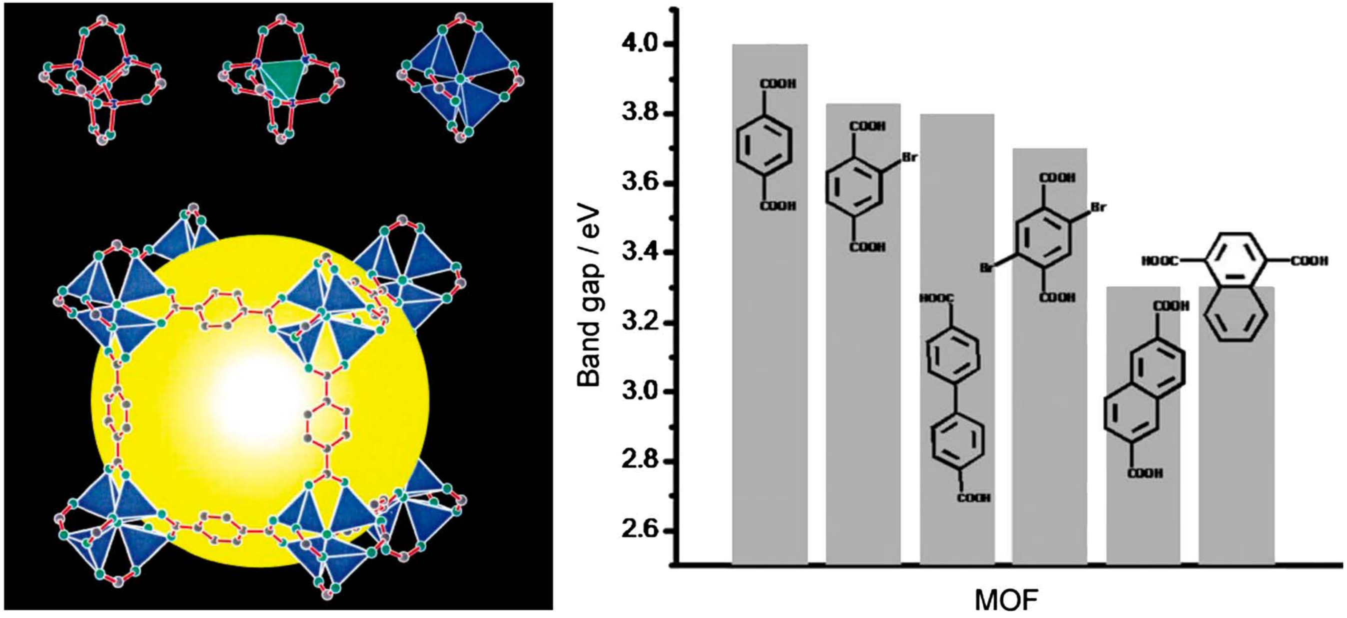

Figure 8.1 Structure of MOF-5 (also known as IRMOF-1) (left); bandgap energy of MOF-5 as a function of linkers constituting the framework. Reprinted from ref. 57 – left and ref. 56 – right.

of the optical absorption yielded a greater photocatalytic activity. Walsh and co-workers both computationally and experimentally found that the introduction of the second amino-group to the same linker lowers the absorption edge from 2.4 eV (NH_2-terephthalate as a linker) down to 1.3 eV for the diaminated MIL-125(Ti), whereas the MOF containing amine-free terephthalates possesses the HOMO–LUMO gap of 3.6 eV.[82] Similar theoretical[83] and experimental studies on UiO-66-type frameworks additionally confirmed the influence of the substituents (NH_2, NO_2, Br) on the light absorption properties and the photocatalytic activity in As(III) oxidation.[84] Interesting results were obtained when a combination of linkers was used for constructing the UiO-66-type MOFs. The authors found that by combining 2-fluoro-1,4-benzenedicarboxylic acid with 2-amino-1,4-benzenedicarboxylic acid the activity of the resulting mixed-linker-MOF in benzyl alcohol photocatalytic oxidation increased by a factor of 3 as compared to the pure NH_2-UiO-66(Zr).[85]

In addition to the strategies altering the LMCT in MOFs, several examples of assembling a MOF of porphyrin-like linkers were documented.[86,87] In these solids the framework is built of bi- or tetradentate porphyrinic entities having intrinsically high visible light absorption capacity. Such MOFs were also reported to demonstrate photocatalytic activity, although in this case the porphyrin core is likely to be responsible rather than the LMCT found in other coordination polymers, as the activity is observed even for materials with redox-inert metals such as Al.[88]

It is worth noting that obtaining a MOF that has desired framework functionality by choice is not always synthetically feasible.[89] In the work of Walsh *et al.*, the MIL-125(Ti)-type framework could only be assembled when using a mixture of 10% of $(NH_2)_2$-TA and 90% of ATA; all the attempts to synthesize pure $(NH_2)_2$-MIL-125(Ti) phase were not successful. Considering these limitations, post-synthetic modifications (PSM)[90] of MOFs are of great importance. One example of such a PSM was recently reported by our group.[91] In this work the NH_2 groups of the ATA linkers were chemically transformed into dye-like molecular fragments after forming the MOF structure.[92] This modification resulted in a material with a significantly red-shifted optical absorption as compared to the parent NH_2-MIL-125(Ti). The modified framework exhibited a greater activity in benzyl alcohol photocatalytic oxidation.

In contrast to the expected destruction of the dye-like moiety at the photocatalytic oxidation conditions, the catalyst remained stable upon recycling. This can probably be explained by the weak redox power of the photogenerated holes within the MR-MIL-125(Ti). Generally speaking, photocatalytic oxidations by MOFs are often mild and much more selective towards intermediate oxidation products compared to those of the classical inorganic semiconductors.[95] At the same time we should point out that many MOFs were successfully applied for decolorization of various organic dyes.[96]

For the purposes of photocatalytic reductions, MOFs can be post-synthetically loaded with organic dyes. Particularly, the UiO-66(Zr) MOF was sensitized with erythrosine B[97] and rhodamine B[98] that were applied in photocatalytic hydrogen evolution. Both of the systems afforded substantial amounts of H_2

gas. However, the downside was that the dyes were dissolved in the catalyst slurry; the catalysts were not fully heterogeneous and the stability of the dyes was questionable. In 2015 Li and co-workers reported a very elegant post-synthetic approach of increasing the visible light absorption of NH_2-UiO-66(Zr) by substituting one of the zirconium atoms within the $Zr_6O_4(OH)_4$ inorganic nodes by titanium as displayed in Figure 8.2.[94] This route holds promise for future research considering the number of MOF structures there are and resembles the doping strategies of titanium dioxide discussed above.

In summary, the optical properties of metal–organic frameworks can be easily manipulated by employing a linker with a desired functionality at the synthesis stage or, alternatively, *via* PSM. Moreover, the optical response can be engineered by using mixed metal clusters (and/or ligands). Examples of such materials were already reported,[99] yet at this stage rational design still appears challenging. Such tuning of optical properties yielded enhancements of the photocatalytic activity of the MOFs. However, the activity of MOF photocatalysts reported thus far is very modest.

One of the intrinsic properties of MOFs that fascinates many researchers around the world is their extremely high surface areas reaching up to 7000 m^2 g^{-1} BET.[100] For the frameworks that are most frequently applied in photocatalysis these values are somehow more modest, *ca.* 1500 m^2 g^{-1} for NH_2-MIL-125(Ti)[101] and 800 m^2 g^{-1} for NH_2-UiO-66(Zr),[102] yet still more than sufficient for providing enough surface area for catalysis. The synthetic effort in the field of photocatalysis with MOFs is not therefore directed toward obtaining materials with higher surface areas as is the case for TiO_2. Moreover, the mechanism behind the MOF photocatalysis is substantially different from that typical for inorganic semiconductors. As highlighted in the beginning of this chapter, one of the key reasons for reducing the particle size of TiO_2 is to diminish the distance the photogenerated charge carriers have to travel

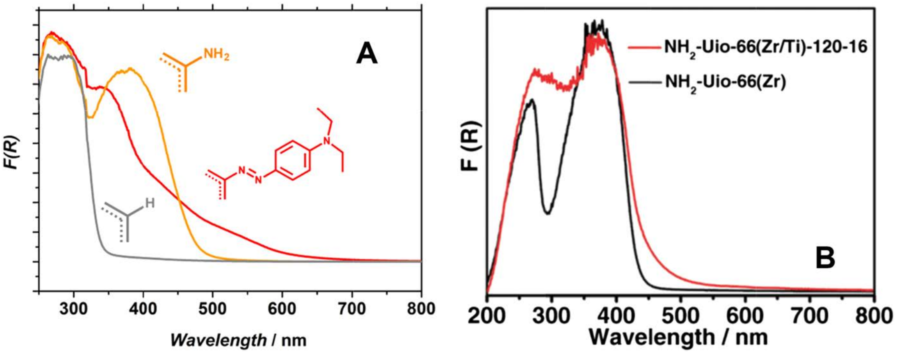

Figure 8.2 Post-synthetic sensitization of NH_2-MIL-125(Ti) with dye-like molecular fragments yielding methyl red-MIL-125(Ti) (MR-MIL-125(Ti)) (A); post-synthetic metal-exchange in NH_2-UiO-66(Zr) and its influence on light absorption properties (B). Reprinted from ref. 91 and 93 – left and ref. 94 – right with permission from the Royal Society of Chemistry.

before they reach the surface and react with the substrates adsorbed on it. The necessity of having mobile charge carriers in MOFs is more questionable. It should be noted that due to the extremely porous nature of coordination polymers, the substrates (reactants) can readily diffuse throughout the MOF crystallite. On the other hand, the rates of photocatalytic reaction can be different at the external surface and in the bulk of the MOF crystallite. This was pointed out by Garcia and colleagues as early as in 2006.[103] They found that MOF-5 exhibited reverse shape selectivity in photocatalytic oxidation of phenols meaning that bulky derivatives of phenol oxidized faster than phenol itself. The diffusion of the bulkier molecules was hindered due to the size restrictions imposed by the MOF lattice. We also speculate that the diffusion of substrates and O_2 is not the only factor influencing this peculiar behavior. Another explanation can be the limited light penetration depth in the absence of photogenerated charge mobility. From that point of view, a detailed study of the photocatalytic activity of MOFs as a function of particle size would shed the light on these processes.

As mentioned above, MOFs were initially perceived as semiconductors based on their optical transitions often resembling band edges and photochemical activity. At the same time photocatalytic activity does not have to originate from a semiconductivity. Inorganic semiconductors fulfill certain requirements such as presence of a delocalized valence band and a conduction band formed by an overlap of a nearly infinite number of orbitals close in energy and distance. Charge transfer in these cases proceeds through the bands. Analogous bands form in organic semiconductors *via* delocalization over extended conjugated π bonds, allowing for charge carrier mobility. A similar overlap must also occur in MOFs in order to classify them as semiconductors.[104] Obviously, the only measure of the semiconductivity of a certain material is a charge mobility within this material. It can either be determined by looking at the current through the material or directly measuring the charge carrier mobility.

A small number of metal–organic frameworks have been reported to conduct charges. These MOFs, based on Cu(I) or Ag(I) ions,[105] or dithiolene-based frameworks,[106] generally have rather small, but discernible, conductivities of 10^{-9}–10^{-3} S cm^{-1}.[105] Another rare example of a 3-D porous metal–organic framework that shows conductivity is based on triazole ligands. Out of a series of materials with the same topology, but having different divalent metal ions, only the conductivity of the framework with Fe(II) ions has been documented.[107] However, more recent works by Dincă and colleagues report an exceptional MOF exhibiting conductivities up to 40 S cm^{-1} as shown in Figure 8.3.[108]

We should emphasize that electroconductivity represents the ability of a given material to conduct electric current. When speaking of photocatalysis and, more generally, light harvesting, photoconductivity–the mobility of electrons and holes generated by electromagenetic radiation–is of greater importance. This parameter can be studied with the help of the photoinduced time-resolved microwave conductivity (TRMC) reported for some

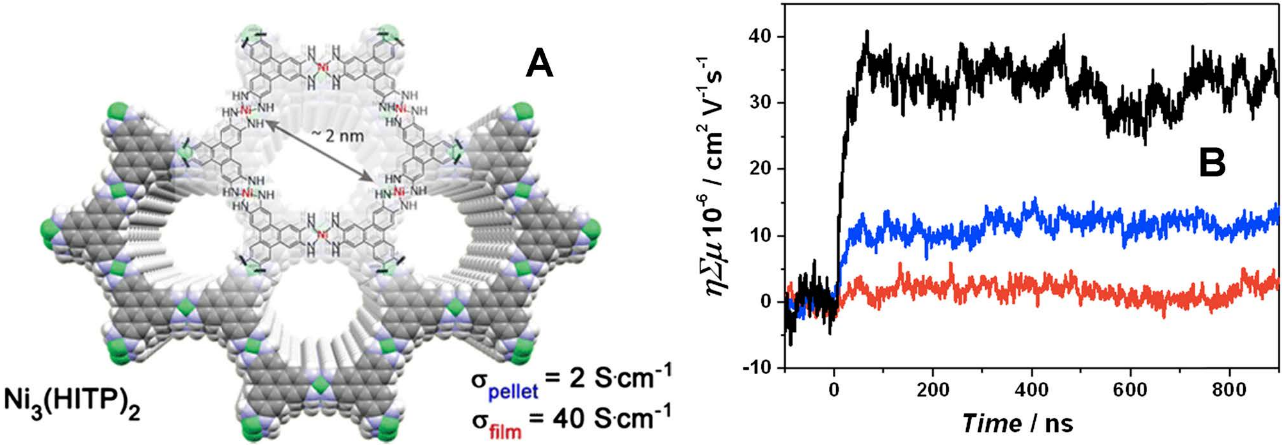

Figure 8.3 MOF with exceptionally high electroconductivity (A); TRMC photoconductivity studies for MIL-125(Ti) at different temperatures: thermal-activated hopping (B). Left – adapted from D. Sheberla *et al.*, *J. Am. Chem. Soc.*, 2014, **136**, 8859–8862. Copyright (2014) American Chemical Society[108] and right – reproduced from ref. 58 and 91 with permission from the Royal Society of Chemistry.

frameworks (see Figure 8.3). The technique assesses the local charge mobility and is an indispensable tool when studying solids for photocatalysis. As a result of such measurements one obtains the product of the charge carrier density and the charge carrier mobility.[109] The signal is obtained with nanosecond time resolution after light absorption. The reported mobility values are in the range between 1×10^{-5} and 4×10^{-5} $cm^2\ V^{-1}\ s^{-1}$. The order of magnitude is rather low compared to conjugated polymers where values of 10^{-3} $cm^2\ V^{-1}\ s^{-1}$ and greater are typical.[109,110] These values have been reported for a MOF with stacked thiafulvalene ligands,[111] a MOF that contains infinite Mn–S chains that should facilitate charge carrier mobility,[112] and MIL-125 a Ti(IV)[113]-containing structure that has also been studied for its photocatalytic behaviour.[114] For the thiafulvalene, and Mn–S chains structures also, the amount of photogenerated mobile charges were determined. The quantum yields are in the order of 10^{-4}–10^{-3}. This thus meant a high intrinsic charge mobility of 0.2 $cm^2\ V^{-1}\ s^{-1}$ for the thiafulvalene framework, and 0.02 $cm^2\ V^{-1}\ s^{-1}$ for the Mn–S chain framework. For the latter structure this corresponds to charge delocalization over 8–12 Mn–S units. However, only a very small fraction (10^{-4}–10^{-3}) of the absorbed photons lead to charges that are mobile.

Considering MIL-125(Ti) as the most representative example of photoactive MOFs to date, it exhibits a low photoconductance (mobility ~ 10^{-5} $cm^2\ V^{-1}\ s^{-1}$ upon 340 nm illumination, see Figure 8.1).[113] Moreover, the conductance is directly proportional to the temperature at which the measurement is carried out, in clear contrast to titania showing mobilities of ~1 $cm^2\ V^{-1}\ s^{-1}$ and nearly independent of temperature.[115,116] This clear difference in behaviour of the two solids suggests that charge transfer in this MOF proceeds *via* so-called thermally-activated hopping due to the isolation of the Ti clusters by the organic linkers in the MOF.[117] The $Ti_8O_8(OH)_4$ clusters in MIL-125(Ti) are too far apart to fulfil the Mott transition conditions (*ca.* 4 Bohr radii).[118,119] Moreover, in most MOFs, the distance between linkers is too large as to allow efficient π–π stacking[120] and there is hardly any orbital overlap, keeping the electrons preferentially in a localized state. This structural feature signifies, as recently pointed out by Lin and colleagues, that MOFs have to be understood as molecules arranged in a crystalline lattice.[121] In the case of photocatalysis, materials like MIL-125(Ti) should therefore be seen as an array of self-assembled molecular catalysts rather than as classical semiconductors. In view of this classification, optical absorption spectra should be interpreted as sets of individual discrete absorption bands, and the HOMO–LUMO gap terminology appears to be more appropriate to describe the discrete character of the electronic transitions in these coordination polymers. For MOF-5, the framework to which semiconductivity has been ascribed the most, Walsh *et al.* computed that no band dispersion occurs in this material, which is in agreement with localized charge carriers and low conductivity.[104] These conclusions are in line with experimental results reported by our research group when photocatalytic activity of iso-reticular Zn-based MOFs and their corresponding monodentate analogues were compared.[122]

Semiconducting behaviour of metal–organic frameworks occurs rarely and is so far of relatively low magnitude. Nevertheless, it has been demonstrated in the literature that upon absorption of photons electron–hole pairs can be generated in MOFs carrying redox activity. In contrast to classical semiconductors, however, in most cases these charges are not mobile and this in turn has a certain influence on photocatalysis. Photocatalysis can be split into a reduction and oxidation half reactions. When the photogenerated charges are not mobile, this essentially means that the catalytic sites for oxidation and reduction must be present in close vicinity to the light absorption and/or charge separation centre. Although the spatial proximity of the photogenerated electrons and holes might cause faster charge recombination thus inhibiting the desired redox transformations, at the same time, the porosity of MOFs facilitates diffusion of reactants and products throughout their crystals, which can compensate for the former.

Similar to the TiO_2-based photocatalysts, MOFs were subjected to active site engineering (ASE).[58] In the case of photocatalysis with MOFs, methods of including additional catalytic sites, to the best of our knowledge, have given the most promising improvements of photocatalytic performance. In contrast to classical semiconductors where ASE is normally restricted to the modification of surfaces by noble metal nanoparticles or, more rarely, transition metal complexes, the synthetic strategies employed for MOFs are much more diverse. The general pathways for using MOFs in photocatalysis are depicted in Figure 8.4.

The first approach is to utilize MOFs as such and carry out photocatalytic transformations by exploiting the LMCT: the MOF organic linkers can act as light absorbers, further transferring the energy of excited states to the clusters composed of only a few metal atoms. This approach generally results in the generation of free charges upon illumination at the appropriate wavelength. However, the photocatalytic performance in this case is rather low. The second strategy is to utilize the extremely large space within the MOF crystals. This space can be then occupied by photocatalytically active species either encapsulated in the cavities of the MOFs or even chemically bound. A variety of substrates can be encapsulated by following this approach: semiconductor nanoparticles,[123] transition metal complexes[124] and others.[125] In this case, the MOF can act either as mere container or participate in the charge transfer process (see Figure 8.4c where a ligand to metal charge transfer (LMCT) is indicated).

As mentioned above, one of the main advantages of using MOFs as carriers for photocatalytically active species is that these guests can be either covalently bound to the framework or encapsulated in its cavities. By doing so, one could prevent leaching of commonly homogeneous catalysts, often consisting of precious metals and being soluble under given reaction conditions. Lin and collaborators reported a series of UiO-67(Zr) materials hosting Ir-, Ru- and Re-coordination complexes that were active in water oxidation,

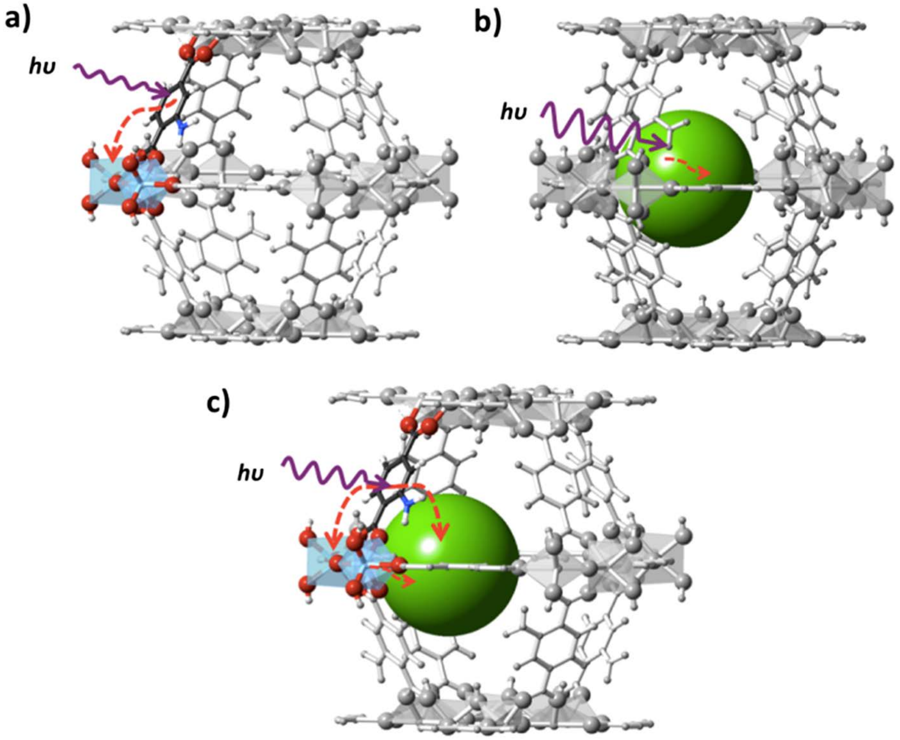

Figure 8.4 Synthetic strategies to obtain photocatalytically active MOFs: (a) the organic linker is acting as absorber and ligand-to-cluster charge transfer occurs; (b) the MOF is used as a carrier for a photocatalyst that directly absorbs light and (c) charge transfer occurs between the MOF scaffold and the encapsulated catalyst.

aza-Henry transformations and CO_2 reduction, respectively.[126] The remarkably high photocatalytic performance compares well with one of the corresponding homogeneous analogues. Moreover, the catalysts were proved to be recyclable evidencing their heterogeneity. A framework with the UiO-67 topology was synthesized following a mixed-linker strategy. Biphenyl-4,4′-dicarboxylic acid as the primary linker was combined with $[Ir(ppy)_2(bpy)]Cl$-derived dicarboxylic acid (see Figure 8.5).[127]

This synthetic method resulted in a crystalline porous material with an iridium content of 2 wt%. Further, platinum nanoparticles (Pt NPs) were deposited within the cavities of the Ir-containing MOF by photodeposition (PD). The proposed mechanism of operation for this bi-functional catalyst was that light absorption takes place at the iridium complex which then separates charges and the photogenerated electrons are injected into Pt NPs. This catalyst assembly exhibited an extremely high activity in H_2 evolution from H_2O (3400 TONs), even outperforming the corresponding homogeneous analogue. The improved activity was associated with the more

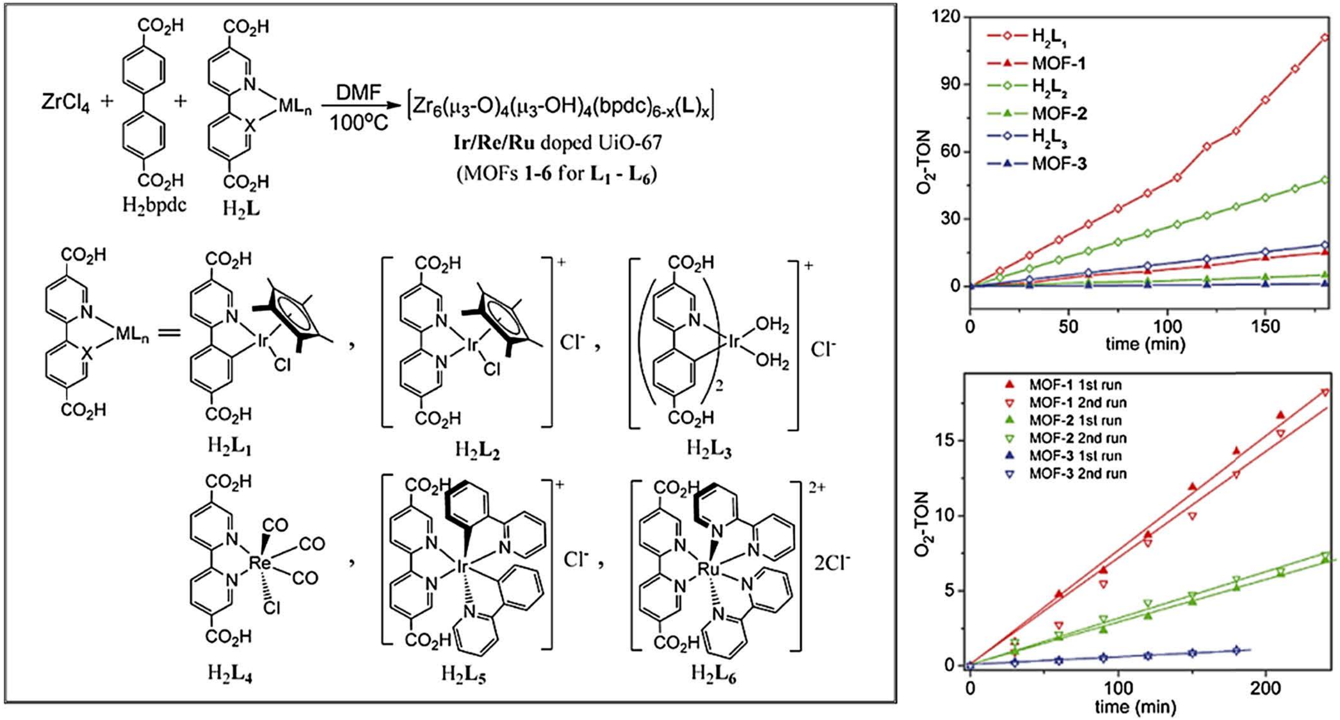

Figure 8.5 Coordinating molecular catalysts to UiO-67(Zr) frameworks: synthetic scheme (left), O_2 evolution as a function of time (O_2-TON) for the doped MOFs and their corresponding homogeneous analogues (top right), recyclability tests (bottom right).[127] Reproduced with permission from C. Wang, K. E. Dekrafft and W. Lin, *J. Am. Chem. Soc.*, 2012, **134**, 7211–7214. Copyright (2012) American Chemical Society.

intimate contact between the photoexcited Ir-complex and the Pt co-catalyst facilitating the charge transfer. Inspired by enzymes found in nature, Ott and co-workers coordinated a molecular di-iron catalyst to the UiO-type MOF for catalysing H_2 evolution.[128] The light absorption was achieved by $Ru(bpy)_3$ photosensitizer. In 2013 Xu and colleagues reported an analogous system based on the redox-innocent MOF-253(Al). In their catalyst the visible light absorption as well as the desirable catalytic site were introduced into the MOF by coordinating $PtCl_2$ to the bipyridine motif of the organic linker.[129] An analogous way of exploiting organic linkers as active catalytic sites was accomplished in porphyrin-based MOFs by Rosseinsky *et al.*[88] They fabricated a MIL-60(Al) type MOF composed of *meso*-tetra(4-carboxyl-phenyl)porphyrin active in H_2 evolution when combined with Pt. Interestingly, the synthesized MOF was free of metal cores within the porphyrin rings, preserving the possibility of engineering the active sites by addition of various metal ions. More recently, another Al-based MOF containing Cu-porphyrin linkers and Zn-based Sn(IV)-porphyrin MOFs were proved to catalyse the CO_2 reduction,[130] however, the photocatalytic performance towards methanol was moderately low.[131]

Metal–organic frameworks were also utilized as matrixes for the encapsulation of polyoxometalates (POMs) for various catalytic applications.[132–134] A Ln^{3+}-based framework containing $[BW_{12}O_{40}]^{5-}$ ions was recently employed for photocatalytic oxidation of thiophene with O_2.[135] The UV light-driven reaction was speculated to proceed *via* the charge separation within the Keggin anions. Another example of a POM-based MOF photocatalyst contains $[Mo_6O_{18}(O_3AsPh)_2]^{4-}$ polyoxoanions and Cu(I) organic motifs. The material is able to catalyze methylene blue degradation.[136]

In all the examples above, the function of the MOF is restricted to that of a container or 'nano-reactor'. It serves as a carrier for species that are active in photocatalysis whereas the remarkable ability of MOFs to absorb light and subsequently separate charges is largely unutilised. The strategy, however, is of great interest as it allows one to anchor active sites in a controlled fashion making them heterogeneous. One of the first examples in which a MOF is utilized as both the container and the light-absorbing unit was reported by Matsuoka and co-workers.[137,138] The presented composite catalyst consists of Pt NPs deposited on NH_2-MIL-125(Ti). The platinum surface is acknowledged to be among the best platforms on which to assemble H–H bonds. As a part of the composite, Pt nanoparticles provide their surface as appropriate catalytic sites required for efficient H_2 production. At the same time the MOF, NH_2-MIL-125(Ti), undergoes photoexcitation by visible light. Mechanistic studies revealed that absorption of visible light by the 2-aminoterephthalates is followed by LMCT, giving rise to Ti^{3+} paramagnetic species detectable by electron paramagnetic resonance spectroscopy. The photogenerated electrons are then injected into Pt NPs acting as electron 'reservoirs' (see Figure 8.6).

The reaction occurs at the surface of the NPs. A similar positive influence was also documented for the case of Pt@NH_2-UiO-66(Zr).[139] Employing noble metal nanoparticles as additional catalytic sites is a common strategy for classical semiconductors as well as MOF-based systems.[97,98,140,141] However, as recently pointed out by Li *et al.*, noble metals can influence the photocatalytic activity of MOFs differently.[142] They found that Pt NPs substantially increased the activity of NH_2-MIL-125(Ti) in photocatalytic CO_2 reduction whereas gold had a negative effect on it. One of the latest examples of employing the full functionality of MOFs was reported by our group. In this work a photocatalytically active NH_2-MIL-125(Ti) was loaded with a cobaloxime, a well-known electrocatalyst for H_2 evolution.[143] The encapsulation resulted in a highly active, recyclable composite Co@MOF that is free of noble metals. Moreover, the experimental proof for the MOF-to-cobaloxime charge transfer was provided (Figure 8.7).

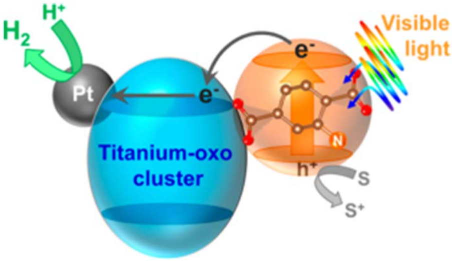

Figure 8.6 Schematic representation of the mechanism of photocatalytic hydrogen evolution catalyzed by Pt-supported NH_2-MIL-125(Ti). Reproduced with permission from Y. Fu *et al.*, *Angew. Chem., Int. Ed.*, 2012, **51**, 3364–3367. Copyright (2012) American Chemical Society.[101]

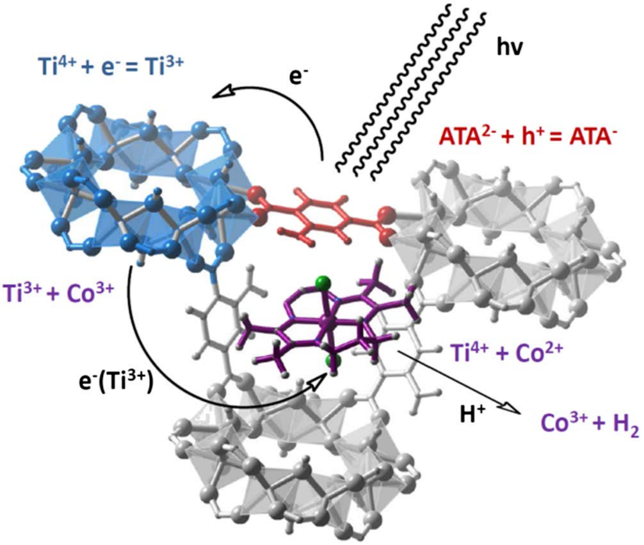

Figure 8.7 Mechanism of hydrogen evolution catalyzed by Co@MOF composite.

8.3 Photocatalytic Reactors

A photocatalytic reactor has to bring the reactants into effective contact with the catalysts and facilitate effective transfer of photons from the light source to the catalyst. The details of reactor geometry and integration of a light source within the reactor design are, therefore, highly important. When using artificial light sources, the main expenses of the process are related to the light source (investment, electricity, maintenance).[144] The key challenge for design is to integrate the photocatalyst and light source in such a way that each part of the catalyst receives the optimal number of photons with the right amount of energy, which complicates scale-up and optimization.

Considerable numbers of different designs have been proposed and investigated by different research groups.[145] Some of the proposed designs are empirically developed whereas others follow more a first-principle approach using mathematical models.[146] The design of photocatalytic reactors using rigorous mathematical models has been carried out mainly during the last two decades.[147–155] Mathematical models are efficient tools to analyse and optimize chemical reactors at different scales. Studies on the mathematical modelling of photocatalytic reactors with integrated modelling of a radiation field have demonstrated great potential.[147,156,157] The complexity of such integrated models poses significant challenges for analysis and for rigorous optimization. Furthermore, many degrees of freedom are available due to the large variety of designs, methods for catalyst preparation, catalyst materials, operating conditions, radiation intensity and light sources, which makes it difficult to optimize the performance of different photocatalytic reactors using all degrees of freedom. In general, photocatalytic reactors can be categorised into two main configurations based on the manner in which the photocatalyst has been deployed: (1) a reactor with suspended photocatalytic particles or, (2) a reactor with an immobilized catalyst on an inert substrate. Within those categories numerous variations exist of which a number of common configurations are discussed in more detail below.

8.3.1 Suspended Systems

In a suspended system, catalyst particles are mixed with a fluid. Suspended systems normally operate at higher catalyst loadings compared to most other photocatalytic reactors, since they utilize the whole volume rather than just a surface.[158] Subsequently, the number of available catalytic active sites per unit of reactor volume increases resulting in an efficient contact between reactant and catalyst with excellent mass transfer characteristics. Although there is typically no external mass transfer resistance in a suspended system, there are other limitations such as internal mass transfer limitations. In addition, achieving a uniform light distribution within this system is difficult, because the particles that are close to the light source shield the particles that are further away. Therefore, when catalyst particles are suspended in the solution, the depth of light penetration is limited.[17,158–160] The aforementioned limitations make it difficult to design a suspended reactor for large-scale applications. Slurry and fluidized bed reactors are two examples of suspended systems that are used for photocatalytic applications.

Slurry photocatalytic reactors have shown great potential to degrade contaminants in aqueous solution[161,162] and to oxidize liquid hydrocarbons.[163–165] However, the separation and recycling of fine catalyst particles from the treated stream remains a major disadvantage of this reactor type.[166] Post-separation of catalyst particles from the reactor effluent is necessary to prevent attrition of catalyst and, consequently, the introduction of new pollutants, which may make the operation of slurry reactors troublesome.[17,167] Furthermore, internal mass transfer limitations may occur due to particle agglomeration.[168]

In a fluidized bed reactor, a fluid (gas or liquid) flows upward in the reactor resulting in suspension of catalyst particles. The catalyst is typically immobilized on an inert support such as, for example, glass beads or sand grains to optimize fluidization. The fluid velocity should be chosen such that the particles are suspended, but are not carried out of the vessel. A fluidized-bed reactor has the ability to process large volumes of fluid with a low pressure drop. However, the success of this reactor type depends on the adequate attachment of the photocatalyst to the supporting particles, because of attrition of the photocatalyst particles by the flowing stream.[169] Figure 8.8 shows a schematic diagram of a bench-scale fluidized-bed that was used to degrade trichloroethylene in a polluted air stream by Dibble and Raupp.[170] Titania as the photocatalyst was supported on silica gel which formed a titania-silica gel. In order to reduce the momentum of the catalyst particles and to prevent them from leaving the reactor with the fluid stream, the top of reactor was designed such that the cross-sectional area was 125% larger compared to the cross-sectional area in the lower part of the reactor to lower the fluid velocity.

8.3.2 Immobilised Systems

8.3.2.1 Flat Plate

Flat plate reactors have been widely used for heterogeneous photocatalysis studies due to the simplicity of the design and ease of operation.[171–173] Flat plate photocatalytic reactors consist typically of two flat plates which are placed at a certain distance from each other forming a channel through which the fluid passes. The catalyst is coated either only on the interior surface of one the plates or on both of them depending on the position of the external or internal light source for illumination of the catalyst surface. Flat plate reactors usually provide a relatively low catalyst surface area and poor photon utilization,[144,174] but are relatively simple to design. An example of a flat plate photocatalytic reactor used by Estivill *et al.*[175] is illustrated in Figure 8.9.

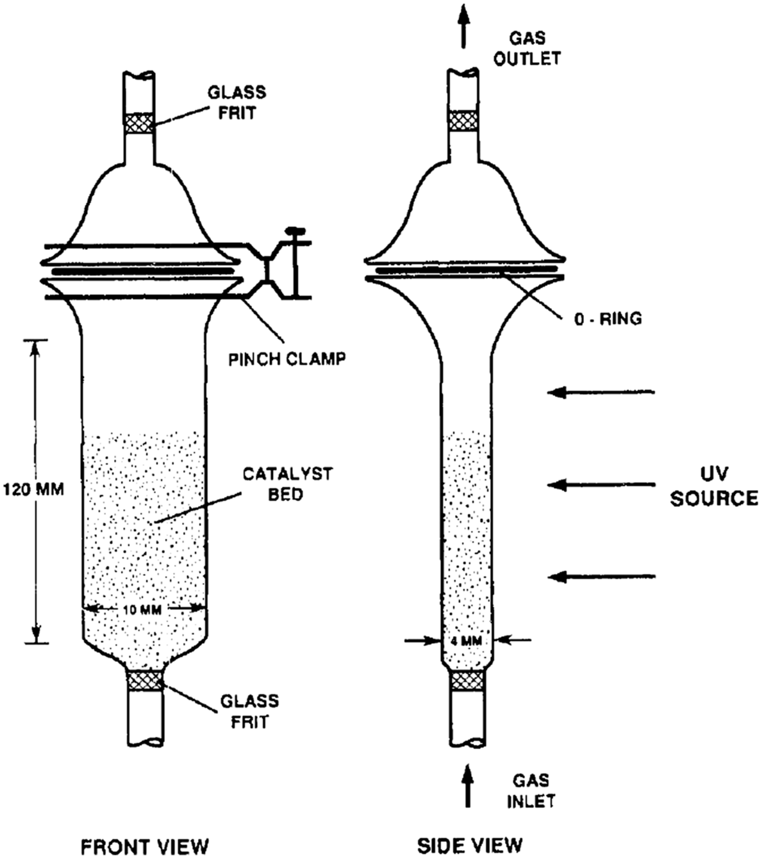

Figure 8.8 Schematic diagram of the fluidized-bed reactor used by Dibble and Raupp[170] Reprinted with permission from L. A. Dibble and G. B. Raupp, *Environ. Sci. Technol.*, 1992, **26**, 492–495. Copyright (1992) American Chemical Society.[170]

8.3.2.2 Honeycomb Monolith Photocatalytic Reactor

Honeycomb monolith photocatalytic reactors have been widely used for emission control of automobile exhausts and for NO_x reduction in power plant flue gases.[150] Typically, honeycomb structures consist of several channels with an internal diameter of about 1 mm while the cross-sectional shape of the channels are normally square or circular. The catalyst is usually coated on the walls of the channels as a thin film. In order to achieve an energy efficient design, investigations have been conducted on the mathematical modelling of mass, momentum and radiation transfer within photocatalytic monolith reactors.[150,154,156] The main advantages of this design are a large ratio of the catalyst surface area over the reactor volume and a low pressure drop. Moreover, the scale-up of the monolithic reactor can be done simply by expanding the number of channels.[176] However, insufficient radiation on the catalyst surface through honeycomb channels might result in a low reaction rate and, therefore,

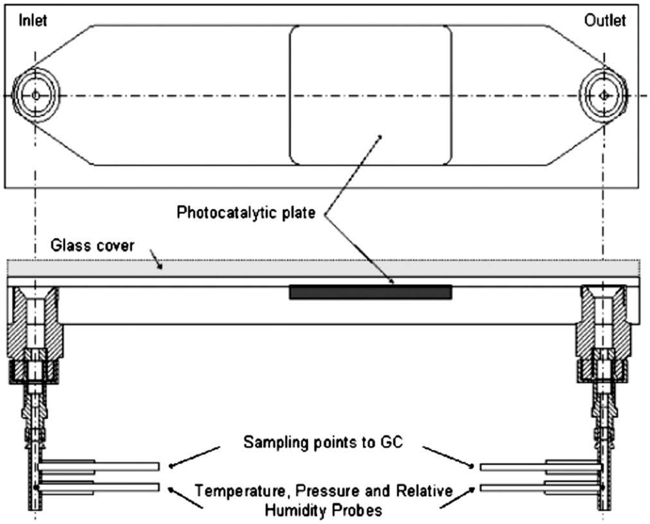

Figure 8.9 A schematic diagram of flat plate photocatalytic reactor used by Estivill *et al.*[175] Reprinted (adapted) with permission from I. Salvadó-Estivill, A. Brucato and G. Li Puma, *Ind. Eng. Chem. Res.*, 2007, **46**, 7489–7496. Copyright (2007) American Chemical Society.[175]

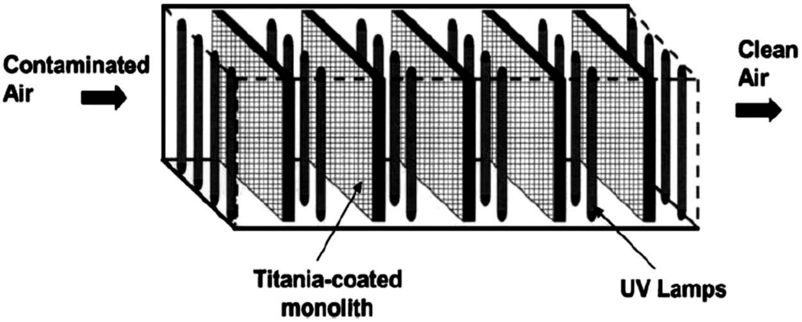

Figure 8.10 Schematic diagram of the monolith reactor used by Hossain and co-workers.[150,156] Reprinted from Hossain *et al.*[150] with permission from John Wiley and Sons. Copyright © 1999 American Institute of Chemical Engineers (AIChE).

low process efficiency.[16,177] An example of a monolith reactor for photocatalytic oxidation of formaldehyde as used by Raupp *et al.*[150,156] is shown in Figure 8.10.

8.3.2.3 Optical Fiber Photocatalytic Reactors

Marinangeli and Olis[178,179] proposed the concept of applying optical fibers as both a support for catalyst immobilization and as a light-distributing guide for photocatalysis. Light travels through the optical fiber by reflection on the fiber wall. In a photocatalytic reactor constructed from such optical fibers, the light beam striking the inner wall of a fiber splits into two parts: one part is absorbed by the catalyst layer coated on the fiber and the remaining light is reflected internally and transmitted along the fiber (see Figure 8.11a). This phenomenon repeats itself along the fibers resulting in the gradual distribution of photons along the reactor length.[159]

The advantages of such a reactor include the more even distribution of light that can be achieved, a large allowable distance between light source and catalyst, and a versatile design in the number of fibers and the distance between them. Furthermore, the back illumination of the catalyst prevents the loss of photons due to scattering or absorption by the reacting medium.[180] However, back illumination of photocatalyst might result in the generation of electron–hole pairs far from the interface of the catalyst and reacting medium, which increases the possibility for recombination of generated electrons and holes before a reaction can occur.[181] Moreover, the optical fibers usually occupy around 20–30% of the reactor space while supplying a relatively low area of catalyst surface.[182] Consequently, the flow rate decreases due to an increase in pressure drop.[16] Oxidation of acetone in an optical fiber photocatalytic reactor employing bare quartz fibers as TiO_2 support was investigated by Choi *et al.*[181]

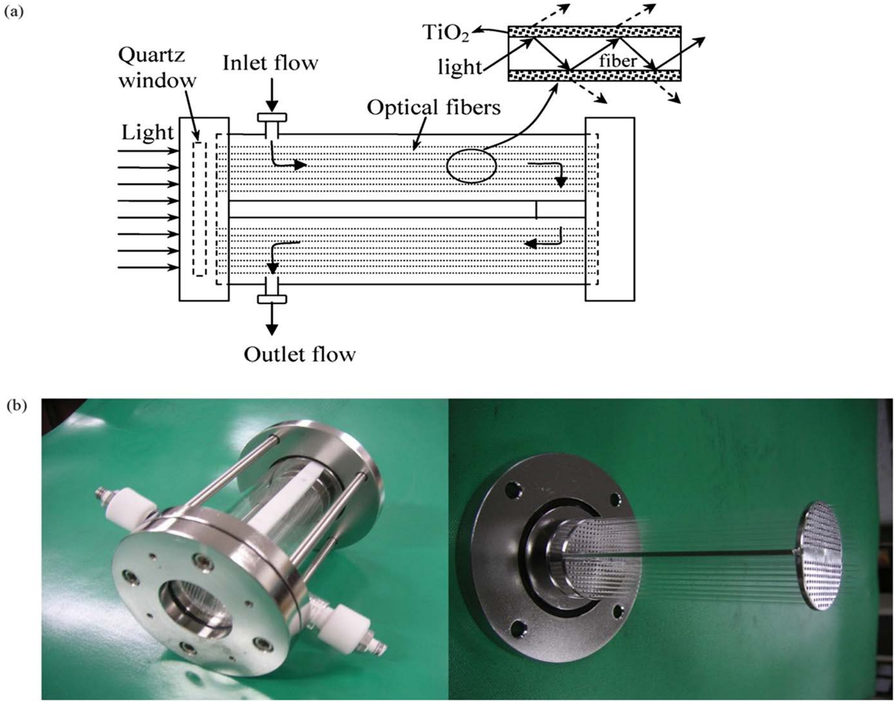

Figure 8.11 (a) Schematic diagram and (b) images of photoreactor with catalyst coated optical fibers by Nguyen *et al.*[183] Reprinted from *Appl. Catal., A*, **335**, T.-V. Nguyen and J. C. S. Wu, Photoreduction of CO_2 in an optical-fiber photoreactor: Effects of metals addition and catalyst carrier, 112–120, Copyright 2008, with permission from Elsevier.

Their results showed a 90% reduction of the intensity of light within 30 cm of a fiber coated with titania, which reveals an exponential decay in the light intensity. Figure 8.11 shows an example of an optical fiber photocatalytic reactor for CO_2 reduction to methanol, which was investigated by Nguyen *et al.*[183]

Lin *et al.*[176] proposed an optical fiber monolith reactor for wastewater treatment. They used a ceramic multichannel monolith as a support for the photocatalyst. They inserted the bare quartz fiber optics as both a light guide and catalyst support into the monolith channels. The reactor performance was tested for degradation of *o*-dichlorobenzene in water. They found an optimum photocatalyst film thickness of 0.4 μm coated on the fibers. This configuration provides a higher photocatalyst surface area compared to an optical fiber reactor. However, the short length of light propagation still remains a disadvantage due to the exponential decay of light along the fiber optics. Du *et al.*[184] modified the proposed design by Lin *et al.* by using "side light" optical fibers instead of normal optical fibers to improve the photon utilization inside the monolith channels (Figure 8.12). Another difference is

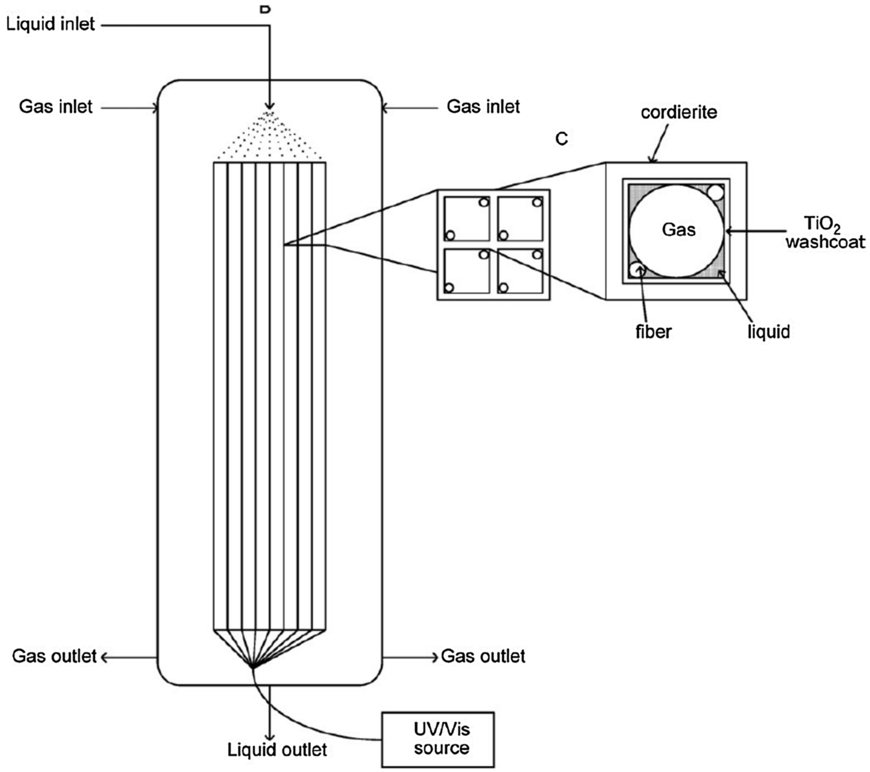

Figure 8.12 Schematic diagram of internally-illuminated monolith photocatalytic reactor.[184] Reprinted from *Appl. Catal., A*, **334**, P. Du, J. T. Carneiro, J. A. Moulijn and G. Mul, A novel photocatalytic monolith reactor for multiphase heterogeneous photocatalysis, 119–128, Copyright 2008, with permission from Elsevier.

that they did not coat the fiber wall with photocatalyst to prevent the light attenuation at the interface of catalyst and reactant. Titania was coated on the inner walls of the monolith channels by a wash coating method. The internally illuminated photocatalytic monolith reactor was tested for photocatalytic oxidation of cyclohexane.

8.3.2.4 Annular Reactors

In an annular reactor, the fluid flows through an annulus region that is bounded by two concentric pipes that have different diameters. The light source may be positioned either at the centre of the reactor or on the outside of the reactor. The walls of the tubes are coated with a layer of photocatalyst. The layer thickness should be thin enough to allow for the photons to illuminate the entire catalyst surface. Similar to the flat plate type of reactor, annular photocatalytic reactors offer a relative low reaction surface.[160] However, an annular geometry offers the advantage of a homogenous light distribution over the catalyst surface and, consequently, optimal photon utilization. In addition, it is possible to approach plug-flow in the annular geometry, which makes this reactor type ideal for studies of the kinetics of photocatalytic reactions.[185] Due to the simple design and operation, annular reactors are the most widely applied photocatalytic reactors for photocatalytic studies.[186] Figure 8.13 shows an annular flow reactor that was used by Imoberdorf *et al.*[153,187,188] They proposed a scaled-up multi-annular photocatalytic reactor for the degradation of pollutants in air streams. Their design was composed of four, 177 cm long, concentric pipes of borosilicate glass while the UV lamp was located at the center. The interior walls of each annulus unit were coated by titania, which provided an active surface area of 5209 cm^2. Such surface area significantly increased when compared to the laboratory reactor of 81 cm^2 active catalyst surface area tested by the same research group. The multi-annular photocatalytic reactor was modelled based on mass, momentum and radiation balances. The results predicted by the model were in good agreement with experimental results.

8.3.2.5 Packed-Bed Photocatalytic Reactors

A packed-bed photocatalytic reactor is composed of a vessel that contains immobilized catalytic particles. The light sources can be located inside or outside of the reactor. The fluid, including the reactants, contacts the illuminated catalyst particles. Quartz and borosilicate glass, which are transparent to UV light, are often used as the packing material. The catalyst is coated as a layer on the catalyst particles, which should be thin enough to allow transmission of a fraction of the UV radiation to the particles that are located further away from the UV source. Consequently, the bed volume can be activated up to a certain depth by the light source. Therefore, the light absorption factor of the catalyst layer is one of the key factors for the design of packed-bed photocatalytic reactors. Guidelines to design packed-bed photocatalytic reactors have been

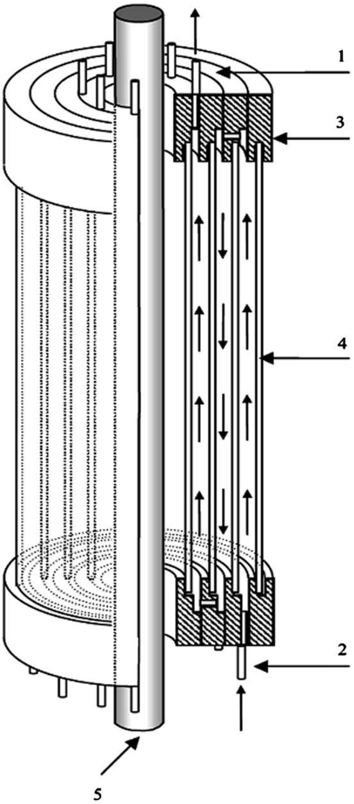

Figure 8.13 Schematic diagram of the annular reactor used by Imoberdorf *et al.*[153,187,188] Reprinted from *Chem. Eng. Sci.*, **62**, Gustavo E. Imoberdorf *et al.*, Simulation of a multi-annular photocatalytic reactor for degradation of perchloroethylene in air: Parametric analysis of radiative energy efficiencies, 1138–1154, Copyright 2007, with permission from Elsevier.

proposed including a cost analysis.[189] Raupp *et al.* developed a mathematical model to predict the behaviour of a continuous packed-bed photocatalytic reactor. Their reactor featured a lamp inside the tube as light source for the oxidation of a pollutant in a gas stream. The model includes a radiation field model within the reactor.[149] The constraints that this design may have are a low surface area to reactor volume ratio and less efficient photon utilization when taking into account both photon absorption and scattering.[149,190] Figure 8.14 shows a schematic diagram of (a) single lamp and (b) multi-lamp packed-bed photocatalytic reactors, which were modelled by Alexiadis *et al.*[189]

8.3.2.6 Microreactors

Micro-reaction systems have attracted much attention for chemical applications and demonstrated significant promise in a wide range of chemical transformations.[191] Microreactors offer a small molecular path for mass

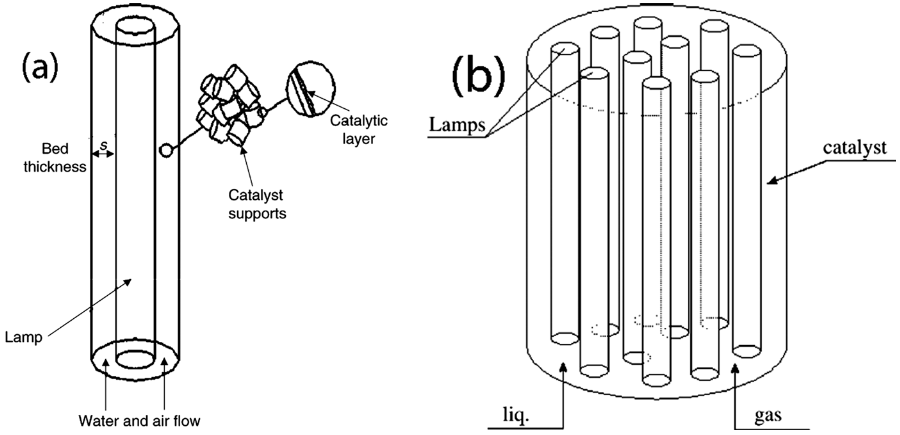

Figure 8.14 Schematic diagram of (a) single lamp and (b) multi-lamp packed-bed photocatalytic reactors used by Alexiadis *et al.*[189] Reprinted from *Chem. Eng. Process.*, **44**, A. Alexiadis and I. Mazzarino, Design guidelines for fixed-bed photocatalytic reactors, 453–459, Copyright 2005, with permission from Elsevier.

transport, fast mixing times, laminar flow conditions and a large specific surface area, which favour fast heat transfer. Microreactors also have a great potential for catalytic applications because of their large surface-to-volume ratio. The ratio of the irradiated surface area of catalyst to reactor volume is one of the crucial factors in the design of a photocatalytic reactor. A microreactor can provide a specific surface area of about 1.410^4 m^2 m^{-3},[192] which is much larger than the typical irradiated specific surface area of conventional photocatalytic reactors.[193] Another advantage of photocatalytic microreactors is that a small light source, and therefore lower radiation cost, is required for a miniaturized reactor. Several studies have investigated the feasibility of using microreactors for photocatalytic applications.[192,194–199] Figure 8.15 shows a microreactor that was used by Gorges *et al.*[194] to decompose 4-chlorphenol in water. Their microreactor consisted of 19 channels each with a cross-section of 200 μm300 μm. Compared to conventional photocatalytic reactors, the irradiated specific catalyst surface area of this microreactor is about 4–400 times larger.

8.3.3 Light Sources

The design of the light source for photocatalysis has a key impact on the efficiency of photocatalytic applications. The rate of photocatalytic reactions depends in general on both the concentrations of the reactants and on the rate of photon absorption by the catalyst. The catalyst has to receive photons with a suitable amount of energy over a large area for optimal performance. At low photon intensities, the reaction rate typically increases linearly with

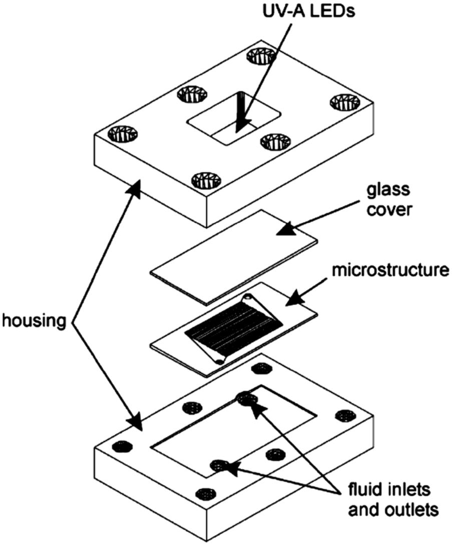

Figure 8.15 Schematic diagram of a photocatalytic micro-reactor used by Gorges *et al.*[194] Reprinted from J. Photochem. Photobiol., A, **167**, R. Gorges, S. Meyer and G. Kreisel, Photocatalysis in microreactors, 95–99, Copyright 2004, with permission from Elsevier.

increasing light intensity due to the increased generation of electron–hole pairs.[3] However, upon further increasing the light intensity, the rate of electrons–hole pair recombination may increase faster than the rate of consumption of electron–hole pairs by the chemical reaction.[3] Therefore, careful design of the radiation field within a photocatalytic reactor is important to maximize reactor performance. Such radiation fields within photocatalytic reactors have been analysed by solving the radiative transfer equations (RTE) for different light sources by applying different numerical methods[147,200–202] including Monte Carlo methods.[152,203–205] In general, the light sources that have been used to activate a photocatalyst can be categorized into two groups: solar radiation and artificial radiation, as described in more detail below.

8.3.3.1 Solar-Based Photocatalytic Reactors

Since only 4–5% of the solar light that reaches the earth is UV light, a great deal of research has been conducted on the development of photocatalysts that can be activated with visible light.[206] In addition to the required bandgap, using sunlight as the radiation source imposes geometrical constraints to the design of photocatalytic reactors. Solar-based photocatalytic reactors normally have a flattened geometry and thus need a large footprint.[207] Nevertheless, it is expected that current interests and developments in the application of solar energy for photocatalysis will even further increase due to the abundance and sustainability of solar energy. The design of solar-based photocatalytic reactors may be based on either an immobilized or suspended catalyst with the option to concentrate solar light before usage. Such concentrated systems use a reflector to direct solar radiation with a solar tracking mechanism. Compared to non-concentrating systems, concentrating systems need a smaller reactor volume for the same light harvesting surface area. Therefore, in the construction of the reactor, more expensive materials can be used. However, concentrated solar-based photocatalytic reactors are not able to harvest diffuse UV radiation, which is of importance especially on cloudy days. Even on a clear day, approximately 50% of the UV light that reaches the earth includes diffuse UV light,[208] which limits the effectiveness of concentrating solar energy.

Non-concentrating solar photocatalytic reactors—whether using a reflector or not—are static systems. They are less expensive to construct and easier to operate compared to concentrating solar photocatalytic reactors.[209] Moreover, they can collect both direct and diffuse UV radiation. Although the collection of solar energy is less efficient due to the absence of concentrating devices, the photonic efficiency is normally higher compared to concentrating reactors due to the lower rate of electron–hole pair recombination at lower radiation intensities.[3] Furthermore, the optical loss is lower compared to the concentrating reactors, especially if no reflective surface is used.[210] However, a much larger photocatalytic surface area is needed compared to concentrating systems and, consequently, the material to build such a reactor should be relatively inexpensive.[210] Non-concentrating solar reactors operate usually at laminar flow, while turbulent flow is more favourable in the term of mass transfer efficiency.[211]

Parabolic trough reactors (PTRs) are an example of a concentrating solar photocatalytic reactor, which consist of parabolic reflectors that concentrate the solar light on a tube located in the centre of the parabola (Figure 8.16). The stream including reactants flows through a tube, which facilitates plug-flow behavior. The reactor size is small and the radiation intensity per reactor volume is high.[212] However, compared to non-concentrating reactors, PTRs are relatively expensive while the optical and quantum efficiency is lower.[212] PTRs have been used to degrade different pollutants in water successfully.[213–216] Compound parabolic concentrator reactors (CPCR) are trough reactors, but with a low ability to concentrate solar light.[217] This type of reactor has static reflectors and differs from a PTR reflector. The reflector of a CPCR usually consists of two parabolas, which are positioned side by side. The focal line is above the connecting line of two parabolas. This geometry allows for the collection of light beams from almost every direction to be concentrated on the focal line. CPCRs combine the characteristics of both concentrating and non-concentrating reflectors: they concentrate the solar light while they are static and collect the direct UV radiation as well as diffuse UV radiation. Figure 8.16a and b show the reflector profile and schematic diagrams of PTRs and CPCRs, respectively. The performances of PTRs and CPCRs were investigated in degradation of different compounds in

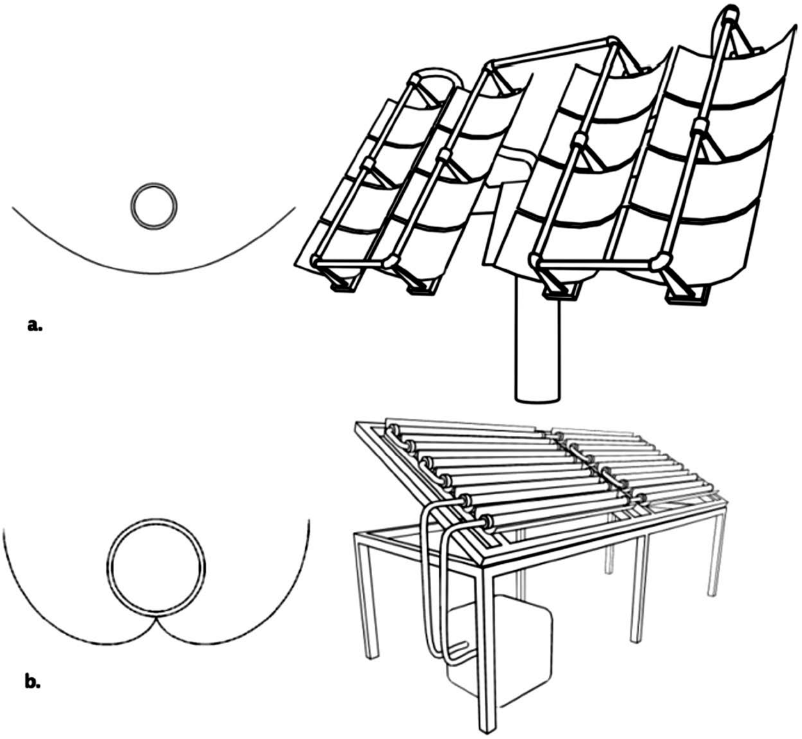

Figure 8.16 Reflector profile and schematic diagram of (a) parabolic trough reactor (PTR) and (b) compound trough reactor (CPCR).[146] Reprinted with permission from R. J. Braham and A. T. Harris, *Ind. Eng. Chem. Res.*, 2009, **48**, 8890–8905. Copyright (2009) American Chemical Society.[146]

water.[214,218–220] Results showed that CPCR performance is more efficient for photocatalytic applications compared to that of PTRs.

Thin-film fixed-bed reactors (TFFBR) are one of the first non-concentrating solar photocatalytic reactors. They generally consist of inclined plates that are coated with a thin film of photocatalyst. The feed stream flows over the catalyst plate as a thin layer.[210] Figure 8.17a shows a schematic drawing of a TFFBR. The efficiency of a TFFBR and a PTR has been compared in some studies.[146,210] Results showed that TFFBRs are more efficient compared to PTRs for the same operating conditions. Moreover, the cost of construction and operation of a TFFBR is considered to be lower than that of a PTR.[210]

A new type of non-concentrating solar photocatalytic reactor is the so-called double sheet skin photocatalytic reactor (DSSR).[221,222] This reactor is made of a transparent box of Plexiglass® with several channels (Figure 8.17b). Some types of Plexiglass® are able to transmit the direct and diffuse UV light with wavelengths shorter than 400 nm. The flow including suspended catalyst and reactants is pumped into the channels. Dillert *et al.*[223] studied a DSSR for the degradation of a biological pollutant in water. They found that to degrade

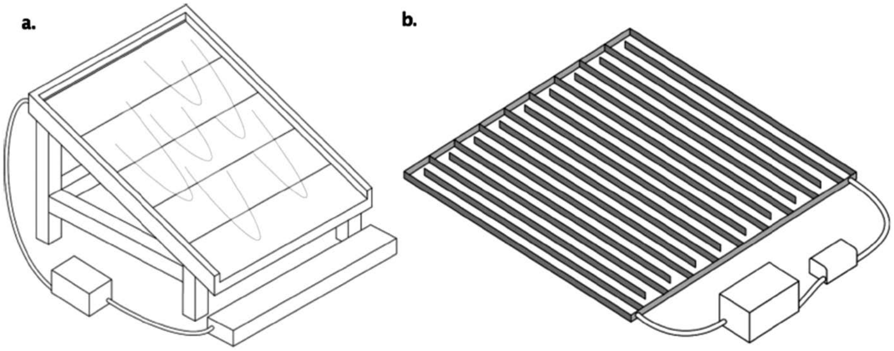

Figure 8.17 Schematic diagram of (a) thin-film fixed-bed photocatalytic reactor (TFFBR) and (b) double skin sheet reactor (DSSR).[146] Reprinted with permission from R. J. Braham and A. T. Harris, *Ind. Eng. Chem. Res.*, 2009, **48**, 8890–8905. Copyright (2009) American Chemical Society.[146]

1 m^3 of contaminated water per day, 50 m^2 of the radiated reactor surface is needed to reach 90% conversion when applying suspended titania (P25) as a catalyst.

8.3.3.2 Artificial Light Sources

Although many efforts have been made to develop photocatalysts that can harness visible light, titania is still the most frequently used photocatalyst which requires ultraviolet (UV) light to be activated. Artificial UV light sources offer independence from location, weather and the day–night cycle. However, additional costs in the form of investments, maintenance and electricity are required when using artificial light sources. In addition, the design of a reactor irradiated by an artificial light source is restricted by the geometry and the size of the light source. Nevertheless, the design of a photocatalytic reactor with an artificial light source can be based on a smaller footprint compared to one using solar light. Furthermore, artificial lights can provide a narrower spectrum of light that better matches the requirements of the photocatalyst compared to solar light.

Classical UV lamps have been used for laboratory and commercial photocatalytic applications. There are several studies dedicated to the analysis and modelling of the radiation field within a reactor based on conventional lamps as the light source.[147] Such lamps have usually a cylindrical shape and are based on mercury discharge or fluorescence. Artificial light sources can be classified into two groups: high and low power UV light sources. High power UV sources, such as medium and high-pressure mercury lamps, generate high intensities of UV light, which can intensify the reaction. However, the quantum yield of titania is known to decrease at high radiation intensities.[207] Therefore, the high power UV sources are usually not favoured in photocatalytic applications.[3] Using low power UV light sources, such as fluorescent or low-pressure mercury lamps, will enhance the quantum yields of photocatalysts. For example, Puma *et al.*[224] compared the performance of low pressure mercury and fluorescent lamps in a falling film photocatalytic reactor for wastewater treatment. Their results showed that a mercury lamp was more efficient than a fluorescent lamp. However, the disadvantages of a mercury lamp include its fragility, toxicity, short life span and issues relating to the disposal of such a lamp.[225]

Alternatively, light-emitting diodes (LEDs) can be used for photocatalytic applications. LEDs are non-toxic, compact and can be applied flexibly within a photocatalytic reactor both in terms of space and time. In addition, LEDs can offer a narrow light spectrum with a peak wavelength tuned for a specific photocatalyst.

In the last few years, several studies have reported the feasibility of using UV LEDs as a light source for photocatalytic applications in both gas and liquid phases.[226–229] These studies showed that LEDs can be promising alternative light sources to conventional UV lamps. This potential will further increase in the future in cases where the costs of LEDs continue to drop. In particular, investigation of the radiation field within a LED-based photocatalytic reactor is needed due to the importance of the rate of photon absorption in the reaction kinetics. Levine *et al.*[229] compared the performance of high power UV LEDs and a black light blue (BLB) lamp for the oxidation of ethanol. Their results showed that at an equivalent average irradiance, the LED-irradiated reactor had a lower reaction rate. They concluded that uniformity of the irradiance on the catalyst surface had a great impact on the reaction efficiency, which stresses the importance of optimizing the arrangement and design of the light source together with the design of the reactor equipment itself to provide the optimum photon utilization in LED-based photocatalytic reactors.

8.4 Conclusions

To unlock the full potential of photocatalysis for enabling a future generation of sustainable chemical processes, novel developments in the design of catalytic materials and novel reactor configurations are highly promising. The synthetic strategies for catalyst development in the case of classical semiconductors such as TiO_2 and novel photocatalysts, such as metal–organic frameworks, are rather similar. Both of them include sensitization towards visible light absorption and the introduction of additional catalytic sites. However, while in the case of TiO_2 charge recombination processes have to be minimized, the absence of intrinsic charge mobility in the case of MOFs imposes certain distinct differences. Moreover, MOFs possess extremely large surface areas and are highly tuneable which greatly enhances the possibilities of employing additional catalytic sites. At this stage semiconductors such as TiO_2 often outperform the MOF-based systems but the growing attention on photocatalysis with MOFs as well as nearly infinite possibilities of designing such systems, provide evidence that this class of materials holds a promise for photocatalytic applications in the coming decades.

Improving mass transfer has been the subject of many studies in chemical reactor design and in this regard, efficient designs have been proposed and developed for different phases. On the other hand, improving the photon transfer within photocatalytic reactors still has much room for improvement. So far, several photocatalytic reactors have been developed and tested to improve the mass and photon transfer simultaneously. Still for many applications, the photocatalytic process efficiency is not economically viable. Using the sun as a sustainable source of photons can improve the economic and environmental performance of the photocatalytic process. However, most of the photocatalysts need UV light to become activated. In this sense, a new generation of light sources such as UV-LEDs can be an attractive alternative for photocatalytic applications. Measuring the amount of photons received and absorbed by a photocatalyst within photocatalytic reactors is challenging, but feasible methods have been developed.[230] Integrated use of *in situ* measuring principles and process modelling tools is a promising way forward to optimize the design of photocatalytic reactors.

References

1. A. Fujishima and K. Honda, *Nature*, 1972, **238**, 37–38.
2. M. A. Fox and M. T. Dulay, *Chem. Rev.*, 1993, **93**, 341–357.
3. M. R. Hoffmann, S. T. Martin, W. Choi and D. W. Bahnemann, *Chem. Rev.*, 1995, **95**, 69–96.
4. J.-M. Herrmann, *Catal. Today*, 1999, **53**, 115–129.
5. B. Kraeutler and A. J. Bard, *J. Am. Chem. Soc.*, 1978, **100**, 5985–5992.
6. A. F. Tooru Inoue, S. Konishi and K. Honda, *Nature*, 1979, **277**, 2.
7. J. Schneider, M. Matsuoka, M. Takeuchi, J. Zhang, Y. Horiuchi, M. Anpo and D. W. Bahnemann, *Chem. Rev.*, 2014, **114**, 9919–9986.
8. Scopus, *web search, keywords: photocatalysis*, 2015.
9. D. O. Scanlon, C. W. Dunnill, J. Buckeridge, S. A. Shevlin, A. J. Logsdail, S. M. Woodley, C. R. A. Catlow, M. J. Powell, R. G. Palgrave, I. P. Parkin, G. W. Watson, T. W. Keal, P. Sherwood, A. Walsh and A. A. Sokol, *Nat. Mater.*, 2013, **12**, 798–801.
10. A. Ibhadon and P. Fitzpatrick, *Catalysts*, 2013, **3**, 189–218.
11. S. G. Botta, J. A. Navío, M. a. C. Hidalgo, G. M. Restrepo and M. I. Litter, *J. Photochem. Photobiol., A*, 1999, **129**, 89–99.
12. T. Hanada, in *Oxide and Nitride Semiconductors*, ed. T. Yao and S.-K. Hong, Springer Berlin Heidelberg, 2009, vol. 12, ch. 1, pp. 1–19.
13. S. R. Pendlebury, X. Wang, F. Le Formal, M. Cornuz, A. Kafizas, S. D. Tilley, M. Grätzel and J. R. Durrant, *J. Am. Chem. Soc.*, 2014, **136**, 9854–9857.
14. M. Barroso, S. R. Pendlebury, A. J. Cowan and J. R. Durrant, *Chem. Sci.*, 2013, **4**, 2724–2734.
15. M. A. Nasalevich, E. A. Kozlova, T. P. Lyubina and A. V. Vorontsov, *J. Catal.*, 2012, **287**, 138–148.
16. T. Van Gerven, G. Mul, J. Moulijn and A. Stankiewicz, *Chem. Eng. Process. Process Intensif.*, 2007, **46**, 781–789.

17. P. S. Mukherjee and A. K. Ray, *Chem. Eng. Technol.*, 1999, **22**, 253–260.
18. K. Hashimoto, H. Irie and A. Fujishima, *Jpn. J. Appl. Phys.*, 2005, **44**, 8269.
19. T. Kawai and T. Sakata, *Nature*, 1980, **286**, 474–476.
20. A. L. Linsebigler, G. Lu and J. T. Yates, *Chem. Rev.*, 1995, **95**, 735–758.
21. R. Li, F. Zhang, D. Wang, J. Yang, M. Li, J. Zhu, X. Zhou, H. Han and C. Li, *Nat. Commun.*, 2013, **4**, 1432.
22. T. Ohno, K. Sarukawa and M. Matsumura, *New J. Chem.*, 2002, **26**, 1167–1170.
23. K. Wenderich, A. Klaassen, I. Siretanu, F. Mugele and G. Mul, *Angew. Chem., Int. Ed.*, 2014, **53**, 12476–12479.
24. M. Gratzel, *Heterogeneous Photochemical Electron Transfer*, CRC Press, Boca Raton, FL, 1989.
25. J. Zhu, F. Chen, J. Zhang, H. Chen and M. Anpo, *J. Photochem. Photobiol., A*, 2006, **180**, 196–204.
26. J. Zhu, W. Zheng, B. He, J. Zhang and M. Anpo, *J. Mol. Catal. A: Chem.*, 2004, **216**, 35–43.
27. L. Palmisano, V. Augugliaro, A. Sclafani and M. Schiavello, *J. Phys. Chem.*, 1988, **92**, 6710–6713.
28. E. Borgarello, J. Kiwi, M. Graetzel, E. Pelizzetti and M. Visca, *J. Am. Chem. Soc.*, 1982, **104**, 2996–3002.
29. S. Yuan, Y. Chen, L. Shi, J. Fang, J. Zhang, J. Zhang and H. Yamashita, *Mater. Lett.*, 2007, **61**, 4283–4286.
30. Z. Wenfang, L. Qingju, Z. Zhongqi and Z. Ji, *J. Phys. D: Appl. Phys.*, 2010, **43**, 035301.
31. W. Choi, A. Termin and M. R. Hoffmann, *J. Phys. Chem.*, 1994, **98**, 13669–13679.
32. H. Yamashita, M. Harada, J. Misaka, M. Takeuchi, Y. Ichihashi, F. Goto, M. Ishida, T. Sasaki and M. Anpo, *J. Synchrotron Radiat.*, 2001, **8**, 569–571.
33. R. Asahi, T. Morikawa, T. Ohwaki, K. Aoki and Y. Taga, *Science*, 2001, **293**, 269–271.
34. K. Nagaveni, M. S. Hegde, N. Ravishankar, G. N. Subbanna and G. Madras, *Langmuir*, 2004, **20**, 2900–2907.
35. J. Li, N. Lu, X. Quan, S. Chen and H. Zhao, *Ind. Eng. Chem. Res.*, 2008, **47**, 3804–3808.
36. D. Li, H. Haneda, S. Hishita, N. Ohashi and N. K. Labhsetwar, *J. Fluorine Chem.*, 2005, **126**, 69–77.
37. W. Kim, T. Tachikawa, T. Majima and W. Choi, *J. Phys. Chem. C*, 2009, **113**, 10603–10609.
38. K. Kalyanasundaram and M. Grätzel, *Angew. Chem. Int. Ed. Engl.*, 1979, **18**, 701–702.
39. B. O'Regan and M. Grätzel, *Nature*, 1991, **353**, 737–740.
40. C. Gomes Silva, R. Juárez, T. Marino, R. Molinari and H. García, *J. Am. Chem. Soc.*, 2010, **133**, 595–602.
41. P. Montes-Navajas, M. Serra and H. Garcia, *Catal. Sci. Technol.*, 2013, **3**, 2252–2258.
42. N. Wang, T. Tachikawa and T. Majima, *Chem. Sci.*, 2011, **2**, 891–900.

43. T. A. Kandiel, A. Feldhoff, L. Robben, R. Dillert and D. W. Bahnemann, *Chem. Mater.*, 2010, **22**, 2050–2060.
44. D. W. Bahnemann, C. Kormann and M. R. Hoffmann, *J. Phys. Chem.*, 1987, **91**, 3789–3798.
45. N. Satoh, T. Nakashima, K. Kamikura and K. Yamamoto, *Nat. Nano*, 2008, **3**, 106–111.
46. Q. Zhang, J.-B. Joo, Z. Lu, M. Dahl, D. L. Oliveira, M. Ye and Y. Yin, *Nano Res.*, 2011, **4**, 103–114.
47. L. V.-E. Juan, C. Ya-Dong, C. W. W. Kevin and Y. Yusuke, *Sci. Technol. Adv. Mater.*, 2012, **13**, 013003.
48. A. M. Doyle, S. K. Shaikhutdinov, S. D. Jackson and H.-J. Freund, *Angew. Chem., Int. Ed.*, 2003, **42**, 5240–5243.
49. N. H. Khdary and M. A. Ghanem, *RSC Adv.*, 2014, **4**, 50114–50122.
50. F. Lakadamyali and E. Reisner, *Chem. Commun.*, 2011, **47**, 1695–1697.
51. F. Lakadamyali, A. Reynal, M. Kato, J. R. Durrant and E. Reisner, *Chem.–Eur. J.*, 2012, **18**, 15464–15475.
52. E. Reisner, D. J. Powell, C. Cavazza, J. C. Fontecilla-Camps and F. A. Armstrong, *J. Am. Chem. Soc.*, 2009, **131**, 18457–18466.
53. P. Mahata, G. Madras and S. Natarajan, *J. Phys. Chem. B*, 2006, **110**, 13759–13768.
54. S. Bordiga, C. Lamberti, G. Ricchiardi, L. Regli, F. Bonino, A. Damin, K. P. Lillerud, M. Bjorgen and A. Zecchina, *Chem. Commun.*, 2004, **10**, 2300–2301.
55. M. Alvaro, E. Carbonell, B. Ferrer, F. X. Llabrés I Xamena and H. Garcia, *Chem.–Eur. J.*, 2007, **13**, 5106–5112.
56. J. Gascon, M. D. Hernández-Alonso, A. R. Almeida, G. P. van Klink, F. Kapteijn and G. Mul, *ChemSusChem*, 2008, **1**, 981–983.
57. H. Li, M. Eddaoudi, M. O'Keeffe and O. M. Yaghi, *Nature*, 1999, **402**, 276–279.
58. M. Nasalevich, M. A. van der Veen, F. Kapteijn and J. Gascon, *CrystEngComm*, 2014, **16**, 4919–4926 .
59. T. Zhang and W. Lin, *Chem. Soc. Rev.*, 2014, **43**, 5982–5993.
60. C. Wang, D. Liu and W. Lin, *J. Am. Chem. Soc.*, 2013, **135**, 13222–13234.
61. G. Ferey, C. Serre, T. Devic, G. Maurin, H. Jobic, P. L. Llewellyn, G. De Weireld, A. Vimont, M. Daturi and J.-S. Chang, *Chem. Soc. Rev.*, 2011, **40**, 550–562.
62. L. E. Kreno, K. Leong, O. K. Farha, M. Allendorf, R. P. Van Duyne and J. T. Hupp, *Chem. Rev.*, 2011, **112**, 1105–1125.
63. J.-R. Li, R. J. Kuppler and H.-C. Zhou, *Chem. Soc. Rev.*, 2009, **38**, 1477–1504.
64. L. J. Murray, M. Dincă and J. R. Long, *Chem. Soc. Rev.*, 2009, **38**, 1294–1314.
65. K. Sumida, D. L. Rogow, J. A. Mason, T. M. McDonald, E. D. Bloch, Z. R. Herm, T.-H. Bae and J. R. Long, *Chem. Rev.*, 2011, **112**, 724–781.
66. P. Horcajada, T. Chalati, C. Serre, B. Gillet, C. Sebrie, T. Baati, J. F. Eubank, D. Heurtaux, P. Clayette, C. Kreuz, J.-S. Chang, Y. K. Hwang,

V. Marsaud, P.-N. Bories, L. Cynober, S. Gil, G. Ferey, P. Couvreur and R. Gref, *Nat. Mater.*, 2010, **9**, 172–178.

67. P. Horcajada, R. Gref, T. Baati, P. K. Allan, G. Maurin, P. Couvreur, G. Férey, R. E. Morris and C. Serre, *Chem. Rev.*, 2011, **112**, 1232–1268.
68. T. Rodenas, I. Luz, G. Prieto, B. Seoane, H. Miro, A. Corma, F. Kapteijn, F. X. Llabrés i Xamena and J. Gascon, *Nat. Mater.*, 2015, **14**, 48–55.
69. T. Rodenas, M. van Dalen, E. García-Pérez, P. Serra-Crespo, B. Zornoza, F. Kapteijn and J. Gascon, *Adv. Funct. Mater.*, 2014, **24**, 249–256.
70. A. Corma, H. García and F. X. Llabrés i Xamena, *Chem. Rev.*, 2010, **110**, 4606–4655.
71. D. Farrusseng, S. Aguado and C. Pinel, *Angew. Chem., Int. Ed.*, 2009, **48**, 7502–7513.
72. J. Gascon, A. Corma, F. Kapteijn and F. X. Llabrés i Xamena, *ACS Catal.*, 2014, **4**, 361–378.
73. B. Civalleri, F. Napoli, Y. Noel, C. Roetti and R. Dovesi, *CrystEngComm*, 2006, **8**, 364–371.
74. M. Fuentes-Cabrera, D. M. Nicholson, B. G. Sumpter and M. Widom, *J. Chem. Phys.*, 2005, **123**, 124713.
75. L.-M. Yang, G.-Y. Fang, J. Ma, E. Ganz and S. S. Han, *Cryst. Growth Des.*, 2014, **14**, 2532–2541.
76. S. S. Kaye, A. Dailly, O. M. Yaghi and J. R. Long, *J. Am. Chem. Soc.*, 2007, **129**, 14176–14177.
77. M. Dan-Hardi, C. Serre, T. Frot, L. Rozes, G. Maurin, C. Sanchez and G. Férey, *J. Am. Chem. Soc.*, 2009, **131**, 10857–10859.
78. J. H. Cavka, S. Jakobsen, U. Olsbye, N. Guillou, C. Lamberti, S. Bordiga and K. P. Lillerud, *J. Am. Chem. Soc.*, 2008, **130**, 13850–13851.
79. K. G. M. Laurier, F. Vermoortele, R. Ameloot, D. E. De Vos, J. Hofkens and M. B. J. Roeffaers, *J. Am. Chem. Soc.*, 2013, **135**, 14488–14491.
80. P. M. Wojciechowski, W. Zierkiewicz, D. Michalska and P. Hobza, *J. Chem. Phys.*, 2003, **118**, 10900–10911.
81. C. G. Silva, I. Luz, F. X. Llabrés I Xamena, A. Corma and H. García, *Chem.–Eur. J.*, 2010, **16**, 11133–11138.
82. C. H. Hendon, D. Tiana, M. Fontecave, C. Sanchez, L. D'arras, C. Sassoye, L. Rozes, C. Mellot-Draznieks and A. Walsh, *J. Am. Chem. Soc.*, 2013, **135**(30), 10942–10945.
83. T. Musho, J. Li and N. Wu, *Phys. Chem. Chem. Phys.*, 2014, **16**, 23646–23653.
84. L. Shen, R. Liang, M. Luo, F. Jing and L. Wu, *Phys. Chem. Chem. Phys.*, 2015, **17**, 117–121.
85. T. W. Goh, C. Xiao, R. V. Maligal-Ganesh, X. Li and W. Huang, *Chem. Eng. Sci.*, 2015, **124**, 45–51.
86. H.-J. Son, S. Jin, S. Patwardhan, S. J. Wezenberg, N. C. Jeong, M. So, C. E. Wilmer, A. A. Sarjeant, G. C. Schatz, R. Q. Snurr, O. K. Farha, G. P. Wiederrecht and J. T. Hupp, *J. Am. Chem. Soc.*, 2012, **135**, 862–869.
87. C. Zou, M.-H. Xie, G.-Q. Kong and C.-D. Wu, *CrystEngComm*, 2012, **14**, 4850–4856.

88. A. Fateeva, P. A. Chater, C. P. Ireland, A. A. Tahir, Y. Z. Khimyak, P. V. Wiper, J. R. Darwent and M. J. Rosseinsky, *Angew. Chem., Int. Ed.*, 2012, **51**, 7440–7444.
89. M. G. Goesten, F. Kapteijn and J. Gascon, *CrystEngComm*, 2013, **15**, 9249.
90. J. S. Seo, D. Whang, H. Lee, S. I. Jun, J. Oh, Y. J. Jeon and K. Kim, *Nature*, 2000, **404**, 982–986.
91. M. A. Nasalevich, M. G. Goesten, T. J. Savenije, F. Kapteijn and J. Gascon, *Chem. Commun.*, 2013, **49**, 10575–10577.
92. D. Jiang, L. L. Keenan, A. D. Burrows and K. J. Edler, *Chem. Commun.*, 2012, **48**, 12053–12055.
93. M. A. Nasalevich, M. G. Goesten, T. J. Savenije, F. Kapteijn and J. Gascon, *Chem. Commun.*, 2015, **51**, 961–962.
94. D. Sun, W. Liu, M. Qiu, Y. Zhang and Z. Li, *Chem. Commun.*, 2015, **51**, 2056–2059.
95. J. Long, S. Wang, Z. Ding, S. Wang, Y. Zhou, L. Huang and X. Wang, *Chem. Commun.*, 2012, **48**, 11656–11658.
96. C.-C. Wang, J.-R. Li, X.-L. Lv, Y.-Q. Zhang and G. Guo, *Energy Environ. Sci.*, 2014, **7**, 2831–2867.
97. Y.-P. Yuan, L.-S. Yin, S.-W. Cao, G.-S. Xu, C.-H. Li and C. Xue, *Appl. Catal., B*, 2015, **168**, 572–576.
98. J. He, J. Wang, Y. Chen, J. Zhang, D. Duan, Y. Wang and Z. Yan, *Chem. Commun.*, 2014, **50**, 7063–7066.
99. Y. Lee, S. Kim, J. K. Kang and S. M. Cohen, *Chem. Commun.*, 2015, **51**, 5735–5738.
100. O. K. Farha, I. Eryazici, N. C. Jeong, B. G. Hauser, C. E. Wilmer, A. A. Sarjeant, R. Q. Snurr, S. T. Nguyen, A. Ö. Yazaydın and J. T. Hupp, *J. Am. Chem. Soc.*, 2012, **134**, 15016–15021.
101. Y. Fu, D. Sun, Y. Chen, R. Huang, Z. Ding, X. Fu and Z. Li, *Angew. Chem., Int. Ed.*, 2012, **51**, 3364–3367.
102. D. Sun, Y. Fu, W. Liu, L. Ye, D. Wang, L. Yang, X. Fu and Z. Li, *Chem.–Eur. J.*, 2013, **19**, 14279–14285.
103. F. X. Llabrés i Xamena, A. Corma and H. Garcia, *J. Phys. Chem. C*, 2006, **111**, 80–85.
104. C. H. Hendon, D. Tiana and A. Walsh, *Phys. Chem. Chem. Phys.*, 2012, **14**, 13120–13132.
105. G. Givaja, P. Amo-Ochoa, C. J. Gomez-Garcia and F. Zamora, *Chem. Soc. Rev.*, 2012, **41**, 115–147.
106. Y. Kobayashi, B. Jacobs, M. D. Allendorf and J. R. Long, *Chem. Mater.*, 2010, **22**, 4120–4122.
107. F. Gandara, F. J. Uribe-Romo, D. K. Britt, H. Furukawa, L. Lei, R. Cheng, X. F. Duan, M. O'Keeffe and O. M. Yaghi, *Chem.–Eur. J.*, 2012, **18**, 10595–10601.
108. D. Sheberla, L. Sun, M. A. Blood-Forsythe, S. Er, C. R. Wade, C. K. Brozek, A. Aspuru-Guzik and M. Dincă, *J. Am. Chem. Soc.*, 2014, **136**, 8859–8862.
109. T. J. Savenije, A. J. Ferguson, N. Kopidakis and G. Rumbles, *J. Phys. Chem. C*, 2013, **117**, 24085–24103.

110. A. Saeki, Y. Koizumi, T. Aida and S. Seki, *Acc. Chem. Res.*, 2012, **45**, 1193–1202.
111. T. C. Narayan, T. Miyakai, S. Seki and M. Dincă, *J. Am. Chem. Soc.*, 2012, **134**, 12932–12935.
112. L. Sun, T. Miyakai, S. Seki and M. Dincă, *J. Am. Chem. Soc.*, 2013, **135**, 8185–8188.
113. M. A. Nasalevich, M. G. Goesten, T. J. Savenije, F. Kapteijn and J. Gascon, *Chem. Commun.*, 2013, **90**, 10575–10577.
114. Y. H. Fu, D. R. Sun, Y. J. Chen, R. K. Huang, Z. X. Ding, X. Z. Fu and Z. H. Li, *Angew. Chem., Int. Ed.*, 2012, **51**, 3364–3367.
115. M. C. Fravventura, D. Deligiannis, J. M. Schins, L. D. A. Siebbeles and T. J. Savenije, *J. Phys. Chem. C*, 2013, **117**, 8032–8040.
116. T. J. Savenije, A. Huijser, M. J. W. Vermeulen and R. Katoh, *Chem. Phys. Lett.*, 2008, **461**, 93–96.
117. R. A. Marcus, *J. Chem. Phys.*, 1956, **24**, 966–978.
118. M. Schiavello, *Heterogeneous Photocatalysis*, Wiley, Chichester, U.K., 1997.
119. N. F. Mott, *Can. J. Phys.*, 1956, **34**, 1356–1368.
120. V. Barone, M. Casarin, D. Forrer, M. Pavone, M. Sambi and A. Vittadini, *J. Comput. Chem.*, 2009, **30**, 934–939.
121. C. Wang, D. Liu and W. Lin, *J. Am. Chem. Soc.*, 2013, **135**, 13222–13234.
122. H. Khajavi, J. Gascon, J. M. Schins, L. D. A. Siebbeles and F. Kapteijn, *J. Phys. Chem. C*, 2011, **115**, 12487–12493.
123. J. He, Z. Yan, J. Wang, J. Xie, L. Jiang, Y. Shi, F. Yuan, F. Yu and Y. Sun, *Chem. Commun.*, 2013, **49**, 6761–6763.
124. J. L. Wang, C. Wang and W. Lin, *ACS Catal.*, 2012, **2**, 2630–2640.
125. J. Juan-Alcaniz, J. Gascon and F. Kapteijn, *J. Mater. Chem.*, 2012, **22**, 10102–10118.
126. C. Wang, Z. Xie, K. E. deKrafft and W. Lin, *J. Am. Chem. Soc.*, 2011, **133**, 13445–13454.
127. C. Wang, K. E. Dekrafft and W. Lin, *J. Am. Chem. Soc.*, 2012, **134**, 7211–7214.
128. S. Pullen, H. Fei, A. Orthaber, S. M. Cohen and S. Ott, *J. Am. Chem. Soc.*, 2013, **135**, 16997–17003.
129. T. Zhou, Y. Du, A. Borgna, J. Hong, Y. Wang, J. Han, W. Zhang and R. Xu, *Energy Environ. Sci.*, 2013, **6**, 3229–3234.
130. Y. Liu, Y. Yang, Q. Sun, Z. Wang, B. Huang, Y. Dai, X. Qin and X. Zhang, *ACS Appl. Mater. Interfaces*, 2013, **5**, 7654–7658.
131. M. H. Xie, X. L. Yang, C. Zou and C. D. Wu, *Inorg. Chem.*, 2011, **50**, 5318–5320.
132. J. Juan-Alcañiz, E. V. Ramos-Fernandez, U. Lafont, J. Gascon and F. Kapteijn, *J. Catal.*, 2010, **269**, 229–241.
133. J. Juan-Alcaniz, M. Goesten, A. Martinez-Joaristi, E. Stavitski, A. V. Petukhov, J. Gascon and F. Kapteijn, *Chem. Commun.*, 2011, **47**, 8578–8580.
134. E. V. Ramos-Fernandez, C. Pieters, B. van der Linden, J. Juan-Alcaniz, P. Serra-Crespo, M. W. G. M. Verhoeven, H. Niemantsverdriet, J. Gascon and F. Kapteijn, *J. Catal.*, 2012, **289**, 42–52.

135. W.-N. Li, F. Lin, X.-X. Li, L.-C. Zhang, W.-S. You and Z.-X. Jiang, *J. Coord. Chem.*, 2013, **66**, 2829–2842.
136. B. Liu, J. Yang, G.-C. Yang and J.-F. Ma, *Inorg. Chem.*, 2012, **52**, 84–94.
137. Y. Horiuchi, T. Toyao, M. Saito, K. Mochizuki, M. Iwata, H. Higashimura, M. Anpo and M. Matsuoka, *J. Phys. Chem. C*, 2012, **116**, 20848–20853.
138. T. Toyao, M. Saito, Y. Horiuchi, K. Mochizuki, M. Iwata, H. Higashimura and M. Matsuoka, *Catal. Sci. Technol.*, 2013, **3**, 2092–2097.
139. D. Sun, Y. Fu, W. Liu, L. Ye, D. Wang, L. Yang, X. Fu and Z. Li, *Chem.–Eur. J.*, 2013, **19**, 14279–14285.
140. L. Shen, W. Wu, R. Liang, R. Lin and L. Wu, *Nanoscale*, 2013, **5**, 9374–9382.
141. M. Wen, K. Mori, T. Kamegawa and H. Yamashita, *Chem. Commun.*, 2014, **50**, 11645–11648.
142. D. Sun, W. Liu, Y. Fu, Z. Fang, F. Sun, X. Fu, Y. Zhang and Z. Li, *Chem.–Eur. J.*, 2014, **20**, 4780–4788.
143. M. Nasalevich, R. Becker, E. V. Ramos Fernandez, S. Castellanos, S. L. Veber, M. V. Fedin, F. Kapteijn, J. N. H. Reek, J. I. van der Vlugt and J. Gascon, *Energy Environ. Sci.*, 2015, **8**, 364–375.
144. M. Birnie, S. Riffat and M. Gillott, *Int. J. Low-Carbon Technol.*, 2006, **1**, 47–58.
145. C. C. Kaan, A. A. Aziz, M. Matheswaran, P. Saravanan and S. Ibrahim, *Heterogeneous Photocatalytic Oxidation an Effective Tool for Wastewater Treatment-A Review*, INTECH Open Access Publisher, 2012.
146. R. J. Braham and A. T. Harris, *Ind. Eng. Chem. Res.*, 2009, **48**, 8890–8905.
147. A. E. Cassano, R. J. Brandi and O. M. Alfanot, *Ind. Eng. Chem. Res.*, 1995, **34**, 2155–2201.
148. M. Pasquali, F. Santarelli, J. F. Porter and P. L. Yue, *AIChE J.*, 1996, **42**, 532–537.
149. G. B. Roupp, J. A. Nico, S. Annangi, R. Changrani and R. Annapragada, *AIChE J.*, 1997, **43**, 792–801.
150. M. M. Hossain, G. B. Raupp, S. O. Hay and T. N. Obee, *AIChE J.*, 1999, **45**, 1309–1321.
151. C. R. Esterkin, A. C. Negro, O. M. Alfano and A. E. Cassano, *AIChE J.*, 2002, **48**, 832–845.
152. G. E. Imoberdorf, O. M. Alfano, A. E. Cassano and H. A. Irazoqui, *AIChE J.*, 2007, **53**, 2688–2703.
153. G. E. Imoberdorf, A. E. Cassano, H. A. Irazoqui and O. M. Alfano, *Catal. Today*, 2007, **129**, 118–126.
154. M. Singh, I. Salvadó-Estivill and G. Li Puma, *AIChE J.*, 2007, **53**, 678–686.
155. V. Tomašić, F. Jović and Z. Gomzi, *Catal. Today*, 2008, **137**, 350–356.
156. G. B. Raupp, A. Alexiadis, M. M. Hossain and R. Changrani, *Catal. Today*, 2001, **69**, 41–49.
157. R. Lakerveld, G. S. J. Sturm, A. I. Stankiewicz and G. D. Stefanidis, *Curr. Opin. Chem. Eng.*, 2014, **5**, 37–41.
158. M. F. J. Dijkstra, A. Michorius, H. Buwalda, H. J. Panneman, J. G. M. Winkelman and A. A. C. M. Beenackers, *Catal. Today*, 2001, **66**, 487–494.

159. C. McCullagh, N. Skillen, M. Adams and P. K. J. Robertson, *J. Chem. Technol. Biotechnol.*, 2011, **86**, 1002–1017.
160. M. F. J. Dijkstra, H. Buwalda, A. W. F. de Jong, A. Michorius, J. G. M. Winkelman and A. A. C. M. Beenackers, *Chem. Eng. Sci.*, 2001, **56**, 547–555.
161. M. L. Satuf, R. J. Brandi, A. E. Cassano and O. M. Alfano, *Appl. Catal., B*, 2008, **82**, 37–49.
162. R. Dillert, D. Bahnemann and H. Hidaka, *Chemosphere*, 2007, **67**, 785–792.
163. P. Du, J. A. Moulijn and G. Mul, *J. Catal.*, 2006, **238**, 342–352.
164. I. Izumi, F.-R. F. Fan and A. J. Bard, *J. Phys. Chem.*, 1981, **85**, 218–223.
165. W. Mu, J.-M. Herrmann and P. Pichat, *Catal. Lett.*, 1989, **3**, 73–84.
166. N. Ma, Y. Zhang, X. Quan, X. Fan and H. Zhao, *Water Res.*, 2010, **44**, 6104–6114.
167. D. Chen and A. K. Ray, *Water Res.*, 1998, **32**, 3223–3234.
168. K. Mehrotra, G. S. Yablonsky and A. K. Ray, *Ind. Eng. Chem. Res.*, 2003, **42**, 2273–2281.
169. K. Reilly, F. Taghipour and D. P. Wilkinson, *Energy Procedia*, 2012, **29**, 513–521.
170. L. A. Dibble and G. B. Raupp, *Environ. Sci. Technol.*, 1992, **26**, 492–495.
171. G. E. Imoberdorf, H. A. Irazoqui, A. E. Cassano and O. M. Alfano, *Ind. Eng. Chem. Res.*, 2005, **44**, 6075–6085.
172. C. Passalía, M. E. Martínez Retamar, O. M. Alfano and R. J. Brandi, *Int. J. Chem. React. Eng.*, 2010, **8**, 1–30.
173. Z. M. Wang, J. Liu, Y. C. Dai, W. Y. Dong, S. C. Zhang and J. M. Chen, *Ind. Eng. Chem. Res.*, 2011, **50**, 7977–7984.
174. Z. Zhang, W. A. Anderson and M. Moo-Young, *Chem. Eng. J.*, 2004, **99**, 145–152.
175. I. Salvadó-Estivill, A. Brucato and G. Li Puma, *Ind. Eng. Chem. Res.*, 2007, **46**, 7489–7496.
176. H. Lin and K. T. Valsaraj, *J. Appl. Electrochem.*, 2005, **35**, 699–708.
177. J. Mo, Y. Zhang, Q. Xu, J. J. Lamson and R. Zhao, *Atmos. Environ.*, 2009, **43**, 2229–2246.
178. R. E. Marinangeli and D. F. Ollis, *AIChE J.*, 1977, **23**, 415–426.
179. R. E. Marinangeli and D. F. Ollis, *AIChE J.*, 1982, **28**, 945–955.
180. C. McCullagh, N. Skillen, M. Adams and P. K. Robertson, *J. Chem. Technol. Biotechnol.*, 2011, **86**, 1002–1017.
181. W. Choi, J. Y. Ko, H. Park and J. S. Chung, *Appl. Catal., B*, 2001, **31**, 209–220.
182. H. Lin and K. Valsaraj, *J. Appl. Electrochem.*, 2005, **35**, 699–708.
183. T.-V. Nguyen and J. C. S. Wu, *Appl. Catal., A*, 2008, **335**, 112–120.
184. P. Du, J. T. Carneiro, J. A. Moulijn and G. Mul, *Appl. Catal., A*, 2008, **334**, 119–128.
185. L. G. Ame´lie Queffeulou, C. Archambeau, H. Le Gall, P.-M. Marquaire and O. Zahraa, *Ind. Eng. Chem. Res.*, 2010, **49**, 6890–6897.
186. Y. Ku, C.-M. Ma and Y.-S. Shen, *Appl. Catal., B*, 2001, **34**, 181–190.

187. G. E. Imoberdorf, A. E. Cassano, O. M. Alfano and H. A. Irazoqui, *AIChE J.*, 2006, **52**, 1814–1823.
188. G. E. Imoberdorf, A. E. Cassano, H. A. Irazoqui and O. M. Alfano, *Chem. Eng. Sci.*, 2007, **62**, 1138–1154.
189. A. Alexiadis and I. Mazzarino, *Chem. Eng. Process. Process Intensif.*, 2005, **44**, 453–459.
190. H. Al-Ekabi, N. Serpone, E. Pelizzetti, C. Minero, M. A. Fox and R. B. Draper, *Langmuir*, 1989, **5**, 250–255.
191. K. F. Jensen, *Chem. Eng. Sci.*, 2001, **56**, 293–303.
192. Y. Matsushita, S. Kumada, K. Wakabayashi, K. Sakeda and T. Ichimura, *Chem. Lett.*, 2006, **35**, 410–411.
193. A. K. Ray and A. A. C. M. Beenackers, *AIChE J.*, 1998, **44**, 477–483.
194. R. Gorges, S. Meyer and G. Kreisel, *J. Photochem. Photobiol., A*, 2004, **167**, 95–99.
195. H. Ge, G. Chen, Q. Yuan and H. Li, *Catal. Today*, 2005, **110**, 171–178.
196. A. Visan, D. Rafieian, W. Ogieglo and R. G. H. Lammertink, *Appl. Catal., B*, 2014, **150–151**, 93–100.
197. Y. Matsushita, N. Ohba, S. Kumada, K. Sakeda, T. Suzuki and T. Ichimura, *Chem. Eng. J.*, 2008, **135**(**Supplement 1**), S303–S308.
198. Y. Matsushita, M. Iwasawa, T. Suzuki and T. Ichimura, *Chem. Lett.*, 2009, **38**, 846–847.
199. M. Krivec, K. Žagar, L. Suhadolnik, M. Čeh and G. Dražić, *ACS Appl. Mater. Interfaces*, 2013, **5**, 9088–9094.
200. G. Imoberdorf and M. Mohseni, *Chem. Eng. Sci.*, 2011, **66**, 1159–1167.
201. M. Motegh, J. J. Cen, P. W. Appel, J. R. van Ommen and M. T. Kreutzer, *Chem. Eng. J.*, 2012, **207**, 607–615.
202. J. Colina-Márquez, F. Machuca-Martínez and G. L. Puma, *Environ. Sci. Technol.*, 2010, **44**, 5112–5120.
203. G. E. Imoberdorf, F. Taghipour and M. Mohseni, *J. Photochem. Photobiol., A*, 2008, **198**, 169–178.
204. G. E. Imoberdorf, G. Vella, A. Sclafani, L. Rizzuti, O. M. Alfano and A. E. Cassano, *AIChE J.*, 2010, **56**, 1030–1044.
205. A. L. L. Zazueta, H. Destaillats and G. Li Puma, *Chem. Eng. J.*, 2013, **217**, 475–485.
206. X. Lang, X. Chen and J. Zhao, *Chem. Soc. Rev.*, 2014, **43**, 473–486.
207. G. Li Puma and P. L. Yue, *Chem. Eng. Sci.*, 2003, **58**, 2269–2281.
208. R. E. Bird, R. L. Hulstrom and L. J. Lewis, *Sol. Energy*, 1983, **30**, 563–573.
209. R. Dillert, A. E. Cassano, R. Goslich and D. Bahnemann, *Catal. Today*, 1999, **54**, 267–282.
210. O. M. Alfano, D. Bahnemann, A. E. Cassano, R. Dillert and R. Goslich, *Catal. Today*, 2000, **58**, 199–230.
211. S. Malato Rodrıíguez, J. Blanco Gálvez, M. I. Maldonado Rubio, P. Fernández Ibáñez, D. Alarcón Padilla, M. Collares Pereira, J. Farinha Mendes and J. Correia de Oliveira, *Sol. Energy*, 2004, **77**, 513–524.
212. S. Malato, J. Blanco, A. Vidal and C. Richter, *Appl. Catal., B*, 2002, **37**, 1–15.

213. C. Minero, E. Pelizzetti, S. Malato and J. Blanco, *Sol. Energy*, 1996, **56**, 411–419.
214. S. Malato, J. Blanco, C. Richter, D. Curcó and J. Gimenez, *Water Sci. Technol.*, 1997, **35**, 157–164.
215. C. Minero, E. Pelizzetti, S. Malato and J. Blanco, *Chemosphere*, 1993, **26**, 2103–2119.
216. S. M. Rodríguez, C. Richter, J. B. Gálvez and M. Vincent, *Sol. Energy*, 1996, **56**, 401–410.
217. S. Malato, P. Fernández-Ibáñez, M. I. Maldonado, J. Blanco and W. Gernjak, *Catal. Today*, 2009, **147**, 1–59.
218. E. R. Bandala, C. A. Arancibia-Bulnes, S. L. Orozco and C. A. Estrada, *Sol. Energy*, 2004, **77**, 503–512.
219. O. A. McLoughlin, S. C. Kehoe, K. G. McGuigan, E. F. Duffy, F. A. Touati, W. Gernjak, I. O. Alberola, S. M. Rodríguez and L. W. Gill, *Sol. Energy*, 2004, **77**, 657–664.
220. S. Parra, S. Malato, J. Blanco, P. Peringer and C. Pulgari, *Water Sci. Technol.*, 2001, **44**, 219–227.
221. D. Bahnemann, *Sol. Energy*, 2004, **77**, 445–459.
222. M. van Well, R. H. Dillert, D. W. Bahnemann, V. W. Benz and M. Mueller, *J. Sol. Energy Eng.*, 1997, **119**, 114–119.
223. R. Dillert, S. Vollmer, M. Schober, J. Theurich, D. Bahnemann, H. J. Arntz, K. Pahlmann, J. Wienefeld, T. Schmedding and G. Sager, *Chem. Eng. Technol.*, 1999, **22**, 931–934.
224. G. Li Puma and P. L. Yue, *Environ. Sci. Technol.*, 1999, **33**, 3210–3216.
225. W.-K. Jo and R. J. Tayade, *Ind. Eng. Chem. Res.*, 2014, **53**, 2073–2084.
226. D. H. Chen, X. Ye and K. Li, *Chem. Eng. Technol.*, 2005, **28**, 95–97.
227. H.-W. Chen, Y. Ku and A. Irawan, *Chemosphere*, 2007, **69**, 184–190.
228. J.-L. Shie, C.-H. Lee, C.-S. Chiou, C.-T. Chang, C.-C. Chang and C.-Y. Chang, *J. Hazard. Mater.*, 2008, **155**, 164–172.
229. L. H. Levine, J. T. Richards, J. L. Coutts, R. Soler, F. Maxik and R. M. Wheeler, *J. Air Waste Manage. Assoc.*, 2011, **61**, 932–940.
230. E. R. Blatchley III, C. Shen, O. K. Scheible, J. P. Robinson, K. Ragheb, D. E. Bergstrom and D. Rokjer, *Water Res.*, 2008, **42**, 677–688.

CHAPTER 9

Photocatalytic Reactors in Environmental Applications

M. ENIS LEBLEBICI[a], GEORGIOS D. STEFANIDIS[a] AND TOM VAN GERVEN*[a]

[a]Process Engineering for Sustainable Systems (ProcESS), Department of Chemical Engineering, KU Leuven, Belgium
*E-mail: Tom.VanGerven@cit.kuleuven.be

9.1 Introduction

Photochemistry deals with the phenomenon of activation of electrons using light of specific wavelengths. This is different to activation with simple heating since the light excites the bond directly without making use of heat transfer.[1] Exciting the bonds and electrons by light thus often yields reactions unattainable by heat. To be able to achieve such excitation solely with heat would pyrolyse the molecule before activating the desired bond in most cases.[1] Photocatalysis involves materials which can be easily activated by light and can catalyse reactions which are otherwise too slow or energy-demanding. Moreover, photochemical reactions which need photons with high energy levels can be carried out by photocatalysis with lower energy photons, thus increasing the efficiency.

This chapter reviews and evaluates the reactor designs which have been reported to integrate photocatalysis in chemical processes. A large amount of scientific work has been performed on photocatalytic reactors in the last 37 years, including 13 500 papers, reviews and reference works. However, the

---

RSC Green Chemistry No. 47
Alternative Energy Sources for Green Chemistry
Edited by Georgios Stefanidis and Andrzej Stankiewicz

Published by the Royal Society of Chemistry, www.rsc.org

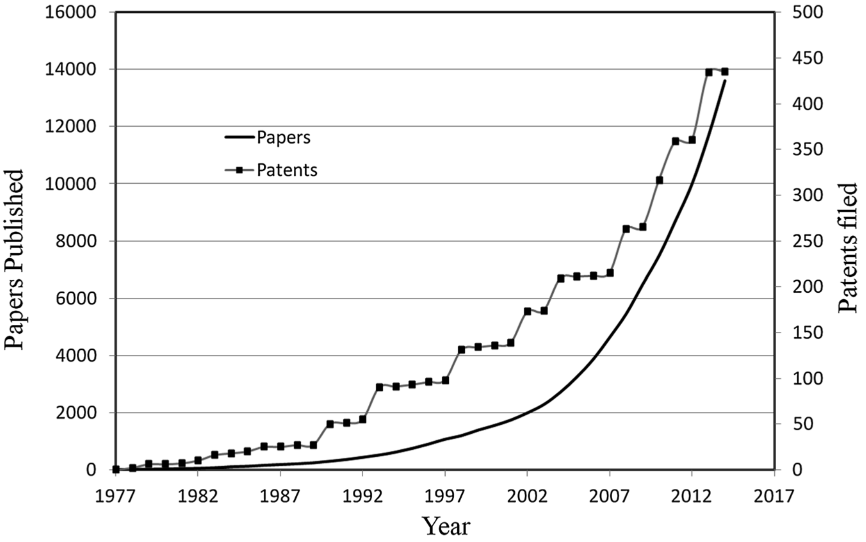

Figure 9.1 Cumulative evolution of published papers and filed patents per year with keywords "photocatalytic reactor". Figures on papers are from Science Direct, figures on patents are from Google patent search.

integration of the photocatalytic reactors into industrial processes is still not achieved.[2] Figure 9.1 shows the number of published papers and filed patents on photocatalytic reactors between 1977 and 2014.

The lack of implementation of photocatalytic reactors in industry is in part due to suboptimal designs.[3] The reason for the difficulty in photocatalytic reactor design comes from their specific challenges. Several challenges for the design of photocatalytic reactors are inherited from conventional catalytic reactors such as the need to have a large specific surface area and high mass transfer rates. Therefore, various reactor configurations that are applied for conventional catalytic applications have been investigated for photocatalytic applications as well.[2,4] Conventional designs, however, are currently being changed using process intensification tools and adapted to photocatalysis. The main optimization and intensification developments focus on the following approaches:[2,4]

1. Overcoming mass transfer limitations: promoting fast adsorption–desorption, increasing catalyst surface;
2. Optimizing photon transfer limitations: optimum lighting strategy and reactor geometry to maximize irradiance;
3. Industrial integration: scale-up, catalyst separation, retrofitting to existing systems.

This work focuses on the different reactor designs in wastewater treatment. Emphasis is on reactors which were patented and/or influenced the ongoing evolution to the optimum design for each application.

9.2 Wastewater Treatment

Wastewater treatment is conventionally performed by biodegradation.[5,6] This is still the predominant treatment method for both industrial and domestic wastewater. However, many of the pollutants are toxic for the biodegradation organisms and/or non-biodegradable.[5] This led to the search for alternative degradation routes. Incineration and chemical processes, namely photolysis and advanced oxidation processes (AOP), were proposed as important routes to degrade the non-biodegradable pollutants.[5,7] Conventional incineration is commonly thought to be a feasible alternative to landfill and diluted discharge but, as presently practised, incineration has low energy efficiency as well as high CO_2 emission since the majority of the fuel is spent in evaporating the wastewater. This limits the future use of incineration.

Photolysis treatment can be applied in two distinct approaches. Direct photolysis utilizes the light wavelength which is directly absorbed by the pollutants to degrade them. On the other hand, photocatalytic AOP utilizes photocatalytic reactions to generate radicals thereby oxidizing the organic pollutants. Even though AOP is indirect, it has an advantage over direct photolysis since, in most cases, organic intermediates of direct photolysis stop absorbing in the same wavelength range and cannot be further photolyzed, thus the chemical oxygen demand (COD) of wastewater cannot decrease further.[8] The radicals generated by photocatalytic AOP are independent of the pollutant concentration. This enables elimination of organic pollutants and the degradation of intermediates in pseudo-first order reaction kinetics.[9–11] This advantage was proven effective in the case of micropollutants with concentrations of $\mu g\ L^{-1}$ down to $ng\ L^{-1}$ which exist in hospital and municipal waste waters and landfill leachates.[12,13] Furthermore many of the pollutants which fall into the micropollutant category are still not regulated and are good candidates for future regulation.[13] New legislation can favour the usage of AOP since these pollutants cannot be eliminated completely with conventional methods.

The catalyst material used in photocatalytic treatment reactors is usually either pure TiO_2 in crystal form or a doped version of this. These dopants can be another semiconductor,[14] such as various transition metals including noble metals, or rare earth elements.[7,15–17] Dopants are utilized to lengthen the maximum excitation wavelength of the photocatalyst and, potentially using the sunlight as the energy source, for radical generation. There are also alternative metal oxide catalysts such as magnetite and maghemite crystals.[18] Even though these dopants and alternatives were successful in broadening the photosensitization spectrum, by far the most common photocatalyst is pure crystalline TiO_2.[4] Among the TiO_2 photocatalysts, the most widely-used one is P25 by Evonik. P25 is a mixture of crystalline TiO_2 nanoparticles in both rutile (20%) and anatase (80%) forms. Figure 9.2 shows the photosensitization wavelengths of the P25 photocatalyst.[19]

The bands shown in Figure 9.2 indicate that light in the near UV spectrum is able to excite both structures. This enables usage of sunlight. However, due to the low UV content of sunlight an artificial UV source, a mercury lamp

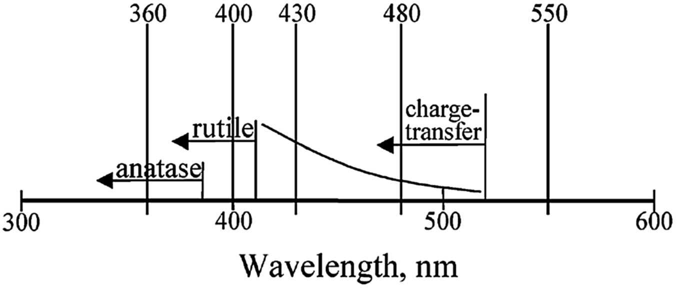

Figure 9.2 Photosensitization wavelengths of TiO_2 crystals which constitute the P25 catalyst. Adapted and reprinted with permission from A. G. Agrios *et al.*, Langmuir, 2004, 5911–5917. Copyright (2004) American Chemical Society.[19]

being the most popular, is used in the research and development of photocatalytic reactors. The UV–LEDs have also been utilized for wastewater treatment with AOP.[20,21] LEDs have the advantages of low power, environmental protection, long lifetime, fast response time (μs) and good mechanical properties.[22] The LED efficiency has reached close to 100 lumens per watt of input electricity whereas this value is around 55–70 lm W^{-1} for standard compact fluorescent lighting.[23] Furthermore, the possibility of periodic illumination further extends the efficiency of LEDs.[24,25]

The majority of the research and exploitation of photocatalysis regarding environmental applications has been performed on effluent treatment, namely the degradation of organic pollutants in industrial wastewater.[26] However, conventional techniques are still in use due to their simplicity, lower operating costs and level of development. Recently, a strategy to combine both conventional and new technologies was proposed, as shown in Figure 9.3.[5]

In this way the AOP can fit in parallel or in series with biodegradation reactors. Figure 9.3 also gives an idea of the main drawback of AOP, namely the high operating costs.[13,27] These operating costs are currently only justified by the successful removal of non-biodegradable pollutants or ones with very high toxicity which cannot be removed otherwise.

Optimal design and process integration alongside more strict environmental regulations can lead the way to integrate the different reactors. This will be discussed in this section on the existing biodegradation systems.

9.2.1 Slurry Reactors

Slurry reactors are the first concept in using photocatalysts for effluent treatment. The advantage of using the slurry reactor is the minimal mass transfer limitations due to the large catalyst surface by dispersing the fine catalyst powder in the reaction medium. Theoretically, the catalyst surface in a slurry reactor can be as large as 170 000 m^2 m^{-3} depending on the catalyst concentration, particle size and the degree of agglomeration.[4] However, a large

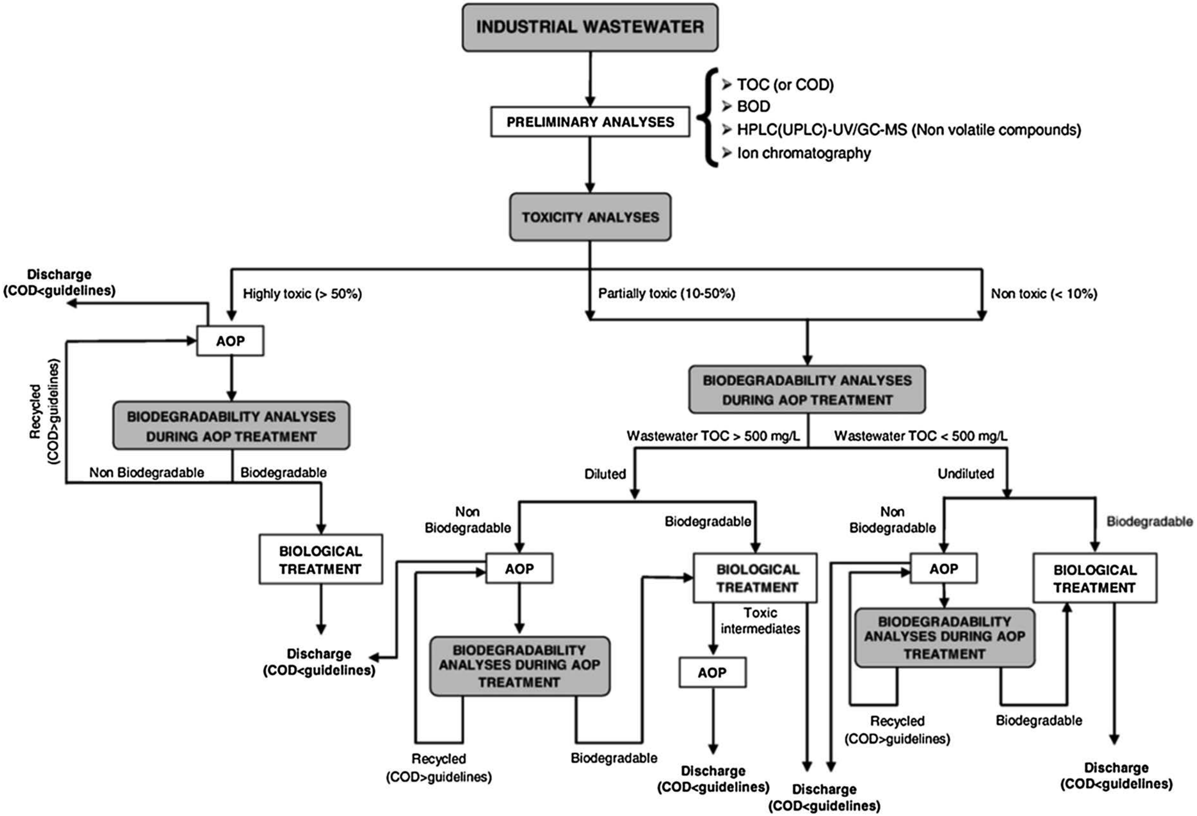

Figure 9.3 Strategy of combining biodegradation with AOP. Reprinted from Science of the Total Environment, 409, I. Oller *et al.*, Combination of Advanced Oxidation Processes and Biological Treatments for Wastewater Decontamination – A review, 4141–4166, Copyright (2011) with permission from Elsevier.[5]

surface area means smaller particles and as the particle size decreases, catalyst recovery becomes an issue resulting in additional cost and lower space–time yield. Larger particles and/or aggregates are simpler to separate but at the expense of catalyst surface area. Furthermore, light penetration in the reaction medium decreases due to absorbing catalyst particles. Depending on the reactor geometry, a portion of the catalyst will not be illuminated, thereby decreasing the reactor yield. Some of the significant studies focusing on these drawbacks for designing industrially applicable photocatalytic slurry reactors are summarized in Table 9.1.

Even though different designs usually involve quite different geometries in the slurry reactors, there are some common physical parameters which govern the efficiency and productivity of all slurry reactors.[32] These parameters are catalyst load, pH and irradiance distribution of the UV light in the reactor volume.

The catalyst load, at lower catalyst concentrations, is directly proportional to the reaction rate. This is expected since more catalyst will introduce more surface area for the degradation process. However, after a threshold

Table 9.1 Proposed slurry reactor designs in the literature.

Name	Application	Significance	Reference
Multi-lamp reactor	Treatment of domestic wastewater. 31 L reaction medium	Reactor design aided by CFD and radiation model. No moving parts in the reactor unit. The designed unit can be multiplied for scale-up. Volumetric reaction rate is in the order of 10^{-8} mol L^{-1} s^{-1}	28
Rotating annular reactor	Phenol degradation. Up to 7.6 L reaction medium	Scalable reactor design. Mixing by moving walls. 0.06×10^{-4} mol L^{-1} min^{-1} reaction rate achieved. The photonic efficiency achieved was 1.4	29
Fountain reactor	Created as a design concept. Not experimented	Industrially applicable design. Analytical modelling has already been done for scaling-up. Up to 10 g L^{-1} catalyst load can be utilized. Down to 0.5 mm slurry film thickness can be reached	30
Photocatalytic membrane reactor	Various AOP applications were tested. Pharmaceutical degradation of contaminated river water was the practical application	Novelty is in the microfiltration membrane which solves the catalyst regeneration problem with flow rates up to 25 L m^{-2} h^{-1}	31

concentration, the additional catalyst has less or no impact on the degradation rate. Moreover, due to shading, high catalyst concentration can even reduce the reactor performance.[28] This threshold value is strongly case-dependent and varies in a broad spectrum of 0.1–8 g L^{-1}.[32]

The pH affects the surface charge of the photocatalyst. Degussa P25 has a point of zero charge (pzc) at pH = 6.25.[33] Lower pH values make the catalyst surface positively charged which promotes the adsorption of anions (*e.g.* phenol, carboxylic acids).[9,21,34] For phenol, a popular anionic substrate, the optimum pH was reported to be between 5 and 7.[35] High pH, *vice versa*, is applicable for cationic substrates (*e.g.* methylene blue, cationic dyes).[36] A high pH promotes adsorption by attracting the cations to the negatively-charged surface.

Irradiance distribution in the slurry reactor affects the rate of generation of the electron–hole pairs on the catalyst surface and is in direct proportion to the reaction rate. However, similar to catalyst loading, this direct relationship is maintained until a threshold irradiance. This critical irradiance was reported as 25 mW cm^{-2} as a universal threshold.[32] For values higher than this irradiance the first order relationship between light intensity and reaction rate becomes half-order, thus decreasing the overall photonic efficiency.

The reason for the existence of these two regimes lies in the mechanism of photocatalysis with TiO_2 which is governed by the generation of electron–hole pairs on the catalyst surface. These pairs are however not stable and they recombine within picosecond timescales. At lower irradiance, more of the generated electron–hole pairs get to partake in chemical reaction than in recombination. At the half-order regime, recombination becomes the dominant step.[32]

Although Carp reports the threshold as a global value, this threshold irradiance value was observed to be lower for immobilized catalysts, proving that mass transfer limitations also play a role in this phenomenon. This observation will be further discussed under the section on immobilized catalysts.

The reactor designs selected for Table 9.1 focus on industrial applicability and scalability which is in parallel with the line of this work. There are other slurry reactor designs which focus on obtaining kinetic constants or proving new lighting or catalyst concepts. They were not included since this chapter focuses on applicable reactor design concepts.

9.2.1.1 Multi-Lamp Reactor (MLR)

This concept aims to optimize the lamp power, number of lamps and positioning of these lamps as well as the hydrodynamics inside the reactor. Its starting point is the annular reactor shown in Figure 9.4a. The standard annular reactor is the most popular slurry reactor,[29] which is basically a tubular reactor with a single lamp at the axis. This design is used in this work as the benchmark continuous process for slurry reactors. Figure 9.4b shows the MLR design with 4 lower output lamps.

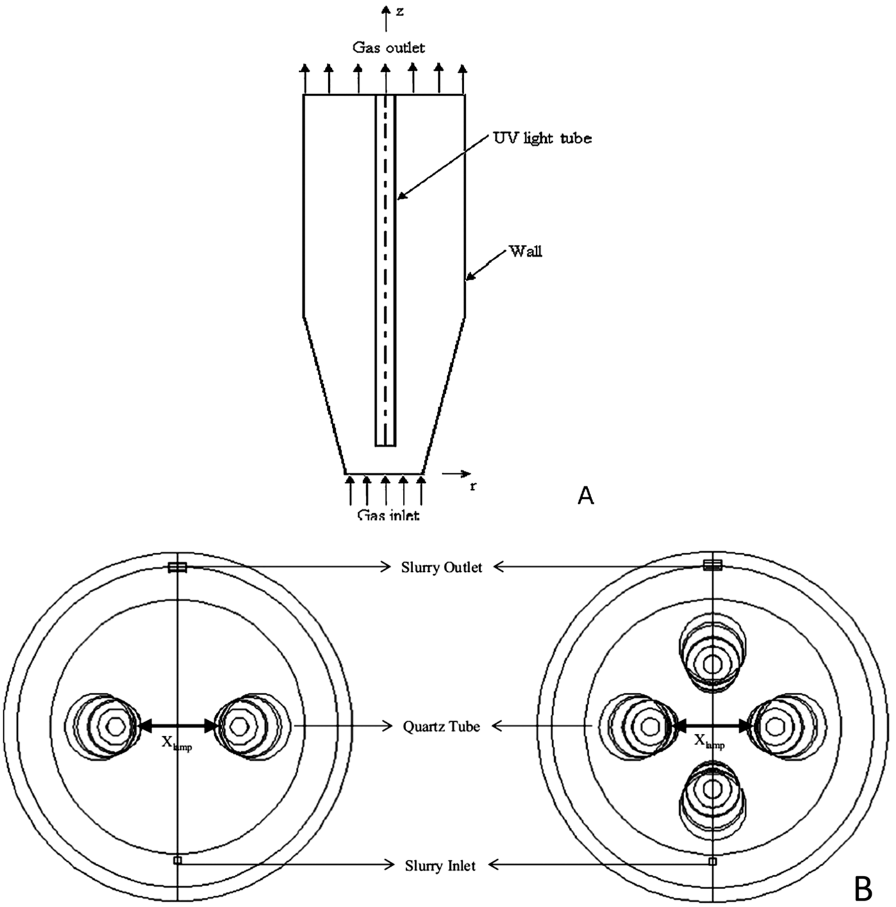

Figure 9.4 (A) Lateral view of a standard annular reactor,[37] (B) axial views of MLR designs (2 and 4 lamps).[28] (A) Reprinted from Chemical Engineering Journal, 172, N. Qi *et al.*, CFD modelling of hydrodynamics and degradation kinetics in an annular slurry photocatalytic reactor for wastewater treatment, 84–95, Copyright (2011), with permission from Elsevier and (B) reprinted from Chemical Engineering Science, 111, Y. Boyjoo *et al.*, CFD simulation of a pilot scale slurry photocatalytic reactor and design of multiple-lamp reactors, 266–277, Copyright (2014), with permission from Elsevier.

As explained previously, a region in an annular reactor with too high an irradiance can have low photonic efficiency. Therefore, a single lamp reactor design has an inefficient (but fast reacting) strongly-illuminated zone close to the lamp and a darker zone away from the lamp. The efficient zone is between these two zones. The MLR aims to keep every location in the reaction medium at a similar irradiance, at values within the range of efficiency.

The efficient range can be identified for different catalysts, catalyst concentrations and substrate molecules with an easy assay. The rate of degradation increases linearly with increasing irradiance in the high photonic efficiency range. At high enough irradiance ranges, the irradiance does not improve the reaction rate linearly any more. The threshold for photonic efficiency has then been reached.

The MLR is a design concept which addresses photon transfer limitations while proposing a scale-up method with multiple lamps. An efficient MLR module can be replicated or extended to the desired size and may be operated with high throughput and efficiency. The main drawback is that it does not address the catalyst recovery issue.

9.2.1.2 Rotating Annular Reactor (RAR)

The RAR was originally developed as a reactive separation platform in 1980.[38] Utilization of the RAR can be seen as another iteration of the annular reactor. In contrast to the MLR, all the lamps are positioned at the reactor's axis,[29] similar to the standard annular design. On the other hand, the RAR focuses on mixing of the slurry in order to irradiate all catalyst particles evenly and to eliminate concentration gradients in radial directions from the lamp. The design is shown in Figure 9.5a.

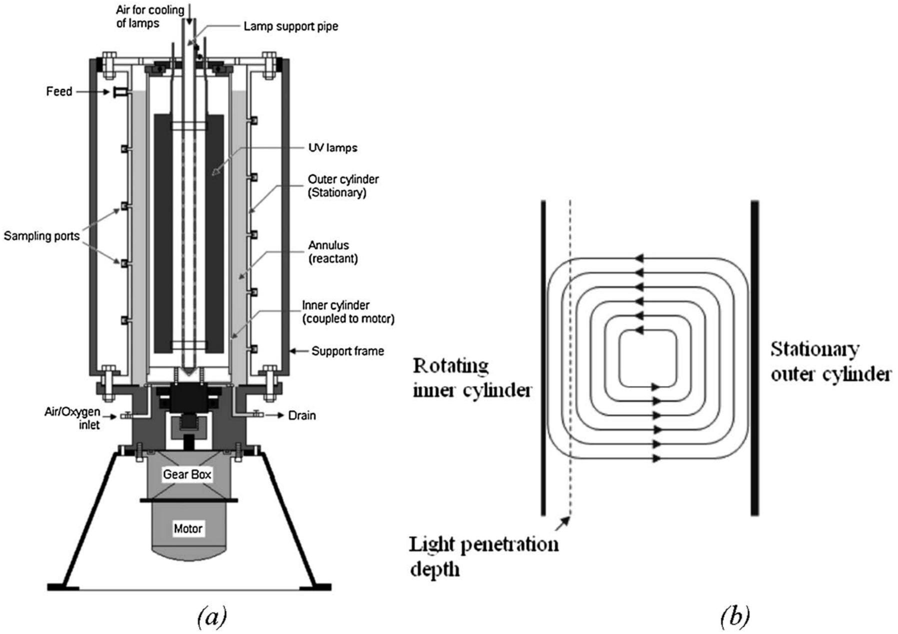

(a) (b)

Figure 9.5 (a) RAR design. (b) Taylor vortices created in the reaction medium. Reprinted from Chemical Engineering Science, 65, M. Subramanian and A. Kannan, Photocatalytic degradation of phenol in a rotating annular reactor, 2727–2740, Copyright (2010) with permission of Elsevier.[29]

Since the apparent reaction rate for the degradation is low, the residence time is usually maintained in the timescale of minutes, which results in a laminar regime. With this way of operating, the annular reactor has the disadvantage of limiting the radial mass transfer to diffusion. The RAR design overcomes this mass transfer limitation by forming Taylor vortices between the rotating and stationary walls, as shown in Figure 9.5b.

The mixing obtained by the RAR is not only enhancing mass transfer by creating laminar mixing but also enabling homogeneous irradiation to all the catalyst particles. Furthermore a higher catalyst concentration (up to 8 g L^{-1} is proven) can be utilized since light penetration does not need to cover all the reactor. Even though this high catalyst concentration blocks the light at a relatively shallow depths, due to the mixing all the catalyst particles will be irradiated evenly (Figure 9.5b).

Rotational motion in the RAR and the vortices created also result in a controlled periodic illumination (CPI) operation. As the catalyst passes through the illuminated zone, the degradation reaction takes place and when the particles are in the dark zone only adsorption–desorption may occur. By controlling the ratio of the illuminated volume to total reactor volume by varying the catalyst concentration and/or lamp output, the CPI duty cycle can also be varied.

The RAR is an improvement in both mass and photon transfer in photocatalytic reactors. It is also straightforward to scale-up by building it taller or multiplying smaller blocks. However, just like the MLR, this concept does not address the issues associated with slurry reactors and the catalyst recovery step.

9.2.1.3 Fountain Reactor (FR)

The FR is a novel design concept invented in 2001.[30] This concept consists of two constituents one being the main slurry reservoir and the second part, on top of the reservoir, is the actual reactor where the reaction takes place as shown in Figure 9.6. The reactor part is called the water fountain and can be designed as a parabolic plate or as a cone placed concentrically with the nozzle. The slurry flows as a film on the plate and is irradiated *via* a solar or an artificial light source.

Even though there is barely any geometrical resemblance, the FR design is focusing on the same problem as the RAR. This problem is mixing and irradiation homogeneity. By mixing the reservoir, all catalyst particles have the same chance to be irradiated and the catalyst concentration can, just like in the RAR, be much higher (up to 10 g L^{-1}) than conventional continuous designs such as the annular reactor.

The residence time of the slurry on the fountain is an important parameter controlling the CPI duty cycle. The ratio of residence time on the fountain to residence time in the reservoir is the duty exactly. Furthermore the flowrate of the fountain also determines the flowing film thickness which should be set according to the light penetration depth at the operating catalyst concentration. The film thickness varies from the nozzle to the edge of the fountain especially in a conic fountain. Parabolic fountain has a more homogeneous film thickness distribution.

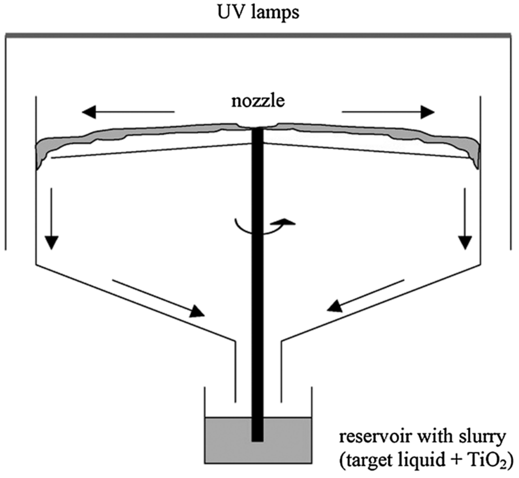

Figure 9.6 Fountain reactor system with an illuminated rotating dome coupled to liquid reservoir.[4] Reprinted from Chemical Engineering and Processing, 46, T. Van Gerven *et al.*, A review of intensification of photocatalytic processes, 781–789, Copyright (2007), with permission from Elsevier.

The FR concept has two main advantages. One is the ability for virtually limitless scale-up. It can be coupled to mixing tanks and the desired reaction rate can be supplied by varying the fountain area. It may even be possible to use solar energy during the day with reactors bearing large enough fountain attachments.

The main drawback of the FR design *per se* is that it is a slurry reactor and the catalyst separation step is still a problem. Its ability of integration to existing systems can be increased if the fountain is not operated as a slurry reactor but with the photocatalyst immobilized at its surface. This would help to integrate the fountain to the existing biodegradation reactors *via* using the algorithm shown in Figure 9.3. The FR is not a patented design and can be further intensified to fit modern industrial needs.

9.2.1.4 Photocatalytic Membrane Reactor (PMR)

The PMR design with a slurry reaction medium is the only integration solution for slurry photocatalytic reactors within existing industrial water treatment systems. The previous design concepts all focus mainly on the first two issues mentioned in Section 9.1 which are photon and mass transfer limitations. The PMR on the other hand almost only focuses on the integration by attempting to solve the catalyst recovery step.

Membrane units in slurry PMRs can, and do, exist in three positions: before the reactor as a pre-treatment unit, within the reactor and after the reactor as catalyst recovery units.[39,40] While using membranes before the reactor can be vital to eliminate any leak of light blocking biodegradation sludge from the ponds to the AOP unit, it is not a design concept at the focus of this work. From a chemical engineering point of view, integrating the previously mentioned slurry reactors with the aid of membranes is more interesting.

The most popular PMR designs are modifications of the most popular slurry reactors, the single lamp or multi-lamp annular reactors. Two of the annular PMR variants are shown in Figure 9.7. The common point on these reactors is the need for high-shear mixing at the surface of the membrane unit. This is needed to clean the photocatalyst particles from membrane surface which may cause fouling. This shear is most popularly supplied by the sparger placed under the membrane,[31,40,41] with the exception of a membrane agitator design (Figure 9.7b).[42] The membranes utilized in the PMR setups are usually polymer microfiltration membranes (polytetrafluoroethylene or polypropylene) with pore sizes varying from 100 nm to 1 μm.

Another commonly-used way of using the membrane is after the reactor as a separate catalyst recovery unit. This method has the advantage of being independent of the reactor design. This is a hollow-tube membrane unit through which the slurry from the reactor is fed and looped back to the reactor. The flow rate is kept high to eliminate fouling; the permeate is free of catalyst particles and is discharged.

The external membrane unit is used in an industrially-applied photocatalytic slurry reactor, namely the Photo-Cat™, Purifics ES Inc. which is a PMR

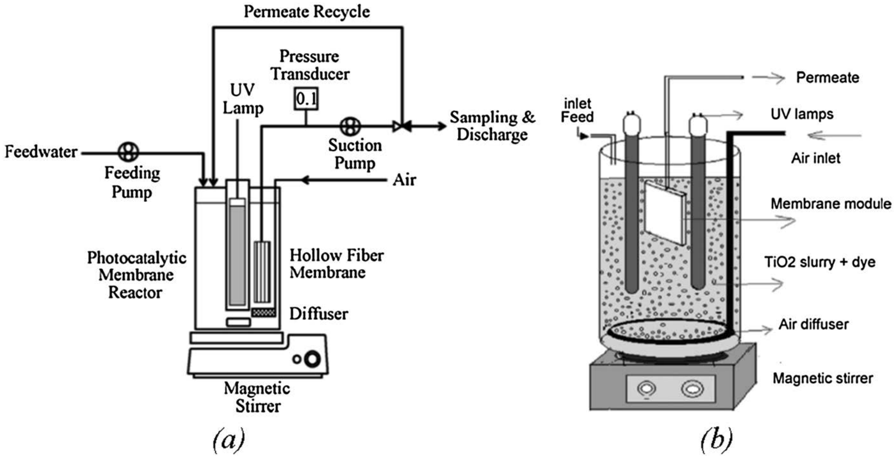

Figure 9.7 (a) Bubble-cleaned PMR annular reactor[31] (b) membrane agitator PMR multi-lamp reactor.[42] (a) Adapted from Journal of Membrane Science, 322, K.-H. Choo *et al.*, Use of photocatalytic membrane reactor for the removal of natural organic matter in water: Effect of photoinduced desorption and ferrihydrite adsorption, 368–374, Copyright (2008), with permission of Elsevier and (b) adapted from Separation and Purification Technology, 71, R. A. Damodar and S.-J. You, Performance of an integrated membrane photocatalytic reactor for the removal of Reactive Black 5, 44–49, Copyright (2010), with permission from Elsevier.

applied for removal of pharmaceuticals, endocrine-disrupting compounds and estrogenic activity from Colorado River water.[39]

The PMR concept appears to be the key to integration of the slurry reactors with industrial and domestic wastewater systems. The reactor designs with embedded catalyst systems are simple and yet still to be applied to practical needs. However, adding an external membrane unit to optimized reactor designs can close the catalyst separation gap between the slurry and immobilized catalyst reactors.

9.2.2 Immobilized Catalyst Reactors (ICR)

The concept of photocatalytic treatment of wastewater may be proven on slurry reactors but the diversity of reactor design concepts with immobilized catalyst is no less than with their slurry counterparts. Naturally, eliminating the difficult catalyst recovery step is the main idea behind coating all the catalyst content on a surface and then irradiating that surface. This is indeed a more practical approach and may seem one step closer to the integration of photocatalysis in industry. However, this concept intensifies the mass and photon transfer limitations, since the transport mechanism of the substrate molecule within the catalyst coating is limited by diffusion. Furthermore, the light penetration is limited to micrometer length scales. This limits the effective catalyst amount making the thickness of coating ineffective on the reaction rate after a certain thickness.[9] The mechanism within the catalyst coating was recently modelled and investigated on a parallel plate reactor[34] using CFD and on a microreactor[43] using analytical modelling.

Since all the catalyst is coated on a surface and light is vital, the reactor geometry needs to maximize the irradiated surface. This is in contrast to maximizing irradiated volume which was the aim of the slurry reactors. Surface maximization without compromising irradiation is a new challenge for chemical engineering. Some of the designs proposed to meet these challenges are shown in Table 9.2.

Similar to the slurry reactor designs, common parameters govern the performance of the reactor. The effect of pH is the same as in slurry designs whereas the irradiance and catalyst loading parameters have different effects on the reactor performance.

The irradiance measured on the catalyst surface is again directly proportional to the reaction rate until the threshold light intensity. However, this threshold was observed to be lower than with slurry designs (<1 mW cm^{-2}) in various studies.[11,34,51,52] This may be due to internal mass transfer limitations in the immobilized catalyst coating. In the slurry reactors there is mixing of the catalyst whereas in immobilized coatings the catalyst is stationary. This keeps the catalyst always under the light for the IC designs. The mixing of particles enables a cyclic operation where the catalyst is irradiated some of the time and in the dark the rest of the time. This allows the adsorption to take place in the dark zones and increases the photonic efficiency as explained in the RAR section. Slurry reactors also have the advantage of high

Table 9.2 Proposed IC reactor designs in the literature.

Name	Application	Significance	Reference
Parallel plate reactor	Various AOP applications in aqueous medium using, mercury lamps and LEDs	Simplest of the ICR. Easy to scale-up. Reaction rate constant – in the order of 0.01 min^{-1} for 1–2 L reaction media	9 and 34
Microreactor	Cortison 21- acetate removal from water	High conversion, high area/volume ratio. Detailed analytical model. Rate constant was shown to be 31 s^{-1} for 1.49 μL reaction medium	43
Optical fibre reactor	Pharmaceutical removal as well as photocatalytic oxidation of cyclohexane. Using short arc mercury lamp	High area/volume ratio. Efficient irradiation. Ability to scale-up using monolith concept	44–47
Foam reactor	2,4 chlorophenol degradation in synthetic aqueous wastewater using LEDs	High area/volume ratio. Flexible design concept able to be applied to different geometries. 0.01 min^{-1} rate constant for 500 mL solutions	48 and 49
Spinning disc reactor	Phenol degradation in synthetic aqueous wastewater with mercury lamps	High area/volume ratio close to microreactor, without the fluid handling problems	50

mass transfer areas which eliminates a major factor for decreasing photonic efficiency and which enables their efficient operation at higher irradiances.

Periodic illumination is also possible in the immobilized catalyst reactors. However improvement in reactor performance *via* periodic illumination is controversial as several studies report no improvement.[29,33,53]

Positioning of the catalyst layer is also an important parameter and its effect is case dependent. If the catalyst is placed before the reaction medium on the light path (back-lighting) the light intensity is higher than placing the catalyst after the reaction medium (front-lighting). However, due to the internal mass transfer limitations, back-lighting is not always favourable.[54] On the other hand, another case favours back-lighting only at higher intensities (2 mW cm^{-2}).[51]

The catalyst load in immobilized catalyst reactors is usually defined as the catalyst thickness. The thickness is usually between 0.5 and 5 microns. Vezzoli *et al.* have reported that any TiO_2 coating thicker than 3 microns has no effect on the reactor performance for irradiances up to 5 mW cm^{-2}.

As shown in Table 9.1, the parallel plate reactor is the starting point from which the microreactor, optical fibre and foam reactor gradually evolved. Spinning disc, on the other hand, is a new design concept with a considerable impact on photocatalysis.

9.2.2.1 Parallel Plate Reactor (PPR)

The parallel plate geometry is the simplest attempt to increase the area to volume (*A*/*V*) ratio by thinking in 2D and keeping the third dimension (thickness of flow area) smaller than the other dimensions. In most of the cases in the literature, this ratio of the third dimension to other dimensions is kept between 30[34] and 150.[9] In other words, a 15 cm long reactor has a flow thickness of 1–5 mm. These values are for the laboratory scale since the industrial reactor would be meters wide and long. The thickness of the PPR is inversely related with the *A*/*V* value giving the relation $A/V = 1/\omega$ where ω is the thickness in meters. A typical 3–5 mm thickness reactor keeps the *A*/*V* at around 200–300 m^2 m^{-3}. An example of parallel plate reactor is shown in Figure 9.8.

The biggest advantage of the PPR is scalability. Its straightforward construction lets it to be built virtually without size limits as long as the capital costs for UV-transparent material are justified. However, size doesn't affect the *A*/*V* ratio since it only depends on the thickness of the PPR. This leads to the main drawback of the PPR which is the low *A*/*V*. This design needs to be built very large in order to achieve the space–time yield of slurry reactors which can carry more catalyst throughout the bulk volume and reach higher *A*/*V* than the PPRs. Furthermore, the light source is another issue with this design. Mercury lamps are omnidirectional and focusing their light on the PPR surface needs additional hardware. LEDs are a powerful alternative and a solution to this issue since they are unidirectional.

The natural solution to the drawbacks of PPRs would be further decreasing the thickness to achieve a higher area per volume. This leads to the sub-mm characteristic length and, thus, the microreactor range.

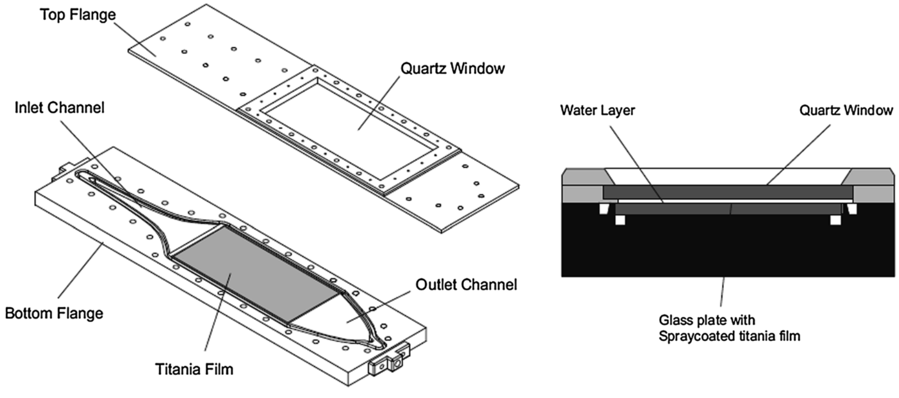

(a) *(b)*

Figure 9.8 (a) Exploded view of a PPR (b) cross-section of the same PPR (ω = 1 mm)[9] both images are adapted from Applied Catalysis A: General, 404, M. Vezzoli *et al.*, Investigation of phenol degradation: True reaction kinetics on fixed film titanium dioxide photocatalyst, 155–163, Copyright (2011), with permission of Elsevier.

9.2.2.2 Microreactor

When the characteristic length is decreased to less than a millimetre, the design is called a microreactor. Microreactors are 2D designs like the PPR. They are used in photocatalysis to overcome mass transfer limitations by exploiting the high A/V ratio. A photocatalytic microreactor designed by Takei and colleagues was an array microchannels placed on a TiO_2 coating. The channels had a thickness (ω) of 3.6 μm and a width of 770 μm which gave the geometry an A/V ratio of 278 000 $m^2\ m^{-3}$.[55] This reactor design is shown in Figure 9.9.

Microreactors are not only advantageous due to the huge A/V ratio but also for their catalyst load. A recent patent reports 23.9 $g\ L^{-1}$ of TiO_2 load which is three times the load of an RAR.[4,56] Furthermore, the wastewater treatment microreactor by Visan *et al.*[43] was calculated to carry a catalyst load of 161 $kg\ m^{-3}$.

Microreactors are a big intensification over the PPR, however they can be further optimized. The channel width of the microreactor shown in Figure 9.9 may be increased for more area without compromising fluid distribution. The current design has empty spaces between the parallel channels. CFD can be a good aid to further optimize the channel width and length. Irradiation of microreactors would also be *via* the UV-LEDs to keep the overall size small[4] and also for the advantages of these light sources discussed in PPR section.

The drawback of the microreactors is the scale-up as well as the light distribution. There are commercial solutions for microreactor scale-up which deliver industrial-scale throughputs however they are not yet optimized for photocatalysis. Maintaining the small characteristic length and scaling-up means folding the reactive surface into a manifold. To irradiate this manifold evenly is another challenge which may involve efficient lighting resources and photon transfer media such as optical fibres.

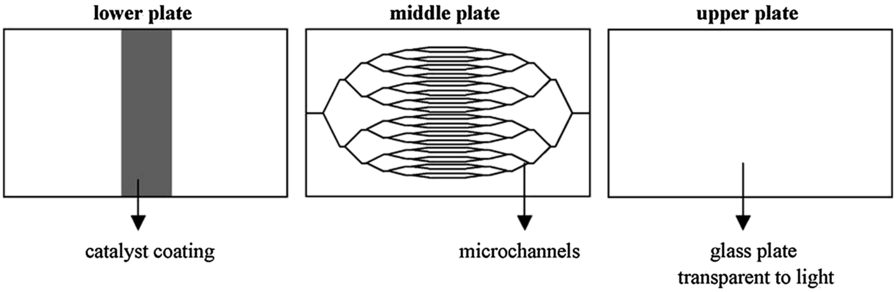

Figure 9.9 The three layers of microreactor[4,55] Reprinted from Chemical Engineering and Processing, 46, T. Van Gerven *et al.*, A review of intensification of photocatalytic processes, 781–789, Copyright (2007), with permission from Elsevier.

9.2.2.3 Optical Fibre Reactor (OFR)

Since high surface area is essential for the reactors with immobilized catalyst, geometries with a manifold of milli- or even microchannels may be needed for more compact designs. The concept of OFR emerged to overcome the potential photon transfer issues in an immobilized catalyst reactor with a 3D geometry. This design uses optical fibres as light distributors and/or catalyst supports.[57] Three main types of OFR design are to be considered here. These design types are shown in Figure 9.10.

The fibres exist in the reactor in three forms: shielded (no illumination just photon transport), stripped (illumination) and TiO_2 coated (catalyst support and illumination). A downside of coating the fibre with catalyst is the loss of light intensity in the axial direction more quickly. The light intensity in the coated fibre decreases to 1% of the initial intensity in 10 cm whereas this value is 40% in a bare fibre,[58] as shown in Figure 9.11.

The first type of OFR is built by coating the optical fibres with the photocatalyst (Figure 9.10a).[44,45,57,59] This has the advantage of increasing the irradiated catalyst coating area dramatically, however since the illumination is behind the coating (back-illumination), due to the mass transfer limitations and decay of light intensity throughout the porous coating, the overall performance is compromised.[4]

To overcome the photon transfer limitations in the first OFR designs, the catalyst was coated on glass beads (Figure 9.10b) and the vessel was irradiated by a bundle of optical fibres.[60] This approach of illumination by the fibres was also utilized for the slurry reactors.[46] Fibres were used in this case to distribute light evenly throughout the vessel and because of the front-lighting, the limitations of the first OFR designs were addressed.

For maintaining front-illumination and increasing the surface area, a monolith reactor with TiO_2 washcoat and square channels (5 mm cell edge) was utilized as a reaction vessel.[46,47,61] A bundle of 100 optical fibres were used for light distribution from a 100 W short-arc mercury lamp (Figure 9.10c). This reactor was utilized for selective oxidation of cyclohexane and proved to have higher photonic efficiency than a top-illuminated tank reactor.

9.2.2.4 Foam Reactor (FR)

Silicon carbide foams with medium surface area have been coated with TiO_2 photocatalyst to achieve a high surface to volume ratio.[48,49,62] The 3D open alveolar structure gives the foam a surface area of 20–30 $m^2\ g^{-1}$. This corresponds to a 2.5 $m^2\ cm^{-3}$ which is obtainable in 2D (parallel plate) geometries only by a microreactor with a characteristic length smaller than 1 μm.

The large surface to volume ratio may be a solution for mass transfer limitations however the 3D geometry blocks the light and introduces photon transfer limitations. Figure 9.12 shows the lighting conformation for the operation of this reactor. It can be seen that he flow distributor is also a light distributor.

The specific reactor shown above was utilized in fact for gas phase degradation reactions, however a similar design was proven effective for the aqueous

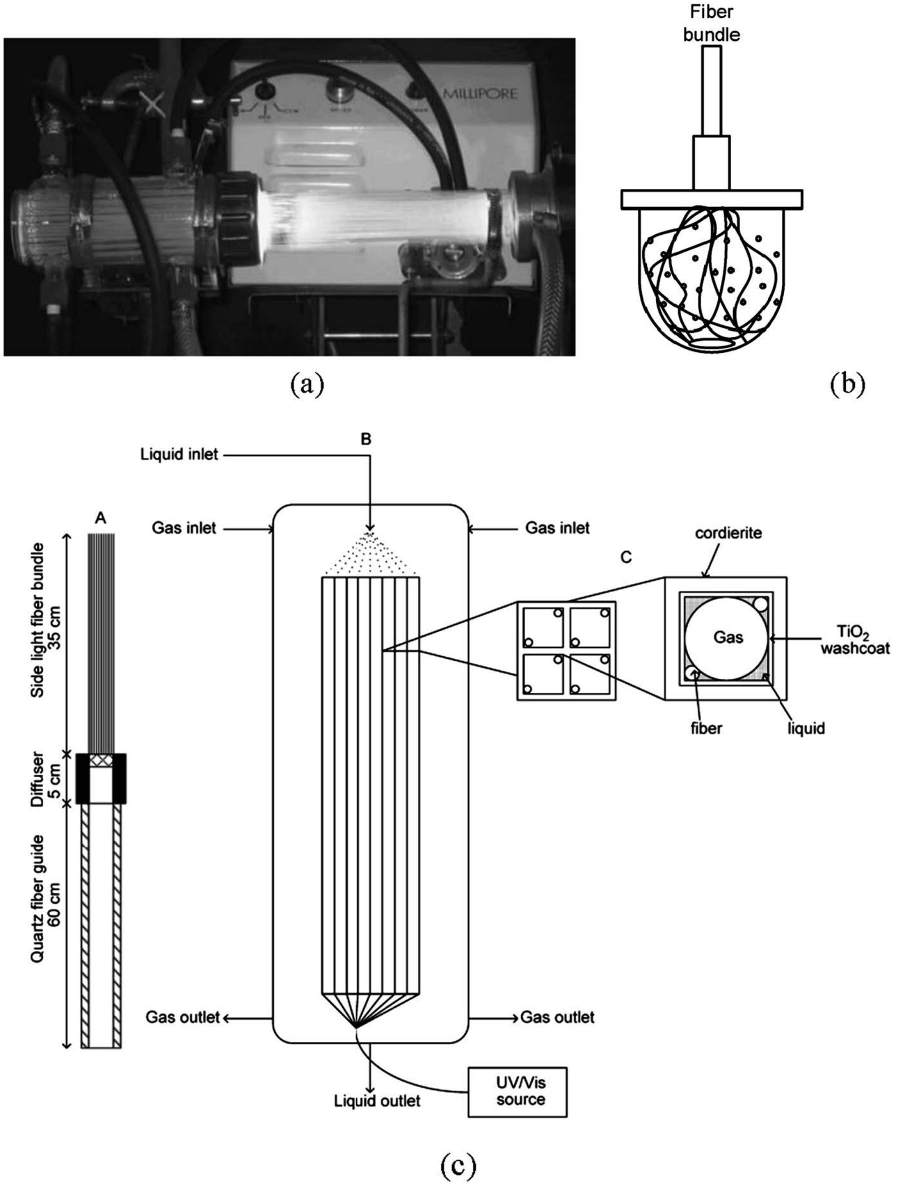

Figure 9.10 Three different OFR designs. (a) First OFR utilizing coated fibres[44] (b) optical fibre illuminated reactor (c) internally-illuminated monolith reactor[46,47] (a) adapted from Applied Catalysis B: Environmental, 62, A. Danion *et al.*, Photocatalytic degradation of imidazolinone fungicide in TiO_2-coated optical fibre reactor, 284–281, Copyright (2006), with permission from Elsevier, (b) and (c) adapted from Applied Catalysis A: General, 334, P. Du *et al.*, A novel photocatalytic monolith reactor for multiphase heterogeneous photocatalysis, 119–128, Copyright (2008), with permission of Elsevier.

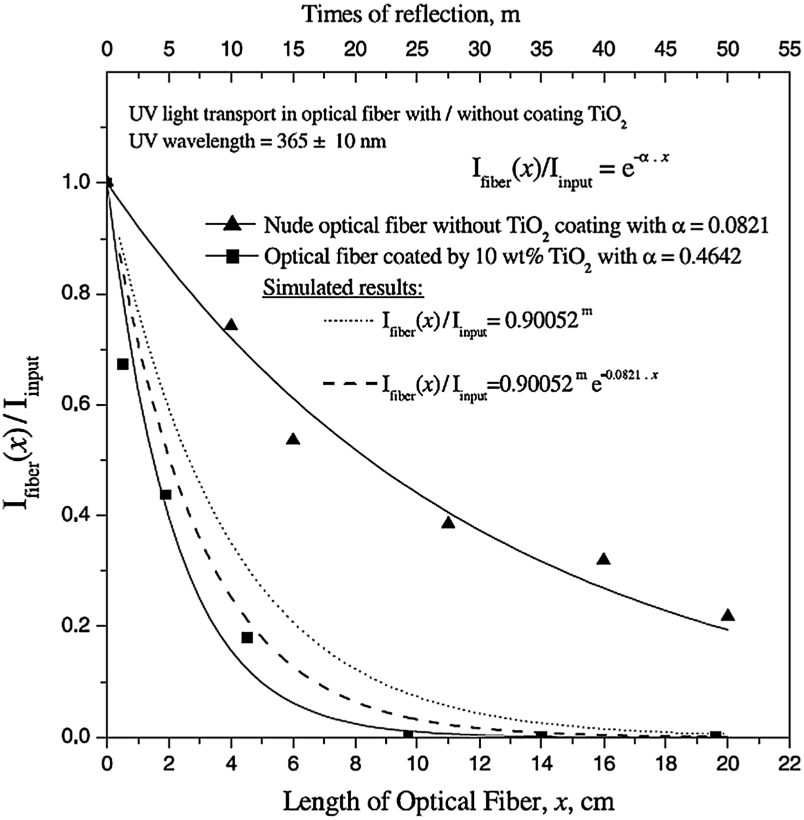

Figure 9.11 Evolution of light intensity in bare and catalyst coated optical fibres.[58] Adapted from Chemosphere, 50, W. Wang and Y. Ku, The light transmission and distribution in an optical fibre coated with TiO_2 particles, 999–1006, Copyright (2003), with permission of Elsevier.

2,4-dichlorophenol degradation.[49] The reaction kinetics (0.0167 min^{-1}) and photonic efficiency (0.002) were of the order of 2D PPRs which shows that this design is not yet optimized. The most probable cause of sub-optimal operation in this case is the photon transfer limitations which can be solved by using photon distributors such as optical fibres.

9.2.2.5 Spinning Disc Reactor (SDR)

Another method used for decreasing the characteristic length of the 2D reactors is to apply centrifugal force on the plate where the catalyst is immobilized. This creates a thin liquid film on the catalyst increasing the A/V ratio.[50] SDR scheme is shown in Figure 9.13. The SDR principle was proven on photocatalytic degradation of 4-chlorophenol in aqueous medium. The SDR managed to decrease the organic substrate concentration of a 10 L vessel by close to two logarithmic levels in 4 hours.

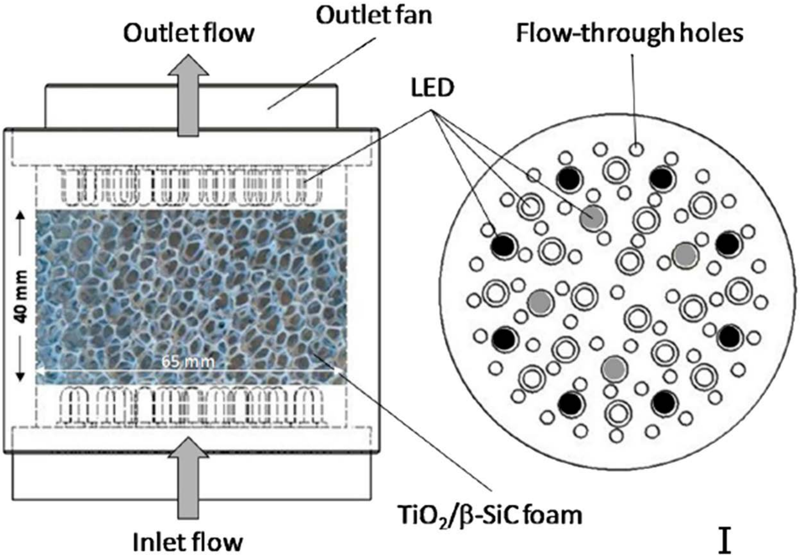

Figure 9.12 Foam reactor scheme and flow distributor with LEDs mounted.[48] Adapted from Applied Catalysis B: Environmental, 154, N. Doss *et al.*, Photocatalytic degradation of butanone (methylethylketone) in a small-size TiO_2/β-SiC alveolar foam LED reactor, 301–308, Copyright (2014), with permission of Elsevier.

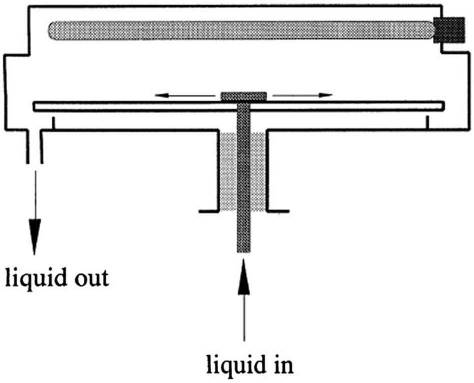

Figure 9.13 The SDR scheme with the mercury lamp on top. Reprinted from Chemosphere, 42, H. C. Yatmaz, The spinning disc reactor – studies on a novel TiO_2 photocatalytic reactor, 397–403, Copyright (2001), with permission of Elsevier.[50]

Although the SDR principle was shown for the first time on water treatment, different new versions have also been developed for use in various reactions. The most interesting for environmental applications is the spinning cloth disc reactor.[63] This design uses cloths as spinning discs and increases the surface area and the residence times of the substrates. This relatively new design can be developed using glass fibre cloth[27] and applied to water treatment.

9.3 Benchmarking Wastewater Treatment Reactors

As explained in the previous sections there are many different photocatalytic reactor design concepts. Trying to evaluate the performance of these reactors is of paramount importance in order to integrate them within existing applications. Evaluation of the reactor's performance and also monitoring the weak points is the key to further process intensification.

Two benchmarks have been used in the literature when comparing reactors. The first benchmark is the apparent first order reaction rate constant k.[43] This benchmark usually has units of min^{-1} depending on the conversion speed of the reactor. This benchmark gives a direct view on the conversion speed of the design which is quite handy when comparing designs. However it does not give an idea of the throughput since it is volume dependent. For example, a PPR working as a loop will give a much lower k when connected to a 10 L vessel than a 50 mL vessel. However it will perform just the same since the active area does not vary. Furthermore this benchmark is dependent on both light intensity and catalyst load.

Another popular benchmark is the photonic efficiency also known as the quantum yield which can be given as,

$$\varepsilon = z\frac{R}{\Phi} \times 100 \tag{9.1}$$

where ε is dimensionless photonic efficiency, R is the reaction rate ($\text{mol L}^{-1}\ \text{s}^{-1}$), z is the amount of electrons transferred per molecule to be degraded and Φ is the photon flux ($\text{mol L}^{-1}\ \text{s}^{-1}$).

ε gives an idea of how efficiently the reactor is utilizing the light. However, it gives no idea of the electrical consumption or the productivity of the reactor. For example, an annular reactor and a parallel plate reactor may have the same photonic efficiency,[34] however they may need lamps of very different powers and they also may have different material throughputs.

Therefore, a need for a better benchmark is definite. The simple benchmark we propose here is the ratio of space–time yield (STY) to the standardized electricity expenditure of the lamp. STY can be calculated by taking the inverse of passage time. The STY here is standardized to the volume (m^3) of wastewater processed from 100 mmol L^{-1} of pollutant to 0.1 mmol L^{-1} of pollutant in a day by 1 m^3 of the reactor. The inlet and outlet concentrations were selected to standardize the degradation to 3 orders of magnitude of concentration decrease. This is a common conversion standard, especially in pharmaceutical and insecticide pollutant elimination.[64] STY can be calculated easily from the apparent reaction rate constant. For a continuous slurry reactor, *i.e.* RAR or MLR, a continuous

PPR operated as a loop and a continuous stirred-tank reactor (CSTR), the model equation can be used.

$$C_{\mathrm{A}} = \frac{C_{\mathrm{A0}}}{1 + k\tau} \tag{9.2}$$

where C_{A} is the output concentration in mmol L^{-1}, C_{A0} is the inlet concentration in mmol L^{-1} and τ is the passage time in days. From the CSTR model, τ can be calculated. Replacing C_{A} by 0.1 mmol L^{-1} and C_{A0} by 100 mmol L^{-1}, the equation then becomes,

$$\mathrm{STY}_{\mathrm{cstr}} = \frac{V_{\mathrm{R}}}{\tau} = \frac{1\mathrm{m}^3}{\tau} = \frac{k}{999} \tag{9.3}$$

where V_{R} is the reactor volume (1 m^3) and k has the units of day^{-1}. For plug-flow photocatalytic reactors such as the microreactor, the STY can be given as;

$$\mathrm{STY}_{\mathrm{pfr}} = \frac{1}{\tau} = -\frac{k}{\ln C_{\mathrm{A}}/C_{\mathrm{A0}}} = \frac{k}{6.908} \tag{9.4}$$

To include the lighting efficiency in the benchmark, the calculated STY was divided by the lamp power and the catalyst load. However, the lamp power was scaled-up to the value which would illuminate 1 m^3 of the reactor by the following relation.

$$\mathrm{LP} = P \times \frac{1\mathrm{m}^3}{V} \tag{9.5}$$

where LP is the standardized lamp power (kW), P is the lamp power of the experimental setup and V is the volume of the reaction medium in the experimental setup (m^3).

Another important parameter affecting the reactor performance is the catalyst load which can be calculated as:

$$\mathrm{CL} = L \times \frac{1\mathrm{m}^3}{V} \tag{9.6}$$

where CL is the standardized catalyst load (kg m^{-3}), L is the catalyst load in the actual setup (g) and V is the volume of the reaction medium in the actual setup (m^3). In conventional catalysis, the benchmarks include the catalyst loading since replacing the spent catalyst is a major expenditure. In this work, however, it is excluded from the benchmark since its consumption by the reactor is very low. In a life cycle assessment of a solar heterogeneous photocatalytic water treatment pilot plant,[65] it is estimated that 20 g of titania photocatalyst is spent for each m^3 of treated water. Assuming a 130 \$ kg^{-1} titania photocatalyst price (www.Alibaba.com search engine), the catalyst

Table 9.3 Three different design concepts benchmarked.

Reactor	k (day^{-1})	STY (day^{-1})	LP (kW)	CL (kg m^{-3})	PSTY (m^3 day^{-1} kW^{-1} kg^{-1})
Microreactor	6×10^6	8.69×10^5	6.71×10^4	161[a]	4.14×10^{-6}
PPR	36	0.036	35	0.07	1.3×10^{-3}
PMR	14.4	0.014	0.22	0.5	6.49×10^{-2}

[a] Catalyst load calculated, assuming 5 μm catalyst thickness for PPR[9] and 1.2 μm catalyst thickness for Microreactor[43] and taking porosity 0.52 from the literature.[34]

cost of the treated water is 0.026 \$ m^{-3}. This is negligible in comparison to the electricity cost which is 0.34 \$ kWh^{-1} (price in Belgium in May 2015) especially when it can take up to 4 kWh of electricity expenditure per m^3 of water.

Hence the overall photocatalytic space–time yield (PSTY) can be given as:

$$\mathrm{PSTY} = \frac{\mathrm{STY}}{\mathrm{LP}} \tag{9.7}$$

The advantage of using the PSTY is to be able to get more idea about the usability of the design than using the k or the ε measures. A microreactor,[43] the PPR shown in Figure 9.8 and a PMR[40] were benchmarked. The data are shown in Table 9.3.

As can be seen in the Table 9.3, different benchmarking parameters lead to different conclusions. According to the k values, the microreactor is, by five orders of magnitude, the best performer of three reactors followed by the PPR which is three times that of the PMR. However, due to the 120 W lamp irradiating a reactor volume of 1.49 μl in the MR setup, the LP value is dramatically higher than the other two which decreases the PSTY benchmark behind both slurry and immobilized catalyst reactors. On the PPR *vs.* PMR side, the PMR rates 50 times better due to the ease of illumination of the slurry reactor with fewer mercury lamps. It should be noted that this benchmark does not include the catalyst recovery step of slurry reactors. PMR recovers the catalyst without additional volume requirement.

Therefore the PSTY benchmark sums up the reactor performances, normalizing very different designs. Furthermore, it shows the weak points in a concept. It is clear: the microreactor does not have a capacity problem but an illumination problem. If there were an UV-LED array of 0.1 W irradiating the reactor, the PSTY would be 13 (m^3 water day^{-1} m^{-3} reactor kW^{-1} lamp) which is 2 to 3 orders of magnitude higher than the competition. A central efficient lighting system with optical distribution can be the solution to this weak point of microreactors in photocatalysis.

9.4 Conclusions

Design concepts to overcome mass and photon transfer limitations shape the current photocatalytic reactors. When compared, the slurry reactors are still more efficient than the immobilized catalyst reactors. However if an effort to scale-up the photocatalytic microreactor (MR) is made, the high area to volume ratio of this design could prove to be the next generation of wastewater treatment.

This scale-up is, however, more complicated than just multiplying the microchannels in an array such as a monolith. The added complication is due the necessity of photon transport to each channel in the array. Hybrid concepts like the internally-illuminated monolith reactor (Section 9.2.2.3) which uses optical fibres and milli-channels can be further investigated to maximize the throughput and efficiency. While using the optical fibres for illumination, it should be taken into account that as shown in Figure 9.11, light intensity decreases as the photons progress through the bare optical fibre.

Here we conclude that to be able to increase the existing levels of throughput and the efficiencies of photocatalytic reactors, focus should be on hybrid designs—with microreactors coupled with new illumination strategies—instead of new design concepts and geometries.

References

1. R. B. Cundall, W. M. Horspool, N. S. Allen, A. Cox and S. T. Reid, *Photochemistry*, The Royal Society of Chemistry, 1996, vol. 27.
2. R. Lakerveld, G. Sturm, A. Stankiewicz and G. Stefanidis, *Curr. Opin. Chem. Eng.*, 2014, **5**, 37–41.
3. G. Mul, T. Van Gerven and A. Stankiewicz, *Novel Concepts in Catalysis and Chemical Reactors*, Wiley-VCH Verlag GmbH & Co. KGaA, 2010, pp. 289–308.
4. T. Van Gerven, G. Mul, J. Moulijn and A. Stankiewicz, *Chem. Eng. Process. Process Intensif.*, 2007, **46**, 781–789.
5. I. Oller, S. Malato and J. A. Sánchez-Pérez, *Sci. Total Environ.*, 2011, **409**, 4141–4166.
6. Y. J. Chan, M. F. Chong, C. L. Law and D. G. Hassell, *Chem. Eng. J.*, 2009, **155**, 1–18.
7. K.-H. Kim and S.-K. Ihm, *J. Hazard. Mater.*, 2011, **186**, 16–34.
8. X.-D. Zhu, Y.-J. Wang, C. Liu, W.-X. Qin and D.-M. Zhou, *Chemosphere*, 2014, **107**, 274–281.
9. M. Vezzoli, W. N. Martens and J. M. Bell, *Appl. Catal., A*, 2011, **404**, 155–163.
10. Q. Xiang, J. Yu and P. K. Wong, *J. Colloid Interface Sci.*, 2011, **357**, 163–167.
11. Z. Wang, J. Liu, Y. Dai, W. Dong, S. Zhang and J. Chen, *J. Hazard. Mater.*, 2012, **215–216**, 25–31.
12. Z. Shu, J. R. Bolton, M. Belosevic and M. G. El Din, *Water Res.*, 2013, **47**, 2881–2889.
13. L. Prieto-Rodríguez, I. Oller, N. Klamerth, A. Agüera, E. M. Rodríguez and S. Malato, *Water Res.*, 2013, **47**, 1521–1528.
14. S. Das and W. M. A. Wan Daud, *Renewable Sustainable Energy Rev.*, 2014, **39**, 765–805.

15. R. Abe, *J. Photochem. Photobiol., C*, 2010, **11**, 179–209.
16. P. R. Gogate and A. B. Pandit, *Adv. Environ. Res.*, 2004, **8**, 501–551.
17. T. H. Lim and S. D. Kim, *Chemosphere*, 2004, **54**, 305–312.
18. M. J. Lima, M. E. Leblebici, M. M. Dias, J. C. B. Lopes, C. G. Silva, A. M. T. Silva and J. L. Faria, *Environ. Sci. Pollut. Res. Int.*, 2014, **21**, 11116–11125.
19. A. G. Agrios, K. A. Gray and E. Weitz, *Langmuir*, 2004, 5911–5917.
20. S. H. Vilhunen and M. E. T. Sillanpää, *J. Hazard. Mater.*, 2009, **161**, 1530–1534.
21. A. Jamali, R. Vanraes, P. Hanselaer and T. Van Gerven, *Chem. Eng. Process. Process Intensif.*, 2013, **71**, 43–50.
22. H. C. Chen and G. Y. Wu, *Opt. Commun.*, 2010, **283**, 4882–4886.
23. O. Comstock, *Today in Energy,* US Energy Information Administration, 2014, http://www.eia.gov/todayinenergy/detail.cfm?id=18671, accessed 26 May 2015.
24. O. Tokode, R. Prabhu, L. A. Lawton and P. K. J. Robertson, *Chem. Eng. J.*, 2014, **246**, 337–342.
25. O. I. Tokode, R. Prabhu, L. A. Lawton and P. K. J. Robertson, *J. Catal.*, 2012, **290**, 138–142.
26. A. Mills and S. Le Hunte, *J. Photochem. Photobiol., A*, 1997, **108**, 1–35.
27. B. P. S. Mukherjee and A. K. Ray, *Chem. Eng. Technol.*, 1999, **22**, 253–260.
28. Y. Boyjoo, M. Ang and V. Pareek, *Chem. Eng. Sci.*, 2014, **111**, 266–277.
29. M. Subramanian and A. Kannan, *Chem. Eng. Sci.*, 2010, **65**, 2727–2740.
30. G. Li Puma and P. L. Yue, *Ind. Eng. Chem. Res.*, 2001, **40**, 5162–5169.
31. K.-H. Choo, R. Tao and M.-J. Kim, *J. Membr. Sci.*, 2008, **322**, 368–374.
32. O. Carp, *Prog. Solid State Chem.*, 2004, **32**, 33–177.
33. O. Tokode, R. Prabhu, L. A. Lawton and P. K. J. Robertson, *Chem. Eng. J.*, 2014, **246**, 337–342.
34. M. E. Leblebici, J. Rongé, J. A. Martens, G. D. Stefanidis and T. Van Gerven, *Chem. Eng. J.*, 2015, **264**, 962–970.
35. S. Ahmed, M. G. Rasul, W. N. Martens, R. Brown and M. A. Hashib, *Desalination*, 2010, **261**, 3–18.
36. E. M. Seftel, M. Niarchos, C. Mitropoulos, M. Mertens, E. F. Vansant and P. Cool, *Catal. Today*, 2015, **252**, 120–127.
37. N. Qi, H. Zhang, B. Jin and K. Zhang, *Chem. Eng. J.*, 2011, **172**, 84–95.
38. F. Visscher, J. van der Schaaf, T. A. Nijhuis and J. C. Schouten, *Chem. Eng. Res. Des.*, 2013, **91**, 1923–1940.
39. S. Mozia, *Sep. Purif. Technol.*, 2010, **73**, 71–91.
40. X. Huang, Y. Meng, P. Liang and Y. Qian, *Sep. Purif. Technol.*, 2007, **55**, 165–172.
41. Y. Meng, X. Huang, Q. Yang, Y. Qian, N. Kubota and S. Fukunaga, *Desalination*, 2005, **181**, 121–133.
42. R. A. Damodar and S. J. You, *Sep. Purif. Technol.*, 2010, **71**, 44–49.
43. A. Visan, D. Rafieian, W. Ogieglo and R. G. H. Lammertink, *Appl. Catal., B*, 2014, **150–151**, 93–100.
44. A. Danion, J. Disdier, C. Guillard, O. Païssé and N. Jaffrezic-Renault, *Appl. Catal., B*, 2006, **62**, 274–281.

45. A. Danion, J. Disdier, C. Guillard, F. Abdelmalek and N. Jaffrezic-Renault, *Appl. Catal., B*, 2004, **52**, 213–223.
46. M. T. Kreutzer, F. Kapteijn, J. A. Moulijn and J. J. Heiszwolf, *Chem. Eng. Sci.*, 2005, **60**, 5895–5916.
47. J. T. Carneiro, R. Berger, J. A. Moulijn and G. Mul, *Catal. Today*, 2009, **147**, 324–329.
48. N. Doss, P. Bernhardt, T. Romero, R. Masson, V. Keller and N. Keller, *Appl. Catal., B*, 2014, **154–155**, 301–308.
49. G. Plantard, V. Goetz, F. Correia and J. P. Cambon, *Sol. Energy Mater. Sol. Cells*, 2011, **95**, 2437–2442.
50. H. C. Yatmaz, C. Wallis and C. R. Howarth, *Chemosphere*, 2001, **42**, 397–403.
51. W.-Y. Wang and Y. Ku, *Water Res.*, 2006, **40**, 2249–2258.
52. K. Wang, H. Tsai and Y. Hsieh, *Appl. Catal., B*, 1998, **17**, 313–320.
53. K. J. Buechler, R. D. Noble, C. A. Koval and W. A. Jacoby, *Ind. Eng. Chem. Res.*, 1999, **38**, 892–896.
54. D. Chen, F. Li and A. K. Ray, *Catal. Today*, 2001, **66**, 475–485.
55. G. Takei, T. Kitamori and H. B. Kim, *Catal. Commun.*, 2005, **6**, 357–360.
56. P. J. Barthe, D. H. Letourneur, J. P. Themont and P. Woehl, *Eur. Pat.*, EP 1415707 A1, 2004.
57. R. E. Marinangeli and D. F. Ollis, *AIChE J.*, 1977, **23**, 415–426.
58. W. Wang and Y. Ku, *Chemosphere*, 2003, **50**, 999–1006.
59. K. Hofstadler, R. Bauer, S. Novalic and G. Heisler, *Environ. Sci. Technol.*, 1994, **28**, 670–674.
60. F. Denny, J. Scott, V. Pareek, G. Ding Peng and R. Amal, *Chem. Eng. Sci.*, 2009, **64**, 1695–1706.
61. P. Du, J. T. Carneiro, J. A. Moulijn and G. Mul, *Appl. Catal., A*, 2008, **334**, 119–128.
62. N. A. Kouamé, D. Robert, V. Keller, N. Keller, C. Pham and P. Nguyen, *Catal. Today*, 2011, **161**, 3–7.
63. X. Feng, D. A. Patterson, M. Balaban and E. A. C. Emanuelsson, *Chem. Eng. J.*, 2014, **235**, 356–367.
64. M. J. Benotti, B. D. Stanford, E. C. Wert and S. A. Snyder, *Water Res.*, 2009, **43**, 1513–1522.
65. I. Muñoz, J. Peral, J. Antonio Ayllón, S. Malato, P. Passarinho and X. Domènech, *Water Res.*, 2006, **40**, 3533–3540.

CHAPTER 10

Plasma-Assisted Nitrogen Fixation Reactions

B. S. PATIL[a], V. HESSEL[a], J. LANG[b] AND Q. WANG*[a]

[a]Laboratory of Chemical Reactor Engineering/Micro Flow Chemistry and Process Technology, Department of Chemical Engineering and Chemistry, Eindhoven University of Technology, P.O. Box 513, 5600 MB Eindhoven, The Netherlands; [b]Innovation Management, Verfahrenstechnik & Engineering, Evonik Industries AG, Rodenbacher Chaussee 4, 63457 Hanau-Wolfgang, Germany
*E-mail: q.wang1@tue.nl

10.1 Introduction

10.1.1 Background – Nitrogen Fixation

Nitrogen, which makes 78% of the Earth's atmosphere, is a basic constituent for sustaining plants and living organisms.[1] Nitrogen constitutes a major part of DNA and RNA, determining the genetic character of all living things. It is also found in plant cells, chlorophyll, enzymes, proteins and amino acids.[2] To most living things, this abundant atmospheric nitrogen is not accessible. Because, before N can be used, the strong triple bond of N_2 must be broken and the N atom must be chemically bonded with other elements such as oxygen and/or hydrogen through a nitrogen fixation process, or with carbon. Some micro-organisms are capable of fixing atmospheric nitrogen and supplying it to plants in a process known as biological nitrogen fixation.[3,4]

RSC Green Chemistry No. 47
Alternative Energy Sources for Green Chemistry
Edited by Georgios Stefanidis and Andrzej Stankiewicz

Published by the Royal Society of Chemistry, www.rsc.org

The other important source for fixed nitrogen is lightning that results from the electrical discharge between two clouds, where conditions are optimal for NO_x formation.[5,6] However, the increasing demand from the global population has intensified agricultural practices and the naturally-fixed nitrogen is no longer sufficient for fulfilling human demands. To cope with this growing demand artificial means of fixing atmospheric nitrogen were developed at the beginning of the 20th century.[7,8]

The most widely used artificial process for the nitrogen fixation is the "Haber–Bosch ammonia synthesis process", which is considered as the most important discovery of the 20th century. Recently, the annual amount of nitrogen fixed by the Haber–Bosch (H–B) process has reached 130 million tons per year, surpassing that fixed naturally in agriculture and doubling the number of humans supported per hectare of arable land.[7,9] After the invention of the H–B process the global population started growing rapidly. Even though there were many other factors, food was the important one. The increase in global population and nitrogen fertilizer consumption follow very similar trends, as shown in Figure 10.1, which also shows the distribution of fixed nitrogen quantities as reported in 2010.[5]

Chemically-fixed nitrogen as ammonia is used in many different forms, ranging from nitric acid to hydrogen cyanide and used for large scale applications in chemistry, *e.g.* fertilizer and plastics manufacture, *etc.*[10] A complete picture of the range of products derived from ammonia is presented in Figure 10.2.

10.1.2 Timeline of N-Fixation Process Development

Investigation on ammonia dates back to 1774; the timeline shows the most significant events in nitrogen fixation process development (see Figure 10.3[14–16]). Here we have focused only on chemical nitrogen fixation.

In the 20th century nitrogen obtained from artificial processes overtook the nitrogen obtained from natural sources (organic and inorganic) thanks to overwhelming efforts put in to fix atmospheric nitrogen, as the atmosphere is an abundant source of nitrogen. A number of successful industrial-scale processes have been investigated, including reactions for the production of nitric oxide (NO), ammonia (NH_3), hydrogen cyanide (HCN) and nitric acid (HNO_3). All these efforts could be combined into the following three main approaches:

1. Combining atmospheric nitrogen and oxygen to form nitric oxide: *e.g.* Birkeland–Eyde electric arc process explained in Section 10.2.1.1[17,18]
2. Use of compounds capable of fixing nitrogen in their structure: *e.g.* cyanamide acid process[10,14,19]
3. Combining atmospheric nitrogen with hydrogen to form ammonia: *i.e.* Haber–Bosch process[20,21]

Birkeland–Eyde successfully developed the electric arc process in Norway in 1903, which is explained in detail in Section 10.2.1.1. The cyanamide acid

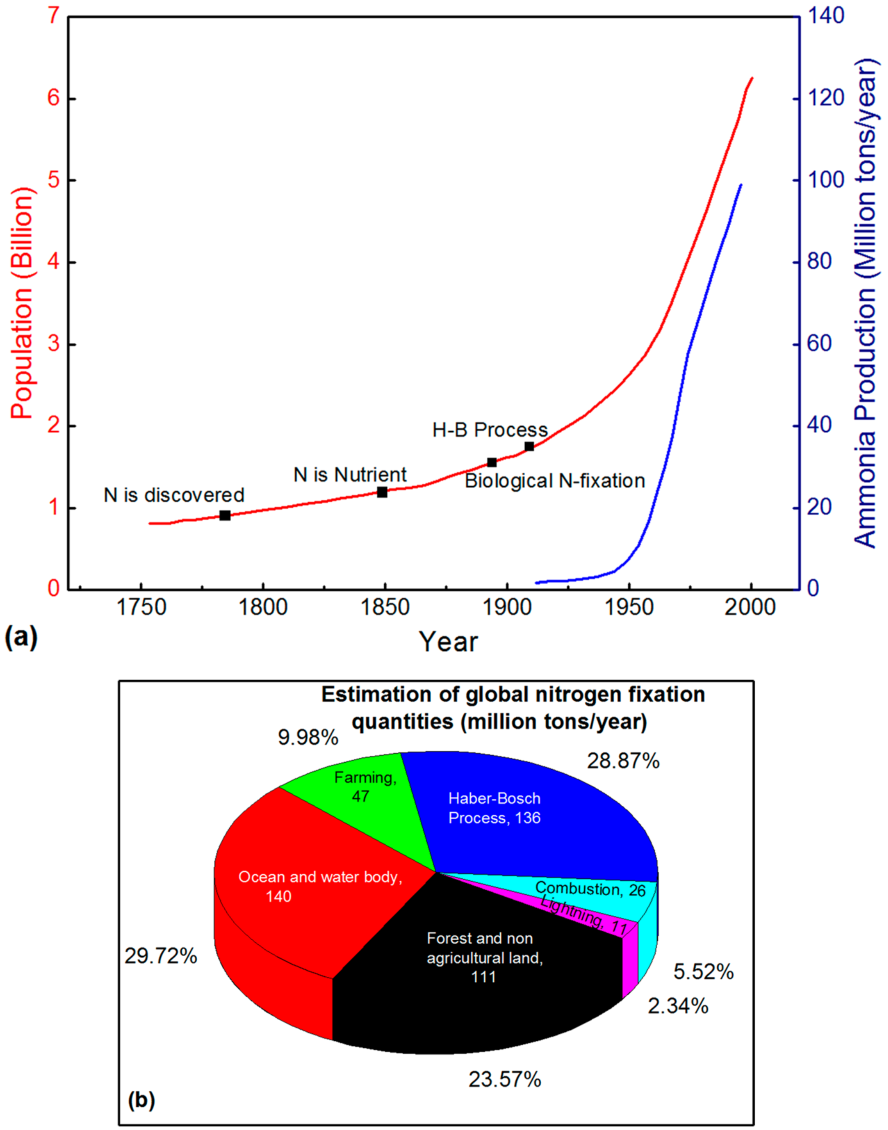

Figure 10.1 A: global population increase and the nitrogen fertilizer consumption trends.[11] B: quantities of fixed nitrogen in million metric tons per year in 2010.[5] Reprinted from Catalysis Today, 256, B. S. Patil *et al.*, Plasma N_2-fixation: 1900–2014, 49–66, Copyright (2015)[12] with permission from Elsevier B.V.

process was developed by German scientists Frank and Caro from 1895–1898. Nitrogen was fixed in the form of calcium cyanamide by reaction of calcium carbide with pure nitrogen. The cyanamide process grew rapidly, reaching its peak in 1918 with 35 plants and total rated capacity for fixing 350 000 tons of nitrogen per year. Both of these processes were very energy intensive[22]

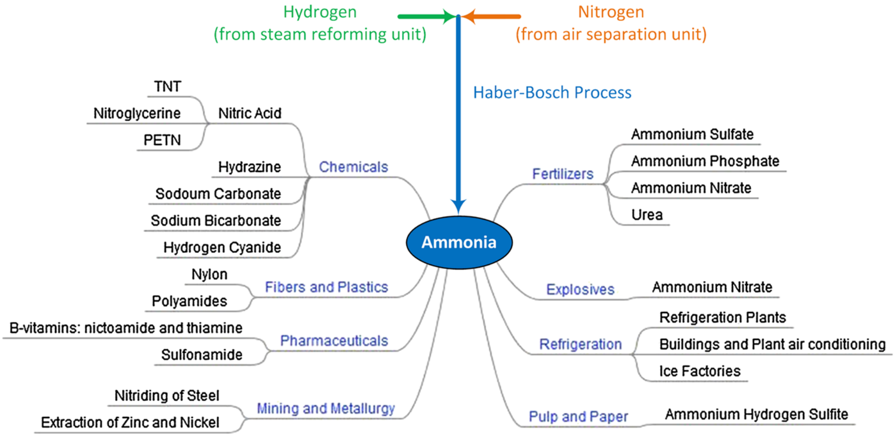

Figure 10.2 Overall picture of nitrogen fixation compounds and their applications.[10,13] Reprinted from Catalysis Today, 256, B. S. Patil *et al.*, Plasma N_2-fixation: 1900–2014, 49–66, Copyright (2015)[12] with permission from Elsevier B.V.

and eventually taken over by the Haber–Bosch process developed in 1908 and commercialized in 1913. The main reasons were comparatively less energy consumption and the higher volumes of ammonia produced. More details on this process can be found elsewhere.[9,19,21] Significant development in technology over the last half century has made it possible to reduce the energy consumption of the Haber–Bosch nitrogen fixation process by almost 3 times to the present energy consumption of 36 GJ per ton of N fixed. This chronological progress is shown in Figure 10.4. The significant development mainly means the development for the upstream units, methane reforming for hydrogen production and high purification nitrogen supply, which takes around 75% of the energy consumption of the whole process, while the synthesis and separation steps only take 25%. It should be noted that all the energy consumption mentioned in following discussions for plasma-assisted nitrogen fixation mainly refers to the energy for the synthesis step.

Even so, the H–B consumes 1–2% of the world's total energy production,[24] 2–3% of world's total natural gas output[21] and emits 300 million metric tons of CO_2 to sustain 40% of world's population.[7,25] The International Energy Agency (IEA) has identified ammonia among 18 chemicals which consume 80% of the total energy demand of the chemical industry and contribute to 75% of GHG emissions.[23] Therefore, even a small improvement in the energy efficiency of this process would bring huge economic savings. However, modern technological and ecological standards require considerable reduction in its environmental footprint and an increase in its energy efficiency, although the H–B process has almost reached its theoretical limits.[26] The IEA has also identified ammonia as the chemical compound with the highest potential to reduce energy and GHG emissions by 2050 through improving the catalyst and the catalytic process.[23]

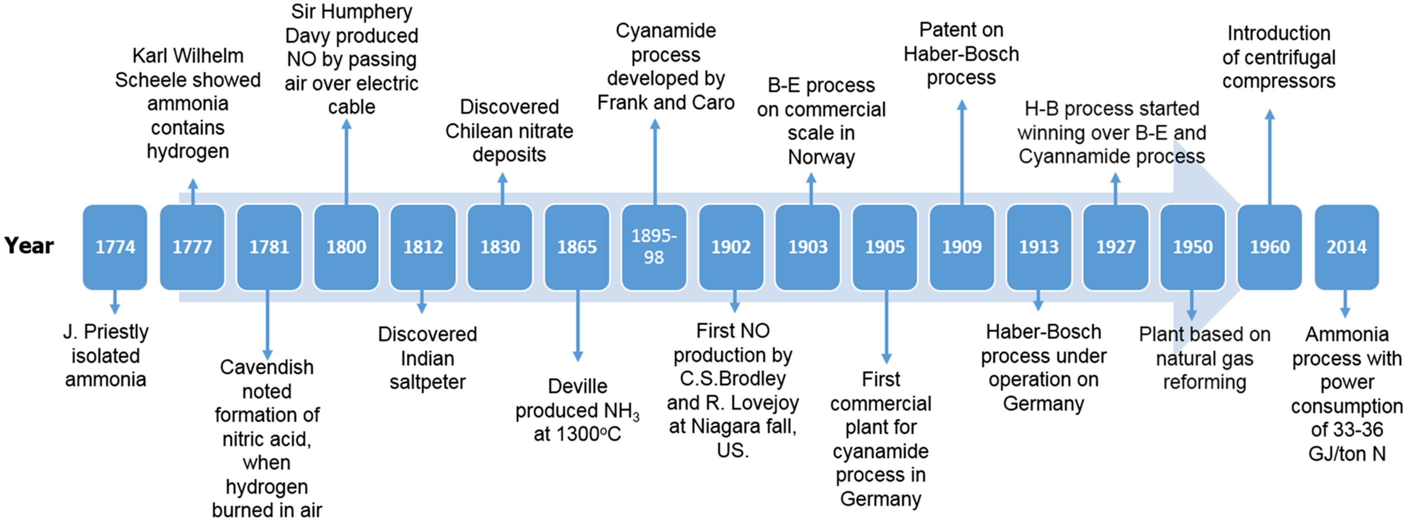

Figure 10.3 Major milestones in chemical nitrogen fixation process development.[14,15] Reprinted from Catalysis Today, 256, B. S. Patil *et al.*, Plasma N_2-fixation: 1900–2014, 49–66, Copyright (2015)[12] with permission from Elsevier B.V.

From Figure 10.5, it can be seen that only the non-thermal plasma process has a lower energy consumption possibility than the H–B process. The most energy-effective mechanism for plasma-chemical NO synthesis is provided by the vibrational excitation of molecules, because most of the energy of non-equilibrium discharges is transferred from electrons to vibrational excitation of N_2 molecules at Te = 1–3 eV.[29] The mechanism of synthesis through vibrational excitation of N_2 is not only the most energy effective but is often the fastest and therefore the most dominating mechanism.[29] It is important to notice that non-thermal plasma has 3 times lower theoretical energy consumption than the H–B process.[26] Therefore, using plasma as an alternative energy to fix nitrogen offers a great potential for the future. Plasma processes

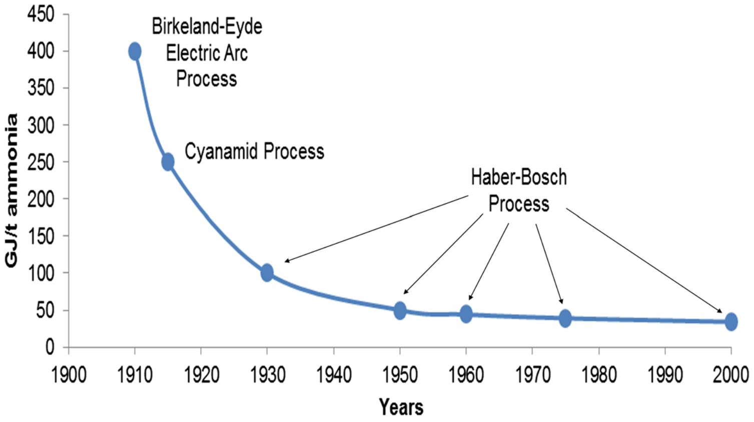

Figure 10.4 Comparison of energy consumption for three N-fixation processes.[23]

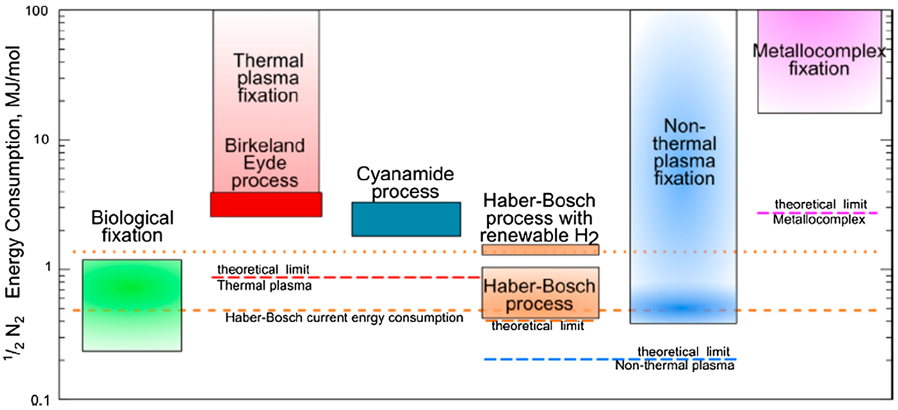

Figure 10.5 Energy consumption for various nitrogen fixing processes, reprinted from Chemical Engineering and Processing, 90, N. Cherkasov *et al.*, A review of the existing and alternative methods for greener nitrogen fixation, 24–33, Copyright (2015)[26] with permission from Elsevier B.V.

on an industrial scale have been reported as a top priority in a number of white papers on process intensification and energy savings.[27,28]

10.1.3 Introduction to Plasmas

Plasma is considered as the fourth state of matter which makes up 99% of the visible universe.[29–31] Plasma processes are among the oldest processes on the earth and may be involved with the origin of life as demonstrated by Miller and Urey's experiments in 1953.[32,33] Plasma is generated by ionization of gases, which takes place when a sufficient amount of electrical energy is supplied to a gas. Plasma contains electrons, neutrals, and highly excited atomic, molecular, ionic and radical species. Plasma is an extraordinary multidisciplinary phenomenon involving physics, electromagnetism and chemistry, *etc.*[29–31] Understanding plasma generation and control is therefore extremely challenging. Plasma can be produced over a wide range of pressures, temperatures, electron temperatures and electron densities. Plasmas are generally classified as high temperature (HTP) or low temperature plasmas (LTP). In HTP, electron and ions are at the same temperature of about 10^7 K. Low temperature plasmas are subdivided into thermal and non-thermal plasmas as shown in Table 10.1.[34] In thermal plasmas, electron, ions and background gas are at the same temperature of about 10^4 K. Arc plasma and plasma torches work with thermal plasma. In non-thermal plasmas, electrons are usually at very high temperatures of the order of 10^5 K because of their smaller mass, whereas ions and background gas are at room temperature. Non-thermal plasmas can be found in atmospheric pressure discharges—pulsed corona, pulsed glow discharge, glow discharge, micro-hollow cathode discharge, dielectric barrier discharge (DBD), RF discharge, microwave discharge, *etc.*[35] Non-thermal plasmas exhibit higher selectivity compared to thermal plasmas. Non-thermal plasmas are the most commonly used plasmas for technological applications. Please refer to standard books on plasma physics and plasma chemistry for more information.[29,30,36]

An energy-efficient and environmentally-benign nitrogen fixation process could be developed by employing non-thermal plasmas.[37,38] In this chapter, there will be a thorough literature review on plasma nitrogen fixation processes for nitric oxide, ammonia, and hydrogen cyanide synthesis between the years 1900 to 2014.

Table 10.1 Classification of plasmas.[34] Reprinted from Catalysis Today, 256, B. S. Patil *et al.*, Plasma N_2-fixation: 1900–2014, 49–66, Copyright (2015), with permission from Elsevier B.V.[12]

Low temperature plasma (LTP)		High temperature plasma (HTP)
Thermal plasma $Te \approx Ti \approx T \leq 2 \times 10^4$ K	Non-thermal plasma $Ti \approx T \approx 300$ K $Ti \ll Te \leq 10^5$ K	$Te \approx Ti \geq 10^7$ K
E.g. arc plasma at normal pressure	*E.g.* low pressure glow discharge, barrier discharge, corona, plasma jets	*E.g.* fusion plasmas

10.2 Plasma-Assisted Nitrogen Fixation

The most fundamental and basic means of fixing nitrogen is the direct reaction of nitrogen with oxygen/hydrogen/carbon under plasma conditions. Plasma nitrogen fixation is generally accomplished by the reaction of nitrogen with oxygen or hydrogen to produce nitrogen oxide (nitric acid) or ammonia, respectively. Nitrogen can also be combined with carbon to produce hydrogen cyanide. In addition, a plasma reactor/process offers advantages such as: simple one-step process, can be operated and stopped instantaneously, provides high energy density for very fast reactions—resulting in smaller units, and is generally non-polluting.[31]

In this section literature reported for plasma nitric oxide, ammonia and hydrogen cyanide synthesis on industrial, pilot and laboratory scales from 1900 to 2014 is reviewed. The main focus is on the reactor configurations, operational regimes, plasma catalysis and energy efficiency.

10.2.1 Plasma Nitric Oxide Synthesis

In plasma nitric oxide synthesis the raw materials (air : nitrogen + oxygen) are available abundantly and are almost free. The nitric oxide production is favored by high temperature processing because of the endothermic nature of the reaction (10.1)[39] and very high dissociation energies of the nitrogen (binding energy of 9.77 eV).[40] The Gibbs free energy for reaction (10.1) is 86.55 kJ $mole^{-1}$ (»0) indicating that it is a very difficult reaction to proceed. These requirements make it necessary to realize this plasma process with affordable energy input and high enough product yield.

$$N_2 + O_2 \rightarrow 2NO; \Delta H = 90 \text{ kJ mol}^{-1} \approx 1 \text{ eV} \tag{10.1}$$

Thermodynamic calculations for the N_2–O_2 system in equilibrium at 1 atmosphere pressure show that the maximum concentration of NO achievable is 6.5% at 3500 K,[41] as shown in Figure 10.6. If the quenching of this product mixture from 3500 K follows thermodynamic equilibrium, then the final concentration of NO would be significantly lower than 6.5%. To attain the equilibrium concentration of NO in thermal plasmas, very rapid cooling following the reaction kinetics is desired.[42] Theoretically, the cooling rate required to freeze the equilibrium composition of the NO in the reactor outlet would be in the order of millions of K per second.[42] This magnitude of quenching rate seems practically infeasible on an industrial scale, therefore employing non-thermal plasma reactors, which operate in strongly non-equilibrium conditions, could be one of the possible solutions to achieve higher NO concentrations.

10.2.1.1 Industrial-Scale Plasma Nitric Oxide Synthesis Processes

Plasma nitrogen fixation was realized by using an electric arc in a process known as the "Birkeland–Eyde (B–E) process" in 1903.[17] In fact, the B–E process is the first plasma process ever realized successfully on an industrial

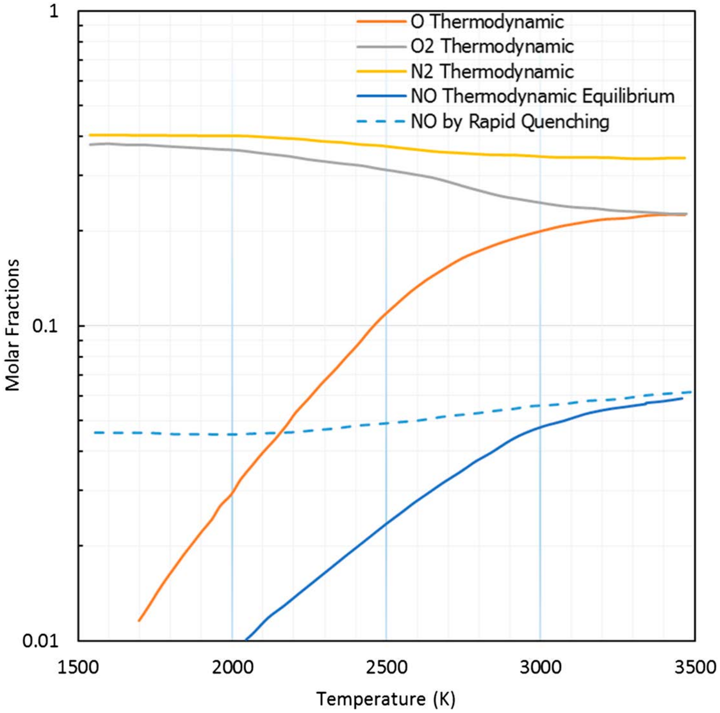

Figure 10.6 Effect of quenching for N_2–O_2 equilibrium mixture. Reproduced from ref. 42 with permission from John Willey and Sons. Copyright © 1966 American Institute of Chemical Engineers.

scale. The final product of this process was nitric acid, produced by first fixing atmospheric nitrogen and oxygen into nitric oxide, then absorbing it in water.

Before the plant at Niagara had discontinued operations a furnace was developed by Prof. Christian Birkeland and engineer Samuel Eyde in Norway, which was successful economically and also from the mechanical aspect.[14] They started a company, the Norwegian Hydro Electric Nitrogen Company (Norsk Hydro), producing nitrogen compounds using electricity, particularly electric arc technology. The Birkeland and Eyde furnace was based on the phenomenon of deflection of an arc by a magnetic field which helped to spread the electric arc through the gas. The experiments were first carried out in 1903 using a 2.24 kW power supply on the developed Birkeland–Eyde furnace. In the next step, a commercial plant working on 111.85 kW was installed, whose successful operation led to installation of a 745.7 kW plant near Arendal, Norway. This successful demonstration resulted into a number of new plasma furnace installations, the biggest of which was a 238.6 MW plasma furnace, fixing 38 ktons of nitrogen in total per year (in 1928).[14,19]

The typical process flow scheme and experimental setup is shown in Figures 10.7 and 10.8. First, air was rapidly passed through a zone of exceedingly

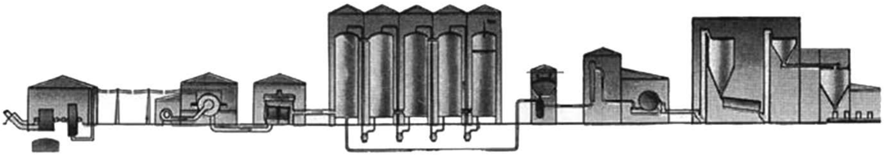

Figure 10.7 The industrial scale model of Birkeland–Eyde nitrogen fixation process; from the power station on the left of the figure to the final fertilizer product to the right.[17] With kind permission from[17] Springer Science and Business Media.

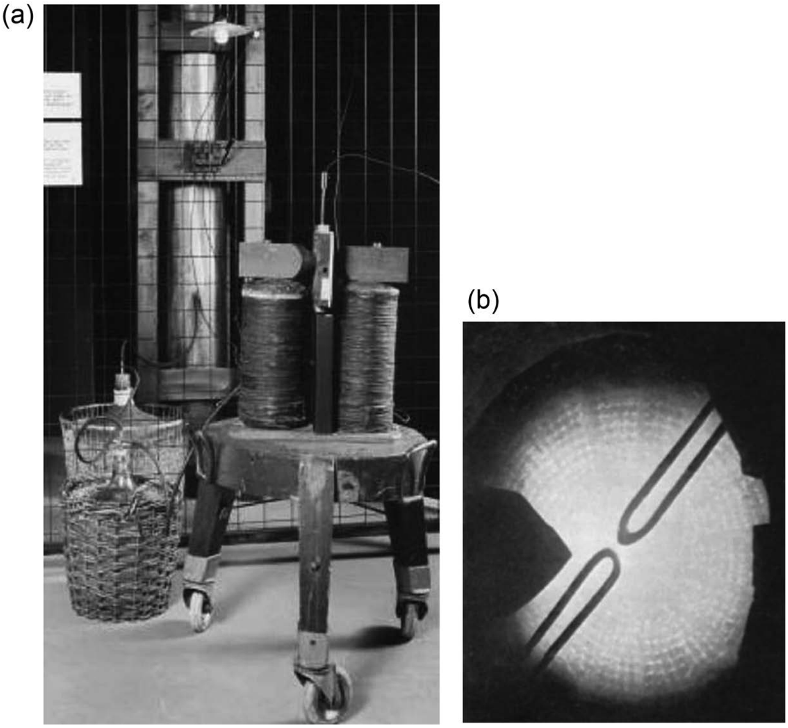

Figure 10.8 A. Birkeland's first experimental nitrogen fixation setup at the university. Nitric acid, converted from the nitric oxide generated in the plasma process, as final product of process was collected in glass container, B. The electric arcs of more than 1 m diameter were produced between 2 electodes.[17] With kind permission from[17] Springer Science and Business Media.

high temperature in an electric arc furnace producing ~1.2 vol% nitric oxide. In the second step, nitric oxide was oxidized to nitrogen dioxide. Finally, nitrogen dioxide was then absorbed in water to produce dilute nitric acid (30%) in a train of absorption columns, including alkaline absorption columns for recovering unabsorbed NO_x.

The theoretical energy required was 1628 kWh for 907 kg of nitrogen. However the total energy supplied to the arc furnace was 61 000 kWh. Less than 3% of the supplied energy was utilized for the reaction, while rest of the supplied energy (97%) was wasted in establishing conditions suitable for the reaction to take place—*e.g.* to obtain 1 ton of fixed nitrogen it was required to process 175 ton of air. Even though equipment had been built to rapidly cool the product gas to avoid decomposition of nitric oxide, it was believed that a large amount of nitric oxide decomposition actually took place.[14]

Various efforts had been put in to improve the performance of the B–E process, such as use of a 50–50% mixture of N_2–O_2, preheating and heat recovery from the process gas and operating the furnace at higher pressure. However, the process had poor energy efficiency as compared to the classical H–B process of ammonia synthesis and also needed high mechanical maintenance, hence it was eventually abandoned by the industry.[14,43]

VIVEX Engineering Ltd (UK) supplies cold plasma technology for HNO_3 production. The company claims to produce 15–35% HNO_3 starting form air with 20% less energy consumption than other processes. This cold plasma process contains high voltage plasma reactors and a series of wet reactors as absorbers.[44]

The company, N2Applied, developed a demonstration plant for nitric oxide production by arc discharge which is being tested and supposed to be used in a local farm for nitrogen fixation in manure.[91] A demonstration plant for nitric oxide production by non-thermal plasma in a containerized plant for de-centralized production of chemicals will be built in Evonik Industries (Germany) as the most important delivery of the European project, MAPSYN.[37]

10.2.1.2 Laboratory Studies on Plasma Nitric Oxide Synthesis

A high industrial relevance of the fixed nitrogen products and benefits offered by plasma has led to numerous efforts on a laboratory scale in the last 100 years to improve the plasma nitrogen fixation process. It is clear from the above discussions that to make the plasma nitric oxide process commercially feasible, energy consumption by the process should be drastically reduced and, at the same time, the amount of nitrogen fixed must be increased several-fold. With the rapid advancement in the under-standing of plasma reaction kinetics due to advanced measurement techniques, a good deal of research on plasma nitrogen fixation has been published by a number of research groups.[45–52] Plasma-assisted nitrogen fixation into nitric oxide has been studied and reported for laboratory-scale processes using air plasma,[48,51,53,54] using N_2–O_2 mixture,[46,47,55] and in argon, argon–nitrogen and nitrogen plasma.[49,55,56] All these efforts in plasma nitric oxide synthesis are analyzed and reported in the following sections, divided in 2 groups: plasma reactor configurations studied and the plasma catalysis.

10.2.1.2.1 Plasma Reactor Configurations. Various plasma types have been investigated to perform the nitric oxide synthesis. Table 10.2 summarizes

Table 10.2 Plasma NO synthesis: summary of reported plasma types and reactor/process configurations. Reprinted from Catalysis Today, 256, B. S. Patil *et al.*, Plasma N_2-fixation: 1900–2014, 49–66, Copyright (2015), with permission from Elsevier B.V.[12]

Process details (plasma type, reactor configuration, and experimental conditions)		Reactants	Feed rate (L min^{-1})		Power	%N-fixation	Concentration of NO	Ref.
			N_2	O_2	kW	%	%	
Radio-frequency plasma	Radio-frequency plasma - 5–7 MHz and atm pressure	N_2 and O_2	17.7	14.3	10	—	—	58
	RF plasma with quench	Air	—	—	—	4	—	59
	RF plasma without quench	Air	—	—	—	2	—	59
	RF plasma 1–2 atm	Air	—	0.5	—	17	—	60
DC thermal plasma	DC plasma jet	N_2 and O_2	5.5	5.5	15	—	—	62
	DC constricted arc	Air	—	0.82	5.2	7	—	63
	Electric arc reactor - 0.5–1 bar and 3000–5000 K	Air	—	—	30 GJ ton^{-1} N_2	—	8 vol% = 0.1 s 12 vol% = 1 m s	57
Inductively coupled plasma	Inductive HF discharge: 40 MHz - Glass tube ID: 10 cm, *L*: 1 m - 6.67–53.32 mbar	N_2–O_2 a. Co-current b. Countercurrent	1–4.5	—	335 kJ L^{-1} of NO	—	9.5 5	46
	Inductive HF discharge: 40 MHz Glass tube ID: 10 cm, *L*: 1 m - 6.67–53.32 mbar - Catalysts: MoO_3 and WO_3 - Surface area/reactor vol. = 0.5	N_2–O_2	1–4.5	—	—	—	19	45
Microwave plasma	Microwave plasma reactor - 2.45 GHz and 20–90 kPa	Air	—	—	—	—	—	69
—	Controlled generation of plasma by setting energy (*E*)/Pressure (*P*) ratio	N_2–O_2	—	—	E/P = 5–15 kV atm^{-1}	—	—	74

the literature reported for plasma NO synthesis with respect to type of plasma, reactor configuration, power source employed and the main results in terms of percentage of nitrogen fixed. The main plasma types investigated are the electric arc of the B–E process,[18,57] radio frequency discharges,[58–61] DC discharges,[62–65] lasers,[66,67] microwave discharges,[68,69] microwave with electron cyclone resonance discharges,[70] glow discharges,[71] dielectric barrier discharges,[72] inductively coupled high frequency discharges,[45,46] and pulsed arc discharges.[53,54]

Various configurations of plasma reactors were reported such as electric arc with expanding reactor geometry,[73,74] reactor with rotating disk,[50,51] DC plasma jet,[52,65] and reactors with various *E*/*P* ratios.[74]

Ingels[57] patented an electric arc reactor to produce nitric oxide by reverse engineering the Birkeland–Eyde furnace. Air is fed to the reactor, an electric arc is produced in the flowing gas, and the magnetic field which is applied at 90°, expands the arc giving a higher plasma volume. This reactor is proposed to operate at lower than 1 bar and the temperature is maintained within the range of 3000 to 5000 K. The energy consumption by the proposed reactor configuration is reported to be 30 GJ ton^{-1} N_2. For a retention time of 0.1 s, NO concentration is claimed to be 8 vol% and for 0.001 second it is found to be 12 vol%. By raising the NO yield from 2% to 10%, energy consumption per ton of N_2 was claimed to reduce by 80%.[57]

A two-stage configuration for plasma nitric acid production is proposed by the combination of hot and cold plasma.[75] Firstly, NO can be produced in the hot plasma, then it could be oxidized to NO_2 in the cold plasma with ozone.[75] High energy lasers are also reported to fix nitrogen by Conrad,[67] where the plasma is produced by the repetitively pulsed high energy laser—a focused beam operating at high temperature with rapid quenching rates. A CO_2 laser was employed with a focusing mirror made of zinc selenide, copper or molybdenum and the product cooling was achieved by the rapid expansion of hot plasma into the surrounding cool gas.[67]

A precise control over plasma generation is the key to increase the energy efficiency. The controlled generation of plasma by actively setting the energy to pressure ratio studied by Chen *et al.*[74] led to 10 times higher nitrogen fixation rates. The *E*/*P* ratio was maintained between 5 and 15 kV atm^{-1} to generate volumetric plasmas and not localized ones.[74] This approach might have maximized vibrationally-excited nitrogen species and hence promoted the reaction for NO synthesis. Also, the ferroelectric support particles of different dielectric constants in the packed bed plasma reactor were found to increase the plasma volume and the number density of the excited nitrogen species.[76]

Amouroux and co-workers published a series of papers in the 1980's on the plasma NO synthesis in non-equilibrium plasma reactors.[45,46,77,78] These studies were conducted in an inductively coupled HF plasma reactor operating at 40 MHz and from 1 to 40 mbar. These measurements suggest that the rotational temperature was around 1500–2000 K, vibrational temperature was 4000–6000 K, and the electronic temperature was around 23 200–34 800 K.

The important conclusion drawn from the study was that the vibrational temperature had a direct relationship with the chemical reactivity. The increased nitric oxide formation was thought to be because of the reaction proceeding through the collision of vibrationally-excited oxygen with N_2.[46]

To improve the energy performance of the plasma nitric oxide synthesis by thermal plasmas, it is very important to increase the heat recovery. Rapid cooling of the product gases is desirable to avoid the ratio of the product to the reactants being adjusted to the less favorable lower temperature equilibrium and to reduce the dissociation of the reaction products. To recover the heat of the product stream two approaches are generally adopted: using heat exchange equipment[79] or rapid cooling of products by employing an expanding reactor geometry.[73] Heat exchange is accomplished by direct or indirect cooling of the product gases with incoming reactant gases. For example, a direct cooling is achieved using 2 clusters of tungsten/molybdenum tubes inside a quartz tube,[79] where the flow directions can be reversed periodically to gain the heat lost by product gases to the W/Mo tubes and *vice versa*. The W/Mo tubes provide both the heat transfer as well as a catalytic surface to achieve higher heat transfer rates and nitric oxide yield.[79] However, nothing has been reported about the % energy efficiency and the nitric oxide yield. For cooling by expansion, Gross and Smith[73] have reported the formation of nitric oxide using an electric arc reactor, where the resulting gases were cooled below dissociation temperature (<1000 °C) by expanding the reactor from 30:1 to 200:1 and contacting with recycled cooled gas. This approach reportedly gave approximately double NO concentration compared to the equilibrium concentration.[73] Sekiguchi *et al.*[80] studied the effect of thermal quenching on the plasma synthesis of nitric oxide using argon plasma and cooling tubes of different diameters. The conversion to nitric oxide increased with decreasing quenching tube diameter, *i.e.* by increasing the heat transfer rate. With the improved understanding of non-thermal plasma reactors, *e.g.* DBD, the low energy efficiency has also been ascribed to energy losses such as heating up the outgoing gas, barriers and electrodes, or losses to the environment.[129] Thus efficient energy recovery is not only necessary for a thermal plasma reactor but also for the non-thermal plasma reactor. Thus it makes more sense to consider the whole process for systematic heat integration. Also, it is difficult to conduct chemistry with adequate selectivity and to incorporate catalysts in thermal arc plasmas. Typically, they also have very high energy consumptions. On the other hand, a non-thermal plasma reactor does not need quenching or rapid cooling of the reaction products as it operates at atmospheric pressure and lower temperatures, offering great potential to make chemical synthesis energy efficient and to incorporate catalysts. However, the non-thermal plasma reactors have not been sufficiently investigated for nitric oxide synthesis. Presently, most of the scientific literature is focusing on the destruction of NO_x gases rather than on the synthesis of NO_x.

Recently, research papers have been published for nitric oxide synthesis in sliding arc[81] and gliding arc discharge reactors.[82] In the sliding discharge, NO production is found to increase and the NO_2 amount decreases with increase in the operating temperature, as directed by the thermodynamic equilibrium of the NO–NO_2 mixture. The highest concentration of NO produced was 1040 ppm (~0.1%) at 420 °C.[81] In this milli-scale gliding arc reactor, 1 vol% of NO_x (=NO + NO_2) is produced with a relatively high energy efficiency of 10 kWh kg^{-1} of NO_x at room temperature. This is thought to be as a result of minimized gas by-passing and intense contact of reactive species inside the plasma region and of the electrical energy given through nanosecond pulses.[82] The NO_x concentration is found to increase with increase in the frequency and the pulse width. As the number of input energy pulses increases with the frequency this indirectly increases the specific energy input (SEI). The NO_2 was also found to be produced in a considerable amount in the gliding arc reactor. As shown in Figure 10.9, increase in the SEI (Figure 10.9A) and increase in the oxygen% (Figure 10.9B) is found to yield higher concentrations of NO_2, suggesting the possible conversion of NO to NO_2 inside the plasma as well as in the reactor exit, which is favored at lower temperature by the thermodynamic equilibrium and kinetics.[82] This demonstrates that the gliding arc, microwave and nano pulse discharge plasma reactors can offer a potential solution and would be interesting to investigate for plasma nitric oxide synthesis.

Despite the available studies on reactor configuration, either for thermal plasma or non-thermal plasma, there is no clear guidance for plasma reactor design for NO_x synthesis. It should be noted that here the plasma reactor means not only the reactor itself but also includes the power supply system. With different researches, it is not that straightforward to compare, even if it concerns the same type of plasma reactor, which is mainly because of the incomparable nature of the power supply system. The intrinsic relationships between the power input and gas discharge, discharge properties and reactor configuration, and reactor configuration and energy efficiency constitute essential knowledge to improve reactor configuration.

Operating a plasma reactor at atmospheric pressure and ambient temperature with the raw materials (nitrogen and oxygen) giving the final products (nitric oxide/nitric acid) directly changes the structure of the conventional Ostwald process considerably. This change will reduce both the operating and capital costs. The use of a heat exchanger, battery and very expensive compressors will become redundant, giving a substantial reduction in the capital cost. However, it will also add new electrical equipment to the process, such as the transformer and electrical power supply system needed for a plasma reactor. Therefore, the holistic process design approach must be followed from the beginning of the new plasma process development, by considering the overall process rather than considering the individual process sections. The holistic design approach focuses, from the beginning, on the analysis of plasma chemical process development from the viewpoint of process engineering, economic and environmental impact.

10.2.1.2.2 Plasma Catalysis for Nitric Oxide Synthesis. The combination of catalyst and the plasma reactor has not been investigated thoroughly for the nitric oxide synthesis and very few researchers have reported

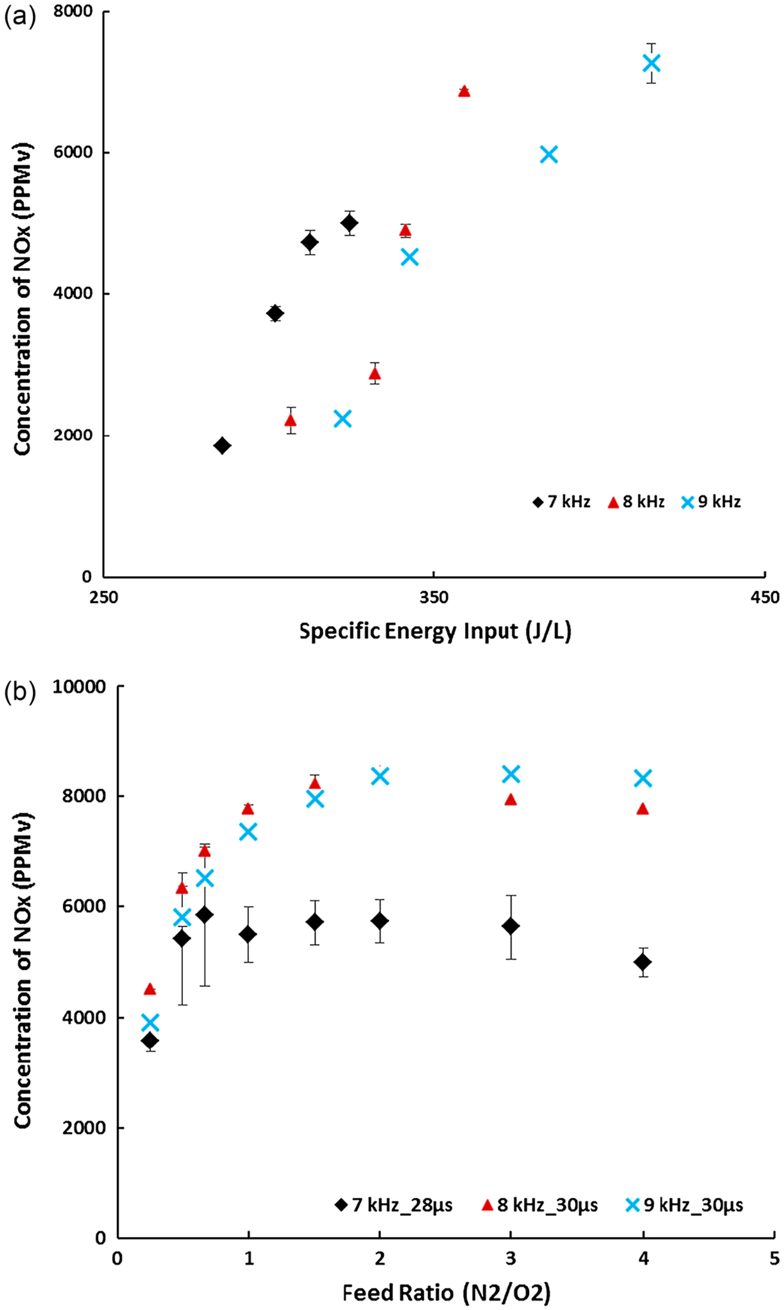

Figure 10.9 Variation of concentration of NO_x with respect to specific energy input (A) and feed ratio (B). Reprinted from ref. 82 with kind permission from Springer Science and Business Media.

it.[45,55,71,78,83–85] Nitric oxide was produced with plasma catalysis by Cavadias and Amouroux.[45,78] The reactor used in this study is schematically shown in Figure 10.10. The yield of nitrogen fixation was about 8% without catalyst; this was increased to 19% by using WO_3 catalyst,[45] as shown in Figure 10.11. To conduct this low pressure process at atmospheric pressure, a fluidized bed reactor was also employed with WO_3/Al_2O_3 as catalyst.[83]

Amourox *et al.* studied the basics of the interaction between the chemical species constituting a plasma and the solid catalyst surface.[7,45] The catalytic materials, transition metal oxides such as WO_3 and MoO_3, were deposited on a support with a large surface area, such as Al_2O_3, MgO and ZrO_2. WO_3 and MoO_3 catalysts are n-type semiconductors and have labile oxygen that can provide required oxygen more easily for the oxidation of nitrogen to NO_x. This labile oxygen could have played an important role in the formation of NO_x. When a vibrationally-excited N_2 molecule arrives on a surface having a labile oxygen it is possible that oxidation takes place much more easily.[47,55,86]

Mutel *et al.*[55] used the same metal oxides deposited on the plasma reactor wall. The energy consumption for the catalytic nitrogen fixation process was found to be 28 MJ kg^{-1} of NO,[55] which gave a 78% improvement in energy efficiency as compared to thermal plasma process of Coudert *et al.*,[64] and 35% in comparison to non-catalytic nitrogen fixation.

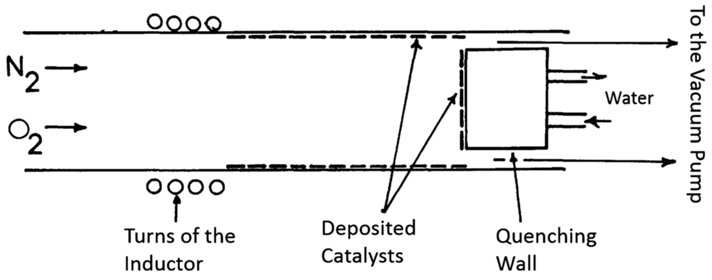

Figure 10.10 Inductively coupled HF plasma reactor with catalyst coated walls. Reproduced from ref. 45 with kind permission from EDP sciences.

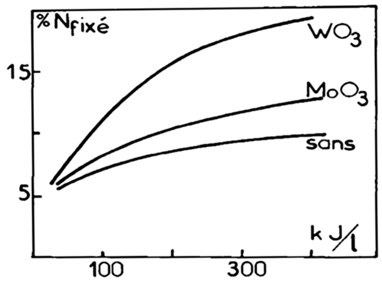

Figure 10.11 Effect of use of catalyst on the rate of nitrogen fixation ($\%N_{fixé}$) as a function of the induced energy (kJ L^{-1}). WO_3 and MoO_3 represent results in presence of catalyst and "sans" shows results without catalyst. (Reproduced from ref. 45 with kind permission of EDP sciences.)

Besides Amourox *et al.*, O'Hare[84,85] has also worked on the plasma catalytic NO synthesis. The catalytic materials patented are tungsten oxide, molybdenum oxide, tantalum, Cr_2O_3, copper cromite, tantalum oxide, magnesium oxide adsorbed on Al_2O_3, ferric oxide, titanium dioxide, silicon dioxide, sodium Y-type zeolite, nickel Y-type zeolite, cobalt Y-type zeolite and manganese X- and Y-type zeolites. O'Hare found that these catalysts also act as a shielding material for the UV radiation generated by electric excitation,[84] to avoid dissociation of the formed product. In another patent,[85] O'Hare claims a process which uses a low-frequency, high-voltage electric arc discharge in combination with catalyst, where the electric arc was formed entirely within the catalyst bed. However, to the best of the authors' knowledge none of these patented catalytic materials have been investigated experimentally to check their suitability for plasma NO_x formation.

Belova *et al.*[71] investigated the nitric oxide synthesis reaction in a glow discharge reactor using Pt, CuO, Fe, Ag gauzes as a catalyst. The experiments had been conducted for nitrogen–oxygen mixtures of 1 : 1 and 1 : 4 ratios. Pt was found to yield the highest nitrogen fixation rate in both scenarios, with NO concentration of 9% (6.5% for the equilibrium condition) for the 1 : 1 mixture. For the 1 : 4 ratio, Pt could produce up to 7.25% NO. For nitric oxide synthesis, the order of catalyst effectiveness is reported as Pt > CuO > Cu > Fe > Ag.[71] Recently, zeolites have also been investigated. Cu-ZSM-5 catalyst was investigated by Sun *et al.*[72] for NO_x formation in a dielectric barrier discharge reactor with a single-stage configuration, however, the main purpose of the study was to investigate favorable process conditions for NO_x removal. In this study temperatures higher than 623 K were found favorable for NO_x formation.

Another possibility could be to use seeding material. Use of seeding material by recycling 5% of the mixture leaving the discharge is reported by Alamaro.[87] It was noted that seeding produced a marked increase in the collision rate and the excitation–dissociation rates, ultimately increasing the NO yield by 10–20% to NO concentration of 6%.

From the literature summarized above, it is evident that very few catalysts have been investigated and reported for plasma NO synthesis. The effects of plasma on the catalyst and *vice versa*, have not been reported for plasma NO fixation in non-thermal plasma reactors. A plasma reactor with provision to achieve faster transport rates with suitable catalyst must be developed to utilize short-lived active species.

10.2.1.3 Mechanism of Plasma Nitric Oxide Synthesis

The limiting step in nitric oxide synthesis is the breaking of the strong triple bond of the N_2 molecule (9.77 eV).[29] Breaking the bond can proceed mostly efficiently *via* reactions of vibrationally-excited nitrogen molecules of lower vibrational states (shown by reaction (10.2)). This reaction is followed by an exothermic reaction (reaction (10.3)) leading to production of nitric oxide and an oxygen atom, which then reacts with nitrogen and closes the reaction chain. This mechanism is known as the Zeldovich mechanism and it is depicted below. Nitric oxide can also be obtained by following the electronic excitation route, but it is limited by high energy cost and its efficiency is much lower than the Zeldovich mechanism.[29]

$$O(^3P) + N_2^{*}\,(^1\Sigma_g^{\ 1}, v) \rightleftharpoons NO(^2\Pi) + N(^4S);\ E_a \approx \Delta H \approx 288\ \text{kJ mol}^{-1} \tag{10.2}$$

$$N + O_2 \rightleftharpoons NO + O;\ \Delta H \approx -96\ \text{kJ mol}^{-1} \tag{10.3}$$

The mechanism of plasma NO synthesis in non-equilibrium plasma reactors without and with catalyst is investigated by Amouroux *et al.*[46] and Rapakoulias *et al.*,[45] respectively. In both the cases, vibrationally-excited nitrogen was found to contribute to NO formation and surface reactions were also found to play an important role. Macheret *et al.* also found that nitric oxide synthesis proceeds most effectively *via* the vibrational excitation of nitrogen.[88]

Amouroux *et al.* studied the synthesis of nitrogen oxide in a high frequency non-equilibrium plasma reactor operated at 6.67–53.3 mbar in countercurrent and co-current fashion.[46] Two possible pathways of NO formation were suggested. The first pathway is from 3000 to 4500 K, which gives the direct synthesis of NO under the condition of high pressure and low nitrogen to oxygen ratio.

$$N_2^{*} + O_2^{*} \rightleftharpoons NO + N + O \tag{10.4}$$

$$N_2^{*} + O \rightleftharpoons NO^{*} + N \tag{10.5}$$

The second pathway extends from 4500 to 6000 K and corresponds to the dissociation of nitrogen. This pathway is favored by low pressure and low nitrogen to oxygen ratio.[46]

$$N_2 + e \longrightarrow N_2^{**} \longrightarrow N + N \tag{10.6}$$

$$N + O_2 \rightleftharpoons NO + O \tag{10.7}$$

The reactivity of nitrogen is found to be proportional to its vibrational excitation. For the countercurrent arrangement (*i.e.* cold oxygen is added to nitrogen plasma) a maximum of 5% nitrogen was fixed at 334.7 kJ L^{-1} N_2, whereas in the co-current configuration, a higher rate of nitrogen fixation, *i.e.* 9.5% for the same energy input, is reported. The important conclusion drawn from this study was that the N-fixing rate decreased with decreasing ratio of surface to reactor volume, suggesting importance of the surface reactions in NO synthesis.

Rapakoulias *et al.*[45] investigated the NO synthesis mechanism for heterogeneous catalysts such as MoO_3 and WO_3. The authors suggested following mechanism of nitric oxide formation in plasma: vibrationally excited nitrogen molecule dissociatively adsorbs on the catalyst surface and then mobile oxygen which was also vibrationally-excited reacts on the surface to give NO. The reaction of adsorbed nitrogen with mobile oxygen was found to be the rate determining step. The proposed reaction mechanism for the catalytic NO synthesis is given by following equations and shown in Figure 10.12.

$$N_2^* \xrightleftharpoons{\text{surface}} 2N_{\text{ads}} \tag{10.8}$$

$$N_{\text{ads}} + O \xrightleftharpoons{\text{surface}} (NO)^*_{\text{ads}} \xrightleftharpoons{\text{desorption}} NO \tag{10.9}$$

Gicquel *et al.* proposed the following reaction mechanism for dinitrogen oxidation on MoO_3 or WO_3 catalysts:[86]

$$N + MoO_3 \rightarrow MoO_3 - N_{\text{ads}} \tag{10.10}$$

$$N_2^* + MoO_3 \rightarrow MoO_3 - N^*_{2_{\text{ads}}} \tag{10.11}$$

$$MoO_3 - N_{\text{ads}} \rightarrow MoO_2 + NO \tag{10.12}$$

$$MoO_3 - N^*_{2_{\text{ads}}} \rightarrow MoO_2 + N_2O^* \tag{10.13}$$

$$N_2O^* + O \rightarrow 2NO \tag{10.14}$$

$$N_2O^* + O(P^3) \rightarrow N_2 + O_2 \tag{10.15}$$

$$MoO_2 + O_2 \rightarrow MoO_3 + O \tag{10.16}$$

$$MoO_2 + O \rightarrow MoO_3 \tag{10.17}$$

This reported mechanisms and data do not really explain: how the catalyst contributes to the increased nitrogen fixation rates, what changes are made in the catalyst morphology or the changes in active site distribution on the support surface due to plasma–catalyst interaction. Better understanding of the synergy mechanism between plasma and catalyst is still the bottleneck for improvement in plasma catalytic reactor design.

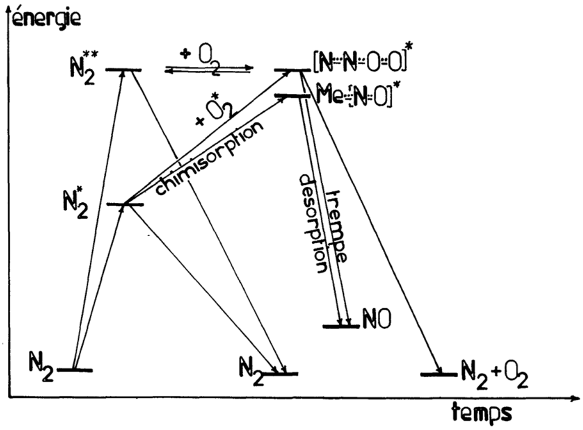

Figure 10.12 Energy diagram-explaining the mechanism of nitric oxide synthesis. Excited states: ** highly dissociative excited state and * moderately excited state. (Reproduced from ref. 45 with kind permission of EDP sciences.)

10.2.1.4 Energy Efficiency of Plasma Nitric Oxide Synthesis

Throughout last century researchers were trying to increase the yield and energy efficiency of the plasma nitric oxide synthesis. On the industrial implementation of plasma nitric oxide synthesis, the Birkeland–Eyde furnaces could produce 1–2% of NO with the energy consumption of about 2.4 MJ mol^{-1}, which corresponds to an energy efficiency of 4% (≈heat of reaction/energy consumption). Other works employing thermal plasma were also not very energy efficient.[29,89,90] Optimization of the thermal plasmas, operation at higher pressures (20–30 atm) and temperatures in the range of 3000–3500 K, made it possible to decrease energy consumption to 0.87 MJ mole^{-1}, which corresponds to an energy efficiency of 11%.[90] Pollo and Banasik[56] performed an energy balance analysis on a thermal plasma reactor designed for NO synthesis. From the total energy supplied, only 0.1% is supplied to the chemical reaction. According to this analysis, a major portion of energy supplied was consumed by the reaction product cooling (quenching) system—approximately 67% of the total energy supplied. This is because the energy in thermal plasmas is distributed over all degrees of freedom including those not effective in NO synthesis.

The energy efficiency of NO synthesis in a non-equilibrium system was found to be different for different mechanisms. The mechanism involving charged and electronically excited species is limited by the high energy cost of the formation of charged and electronically excited particles—the energy efficiency is generally not more than 3%.[29] Vibrational excitation of the molecules is the most energy efficient and therefore the most dominating mechanism of NO synthesis in non-equilibrium plasmas. Unlike thermal plasma, in non-thermal plasmas, energy can be selectively channeled to effective NO synthesis routes. For the plasma catalysis studies, the optimal value of the energy consumption was reported as 28 MJ kg^{-1} of NO with 6 mole% of NO.[55]

Table 10.3 summarizes the energy consumption values reported for the plasma nitric oxide synthesis by different types of plasma. The comparison of the energy consumption and NO concentration for main plasma NO synthesis studies are shown in Figure 10.13. The energy consumption numbers reported in this section and graph are only for the reactors and not for the overall process.

Rapakoulias *et al.*[45] calculated the energy yield for 3 different approaches to plasma NO synthesis, these are shown in Figure 10.14. They are ionic, dissociation, and catalytic routes with energy requirements of 15 eV, 9.77 eV, and 6–7 eV respectively. The highest energy efficiency is given by the catalytic route (31%) followed by dissociation (20%) and the ionic route (13%).

Therefore, it seems necessary to develop an understanding and utilize the synergetic effect of catalyst and non-thermal plasma to reduce the energy consumption and to increase the nitrogen fixation rate. To take the plasma NO process to a commercial scale, if using conventional fuel energy resource, the energy consumption of overall process must be brought below that of the Haber–Bosch process *i.e.* 33–35 GJ ton^{-1} N_2[20] and the NO yield must be increased considerably.

Table 10.3 Summary of the literature reported energy consumptions for plasma nitric oxide(s) synthesis.

Type of plasma	Products/ concentration	Energy consumption (MJ mol^{-1})	Ref.
Birkeland–Eyde arc furnace	1–2% of NO	2.4	18
Thermal plasma	NO	0.87	90
- High quenching			
- Low quenching	NO	1.93	
Thermal plasma	NO_2	10.61	89
Radio-frequency discharge	HNO_3	19.3	61
Laser	NO_x	9.65	66
Rotating disk configuration	NO 4.7%	3.5	50 and 52
Jet arc generator	NO (6.5%)	4	64
Plasma beam discharge	NO	0.96	127
DC plasma generator	NO	0.84	65
Glow discharges	NO	0.67	128
Pulsed microwave discharge	NO	0.6	68
Electron cyclotron resonance	NO	0.3	70
Sliding discharges	NO and NO_2 (0.1%)	15.4	81
Gliding arc discharge	NO and NO_2 (1%)	1.43	82

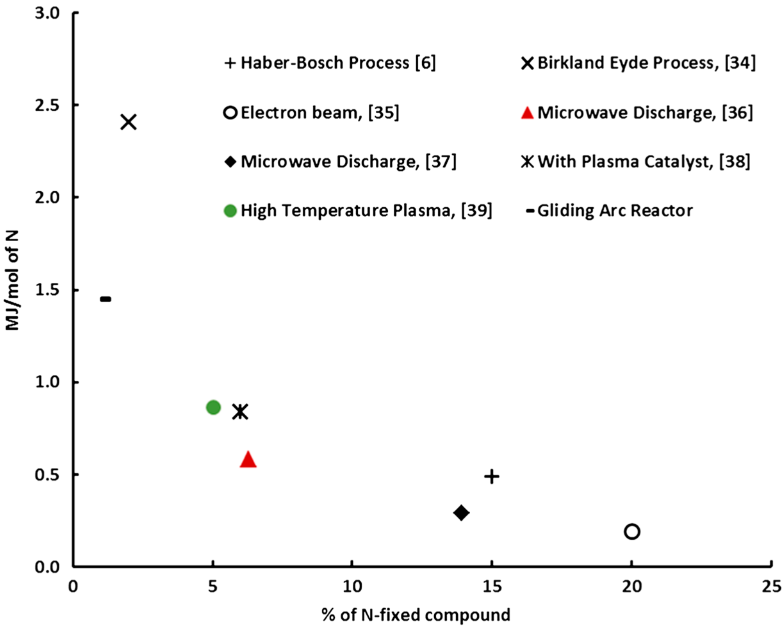

Figure 10.13 Comparison of energy consumption and concentration of fixed nitrogen for plasma NO synthesis. (The energy consumption numbers reported are only for the reactors and not for the overall process, except in case of B–E and H–B process.)

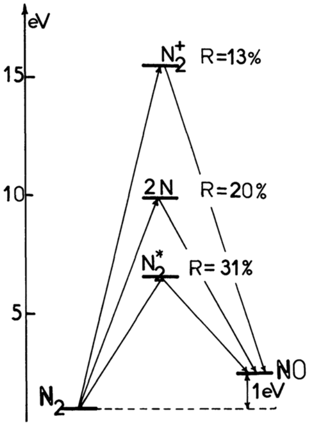

Figure 10.14 Theoretical energy yield for 3 different routes of NO synthesis. Reproduced from ref. 45 with kind permission from EDP sciences.

10.2.1.5 Applications Beyond Nitric Acid

In addition to using fixed nitrogen in the form of nitric acid, it has been investigated for other applications as well. Papers published in following fields of applications are summarized below together with some knowledge from them.

10.2.1.5.1 Direct Agricultural Fertilizer. The NO produced with lower concentrations in plasma processes can be used directly as a fertilizer component rather than producing urea or ammonium nitrate. This lower concentration of NO could be absorbed in water to get a dilute concentration of HNO_3, which could be directly mixed with organic farm wastes (*e.g.* manure) and used as an N-rich organic mixture fertilizer for farming. This approach proposed to reduce the loss to the environment of nitrogen through denitrification, thereby considerably eliminating serious environmental issues related to loss of nitrogen. In the long term this could help reduce the fertilizer used by farmers and preserve the environment.[91]

10.2.1.5.2 Medical Use. Inhaled NO has been extensively used in clinical treatment of pulmonary hypertension, high altitude pulmonary edema, *etc.* Generally, bottled NO is used in hospitals, however it is inconvenient and expensive to use. Various plasma types such as corona, dielectric,[92] shielded sliding discharge[81] and pulsed arc discharge[54,93] have been employed to obtain NO for medical uses. Beside NO, these plasma chemical processes also produce NO_2, N_2O_5 and ozone, which are toxic upon inhalation.[54,92,93] Therefore, product gases need additional processing to get rid of harmful NO_2 and O_3. This is done in a converter packed with catalyst or by operating the reactor higher temperatures.[82] The catalysts reported for use in the converter are Mo,[54] Mo_2C with Ni.[92] This application mainly requires to generate

NO on site[54] and to obtain maximum of NO/(NO + NO_2) output. A similar device with a heat exchanger was patented by Castor and Hamer.[93] This device consists of a DBD reactor (for production of NO) and a converter (to convert NO_2/N_2O_5 to NO) acting as a heat exchanger.

10.2.1.5.3 In Liquid. In a typical plasma nitric oxide process, NO is first oxidized to NO_2, then NO_2 is absorbed in water to form HNO_3. Instead, Bian *et al.*[94] allowed plasma of feed gas (mixture of N_2–O_2) to be bubbled directly into the liquid phase. Bian *et al.* analyzed plasma nitrogen fixation using a pulsed high voltage discharge. Reaction products distribute into the two phases: the liquid phase containing HNO_2 and HNO_3 and the gas phase consisting of NO and NO_2. The energy yield was reported to be 820 kWh kg^{-1} of HNO_3.

10.2.1.5.4 Lightning. Fixation of nitrogen by lightning is of great importance to understand the environmental chemistry and evolution of the atmospheres on Earth, Venus and Mars. Numerous studies had been performed to understand the global nitrogen fixation rates by lightning. The NO_x gases produced by lightning play a key role in photochemistry of the atmosphere mainly due to production and control of ozone in the troposphere and stratosphere. These studies have been carried out with aim of understanding the global NO production by lightning using arc[95] and corona[96] discharges.

10.2.2 Plasma Ammonia Synthesis

The reaction for plasma ammonia synthesis from nitrogen and hydrogen is an exothermic reaction as can be seen from the heat of reaction (10.18). In case of the ammonia synthesis reaction, kinetics favors high temperature for higher reaction rates and thermodynamics favors low temperature processing to achieve higher yields. However, the dissociation of N_2 is a strongly endothermic reaction and requires high energy input. It must be noted that plasma ammonia synthesis requires expensive hydrogen in addition to readily available nitrogen.

$$N_2 + 3H_2 \rightleftharpoons 2NH_3;\ \Delta H = -46.27\ \text{kJ mol}^{-1} \tag{10.18}$$

10.2.2.1 Laboratory-Scale Efforts to Improve Plasma NH_3 Synthesis Process

To date, no plasma NH_3 synthesis processes have been developed and implemented on the industrial or pilot scales. However, numerous efforts have been made at the laboratory scale to develop a plasma process operating at milder temperatures and pressures compared to the widely accepted Haber–Bosch process. All these studies are reported in this section in two categories: plasma reactor configurations and plasma catalysis.

10.2.2.1.1 Plasma Reactor Configurations. Non-equilibrium plasmas which operate at ambient temperature are widely investigated as a promising alternative to produce ammonia from a N_2–H_2 mixture *via* NH radicals. Synthesis of ammonia has been reported for glow discharge plasma,[97,98] microwave plasma,[99–102] radio-frequency plasma,[99,103] electron cyclone resonance (ECR),[104] dielectric barrier discharge plasma[105–107] and expanding plasma[108] reactors. These studies have been summarized in Table 10.4

Sugiyama *et al.* (1986) studied ammonia synthesis using *glow discharge plasma* at low pressure. The reactor arrangement used in this study is shown in Figure 10.15.[97] This study speculates that the ammonia production process occurs on the surface.

Microwave discharge (2450 MHz and 1.2 kW) and *radio-frequency discharge* (13.56 MHz) were investigated under similar experimental conditions.[99–102] Twice the amount of ammonia was produced when using microwave discharge than radio-frequency discharge, as shown in Figure 10.16.[99] The maximum yield of ammonia was obtained for the optimal experimental conditions—power input of 150 W and hydrogen to total flow ratio of 0.75. It was concluded that the ammonia molecule is formed not only by reaction of NH radicals with hydrogen atoms but also with hydrogen molecules.[100] The synergetic effect of catalysts and microwave and radio-frequency discharge plasmas on the synthesis of ammonia and hydrazine was also investigated.[101] When radio-frequency discharge plasma was employed, the yield of ammonia and hydrazine were found to increase while using microwave plasma resulted in a higher yield of ammonia, however the yield of hydrazine decreased. Addition of hydrogen to microwave plasma reduces the ammonia production, while hydrogen injection in the afterglow region gave a higher concentration of ammonia, increasing approximately by a factor of 20.[102] The dilution of plasma gas with argon flow up to 10 L min^{-1} resulted in a 25–30% higher ammonia production rate. Beyond 10 L min^{-1} flow of argon, the ammonia production rate was found to decrease. This could be because of reduced absolute amounts of N_2.

The synthesis of ammonia was also investigated in *ECR plasmas*,[104] where XPS spectral analyses were performed to identify the species adsorbed on the stainless steel substrate. The proposed mechanism of the ammonia synthesis consists of three steps; dissociative adsorption of nitrogen molecules as well as NH_x radicals, then reaction between adsorbed species and hydrogen from the plasma and finally desorption of the product.

The abovementioned reactors and configurations were operated at reduced pressure, which is not very attractive for industrial scale applications. Due to the ease of testing various catalyst materials and operation at atmospheric conditions, dielectric barrier discharge reactors have also been investigated for plasma ammonia synthesis.

Bai *et al.*[105] used a *micro gap dielectric barrier discharge* plasma to synthesize ammonia at ambient pressure. The gap between the discharge electrodes was 0.47 mm. The dielectric layer of 0.25 mm alpha-Al_2O_3 powder was sprayed on both sides of the discharge electrodes. The concentration of ammonia was found to increase by increasing discharge power per area,

Table 10.4 Summary of literature reported on plasma ammonia synthesis. Reprinted from Catalysis Today, 256, B. S. Patil *et al.*, Plasma N_2-fixation: 1900–2014, 49–66, Copyright (2015),[12] with permission from Elsevier B.V..

Type of plasma reactor/plasma source/ process conditions		Gases used	Catalysts/electrode material	Results	Ref.
Glow discharge plasma	Glow discharge plasma - $P = 13.33$ mbar and $I = 6$ mA	N_2 and H_2 (1 : 3)	Basic oxides: CaO, MgO Acidic oxides: Al_2O_3, WO_3 and SiO_2–Al_2O_3	• Basic oxides were more active for NH_3 synthesis • Ammonia production occurs at surface	97
	Glow discharge plasma - 60 Hz, 15 kV, 200 W	N_2 (22.7 mL s^{-1}) and H_2 (24.6 mL s^{-1})	Al, Fe, Cu, Zn, Ag, Pt, SS (stainless steel)	• Order of catalytic activity found to be Pt > SS > Ag > Fe > Cu > Al > Zn	98
Microwave discharge plasma	Microwave discharge (2450 MHz and 1.2 kW) Radio-frequency discharge (13.56 MHz) - 650 Pa, 200 W	N_2 and H_2 (1 : 4) 1.2 lit h^{-1}	—	• Microwave discharge had one order of magnitude higher concentration of NH_x radicals, hence gave higher ammonia production, because of the higher power input in MW than RF discharge	99
	Microwave discharge - 30–280 W - 260–2600 Pa	N_2 and H_2	—	• Ammonia yield increases with decreasing pressure	100
	Microwave plasma discharge Atmospheric pressure - 1.3 kW and frequency of 2.45 GHz	N_2, Ar, He and H_2 total flow: 15 lit min^{-1}	—	• Gas quenching is found as most effective for ammonia production	102
Radio frequency discharge	Radio-frequency discharge - 13.6 MHz at 6.67 mbar	N_2 and H_2 (1 : 4)	Iron wires	• Yield increased with number of wires • Iron wire resulted in increased concentration of ammonia by 2 times and 2 order of magnitude more hydrazine	103
	Microwave and radio-frequency discharge plasmas - 6.67 mbar, 180 W	N_2 and H_2	Iron wire, molybdenum wires	• Microwave plasma resulted in higher yield of ammonia, the yield of hydrazine decreased	101

(*continued*)

Table 10.4 (*continued*)

Type of plasma reactor/plasma source/process conditions		Gases used	Catalysts/electrode material	Results	Ref.
ECR plasma	ECR plasma - 600 Pa, 200 W	N_2 and H_2	SS	• N_2 dissociatively adsorbed on stainless steel surface; acts as catalyst	104
DBD reactor	Micro gap dielectric barrier discharge - Discharge gap = 0.47 mm, 10 kHz, energy density = 0.8 W cm^{-2}	N_2 and H_2	Alpha-Al_2O_3 powder as dielectric	• Ammonia with yield of 12 500 ppm (1.25%) • Energy efficiency of the ammonia synthesis found to be 1.53–1.83 g kWh^{-1}	105
	Micro-gap DBD reactor - Discharge gap of 0.47 mm and 0.64 mm	CH_4 and N_2	Alpha-Al_2O_3 powder smeared on electrodes	• Yield of ammonia is found to be 8000 ppm for the residence time of 1.6 s • Hydrogen was reported to be 9.1% (v/v)	106
	DBD reactor packed with a tubular membrane-like catalyst - atm pressure, 2.5–4.5 kV and 21.5 kHz	N_2 and H_2 (1 : 3)	Al, Ru	• No change in discharge current and power consumption	107
Expanding plasma	Expanding thermal plasma - 40 kPa in thermal arc and 20 pa in expanding section - 2–8 kV	N_2, H_2 and argon	—	• Maximum molar fraction of NH_3 is 30%, giving 33% efficiency in ammonia generation	108
Strong electric field	Strong electric field non-equilibrium plasma - 140 kV cm^{-1}, 0.12 ms, 1.2 kV ns^{-1}, 500 Hz	N_2 (0.06 m^3 h^{-1}) and H_2 (0.076 m^3 h^{-1})	MgO	• Ammonia synthesis at atmospheric pressure • Concentration of ammonia reached 5000 ppm	110

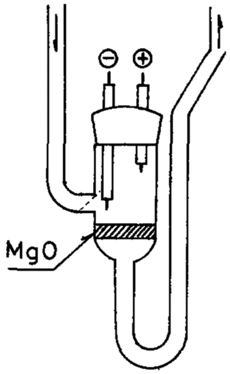

Figure 10.15 Glow discharge reactor for ammonia synthesis. Reproduced from ref. 97 with kind permission from Springer Science and Business Media.

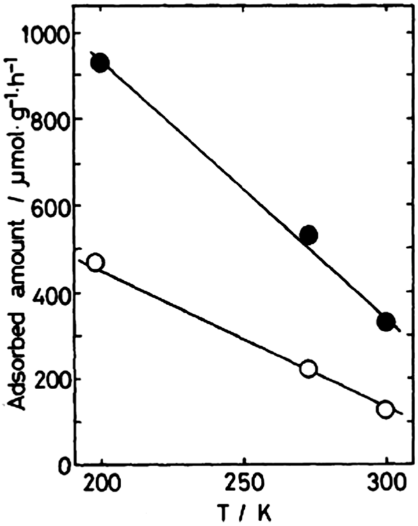

Figure 10.16 Absorbed amount of ammonia in ○ radiofrequency discharge and ● microwave discharge. Reproduced from ref. 99 with kind permission from Springer Science and Business Media.

voltage, gas temperature, and volume ratio of N_2 to H_2. The increase in power input increases the collision rate and hence density of the reactive species. 9.8 kHz was found to be the optimum frequency for ammonia synthesis. The increase in the total gas flow resulted in a decreased ammonia concentration because of the reduced residence time. The final product was mainly ammonia with yield of 12 500 ppm (1.25%). The energy efficiency of the ammonia synthesis found to be 1.53–1.83 g kWh^{-1}.

Direct use of methane as hydrogen source is also investigated for plasma ammonia synthesis. The synthesis of ammonia from CH_4 and N_2 in a micro-gap DBD reactor is reported by Bai *et al.*[106] The highest yield of ammonia is found to be 8000 ppm for the residence time of 1.6 s. This reactor configuration was also found to generate hydrogen, reported to be 9.1% (v/v). The results obtained are shown in Figure 10.17. The addition of argon into the DBD plasma reactor was found to have positive effect on the plasma ammonia synthesis, increasing the conversion of H_2 to NH_3 from 1.7% to 4.2%, making the plasma more uniform and intense.[109]

Mizushima *et al.*[107] reported the synergetic effect of plasma and catalyst for the ammonia synthesis using a *DBD reactor packed with a tubular*

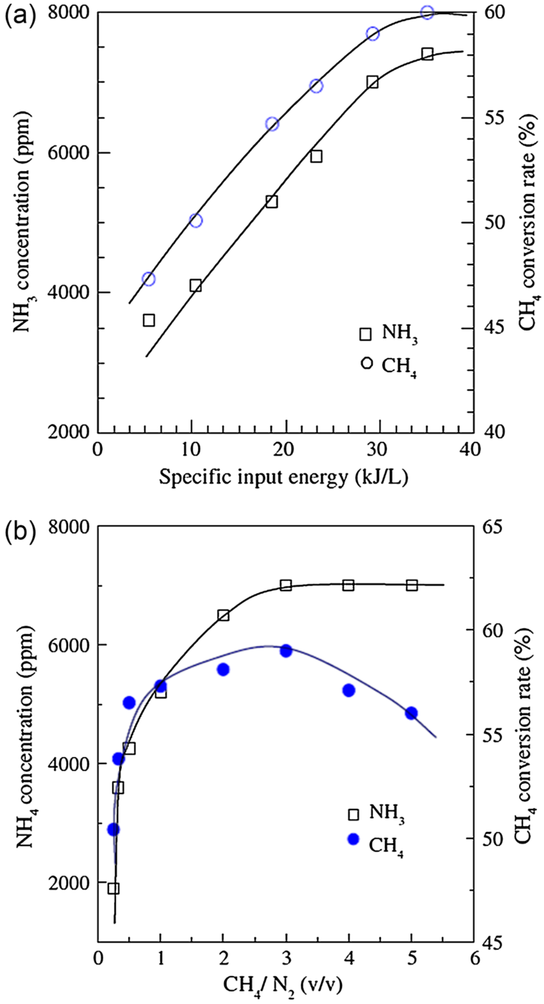

Figure 10.17 Effect of specific energy input, discharge gap, volume ratio of CH_4/N_2, residence time and gas temperature on the concentration of ammonia and conversion of CH_4. Reproduced from ref. 106 with kind permission from Springer Science and Business Media.

membrane-like catalyst, alumina and ruthenium, shown in Figure 10.18. A gas mixture of nitrogen and hydrogen was introduced in the plasma reactor which operates at ambient conditions and an applied voltage and frequency of 2.5–4.5 kV and 21.5 kHz, respectively. Increasing flow rate leads to an increase in the energy efficiency, reaching up to 5.5×10^9 mole J^{-1}, possibly because of reduced decomposition of ammonia due to short residence time in the plasma region. Interestingly, even when ammonia yield and energy efficiency trends were similar, the optimal H_2/N_2 values were found to be 3 and 5 with catalyst and without catalyst, respectively. This suggests two different mechanisms are followed for the ammonia synthesis in the presence and absence of catalyst. For this study the NH radical is found to be the precursor for NH_3 formation. As the current and energy consumption was unchanged in the reactor with a membrane then, most probably, Ru and alumina might not have acted as the plasma condition modifier, but as catalysts to promote ammonia formation.

van Helden *et al.*[108] investigated the efficiency and formation mechanism of ammonia from N_2–H_2 plasma under various plasma conditions. They used an *expanding thermal plasma* setup to investigate ammonia synthesis. In this setup, plasma production, plasma transport and plasma–surface interaction have been separated geometrically. The relation between ammonia formation and fluxes of N and H radical has been studied by investigating ammonia formation in expanding plasmas generated in the following four ways

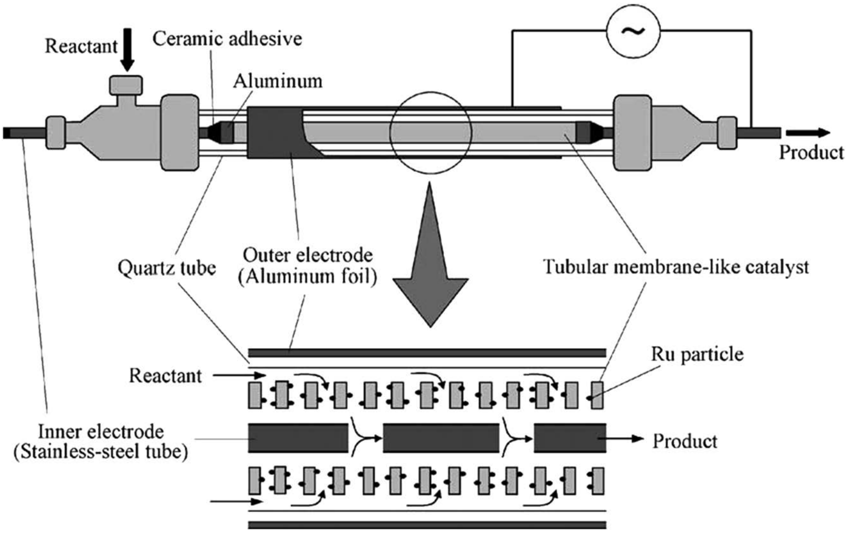

Figure 10.18 Dielectric barrier discharge reactor with a tubular membrane like catalyst. Reprinted from Applied Catalysis A: General, 265, T. Mizushima *et al.*, Tubular membrane-like catalyst for reactor with dielectric-barrier-discharge plasma and its performance in ammonia synthesis, 53–59, Copyright (2004)[107] 2004 with permission from Elsevier.

shown in Figure 10.19. This way gave a better controllability over the plasma conditions and plasma chemistry. A gas mixture is fed into a high pressure cascaded arc plasma reactor (at 40 kPa) operating at an applied voltage range of 2–8 kV. Then this plasma expands supersonically into a low pressure vessel (at 20 Pa). In comparison to the Haber–Bosch process, where N_2 dissociatively adsorbs on the catalyst surface, the N_2 and H_2 atoms are dissociated into free radicals during their passage in the plasma zone. A clear dependence of the ammonia production on the fluxes of atomic N and H radicals is seen, meaning that expanding N_2 and H_2 together gave highest ammonia density. Expanding hydrogen and adding nitrogen resulted in no ammonia formation, indicating the necessity of dissociation of both N_2 and H_2 for ammonia formation. It was also reported that the ammonia production is independent of the wall material. For a hydrogen ratio of 0.7, the maximum molar fraction of NH_3 was 30%, giving 33% efficiency in ammonia generation. The result of the study established that the ammonia is formed at the surface by plasma–surface interaction and stepwise addition reaction between adsorbed nitrogen and hydrogen radicals.[108]

Plasma ammonia synthesis with non-equilibrium plasma reactors is only scantily investigated. New non-equilibrium plasma reactors such as the gliding arc seem to offer a new possibility. Thorough understanding on the mechanism of plasma NH_3 formation still needs to be gained to efficiently develop plasma types and reactor configurations for plasma ammonia synthesis.

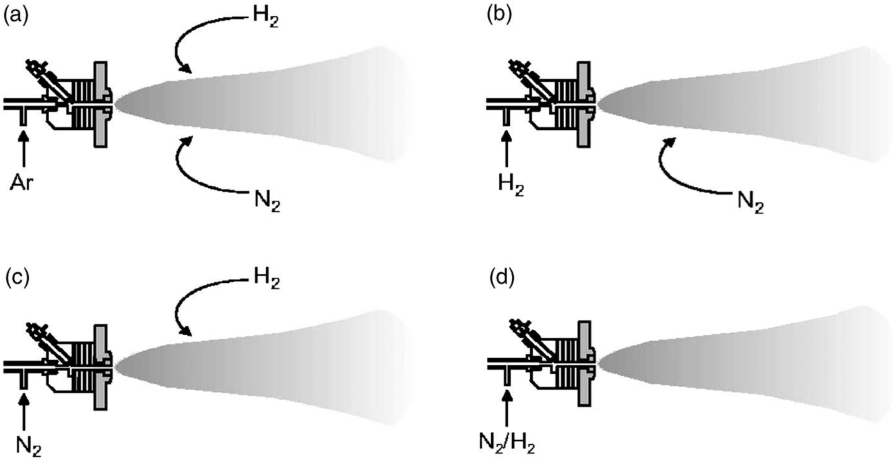

Figure 10.19 Schematic of expanding plasma cases; a. Expanding Ar to which mixture of N_2 and H_2 were added, b. Expanding H_2 plasma to which N_2 plasma were added, c. Expanding N_2 plasma to which H_2 plasma was added, d. Expanding N_2–H_2 plasma. Reprinted with permission from J. H. van Helden, W. Wagemans, G. Yagci, R. a. B. Zijlmans, D. C. Schram, R. Engeln, G. Lombardi, G. D. Stancu and J. Röpcke, *J. Appl. Phys.*, 2007, **101**, 043305.[108] Copyright 2007, AIP Publishing LLC.

10.2.2.1.2 Plasma Catalysis for Ammonia Synthesis. As can be learnt from the above section, the surface reaction of N and H is an important step in plasma ammonia synthesis. This gives motivation to investigate various types of catalytic materials in plasma reactors and one can expect that employing the right catalyst in the plasma reactor can selectively accelerate the reaction rate considerably. Various metal catalysts and their synergetic effect have been investigated and found to enhance the yield of ammonia. These studies are briefly summarized below.

Acidic oxide, basic oxide and metals have been investigated as catalysts by Sugiyama *et al.*[97] Magnesium and calcium oxides showed a catalytic effect in the ammonia synthesis when the reaction was carried out in the presence of H_2–N_2 plasma, although they are catalytically inactive in the thermal ammonia synthesis. Acidic oxides (Al_2O_3, WO_3, and SiO_2–Al_2O_3) showed no tendency to produce ammonia. The reactor arrangement used in this study is shown in Figure 10.15. It is speculated that the ammonia production process occurs at the catalyst surface. Excited nitrogen is assumed to dissociatively adsorb on the catalyst surface then later combine with hydrogen from the gas phase to form NH(a) or NH_2(a) and finally to yield ammonia.

Yin and Venugopalan investigated Pt, SS, Ag, Fe, Cu, Al and Zn (SS = stainless steel) at low pressure using a 60 Hz glow discharge. The order of catalytic activity found was Pt > SS > Ag > Fe > Cu > Al > Zn. Pt had the highest catalytic activity and electron work function[98] as shown in Figure 10.20. Iron wire was also found to have a catalytic effect on ammonia and hydrazine synthesis,[103] increasing the yield of ammonia two-fold and hydrazine by two order of magnitude. Increasing the surface area of catalyst by increasing the number of iron wires gave increased yields of the products. Hydrazine was reported to form from the reaction between adsorbed ammonia on the iron wire and NH_x radicals formed in the plasma as well as by the reaction between adsorbed

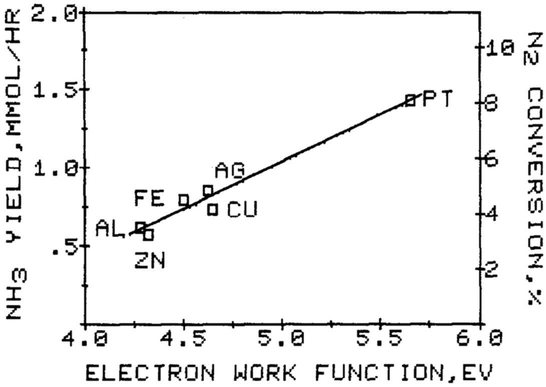

Figure 10.20 N_2 conversion and NH_3 yield as function of electron work function for the electrode material. Reproduced from ref. 98 with kind permission from Springer Science and Business Media.

NH_2 and NH_2 radicals from the plasma. Uyama *et al.* also supported a similar reaction scheme by XPS studies which concluded that the nitrogen molecule dissociatively adsorbs on the catalyst surface and forms NH_x radicals by reaction with hydrogen in the plasma which later leads to formation of NH_3 and N_2H_4. In the presence of catalyst, ammonia and hydrazine yields are reported to be considerably higher with plasma than without plasma, showing the synergy between plasma and catalyst.

Shigeyuki *et al.*[101] also investigated the synergetic effect of catalysts (iron wire and molybdenum wire) and plasmas on the synthesis of ammonia and hydrazine. Here also, iron wire gave a higher yield of ammonia than molybdenum wire. Bai *et al.*[110] used MgO as catalyst which was smeared on the electrode surface in a DBD reactor. The catalyst and micro-plasma increased the yield of ammonia by 1.54–1.75 times and the overall ammonia concentration obtained was 0.5% (v/v).

Mizushima *et al.*[111] used a plasma DBD reactor with membrane-like alumina tubes loaded with Ru, Pt, Ni and Fe. Metal loading on alumina porous tube resulted in increased ammonia yield. The sequence of catalytic activity was found to be Ru > Ni > Pt > Fe > bare alumina membrane. Two possible paths of ammonia formation were identified in a DBD reactor without catalyst: 1. Reaction in the gas phase and 2. Reaction on the surface of the reactor wall. As the rate of reaction did not increase appreciably with increasing power, because of the limited surface area, it was concluded that the surface reaction is the dominant pathway for the ammonia formation. The mechanism of ammonia formation in the presence of catalyst was also investigated and the proposed mechanism is shown in Figure 10.21. From temperature programmed desorption (TPD) studies, it was found that the N species were adsorbed on the alumina surface rather than on the active metal surface. Active metals (such as Ru) enhance the hydrogenation of adsorbed nitrogen atoms to form ammonia. It was concluded that the hydrogenation of the adsorbed nitrogen species was the rate limiting step rather than the dissociative adsorption of the nitrogen, justifying the different ammonia yields obtained for the various supporting metal particles used.

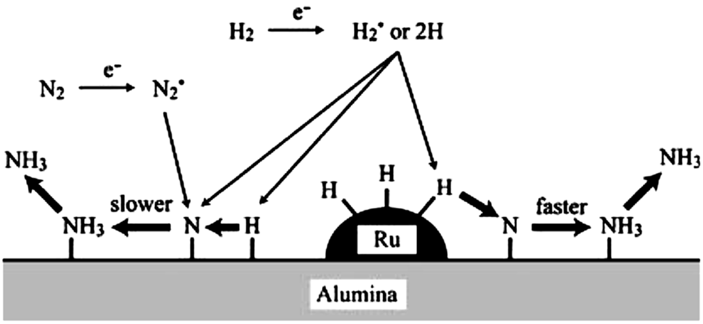

Figure 10.21 Proposed ammonia formation pathway on Ru/Alumina in N_2–H_2 plasma. Reproduced from ref. 111 with kind permission from Springer Science and Business Media.

Only a limited number of catalytically active metals and supports have been investigated for plasma ammonia synthesis. Various combinations of active metals, support and plasma discharge must be thoroughly investigated to realize a plasma ammonia synthesis competitive with the commercial nitrogen fixation process. There is still lack of information on the rate limiting steps and the important side-reactions. A comprehensive reaction modeling of the involved plasma reactions could answer these questions methodically.

10.2.2.2 Energy Requirement for Plasma Ammonia Synthesis

The energy requirement for plasma ammonia synthesis has not been at the focal point of the reported research; very few studies have emphasized the energy efficiency and energy consumption. For a DBD reactor, Bai *et al.* reported an energy consumption of 1.53–1.83 g kWh^{-1} for 6000 ppm of ammonia[106] and 36 kJ L^{-1} for 7250 ppm of ammonia produced.[106] The industrial Haber–Bosch process for ammonia synthesis demands around 30–35 GJ ton^{-1} of ammonia, depending on the hydrogen source.[20] The plasma ammonia synthesis process must have an energy consumption less than 33 GJ ton^{-1} of ammonia (0.48 MJ mol^{-1} of nitrogen).

10.2.2.3 Applications of Plasma NH_3 Synthesis

Ammonia produced by the plasma process could find applications beyond the conventional application areas, as depicted in Figure 10.2. Plasma ammonia synthesis has been investigated for the very practical and interesting applications of destruction of NO_x gases emitted by vehicles and chemical processes. The ammonia produced from air using plasma energy reacts with emitted NO_x gases on a catalyst to decompose NO_x into N_2 and H_2O.[112]

The possibility of ammonia synthesis on a smaller scale and in portable containers has been investigated for use in fertilizer production onsite, avoiding transportation and distribution problems.[113,114] The University of Minnesota successfully built the first small-scale ammonia plant running on wind energy and using air and water as feeds. The energy consumption of this plant is reported to be 60 GJ ton^{-1} NH_3, which is higher than the Haber–Bosch process. However, a new optimized plant is expected to achieve an energy consumption of 28.8 GJ ton^{-1} NH_3, lower than the Haber–Bosch process.[115] Ammonia also holds great potential to be used as a green fuel for automobiles.[116,117] Plasma ammonia production holds great potential for these applications *i.e.* for remote (localized) fertilizer production and future fuel production.

10.2.3 Hydrogen Cyanide Synthesis

10.2.3.1 Conventional Hydrogen Cyanide Processes

Hydrogen cyanide is commercially produced mainly by the Andrussow and Blausaeure–Methan–Ammoniak (BMA) processes.[118] The Andrussow process uses ammonia, methane and air as starting materials to follow an ammoxidation route while the BMA process follows the ammonia dehydrogenation route using ammonia and methane in the absence of air. The Andrussow process was developed in 1930 at IG Farben, Germany, whereas the BMA process was developed by Degussa–Huls in the 1950s. Besides these two processes, the Shawinigan process is also used to produce HCN where electricity is available cheaply, as this process needs a huge amount of electricity to supply the heat of reaction. Less conventional methods such as solid oxide fuel cell and microplant can also be used to produce hydrogen cyanide.[119] These processes have one or more disadvantages such as high operational temperature and high energy requirement, or an extended purification step requirement because of low yields.

10.2.3.2 Plasma Hydrogen Cyanide Process

Hydrogen cyanide has been successfully produced from the C and H_2 elements in nitrogen plasma with consumable graphite, which has given a conversion rate of consumable carbon of over 50%.[120] The reaction to produce HCN from its elements can be represented by reaction eqn (10.19).

$$2C + H_2 + N_2 \rightarrow 2HCN;\ \Delta H = -126\ \text{kJ mol}^{-1} \qquad (10.19)$$

Hydrogen cyanide production from nitrogen plasma with ammonia and methane has also been widely reported in the literature.[77,121–124] The following exchange reaction equations were proposed for this system[121] with the nitrogen molecule in three types of excited state: N_2^{**}- highly dissociative excited state, N_2^{*}- moderately excited state and N_2'- little excited state. The main by-product of the reaction was acetylene.[121,123]

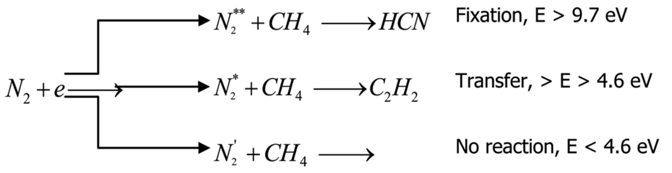

(10.20)

10.2.3.3 Kinetics and Mechanism of Plasma HCN Synthesis

The kinetics of the formation of hydrogen cyanide from methane and ammonia in microwave plasma was studied by Juul-Dam and Brockmeier at 10 to 25 torr. Conversion to HCN was found to be 9–78% for the given range of gas flow rates and microwave power. The formation of HCN followed a first order mechanism with a rate constant of 0.035 liter per watt hour.[122] Leutner investigated the formation of hydrogen cyanide from four different starting materials: from elements, from ammonia and carbon, from methane + nitrogen and from methane + ammonia and reported more than 50% conversion of the carbon source.[123]

Rapakoulias and Amouroux proposed two exchange reactions between the nitrogen and methane system, as shown in eqn (10.20). Because of the energy requirement, the fixation reaction (synthesis of HCN) was suggested to be more probable. The HCN conversion increased and acetylene conversion decreased with increase in specific energy, increase of pressure and with increase in nitrogen flow rate.[121] This study also reports a significant increase in hydrogen cyanide synthesis in the presence of a metallic grid in the following order Mo > W > Ta > Fe > Cu, as shown in Figure 10.22. The reaction mechanism proposed by Rapakoulias and Amouroux[121] for the plasma hydrogen cyanide synthesis is shown in Figure 10.23.

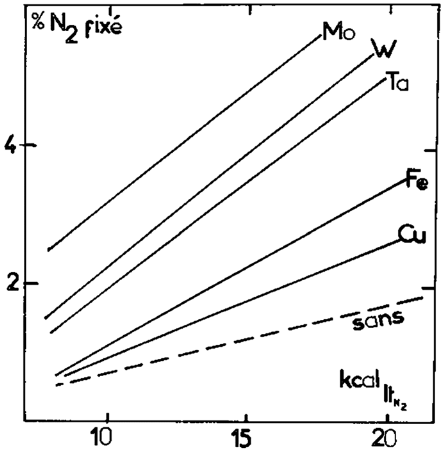

Figure 10.22 Rate of nitrogen fixation (%$N_{fixé}$) for the nitrogen-methane plasma reactions in presence of different metallic grids as a function of energy input (kJ L^{-1}). (Reproduced from ref. 121 with kind permission of EDP sciences.)

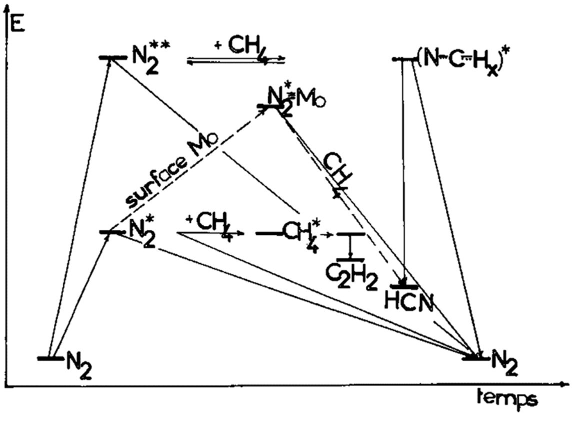

Figure 10.23 Reaction mechanism proposed for the hydrogen cyanide synthesis from methane and nitrogen. Excited states: ** highly dissociative excited state and * moderately excited state. (Reproduced from ref. 121 with kind permission of EDP sciences.)

Amouroux and Rapakoulias identified two regions of operation for HCN synthesis from N_2–CH_4; one corresponding to the HCN synthesis (from 1700 K to 2700 K) and another region corresponding to the C_2H_2 synthesis (1000 K to 2100 K).[125] For plasma HCN formation in non-equilibrium nitrogen plasma, the following two crucial steps could be distinguished: an endothermic step associated with decomposition of reactants and the exothermic step of reaction product quenching.[126] Freeman and Mentzer found increased HCN formation when diluted with argon and it had second order dependency on the plasma composition.[124]

10.3 Conclusions and Outlook

Plasma assisted nitrogen fixation reactions have been investigated extensively over the last century. Plasma nitric oxide synthesis was commercialized as early as in 1903, however it was eventually abandoned because of its poor energy efficiency using a thermal plasma. Theoretically, the energy consumption of nitrogen fixation by non-thermal plasma can be lower than the Haber–Bosch process because the most energy-effective mechanism for plasma chemical NO synthesis is provided by the vibrational excitation of molecules in a non-thermal plasma. Since that time many efforts have been made to improve the plasma NO, NH_3 and HCN syntheses; these included investigation of the different types of plasma reactor, synergy between plasma and catalyst as well as the improvement of the heat exchange. Gliding arc, microwave and nano pulse plasma reactors with combination of catalysts could afford the potential candidate to make plasma nitrogen fixation processes energy efficient. For this, it is a prerequisite to understand the fundamental effects of plasma on the catalyst and *vice versa*. The synergy mechanism between plasma and catalyst is essential for better reactor design and scaling-up. Despite the plasma ozone production process having been commercialized, the knowledge necessary for the scale-up of plasma processes is relatively underdeveloped. The atmospheric pressure plasma reactors which have the potential for industrial application demand further research in order to precisely control the EEDF of the plasma to the benefit of vibrational excitation of nitrogen, which is one of the essential ways for improving the energy efficiency.

The most energy-consuming step in a complete Haber–Bosch process from hydrogen production to ammonia is actually the step of methane reforming for hydrogen production. The discussion in this chapter has been of work being carried out on plasma reaction/reactors without considering the energy consumption for raw chemicals supply and separation steps following the reaction. For NO_x synthesis by plasma, air can be the direct feeding gas only if no larger proportion of oxygen is needed. Energy consumption on air separation therefore needs to be considered. For NH_3 synthesis, the operation condition is totally changed from high pressure and high temperature in the Haber–Bosch process to low pressure and low temperature in a plasma process, which will significantly influence the purification steps which follow.

This requires a detailed process simulation and evaluation (in the sense of economic and ecological effect) in order to fairly assess the whole process and benchmark compared to the existing Haber–Bosch process.

The last century witnessed enormous advancement in technologies for renewable energy production and its distribution. Solar and wind energy production have taken center stage among all renewable energies. Recently, the concept of containerized plant and de-centralized chemicals production has been gaining an acceptance in chemical industry. The research fields of plasma and catalysis have gained a higher understanding of the basic phenomena. These recent advances and the urge to form interdisciplinary collaborations have brought a new paradigm for plasma processes. It is necessary to combine renewable energy sources to compensate the high energy demand of the plasma processes. It is interesting from a sustainability viewpoint to employ renewable energy or a mixture of conventional and renewable energies with plasma processes. Plasma processes are more attractive on a smaller scale, such as the container/modular plant scale, to decentralize chemical production and bring benefit to remote places. This paradigm shift towards preference for localized chemicals production and the changing scenario of renewable electricity cost would give a new boost to plasma-assisted nitrogen fixation processes and the use of plasma as an alternative energy source for chemicals production. Consideration of the usage of renewable energy in process design will definitely change the environmental profile of plasma processes towards being greener. The decreasing price of renewable electricity in the future will enable plasma nitrogen fixation to become an economic process.

Acknowledgements

This research is kindly funded by the EU project MAPSYN: Microwave, Acoustic and Plasma SYNtheses, under grant agreement no. CP-IP 309376 of the European Community's Seventh Framework Program. This chapter was adapted from B.S. Patil, Q. Wang, V. Hessel, J. Lang Plasma N_2-Fixation: 1900–2014, 256(1) 2015, 49–66, Copyright @2015, with kind permission from Elsevier B.V.

References

1. UNEP and WHRC, *Reactive Nitrogen in the Environment: Too Much or Too Little of a Good Thing*, United Nations Environment Programme, Paris, 2007.
2. V. Smil, *Ambio*, 2002, **31**, 126–131.
3. C. P. Chanway, R. Anand and H. Yang, in *Advances in Biology and Ecology of Nitrogen Fixation*, ed. T. Ohyama, InTech, 2014, pp. 3–21.
4. D. F. Bezdicek and A. C. Kennedy, *Microorganisms in Action*, Blackwell Scientific Publications, 1998.

5. D. E. Canfield, A. N. Glazer and P. G. Falkowski, *Science*, 2010, **330**, 192–196.
6. I. L. Pepper, C. P. Gerba and T. J. Gentry, *Environmental Microbiology*, 3rd edn, 2015.
7. J. W. Erisman, M. A. Sutton, J. Galloway, Z. Klimont and W. Winiwarter, *Nat. Geosci.*, 2008, **1**, 636–639.
8. J. N. Galloway, *Environ. Pollut.*, 1998, **102**, 15–24.
9. V. Smil, *Enriching the Earth: Fritz Haber, Carl Bosch, and the Transformation of World Food Production*, MIT Press, 2004.
10. G. R. Maxwell, *Synthetic Nitrogen Products–A Practical Guide to the Products and Processes*, Kluwer Academic Publishers, New York, 2004.
11. J. N. Galloway and E. B. Cowling, *Ambio*, 2002, **31**, 64–71.
12. B. S. Patil, Q. Wang, V. Hessel and J. Lang, *Catal. Today*, 2015, **256**, 49–66.
13. J. M. Modak, *Resonance*, 2002, 69–77.
14. F. A. Ernst, *Fixation of Atmospheric Nitrogen*, Industrial Chemical Monographs, Chapman and Hall Ltd, 1928.
15. Ammonia Timeline: The Early Years, *Chem. Eng. Prog.*, 2005, 57–62.
16. R. E. Krebs, *The History and Use of Our Earth's Chemical Elements: A Reference Guide*, Greenwood Press, Westport, 2006.
17. A. Egeland and W. J. Burke, *Kristian Birkeland*, Springer, Netherlands, 2005, vol. 325, pp. 109–130.
18. K. R. Birkeland, *Trans. Faraday Soc.*, 1906, **2**, 98–116.
19. A. S. Travis, *The Synthetic Nitrogen Industry in World War I: its Emergence and Expansion*, Springer, Fargo, North Dakota, USA, 2015.
20. M. Appl, *Ullmann's Encycl. Ind. Chem.*, 2012, 139–225.
21. M. Appl, *50th Anniversary of the IFA Technical Conference*, 1997, p. 25.
22. G. J. Leigh, *Nitrogen Fixation at the Millennium*, Elsevier Science, 2002.
23. International Energy Agency-IEA, *Technology Roadmap: Energy and GHG Reductions in the Chemical Industry via Catalytic Processes*, 2013.
24. R. R. Schrock, *Proc. Natl. Acad. Sci. U. S. A.*, 2006, **103**, 17087.
25. E. Cowling, J. Galloway, C. Furiness, M. Barber, T. Bresser, K. Cassman, J. W. Erisman, R. Haeuber, R. Howarth, J. Melillo, W. Moomaw, A. Mosier, K. Sanders, S. Seitzinger, S. Smeulders, R. Socolow, D. Walters, F. West and Z. Zhu, *Sci. World J.*, 2001, **1**, 1–9.
26. N. Cherkasov, A. O. Ibhadon and P. Fitzpatrick, *Chem. Eng. Process.*, 2015, **90**, 24–33.
27. S. Samukawa, M. Hori, S. Rauf, K. Tachibana, P. Bruggeman, G. Kroesen, J. C. Whitehead, A. B. Murphy, A. F. Gutsol, S. Starikovskaia, U. Kortshagen, J.-P. Boeuf, T. J. Sommerer, M. J. Kushner, U. Czarnetzki and N. Mason, *J. Phys. D: Appl. Phys.*, 2012, **45**, 253001.
28. Creative Energy, *European Roadmap for Process Intensification*, 2008.
29. A. Fridman, *Plasma Chemistry*, Cambridge University Press, New York, 2008.
30. M. A. Lieberman and A. J. Lichtenberg, *Principles of Plasma Discharges and Materials Processing*, Wiley, 2005.
31. P. Fauchais and J. Rakowitz, *J. Phys.*, 1979, **40**, C7-289–C7-312.
32. S. L. Miller, *Science*, 1953, **117**, 528–529.

33. S. L. Miller and H. C. Urey, *Science*, 1959, **130**, 245–251.
34. R. Hippler, *Low Temperature Plasma Physics: Fundamental Aspects and Applications*, Wiley-VCH, 2001.
35. A. P. Napartovich, *Plasmas Polym.*, 2001, **6**, 1–14.
36. *Nonthermal Plasma Chemistry and Physics*, ed. J. Meichsner, M. Schmidt, R. Schneider and H.-E. Wagner, 2013.
37. V. Hessel, G. Cravotto, P. Fitzpatrick, B. S. Patil, J. Lang and W. Bonrath, *Chem. Eng. Process.*, 2013, **71**, 19–30.
38. V. Hessel, a. Anastasopoulou, Q. Wang, G. Kolb and J. Lang, *Catal. Today*, 2013, **211**, 9–28.
39. M. Thiemann, E. Scheibler and K. W. Wiegand, *Ullmann's Encyclopedia of Industrial Chemistry*, Wiley-VCH Verlag GmbH & Co. KGaA, 2000.
40. D. C. Frost and C. A. MCDowell, *Proceedings of the Royal Society of London. Series a, Mathematical and Physical Sciences*, 1956, vol. 236, pp. 278–284.
41. F. Coudert J, Universitt de Limoges, 1978.
42. P. R. Ammann and R. S. Timmins, *AIChE J.*, 1966, **12**, 956–963.
43. V. Smil, *Sci. Am.*, 1997, **76**, 76–81.
44. VIVEX Engineeirng Ltd., 2014.
45. D. Rapakoulias, S. Cavadias and J. Amouroux, *Rev. Phys. Appl.*, 1980, **15**, 1261–1265.
46. J. Amouroux, S. Cavadias, D. Rapakoulias and J. Amouroux, *Rev. Phys. Appl.*, 1979, **14**, 961–968.
47. S. Cavadias and J. Amouroux, *Bull. Soc. Chim. Fr.*, 1986, **2**, 147–158.
48. I. Pollo, K. Hoffmann-Fedenczuk and L. Fedenczuk, in *Int. Symp. Plasma Chem.*, ed. B. Waldie and G. A. Farnell, 1981, vol. 2, pp. 756–760.
49. I. Pollo and S. Banasik, *Chem. Plazmy*, 1978, 259–270.
50. J. Krop and I. Pollo, *Chemia*, 1981, **678**, 51–59.
51. J. Krop and I. Pollo, *Chemia*, 1980, **633**, 25–33.
52. J. Krop, E. Krop and I. Pollo, *Chem. Plazmy*, 1979, 242–249.
53. T. Namihira, S. Tsukamoto, D. Wang, S. Katsuki, H. Akiyama, R. Hackam and K. Okamoto, *12th IEEE Int. Pulsed Power Conf. (Cat. No.99CH36358)*, 1999, vol. 2, pp. 1313–1316.
54. T. Namihira, S. Katsuki, R. Hackam, H. Akiyama and K. Okamoto, *IEEE Trans. Plasma Sci.*, 2002, **30**, 1993–1998.
55. B. Mutel, O. Dessaux and P. Goudmand, *Rev. Phys. Appl.*, 1984, **19**, 461–464.
56. I. Pollo and S. Banasik, *Chemia*, 1979, **631**, 377–378.
57. R. Ingels, WO 2012/150865 A1, 2012.
58. C. P. Bequin, J. B. Ezell, A. Salvemini, J. C. Thompson, D. G. Vickory and J. L. Margrave, *The Application of Plasma to Chemical Synthesis*, MIT Press, Cambridge, Massachussetts, 1967.
59. M. J. LaRoche, *La Chimie des hautes temperatures*, CNRS, Paris, 1955.
60. K. Jackson and M. S. Bloom, BP 915771, 1963.
61. W. S. Partridge, R. B. Parlin and B. J. Zwolinski, *Ind. Eng. Chem.*, 1954, **46**, 1468–1471.

62. A. V. Grosse, C. S. Stokes, J. A. Cahill and J. J. Correa, *Final Annual Report*, Philadelphia, Pennsylvania, 1961.
63. R. Timmins and P. Amman, *Plasma Applications in Chemical Processes*, Mir (World), Moscow, 1970.
64. J. F. Coudert, J. M. Baronnet, J. Rakowitz and P. Fauchais, *Symp. Int. Chim. Plasmas*, 1977, 1.
65. J. M. Baronnet, J. F. Coudert, J. Rakowitz, E. Bourdin and P. Fauchais, *Nitrogen Oxides Synthesis in a D.C. Plasma Jet*, Zurich, 1979.
66. M. Rahman and V. Cooray, *Opt. Laser Technol.*, 2003, **35**, 543–546.
67. R. W. Conrad, US 4167463, 1979.
68. L. S. Polak, A. A. Ovsiannikov, D. I. Slovetsky and F. B. Vurzel, *Theoretical and Applied Plasma Chemistry*, Nauka (Science), Moscow, 1975.
69. H. Matsuuchi, US8425852, 2013.
70. R. I. Asisov, V. K. Givotov, V. D. Rusanov and A. Fridman, *Sov. Phys.*, 1980, **14**, 366.
71. V. M. Belova, E. N. Eremin and A. N. Maltsev, *Russ. J. Phys. Chem.*, 1978, **52**, 968–970.
72. Q. Sun, A. Zhu, X. Yang, J. Niu and Y. Xu, *Chem. Commun. (Cambridge, U. K.)*, 2003, **5**, 1418–1419.
73. A. V. Grosse and E. W. Smith, US 3666408 A, 1972.
74. H. L. Chen, US4399012, 1981.
75. L. F. A. Diaz, MX2008 n013634A, 2008.
76. Y. Uchida, K. Takaki and K. Urashima, *IEEE Trans. Dielectr. Electr. Insul.*, 2004, **11**, 291–297.
77. J. Amouroux and D. Rapakoulias, in *3rd Commun. Symp. Int. Chim. Plasmas*, ed. P. Fauchais, 1977, vol. 1.
78. J. Amouroux, D. Rapakoulias and S. Cavadias, CH 645321 A5, 1984.
79. L. R. O'Hare, US 4833293, 1989.
80. H. Sekiguchi, A. Kanzawa and T. Honda, *Plasma Chem. Plasma Process.*, 1989, **9**, 257–275.
81. M. A. Malik, C. Jiang, R. Heller, J. Lane, D. Hughes and K. H. Schoenbach, *Chem. Eng. J.*, 2016, **283**, 631–638.
82. B. S. Patil, J. Rovira Palau, V. Hessel, J. Lang and Q. Wang, *Plasma Chem. Plasma Process.*, 2016, **36**, 241–257.
83. J. Amouroux and S. Cavadias, US 4469509, 1984.
84. L. R. O'Hare, US 4451436, 1984.
85. L. R. O'Hare, US 4877589, 1989.
86. A. Gicquel, S. Cavaidas and J. Amouroux, *J. Phys. D: Appl. Phys.*, 1986, **19**, 2013–2042.
87. M. Alamaro, US4287040, 1981.
88. S. O. Macheret, V. D. Rusanov, A. A. Fridman and G. V Sholin, *Pis'ma Zh. Tekh. Fiz.*, 1978, **4**, 346–351.
89. E. D. Mccollum and F. Daniels, *Ind. Eng. Chem.*, 1923, **15**, 1173–1175.
90. L. S. Polak and V. S. Shchipachev, *Kinetics and Thermodynamics of Chemical Reactions in Low Temperature Plasma*, Nauka (Science), Moscow, 1965.

91. R. Ingels, D. Graves, S. Anderson and R. Koller, *International Fertiliser Society*, International Fertiliser Society, London, UK, 2015, pp. 1–27.
92. R. Castor and T. Hammer, US 6955790, 2005.
93. X. Wang, Q. Yang, C. Yao, X. Zhang and C. Sun, *Energies*, 2011, **4**, 2133–2150.
94. W. Bian, X. Song, J. Shi and X. Yin, *J. Electrostat.*, 2012, **70**, 317–326.
95. Y. Wang, A. W. DeSilva, G. C. Goldenbaum and R. R. Dickerson, *J. Geophys. Res.*, 1998, **103**, 19149–19159.
96. D. Nna Mvondo, R. Navarro-Gonzalez, C. P. P. McKay, P. Coll and F. Raulin, *Adv. Space Res.*, 2001, **27**, 217–223.
97. K. Sugiyama, K. Akazawa, M. Oshima, H. Miura, T. Matsuda and O. Nomura, *Plasma Chem. Plasma Process.*, 1986, **6**, 179–193.
98. K. S. Yin and M. Venugopalan, *Plasma Chem. Plasma Process.*, 1983, **3**, 343–350.
99. H. Uyama and O. Matsumoto, *Plasma Chem. Plasma Process.*, 1989, **9**, 13–24.
100. H. Uyama and O. Matsumoto, *Plasma Chem. Plasma Process.*, 1989, **9**, 421–432.
101. S. Tanaka, H. Uyama, O. Matsumoto and O. Matsumoto, *Plasma Chem. Plasma Process.*, 1994, **14**, 491–504.
102. J. Nakajima and H. Sekiguchi, *Thin Solid Films*, 2008, **516**, 4446–4451.
103. H. Uyama, T. Nakamura, S. Tanaka and O. Matsumoto, *Plasma Chem. Plasma Process.*, 1993, **13**, 117–131.
104. H. Kiyooka, O. Matsumoto and O. Matsumoto, *Plasma Chem. Plasma Process.*, 1996, **16**, 547–562.
105. M. Bai, Z. Zhang, X. Bai, M. Bai and W. Ning, *IEEE Trans. Plasma Sci.*, 2003, **31**, 1285–1291.
106. M. Bai, Z. Zhang, M. Bai, X. Bai and H. Gao, *Plasma Chem. Plasma Process.*, 2008, **28**, 405–414.
107. T. Mizushima, K. Matsumoto, J. Sugoh, H. Ohkita and N. Kakuta, *Appl. Catal., A*, 2004, **265**, 53–59.
108. J. H. van Helden, W. Wagemans, G. Yagci, R. a. B. Zijlmans, D. C. Schram, R. Engeln, G. Lombardi, G. D. Stancu and J. Röpcke, *J. Appl. Phys.*, 2007, **101**, 043305.
109. J. Hong, S. Prawer and A. B. Murphy, *IEEE Trans. Plasma Sci.*, 2014, 42, 2338–2339.
110. B. Mingdong, B. Xiyao and Z. Zhitao, *Plasma Chem. Plasma Process.*, 2000, **20**, 511–520.
111. T. Mizushima, K. Matsumoto, H. Ohkita and N. Kakuta, *Plasma Chem. Plasma Process.*, 2006, **27**, 1–11.
112. J. Gieshoff and J. Lang, US 6471932, 2002.
113. M. Reese, *Wind to Ammonia: An Update Presenter Overview*, 2007.
114. M. Reese, *Lessons Learned in Developing a Wind to Ammonia Pilot Plant Why Home Grown Energy?*, 2012.
115. D. G. Tiffany, *Wind to Ammonia Project Update Today's Talk*, 2011.
116. W. Avery, *Int. J. Hydrogen Energy*, 1988, **13**, 761–773.

117. E. Morgan, J. Manwell and J. McGowan, *Renewable Energy*, 2014, **72**, 51–61.
118. E. Gail, S. Gos, R. Kulzer, J. Lorosch, A. Rubo, M. Sauer, R. Kellens, J. Reddy, N. Steier and W. Hasenpusch, *W. Ullmann's Encyclopedia of Industrial Chemistry*, 2012, pp. 673–710.
119. N. Kiratzis and M. Stoukides, *J. Electrochem. Soc.*, 1987, **134**, 1925–1929.
120. V. J. Ibberson, M. W. Thring and P. Chemical, *Ind. Eng. Chem.*, 1969, **61**, 48–61.
121. D. Rapakoulias and J. Amouroux, *Rev. Phys. Appl.*, 1980, **15**, 1251–1259.
122. T. Juul-Dam and N. F. Brockmeier, *Ind. Eng. Chem. Prod. Res. Dev.*, 1970, **9**, 388–397.
123. H. W. Leutner, *Ind. Eng. Chem. Process Des. Dev.*, 1963, **2**, 315–318.
124. M. P. Freeman and C. C. Mentzer, *Ind. Eng. Chem. Process Des. Dev.*, 1970, **9**, 39–42.
125. J. Amouroux and D. Rapakoulias, *Rev. Phys. Appl.*, 1977, **12**, 1013–1021.
126. D. Rapakoulias and J. Amouroux, *Rev. Phys. Appl.*, 1979, **14**, 961–968.
127. A. M. Alekseev, V. M. Atamanov, E. M. Erastov, A. A. Ivanov, S. I. Krasheninnikov, G. B. Levadnii, Y. F. Nasedkin, V. A. Nikiforov and Y. M. Pustovoit, *Int. Symp. Plasma Chem.*, 1979, **2**, 427–432.
128. A. K. Vakar, V. P. Denisenko and V. D. Rusanov, *3rd Int. Symposium on Plasma Chemistry (ISPC-3)*, Limoge, France, 1977, p. 10.
129. T. Kappes, W. Schiene and T. Hammer, *Energy balance of a dielectric barrier discharge for hydrocarbon steam reforming*, vol. 1 and 2, HAKONE 8: International Symposium on High Pressure, Low Temperature Plasma Chemistry Proceedings, 2002.

CHAPTER 11

Higee Technologies and Their Applications to Green Intensified Processing

KAMELIA V. K. BOODHOO

School of Chemical Engineering and Advanced Materials,
Newcastle University, Newcastle upon Tyne, NE1 7RU, UK
*E-mail: kamelia.boodhoo@ncl.ac.uk

11.1 Introduction

In recent years, centrifugal field or Higee technologies have gained much prominence, notably as promising examples of process intensification technologies. As such, they are also regarded as having the potential to deliver green chemical processing by virtue of their ability to achieve waste minimisation at source primarily by enhancing process selectivities, thereby reducing by-product formation and using less raw material and by enabling the use of minimal amounts of solvent.

The basic operating principle of centrifugal field technologies relies on the application to processing fluids of large forces created on a rotating surface or in an enclosed volume. Depending on the rate of rotation, forces as high as 1000 g can be imposed on fluids, resulting in the flow of thin films of the order of 50–500 microns[1,2] or small droplets[3] which have been shown to give significant processing advantages. For instance, very short, controllable

RSC Green Chemistry No. 47
Alternative Energy Sources for Green Chemistry
Edited by Georgios Stefanidis and Andrzej Stankiewicz

Published by the Royal Society of Chemistry, www.rsc.org

residence times, of the order of seconds, near ideal plug flow behaviour, enhanced heat and mass transfer due to the extremely short path lengths and high surface area per unit volume (as highlighted in Figure 11.1) are all characteristic features offered by thin film flow hydrodynamics.[4] It is particularly noteworthy that these features can be achieved not only in laboratory scale equipment but also in scaled-up designs of these centrifugal technologies,[1] which is a clear benefit when compared to conventional stirred tank technologies.

A number of configurations currently exist for continuous flow technologies based on centrifugal field environments. Those that have gained much attention in recent years include the spinning disc reactor (SDR) and the rotating packed bed (RPB). These technologies, in particular their design features, operating principles, unique characteristics and examples of their applications to green chemical processing, are the focus of this chapter. Variants of these systems which have emerged in recent years will also be highlighted.

11.2 Spinning Disc Reactor (SDR)

11.2.1 Design and Operating Principles

A typical SDR consists of a horizontal disc surface which may be smooth or may include turbulence-inducing structures such as concentric or spiral grooves. On rotation of this surface, the imposed centrifugal force causes liquids fed to the spinning surface to flow in the form of highly sheared thin films with numerous surface ripples, as depicted in Figure 11.2. These hydrodynamic characteristics are associated with turbulence-inducing fluid dynamics which is responsible for excellent mixing and heat and mass transfer characteristics prevailing in the flowing films.

Figure 11.3 shows a schematic diagram of the SDR with provision for internal heat transfer fluid circulation. The process liquid feeds are pumped through the inlet tubes normally positioned at the centre of the disc and

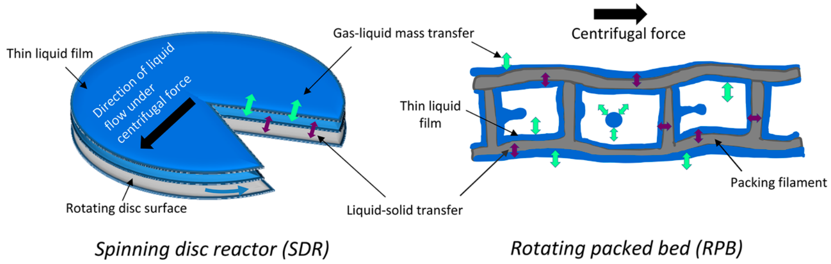

Spinning disc reactor (SDR)

Rotating packed bed (RPB)

Figure 11.1 Thin film processing in spinning disc reactor and rotating packed bed, illustrating the short diffusion/conduction path lengths and high surface area for heat/mass transfer. (Reprinted from ref. 4 ©2013 John Wiley & Sons.)

Figure 11.2 Thin, wavy film flow on a rotating disc. (Reprinted from ref. 1 ©2013 John Wiley & Sons.)

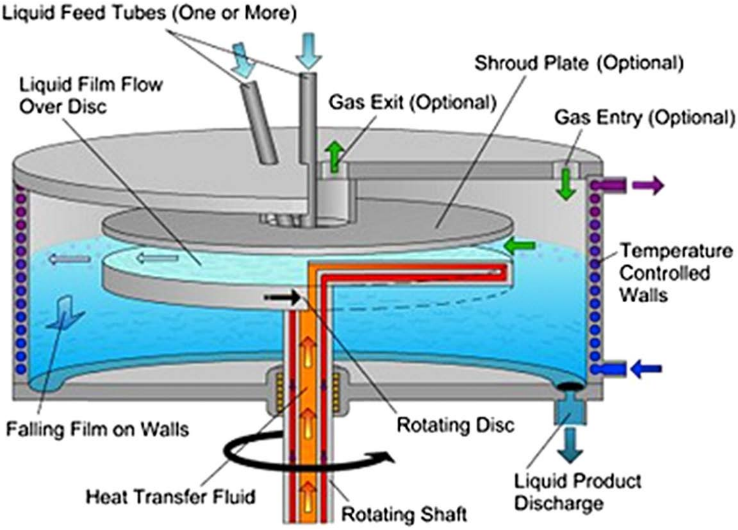

Figure 11.3 Schematic of a spinning disc reactor with internal heat transfer. (Reprinted from ref. 5 ©2005 with permission from IChemE Publications.)

onto the surface of the spinning disc below. Depending on the application the feeds may also be located at different radial positions across the disc. Disc rotation is driven by an electrical motor through a shaft, the speed of which can be controlled typically between 300 rpm and 4000 rpm. Disc diameters usually vary between 0.1 m for laboratory scale equipment and 1.0 m for pilot/industrial scale equipment. After impacting the surface of the disc the liquid feeds are forced outward by the centrifugal force creating a very highly sheared thin film. Film thicknesses on a fully wetted surface in the SDR typically range from 50 μm to 500 μm. Once the liquid reaches the edge of the disc it is flung onto the temperature controlled stationary walls of the reactor. The liquid is discharged from the reactor through an outlet at the base of the stationary housing enclosing the rotating element. The lid of the reactor can be configured for the insertion of several liquid feed streams at different radial positions to enable different reaction zones on a given disc. Similar considerations can be extended to optional gas inlets/outlets to accommodate gas–liquid processing. Provision for purging the system with an inert gas can also be incorporated in the reactor setup.

Depending on the heat transfer fluid used, the operating temperature of a spinning disc can be set at between −20 °C and 300 °C, or even higher if radiant heaters are used instead of a heat transfer fluid. Appropriate seals between the rotating shaft and the stationary housing can also allow operation under vacuum or at pressures of up to 10–20 bars. The overall heat transfer coefficient in a spinning disc reactor with internal heat transfer capability can be as high as 10 kW m^{-2} K^{-1},[3,6,7] which is up to 10× higher than that obtained in other heat transfer devices. This, combined with the large surface area per unit volume offered by the thin films (typically of the order of 20 000 m^2 m^{-3}), allows a small spinning disc to handle very large thermal duties for tight control of highly exothermic reactions. Recent studies using a thermal imaging camera for a visual representation of the temperature profiles of a thin film across a rotating disc surface clearly highlight the beneficial effect of operating at high disc rotational speeds of 2000 rpm for rapid heating of a film flowing across a spinning disc (Figure 11.4).

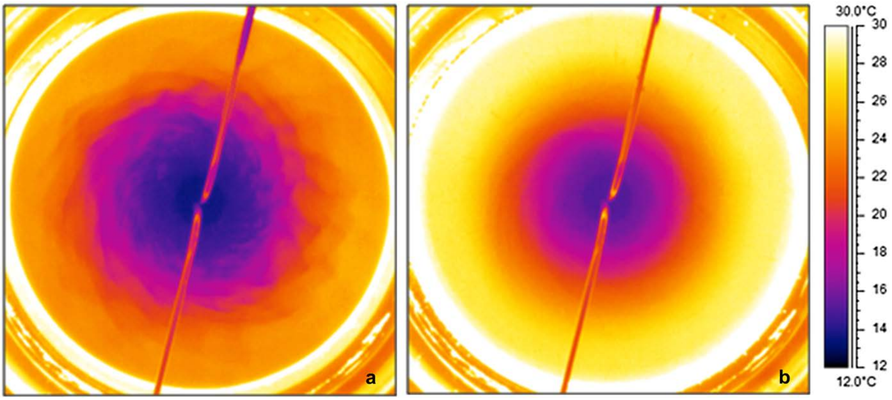

Figure 11.4 Thermograms for thin film flow in SDR (Q = 10 mL s^{-1}, working fluid: water) (a) N = 500 rpm (b) N = 2000 rpm. (Reprinted from Applied Thermal Engineering, 44, D. Ghiasy *et al.*, Thermographic analysis of thin liquid films on a rotating disc: Approach and challenges, 39–49, Copyright (2012) with permission from Elsevier.[8])

11.2.2 Green Processing Applications of SDR

Processes that are ideally suited for SDR application involve those that are kinetically fast (half-lives typically of less than a minute), highly exothermic and involve competitive reaction steps. With such characteristics, these processes could benefit from the following SDR features: (1) the rapid micromixing in the intense fluid dynamics environment[9] (with micromixing time τ_m of the order of milliseconds[10,11]) to enable the reaction to proceed at its inherently fast rate, (2) the excellent heat transfer capabilities to enable the reaction to be performed under controlled, isothermal conditions for product yield optimisation, (3) the plug flow conditions in the thin films[12] to suppress by-product formation or further reaction downstream of the desired product and (4) the very short residence time to prevent product degradation at high reaction temperatures *etc.* for excessive time periods. Typical reactions include polymerisations, crystallisations or precipitations and food processes.

A comprehensive review of SDR processing related to green chemistry applications has recently been compiled.[1] Selected examples of relevance are included within the present chapter alongside more recently published work involving, for instance, enzymatic transformations.

11.2.2.1 Polymerisations

Greener processing of polymerisations in SDRs is made possible through minimal solvent use. Solvents are typically used in conventional large scale polymerisation reactions to dilute the concentrations of monomer and polymer in order to have a more controllable process in terms of its exothermicity, viscosity, *etc.* In the SDR however, the thin film's hydrodynamics enables the process to be safely controlled even at high monomer concentrations (as in the cationic polymerisation of styrene catalysed by a silica-supported BF_3 Lewis acid catalyst[6]) or even with neat monomer (*e.g.* photo-polymerisation of *n*-butyl acrylate[13]). The enhanced properties of the polymer product from the SDR (*e.g.* molecular weight M_r, polydispersity index PDI) compared to processing under conventional conditions (as highlighted in Table 11.1 below) represent an added distinct advantage for performing these polymerisations in the thin film environment of the SDR system.

The use of UV light as an alternative form of energy for initiating polymerisation reactions or any other types of photo-reactions on a spinning disc opens up another interesting avenue for 'greening' such processes. In general, with a brief but intense UV illumination even under ambient temperature conditions, a large amount of free radicals can be formed from a photo-sensitive compound leading to fast reactions as well as a clean process as it generally does not involve any solvent.[14] However, despite these advantages, photo-initiated reactions are rather limited in conventional engineering equipment with large bulk volumes by the process inefficiency resulting from the very short penetration depth of the UV radiation, typically a few centimetres at the most. The opportunity offered to such photo-induced

Table 11.1 Cationic polymerisation in batch and SDR using 1.3 wt% BF_3 suspended in 1,2-dichloroethane (Reprinted from ref. 6 with permission from John Wiley and Sons. Copyright © 2006 Wiley Periodicals, Inc.).

Reactor type	Run no.	[St]% w/w	Reaction temp. (°C)	Residence time (s)	Conversion (%)	Ave. rate of conversion (% s^{-1})	M_r	PDI
Batch	B4[a]	49	13	1800	10	0.0056	12 032	2.0
Batch	B8[b]	49	97	60	94	1.57	4100	3.12
SDR	S14[c]	49	40	1.0	7.6	7.6	24 679	1.68
SDR	S21[c]	75	40	1.1	7.8	7.1	25 050	1.46
SDR	S26[d]	75	40	0.9	9.5	10.6	14 593	1.60
SDR	S31[d]	75	20	1.0	4.1	4.1	17 045	1.73

[a] Temperature controlled at 7 °C; initial temperature of monomer = 21.5 °C.
[b] Temperature controlled at 40 °C; initial temperature of monomer = 36 °C.
[c] Disc diameter = 100 mm; disc speed = 200 rpm; flow rate = 0.7 mL s^{-1}.
[d] Disc diameter = 200 mm; disc speed = 400 rpm; flow rate = 1.5 mL s^{-1}.

processing by the formation of continuous and controllable films in the SDR of thicknesses well within the penetration depth limits of UV light represents an exciting prospect for development in this area of application. Experimental studies involving the UV-initiated photo-polymerisation of *n*-butyl acrylate (*n*-BA)[13] and, more recently, photo-copolymerisation of vinyl acetate with *n*-butyl acrylate (VAc-BA)[15] demonstrate the potential of the SDR technology for this particular type of application.

For the *n*-BA photo-polymerisation, the rate of photo-polymerisation in the SDR was observed to be extremely high, with conversions in excess of 90% obtained within a residence time of approximately 2 s and upon exposure to a moderate UV intensity of 25 mW cm^{-2} (Figure 11.5). The highly-sheared, well-mixed film in the SDR generally outperforms photo-polymerisation in a thin static film of comparable thickness, both in terms of the rate of polymerization and the polymer properties.[13] The rapid mixing and good temperature control maintained in the thin film on the rotating disc enable a faster and more controllable polymerization to occur than is possible in a static film of comparable film thickness.

The photo-copolymerisation of VAc-BA showed similar beneficial effects of SDR processing (Figure 11.6). A conversion of 37% was achieved in one disc pass, corresponding to a residence time of about 5 s, a UV intensity of 106 mW cm^{-2} and an initiator concentration of 5% (w/w). Comparable levels of conversion could be obtained in a static film but only after longer residence times under otherwise identical operating conditions. The overall monomer conversion in the SDR is influenced by the UV exposure time and the extent of light absorption during the exposure time which in turn influences the initiator decomposition efficiency on the disc surface. It is shown that the largest amount of light is absorbed in one disc pass under hydrodynamic conditions in the SDR that gives rise to longest UV exposure times, which also correspond to highest overall conversions achieved. Higher UV intensities and higher initial photo-initiator concentration are also beneficial in this

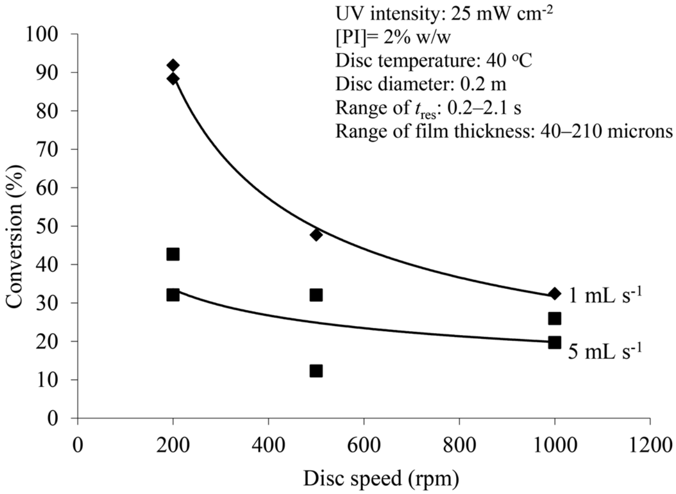

Figure 11.5 Photo-polymerisation of *n*-butyl acrylate in the SDR. (Reprinted with permission from K. V. K. Boodhoo, W. A. E. Dunk, and R. J. Jachuck, *Advances in Photoinitiated Polymerisations*, ed. K. Belfield and J. Crivello, American Chemical Society, Washington D.C., 2003, ACS Symp. Ser. 847, pp. 437–450. Copyright (2013) American Chemical Society.[13])

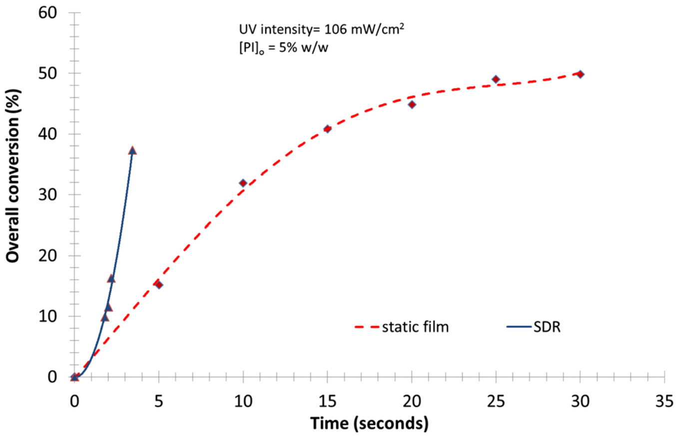

Figure 11.6 Comparison of photo-coplymerisation of VAc and *n*-BA in SDR and in static films. (Reprinted from Chemical Engineering and Processing, 71, C. G. Dobie *et al.*, An evaluation of the effectiveness of continuous thin film processing in a spinning disc reactor for bulk free-radical photo-copolymerisation, 97–106, Copyright (2013) with permission from Elsevier.[15])

respect. The efficiency of initiator decomposition and therefore monomer conversion can be optimised by reducing the flow rate of the feed stream without any additional energy input.

These studies demonstrate the exciting and industrially viable opportunity for performing continuous photo-polymerization of monomers in bulk in the SDR. There are clear indications that the SDR, with its ability to produce thin, controllable and highly mixed films in continuous flow, even on scale-up, offers much scope for exploiting the relatively untapped possibilities presented by photochemistry applications in general. The potential for significant energy savings offered by the SDR[16] in combination with the benefits of UV processing can provide a realistic energy-efficient solution for many processes.

11.2.2.2 Reactive Precipitations

There is a drive in many industries to produce nanoparticles or nanocrystals which, by definition, are between 1 and 100 nm in diameter. This interest stems from the superior physical and chemical properties offered by these nano-sized particulate materials including greatly improved mechanical strength of materials (*e.g.* in polymer nanocomposites, bone cement), thermal stability, catalytic activity and larger surface area for easier dissolution as drugs. Ideal equipment for producing such nano-sized materials should have very rapid and uniform micromixing characteristics in order to create high levels of supersaturation and ultimately high nucleation rates throughout the processing volume. The SDR, with its micromixing time of the order of milliseconds,[10,11] readily fulfills this requirement.

There have been a number of experimental studies that have highlighted the potential of the SDR to be employed as an effective precipitation device producing small, tailored particle sizes with excellent uniformity in size and therefore application characteristics. In reactive precipitation processes, for instance, barium sulphate crystals of 0.7 μm have been obtained.[17,18] More recent work[19] has demonstrated the synthesis of narrowly size-distributed nano-titanium dioxide (TiO_2) particles of around 1 nm *via* the reactive precipitation of tetraisopropoxide (TTIP) with water under ambient temperature conditions (Figure 11.7). Overall, the optimized operating conditions for generating smaller particles with narrower distributions include a combination of high disc rotational speeds, high flow rates and textured disc surfaces such as a grooved disc. Interestingly, Chan *et al.*[20] have reported the production of *in situ* anatase TiO_2 in a SDR operating at elevated temperatures of 400–500 °C without any further calcination step, demonstrating an integrated reaction downstream processing procedure with potential time/energy saving benefits.

Tai and co-workers have demonstrated the synthesis of nanoparticles of silver[21] of less than 10 nm diameter *via* the application of a greener precipitation process based on the use of glucose, an environmentally benign reagent employed as the reducing agent. An even greener method of silver nanoparticles synthesis involves the use of glucose in combination with a more environmentally friendly protecting agent such as starch to prevent agglomeration, instead of the more commonly employed polyvinyl pyrrolidone (PVP).[21–23] An alternative 'green' approach adopted in the synthesis of superparamagnetic magnetite nanoparticles has been reported by Chin *et al.*[24]

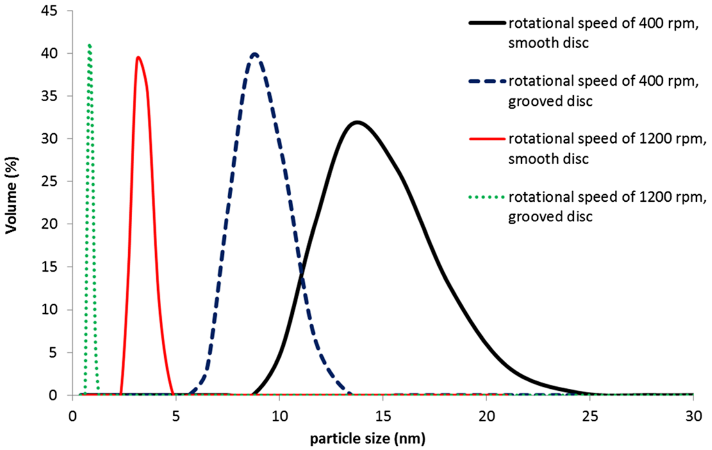

Figure 11.7 Nano-TiO_2 particles formed from reactive precipitation in SDR under different operating conditions. (Reprinted from Chemical Engineering Journal, 258, S. Mohammadi *et al.*, Synthesis of TiO2 nanoparticles in a spinning disc reactor, 171–184, Copyright (2014) with permission from Elsevier.[19])

Alginic acid, a natural biopolymer originating from algae, was employed as a surfactant to stabilize the Fe_3O_4 particles during processing in the SDR. The ability to inject the alginic acid into the magnetite particle suspension and achieve uniform mixing of the two streams on the rotating disc constituted a considerable processing advantage in producing highly stable particles of about 10 nm and of very narrow size distribution.

11.2.2.3 Catalytic/Enzymatic Transformations

A number of applications have been documented in the literature in relation to enhancement of catalytic reactions in the SDR. One of the earliest studies investigated was the reaction between a ketone and chloroacetonitrile in tetrahydrofuran (commonly known as Darzen's reaction) in the presence of a phase-transfer catalyst dissolved in an aqueous phase of potassium hydroxide.[7] The target product of this reaction is a valuable drug intermediate. Two key characteristic features of SDR processing, namely the rapid liquid–liquid mass transfer at high disc speeds and the short residence times, resulted in enhanced selectivity and higher product purity even under ambient conditions when benchmarked against the conventional batch process.

More interestingly, however, are the potential downstream processing and associated environmental benefits of fixing a solid-supported catalyst onto the rotating disc surface without compromising the reaction rate and selectivity. This was successfully demonstrated in a fine chemical process commonly carried out in the fragrance industry involving the re-arrangement of α-pinene oxide catalysed by a thin disc coating of silica-supported zinc triflate catalyst.[25] The immobilisation of the catalyst enabled the catalyst separation step to be eliminated, representing important environmental and economic advantages as the need for expensive and potentially harmful, volatile solvents typically used in the washing and recovery process could be removed. In spite of the catalyst immobilisation which, in conventional technologies may result in loss of active sites and therefore lower reaction rates, faster reaction rates and improved selectivity were achieved in the thin film SDR. The experimental outcomes suggested that better mixing and much shorter and controllable residence times were responsible for the observed improvements in the continuous SDR process.

More recently, Patterson and co-workers have demonstrated the combined UV processing advantages in thin films with enhanced catalytic degradation of wastewater using suspended TiO_2 catalyst in a SDR.[26]

Recent work on enzymatic transformations using enzymes supported on a cloth fixed on a rotating horizontal disc has highlighted the benefits of bioprocessing using the thin films of the SDR.[27] The study, which was focused on the hydrolysis of tributyrin using lipase enzyme immobilised on a woollen cloth fixed to the rotating disc surface, demonstrated an increase in reaction rate compared to processing with immobilised enzymes in a conventional agitated batch vessel (Figure 11.8). This rate enhancement is attributed to improved mass transfer between the reactant tributyrin and the immobilised lipase enzyme, enabled by the smaller droplet sizes of the emulsion

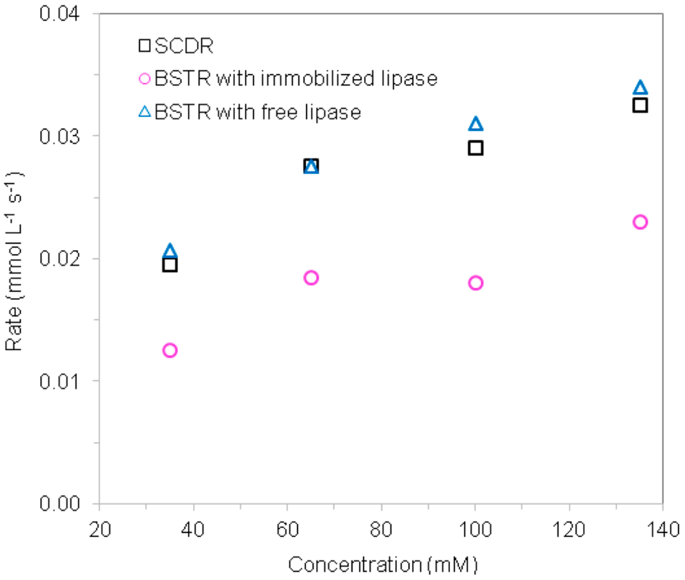

Figure 11.8 Rate enhancement of enzymatic hydrolysis of tributyrin in SCDR and conventional batch vessel. (Reprinted from Chemical Engineering Journal, 221, X. Feng *et al.*, The spinning cloth disc reactor for immobilized enzymes: A new process intensification technology for enzymatic reactions, 407–417, Copyright (2013) with permission from Elsevier.[27])

produced and the higher shear rate in the thin film of the spinning cloth disc reactor (SCDR). It is thought that the woollen cloth provides a certain degree of protection to the enzyme immobilised in its structure, thus preventing its deactivation by the high shear stress imposed by the liquid film flowing past.

11.2.3 Rotor–stator SDR

A variant of the thin film SDR described in Section 2.2 above is the more recently developed rotor–stator SDR (RSSDR)[28] which involves fluid flow in small channels, of a few millimeters in height, formed by the space between a rotating disc and a stationary disc as shown in Figure 11.9. High shear forces, created within the film as it passes in the channel between the rotor and stator surfaces, are responsible for intimate contact between fluid streams. Volumetric mass transfer coefficients as high as 250 s^{-1} have been reported for immiscible liquid systems at a rotational speed of 1600 rpm,[28] which, in combination with the high surface area to volume ratio offered by the thin enclosed film, enable rapid mass transfer processes to occur during passage within the channels. The rotor–stator SDR has been applied to a range of multiphase processes involving liquid/liquid extractions,[28] gas/liquid mass transfer[29] and liquid/solid reaction systems.[30]

11.3 Rotating Packed Bed (RPB)

11.3.1 Design and Operating Principles

Similar operating principles as those encountered in a SDR are applicable in a rotating packed bed (RPB); high centrifugal accelerations, typically of the order of 100–1000 g, are imposed on the processing fluids due to rotation of the bed. The primary difference between the SDR/RSSDR and RPB designs is that whilst the former operate on the basis of a liquid impinging on a flat,

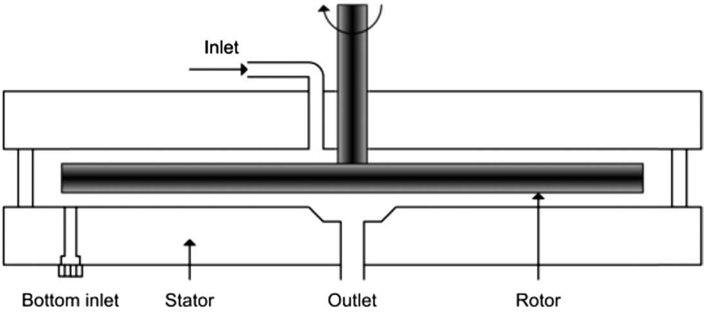

Figure 11.9 Rotor–stator SDR equipment. (Reprinted from Chemical Engineering Journal, 185, F. Visscher *et al.*, Liquid–liquid mass transfer in a rotor–stator spinning disc reactor, 267–273, Copyright (2012) with permission from Elsevier.[28])

usually horizontal, spinning surface to form thin liquid films as in the SDR or on the basis of multiphase flow in a very narrow, empty channel as in the RSSDR, the RPB relies on the use of structured packing elements of an axial depth of at least 10 mm rotating in an enclosed volume to achieve intimate contact between the phases. The reactor volume of the RPB is therefore much higher than that of the SDR or even the RSSDR. The packing characteristics, particularly its specific surface area and its voidage, are key parameters which influence the mass transfer capability and pressure drop/energy consumption of the device. A range of packing structures have been employed with specific surface areas typically in the range of 500–5000 m^2 m^{-3}, and voidages typically between 40 and 95%, with the higher surface areas and voidages greater than 85% preferred for optimal performance.[3,31,32]

Gas/liquid or liquid/liquid flow arrangement within the reactor is usually counter-current to maximise the concentration driving force for mass transfer, although co-current[33] and cross-flow[34,35] configurations are also possible in practice. In the counter-current flow arrangement (Figure 11.10), the less dense phase will be injected from the periphery of the rotor and will flow against the centrifugal force through the packing towards the exit region in the centre or the eye of the rotor. The denser phase meanwhile enters from the centre of the rotor and is flung under the action of the centrifugal force towards the outer edges of the packed bed from where it disengages from the rotor into a collector.

Visual investigations into the hydrodynamic behaviour of liquid in an RPB have shown that various flow regimes are obtained depending on the angular velocity ($r\omega$) of the fluid. Generally, pore flow or rivulet flow, as depicted in Figure 11.11, is dominant at low rotational speeds which is indicative of liquid maldistribution and incomplete wetting of the packing surface whilst

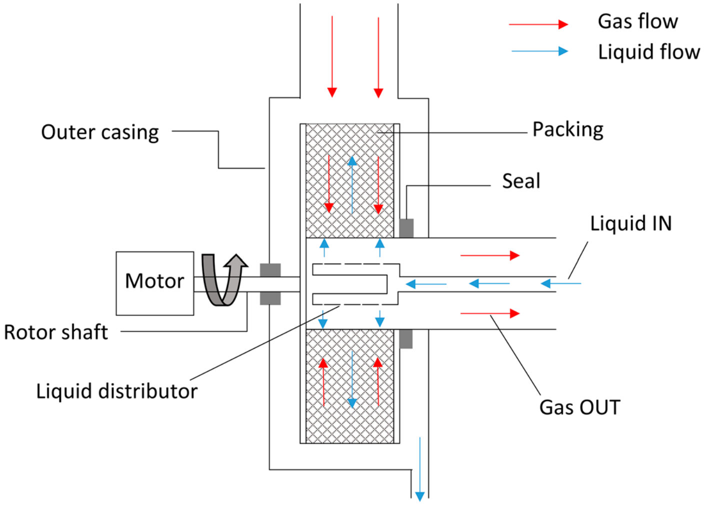

Figure 11.10 Schematic of a counter-current flow RPB.

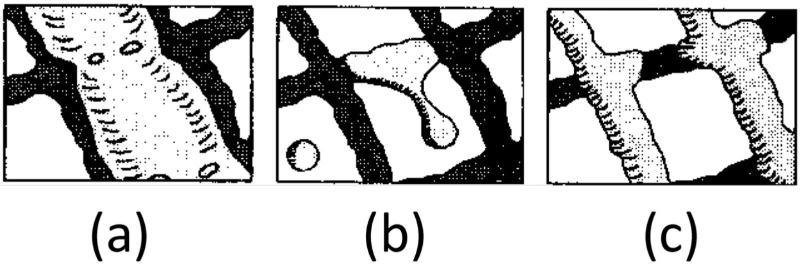

Figure 11.11 Liquid flow regimes in an RPB: (a) pore (rivulet) flow (b) droplet flow and (c) film flow. (Reprinted from Chemical Engineering Science, 51, J. R. Burns and C. Ramshaw, Process intensification: Visual study of liquid maldistribution in rotating packed beds, 1347–1352, Copyright (1996) with permission from Elsevier.[36])

droplet flow was seen to become more prominent at high rotational speeds.[36] It was also highlighted that thin film flow may be rather difficult to sustain in a high acceleration environment where the liquid is constantly hitting packing elements or filaments. Further work has since revealed that this may indeed be the case, although the turbulence induced by such disturbances in the path of the high velocity liquid flow may still be conducive to a significant enhancement in multiphase mass transfer.[37] The latter work also clearly demonstrates that the liquid trajectory from the central inlet towards the periphery is predominantly in a radial direction, confirming the observations made in earlier studies.[31,36]

RPBs have been considered strong contenders for gas–liquid separation processes such as absorption and stripping, conventionally carried out in packed bed towers operating under gravity, mainly because of the considerable enhancement in volumetric mass transfer coefficient, k_La. Values for k_La as high as 2.7 s^{-1} have been reported in an RPB operating at 200 g with structured packings, representing an enhancement of about 40× the corresponding value in a packed column under 1 g acceleration.[31] One other distinct advantage of the RPB over a conventional packed column is that much high flow rates can be processed before flooding occurs due to the high gravity environment that exists in the RPB. Or alternatively, for similar throughputs as those in a ‘1 g’ packed bed tower, the footprint of the RPB can be significantly reduced.[38]

11.3.2 Green Processing Applications of RPB

The key characteristics of enhanced mass transfer, rapid micromixing and short residence times presented by the RPB have enabled its application to a wide range of separation processes such as distillation, absorption, desorption/gas stripping and, more recently, reactions such as precipitation/crystallisation and biotransformations. Its compact design makes it especially attractive for offshore applications such as the de-oxygenation of seawater.[3]

One of its limitations, however, is the difficulty in controlling heat removal from exothermic processes taking place in the packed bed due to the lack of provision for an internal heat transfer system within the bed, as highlighted in a recent study involving a fermentation process.[39]

11.3.2.1 Absorption Processes

11.3.2.1.1 Carbon Capture Applications. Although distillation was one of the earliest applications of the RPB,[40] there has been much renewed interest in the technology for carbon capture applications which have important environmental benefits. In particular, capture of CO_2 from waste gas streams emanating from power plants and petroleum/bulk chemicals plants is an area of significant interest that has grown as a result of initiatives such as the Kyoto Protocol. The drive for the search and implementation of new technologies such as the RPB for CO_2 capture stems from multiple needs: (1) to overcome the mass transfer limitations of traditional separation units such as packed towers for more energy-efficient and cost-effective engineering solutions and (2) to handle extremely large mass flows that are typical of large CO_2 producers such as fossil fuel power stations. Conventional packed towers are inadequate in their current form to cope with the processing throughputs required in these situations.[41] The enhanced gas–liquid mass transfer in a RPB gives it a processing edge in effectively extracting CO_2 from waste gas streams, and thus makes the large-scale capture of CO_2 a more economically viable prospect. Several studies have demonstrated the effectiveness of the RPB as a gas–liquid contactor for CO_2 absorption into solvents such as alkanolamines.[38,42] A review of these studies and others involving a range of other potentially greener solvents, such as ionic liquids for CO_2 absorption, in the RPB has recently been published.[41]

More recently, the carbonation of solid wastes such as steelmaking slags from steel manufacturing plants in the RPB has been reported.[43,44] The authors have highlighted the improved CO_2 removal efficiency and carbonation conversion of steelmaking slag in an RPB in comparison to processing in an autoclave or a slurry reactor. Rapid mass transfer gives high CO_2 removal efficiency in processing times of under 1 minute, all under ambient temperature and pressure conditions.[44] This method of CO_2 sequestration has greener credentials and sustainable attributes compared to conventional absorption processes using amine solvents for instance as it involves the use of waste materials to capture CO_2.[45]

11.3.2.1.2 SO_2 and NO_x Absorption. Although the focus lately has primarily been on CO_2 sequestration in order to meet environmental legislation, there is equally promising potential for other environmentally harmful gases such as NO_x and SO_2 to be removed from waste gas streams *via* gas–liquid absorption processes in the RPB.[46,47]

In flue gas desulphurisation, for example, SO_2 absorption in sodium citrate solution in a counter-current RPB at 900 rpm gives an SO_2 removal efficiency of 98% from the simulated flue gas when fresh sodium citrate solution is employed.[46] Co-current operation, which has the advantage of lower gas pressure drop over counter-current operation and therefore lower operating cost, can also give comparably high SO_2 removal efficiency (Figure 11.12).[33]

11.3.2.2 Reactive Precipitations

Many examples have been reported in the literature for gas–liquid and liquid–liquid reactive precipitation in the RPB of a range of nanoparticles such as $CaCO_3$, $Al(OH)_3$ and $SrCO_3$ amongst many others.[48,49] In comparison with conventional technologies, such as stirred tank reactors, the RPB gives much smaller particles, of the order of tens of nm,[49] as well as improved control of their size distribution, as highlighted in Figure 11.13. These effects have been attributed to the higher micromixing intensity that can be achieved in the RPB between the two reacting streams during the precipitation process, an effect that is similarly obtained in the SDR as discussed earlier in Section 11.2.2.2.

11.3.3 Novel Variations of RPB designs

A more recent design which originates from the RPB concept is the rotating zigzag bed (RZB)[50] which involves a series of concentric rotor rings alternating with concentric stator rings along the radial direction of the reactor

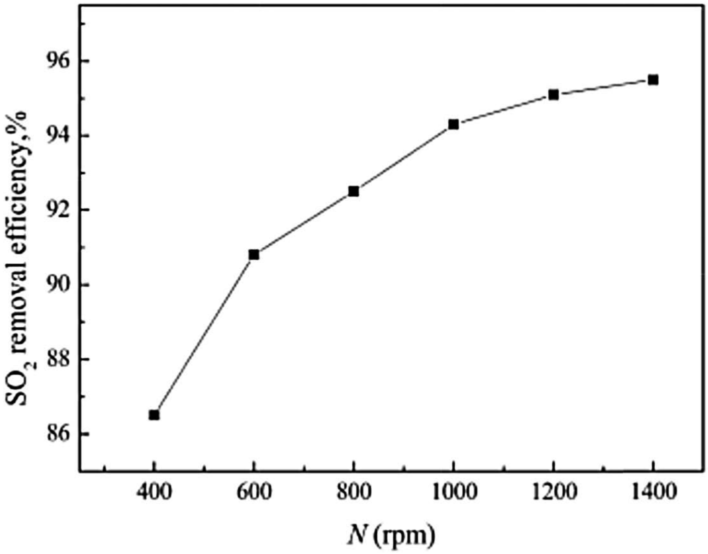

Figure 11.12 SO_2 removal efficiency in ammonia solution in a co-current RPB. (Reprinted with permission from G.-W.Chu, Y. Luo, C.-Y. Shan, H.-K. Zou, Y. Xiang, L. Shao, and J.-F. Chen, Absorption of SO_2 with Ammonia-Based Solution in a Co-current Rotating Packed Bed. *Ind. Eng. Chem. Res.* 2014, **53**, 15731. Copyright (2014) American Chemical Society.[33])

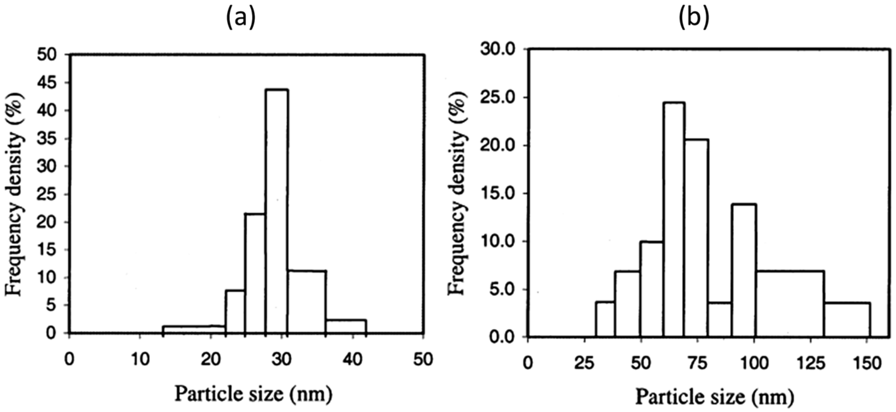

Figure 11.13 Comparison of particle size distribution of $CaCO_3$ in (a) RPB and (b) conventional technology. (Reprinted with permission from J.-F. Chen, Y.-H. Wang, F. Guo, X.-M. Wang, and C. Zheng, Synthesis of nanoparticles with Novel Technology: High-Gravity Reactive Precipitation. *Ind. Eng. Chem. Res.* 2000, **39**, 948. Copyright (2000) American Chemical Society.[49])

(Figure 11.14(a)). The main difference between this design and the original RPB is the absence of packing material in the rotor–stator gaps. It is essentially directly comparable with the rotor–stator SDR concept highlighted in Section 11.2.3 but with a number of obstacles (inducing potentially greater shear stress in the processing streams) presented by the alternating perforated rotating and plain surface stationary baffles which result in a zigzag flow path for the gas and liquid streams (Figure 11.14(b)). Recent literature suggests that improvements in micromixing and mass transfer coefficients are achieved in this novel rotor–stator design compared to a conventional RPB[51,52] and several industrial applications including multistage distillation and stripping processes are reported to have been successfully demonstrated.[50]

11.4 Concluding Remarks

Great strides have been made in the design, development and application of Higee technologies in the last two decades. The original designs of the SDR and the RPB as well as the novel versions such as the RSSDR and the RZB, as discussed in this chapter, offer distinct processing advantages as a result of their enhanced fluid dynamics and associated transport and mixing characteristics. The ability of these technologies to deliver greener chemical processing is invariably related to their significantly improved processing efficiency, even under challenging conditions of operation, for example in the highly viscous polymerisation systems applied in the SDR. This allows waste minimisation at source in environmentally friendly processes as highlighted in several examples throughout this chapter.

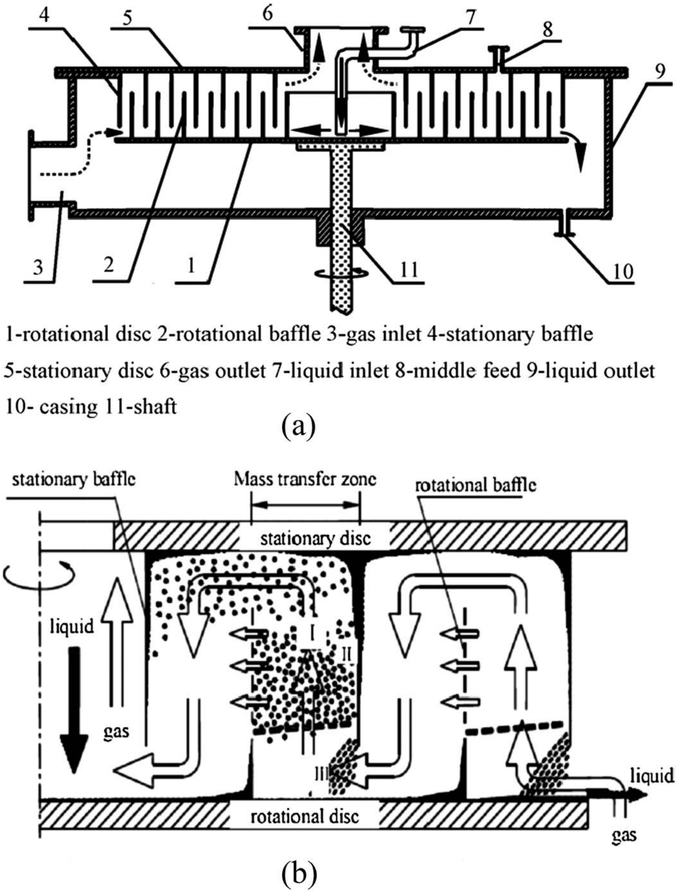

Figure 11.14 (a) Schematic of the novel rotating zigzag bed (RZB) (b) zigzag flow path of gas and liquid flows between rotating and stationary baffles. (Reprinted from Chemical Engineering Research and Design, 89, G. Q. Wang *et al.*, Progress on Higee distillation – Introduction to a new device and its industrial applications, 1434–1442, Copyright (2011) with permission from Elsevier.[50])

References

1. K. V. K. Boodhoo, *Process Intensification for Green Chemistry: Engineering Solutions for Sustainable Chemical Processing*, ed. K. V. K. Boodhoo and A. Harvey, Wiley-Blackwell, Oxford, 1st edn, 2013, ch. 3, pp. 59–90.
2. J. R. Burns, C. Ramshaw and R. J. Jachuck, Measurement of liquid film thickness and the determination of spin-up radius on a rotating disc using an electrical resistance technique, *Chem. Eng. Sci.*, 2003, **58**, 2245.
3. D. A. Reay, C. Ramshaw and A. Harvey, *Process Intensification: Engineering for Efficiency, Sustainability and Flexibility*, Elsevier, Oxford, 2008.

4. K. V. K. Boodhoo and A. P. Harvey, *Process Intensification for Green Chemistry: Engineering Solutions for Sustainable Chemical Processing*, ed. K. V. K. Boodhoo and A. Harvey, Wiley-Blackwell, Oxford, 1st edn, 2013, ch. 1, pp. 1–30.
5. C. Ramshaw and S. Cook, Spinning around, *Chem. Eng.*, 2005, **774**, 42.
6. K. V. K. Boodhoo, W. A. E. Dunk, M. Vicevic, R. J. Jachuck, V. Sage, D. J. Macquarrie and J. H. Clark, Classical cationic polymerisation of styrene in a spinning disc reactor using silica-supported BF3 catalyst, *J. Appl. Polym. Sci.*, 2006, **101**, 8.
7. P. Oxley, C. Brechtelsbauer, F. Ricard, N. Lewis and C. Ramshaw, Evaluation of spinning disc reactor technology for the manufacture of pharmaceuticals, *Ind. Eng. Chem. Res.*, 2000, **39**, 2175.
8. D. Ghiasy, K. V. K. Boodhoo and M. T. Tham, Thermographic Analysis of Thin Liquid Films on a Rotating Disc: approach and challenges, *Appl. Therm. Eng.*, 2012, **44**, 39.
9. K. V. K. Boodhoo and S. Al-Hengari, Micromixing characteristics in a small scale spinning disk reactor, *Chem. Eng. Technol.*, 2012, **35**, 1229.
10. S. Mohammadi, L. Turetta and K. V. K. Boodhoo, Characterisation of liquid/liquid micromixing and power dissipation in spinning disc reactors, *Paper presented at 5th European Process Intensification Conference (EPIC5)*, Nice, France, 26 Sept–02 Oct 2015.
11. N. C. Jacobsen and O. Hinrichsen, Micromixing efficiency of a spinning disk reactor, *Ind. Eng. Chem. Res.*, 2012, **51**, 11643.
12. S. Mohammadi and K. V. K. Boodhoo, Online conductivity measurement of residence time distribution of thin film flow in the spinning disc reactor, *Chem. Eng. J.*, 2012, **207–208**, 885.
13. K. V. K. Boodhoo, W. A. E. Dunk and R. J. Jachuck, *Advances in Photoinitiated Polymerisations*, ed. K. Belfield and J. Crivello, American Chemical Society, Washington D.C., 2003, vol. 847, ACS Symp. Ser., pp. 437–450.
14. A. Ledwith, Photoinitiation of polymerization, *Pure Appl. Chem.*, 1977, **49**, 431.
15. G. Dobie, M. Vicevic and K. V. K. Boodhoo, An evaluation of the effectiveness of continuous thin film processing in a spinning disc reactor for bulk free-radical photo-copolymerisation, *Chem. Eng. Process.*, 2013, **71**, 97.
16. D. Ghiasy and K. V. K. Boodhoo, *Process Intensification for Green Chemistry: Engineering Solutions for Sustainable Chemical Processing*, ed. K. V. K. Boodhoo and A. P. Harvey, Wiley-Blackwell, Oxford, 1st edn, 2013, ch. 15, pp. 379–392.
17. L. M. Cafiero, G. Baffi, A. Chianese and R. J. Jachuck, Process intensification: precipitation of barium sulfate using a spinning disk reactor, *Ind. Eng. Chem. Res.*, 2002, **41**, 5240.
18. A. M. Dehkordi and A. Vafaeimanesh, Synthesis of barium sulfate nanoparticles using a spinning disk reactor: effects of supersaturation, disk rotation speed, free ion ratio, and disk diameter, *Ind. Eng. Chem. Res.*, 2009, **48**, 7574.

19. S. Mohammadi, A. Harvey and K. V. K. Boodhoo, Synthesis of TiO_2 nanoparticles in a spinning disc reactor, *Chem. Eng. J.*, 2014, **258**, 171.
20. B. C. Y. Chan, X. Wang, L. K. W. Lam, J. M. Gordon, D. Feuermann, C. L. Raston and H. Tong Chua, Light-driven high-temperature continuous-flow synthesis of TiO_2 nano-anatase, *Chem. Eng. J.*, 2012, **211–212**, 195.
21. C. Y. Tai, Y. H. Wang, Y. W. Kuo, M. H. Chang and H. S. Liu, Synthesis of silver particles below 10 nm using spinning disk reactor, *Chem. Eng. Sci.*, 2009, **64**, 3112.
22. C. Y. Tai, Y. H. Wang and H. S. Liu, A green process for preparing silver nanoparticles using spinning disc reactor, *AIChE J.*, 2008, **54**, 445.
23. P. Raveendran, J. Fu and S. L. Wallen, Completely "green" synthesis and stabilization of metal nanoparticles, *J. Am. Chem. Soc.*, 2003, **125**, 13940.
24. S. F. Chin, K. S. Iyer, C. L. Raston and M. Saunders, Size selective synthesis of superparamagnetic nanoparticles in thin fluids under continuous flow conditions, *Adv. Funct. Mater.*, 2008, **18**, 922.
25. M. Vicevic, K. V. K. Boodhoo and K. Scott, Catalytic isomerisation of α-pinene oxide to campholenic aldehyde using silica supported zinc triflate catalysts: II. performance of immobilised catalysts in a continuous spinning disc reactor, *Chem. Eng. J.*, 2007, **133**, 43.
26. I. Boiarkina, S. Pedron and D. A. Patterson, An experimental and modelling investigation of the effect of the flow regime on the photocatalytic degradation of methylene blue on a thin film coated ultraviolet irradiated spinning disc reactor, *Appl. Catal., B*, 2011, **110**, 14.
27. X. Feng, D. A. Patterson, M. Balaban, G. Fauconnier and E. A. C. Emanuelsson, The spinning cloth disc reactor for immobilized enzymes: A new process intensification technology for enzymatic reactions, *Chem. Eng. J.*, 2013, **221**, 407.
28. F. Visscher, J. van der Schaaf, M. H. J. M. de Croon and J. C. Schouten, Liquid–liquid mass transfer in a rotor–stator spinning disc reactor, *Chem. Eng. J.*, 2012, **185–186**, 267.
29. M. Meeuwse, J. van der Schaaf, B. F. M. Kuster and J. C. Schouten, Gas-liquid mass transfer in a rotor–stator spinning disc reactor, *Chem. Eng. Sci.*, 2010, **65**, 466.
30. M. Meeuwse, S. Lempers, J. van der Schaaf and J. C. Schouten, Liquid-solid mass transfer and reaction in a rotor–stator spinning disc reactor, *Ind. Eng. Chem. Res.*, 2010, **49**, 10751.
31. D. P. Rao, A. Bhowal and P. S. Goswami, Process Intensification in Rotating Packed Beds (HIGEE): An Appraisal, *Ind. Eng. Chem. Res.*, 2004, **43**, 1150.
32. J. R. Burns, C. Jamil and C. Ramshaw, Process Intensification: Operating Characteristic of Rotating Packed Beds-Determination of Liquid Hold-Up for a High-Voidage Structured Packing, *Chem. Eng. Sci.*, 2000, **55**, 2401.
33. G.-W. Chu, Y. Luo, C.-Y. Shan, H.-K. Zou, Y. Xiang, L. Shao and J.-F. Chen, Absorption of SO_2 with Ammonia-Based Solution in a Cocurrent Rotating Packed Bed, *Ind. Eng. Chem. Res.*, 2014, **53**, 15731.

34. N. Goswami, S. Basu, A. Bhowal and S. Datta, Concentration of solution in cross-flow rotating packed bed contactor, *Chem. Eng. Res. Des.*, 2015, **95**, 281.
35. F. Guo, C. Zheng, K. Guo, Y. Feng and N. C. Gardner, Hydrodynamics and Mass Transfer in Cross Flow Rotating Packed Bed, *Chem. Eng. Sci.*, 1997, **52**, 3853.
36. J. R. Burns and C. Ramshaw, Process Intensification: Visual Study of Liquid Maldistribution in Rotating Packed Beds, *Chem. Eng. Sci.*, 1996, **51**, 1347.
37. Z.-Y. Yan, C. Lin and Q. Ruan, Hydrodynamics in a Rotating Packed Bed. I. A Novel Experimental Method, *Ind. Eng. Chem. Res.*, 2012, **51**, 10472.
38. M. S. Jassim, G. Rochelle, D. Eimer and C. Ramshaw, Carbon Dioxide Absorption and Desorption in Aqueous Monoethanolamine Solutions in a Rotating Packed Bed, *Ind. Eng. Chem. Res.*, 2007, **46**, 2823.
39. K. V. K. Boodhoo, C. D. Cartwright, M. Vicevic, M. A. Prieto and M. Tortajada, Development of a Higee bioreactor (HBR) for production of polyhydroxyalkanoate: Hydrodynamics, gas–liquid mass transfer and fermentation studies, *Chem. Eng. Process.*, 2010, **49**, 748.
40. C. Ramshaw, HiGee Distillation-An Example of Process Intensification, *Chem. Eng.*, 1983, **389**, 13.
41. M. Wang, A. S. Joel, C. Ramshaw, D. Eimer and N. M. Musa, Process intensification for post-combustion CO_2 capture with chemical absorption: A critical review, *Appl. Energy*, 2015, **158**, 275.
42. C. C. Lin, W. T. Liu and C. S. Tan, Removal of Carbon Dioxide by Absorption in a Rotating Packed Bed, *Ind. Eng. Chem. Res.*, 2003, **42**, 2381.
43. E. E. Chang, S. Y. Pan, Y. H. Chen, C. S. Tan and P. C. Chiang, Accelerated Carbonation of Steelmaking Slags in a High-gravity Rotating Packed Bed, *J. Hazard. Mater.*, 2012, **227–228**, 97.
44. S. Y. Pan, P. C. Chiang, Y. H. Chen, C. S. Tan and E. E. Chang, Ex Situ CO_2 Capture by Carbonation of Steelmaking Slag Coupled with Metalworking Wastewater in a Rotating Packed Bed, *Environ. Sci. Technol.*, 2013, **47**, 3308.
45. S. Y. Pan, A. Chiang, E.-E. Chang, Y.-P. Lin, H. Kim and P.-C. Chiang, An Innovative Approach to Integrated Carbon Mineralization and Waste Utilization: A Review, *Aerosol Air Qual. Res.*, 2015, **15**, 1072.
46. X. Jiang, Y. Liu and M. Gu, Absorption of sulphur dioxide with sodium citrate buffer solution in a rotating packed bed, *Chin. J. Chem. Eng.*, 2011, **19**, 687.
47. Y. Li, Y. Liu, L. Zhang, Q. Su and G. L. Jin, Absorption of NO_x into nitric acid solution in rotating packed bed, *Chin. J. Chem. Eng.*, 2010, **18**, 244.
48. H. Zhao, L. Shao and J. F. Chen, High-gravity process intensification technology and application, *Chem. Eng. J.*, 2010, **156**, 588.
49. J.-F. Chen, Y.-H. Wang, F. Guo, X.-M. Wang and C. Zheng, Synthesis of nanoparticles with Novel Technology: High-Gravity Reactive Precipitation, *Ind. Eng. Chem. Res.*, 2000, **39**, 948.

50. G. Q. Wang, Z. C. Xu and J. B. Ji, Progress on Higee distillation—Introduction to a new device and its industrial applications, *Chem. Eng. Res. Des.*, 2011, **89**, 1434.
51. G. W. Chu, Y. H. Song, H. J. Yang, J. M. Chen, H. Chen and J. F. Chen, Micromixing efficiency in a novel rotor–stator reactor, *Chem. Eng. J.*, 2007, **128**, 191.
52. Y. Li, B. Sun, Z. Zeng, Y. Song, J. Chen, G. Chu, J. Chen and L. Shao, A Study on the Absorption of Ammonia into Water in a Rotor-Stator Reactor, *Can. J. Chem. Eng.*, 2015, **93**, 116.

CHAPTER 12

High-Gravity Operation in Vortex Chambers for the Generation of High-Efficiency Fluidized Beds

WALDO ROSALES TRUJILLO[a] AND JURAY DE WILDE*[a]

[a]Université Catholique de Louvain, Materials and Process Engineering (iMMC-IMAP), Place Sainte Barbe 2, 1348 Louvain-la-Neuve, Belgium
*E-mail: Juray.DeWilde@UCLouvain.be

12.1 Introduction on Fluidization in a High-G Field

Fluidized beds are used in a variety of processes, for example in fluid catalytic cracking (FCC), coal combustion, particle drying and coating, *etc.* A variety of fluidization regimes exists, from a bubbling bed in which there is no net transport of solids to a riser in which both gas and solids move upwards with a slip velocity equal to the terminal velocity of the particles.[1] The range of process conditions resulting in a given fluidization regime and the related performance of fluidized beds are limited. Limitations encountered are closely related to the role of earth gravity in (conventional) fluidized beds:

(i) The gas–solid slip velocity and related coefficients of gas–solid mass, momentum and heat transfer are limited by the terminal velocity of the particles in the earth gravity field.

RSC Green Chemistry No. 47
Alternative Energy Sources for Green Chemistry
Edited by Georgios Stefanidis and Andrzej Stankiewicz

Published by the Royal Society of Chemistry, www.rsc.org

(ii) The particle bed density decreases gradually with increasing gas velocity, as the particle bed expands. At gas velocities beyond the terminal velocity of the particles, the particles are entrained with the gas and the particle bed density further decreases. The solids volume fraction in risers is only a few percent.

(iii) Meso-scale non-uniformities in the particle bed occur and play a major role in the performance of fluidized bed devices. Under dense conditions, bubbling occurs, under dilute conditions, clustering. Both are detrimental for gas–solid contact and related interfacial transfer and reactions.

(iv) Large-scale non-uniformities, like channeling and slugging, may occur and put constraints on the particle bed width-to-height ratio. The latter should, for example, be sufficiently small in order to avoid channeling.

(v) Fine or light cohesive powders (typically <30 μm) fluidize poorly. The inter-particle van der Waals forces dominate the gravity- and gas–solid drag-related forces. The limitations on the latter were already referred to in (i).

To overcome these limitations, fluidization in a high-gravity (high-G) field can be considered. For ferromagnetic particles, fluidization in a magnetic field was developed. A more generally applicable technology is based on the particle inertial forces in cylindrically-shaped rotating particle beds. The process gas is then fed through the outer cylindrical wall of the fluidization chamber and flows radially inwards towards a centrally positioned chimney for evacuation. The particle bed width is now to be defined in the tangential direction (circumference), the particle bed height in the radial direction. Compared to conventional fluidized beds, the particle bed width-to-height ratio is much higher, allowing more feed gas per unit surface area of particle bed and shorter gas phase residence times. Despite the high particle bed width-to-height ratios, channeling can be avoided by high-G operation.

Two rotating fluidized bed technologies have been developed, essentially differing in the way the particle bed rotational motion is introduced. The first technology, referred to as rotating fluidized bed (RFB), makes use of a motor to rotate the fluidization chamber fast around its axis of symmetry. The process gas is injected radially *via* multiple perforations. In the second technology, with the rotating fluidized bed in a static geometry (RFB-SG), use is made of a vortex or whirl chamber in which the process gas is injected tangentially *via* multiple slots. In RFBs, the fluidization gas flow rate and the particle bed rotation speed can be independently controlled. In RFB-SGs the two are coupled, the coupling depending on the vortex chamber design and the type of particles fluidized. The flow patterns in RFBs have been studied by different research groups.[2–9] Applications in gas phase polymerization[10] and in the production and coating of fine powders[11–14] have been reported. The major disadvantage of RFBs is the rotating geometry, making scale-up and commercialization challenging. For that reason, the use of vortex chambers

(RFB-SGs) has recently attracted more attention. This chapter summarizes the state of the art in RFB-SG research and development.

12.2 Rotating Fluidized Beds in a (Static) Vortex Chamber

In RFB-SGs, the process gas is injected tangentially in a vortex chamber (Figure 12.1).[15–19] Particles are entrained by the gas, resulting in a rotational motion of the particle bed. The gas flows radially inwards through the particle bed and leaves the vortex chamber *via* a centrally positioned chimney. Due to their inertia, particles do not follow the gas phase flow path. Considering a frame moving with a particle, the balance between the particle inertial forces (centrifugal and Coriolis force) and the radial gas–solid drag force determines if the particle is entrained into the chimney or stays in the vortex chamber. The Coriolis effect allows a particle that is entrained radially inwards to convert its radial momentum into tangential momentum. To achieve this before losing the particle into the chimney requires a correct vortex chamber and chimney design.

Single- and multiphase flows in vortex chambers have been studied since the late sixties.[15–17] The optimization of the operating conditions and the vortex chamber design has been addressed. Feeding a single phase only, a free vortex type flow pattern develops. The loss of this flow pattern in the presence of particles has important consequences on the force balance in the vortex chamber and on the design requirements of the latter. Typically, a high solids

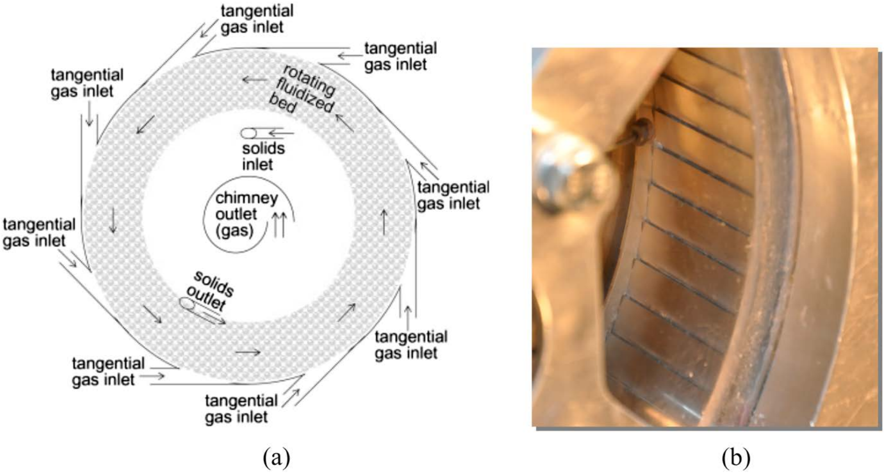

Figure 12.1 (a) The use of a vortex chamber to generate a rotating fluidized bed in a static geometry. (b) Detailed view of the gas inlet slots in a 72 × 0.5 mm slots vortex chamber. (Reproduced from De Wilde and de Broqueville with permission from John Wiley and Sons. Copyright © 2007 American Institute of Chemical Engineers (AIChE).)[19]

concentration in the rotating particle bed is aimed at. Apart from gas–solid flows, gas–liquid flows,[20,21] *e.g.* for fine particulates removal from flue gases, and liquid–solid flows[22,23] have been considered. In a vortex chamber type gas–liquid contactor, high-G operation results in smaller bubbles and more efficient mass transfer. The present paper focuses on gas–solid fluidized beds in vortex chambers and high-G operation, allowing us to neglect the effect of gravity. In an RFB-SG of a given design, the latter requires sufficiently high gas flow rates. The hydrodynamic characteristics of RFB-SGs are discussed in Section 12.3, whereas Section 12.4 addresses the most important design aspects of RFB-SGs. Sections 12.5 and 12.6 deal with potential applications of RFB-SGs. Finally, extensions of the concept and multi-zone operation are discussed in Section 12.7.

The difference between vortex chamber and Torbed technology should be emphasized. In a Torbed[24–27] the process gas is injected tangentially *via* multiple gas inlet slots integrated in the bottom-end wall of the cylindrical fluidization chamber and is forced to leave *via* the top-end. The particles are suspended on the rotating gas flow that is generated (tornado effect) and are fluidized vertically against earth gravity, so operation is essentially not high-G.

12.3 Hydrodynamic Characteristics

12.3.1 Fluidization in the Tangential and Radial Direction

In RFB-SGs, a distinction can be made between fluidization in the tangential and radial directions. The particle bed is always fluidized in the tangential direction. Whether fluidization in the radial direction occurs depends mainly on the vortex chamber design and the type of particles used.[19,28] Figure 12.2 shows the particle bed in a vortex chamber of given design and applying given operating conditions using two types of particles: (a) 2 (length)–5 (diameter) mm diameter HDPE polymer pellets and (b) 300 µm alumina particles. With the polymer pellets, the particle bed is radially not fluidized and a so-called concentrated pseudo-fluidized layer (CPL) is formed. The 'packed' bed is supported by the cylindrical outer wall of the vortex chamber. With the alumina particles, on the other hand, the bed is radially fluidized. The latter is reflected in the relation between the pressure drop over the particle bed and the gas flow rate, as shown in Figure 12.3. When the bed is radially packed, the pressure drop over the particle bed increases with increasing gas flow rate. When the particle bed is radially fluidized, the pressure drop over the particle bed is seen to become independent of the gas flow rate—a behavior well known from conventional fluidized beds.[1] Radial fluidization of the particle bed implies a reduction of the bed density and increases the presence of particles in the particle bed freeboard region. This facilitates the loss of particles *via* the chimney. As will be discussed in Section 12.4, a careful design of the vortex chamber allows optimizing the ratio of the radial gas–solid drag force and the inertial forces exerted on the particles and as such increasing the particle bed density and reducing the loss of solids *via* the chimney.

(a) 2–5 mm polymer pellets (b) 300 μm Alumina

Figure 12.2 Fluidization of different types of particles in an RFB-SG of given design. Vortex chamber: $D = 36$ cm, $L = 13.5$ cm, $n = 12$, $s = 4$ mm, $\lambda = 0.042$. Operating conditions: total gas flow rate: 0.2 Nm^3 s^{-1}, continuous operation with side solids inlet and outlet, solids loading: 1–1.5 kg. (a) 2–5 mm HDPE polymer pellets; (b) 300 μm alumina. (Reproduced from De Wilde and de Broqueville with permission from John Wiley and Sons. Copyright © 2007 American Institute of Chemical Engineers (AIChE).)[19]

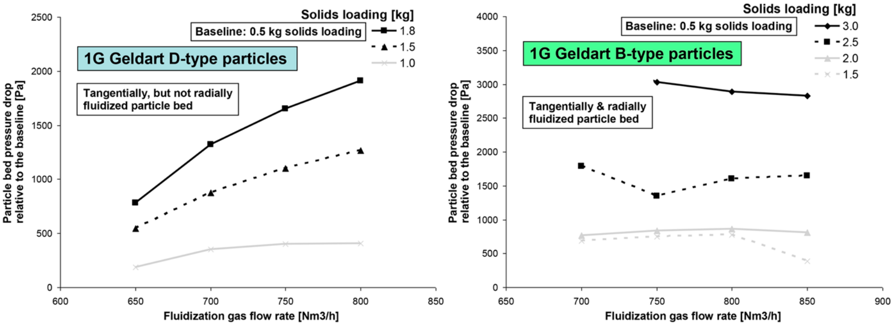

(a) 2–5 mm polymer pellets (b) 300 μm salt

Figure 12.3 Detection of radial fluidization when fluidizing different types of particles in an RFB-SG of given design. Pressure drop over the particle bed as a function of the fluidization gas flow rate for different solids loadings. Vortex chamber: $D = 24$ cm, $L = 11.5$ cm, $n = 24$, $s = 2.3$ mm, $\lambda = 0.073$. Continuous operation with side solids inlet and chimney outlet. (a) 2–5 mm HDPE polymer pellets; (b) 300 μm salt. (From De Wilde.)[32]

12.3.2 Free Vortex *Versus* Solid Body Type Rotation and Flexibility in the Solids Loading

In the absence of particles a free vortex forms in the vortex chamber. When feeding particles the free vortex is lost. This is reflected in an initial decrease of the pressure drop over the vortex chamber. The different flow patterns are illustrated in Figure 12.4(a) showing the normalized circulation ($\Gamma = v_t r$) as a function of the normalized radial coordinate, both in the absence and presence of a particle bed,[18] and in Figure 12.4(b) showing the rotational speed as a function of the solids loading at different normalized radial positions.[17] In general, the particle bed flow pattern is between solid body and free vortex type.[17,18,29,30] From detailed CFD simulations, a relation with radial fluidization and the formation of meso-scale non-uniformities could be demonstrated.[31] With the dense and uniform particle bed of 3 mm polymer pellets shown in Figure 12.2, the particle bed rotates nearly like a solid body, although radial mixing in the particle bed was fast.[32] In the particle bed freeboard region, the particle concentration is much lower than in the particle bed and a behavior approaching free vortex type can be expected. The latter was confirmed from experimental measurements (Figure 12.4(a))[18] and computational fluid dynamics (CFD) simulations.[33] As will be described in Section 12.4.3 on the chimney design, advantage can be taken of the behavior in the particle bed freeboard region. In the central region where the chimney is located, the outflow destroys the free vortex and a quasi-solid body type flow pattern was observed (Figure 12.4(a)).[18,34]

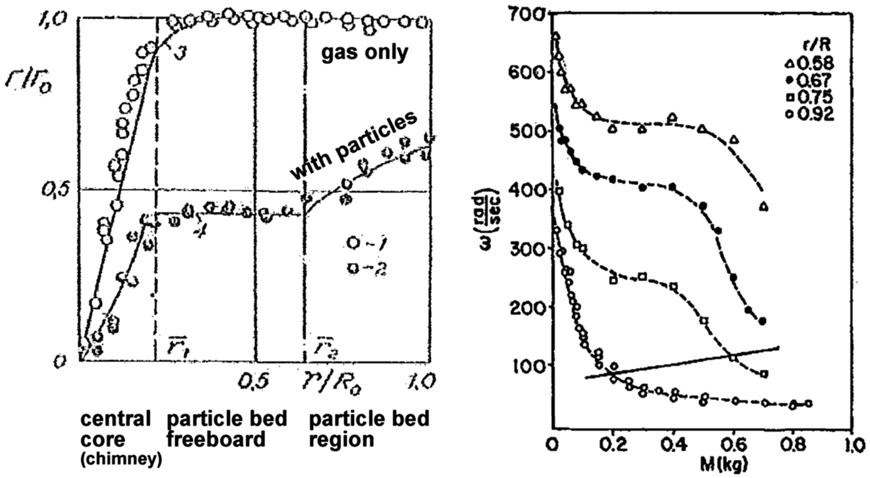

(a) (b)

Figure 12.4 (a) Normalized circulation ($\Gamma = v_t r$) as a function of the normalized radial position in the vortex chamber (subscript $_0$ indicates at the chamber outer wall) in the absence and presence of particles. Vortex chamber: $D = 36$ cm, $L = 6$ cm, $D_c = 8$ cm, $n > 20$, $\lambda = 0.099$. Operating conditions: solids loading: 1 kg of sand particles ($\rho_s = 1900$ kg m^{-3}, $d_p = 2$ mm). (Adapted from Volchkov *et al.* Taylor & Francis Ltd. http://www.informaworld.com.)[18] (b) Rotational speed as a function of the solids loading for different radial positions in the vortex chamber. Vortex chamber: $D = 30.5$ cm, $L = 6.3$ cm, $D_c = 15 \rightarrow 8$ cm (convergent), $n = 12$, $s = 0.3$ mm, $\lambda = 0.00376$. Operating conditions: talc particles ($\rho_s = 2700$ kg m^{-3}, $d_p = 20$ µm). (From Anderson *et al.* with permission from the American Institute of Aeronautics and Astronautics (AIAA).)[17]

Figure 12.4(b) deserves some further discussion. The initial feeding of solids drastically reduces the rotational speed at all radial positions in the vortex chamber, as explained above. From a certain solids loading onwards, however, in a given solids loading range, only a minor influence of the solids loading on the rotational speeds is observed. Because of the required balance between the centrifugal force and the radial gas–solid drag force, this is an important characteristic assuring a certain flexibility with respect to the solids loading. It also suggests that in this region the bed grows without causing drastic changes in the bed density. At too high solids loadings, the rotational speeds are again seen to decrease sharply, due to increasing frictional losses arising from the dense peripheral cloud.[17] Also, as more particles enter the particle bed freeboard region, the free vortex in this region—which contributes to the acceleration of the dense particle bed—is destroyed. Measurements of the effect of the solids loading on the particle bed porosity by Volchkov *et al.*[35] during grain drying in a vortex chamber of given design confirm the above-described behavior and a certain flexibility with respect to the solids loading. Finally, it should be remarked that in certain cases, a hysteresis effect is observed when measuring the flow pattern as a function of the solids loading.

12.3.3 Flexibility in the Gas Flow Rate

A unique feature of RFB-SGs is the flexibility in the gas flow rate. Indeed, when increasing the gas flow rate, both the radial gas–solid drag force and the counteracting centrifugal force increase. Depending on the vortex chamber design and the operating conditions, in particular the type of particles fluidized, the increase of the centrifugal force with increasing gas flow rate will be more or less pronounced than the increase of the radial gas–solid drag force. As such, under certain conditions, radial bed contraction rather than radial bed expansion will occur when increasing the gas flow rate. Volchkov *et al.*[35] experimentally showed a decrease of the bed porosity with increasing gas flow rate for a given vortex chamber design and particles. The flexibility in the gas flow rate of RFB-SGs is reflected in the dependence of the terminal velocity of the particles on the gas flow rate, as illustrated in Figure 12.5.[36] Using a theoretical model for the flow pattern in vortex chambers and neglecting the effect of gravity, Sazhin *et al.*[34] showed that the retention capacity of vortex chambers should be relatively independent of the air flow rate. The retention capacity is the solids loading remaining in the vortex chamber after stopping the solids feeding. Experimental observations by Kochetov *et al.*[15,16] and by Anderson *et al.*[17] show, however, a different behavior—the retention capacity increasing strongly with increasing gas flow rate in a given gas flow rate and corresponding solids loading (retention capacity) range (see Figures 12.13(c) and 12.14(a) discussed later). This could be explained by the role of gravity which cannot be neglected at low gas flow rates. At sufficiently high gas flow rates, Kochetov *et al.*[15,16] indeed observed the dependence on the gas flow rate to vanish. Another explanation could be that the flow behavior

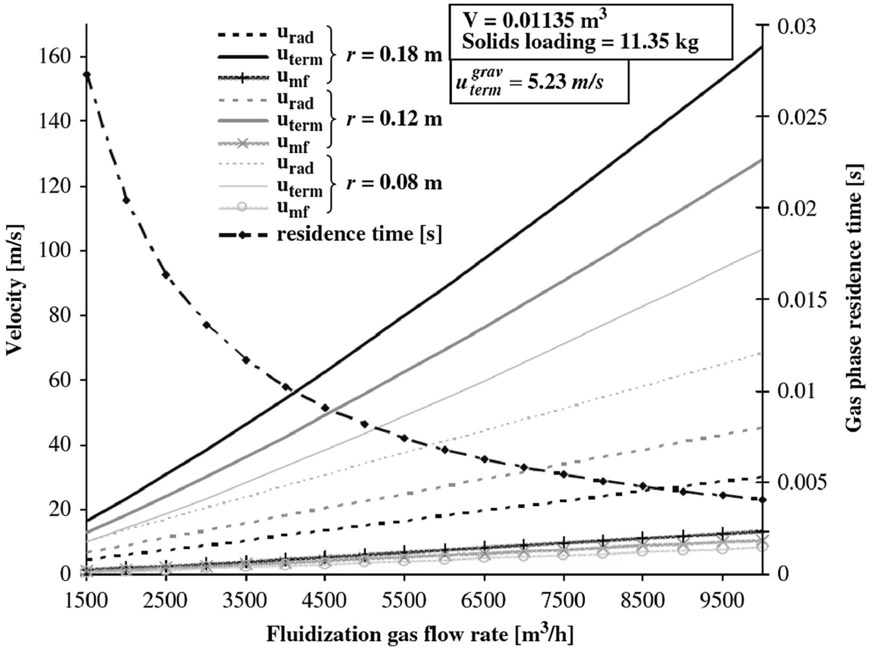

Figure 12.5 Illustration of the dependence of the minimum fluidization velocity and of the terminal velocity of the particles on the gas flow rate in RFB-SGs. (Reprinted from Chemical Engineering Science, 64, de Broqueville and De Wilde, Numerical investigation of gas–solid heat transfer in rotating fluidized beds in a static geometry, 1232–1248, Copyright (2009) with permission from Elsevier.)[36]

in the vortex chamber changes drastically when introducing solids up to a given solids loading. Doing experiments at relatively high gas flow rates and with continuous solids feeding and as such relatively high solids loadings, De Wilde and de Broqueville[19,28] confirmed a minor influence of the gas flow rate on the solids loading for a given solids feeding rate and on the particle bed stability.

The key for flexibility in the gas flow rate of RFB-SGs is the effect of the gas flow rate on the particle bed rotational speed. In a given gas flow rate range, a nearly linear increase of the particle bed rotational speed with the gas flow rate is observed. At higher gas flow rates, as shear grows in importance, the particle bed rotational speed increases less than proportionally with the gas flow rate. The range of gas flow rates in which a linear increase can be obtained depends on the type of particles fluidized and on the vortex chamber design, discussed in detail in Section 12.4. It can be noted in this context that Loftus *et al.*[20] working on a gas–liquid vortex chamber type contactor observed an increase of the mass of liquid contained in the chamber with increasing air flow rate, but that this increase was strongly dependent on the chamber design.

12.3.4 Large-Scale Non-Uniformities and Bed Stability

Bed stability and the absence of large-scale non-uniformities causing a complete bypass of the particles by the gas are crucial for industrial applications of fluidized beds. In RFB-SGs gas is fed to the vortex chamber from a gas distribution chamber *via* multiple inlet slots. Only the total gas flow rate is controlled, not the gas flow rate through each individual inlet slot. A non-uniform gas distribution over the different gas inlet slots can occur. Furthermore, within each inlet slot, a non-uniform distribution of the gas in the axial direction can occur. Non-uniformities in the gas distribution are closely related with large-scale non-uniformities in the particle bed.[31]

Channeling in the particle bed occurs in combination with a non-uniform distribution of the gas in the axial direction. Friction of particles with the end walls plays an important role in the appearance of channeling, particles being decelerated and accumulating near the end walls. This may cause most of the gas to enter towards the axial center of the vortex chamber. Particle bed slugging occurs in combination with a non-uniform distribution of the gas over the different gas inlet slots. The rotational motion of the particles causes a non-stationary distribution of the gas over the gas inlet slots, most of the gas entering the vortex chamber through inlet slots not facing the resistance of particles.

Figure 12.6 shows a map of the different regimes observed when fluidizing 1G-Geldart D-type,* 3 mm diameter PE pellets in a 24 cm diameter, 5 cm long vortex chamber with 12 gas inlet slots, 3 mm wide each (* high-G operation results in a shift in the Geldart classification of particles as shown by Qian *et al.*).[9] Channeling is observed at very small solids loadings. At somewhat higher solids loadings, slugging occurs. Finally, at sufficiently high solids loadings, solids phase stresses in the slugging regime become too high and a stable and uniform rotating particle bed forms. Figure 12.6 also nicely illustrates the flexibility in the gas flow rate in RFB-SGs discussed in the previous section. The gas flow rate is seen to have only a minor effect on the particle bed stability and on the occurrence of large-scale non-uniformities.

Figure 12.6 showed that a sufficiently high solids loading is crucial to avoid large-scale non-uniformities and to obtain a stable and uniform rotating particle bed. The solids loading in the vortex chamber that can be built up with a given solids feeding rate depends on the rate of solids losses *via* the chimney for the given solids loading. The latter depends on the vortex chamber design, more particularly the gas inlet and chimney design. Hence, the vortex chamber design will play a crucial role in extending the range of operating conditions in which large-scale non-uniformities can be avoided.

Large-scale non-uniformities inside the vortex chamber can be easily detected from pressure measurements. This is illustrated in Figure 12.7. Channeling can be detected from a difference in pressures measured at the outer cylindrical wall of the vortex chamber, close to an end wall and in the axial center of the vortex chamber respectively. Slugging can be identified from fluctuations in time of the pressure at any point in the vortex chamber.[37]

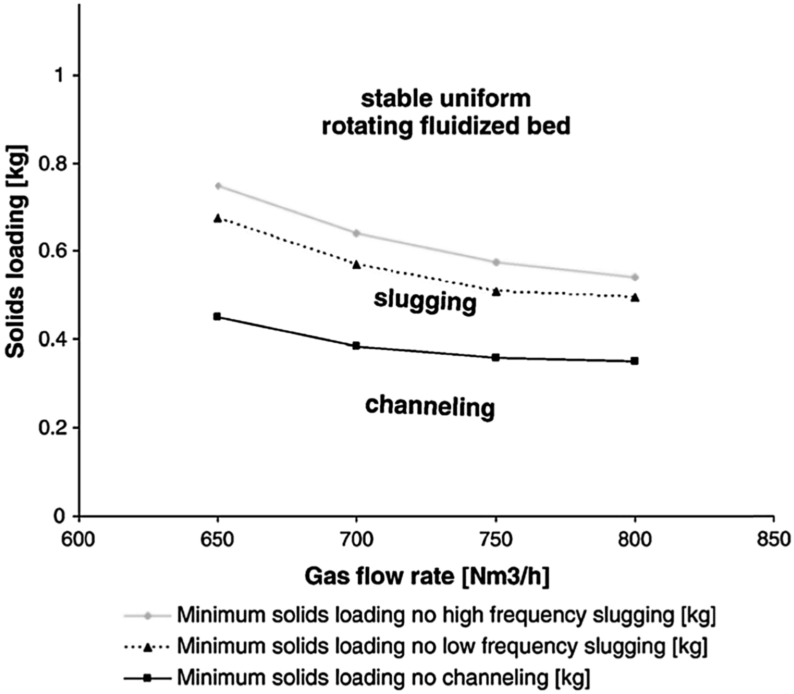

Figure 12.6 Flow regime map with 2–5 mm polymer pellets. Vortex chamber design: see Figure 12.3. (Reprinted from Powder Technology, 183, De Wilde and de Broqueville, Experimental investigation of a rotating fluidized bed in a static geometry, 426–435, Copyright (2008) with permission from Elsevier.)[28]

Vortex chambers have also been tested for liquid–solid fluidization. In this case, both rarefied and condensed stable states of the particle bed have been observed, the rarefied states being different with large and small particles (see Goldshtik *et al.*).[23]

12.3.5 Meso-Scale Non-Uniformities

Meso-scale non-uniformities in the form of bubbles are well known to appear in conventional fluidized beds. Their presence is detrimental for the conversion of heterogeneous catalytic reactions. High-G operation was shown to result in improved particle bed uniformity, bubble formation to a certain extent being suppressed. In cases where bubbles are formed in RFB-SGs, they are formed in the vicinity of the gas inlet slots and they propagate both tangentially and radially through the particle bed (Figure 12.8). Bubble formation in RFB-SGs strongly depends on the type of particles fluidized and the vortex chamber design. De Wilde and de Broqueville[19] observed complete absence of bubbles with 1G-Geldart D-type, 3 mm diameter PE pellets in a 24 cm diameter, 5 cm long vortex chamber with 12 gas inlet slots,

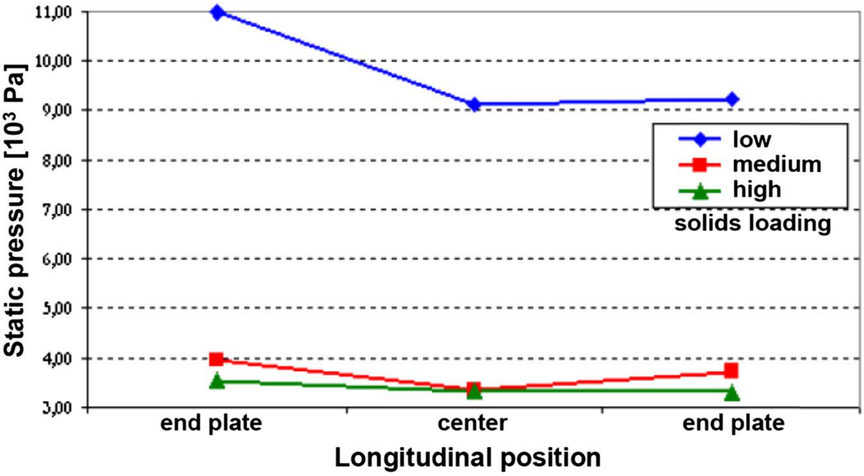

Figure 12.7 Static pressure at the outer cylindrical wall of the vortex chamber. Indication of channeling at low solids loadings. Total gas flow rate of 0.2 Nm^3 s^{-1} and 2–5 mm polymer pellets. Vortex chamber design: see Figure 12.3. (De Gruyter [International Journal of Chemical Reactor Engineering], Walter De Gruyter GmbH Berlin Boston, [2007]. Copyright and all rights reserved. Material from this publication has been used with the permission of Walter De Gruyter GmbH.)[37]


$t=0\cdot10^{-3}$ s $t=8\cdot10^{-3}$ s $t=16\cdot10^{-3}$ s

Figure 12.8 Bubble formation and motion in an RFB-SG visualized by means of a high speed CCD camera at 1000 frames s^{-1} focusing on the vicinity of a single gas inlet slot. Vortex chamber design: see Figure 12.2. Total gas flow rate: 0.2 m^3 s^{-1}, solids loading: 1.1 kg, 300 μm alumina particles. (From De Wilde.)[32]

3 mm wide each. Using the same vortex chamber with 1G-Geldart B-type, 300 μm diameter alumina particles, significant bubble formation was observed (Figure 12.8).

Crucial in suppressing bubble formation and improving the particle bed uniformity in RFB-SGs is the hydrostatic pressure drop over the particle bed which is determined by the solids loading in the vortex chamber and the particle bed rotational speed. Working with 70 and 85 μm FCC catalyst, Trujillo and De Wilde[30] demonstrated the role of the vortex chamber design.

12.3.6 Further Remarks on the Gas and Solids Phase Flow Pattern

The flow pattern in RFB-SGs deserves some further discussion. It is crucial for modeling RFB-SGs and for evaluating their potential for given applications. As mentioned in Section 12.3.2, the gas phase flow pattern changes drastically with the presence of particles in the vortex chamber. CFD and experimental studies have shown that upon contact with the particle bed, the gas injected tangentially at high velocity is rapidly tangentially decelerated. This is reflected in a deflection of the flow path in the radial direction, as seen in Figure 12.9(a). Additional deflection in the radial direction is observed when the gas injected *via* a given gas inlet slot approaches the next gas inlet slot. As a result, mixing between gases injected *via* successive gas inlet slots is very limited. This is illustrated in Figure 12.9(a), showing the gas phase concentration of a tracer component A (red) that was injected through two of the gas inlet slots only.[32] The results of this CFD study were confirmed by experiments with a smoke tracer (Figure 12.9(b)). Hence, a plug flow type flow pattern for the gas phase in the RFB-SG may be a reasonable approximation for a first evaluation of the performance of RFB-SGs, provided that bubble formation can be avoided.

The particle bed and gas phase hydrodynamics are very different. Mixing in the particle bed is pronounced. In the tangential direction mixing is dominated by the particle bed rotational motion. In the radial direction, shear in the particle bed and radial fluidization contribute to the mixing. De Wilde[32] studied the particle bed mixing by means of step response experiments with colored particles. A response approaching that of a perfectly mixed particle bed was found at sufficiently high particle bed rotational speeds, that is, at sufficiently high gas flow rates (Figure 12.10). Staudt *et al.*[38] developed an RFB-SG reactor model based on the assumption of a well-mixed particle bed and a plug flow type behavior of the gas phase. It was used to evaluate the potential of RFB-SGs for the low-temperature pyrolysis and gasification of biomass. The assumption of a well-mixed particle bed was justified from a comparison of the time scales of reaction and mixing, the particles making on average multiple turns in the vortex chamber while reacting. With poly-disperse particles, segregation occurs in the vortex chamber and the assumption of a well-mixed particle bed may no longer hold. Grain cleaning in vortex chambers makes use of the segregation between the grain particles and impurities such as seeds.[35]

With decreasing particle size and/or density, achieving a dense and uniform particle bed becomes increasingly difficult. Radial fluidization of the particle bed cannot be avoided and a complex particle bed density profile develops. This was confirmed by rapid camera observations (*viz.* Figures 12.5 and 12.8) and CFD simulations. Anderson *et al.*[17] carried out X-ray absorption experiments to determine the particle bed density profiles in rotating fluidized beds of fine powders: talc (d_p = 20 μm, ρ_s = 2700 kg m^{-3}), tungsten (d_p = 12 μm, ρ_s = 19 100 kg m^{-3}), and zinc (d_p = 10 μm, ρ_s = 7000 kg m^{-3}).

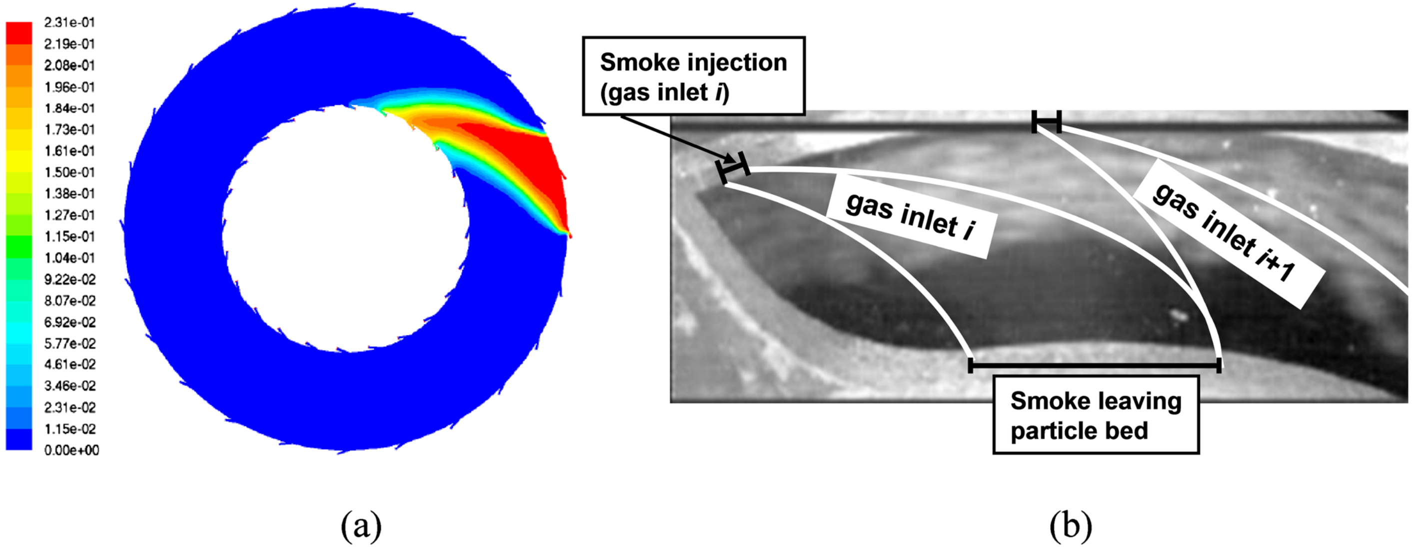

Figure 12.9 Visualization of the gas phase flow pattern in an RFB-SG. (a) CFD simulation of the motion of a tracer injected *via* two of the gas inlet slots. (b) Experiments with smoke injection *via* one of the gas inlet slots. (From De Wilde.)[32]

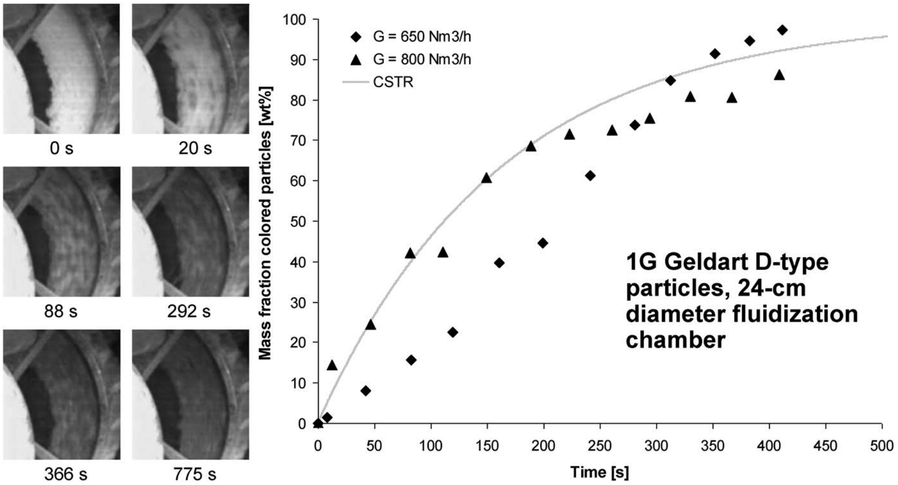

Figure 12.10 Particle bed mixing in RFB-SGs. Response in the mass fraction of colored particles at the outlet to a step change in the color of the particles fed at $t = 0$ s. Data at different gas flow rates and comparison with the theoretical curve for a well mixed particle bed. Vortex chamber design: see Figure 12.3. Experiments with 2–5 mm polymer pellets. (From De Wilde.)[32]

Figure 12.11 shows a picture of a rotating particle bed of talc powder and the radial profiles of the axially-, tangentially- and time averaged particle bed density at different solids loadings measured by X-ray absorption. Typical particle bed density contours deduced from the X-ray absorption measurements are shown in Figure 12.11(c). The gas jet entering the chamber causes significantly lower particle bed densities along the wall (see also Figure 12.8). Also, accumulation of particles is observed, upstream of the region where most of the gas injected *via* a given slot deflects radially into the particle bed, that is, upstream of the next gas inlet slot. Referring to Figure 12.11, note that the loosely packed bed density of talc is about 0.5 gm cm^{-3}, so that quite dense rotating fluidized beds of fine particles could be obtained.

Axial uniformity in the vortex chamber is an extremely challenging issue. Near the end walls, friction reduces the rotational motion, generating a boundary layer flow. Figure 12.12 shows the axial profiles of the radial gas velocity in the absence and presence of 2–5 mm diameter wheat grain particles (the chamber length was 26 mm). The presence of a rotating particle bed improves the axial uniformity in the vortex chamber. Nevertheless, a reduction of the centrifugal acceleration can cause a lack of cyclostrophic balance. As such, a secondary flow of particles towards the axis can be generated along the end walls.[23] This phenomenon becomes the more important with decreasing particle size and can cause an excessive loss of particles *via* the chimney. Ways to adapt the vortex chamber design to reduce this effect are discussed in Section 12.4.

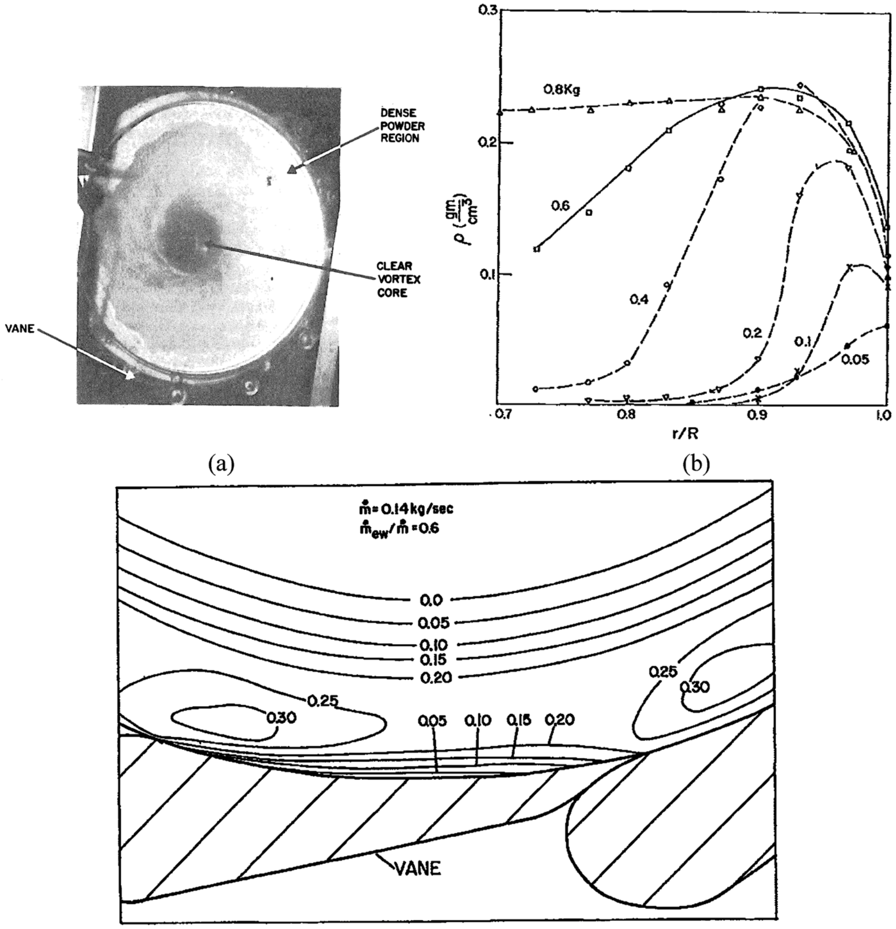

(a) (b)

(c)

Figure 12.11 Fluidization of fine talc powder ($d_p = 20\ \mu\text{m}, \rho_s = 2700\ \text{kg m}^{-3}$) in a vortex chamber. Vortex chamber: $D = 30.5$ cm, $L = 6.3$ cm, $ns = 0.36$ cm, $\lambda = 0.00376$. Operating conditions: total gas flow rate: 0.117 $\text{Nm}^3\ \text{s}^{-1}$, solids loading: 0.05–0.8 kg. (a) Picture of the rotating particle bed; (b) radial profiles of the axially-averaged particle bed density at different solids loadings measured by X-ray absorption (100 kV, 15 ma, typical exposure time: 1 s); (c) typical particle bed density contours deduced from X-ray absorption measurements for a solids loading of 0.4 kg. (From Anderson *et al.* with permission from the American Institute of Aeronautics and Astronautics (AIAA).)[17]

Volchkov *et al.*[35] pointed out the similarity between fluidization in a vortex chamber and vibrational fluidization. This is due to the motion of the particle bed with respect to the gas inlet slots, particles moving periodically through zones where the aerodynamic forces are sufficient and insufficient for fluidization of the bed and particles periodically interacting with the wall. The importance of this effect depends on the characteristics of the particles

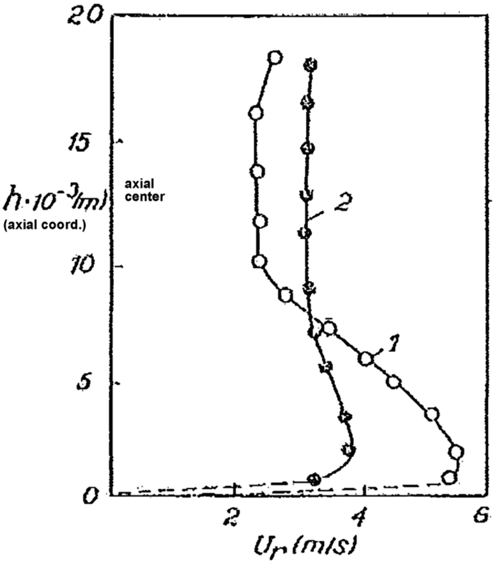

Figure 12.12 Illustration of boundary layer flow. Experimentally measured axial profiles of the radial gas velocity. 1. In the absence of particles; 2. In the presence of particles. Vortex chamber: $D = 20$ cm, $L = 2.6$ cm, $D_c = 10$ cm, $n > 20$, $\lambda = 0.0518$. Operating conditions: solids loading: 0.15 kg of wheat grain particles ($\rho_s = 1200$ kg m^{-3}, $d_p = 2$–5 mm). (Adapted from Volchkov *et al.* Taylor & Francis Ltd. http://www.informaworld.com.)[18]

fluidized. Observations and calculations by Volchkov[35] in the context of grain drying and cleaning show that (radial) fluidization of the bed can occur even in cases when the aerodynamic forces calculated with the mean gas velocity are substantially smaller than the centrifugal force. Volchkov *et al.*[35] adapted a criterion for vibrational fluidization for application to RFB-SGs.

12.4 Design Aspects

12.4.1 Design Objectives

The design of an RFB-SG aims at (i) maximizing the particle bed density and improving the particle bed uniformity and (ii) independently controlling the gas and solid phase residence times. Both (i) and (ii) imply minimizing the loss of solids *via* the chimney, serving as the main gas outlet.

12.4.2 Gas Inlets

The gas inlet design is one of the important factors determining the solids retention capacity of vortex chambers. The number (n) and size (s) of gas inlet slots of vortex chambers that have been studied cover a wide range.

Kochetov *et al.*[15,16] originally started from a vortex chamber with a single gas inlet slot and then added inserts to increase the number of gas inlet slots to 5 or 6. They also considered a non-uniform distribution of the gas inlet slots to reduce the effect of gravity and the solids losses *via* the chimney. Note that at sufficiently high particle bed rotational speed (high-G), the effect of gravity should be negligible. As seen from Figure 12.13(b), with a single gas inlet slot, the particle bed is strongly non-uniform and the gas–particle contact poor. From theoretical considerations, Sazhin *et al.*[34] conclude that at least 4 gas inlet slots are required to obtain an axisymmetric radial outflow from the vortex chamber. Experimental observations by Kochetov *et al.*[15,16] and Trujillo *et al.*[33] confirm an initial drastic improvement of the particle bed uniformity with increasing number of gas inlet slots. Figure 12.13(c) shows the effect of the gas inlet design on the solids retention capacity, *i.e.* at zero solids feeding rate, as a function of the gas flow rate. It is important to mention that Kochetov *et al.*[15] observed an increase of the solids retention capacity with increasing gas flow rate up to a certain gas flow rate only. In this gas flow rate range, the influence of gravity cannot be neglected. At gas flow rates sufficiently high for the effect of gravity to become negligible, the solids retention capacity is seen to become nearly independent of the gas flow rate (Figures 12.13(c) and 12.14(a)), as explained in Section 12.3.3. The influence of gravity

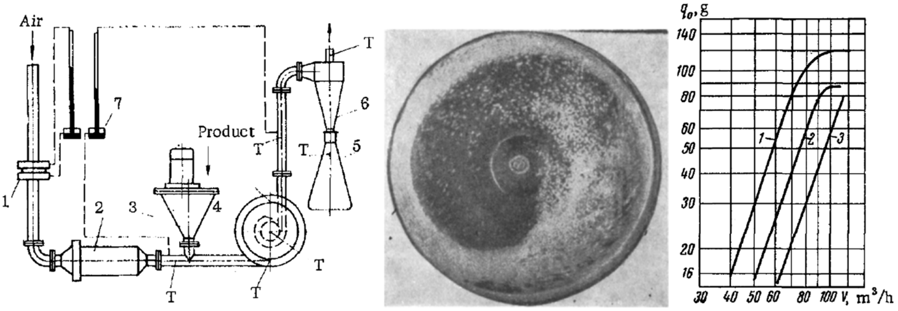

(a) (b) (c)

Figure 12.13 (a) and (b): A rotating particle bed in a vortex chamber with a single gas inlet slot, tangentially injecting the gas–solid mixture. Vortex chamber: $D = 24$ cm, $L = 3.5$ cm, $ns = 1.5$ cm, $\lambda = 0.02$. (From Chemical and Petroleum Engineering, Hydrodynamics and heat exchange in vortex drying chambers, 5, 1970, Kochetov *et al.*, Figures (a) and (b) with permission of Springer.)[16] (c) Solids retention capacity (zero solids feeding rate) as a function of the air flow rate for different gas inlet configurations: 1. Five gas inlet slots in the lower part of the chamber; 2. One single gas inlet slot; 3. Six uniformly distributed gas inlet slots. Vortex chamber as in (a) and (b), but $ns = 2$ cm, $\lambda = 0.027$. (c) Reproduced from Chemical and Petroleum Engineering, 5, L. M. Kochetov *et al.*, Experimental determination of the optimal ratios of structural dimensions in the whirl chamber for drying granular materials, Copyright (1969) with permission from Elsevier.[15]

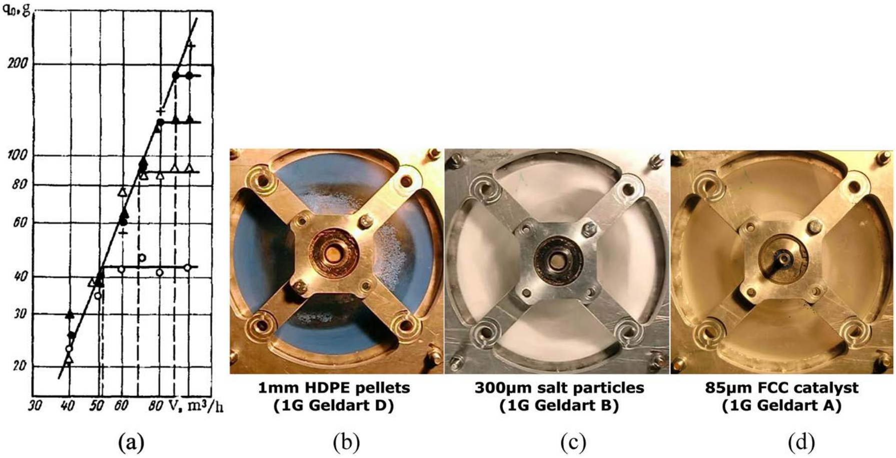

(a) (b) (c) (d)

Figure 12.14 Fluidization of different types of particles in a vortex chamber of given design. (a) Solids retention capacity (zero solids feeding rate) as a function of the air flow rate. Polystyrene particles: ○ d_p = 0.25–0.5 mm; △ d_p = 0.5–1.0 mm; ▲ d_p = 1.2–1.5 mm; ● d_p = 1.5–2.0 mm. Vortex chamber: D = 24 cm, L = 3.5 cm, ns = 1.5 cm, λ = 0.02. (From Kochetov *et al.*)[16] (b)–(d) Fluidization at given gas (700 Nm^3 h^{-1}) and solids (8.35 g s^{-1}) feeding rates. Vortex chamber: D = 24 cm, L = 5 cm, n = 24, s = 3 mm, λ = 0.096. (From Trujillo and De Wilde.)[30,32]

also explains why Kochetov *et al.*[15] observed a superior performance in terms of solids retention capacity with 5 gas inlet channels located in the lower part of the vortex chamber and with a single gas inlet channel also located in the lower part of the vortex chamber than with 6 uniformly distributed gas inlet channels. Indeed, as seen in Figure 12.13(c), the performance of the chamber with 6 uniformly distributed gas inlet channels starts to catch up with the other vortex chamber configurations at high gas flow rates. As mentioned earlier, high-G operation is the focus of this chapter. In later work on the drying of granular materials in vortex chambers, Kochetov *et al.*[16] stress the necessity of using multiple gas inlet channels when drying fine particles. Volchkov *et al.*[18] also indicated that a sufficiently high number of gas inlet slots (>20) is required to optimize the circulation rate of the particle bed for a given gas flow rate per unit chamber length.

The optimization of the gas inlet design is complex as it involves both the number and size of the gas inlet slots. For a given gas flow rate per meter length vortex chamber, the fraction λ of the chamber circumference taken by the gas inlet slots ($\lambda = ns/\pi D$) is an important design parameter and determines the gas injection velocity and as such the amount of tangential momentum injected into the chamber. Carrying out experiments with a variety of vortex chambers, Kochetov *et al.* (1969a) found an optimal value of λ between 0.025 and 0.038. In their experiments with fine talc (d_p = 20 µm, ρ_s = 2700 kg m^{-3}), tungsten (d_p = 12 µm, ρ_s = 19 100 kg m^{-3}), and zinc (d_p = 10 µm, ρ_s = 7000 kg m^{-3}) powders, Anderson *et al.* (1972) used a vortex chamber with a much smaller λ of 0.00376 (the vortex chamber was equipped with 12 slots of 0.3 mm only – see Figure 12.11). Volchkov *et al.*,[18] on the other hand, used vortex chambers with relatively large λ (between 0.05 and 0.1). Proper functioning with different types of relatively large particles only (d_p = 2–8 mm – sand, corn, wheat grain, plastic) was, however, reported. Trujillo and De Wilde[30] revealed that as the particle size and/or density reduce(s), the maximum allowable λ decreases and derived a theoretical design criterion. Focusing on the optimal number of gas inlet slots (n), from theoretical calculations and considering relatively large particles (≥100 µm), Sazhin *et al.*[34] conclude that for a given λ, increasing the number of gas inlets slots above 4 does not lead to a further improvement of the particle bed uniformity and/or rotational speed. Experimental studies by De Wilde and de Broqueville[19] and Trujillo *et al.*[33] showed, however, that, in particular when fluidizing fine particles, a higher number of gas inlet slots is advantageous. Achieving a sufficiently low value of λ then requires extremely small gas inlet slot widths (see *e.g.* Figure 12.16 discussed later).

Particle entrainment into the chimney and the gas inlet design are seen to become the more critical with decreasing particle size and/or density. This is illustrated in Figure 12.14(a)–(d) focusing on the performance of a vortex chamber of given design with different types of particles. Figure 12.14(a) compares the solids retention capacity (zero solids feeding rate) as a function of the gas flow rate when fluidizing different fractions of polystyrene.[16] The solids retention capacity (at sufficiently high gas flow rates) is seen to decrease significantly with decreasing particle size. As shown in Figure 12.14(b)–(d), the sensitivity with respect to the particle characteristics was confirmed when feeding solids continuously, operating at given gas and solids feeding rates.[30] Note the relatively large value of λ (0.096) in this case and that no particle bed could be obtained with the 70 µm FCC catalyst particles.

A force balance determines whether particles will be entrained into the chimney and as such determines the particle bed density and uniformity. To avoid such entrainment, the centrifugal force should at least compensate the radial gas–solid drag force. Both forces are generated by the gas flow, but the ratio of the centrifugal force and the radial gas–solid drag force can be modified by the RFB-SG design and in particular the gas inlet design. The particle bed rotational speed is determined by the amount of tangential momentum injected with the gas ($S_{inj}\rho_{inj}u_{inj}u_{inj}$ with S_{inj} the total gas inlet surface area, $S_{inj} = nsL$). For a given gas mass flow rate fed ($S_{inj}\rho_{inj}u_{inj}$) the amount of tangential momentum injected can, hence, be varied by changing u_{inj} *via* S_{inj}. The latter is determined by the number of gas inlet slots and their size. Design criteria accounting for the particle characteristics were derived by Trujillo and De Wilde.[30] The required gas inlet slot width is seen to decrease with decreasing particle size, as illustrated in Figure 12.15.

Trujillo and De Wilde[30,39] experimentally demonstrated the impact of the gas inlet design on the particle bed rotational speed and the related solids losses *via* the chimney and particle bed density and uniformity. Figure 12.16 shows the particle bed obtained with 70 µm FCC catalyst powder for given

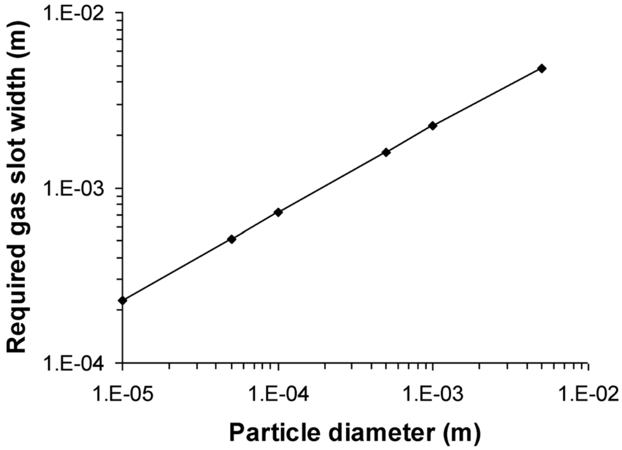

Figure 12.15 Theoretical relation between the gas inlet slot width and the particle diameter. Case study: $\rho_s = 1500$ kg m^{-3}, $\rho_g = 1$ kg m^{-3}, $d_t = 0.24$ m, $\varepsilon_s = 0.35$, $n = 72$, $f_{tm} = 12.5\%$.

operating conditions and using different gas inlet slot designs. By reducing the gas injection surface area and as such increasing the gas injection velocity, the ratio of the centrifugal force and the radial gas–solid drag force could be increased and a dense and stable rotating particle bed could be obtained—as theoretically predicted. Similar observations were made by Ekatpure *et al.*[40] With 70 μm FCC catalyst particles, no stable bed could be obtained using a vortex chamber with $\lambda = 0.127$ (36 × 6 mm slots in a 0.54 m diameter vortex chamber). Reducing the slot size to 2 mm (and as such λ to 0.042) allowed a stable bed to be obtained. With heavier polymer particles ($\rho_s = 950$ kg m^{-3}, $d_p = 0.9$, 1.6 and 2.4 mm), a stable bed could also be obtained in the vortex chamber with $\lambda = 0.127$. The influence of the gas inlet design and resulting gas injection velocity on the solids loading in the vortex chamber as a function of the solids feeding rate is quantitatively shown in Figure 12.16(b). The effect of the balance between centrifugal force and radial gas–solid drag force on the suppression of meso-scale non-uniformities is equally important. In the experiments of Anderson *et al.*,[17] for example, there was little indication of bubbling when fluidizing fine talc ($d_p = 20$ μm, $\rho_s = 2700$ kg m^{-3}), tungsten ($d_p = 12$ μm, $\rho_s = 19100$ kg m^{-3}), and zinc ($d_p = 10$ μm, $\rho_s = 7000$ kg m^{-3}) powders in a vortex chamber with a small λ of 0.00376, in contrast to observations in vortex chambers with larger λ[19] (De Wilde, – see Figure 12.8[32]).

Another important aspect of RFB-SGs is the axial uniformity of the particle bed and channeling, as described in Section 12.3.4. Studying the drying of granular material ($d_p = 3.5$ mm, $\rho_s = 1420$ kg m^{-3}) in a drying chamber with a relatively large λ of 0.1, Dvornikov and Belousov (2011) measured the mean particle bed rotational speed near the end wall and in the axial center of the vortex chamber by means of laser Doppler velocimetry (LDV) and a rotating antenna, respectively. Significantly higher mean particle bed rotational speeds were observed in the axial center of the vortex chamber than near

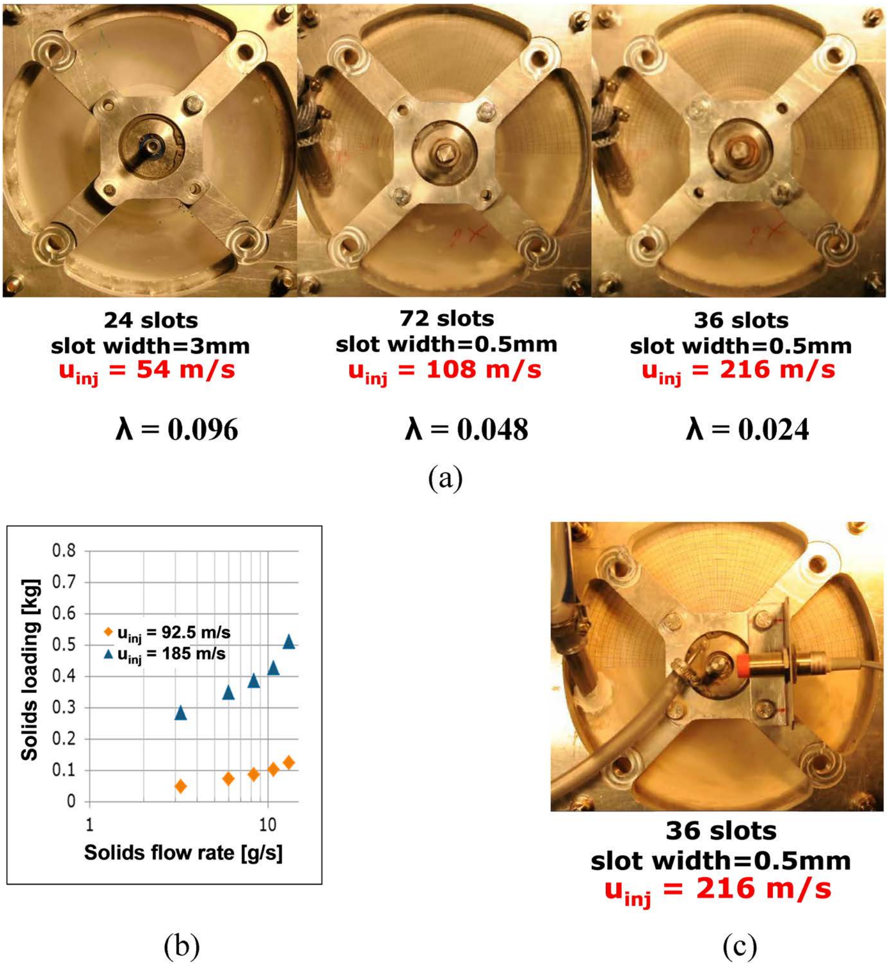

Figure 12.16 Influence of the gas inlet design and resulting gas injection velocity on the solids retention in the vortex chamber for given gas and solids feeding rates. (a) Solids feeding rate: 8.35 g s^{-1}; (b) varying solids feeding rate; (c) solids feeding rate: 20.08 g s^{-1}. Other vortex chamber characteristics and operating conditions: see Figure 12.14. (From Trujillo and De Wilde.)[30,32]

the end walls, despite the use of relatively heavy particles. Trujillo and De Wilde[30] compared the particle bed rotational speed near the end wall (measured using a high speed CCD camera) and in the axial center of the bed (measured using a rotating antenna) for different vortex chamber gas inlet designs. Figure 12.17 illustrates their findings. A sufficiently high pressure drop over the gas inlet slots is required to assure a uniform distribution of the gas (and solids). Again, it can be theoretically shown that with decreasing particle size, the maximum allowable λ guaranteeing axial uniformity decreases, consistent with experimental observations.[30] It should finally be remarked that there are construction limits to be accounted for. With a

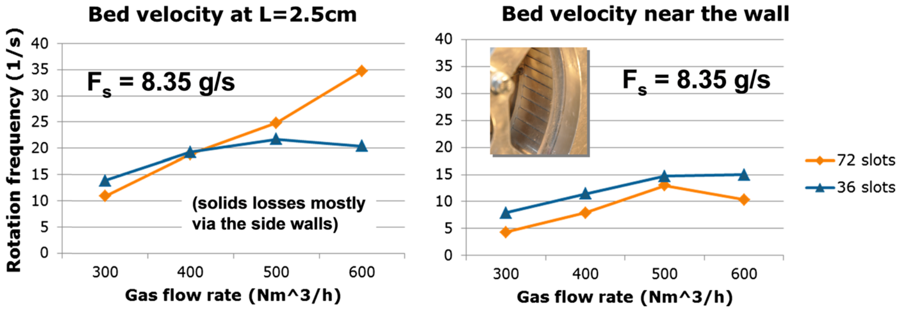

Figure 12.17 Particle bed rotation frequency as a function of the gas flow rate with two different gas inlet designs (36 and 72 × 0.5 mm gas inlet slots). Comparison of the rotation velocity near the end wall (right) and the axial center of the bed (left) to detect channeling. Other vortex chamber characteristics and operating conditions: see Figure 12.14. (From Trujillo and De Wilde.)[30,32]

limited number of gas inlet slots, high gas injection velocities and pressure drops over the gas inlets can be achieved with relatively large slots (*e.g.* 4 slots of minimum 5 mm in Sazhin *et al.*[34]). In cases where more gas inlet slots are required to assure tangential particle bed uniformity, the slot size has to be reduced to maintain high gas injection velocities and pressure drops over the gas inlets. The construction and operation of vortex chambers with slot widths below 0.2 mm is challenging.

12.4.3 Gas Outlet/Chimney

Often, radial entrainment of solids cannot be avoided completely. This is particularly true near the end walls where friction reduces the particle bed rotational motion and the resulting centrifugal acceleration. The lack of cyclostrophic balance generates a secondary, or boundary layer flow of particles towards the axis along the end walls.[23] The chimney design is crucial in minimizing the rate of solids losses *via* the chimney. A variety of designs has been developed and tested. A first category makes use of a cyclone flow exit tube with a guide slot, as for example shown in Figures 12.1, 12.2 and 12.19. A second category is that of the vortex finder, an open-ended tube which enters the chamber over a small length, as such avoiding particles entrained along the end wall connected to the chimney, to enter directly into the chimney. Loftus *et al.*[20,33] found the vortex finder to improve the bed stability and to be more efficient in reducing the solids losses *via* the chimney than a cyclone flow exit tube with a guide slot. Note that the secondary flows near the end walls can be used to remove the heavy phase from the chamber, largely separated from the light phase, as shown in Figure 12.19.

A particle entrained into the particle bed freeboard region can be recovered by the bed, making use of the Coriolis effect. To take advantage of this effect before losing the particle into the chimney, the latter must be sufficiently small, as shown in Figure 12.18. This comes at the cost of an increased pressure drop over the chimney. Testing a variety of chamber dimensions, Kochetov *et al.*[15] found an optimum chimney diameter between 0.3 and 0.5 times the gas distribution chamber diameter. Too high a pressure drop over the chimney can be avoided by using a dual-chimney design, as shown in Figure 12.19.[20] Experiments by Loftus *et al.*[20] confirm that the bed stability and solids retention can be improved by reducing the chimney diameter. If the solids concentration in the freeboard region is sufficiently low, a flow pattern close to free vortex develops in this region. This is particularly advantageous for recovering particles, their rotational speed increasing with decreasing distance from the chimney. In such case, the dense particle bed rotational motion is driven by two mechanisms acting on two of its boundaries: (i) by the tangential injection of gas and (ii) by the free vortex in the particle bed freeboard region.

Studying the aerodynamics and mass and heat transfer of gas–solid fluidized beds in vortex chambers, Volchkov *et al.*[18] considered profiling the end wall of the RFB-SG connected to the chimney to balance the centrifugal force and the radial gas–solid drag force throughout the vortex chamber. Indeed, as the process gas moves radially inwards, the radial gas velocity and related radial gas–solid drag force increase if the decrease of the circumference is not compensated for by profiling the end wall. A profiled end wall was also used by Kuzmin *et al.*[21] in their investigation of a vortex type gas–liquid bubbling reactor. The calculation of the end wall profile by Kuzmin *et al.*[21] was

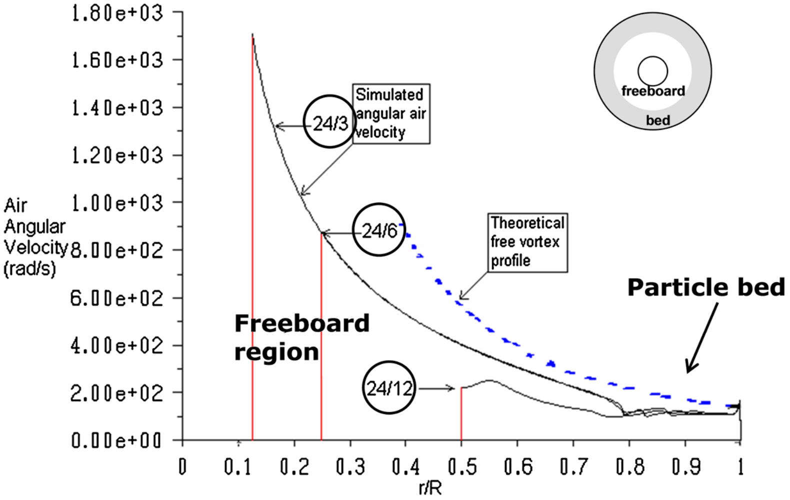

Figure 12.18 Influence of the chimney diameter on the radial profile of the angular velocity in the particle bed freeboard region. CFD simulations of a 24 cm diameter vortex chamber with three different chimney diameters: 3, 6 and 12 cm. Comparison at equal gas flow rate and solids loading of 60 μm FCC catalyst. (From Trujillo *et al.*)[33]

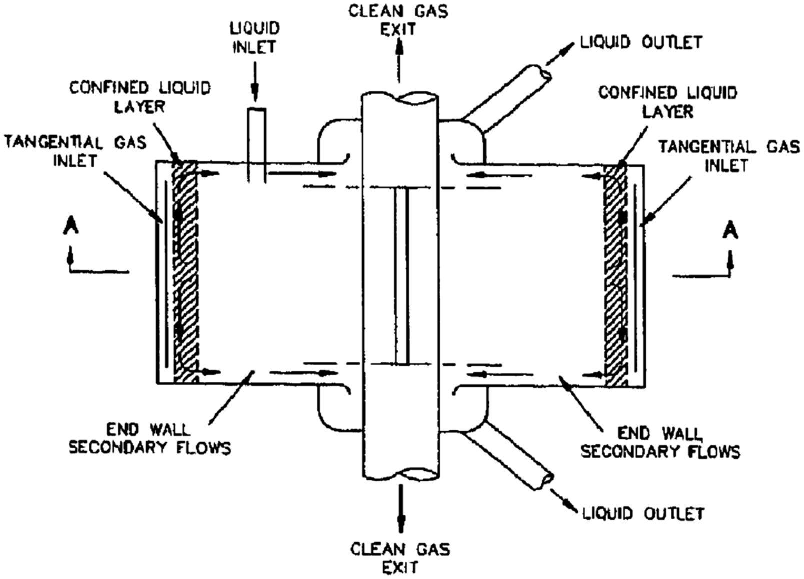

Figure 12.19 Dual-chimney design with cyclone flow exit tube with a guide slot. Gas–liquid flow with specific liquid outlet design. (Reproduced from Loftus *et al.* with permission from John Wiley and Sons. Copyright © 1992 American Institute of Chemical Engineers.)[20]

based on a solid body type behavior of the gas–liquid bed. Kuzmin *et al.*[21] found the influence of profiling the end wall to be important and positive. With gas–solid flows, profiling the end wall has, however, the disadvantage of destroying a free vortex type flow pattern in the particle bed freeboard region. This may as such lead to an increase of the entrainment of solids into the chimney. To avoid such entrainment, Kuzmin *et al.*[21] proposed to mount a concentric ring at the inner boundary of the profiled end wall (Figure 12.20). Such a concentric ring can also be used with flat end walls.[15]

To suppress the boundary layer flow causing particle losses *via* the chimney, a particular chimney design was developed by Anderson *et al.*[17] in their experiments with fine talc (d_p = 20 μm, ρ_s = 2700 kg m^{-3}), tungsten (d_p = 12 μm, ρ_s = 19 100 kg m^{-3}), and zinc (d_p = 10 μm, ρ_s = 7000 kg m^{-3}) powders. As shown in Figure 12.21(a), suppressing the boundary layer flow is achieved by positioning additional nozzles for secondary gas injection concentric with the gas outlet which is located centrally at the end of a tapered annex. Figure 12.21(b) illustrates the influence of the secondary gas injection on the rate of solids losses *via* the chimney. A rate coefficient for the particle losses *via* the chimney is defined based on the experimentally observed exponential decrease of the solids loading in the vortex chamber when stopping the solids feeding at (initial) solids loading M_0 to be $M = M_0 \exp[-kt]$. A certain amount of secondary gas injection permits significantly reducing the rate of solids losses *via* the gas outlet for a given solids loading in the vortex chamber. At sufficiently high secondary gas injection flow rates, however, the influence

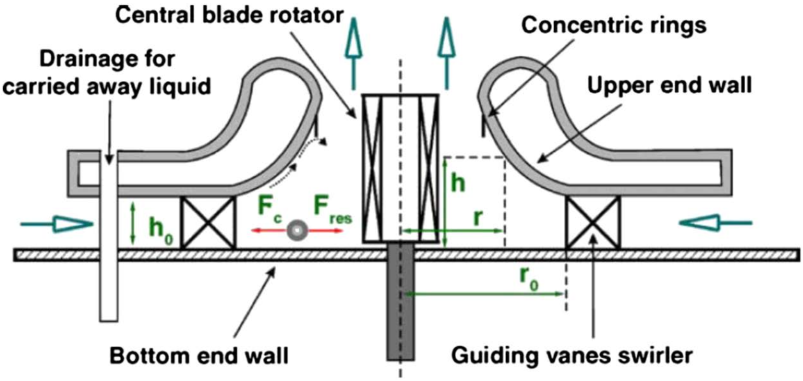

Figure 12.20 Profiled end wall and concentric ring. (Reprinted from Chemical Engineering Journal, 107, Kuzmin *et al.*, Vortex centrifugal bubbling reactor, 55–62, Copyright (2015) with permission from Elsevier.)[21]

of a further increase of the secondary gas injection flow rate is limited and it is mainly the total gas flow rate that determines the solids retention in the vortex chamber, at least up to a certain gas flow rate (see Section 12.3.3).

12.4.4 Solids Inlet

Focusing on continuous operation, it was found that the solids feeding can disturb the particle bed. Hence, a careful solids inlet design is required. Two options will be discussed here, keeping in mind that other solutions may exist. A first possibility is to inject the solids *via* an inlet tube pierced through one of the end walls, eventually under an angle to introduce them with a tangential velocity component as well. This type of solids inlet can be positioned in the particle bed freeboard region. A peripheral slot in one of the end walls has been used as well.[41] It is important to note that solids feeding typically hardly contributes to the amount of tangential momentum injected in the vortex chamber. End wall solids inlet configurations were shown to function correctly with a variety of particles in a relatively wide range of solids feeding rates.[19,28,30,41,42] At too high solids feeding rates, the impact of the side solids injection on the particle bed hydrodynamics may, however, become too important and the particle bed uniformity may be lost. Direct entrainment of the solids feed into the chimney outlet should also be avoided. In their biomass drying experiments, Eliaers and De Wilde[43] observed this phenomenon. It resulted in part of the biomass feed bypassing the particle bed which was reflected in the distribution of the humidity of the biomass leaving the drying chamber, as shown in Figure 12.22. Note that Kuzmin *et al.*[21] used end wall liquid injection when studying a vortex chamber-based gas–liquid reactor.

An alternative way of injecting the solids is *via* the outer cylindrical wall of the vortex chamber, *via* separate inlet slots or with the gas. Volchkov *et al.*[18] fed the solids in the axial center of the vortex chamber through the outer cylindrical wall, but it is unclear whether separate slots for the solids were used or whether the solids were fed with the gas. Of course, when feeding

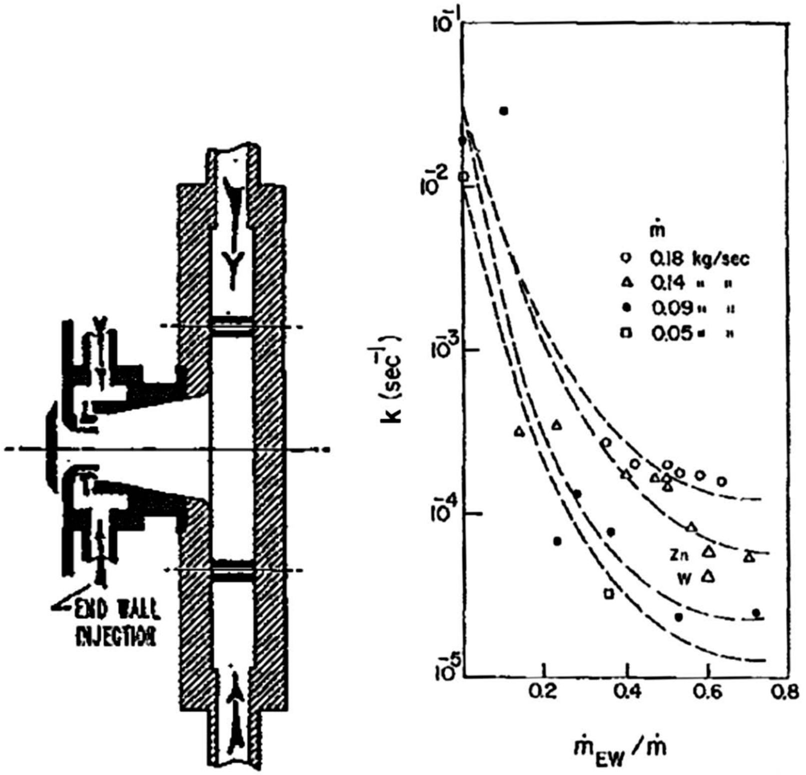

(a) (b)

Figure 12.21 Vortex chamber with secondary gas injection *via* additional nozzles positioned concentric to the central gas outlet at the end of a tapered annex. (a) Schematic representation; (b) rate coefficient for particle losses *via* the gas outlet (chimney) as a function of the normalized secondary gas flow rate for different total gas flow rates. $\dot{m}_{\mathrm{EW}}$: secondary (end wall) gas flow rate; $\dot{m}$: total gas flow rate. (From Anderson *et al.* with permission from the American Institute of Aeronautics and Astronautics (AIAA).)[17]

solids *via* slots, their width must be sufficient to prevent blockage by particles. As discussed in Section 12.4.2, the width of the gas inlet slots is critical for obtaining a stable and dense rotating particle bed and the required gas inlet slot width depends on the particle characteristics, the required gas inlet slot width decreasing with decreasing particle size. Hence, feeding the particles *via* the gas inlet slots is not evident. Another issue is that in standard RFB-SG technology, the tangential momentum of the particle bed is to be supplied by the injected gas. CFD simulations by Trujillo and De Wilde[31] illustrated the disturbing effect on the particle bed hydrodynamics of feeding the solids radially *via* separate inlet slots in the outer cylindrical wall of the vortex chamber (Figure 12.23). Experimental tests and CFD simulations in

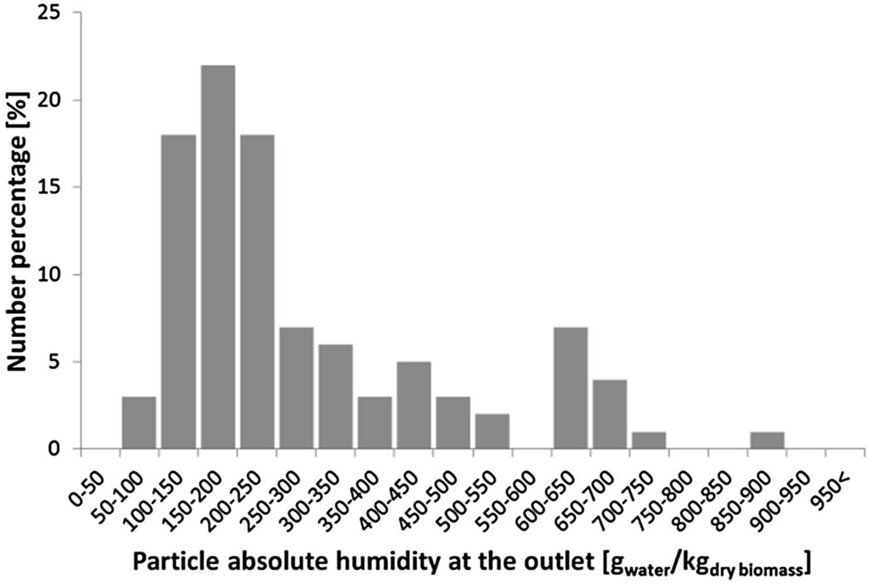

Figure 12.22 Drying of biomass in an RFB-SG. Bimodal distribution of the outlet biomass humidity indicating biomass bypassing the particle bed and going directly from the side solids inlet into the chimney. (From Eliaers and De Wilde. Taylor & Francis Ltd. http://www.informaworld.com.)[43]

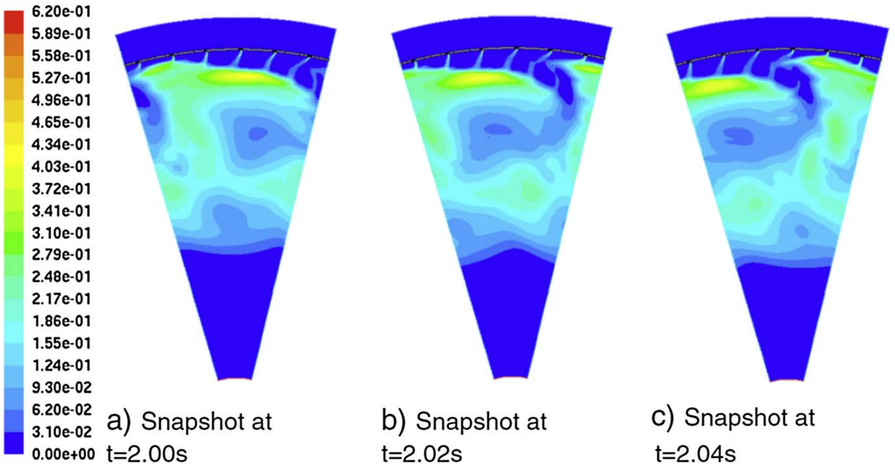

a) Snapshot at t=2.00s

b) Snapshot at t=2.02s

c) Snapshot at t=2.04s

Figure 12.23 CFD simulation of the gas–solid flow pattern in an RFB-SG. Evolution of the solids volume fraction in time. Vortex chamber diameter: 1.2 m, 72 × 0.5 mm gas inlet slots, 72 radial solids inlet slots, 80 µm FCC catalyst. (Reprinted with permission from Powder Technology, 221, Trujillo and De Wilde, Fluid catalytic cracking in a rotating fluidized bed in a static geometry: a CFD analysis accounting for the distribution of the catalyst coke content, 36–46, Copyright (2007) with permission from Elsevier.)[31]

which the solids were injected *via* the gas inlet slots showed, however, more positive results. As mentioned above, this imposes restrictions on the width of the gas inlet slots.

12.4.5 Solids Outlet

For processes requiring continuous solids feeding and removal, the solids outlet design is crucial. Different solids outlet designs have been reported in the literature. The solids can, for example, be removed *via* a tube pierced through one of the end walls. De Wilde and de Broqueville[19] demonstrated fluidization of 1G-Geldart D-type, 3 mm polymer pellets in an RFB-SG, continuously feeding and removing particles *via* a side solids inlet and a side solids outlet, respectively. With the vortex chamber design and type of particles used in those experiments, the particle bed freeboard region was free of particles and no solids losses *via* the chimney were observed. The radial position of the side solids outlet on the end wall was shown to affect the particle bed height, that is, the solids loading in the vortex chamber, for a given solids feeding rate.

When fluidizing lighter particles, alternative ways of removing the solids from the vortex chamber may have to be considered—*via* the chimney with the gas or even *via* a solids outlet in the outer cylindrical wall of the vortex chamber. In the context of the development of a vortex liquid piston engine, different configurations for combining in- and outflow *via* the slots were considered by Goldshtik *et al.*[23] A configuration with a divided channel was found to perturb the flow in the vortex chamber due to symmetry breaking. Evacuating the solids *via* the gas outlet (chimney) reduces the degree of freedom with respect to the residence time of the particles in the particle bed and forces the particles to enter the particle bed freeboard region. A too high solids concentration in the particle bed freeboard region will hinder a free vortex type flow pattern to develop in this region. This is detrimental for the particle bed density and stability and results in a reduction of the solids loading in the vortex chamber for a given solids feeding rate. When fluidizing smaller and/or lighter particles, the importance of boundary layer flows along the end walls for particle entrainment into the gas outlet has been recognized. Loftus *et al.*[20] took advantage of this effect to remove solids from the vortex chamber separately from the gas *via* a specially designed solids outlet to be used in combination with a vortex finder (Figure 12.19). Volchkov *et al.*[18] proposed a cyclone type system to recover the solids from the vortex chamber. The authors report that this configuration could be effectively implemented with different types of relatively large particles (d_p = 2–8 mm) – sand, corn, wheat grain and plastic. The behavior of this type of solids recovery system when fluidizing smaller/less dense powders remains to be studied. Dvornikov and Belousov[41] used an annular slot in one of the end plates to remove the solids. Again, only relatively large particles (d_p = 3.5 mm, ρ_s = 1420 kg m^{-3}) were used.

12.4.6 Other Design Aspects

Cylindrical, polygonal, or complex-shaped vortex chambers can be designed. Experimental and numerical studies showed that the polygonal design offers advantages with respect to the crucial transfer of tangential momentum from the injected gas to the particle bed.[32] In a cylindrical vortex chamber, friction with the wall in the immediate vicinity of the gas inlet slots hinders the tangential acceleration of the particles. The construction of the vortex chamber is also greatly facilitated by adopting a polygonal design and attrition in the particle bed may be reduced. Few data are available on this matter. De Wilde[44] reported a negligible amount of attrition in an experiment with 3 mm polymer pellets using a polygonal vortex chamber design. With 300 μm kitchen salt particles, some attrition was, however, observed.

The effect of the length of the vortex chamber was already briefly discussed in Section 12.4.2 on the gas inlet design. Increasing the pressure drop over the gas inlet slots allows improving the axial uniformity in the vortex chamber. There are, however, limits. Kochetov *et al.*[15] carried out experiments with different chamber designs and found that axial particle bed uniformity could only be guaranteed for chamber lengths below half the chamber diameter. More recent experimental data seem to confirm this limitation.[17–19,28,30,32]

When operating above atmospheric pressure, the process gas is fed to the vortex chamber from a gas distribution chamber. Different gas distribution chambers have been proposed in the literature, helix type as well as tangentially- and radially-fed. Trujillo and De Wilde[30] showed that if the pressure drop over the gas inlet slots of the vortex chamber is sufficiently high, *i.e.* if the gas injection surface area of the vortex chamber is sufficiently small, the impact of the type of gas distribution chamber used on the flow pattern in the vortex chamber is minor.

12.5 Intensification of Interfacial Mass and Heat Transfer

One of the advantages of fluidizing in a high-G field is that operation at higher gas–solid slip velocities is possible. This is in particular beneficial for interfacial mass and heat transfer, the coefficients of interfacial mass and heat transfer increasing with increasing gas–solid slip velocity. A theoretical and CFD study of the potential of RFB-SGs for intensifying interfacial heat transfer was presented by de Broqueville and De Wilde.[36] It was shown that the terminal velocity of the particles—which determines the maximum possible gas–solid slip velocity—is proportional to the square root of the centrifugal force. Furthermore, experimental observations with Geldart D- and B-type particles showed that the particle bed rotational speed in RFB-SGs is proportional to the gas flow rate in a wide range of gas flow rates.[28,30,42] Hence, there is a unique potential for intensifying interfacial mass and heat transfer when fluidizing particles in an RFB-SG. The CFD study of de Broqueville and De

Wilde[36] confirmed this potential. The response of the particle bed temperature to a step change in the fluidization gas temperature was simulated, both for a conventional fluidized bed and for an RFB-SG. The characteristics of the fluidization chambers simulated and the operating conditions used are summarized in Table 12.1. It was demonstrated that higher specific gas flow rates, *i.e.* per m^3 particle bed, and higher gas–solid slip velocities allowed the particle bed to heat up much faster in the RFB-SG than in the conventional fluidized bed (Figure 12.24). Furthermore, mixing in the particle bed, driven by the particle bed rotational motion (see also Section 12.3.6), results in an improved particle bed temperature uniformity (Figure 12.25).

The intensification of interfacial mass and heat transfer make RFB-SGs potentially interesting for the drying of granular materials. Kochetov *et al.*[16,18]

Table 12.1 Vortex chamber characteristics and operating conditions for the 2D CFD study of interfacial heat transfer. (Reprinted from Chemical Engineering Science, 64, de Broqueville and De Wilde, Numerical investigation of gas–solid heat transfer in rotating fluidized beds in a static geometry, 1232–1248, Copyright (2009) with permission from Elsevier)[36]

Conventional fluidized bed		Rotating fluidized bed in a static geometry
Gas distribution chamber	/	Outer diameter (m): 54×10^{-2} Number of gas inlets: 12 Gas inlet width (m): 3.5×10^{-2}
Fluidization chamber	Width (m): 15×10^{-2} Height (m): 50×10^{-2} Number of gas inlets: 7 Gas inlet width (m): 2×10^{-3}	Outer diameter (m): 36×10^{-2} Number of tangential gas inlet slots: 24 Gas inlet slot width (m): 2.3×10^{-3} Number of solids inlets: 24 Solids inlet slot width (m): 5×10^{-3}
Chimney	/	Diameter (m): $12–13 \times 10^{-2}$ Number of outlet slots: 1 Outlet slot width (m): 8×10^{-2}
Solid particles	Diameter (m): 700×10^{-6} Density (kg m^{-3}): 2500 Restitution coefficient for particle–particle collisions (e): 0.9 Specularity coefficient for particle–wall ($\o$): 0.2 Initial temperature (K): 300 Mass in the fluidization chamber (kg $m_{\text{length fluid.chamber}}^{-1}$): 33.75	Mass fed* to the fluidization chamber (kg $m_{\text{length fluid.chamber}}^{-1}$): 33.75 * fed during first 5.63 s of the simulation
Fluidization gas	Flow rate (m^3 (h $m_{\text{length fluid.chamber}})^{-1}$) (a) 195 (b) 540 (c) 1080 Temperature (K): 300 → 400 at time t_0	Flow rate (m^3 (h $m_{\text{length fluid.chamber}})^{-1}$): (a) 29 800 (b) 59 600

introduced vortex chamber technology for the removal of superficial moisture from several materials such as MSN copolymer, sulfanilamide, melalite, emulsion polystyrene or sand. Table 12.2 summarizes the results of Kochetov *et al.*,[16] using a vortex chamber as shown in Figure 12.13(b) but with multiple gas inlet slots when drying fine particles (5 gas inlet channels in the lower part of the chamber or 6 evenly distributed). Volchkov *et al.*[18] studied continuous sand drying. Few results of the drying of wheat grains were also reported. The experiments demonstrated that deep dehydration of sand ($\Delta\varphi$ = 0.15–0.2) can be achieved with particle residence times as small as 3–5 s. Volchkov *et al.* (1993) indicated that aerodynamic blow-off of superficial moisture could significantly contribute to the removal of water from the sand particles, in particular when operating at mild temperatures. So far, it is unclear to what extent the liquid droplets blown off evaporate. With grain materials, containing bound and capillary moisture, a number of measurements showed that fast initial drying can be achieved by using RFB-SGs, the rate of final drying being determined by intra-particle diffusion. Volchkov *et al.*[18]

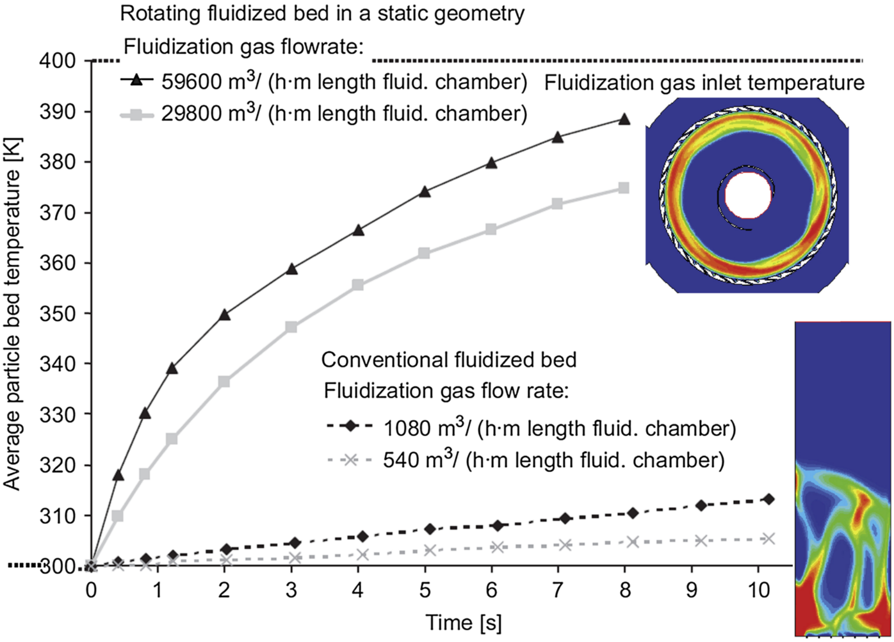

Figure 12.24 2D CFD simulations of the response of the average particle bed temperature to a step change in the gas phase temperature from 300 to 400 K at $t = 0$ s. Comparison of conventional fluidized bed and RFB-SG technology. Embedded figures in color: snapshot of the solids volume fraction profiles. Fluidization chamber design and operating conditions: see Table 12.1. (Adapted from Chemical Engineering Science, 64, de Broqueville and De Wilde, Numerical investigation of gas–solid heat transfer in rotating fluidized beds in a static geometry, 1232–1248, Copyright (2009) with permission from Elsevier.)[36]

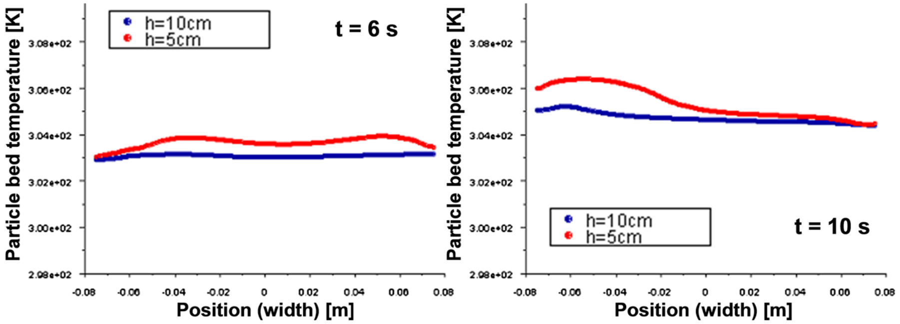

Conventional fluidized bed

Fluidization gas flow rate = $540\ \mathrm{m}^3 / (\mathrm{h} \cdot \mathrm{m}_{\text{length fluid. chamber}})$

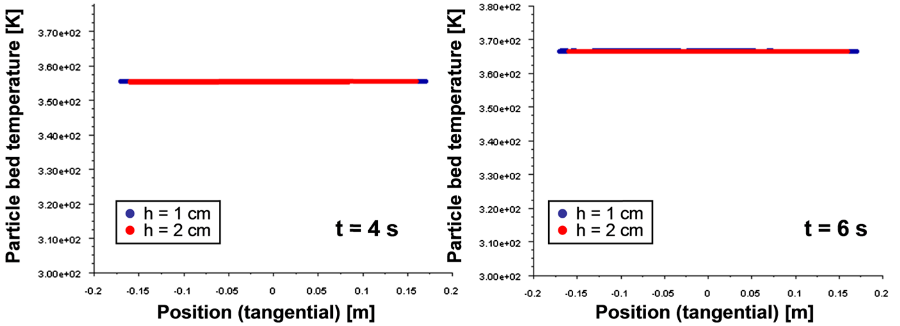

Rotating fluidized bed in a static geometry

Fluidization gas flow rate = $29800\ \mathrm{m}^3 / (\mathrm{h} \cdot \mathrm{m}_{\text{length fluid. chamber}})$

Figure 12.25 2D CFD simulations of the response of the particle bed temperature to a step change in the gas phase temperature from 300 to 400 K at $t = 0$ s. Comparison of the particle bed temperature uniformity in a conventional fluidized bed and in an RFB-SG. Fluidization chamber design and operating conditions: see Table 12.1. (Reprinted from Chemical Engineering Science, 64, de Broqueville and De Wilde, Numerical investigation of gas–solid heat transfer in rotating fluidized beds in a static geometry, 1232–1248, Copyright (2009) with permission from Elsevier.)[36]

report that within 3 s, the humidity of wheat could be decreased from 20 to 18% in an RFB-SG—the operating temperature is not specified. Data of the coefficient of heat transfer between air and grain particles as a function of the grain heating time are shown in Figure 12.26. The model predictions presented were based on a mass-based average temperature of the grain particles, which is strictly only valid for grain particle Biot numbers smaller than unity. Volchkov *et al.*[18,35] report the development of a vortex chamber-based apparatus for heating, drying, and cleaning of grain materials with production rates of 2 to 30 tons h^{-1}. For the vortex grain heaters with a production rate of 20 tons h^{-1}, a 45% increase of efficiency with respect to existing mining drying apparatus and a 10% decrease of the specific expenditures for

Table 12.2 Drying of different materials in a vortex chamber. (With kind permission from Springer Science and Business Media: Chemical and Petroleum Engineering, Hydrodynamics and heat exchange in vortex drying chambers, 5, 1970, 1969b, L. M. Kochetov *et al.*, Table 1)[16,a].

Material	Output (kg h^{-1})	Air flow rate (kg h^{-1})	Gas temperature (°C)		Material moisture content (%)		Average time material in apparatus (sec)
			Initial	Final	Initial	Final	
MSN copolymer	16.0	120	140	90	8.0	0.5	11
Sulfanilamide	18.0	96	180	106	12.0	0.1	23
Melalite	3.6	102	185	130	40.0	1.5	185
Emulsion polystyrene	2.8	50	140	100	27.0	0.60	15

[a] Note: In drying the finely divided materials (polystyrene, sulfanilamide, MSN copolymer) inserts were mounted within the vortex chambers, permitting gas to be supplied by several channels to the rotating annular layer of particles.

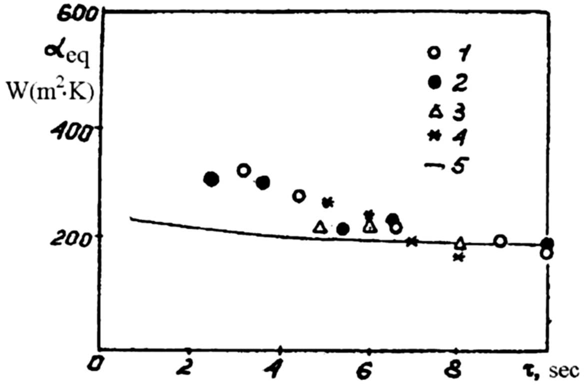

Figure 12.26 Effective coefficient of heat transfer between the gas and the grain particles as a function of the grain heating time in the vortex chamber. 1. $Re = \rho_g u_{inj} d_p / \mu_g = 2600$; 2. Re = 1800; 3. Re = 2000; 4. Re = 2300 (industrial test); 5. Calculation for a single particle, Re = 1800, Bi = 1.26. Industrial test: grain flow rate: 30 tons h^{-1}, grain inlet temperature: 11 °C, grain inlet moisture content: 25%, air flow rate (vortex chamber): 22.5 tons h^{-1}, air inlet temperature (vortex chamber): 206 °C. (Republished with permission of Begell House, from E. P. Volchkov *et al.*, Heat Transfer Res., 2003, 37, 486; permission conveyed through Copyright Clearance Center, Inc.)[35]

drying (fuel) are claimed. For grain drying, vortex chambers have been used as such or in combination with a shaft dryer. In the latter case, the vortex chamber is installed upstream of the shaft dryer and serves for efficient initial grain drying and cleaning.

Drying of (porous) woody biomass in an RFB-SG at relatively low temperatures ($T_{bed} = 318.15$ K) was experimentally studied by Eliaers and De Wilde.[43] A direct comparison between the performance of a conventional fluidized

Table 12.3 Fluidization chamber characteristics and operating conditions for the drying of biomass (From Eliaers and De Wilde. Taylor & Francis Ltd. http://www.informaworld.com)[43]

	Conventional fluidized bed	Rotating fluidized bed in a static geometry
Dimensions	$D = 0.10$ m $H = 1.50$ m $V = 11.8$ L	$D = 0.43$ m D (chimney) = 0.10 m $L = 0.05$ m $V = 6.9$ L
Gas distribution	Cone and perforated plate	72, 30° inclined gas inlet slots, each 2 mm wide
Solids feeding	*Via* side wall at $h = 0.05$ m	*Via* end wall
Particle characteristics	Pelletized wood, cylindrically shaped, $d_p = 4$ mm, $h_p = 4$ mm	
Operating conditions		
T_{bed} [K]	318.15	
P_{out} [Pa]	101 325	
Gas mass flow rate [$Nm^3\ h^{-1}$]	110	700
Solids mass flow rate [$g_{humid\ biomass}\ s^{-1}$]	1, 2, 3, 6, 9	3, 6, 9, 12, 15, 18
Solids inlet humidity [$g_{water}\ kg_{dry\ biomass}{}^{-1}$]	850	

bed (FB) and an RFB-SG was made. Both the performance in terms of the biomass feed rate per m^3 drying chamber and in terms of the air utilization were evaluated. Table 12.3 summarizes the drying chamber characteristics and the operating conditions used for the experiments. Figure 12.27 illustrates the process intensification that could be achieved by using an RFB-SG wherein, per m^3 drying chamber and per s, about one order of magnitude more biomass could be dried to a given degree of humidity than in the FB. At low biomass outlet humidity, intra-particle diffusion limitations become important and less advantage can be taken from the intensification of interfacial mass and heat transfer. The process intensification comes at the cost of a significantly higher gas flow rate, but the air can be equally well used. Indeed, as seen from Figure 12.28, for a given biomass outlet humidity, the air humidity increases equally in the FB and in the RFB-SG. Eliaers and De Wilde[43] showed that the process intensification achieved by using the RFB-SG was mainly due to an increase of the particle bed density and an improved particle bed uniformity, the gas–solid slip velocities in the RFB-SG being only slightly higher than in the FB under the conditions imposed. The contribution of aerodynamic blow-off was found small under the conditions studied. Interfacial mass and heat transfer could be further intensified by optimizing the RFB-SG drying chamber design and the operating conditions. The importance of the solids inlet design for avoiding wet biomass fed to be entrained directly into the chimney, as such bypassing the particle bed, was already discussed in Section 12.4.4 (see Figure 12.22).

Theoretically, Eliaers *et al.*[45] showed that the intensification of interfacial mass, heat and momentum transfer in RFB-SGs opens perspectives for particle coating applications. In a subsequent study, the low-temperature coating

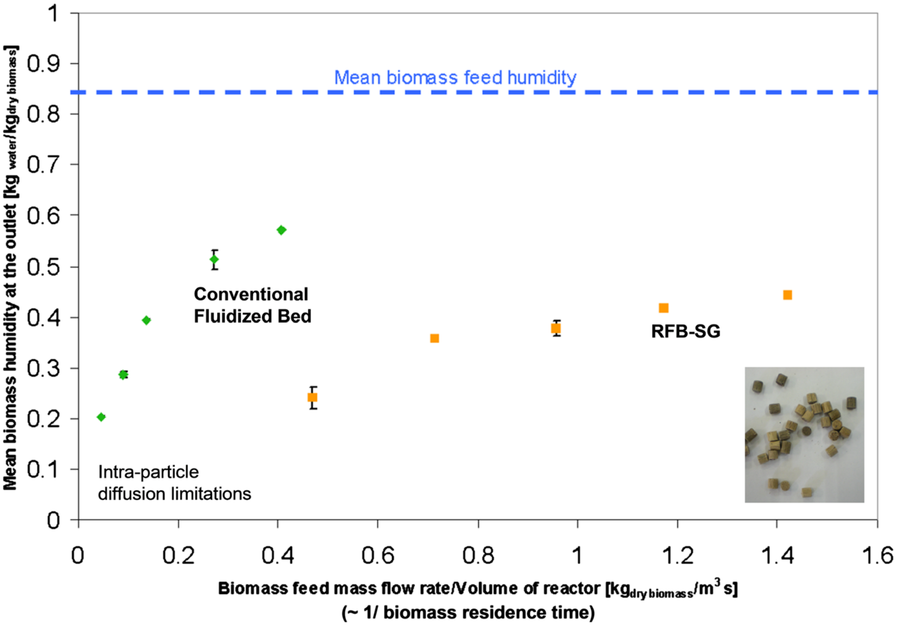

Figure 12.27 Drying of woody biomass in a conventional fluidized bed and in an RFB-SG. Mean biomass humidity at the inlet and at the outlet as a function of the specific biomass feed rate. Fluidization chamber characteristics and operating conditions: see Table 12.3. (From Eliaers and De Wilde. Taylor & Francis Ltd. http://www.informaworld.com.)[43]

of Geldart-C type powders with an aqueous polymer solution was experimentally demonstrated.[43,46]

12.6 Intensification of Heterogeneous Catalytic Reactions

Fluidized bed reactors were developed for the catalytic cracking of gas oil in the early 1940s (FCC: fluid catalytic cracking). Since then, they have been introduced for carrying out a variety of heterogeneous non-catalytic and catalytic reactions on an industrial scale—either because of their excellent heat transfer properties or because they allow continuous regeneration of a deactivating catalyst. The limitations of conventional fluidized bed reactors presented in Section 12.1 can be overcome by using an RFB-SG. In the latter, the particle bed is, however, relatively thin (order of centimeters) and the gas velocities are high. Hence, the gas phase residence time is much smaller than in a conventional fluidized bed. The higher particle bed density and improved particle bed uniformity should compensate for this and should allow achieving sufficiently high conversions. Trujillo and De Wilde[31,39] verified this for the catalytic cracking of gas oil by means of detailed CFD simulations and evaluating different vortex chamber designs. Details of the CFD simulations are summarized in Table 12.4. As shown in Figure 12.29, it was shown that sufficiently

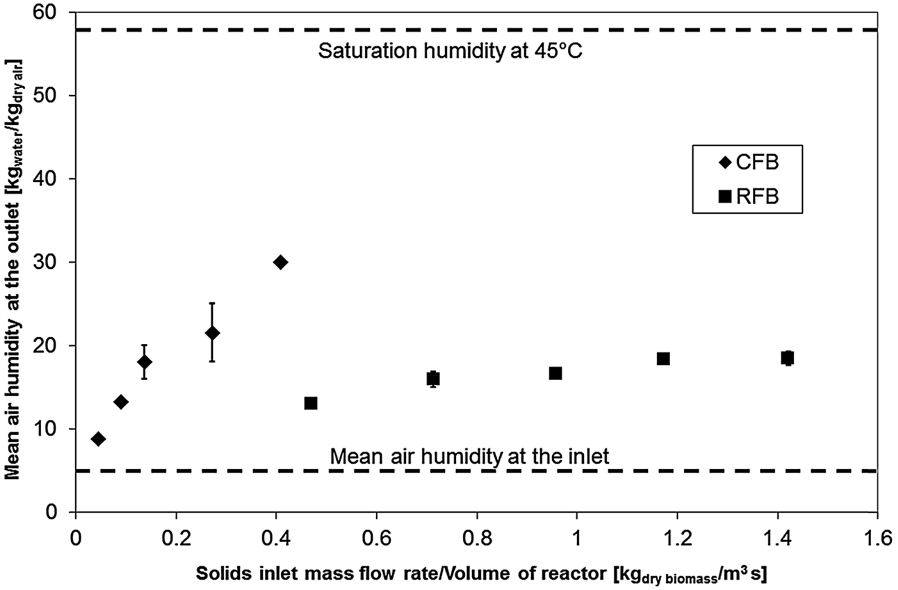

Figure 12.28 Drying of woody biomass in a conventional fluidized bed and in an RFB-SG. Mean air humidity at the inlet and at the outlet as a function of the specific biomass feed rate. Fluidization chamber characteristics and operating conditions: see Table 12.3. (From Eliaers and De Wilde. Taylor & Francis Ltd. http://www.informaworld.com.)[43]

Table 12.4 2D CFD simulation of fluid catalytic cracking (FCC) in an RFB-SG. Vortex chamber characteristics and operating conditions. Mass flow rates expressed per m length of vortex chamber. (Reprinted with permission from Powder Technology, 221, Trujillo and De Wilde, Fluid catalytic cracking in a rotating fluidized bed in a static geometry: a CFD analysis accounting for the distribution of the catalyst coke content, 36–46, Copyright (2007) with permission from Elsevier)[31]

Distribution chamber	Gas mass flow rate	8.35	$kg\ s^{-1}\ m^{-1}$
	Gas inlet density	4.72	$kg\ m^{-3}$
	Gas inlet temperature	775	K
Fluidization chamber	Number of slots	72	—
	Slots width	0.5	mm
	Outer radius	0.6	m
	Inner radius (chimney)	0.1	m
	Particle diameter	80	μm
	Particle density	1500	$kg\ m^{-3}$
	Catalyst mass flow rate	181.44	$kg\ s^{-1}\ m^{-1}$
	Catalyst volume fraction at the inlets	0.3	—
	Catalyst initial coke content	0.15	wt%
	Catalyst inlet temperature	775	K
	Feed catalyst-to-oil ration	21.75	—

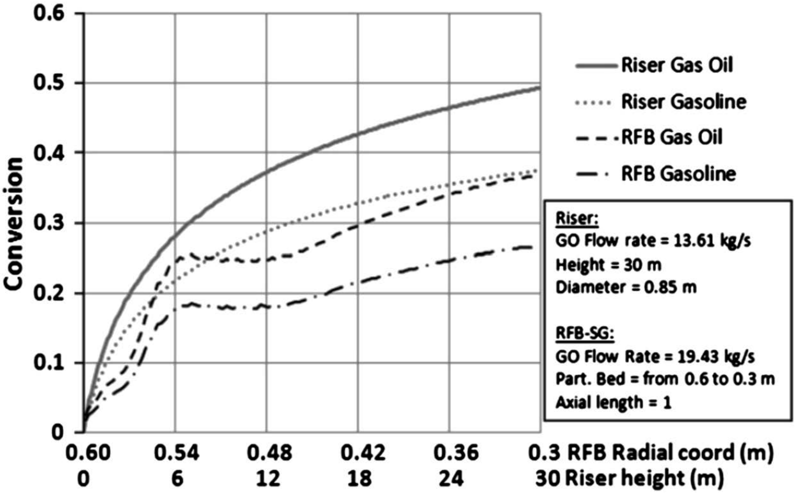

Figure 12.29 2D CFD simulation of fluid catalytic cracking (FCC) in an RFB-SG. Gas oil conversion and conversion into gasoline as a function of the distance in the particle bed. Comparison with a reference riser technology (characteristics given in the figure). Vortex chamber characteristics and operating conditions: see Table 12.4. (Reprinted with permission from Powder Technology, 221, Trujillo and De Wilde, Fluid catalytic cracking in a rotating fluidized bed in a static geometry: a CFD analysis accounting for the distribution of the catalyst coke content, 36–46, Copyright (2007) with permission from Elsevier.)[31]

high conversions can be achieved in RFB-SGs. Furthermore, from a comparison with riser technology, the process intensification potential of RFB-SGs was confirmed. Process intensification by about one order of magnitude was demonstrated. Trujillo and De Wilde[39] also showed that even more process intensification could be achieved using a more active catalyst and/or operating at higher cracking temperatures. This is possible because of the short gas phase residence time and excellent particle bed mixing and resulting particle bed temperature uniformity. Taking a similar CFD simulation-based approach, Ashcraft *et al.*[47] demonstrated the significant process intensification that can be achieved by using a vortex chamber-generated rotating fluidized bed reactor for the simultaneous adsorption of SO_2 and NO_x from flue gas, a process conventionally carried out in a circulating fluidized bed riser.

12.7 Extensions of the Concept and Multi-Zone Operation

RFB-SGs can be designed for multi-zone operation, either in the tangential (Figure 12.9) or in the axial direction (Figure 12.30). Specific gases could as such be injected *via* a number of gas inlet slots or a part of the gas inlet slots and different reaction zones could be integrated into one single vortex

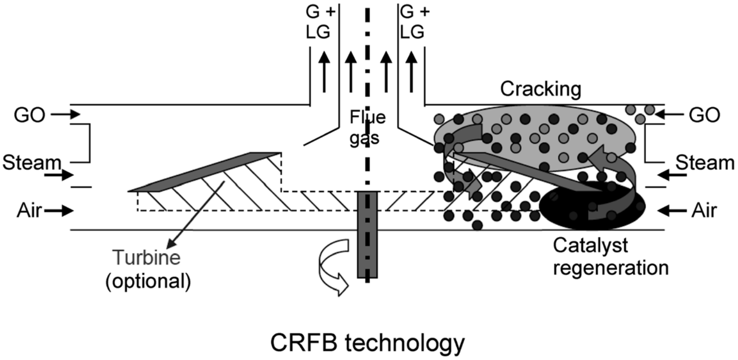

Figure 12.30 Illustration of axial multi-zone operation in an RFB-SG. (De Gruyter [International Journal of Chemical Reactor Engineering], Walter De Gruyter GmbH Berlin Boston, [2011]. Copyright and all rights reserved. Material from this publication has been used with the permission of Walter De Gruyter GmbH.)[38]

chamber. Another potentially interesting application is the injection of a very hot gas in one zone of the RFB-SG, limiting the time of exposure of the particle bed to high temperatures, but allowing supply of sufficient heat to the particle bed. CFD simulations have shown that even with extreme differences in the temperatures of the gases fed to the different zones of the vortex chamber reactor, the resulting differences in the particle bed temperature remain remarkably small due to the mixing in the particle bed (Staudt *et al.*, 2011). Experimental tests of fine particle coating with an axially non-uniform heat supply confirmed this finding.[43]

In the context of axial multi-zone operation, the concept of a circulating rotating fluidized bed (CRFB) was developed. In CRFBs, an axial–radial circulation of the particle bed is introduced and superimposed on the particle bed rotational motion. Eliaers and De Wilde[43] observed that such circulation occurs naturally in RFB-SGs because of axial gradients in the particle bed rotation velocity in the vicinity of the end walls. The axial–radial circulation can, however, be intensified and controlled by means of an axially non-uniform gas distribution, as demonstrated by Staudt *et al.*[38] by means of three-dimensional periodic domain CFD simulations. The latter aimed at demonstrating that a significant axial circulation in the particle bed could be obtained without introducing axial mixing in the gas phase. Gases of different temperature and composition were introduced in different axial zones of the vortex chamber. Gas A was injected in the top section at 300 K, whereas gas B was injected in the bottom section at 950 K. As seen in Figure 12.31, significant axial circulation in the particle bed resulted in a quite uniform particle bed temperature, despite the significant difference in the temperatures of the different gases injected. Axial mixing of the gases is, however, minimal, the radial velocity of the gases being relatively high. Hence, gases A and B could be separately evacuated from the vortex chamber *via* two chimneys

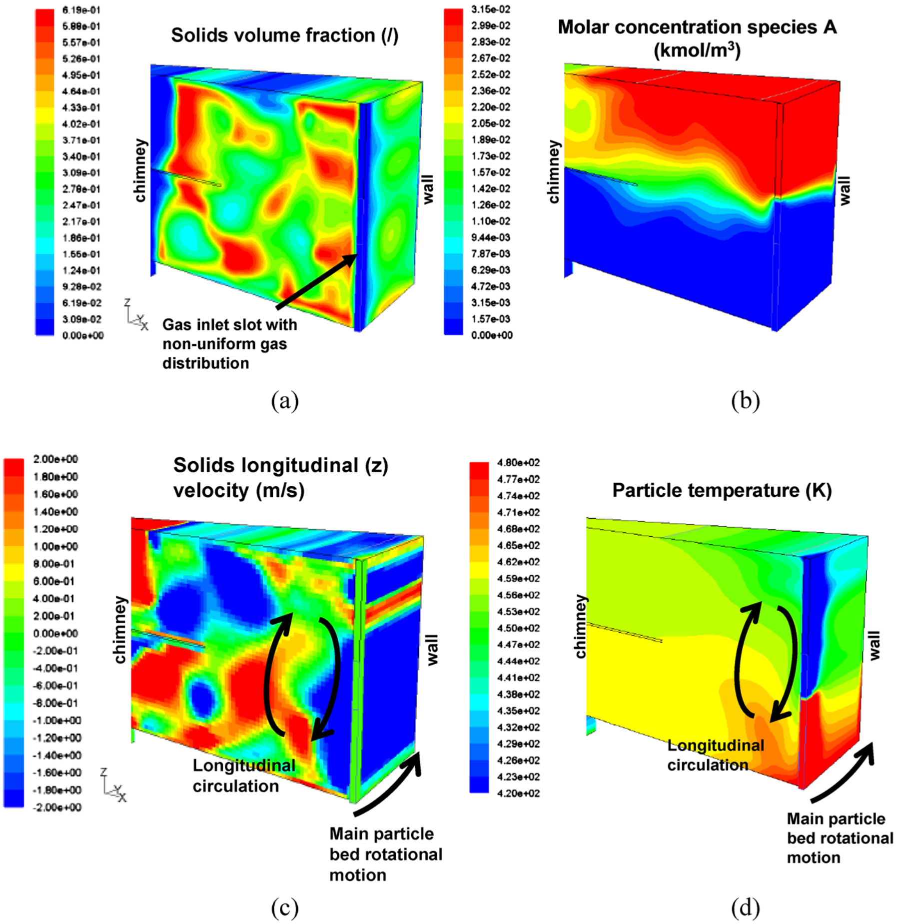

Figure 12.31 Circulating rotating fluidized bed (CRFB) (D = 240 mm, L = 50 mm). Demonstration by means of 3D periodic domain CFD simulations of longitudinal circulation of particles in a CRFB. Profiles of (a) the solids volume fraction, (b) gas composition, (c) axial solids velocity and (d) particle bed temperature. Cold gas A (300 K) injected *via* the top section of the gas inlet slot, hot gas B (950 K) injected *via* the bottom section of the gas inlet slot. (De Gruyter [International Journal of Chemical Reactor Engineering], Walter De Gruyter GmbH Berlin Boston, [2011]. Copyright and all rights reserved. Material from this publication has been used with the permission of Walter De Gruyter GmbH.)[38]

located in the opposite end walls. The CFD simulations by Staudt *et al.*[38] also demonstrated that it is possible to supply a sufficient amount of heat to the particle bed by means of a very hot gas injected through a number of gas inlet slots and/or part of the gas inlet slots. The use of a secondary gas outlet can also be considered in CRFBs (Figure 12.30). CFD simulations by Staudt *et al.*[38] (Figure 12.31) confirmed this allows separate evacuation of the gases moving through, or produced in, different axial zones of the reactor.

Staudt *et al.*[38] numerically evaluated the potential of RFB-SGs and CRFBs for the low-temperature pyrolysis and gasification of biomass. In the CRFB, a biomass pyrolysis and a char combustion zone are integrated, the combustion of the char generating the heat required for the pyrolysis of the biomass. The axial circulation makes the solids (char and eventually a high heat capacity inert solid, *e.g.* sand) move in a closed loop between both reaction zones. The fresh air enters the vortex chamber in the char combustion zone. This prevents the air fed from burning the gas produced by the biomass primary pyrolysis, the biomass being injected in between the two reaction zones. The solids circulation and particle bed mixing result in a relatively low temperature difference between the two reaction zones. Hence, the biomass pyrolysis can be carried out at higher temperatures without exceeding the ash melting temperature in the char combustion zone. Without sand circulation, the specific biomass conversion rate—a measure of the process intensification, *i.e.* the amount of biomass converted per m^3 reactor and per s—is about one order of magnitude higher in CRFBs than in circulating fluidized bed risers. RFB-SGs allow about two orders of magnitude process intensification, but CRFBs allow for further optimizing the liquids production while somewhat reducing the char production. The produced dry gas contains less CO and more CO_2 and H_2, but its LHV (including liquids) is comparable. The circulation of a sand–char mixture was shown to allow a further increase of the specific biomass inlet flux and the specific biomass conversion rate, while hardly affecting the product distribution and the LHV of the produced dry gas. Finally, the use of two separate gas outlets for the biomass pyrolysis and char combustion zones in a CRFB allowed almost a doubling the LHV of the produced dry gas, the flue gas being evacuated separately.

Kuzmin *et al.*[21] (gas–liquid) and de Broqueville and De Wilde[19] (gas–solid) developed a rotating chimney that can be integrated in RFB-SGs or CRFBs. The centrally positioned chimney (Figure 12.32) rotates in the same sense as the rotating particle bed, but can rotate at higher rotational speeds. The increase of the centrifugal force in the vicinity of the chimney allows reducing the rate of solids losses *via* the chimney for a given solids loading and fluidization gas flow rate. Experimental studies of RFB-SGs equipped with a rotating chimney were presented by De Wilde and de Broqueville.[29,42] These studies confirmed the theoretically predicted behavior and showed that the rotating chimney can be used to control the average particle residence time in the vortex chamber. An interesting feature was demonstrated with Geldart B-type particles. With the given vortex chamber design and operating conditions, the particle bed was radially fluidized and a bubbling bed was observed, at least with a static chimney. As shown in Figure 12.33, the rotating chimney permitted increase in the solids loading and the particle bed density and suppression of bubbling, the rotating chimney acting like a compressor on the particle bed. Hence, quite dense and uniform particle beds could be obtained in a wider range of particle bed rotational speeds.

Finally, cylindrical, conical, and hybrid vortex chambers have been used for the generation of a rotating fluidized bed. A grain dryer making use of a

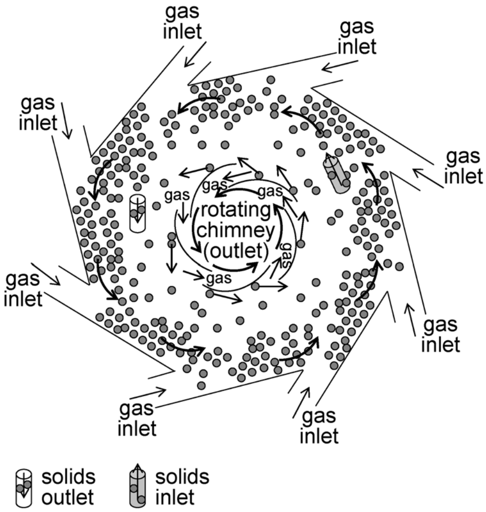

Figure 12.32 The use of a rotating chimney in a vortex chamber. (Reproduced from De Wilde and de Broqueville with permission from John Wiley and Sons. Copyright © 1987 American Institute of Chemical Engineers.)[42]

hybrid design was used by Volchkov *et al.*[35] and Dvornikov and Belousov.[41] The gas flow rates to the cylindrical and different conical vortex chambers can be independently controlled, introducing a kind of multi-zone operation.

12.8 Conclusions and Outlook

In rotating fluidized beds in a static geometry (RFB-SG), high-G operation is achieved by the tangential injection of the fluidization gas in a so-called vortex or whirl chamber with multiple gas inlet slots in its outer cylindrical wall. RFB-SGs offer interesting hydrodynamic characteristics. High-G operation in particular allows operating a dense particle bed at high gas–solid slip velocities. The particle bed uniformity is improved and the fluidization of fine powders facilitated. A particular feature of RFB-SGs is the flexibility in the gas flow rate, the latter affecting both the centrifugal force and the counteracting radial gas–solid drag force in similar ways. Another important feature is that radial fluidization of the particle bed is not really necessary to achieve good particle bed mixing, the particle bed being essentially tangentially fluidized. Finally, it was shown that although the macro-scale particle bed behavior with respect to its rotational motion approaches that of a solid body, the behavior in the particle depleted freeboard region approaches that of a free vortex.

The hydrodynamic characteristics of RFB-SGs require a careful vortex chamber design, in particular when fluidizing fine powders. The importance of the gas inlet and outlet (chimney) design and of the solids inlet and outlet design is discussed and different configurations presented. In general, smaller/lighter particles require the use of smaller gas inlet slots and a smaller chimney.

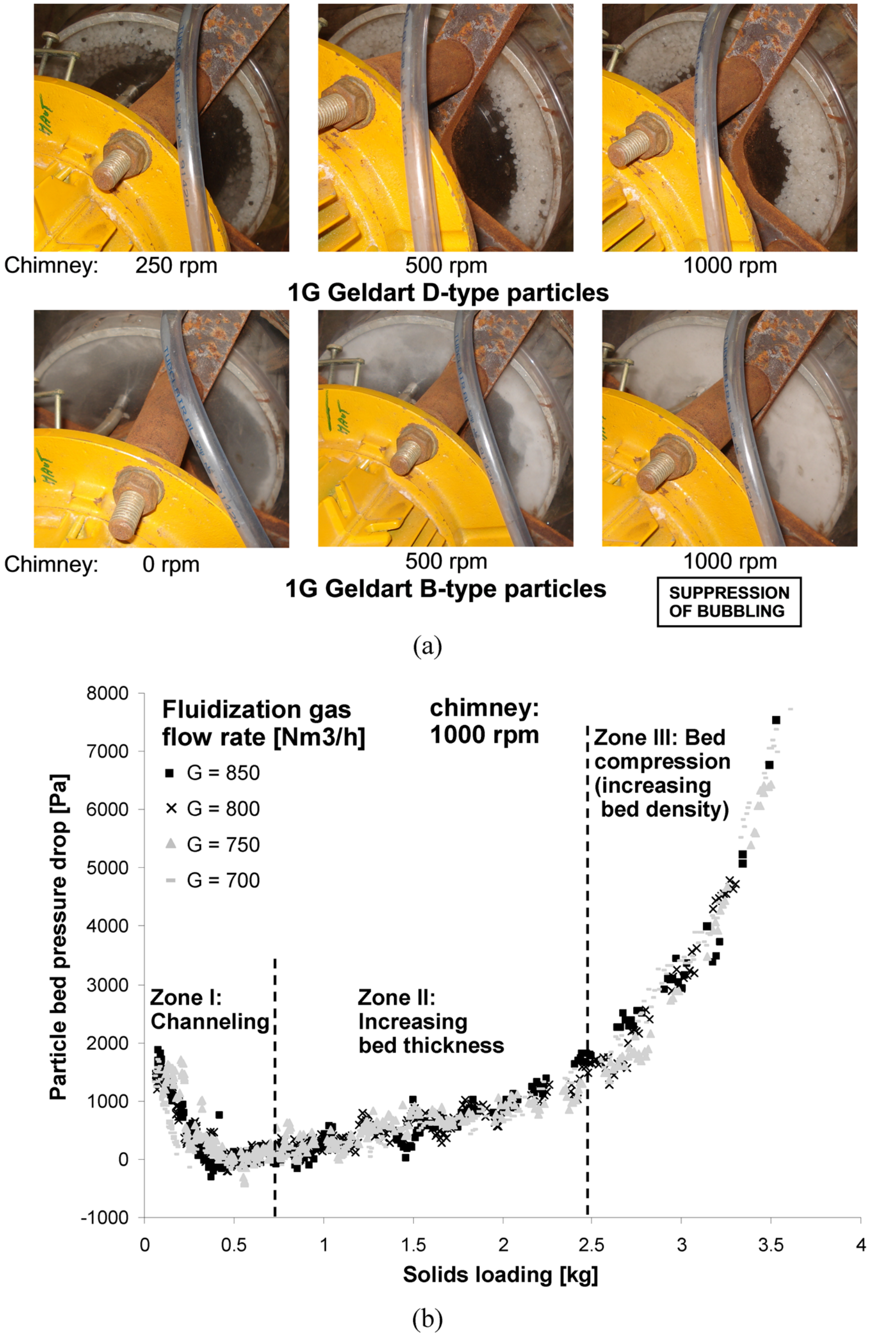

Figure 12.33 (a) Influence of the rotational speed of a rotating chimney on the solids loading and particle bed density and uniformity in an RFB-SG operated at given gas and solids feeding rates and with 2–5 mm polymer pellets (top) and 300 μm salt particles (bottom). Suppression of bubbling at high solids loadings of 300 μm salt due to compression of the particle bed by the rotating chimney. (b) Pressure drop over the particle bed as a function of the solids loading when fluidizing 300 μm salt particles with a chimney rotating at 1000 rpm. Vortex chamber design: see Figure 12.3. (Reproduced from Powder Technology, 199, De Wilde and de Broqueville, a rotating chimney for compressing rotating fluidized beds, 87–94, Copyright (2010) with permission from Elsevier.)[29]

The analysis of some (potential) applications of RFB-SGs illustrates the significant increase in efficiency that can be achieved by operating high-G. The intensification of interfacial mass and heat transfer is particularly promising for particle drying, coating and granulation. The intensified interfacial momentum transfer leading to denser and uniform beds, combined with extremely short contact times between the process gas and the particles (*e.g.* catalyst) opens perspectives for carrying out reactions with improved efficiency and selectivity.

A variety of extensions of the concept can be imagined. Different types of multi-zone operation are possible and open perspectives for further improved efficiency, *e.g.* by internal circulation of the solids between different reaction zones.

References

1. G. F. Froment, K. B. Bischoff and J. De Wilde, *Chemical Reactor Analysis and Design*, 3rd edn, 2010.
2. D. G. Kroger, E. K. Levy and J. C. Chen, *Powder Technol.*, 1979, **24**, 9.
3. R. Chevray, Y. N. I. Chan and F. B. Hill, *AIChE J.*, 1980, **26**, 390.
4. L. T. Fan, C. C. Chang, Y. S. Yu, T. Takahashi and Z. Tanaka, *AIChE J.*, 1985, **31**, 999.
5. J. H. Saunders, *Powder Technol.*, 1986, **47**, 211.
6. Y.-M. Chen, *AIChE J.*, 1987, **33**, 722.
7. G.-H. Qian, I. Bagyi, R. Pfeffer, H. Shaw and J. G. Stevens, *Powder Technol.*, 1998, **100**, 190–199.
8. G.-H. Qian, I. Bagyi, R. Pfeffer, H. Shaw and J. G. Stevens, *AIChE J.*, 1999, **45**, 1401.
9. G.-H. Qian, I. Bagyi, I. W. Burdick, R. Pfeffer, H. Shaw and J. G. Stevens, *AIChE J.*, 2001, **47**, 1022–1034.
10. A. Ahmadzadeh, H. Arastoopour and F. Teymoour, *presented in part at the AIChE Annual meeting*, Cincinnati, OH, USA, 2005.
11. S. Watano, Y. Imada, K. Hamada, Y. Wakamatsu, Y. Tanabe, R. N. Dave and R. Pfeffer, *Powder Technol.*, 2003, **131**, 250.
12. S. Watano, H. Nakamura, K. Hamada, Y. Wakamatsu, Y. Tanabe, R. N. Dave and R. Pfeffer, *Powder Technol.*, 2004, **141**, 172.
13. J. A. Quevedo, H. Nakamura, Y. Shen, R. N. Dave and R. Pfeffer, *presented in part at the AIChE Annual meeting*, Cincinnati, OH, USA, 2005.
14. J. A. Quevedo, R. Pfeffer, Y. Shen, R. N. Dave, H. Nakamura and S. Watano, *AIChE J.*, 2006, **52**, 2401.
15. L. M. Kochetov, B. S. Sazhin and E. A. Karlik, *Khim. Neft. Mashinostr.*, 1969, **2**, 10.
16. L. M. Kochetov, B. S. Sazhin and E. A. Karlik, *Khim. Neft. Mashinostr.*, 1969, **9**, 10.
17. L. A. Anderson, S. H. Hasinger and B. N. Turman, *J. Spacecr. Rockets*, 1972, **9**, 311.

18. E. P. Volchkov, V. I. Terekhov, A. N. Kaidanik and A. N. Yadykin, *Heat Transfer Eng.*, 1993, **14**, 36.
19. J. De Wilde and A. de Broqueville, *AIChE J.*, 2007, **53**, 793.
20. P. J. Loftus, D. B. Stickler and R. C. Diehl, *Environ. Prog. Sustainable Energy*, 1992, **11**, 27.
21. A. O. Kuzmin, M. Kh. Pravdina, A. I. Yavorsky, N. I. Yavorsky and V. N. Parmon, *Chem. Eng. J. (Amsterdam, Neth.)*, 2005, **107**, 55.
22. B. A. Folsom, I. Two-phase flow in vertical and annular fluidized beds. II. Unsteady disturbances in axial compressors, *PhD Thesis*, California Institute of Technology, 1974.
23. M. Goldshtik, F. Hussain and R. J. Yao, *Sādhanā*, 1997, **22**, 323.
24. C. Dodson, *Chem. Eng. – London*, 1996, **605**, 13.
25. J. Shu, V. I. Lakshmanan and C. E. Dodson, *Chem. Eng. Process.*, 2000, **39**, 499.
26. R. Turton and X. X. Cheng, *Powder Technol.*, 2005, **150**, 78.
27. G. A. Wellwood, Hydrodynamic behaviour of the Torbed reactor operating in fine particle mode, *PhD Thesis*, University of Queensland, 2000.
28. J. De Wilde and A. de Broqueville, *Powder Technol.*, 2008, **199**, 87.
29. J. De Wilde and A. de Broqueville, *Powder Technol.*, 2010, **199**, 87.
30. W. Rosales Trujillo and J. De Wilde, *Theoretical and Experimental Study of Fine Particle Fluidization in a Rotating Fluidized Bed in a Static Geometry*, Université catholique de Louvain, 2012.
31. W. Rosales Trujillo and J. De Wilde, *Powder Technol.*, 2012, **221**, 36.
32. J. De Wilde, *presented in part at the the Prof. Robert Pfeffer seminar, International Fine Particles Research Institute (IFPRI), IFPRI Annual General Meeting 2010*, Liège, Belgium, 2010.
33. W. Rosales Trujillo, M. Abouahi and J. De Wilde, *presented in part at the XIIIeme Congrès de la Société Française de Génie des Procédés (SFGP 2011)*, Lille, France, 2011.
34. B. S. Sazhin, L. M. Kochetov and A. S. Belousov, *Theor. Found. Chem. Eng.*, 2008, **42**, 125.
35. E. P. Volchkov, N. A. Dvornikov and A. N. Yadykin, *Heat Transfer Res.*, 2003, **37**, 486.
36. A. de Broqueville and J. De Wilde, *Chem. Eng. Sci.*, 2009, **64**, 1232.
37. J. De Wilde, A. Habibi and A. de Broqueville, *Int. J. Chem. React. Eng.*, 2007, **5**, A106.
38. N. Staudt, A. De Broqueville, W. Rosales Trujillo and J. De Wilde, *Int. J. Chem. React. Eng.*, 2011, **9**, A43.
39. W. Rosales Trujillo and J. De Wilde, *presented in part at the AIChE Annual Meeting*, Minneapolis, Minnesota, USA, 2011.
40. R. Ekatpure, V. U. Suryawansh, G. J. Heynderickx, A. de Broqueville and G. B. Marin, *Chem. Eng. Process.*, 2011, **50**, 77–84.
41. N. A. Dvornikov and P. P. Belousov, *J. Appl. Mech. Tech. Phys.*, 2011, **52**, 206.
42. J. De Wilde and A. de Broqueville, *AIChE J.*, 2008, **54**, 2029.

43. P. Eliaers and J. De Wilde, *presented in part at the 2012 Annual AIChE Meeting*, Pittsburgh, USA, 2012.
44. J. De Wilde, *Catal. Rev.*, 2010, **23**, 18.
45. P. Eliaers, W. Rosales Trujillo and J. De Wilde, *Production and coating of fine particles in a rotating fluidized bed in a static fluidization chamber: Evaluation of different technologies*, Report for FrieslandCampina, 2011.
46. P. Eliaers, A. de Broqueville, A. Poortinga, T. van Hengstum and J. De Wilde, *Powder Technol.*, 2014, **258**, 242.
47. R. W. Ashcraft, G. J. Heynderickx and G. B. Marin, *Chem. Eng. J. (Amsterdam, Neth.)*, 2012, **207**, 195.

Subject Index